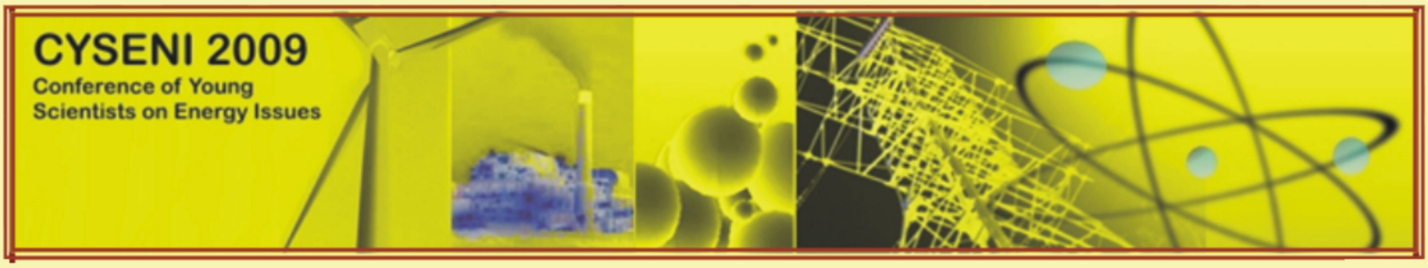

Conference of Young Scientists on Energy Issues

ISSN 1822-7554

Conference proceedings
www.cyseni.com
28 – 29 May, 2009

Dear Reader of the Proceedings,

Conference of ***Young Scientists on Energy Issues 2009*** is already a sixth conference. Initiative came from young, enthusiastic researchers who realised that around ourselves we do have young, smart and science-oriented young people in the energy field, who need an event to come together and share their views, ideas, success and disappointment stories. The very beginning was year 2004, when young researchers with the supervision of experienced scientists from only Lithuanian Energy Institute organised a conference. In 2005 it became a national conference with participants from Kaunas University of Technology, Vilnius Gediminas Technical University, Vilnius University, Vytautas Magnus University – in fact from all science and education institutions of Lithuania involved in energy-related topics. Year 2006 was devoted to strengthen status of the conference among young researchers and their experienced supervisors and bring the message that only joint efforts in a small country we can reach our targets. In 2007 organising committee decided to put emphasis on regional and international dimension. In the conference we had papers from neighbouring countries – Belarus and Poland. We realised that facing challenges in energy research we have to bring together as many young researchers as possible to create a critical mass to be competent and competitive for the future research. Thus, conference is not only increasing the competence with involvement of best experienced scientists as peer reviewers, involving the review process participants of the conference as educational exercise, but also expanding geographically. In 2008 we already had papers and participants from Belarus, Estonia, Latvia, Lithuania, Russia, and India. In 2009 we had papers from Belarus, Estonia, Italy, Latvia, Lithuania, Nigeria, and Ukraine. Young scientists in the conference of ***Young Scientists on Energy Issues 2009*** have an auditorium to share their views and findings of the research, a possibility to evaluate achievements and hear critical comments for the improvements. We will keep this momentum in the future ***Young Scientists on Energy Issues*** conferences as well. Thus, we already now invite you to conference of ***Young Scientists on Energy Issues 2010***, which will be held in 27-28 May, 2010 in Kaunas, Lithuania.

Organisers

CONTENT

I. Hydrogen and fuel cells (11)

II. Renewable energy sources and their use (5)

III. Smart energy networks (2)

IV. Energy efficiency and savings (4)

V. Knowledges for energy policy making (5)

VI. Investigations in the fields of thermal physics, Fluid mechanics and metrology (9)

VII. Nanosciences and nanotechnologies, investigations on multifunction materials (3)

VIII. Investigations of combustion and plazma processes (9)

IX. Global change and ecosystem (2)

X. Fusion energy (2)

XI. Nuclear fission and radiation protection (9)

CYSENI 2009, May 28-29, Kaunas, Lithuania
ISSN 1822-7554, www.cyseni.com

ARTEFACTS OF PHYSICAL VAPOUR DEPOSITION IN PERFORMANCE OF Mg-Ni HYDROGEN STORAGE SYSTEM

S. Tuckute, M. Lelis
Faculty of Nature Sciences
Vytautas Magnus University
Vileikos St. 8, Kaunas, LT-44404 – Lithuania
Phone: +370 37 327 910
E-mail: s.tuckute@gmail.com

E. Wirth
Centre for Hydrogen Energy Technologies
Lithuanian Energy Institute
Breslaujos str. 3, Kaunas, LT-44403 – Lithuania
Phone: +370 37 401909
E-mail: wirth@mail.lei.lt

ABSTRACT

The aim of the presented work is to investigate whether any "fingerprints" of specialities of physical vapour deposition technique act on the performance of well known Mg-Ni hydrogen storage system. For this purpose magnetron co-sputtering technique was used to produce nanocrystalline Mg-Ni films, which were delaminated and taken for measurement of number of pressure-composition-isotherms. Hydrogenation/dehydrogenation cycling is believed to have caused modification of the investigated nanocrystalline materials. The derived dissociation enthalpies of the corresponding hydrides, MgH_2 and Mg_2NiH_4, were found to be coherent with values reported in literature, with the exception of two samples. In addition, one of these samples showed a third plateau pressure pointing to the presence of a hydrogenated metastable phase.

Keywords: Mg_2NiH_4, hydrogen storage, nanomaterials, PCI

1. INTRODUCTION

Lately fossil fuels became troublesome for several reasons – decreasing supplies, rising prices, political instability in oil exporting countries and unacceptable environmental risk. Either issue is serious enough to initiate an immediate action, thus alternative energy sources such as hydro, wind and solar power having a minimal environmental impact again became one of the top scientific and industrial issues [1]. Every year new power plants using renewable energy are projected and built worldwide. However, almost all sorts of renewable energy sources are flow limited and the electricity generation by wind or solar plants is very unstable and strongly depends on weather condition. As one of the most promising ways to achieve stable and reliable electricity generation by wind and solar power plants (without undesired power variations) is to combine them with hydrogen systems [2], however these systems deal with critical issues related to safe, compact, lightweight and cheap hydrogen storage.

Up to date there are three main ways of hydrogen storage: (i) hydrogen storage as pressurised gas; (ii) liquefied hydrogen; and (iii) solid state materials of physisorbed or chemisorbed hydrogen storage [3]. But only the later has the potential to meet the requirements for the long term hydrogen storage systems. As no one of currently known systems can meet the requirements, great efforts are made to investigate various solid state hydrogen storage materials and to improve their properties to reach the goals set by the international industry and modern society [4]. In this light nano-engineering comes as the most promising tool for the manufacturing of suitable hydrogen storage systems.

Most of researchers in the hydrogen storage area work with the ball milling technologies which are relatively simple and easy to use. However, there are more of the nanotechnologies for the choice which have potential to provide bigger possibilities for the modification of material properties [5]. Moreover, wider possibilities also give additional advantages looking for the undiscovered fundamental understanding of hydrogen storage materials. Thus, in this work it was decided to use magnetron sputtering technology and to deposit Mg-Ni thin films. Later to delaminate them from the substrate and to investigate their thermodynamical properties using volumetric hydrogen sorption, make investigations of these systems and compare the received results with ones known for powder material.

The Mg-Ni (and consequently Mg_2NiH_4) system was chosen for two reasons. Firstly, this system has been widely explored in powder form and there are lots of reported data for it, but still there are little data about it in thin film form. These factors are greatly favourable to perform a thermodynamical study of two forms of the same system and to identify if there are any differences between powder and thin films which might be a fingerprint of a magnetron sputtering technique. As there are no such comparison and this point of view can give fundamental insight towards the ways on how to apply nano-engineering to get hydrogen storage materials with enhanced characteristics.

2. EXPERIMENTAL METHODOLOGY

2.1. Sample preparation

The Mg-Ni alloys were deposited on quartz glass substrates using a physical vapour deposition system equipped with two independent DC magnetron sputtering sources. A vacuum system consisting of mechanical and diffusion pumps enabled a base pressure of $2x10^{-3}$ Pa. Afterwards, Ar (99.999%) gas was injected to the vacuum chamber and its flow was controlled to keep a constant pressure of 0.4 Pa. Metallic Mg (99.98%) and Ni (99.999%) disks of 100 mm diameter each were used as target materials for the magnetron sources.

The calibration procedure is analogous to one described in [6], except that the sample weight was used instead of measuring the film thickness. After the film deposition rates of separate magnetrons at various currents had been determined. Five different Mg/Ni ratio samples were produced. Sample indexing together with Mg and Ni magnetron currents are given in table 1.

Table 1. Sample indexing and deposition conditions

Sample number	Mg magnetron current (A)	Ni magnetron current (A)
1	1	0.3
2	1	0.5
3	1	0.7
4	1	0.9
5	0,5	0.5

The as-produced delaminated flakes from films were afterwards manually crushed to produce coarse powders of one gram in weight. The powders were then analysed by X-ray powder diffraction (XRD, *θ/2θ* setting with Cu Kα radiation, Philips Analytical X'pert) and by scanning electron microscopy (SEM, Leo Supra 50) equipped with X-ray energy dispersive spectroscopy (EDS, Inca Oxford Instruments). Subsequently the samples were loaded on a volumetric automated gas reaction controller (GRC, commercial instrument built by Advanced Materials Corporation, Pittsburgh, USA), for hydrogen activation and for performing sorption measurements.

The activation procedure started with out-gassing during 12h at 473K and was followed by a number of soak/release cycles. During soak the sample chamber was filled with hydrogen at 30.4 bar for 90 min at 573 K, whereas during the release mode the chamber was maintained at 573K for 60 min under vacuum (1:2 x 10^{-2} mbar). Full activation was considered achieved when the hydrogen storage of the sample stabilises over three consecutive cycles. The required number of cycles for full activation, for each sample, is given in Table 2.

Table 2. Number of activation cycles, values of enthalpy of dissociation of the present hydrides and respective standard deviations

Sample number	Number of activation cycles	$\Delta H_{des\ \mathrm{Mg_2NiH_4 \rightarrow Mg_2Ni}} (kJ/mol)$	$\Delta H_{des\ \mathrm{MgH_2 \rightarrow Mg}} (kJ/mol)$
1	22	64 ± 1	77 ± 1
2	27	66 ± 1	78 ± 1
3	32	70 ± 1	79 ± 1
4	26	65 ± 1	76 ± 1
5	27	71 ± 1	-
Literature value [7]		64	74.5

Following activation, pressure-composition-isotherms (PCIs) were acquired at five different temperatures (513, 543, 573, 603 and 623 K) at a maximum pressure of 20.3 bar. At the end of the absorption/desorption runs, the samples were again microscopically analysed by XRD and SEM. The enthalpy of dissociation of the hydrides was determined by the construction of the van't Hoff plots.

3. RESULTS

3.1. Hydrogen sorption measurements

The number of hydrogenation cycles required for each sample activation (Table 2) ranged between 20 and 35 cycles. No direct relationship could be identified between the actual number of these activation cycles and the deposition conditions. Fig. 1 illustrates the PCIs obtained for all samples at 573 ± 2K. The overall storage capacities for samples 1–4 are in the same range (3.90–4.18 wt %) with the maximum storage capacity obtained for sample 1, where the longest $Mg \leftrightarrow MgH_2$ plateau is found. Three samples (samples 1, 2 and 4) exhibit double-plateau pressure behaviour. The lower plateau can be attributed to the transition $Mg \leftrightarrow MgH_2$, whereas the upper one to the transition $Mg_2Ni \leftrightarrow Mg_2NiH_4$. The main difference between the samples (Fig. 1) is the length of their plateaus. The hydrogen weight percent of each phase is given on the top of each curve (Fig. 1). Examination of the data indicates that the Mg_2Ni phase is maximised for a deposition condition (I_{Ni} = 0.5 A for sample 2). However, the sample with the maximum nickel intensity is not the one with the predominance of the Mg_2Ni phase.

The PCI curves for samples 3 (Fig. 1c) and 5 (Fig. 1e) show an anomalous behaviour. In the case of sample 3, for the second part of the curve, a short Mg_2Ni plateau can be identified, and then the increase of pressure leads to a steep curve for absorption and finally, to a third plateau. On the other hand, sample 5 (Fig. 1e) deviates from the standard double plateau by showing a single plateau. In addition, the hydrogen storage capacity of this sample is decreased by almost a factor of two, compared to the rest.

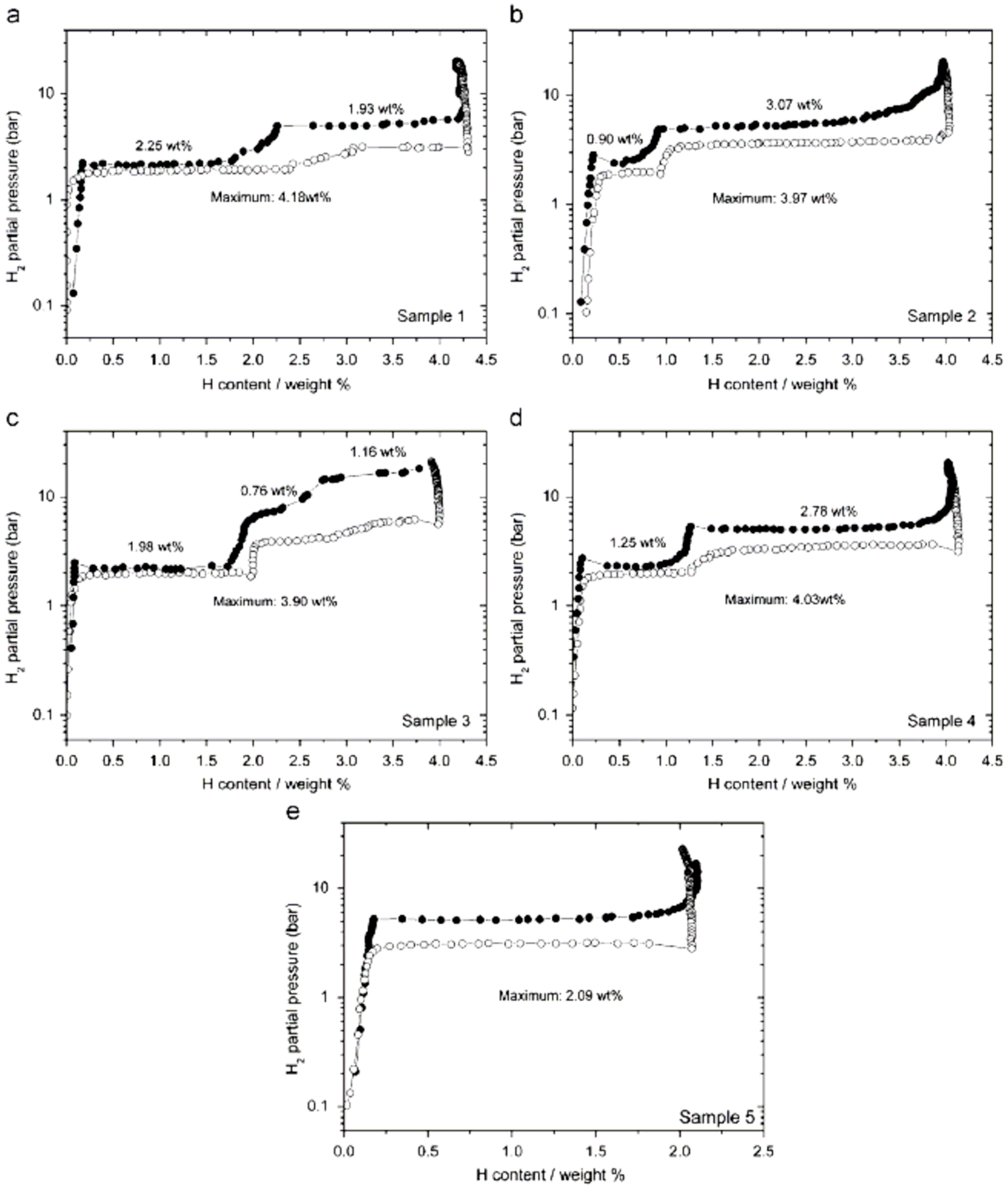

Fig. 1. Pressure-composition-isotherm at 573K for the samples with an $I_{Mg} = 1$: (a) $I_{Ni} = 0.3$, (b) $I_{Ni} = 0.5$, (c) $I_{Ni} = 0.7$, (d) $I_{Ni} = 0.9$ and (e) $I_{Ni} = 0.5$ and $I_{Mg} = 0.5$. Filled symbols correspond to the absorption mode, open symbols correspond to the desorption mode

The dissociation enthalpy derived from van't Hoff plots, obtained in desorption mode for each sample, is found to be comparable for the samples 1, 2 and 4 (Table 2). They are also consistent with the literature values [7], confirming the presence of Mg and Mg_2Ni phases in the samples investigated. The calculated enthalpy of dissociation for the $Mg \leftrightarrow MgH_2$ transition for sample 3 is also in agreement with the literature data. As described earlier, the rest of the curve for this sample though is very different from the others, assuming that its upper plateau corresponds to Mg_2Ni. The enthalpy for this second plateau does not correspond to the literature value (Table 2). Surprisingly, the unique plateau of sample 5 exhibited an enthalpy value of equal magnitude as sample 3. This indicates a probable formation of the same material phase for both samples (3 and 5). Finally, it was not possible to calculate the enthalpy of dissociation corresponding to the third plateau of sample 3, since it appears only above 573 K.

To investigate further this behaviour, XRD studies were undertaken in an attempt to identify and confirm the phases present.

3.2. Structural and microstructural analysis

The XRD patterns obtained prior to hydrogenation are shown in Fig. 2 and after hydrogenation in Fig. 3. Looking at Fig. 2 we can conclude that all the patterns backgrounds confirmed the presence of amorphous material. The detected crystallite phases were exclusively the Mg and Mg_2Ni phases, with the exception of sample 5 where there was an indication of the presence of the Ni phase. No direct evidence of an extra phase was found to where the third plateau displayed by sample 3 could be assigned. This issue is subject of further investigations. The crystallite sizes were found to be in the 20–100 nm range, confirming the presence of nanocrystals.

SEM analysis of the samples before hydrogenation (Fig. 4) showed that the particles were very coarse (some particles were bigger than 100 mm). Backscattered electron imaging revealed zones of slight heterogeneity also (Fig. 4a). The examination of the phase diagram of the system [8] established that neither Mg nor Mg_2Ni phase can accommodate the composition range which was observed in the subsequent EDS analysis. Consequently, the heterogeneity is not due to the formation of different phases as verified by quantitative EDS chemical analysis, it could be attributed to different levels of Ni and Mg enrichment.

Sample 3 was found to be more heterogeneous in terms of volume and morphology than the other samples (Fig. 4b) exhibiting a multiple layering between Ni-rich and Mg-rich zone. This behaviour was confirmed by examining a second sample which was produced using the same deposition parameters.

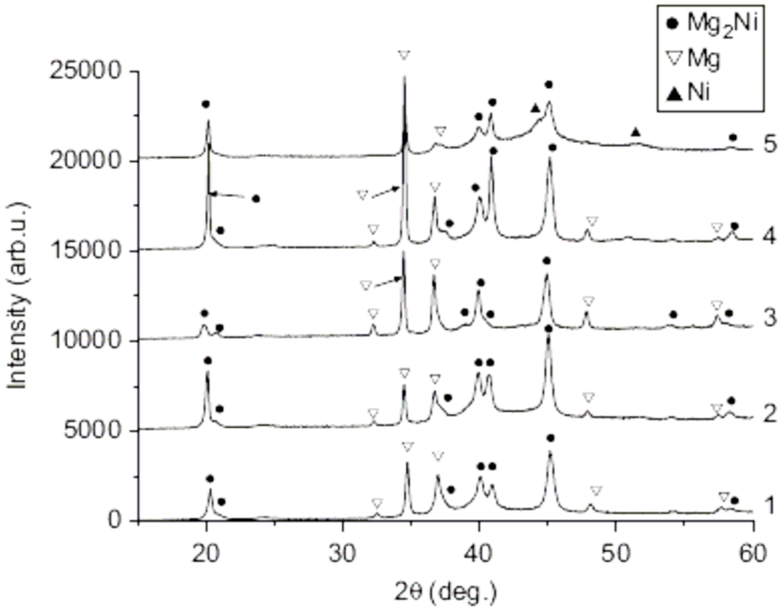

Fig. 2. XRD patterns of the five samples before hydrogenation

The modifications induced in the sample structure by the hydrogen exposure are demonstrated by the XRD patterns (Fig. 3) and SEM images (Fig. 4). The phases detected for samples 1–4 were Mg and Mg_2Ni while amorphous material was still visible after cycling. No $MgNi_2$ was detected in the cycled samples. Earlier work [9] though reported the formation of $MgNi_2$ after a number of cycles which was also decreasing the hydrogen storage capacity of the material. In the case of sample 5, the XRD pattern indicated the disappearance of the Mg phase and the emergence of the $MgNi_2$ phase (Fig. 3). This agrees with the reduced hydrogen storage capacity that we have found for this sample in the hydrogen sorption measurements.

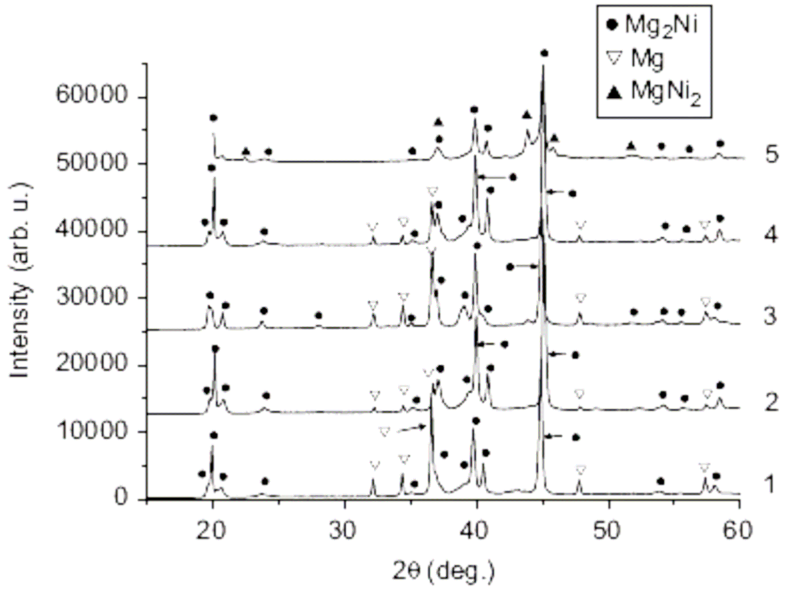

Fig. 3. XRD patterns of the five samples after hydrogen exposure

The presence of Mg_2Ni in samples 3 and 5, confirmed that the plateau on the corresponding PCI curve was the $Mg_2Ni \leftrightarrow Mg_2NiH_4$ transition. However, the origin of the difference in the enthalpy for these two samples as compared to the literature values was not explained.

The size of crystallites was generally in the same range (30–60 nm) with the ones calculated before hydrogenation, indicating that there is no significant crystal size evolution induced by the hydrogenation cycles.

SEM images (Fig. 4) of the hydrogen exposed samples highlighted the effect of the succession of hydrogenation/dehydrogenation cycles on the original material. The coarse grains were found to be fragmented in small particles of an average size of 1 mm (Fig. 4c) while their original shape remained. This is consistent with the progressive fragmentation of this material as reported in the literature [10–11]. Finally, some zones appear to stay unaffected by the exposure to hydrogen (Fig. 4d) most probably being amorphous.

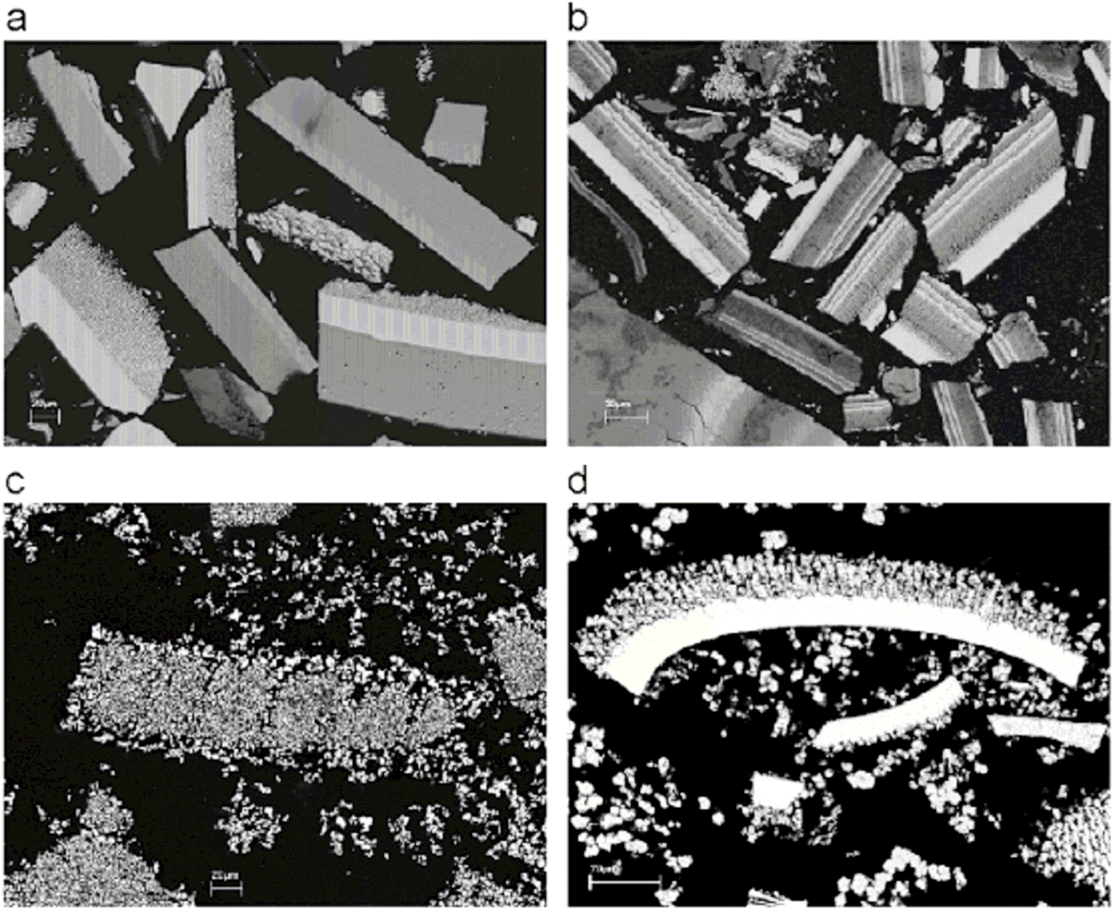

Fig. 4. Backscattered electron SEM picture before hydrogen exposure (a and b) and after hydrogen exposure (c and d): (a) small gradients of compositions are visible for all samples (the sample 1 is shown here); (b) the sample 3 showed many layers; (c) the coarser particles are reduced in fine grains (sample 4) and (d) some zones remained unaffected by the hydrogen (sample 5)

4. DISCUSSIONS

It is widely known that different nano-engineering techniques provide promising possibilities to modify the unsatisfactory properties of hydrogen storage materials. During this work we have compared thermodynamic properties of Mg-Mg_2Ni system in powder and thin film form. The initial assumption that magnetron sputtering should leave its "fingerprints" in properties of synthesised material and its performance was confirmed. We have registered the presence of amorphous material in every sample which might be directly linked to the artefact of physical vapour deposition technique. Furthermore, the long deposition time together with disproportion of wear-out of Mg and Ni cathodes might be responsible for slight heterogeneities of samples.

Also the analysis of the results has not yet permitted to explain two features observed here: the slight difference with the literature data in the dissociation enthalpy of Mg_2NiH_4 for the samples 3 and 5, assuming that the same phase is formed, and the presence of a third plateau for sample 3. In our opinion this might be related to either of the following specialities of film samples: i) they were handled in air atmosphere, thus there might be an oxide layer which influences overall performance, however, it is supposed to be removed during activation process; ii) unexplained results might be related to the presence of amorphous phase and its different properties; iii) there might be special microstructural structural conditions (the results of microstrains) which help to form metastable phases and influences thermodynamical performance of investigated materials.

5. CONCLUSIONS

Nanocrystalline Mg–Ni alloy powder was produced via magnetron co-sputtering with a certain degree of heterogeneity. The formation of $MgNi_2$ during hydrogen activation was only observed in the sample with the higher Ni content. The values of enthalpy of dissociation of the corresponding hydrides, MgH_2 and Mg_2NiH_4, as calculated via the respective van't Hoff plots, were coherent with the literature values except for two samples. In addition, one of these samples showed a third plateau and the presence of a hydrogenated metastable phase. This behaviour is currently under investigation.

The present work gave a first insight into some of the mechanisms occurring during the hydrogen activation of nanostructured powders produced by the physical vapour deposition technique and also of their sorption behaviour.

6. ACKNOWLEDGEMEN

This work has been financially supported by Lithuanian State Science And Studies Foundation project: "Development of multifunctional materials heterostructures for hydrogen fuel cells" (Contract No. C-15/2008/02, Acronym: H2technologijos). M. Lelis activities were supported by the Nordic Energy research program project: "Nordic Centre of Excellence on Hydrogen storage Materials" (Contract No. 06-HYDRO-C15).

REFERENCES

1. "Annual Energy Outlook 2008 (Revised Early Release)", Energy Information Administration (Official Energy Statistics from the U.S. Government), March 2008 – http://www.eia.doe.gov/oiaf/aeo/
2. USA DOE "Hydrogen Posture Plan", 2004 – http://www1.eere.energy.gov/hydrogenandfuelcells/pdfs/hydrogen_posture_plan.pdf.
3. L. Schlapbach, A. Züttel. Hydrogen-storage materials for mobile applications. Insight review article, Swiss Federal Laboratories for Materials Research and Testing, University of Fribourg, Physics Department, CH-1700, Switzerland. 2001, p. 353–358.
4. S. Shi, I-Y. Hwang. Research frontier on new materials and concepts for hydrogen storage. International Journal of Hydrogen Energy, USA. 2007, p. 224–228.

5. V. Berube, G. Radtke, M.S. Dresselhaus and G. Chen. Size Effects on the Hydrogen Storage Properties of Nanostructured Metal Hydrides. International Journal of Energy Research. 2007, p. 637–663.
6. J. Isidorsson, I. A. M. E. Giebels, M. di Vece and R. Griessen. Electrochromism of Mg-Ni hydride switchable mirrors. Solar and Switching Materials. 2001, p. 128–137.
7. http://hydpark.ca.sandia.gov
8. H. Feufel and F. Sommer. Thermodynamic investigations of binary liquid and solid Cu-Mg and Mg-Ni alloys and ternary liquid Cu-Mg-Ni alloys. Journal of Alloys and Compounds. 1995, p. 42–54.
9. M. Y. Song. Phase separation of Mg_2Ni by hydriding–dehydriding cycling. Journal of Alloys and Compounds. 1999, p. 297–301.
10. K. J. Gross, P. Spatz, A. Züttel and L. Schlapbach. Mechanically milled Mg composites for hydrogen storage the transition to a steady state composition. Journal of Alloys and Compounds. 1996, p. 206–213.
11. Z. Dehouche, R. Djaozandry, J. Goyette and T. K. Bose. Thermal cyclic charge and discharge stability of nanocrystalline Mg_2Ni alloy. Journal of Alloys and Compounds. 1999, p. 312–318.

WATER ELECTROLYSIS – TRADITIONAL AND UNCOMMON ASPECTS

M. Vanags, J. Kleperis, G. Bajars, G. Vaivars
Institute of Solid Sate Physics
University of Latvia
Kengaraga 8, LV-1063, Riga – Latvia
Phone: +371 67262145
E-mail: sf11053@gmail.com

ABSTRACT

In our work the water is used as electrolyte, and cell is made from cylindrical steel electrodes. In an uncommon aspect of electrolysis, the cell can be represented as capacitor for definite regime of applied voltage. We used short voltage pulses to initiate hydrogen/oxygen evaluation below electrochemical potential of electrodes in the cell, i.e. without ionic current in electrolyte. It was achieved increas of efficiency in electrolysis using mixed DC + AC power and electrodes of special construction. Such research is very important, if electricity from renewables is used for electrolysis, because in hydrogen produced by such a way, greenhouse-gas emissions are minimized.

Keywords: water electrolysis, resonance circuit, capacitor cell

1. INTRODUCTION

Hydrogen as an energy storage media has attracted world-wide attention as a possible solution of energy and environmental problems. The technology challenge facing application of hydrogen devices is of great complexity and scale and needs very high technical competencies, therefore this challenge is tackled in a focused and coherent way at EU level. The JTI on “Fuel Cells and Hydrogen” is to implement a programme of research, (RTD&D) activities in Europe in the fields of hydrogen technologies (fuel cells, electrolysers, storage containers, etc.) [1]. Water electrolysis is considered as an important method for large-scale production of “green” hydrogen, especially when electricity from renewable sources (sun, wind, water) is used [2]. Different electrolysers mostly based on alkali electrolysis and proton exchange membranes (PEM) nowadays are available in the market for the generation of hydrogen [3]. Conventional electrolysis using alkaline solutions has some disadvantages as extra heat, interaction between electrodes and alkali, necessity for reinforced containers and storage place. PEM based devices are expensive due to complicate polymer membrane (mostly Nafion) and Ru/Pt based catalysts. Also, it is known that the cost for water electrolysis using DC power still dominates a large part of the hydrogen production cost [3]. Is it possible to find more efficient way for classical electrolysis, using only water as electrolyte and at lower energy consumption and lower cost?

In our work the research on the non-traditional electrolysis method is analyzed, using alternative current pulses with different form and combined in different groups.

2. THEORETICAL CONSIDERATIONS

In the conventional DC electrolysis of water, hydrogen is generated as a result of electron transfer from the cathode electrode to adsorbed hydrogen ions on the cathode surface, when the applied voltage between the anode and the cathode exceeds the water decomposition voltage (about 1.4–1.8 V, the sum of the theoretical water decomposition potential

E_o=1.229 V for the reaction $H_2O \rightarrow H_2 + \frac{1}{2}O_2$ and an overvoltage of about 0.2–0.6 V depending on electrode material [4]. DC electrolysis always is a diffusion limited process and the current flow in electrolyte is determined by the diffusion coefficient of ions. It is therefore difficult to increase the input power for a constant volume electrochemical cell without reduction in electrolysis efficiency. When applied voltage is increased in DC electrolysis, the current increases so that hydrogen generation rate increases, but the efficiency compared with the ideal generation rate decreases. The decrease in efficiency can be explained mainly because an electron with high energy can only reduce one hydrogen ion so that the difference between the applied voltage and the decomposition voltage is dissipated as heat.

A survey of the different approaches for splitting water (electrolysis, plasmolysis, magnetolysis, magmalysis, photolysis, photoelectrochemical methods, radiolysis, catalytic and biocatalytic decomposition) was made Bockris et all (1985) [4]. These water splitting techniques are all part of a massive effort by the scientific community to find a plentiful, clean, and inexpensive source of fuel. One more new approach is intensively discussed during 30 years already – high voltage/short pulse water decomposition (for example, see patents of Puharich (1983) [5], Horvath (1976) [6], Spirig (1978) [7], Themu (1980) [8], Meyer (1986, 1989, 1992) [9–11], Santilli (2001) [12], Chambers (2002) [13], Shimizu (2006) [14]). Pure water has a very high dielectric constant, therefore exist an open circuit reversible threshold for water splitting, in which the water molecules behave as capacitor charging and discharging.

In our work the water electrolysis cell (WEC) represents two co-axial steel cylinders soaked in deionized water. Dielectric permittivity of deionized water is 78.5 (at 25°C), therefore it could be good dielectric, and WEC could be considered as capacitor with defined capacity. The resonance circuit is obtained in serial connection of WEC and induction coil, were voltage resonance must be observed. When blocking diode is added to this serial connection, known Mayer's [9–11] circuit (Fig. 1) is obtained (ground bed is avoided using transformer).

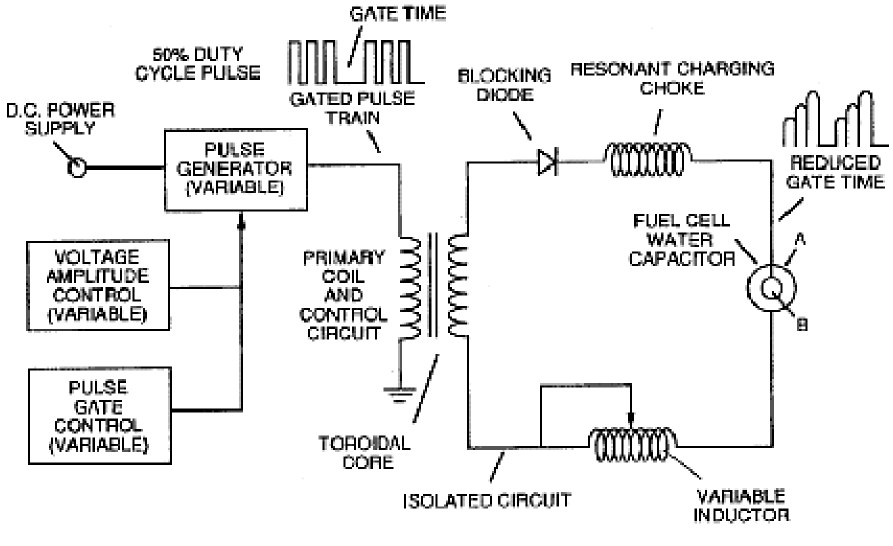

Fig. 1. Basic electrical circuit used as pulse generator for electrolysis (from Meyer [9–11])

Similar scheme is used in electronics for portable power supply units, with an objective to reach step charging effect. Working principle of the power supply unit is: one-polar impulse with frequency of serial resonance circuit is given to entry, and voltage resonance must be reached on capacitor. At the end of pulse capacitor discharge is not possible due blocking diode.

Serial oscillation circuit contains coil, capacitor, and omic resistivity from connections and wires. Capacitor in our case is WEC with clean water having high dielectric constant. Serial oscillation circuit at resonance frequency has potential on capacitor (or coil) Q times larger as supplied voltage (Q is circuit's quality factor *quality factor*):

$$Q = \frac{1}{R}\sqrt{\frac{L}{C}}, \tag{1}$$

where: *L – coil inductivity (H), C – capacity of WEC capacitor (F), R – active or omic resistivity (Ω)*

All parameters in equation (1) must be determined at resonance frequency, when circuit's impedance is in minimum (when imaginary resistivity in circuit is zero). The equation for impedance is the following:

$$Z = \sqrt{R^2 + (X_L - X_C)^2}, \tag{2}$$

where: X_L *– inductive resistance (Ω),* X_C *–capacitaive resistance (Ω).*

In case when both inductive and capacitative resistances are equal, the resonance is achieved. Resonance frequency is determined from::

$$\omega_{res} = \frac{1}{\sqrt{LC}}. \tag{3}$$

The potential must increase on coil or capacitor if *quality factor* is greater 1. It was already mentioned that electrolysis occurs at voltage above $E_o=1,23V$. It is possible to make water electrolysis at voltage below *1.23V*, if circuit`s *quality factor* Q is greater than 1 in resonant circuit just discussed. Applied voltage E_a on capacitor WEC must be multiplied with Q and electrolysis occurs at condition $E_a \cdot Q > E_0$. As soon electrolysis occurs, capacitor is break through, circuit's *quality factor* decreases and voltage on capacitor drops down till value $E_a<E_o$ and electrolysis stops. Water between capacitor plates relax back with high dielectric value, the circuit's albums growth up again, and at resonance state again $E_a \cdot Q > E_0$ and electrolysis occurs and so on. The power supply to WEC in such circuit must be in the form of pulses with frequency ω_{res} formed in packages with lower frequency.

Already in [15] we tried to find resonance in WEC by applying voltage above 5 V on the cell. It was found that limited capacity was obtained due to high internal conductivity in WEC even with distilled water as electrolyte. In the present work, we have examined the applicability of DC under 1.23 V and pulses with different freguency to reach water electrolysis with limited power supply.

3. EXPERIMENTAL

Water electrolysis cell WEC is cylindrical, made from two coaxial steel electrodes. The tubes from steel 304 (12X18H10T, composition given in Table 1) with inner diameter of outer electrode – 22.3 mm, outer diameter of inner electrode – 19.5 mm, height of both cylindrical electrodes – 131 mm were used.

Table 1. Percentage composition of steel

Element	C	Si	P	S	Ti	Cr	Mn	Fe	Ni	Cu
Composition (wt%)	0.12	0.83	0.04	0.02	0.67	17.88	2.02	68.36	9.77	0.29

The distance between both electrodes was made equal using six special clamps for centring (Fig. 2).

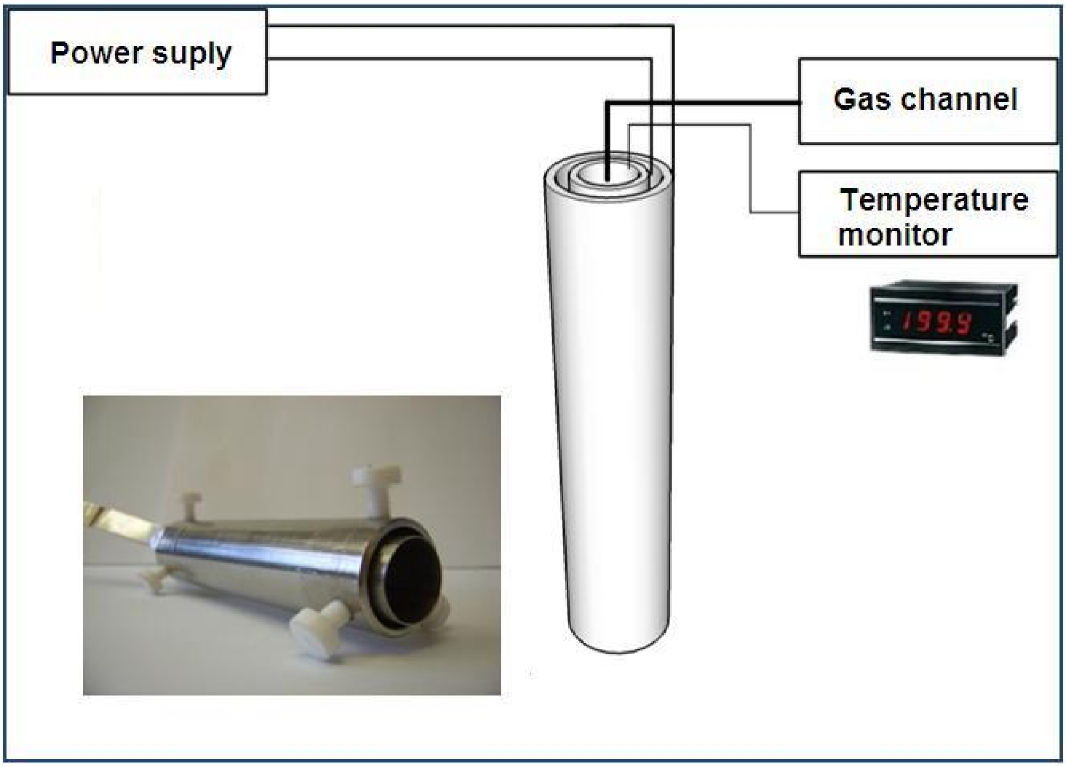

Fig. 2: Experimental setup of water electrolysis cell and measurents

It was necessary because after immersion of electrodes in deionized water (conductivity ~ 0.1 μS), the resistance between electrodes decreased to 10 KΩ. Possible reason could be the surface conductivity of clamps, therefore the smaller connection between both coaxial cylinders, the higher resistance. Solution was found using plastic clamps having sharp glass at the end to provide less contact area. The WEC made from such centring clamps maintain the highest resistance (28 kΩ) after immersion in deionized water.

Electrical circuit was made using signal generator GwInstek GFG-3015 connected to the gate of field transistor BUZ350 (Fig. 3). The source pin of transistor was connected with ground contacts of both signal generator and power supply unit HQ Power PSS-2010. Plus pole from power supply unit was connected with initial winding of special impulse transformer, which prime coil (final output) was connected with drown pin of field transistor. This circuit provides pulse supply till frequencies 150 MHz, voltage 30V and current 10 A. It is possible to programm pulses with different forms, packages, sweep, etc. using generator GwInstek GFG-3015. WEC is connected in serial with induction coil and blocking diode with secondary coil of impulse transformer.

Current and voltage in serial circuit are controlled with HAMEG 8115-2 power meter and osciloscope GwInstek GDS-2204. The frequency of pulses is at least ten times higher than the frequency of pulse packages.

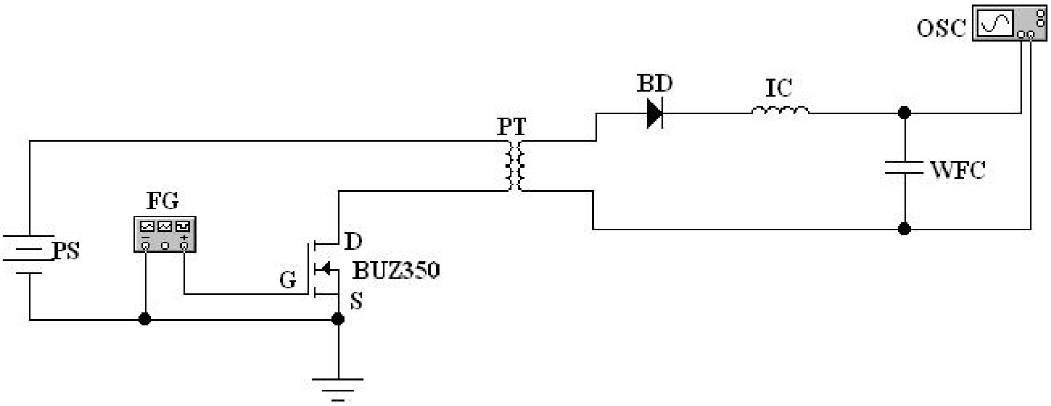

Fig. 3. Electrical circuit used in experiments: FG – signal generator, PS – power supply, BUZ350 – electronic switch, PT – impulse transformer, BD – blocking diode, IC – induction coil, FC – water electrolysis cell

4. RESULTS AND DISCUSSION

The resonanse is achieved as a step charging effect with pulse freguency 20 kHz, pulse package frequency 1 kHz and coil with inductivity 1mH (Fig. 4).

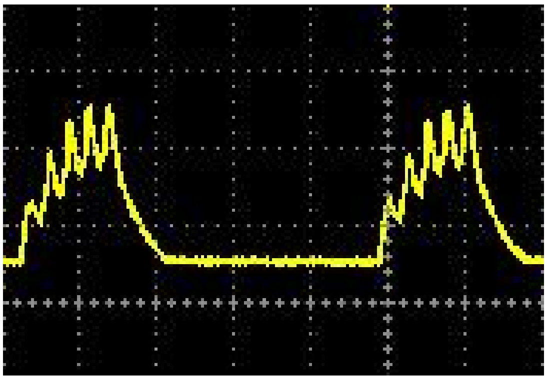

Fig. 4. Step charging effect

It is important to reduce DC power supply below standard water splitting potential 1.23 V, and reach electrolyses with resonanse in serial circuit, when due to step charging the summary voltage on cell exceeds water splitting potential in the experiment. The best result was achieved in the experiments using DC power 0.9 V, frequency 5 kHz, when voltage 1.7 V was obtained on electrolysis cell (Fig. 5).

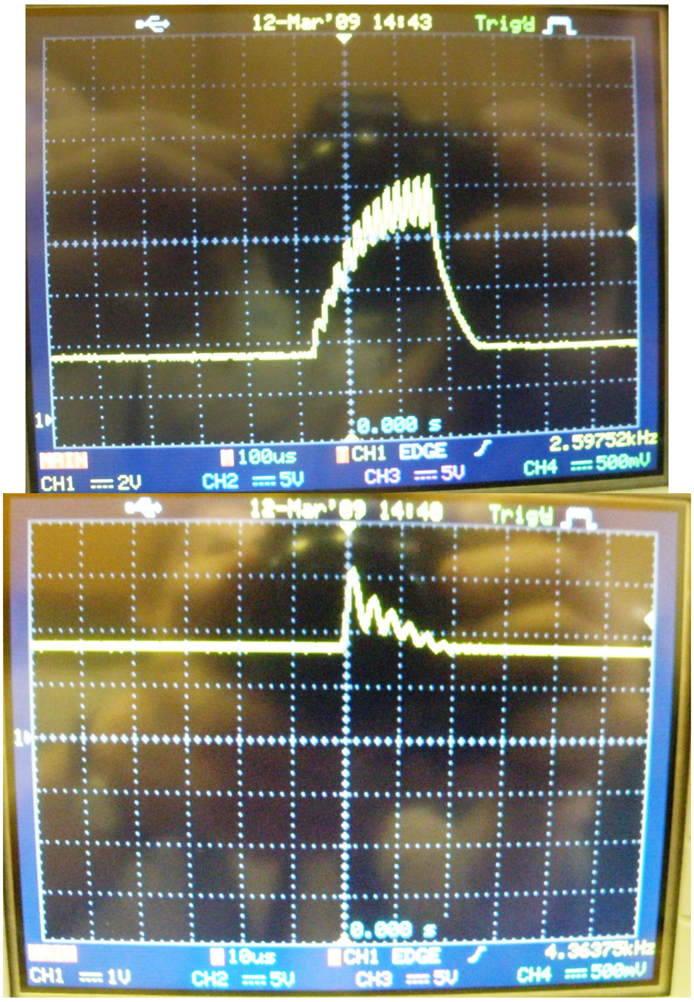

Fig. 5. Situation when voltage on electrolysis cell exceeds applied DC power

As it is seen from volt-amperic curve of water electrolysis cell (Fig. 6), the water splitting started at 1.54 V already.

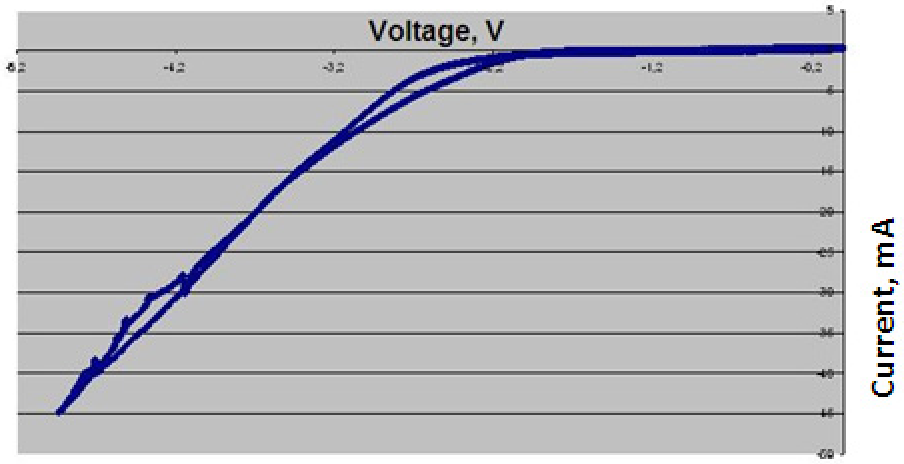

Fig. 6. Volt-amperic curve of water electrolysis cell

CONCLUSIONS

By using cylindrical electrodes and distilled water electrolyte for water electroysis cell in serial circuit with induction coil and blocking diode, it is possible to achieve resonance condition at definite frequence. In such case it is possible to achieve a situation, when water splitting is possible at applied direct current voltage below electrochemical splitting threshold.

5. ACKNOWLEDGMENT

We would like to thank National State Program in Energetic and University of Latvia for financial support in researches and preparation of patent application.

REFERENCES

1. Momirlan, M. and Veziroglu, T.N. Current status of hydrogen energy. Renewable and Sustainable Energy Reviews, 6, (2002), p. 141–179.
2. Roy, A., Watson, S., and Infield, D. Comparison of electrical energy efficiency of atmospheric and high-pressure electrolysers. International Journal of Hydrogen Energy, 2006, Article in Press.
3. Ivy, J. Summery of electrolytic hydrogen production: milestone completion report, NREL/MP-560-35948. (2004), http://www.nrel.gov/docs/fy04osti/36734.pdf Website last accessed on 02-02-2007.
4. Bockris, J.O`m., Dandapani, B., Cocke, D., and Ghoroghchian, J. On the spltting of water. Int. J. Hydrogen Energy, 10, (1985), p. 179–201.
5. Puharich, H.K. Method & Apparatus for Splitting Water Molecules. US Patent # 4,394,230, (1983).
6. Horvath, St. Electrolysis apparatus. US Patent 3954592 (1976).
7. Spirig, E. Water decomposing apparatus. US Patent 4113601 (1978).
8. Themu, C.D. High voltage electrolytic cell. US Patent 4316787 (1980).
9. Meyer, S.A. Electric pulse generator. US Patent 4613779 (1986).
10. Meyer, S.A. Gas generator voltage control circuit. US Patent 4798661 (1989).
11. Meyer, S.A. Process and apparatus for the production of fuel gas and the enhanced release of thermal energy from such gas. US Patent 5149407 (1992).
12. Santilli, R.M. Durable and efficient equipment for the production of a combustible and non-pollutant gas from underwater arcs and method therefore. US Patent 6183604 (2001).
13. Chambers, S.B. Method for producing orthohydrogen and/or parahydrogen. US Patent 6419815 (2002).
14. Shimizu…
15. Martins Vanags, Peteris Shipkovs, Janis Kleperis, Gunars Bajars, Andrejs Lusis. Water Electrolyses – Unconventional Aspects. Proceeding 2nd International Hydrogen Energy Congress and Exhibition IHEC 2007 Istanbul, Turkey, 13–15 July 2007.

PLASMA ACTIVATED HYDROGEN PERMEATION THROUGH THIN METAL MEMBRANES

A. Bačianskas
Vytautas Magnus University
Vileikos St. 8, Kaunas – Lithuania
Phone: 868434213
E-mail: aliusb@xxx.lt

ABSTRACT

The technical characteristics of the membranes are very sensitive to the chemical contaminants of the working gas mixture, such as sulphur, chlorine and CO. In the present work, the feasibilities of hydrogen separation from ionized hydrogen-carbon compounds are considered. It is shown that membrane feed surface may be protected from the poisoning effects using hydrogen separation by plasma technologies. Preliminary studies have shown that the removal of inorganic surface impurities may be realized by the physical sputtering in the working gas pressure range 1 - 10 Pa, and the removal of organic and carbonaceous chemical compounds may be performed by plasma-chemical etching in the working gas pressure range 60-80 Pa.

Keywords: membranes, hydrogen, separation, plasma

1. INTRODUCTION

Effective membranes suitable for the hydrogen separation from the gas mixture are widely studied. Membranes have limited industrial use despite of the considerable efforts of researchers. Today, the membranes are used in ammonia production and electronics technologies. Selection of membranes (material, thickness, operating temperature and pressure) depends on the working gas composition, the desired gas purity, the process efficiency and the cost. Table 1 includes the list of membranes which are currently used and under investigations and their main characteristics.

Table 1. The classification of membranes used for hydrogen separation [1]

	Dense polymer	Micro porous ceramic	Dense metallic	Porous carbon	Dense ceramic
Temperature range	< 100°C	200°C–600°C	300°C–600°C	500°C–900°C	600°C–900°C
H_2 selectivity	low	5–139	> 1000	4–20	> 1000
H_2 flux (10^{-3} mol/m^{2}s) at dP=1 bar	low	60–300	60–300	10–200	6–30
Stability issues	Swelling, compaction, mecanical strength	Stability in H_2O	Phase transition	Britle, oxidising	Stability in CO_2
Poisoning issues	HCl, SO_x, (CO_2)		H_2S, HCl, CO	Strong adsorbing vapours, organics	H_2S

Materials	Polymers	Silica, alumina, zirconia, titania, zeolites	Palladium alloy	Carbon	Proton conducting ceramics (mainly $SrCeO_{3-\delta}$, $BaCeO_{3-\delta}$)
Transport mechanism	Solution/diffusion	Molecular sieving	Solution/diffusion	Surface diffusion: molecular sieving	Solution/diffusion (proton conduction)
Development status	Commercial by Air Products, Linde, BOC, Air Liquide	example few cm^2 (small samples)	Comercial by Johnson Matthey propotype	Small membrane modules commercial, mostly small samples (cm^2) available for testing	Small samples available for testing

Metal membranes play a vital role in hydrogen purification. Defect-free membranes exhibit excellent selectivity and provide high fluxes, resistance to poisoning, long operational lifetimes and low cost. Alloying offers one route to improve properties of membranes based on pure metals [2].

The scheme of the membrane used for hydrogen separation is presented in Fig. 1. The working gas mixture is flown over the membrane. Molecular hydrogen, as reaction product, is adsorbed on the membrane surface and transported from the surface into the bulk. The reaction products and not adsorbed hydrogen leave the reactor.

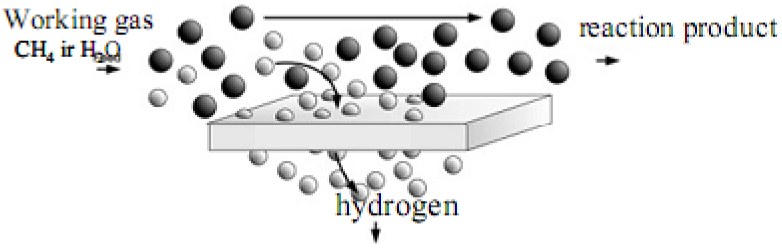

Fig. 1. The scheme of membrane used for hydrogen separation [1]

This work considers the feasibilities of fabrication of thin dense metallic hydrogen separating membrane on the top of the thick (up to 0.5 mm thick) of porous, made of Al_2O_3, layer formed on stainless steel substrate. The diffusion mechanism of hydrogen through the metal membrane gives high membrane selectivity for hydrogen, however, small hydrogen flow. Fig. 2 schematically illustrates hydrogen transport mechanism through thin dense membrane. It includes five stages: (i) the adsorption of the molecular hydrogen, (ii) the H_2 dissociation, (iii) the diffusion of atomic hydrogen through the membrane, (iv) the H_2 recombination (the formation of molecular hydrogen), and (v) the H_2 desorption. To increase this flow, the metal membrane has to be very thin (20–50 μm thick). This membrane can be deposited on the surface of porous electrode using physical vapour deposition technologies, for example, magnetron sputtering technique [3]. Porous membrane has a low selectivity, but it permeates large gas flows. Two-layered membrane, consisting of a thin metal hydrogen separating film on the surface of porous ceramic coating, increases the efficiency of the membrane. Thin membrane performs hydrogen separation, and thick porous electrode guaranties the mechanical stability of the membrane. The formation technology of thick porous Al_2O_3 layer has been considered in publication [4].

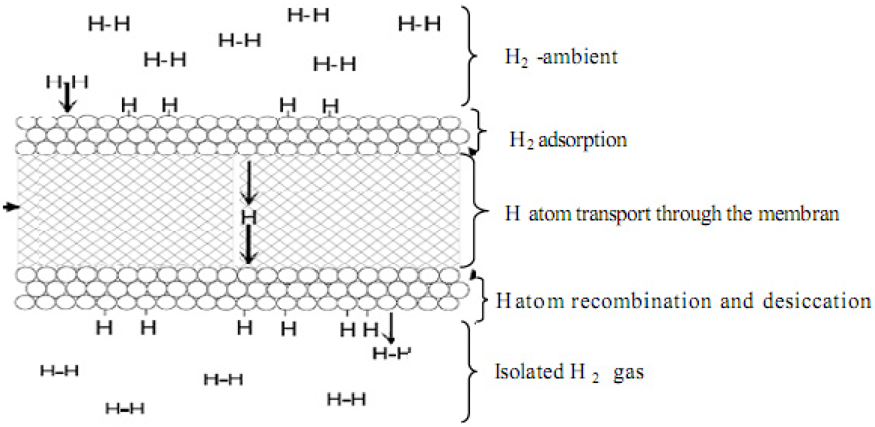

Fig. 2. Schematic presentation of the hydrogen transport mechanism through a thin dense membrane

2. PROCESSES ON THE SURFACE OF MEMBRANES IN REACTIVE PLASMA

2.1. Model

Model aims to illustrate feasibilities of hydrogen separation from ionized gases including hydrocarbon compounds using membrane technologies. The main advantages of plasma technologies are the following: (i) the hydrogen ions extracted from plasma are accelerated and ion implanted in the near surface region of membrane avoiding permeation hindrances formed by the surface barrier, (ii) the energetic carbon ions perform removal of surface contaminants by physical sputtering, and (iii) the hydrogen and oxygen atoms react with adsorbed carbon atoms forming volatile compounds (chemical sputtering) and remove carbon deposits. In previous studies [5] it has been shown that for the reactive plasma the mechanism of chemical sputtering prevails in the range of high working gas pressures (above 60 Pa), and the physical sputtering dominates in the range of pressures less than 10 Pa. The model is based on the analysis of the heterogeneous chemical reactions on the membrane surface

$$\left(\frac{dc_i}{dt}\right)_{Ch} = \sum_j c_j R_{ji} - c_i \sum_j R_{ij} , \tag{1}$$

where R_{ij} – the frequency probability of the reaction for i and j components, c_i – the partial surface concentration of i atoms ($\sum c_i = 1$).

Let us consider CH_4 as the working gas. Plasma generated in CH_4 gas consists of a mixture of CH_4, CH_3, CH_2, CH, C and H atoms and molecules in neutral, ionized and excited states. Concentration of ions in plasma for this case does not exceed 1–5%. Positive ions are accelerated through the space charge layer in front of the membrane surface. Their energy depends on the negative bias voltage of membrane which may be verified in the range 100–1000 eV. The incident energetic ions sputter the membrane surface atoms (physical sputtering) and remove inorganic contaminants arriving from the working gas. At the same time, atoms and ions arriving from plasma are adsorbed on the membrane surface and take part in possible reactions. In the present work, of the various possible chemical reactions we consider as dominant the following

$$C+4H \rightarrow CH_4\uparrow \tag{2}$$

The reaction products are the volatile compound, CH_4. Which leaves the surface at room temperature removing carbon atoms from the membrane surface. For this simplified case, the graphite surface is covered by two components: C and CH_4 with surface concentrations c_1 – for carbon, and c_2 – for CH_4. The concentration of C in deeper monolayers is $n_1=1$. Thus, eq. (1) may be rewritten for two components on the surface as

$$\frac{dc_1}{dt} = \frac{dc_2}{dt} = w_2 c_2 - R_{12} c_1 , \tag{3}$$

where w_2 is the desorption frequency probability of CH_4 molecules. It is seen that the surface composition approaches exponentially the steady state values, and the steady state surface erosion rate is equal to

$$V_{S,st} = w_2 \frac{w_1 + R_{12}}{w_2 + R_{12}} , \tag{4}$$

where w_1 is the desorption frequency probability of C atoms.

This model is simple when parameters describing kinetics of reactions are expressed in units of frequency probabilities for corresponding processes. For practical applications it is important to have dependences of reaction rates as function of controllable technological parameters, such as, pressure and temperature. We will follow the scheme suggested in [6]. The frequency probability of chemical reaction, R, may be expressed as function of surface concentrations of reactive components. The reaction rate for eq. (2) may be written as

$$R_{12} = K[H]^4 , \tag{5}$$

where K – the heterogeneous reaction rate and [H] – the surface concentration of hydrogen. In this case, the additional equation which describes the dependence of surface concentration of on the technological parameters is necessary. Usually, so kind equations are empirical and based on the analysis of experimental results.

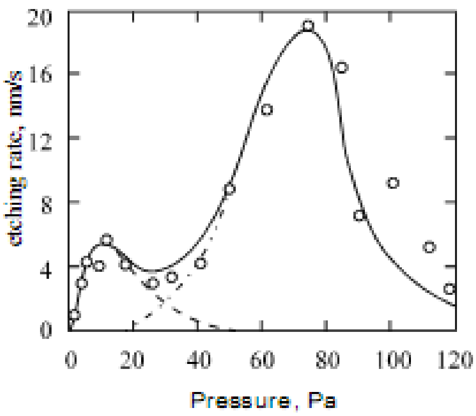

Fig. 3. The dependence of surface erosion rate on the working gas pressure [6]

The surface concentration of components generated in plasma on the working gas pressure may be written as [6]

$$[A] = N_{OA} p^{\xi_i p} e^{-x_A p}, \tag{6}$$

where N_{OA}, ξ_A, x_A – the empirical coefficients depending on the reactor design and experimental conditions. In this way,

$$R_{12} = K_1 p^{4\xi} e^{-xp}. \tag{7}$$

The positive ions extracted from plasma bombard membrane surface with energy $\varepsilon = q(\varphi_{p1} - \varphi_{s1})$, where φ_{p1} and φ_{s1} are the plasma and membrane potentials, correspondingly. Following the same scheme and the methodological approach suggested in [6] we obtain that

$$w_1 = a_1 (\varphi_{pl} - \varphi_{sl})^{3/2} e^{xp}, \tag{8}$$

$$w_2 = a_2 (\varphi_{pl} - \phi_{sl})^{3/2} e^{-xp} + w^{(T)}; \tag{9}$$

where a_1 and a_2 are the empirical coefficients.
Assuming that

$$\varphi_{pl} - \varphi_{sl} = 470 e^{-0.07p}. \tag{10}$$

where p is the working gas partial pressure in the reactor, after insertion of (10) into (8) and (9) equations, and (7) into (4) equation, the dependence of surface erosion rate on the working gas pressure is obtained. Solid line in Fig. 3 shows the calculated dependence for $a_1=3.285\times10^{-4}\,s^{-1}$, $a_2=0.365\times10^{-4}\,s^{-1}$, $K_1=9.13\times10^{-6}\,Pa^{-4}$, $\xi = 1$, $x = 0.005 Pa^{-1}$ which is in good agreement with the experimental results.

In this way, theoretical model explains the experimental dependence of the erosion rate on the pressure. The model grounds the suggestion that hydrogen separation from the hydrocarbon ionized gases may be performed if the working gas pressure is changed in time: (i) when the working gas pressure less than 10 Pa, hydrogen is implanted in the near surface region of membrane and efficiently transported through it, and (ii) after the membrane surface is contaminated by carbon arriving from the working gas, the working gas pressure has to be increased up to 60-80 Pa for the removal of deposited carbon layer by chemical etching.

2.2. Adsorption of C on W under ion irradiation

The basic model predictions have been used to explain experimental results of C transport in W films. The conditions on W films are similar to those taking place on the membranes immersed in reactive plasma. The experimental details are presented in [7]. It has been observed that C penetration depth in W under plasma irradiation depends on the working gas pressure. Three regimes have been distinguished: (i) the surface erosion rate exceeds C adsorption rate, (ii) the C adsorption rate prevails surface erosion, and (iii) the adsorption and erosion rates are equal. It is not fully understood behavior of adsorbed C atoms and their subsequent transport mechanism from the surface into the material volume under ion radiation for high temperatures. In the present work, it is shown that the observed experimental results may be explained on the basis of the above considered physical model. Fig. 4 illustrates C distribution profiles in W film, measured by the secondary ion emission mass spectroscopy (SIMS) technique after deposition of C under ion irradiation: curve 1 - the surface erosion rate exceeds the C adsorption rate, curve 2 – the C adsorption rate is approximately equal to the membrane surface erosion rate, and curve 3 – the C adsorption rate exceeds the membrane surface erosion rate. It is seen that C atoms are efficiently transported from the surface of membrane into the bulk of material when the adsorption rate of C atoms in the membrane is approximately equal to the rate of erosion. For this case, the membrane surface is only partially covered by C atoms. This is confirmed by the studies of the membrane surface views in the scanning electron microscope (SEM). Typical views are presented Fig. 4: a – the W membrane partially covered by C atoms, and b - the membrane fully coated with C atoms.

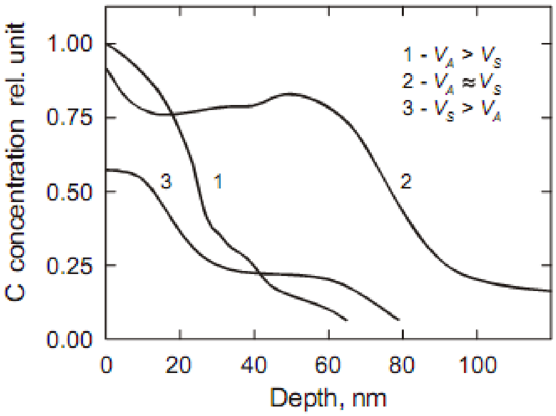

Fig. 4. The distribution profiles of C atoms in W film [7]: curve 1 – the surface erosion rate exceeds C adsorption rate, curve 2 - the surface erosion and C adsorption rates are approximately equal, and curve 3 - the C adsorption rate exceeds the surface erosion rate

It is seen that C transport from the surface into the bulk is efficient when W surface is partially covered by C atoms. To avoid C contamination effects the C surface concentration has to be minimized. It may be realized if to form working gas mixture including oxygen. It is well known that carbon deposits are efficiently removed in oxygen plasma.

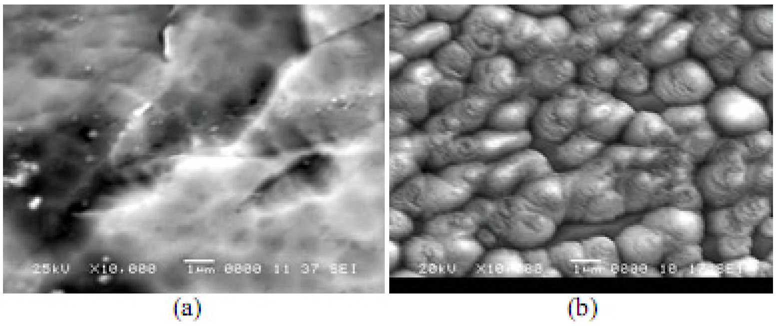

Fig. 5. Surface views of W film in SEM [7]: a – the surface erosion rate exceeds C adsorption rate, and b - the C adsorption rate exceeds the surface erosion rate

It is seen that C transport from the surface into the bulk is efficient when W surface is partially covered by C atoms. To avoid C contamination effects the C surface concentration has to be minimized. It may be realized if to form working gas mixture including oxygen. It is well known that carbon deposits are efficiently removed in oxygen plasma.

CONCLUSIONS

The feasibilities of hydrogen separation from the ionized hydrocarbon compounds using membrane technologies have been considered. The main advantages of plasma technologies: (i) the diminished role of surface barrier for hydrogen transport from the surface into the bulk, (ii) the realization of physical and chemical removal of contaminants arriving from the working gas, and (iii) oxygen additives in working gas may be used for the removal of carbon deposits.

The dominance of the processes of physical sputtering of inoragnic compounds and chemical etching of carbonaceous compounds depends on the working gas pressure.

REFERENCES

1. Kluiters S.C.A. Status review on membrane systems for hydrogen separation, 2004, Intermediate report EU project MIGREYD NNES-2001-670, http:/www.ecn.nl/does/libraray/report2004/c04102.pdf.
2. Laukaitis G. Membrane Technology and Applications for Sustainable Hydrogen Production and Fuel Cells, VDU-LEI, 2008, 350 p.
3. Zhang H., Li D.Y., Effects of sputtering condition on tribological properties of tungsten coatings Wear 255 (2003), p. 924–932;
4. Pranevicius L., Pranevicius L. L., Valatkevicius P., Valincius V. Plasma spray deposition of Al-Al_2O_3 coatings doped with metal oxides: catalytic applications, Surface and Coatings Technology 123 (2000), p. 122–128.
5. Galdikas A., Pranevicius L. Interactions of ions with condenced matter. // Horizons in World Physics, Volume 229, Nova Science Publishers, Inc., Huntington, New York, 2000, 176 p.
6. Pranevicius L.. Coating Technology: Ion Beam Deposition // Satas and Associates, Warwick, Rhode Island (USA), 1993, 453 p.
7. Pranevicius L.L., Milcius D., Bobrovaite B., Templier C., Pranevicius L. Plasma erosion of tungsten films with different carbon content, Thin Solid Films 516 (2008) 7340-7344.

CYSENI 2009, May 28-29, Kaunas, Lithuania
ISSN 1822-7554, www.cyseni.com

POLYMER MEMBRANES FOR FUEL CELLS

J. Hodakovska, J. Kleperis
Institute of Solid State Physics, University of Latvia
Kengaraga 8, LV-1063, Riga, Latvia
Phone: +371 67262145
Email: julia_h_lv@yahoo.co.uk

ABSTRACT

The one between most promising clean energy sources is hydrogen fuel cell, since it does not generate toxic gases and other hazardous compounds. Low temperature fuel cells currently are an important research topic in all leading automobile and energy industries. Some fuel cell products already reached the threshold of commercialization and is coming on market. Among various kinds of fuel cells, polymer electrolyte membrane (PEM) fuel cells are easy to be miniaturized and suited as energy sources for automobiles as well as domestic applications and portable devices.

The main part of PEM fuel cell is the polymer electrolyte membrane, as it defines the properties needed for other components of the cell and is the key component of it. The membrane is one from two most expensive parts of fuel cell (second is catalyst), so it is one of the areas that needs more researches. Nowadays the membrane materials are either expensive due to complicated synthesis and used nature-unfriendly (poisonous or cancerogenic) compounds. Some of it's properties (proton conductivity, water absorbtion, mechanical or chemical stability) are limiting their use in fuel cells.

This report is dedicated on fuel cell membranes and gives short review about the development of polymeric membranes for PEM fuel cells in different aspects. The proton conductivity and gravimetric researches is presented for some commercial and self made membranes in experimental part. Their power characteristics are tested for possibility to use them in the fuel cells.

Keywords: proton conductivity, polymer membranes

1. INTRODUCTION

During the last years a lot of attention has been paid to energy production and supply, involving different aspects: production, storage, decreased consumption, and increased efficiency. Energy now is one of the most valuable things on Earth since it is not possible to imagine life of any modern society without it. In all areas of social life, and in all sectors of industry, including transport, we are consuming huge amounts of energy, using fossil fuels. Such a dependence on directly non-renewable sources could lead to energy deficit in future or according to most dramatic scenarios could bring humankind back to Stone Age. Renewables are most obvious solution of this situation, but there are some important shortages yet: limited availability (the Sun in daytime, the wind – chaotically), necessity for storage, expensive technologies.

One of the promising ways of storing energy is hydrogen, because it has high energy density to weight [1]. Hydrogen could be produced, stored and consumed in several ways, including direct burning. But the most efficient is hydrogen chemical burning in fuel cell due to high theoretical efficiency, reaching 83% for hydrogen's higher heating value and 94.5% for lower heating value. This is much more than today's engines reach [2, 3]. Proton conductive membrane is one of the basic constituent of fuel cell and is necessary to improve it.

Proton conductive polymer membranes found applications in many commercial electrochemical systems used in polymer electrolyte membrane (PEM) fuel cells, direct methanol fuel cells (DMFC), PEM electrolysers, water purification systems; gas sensors, etc. There is a need for new polymer electrolyte membrane materials which are used in the PEM that are cheaper and more conductive than the current perfluorosulfonic acid materials (most known Nafion®). These new materials should be durable for up to 10.000 hours. For direct methanol fuel cells, new membranes with reduced methanol permeability and increased stability are required. Also, often production of the polymer itself requires expensive technologies and/or materials. Sometimes polymers' burning could release carcinogenic components during fires. All these topics are important when new technologies are developed.

In this article we report on properties of new sulfonated poly (ether-ether-ketone) (SPEEK) membranes, using thermagravimetric (TG) analysis and conductivity measurements, comparing it to Nafion-type commercial membranes.

2. EXPERIMENTAL

2.1. Materials

Two different polymers were studied, including commercially produced Nafion115 and home-made sulfonated poly(ether-ether-ketone) (SPEEK). Both polymers have similar mechanism of proton conductivity – via SO_3H-groups (Fig. 1). Nafion is one of the best known polymers for commercial fuel cells today, due to its high proton conductivity at low temperatures (below 100°C). SPEEK based membranes also have received lot of attention during the last years.

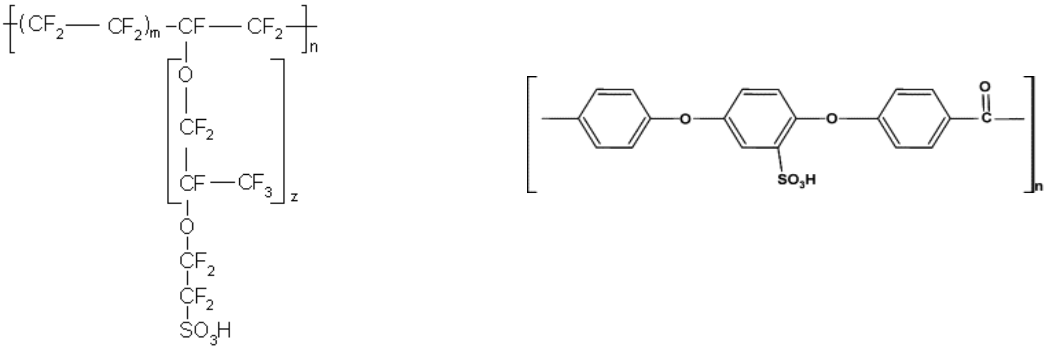

Fig. 1. Nafion (left) and SPEEK (right) structural forms

Nafion115 membrane is produced by DuPont [4]. SPEEK was prepared from poly(ether-ether-ketone) (PEEK) supplied by Aldrich and according to procedure described elsewhere [5]. Polymer was cast on glass with resulting membrane's thickness equivalent to the one of Nafion115.

2.2. Methodology

2.2.1. Thermogravimetric (TG) and differential thermal analysis (DTA)

Thermogravimetric (TG) analysis was performed with SHIMADZU DTG-60 instrument in Ar atmosphere (Ar 5.0 from AGA Ltd.) with flow 50 ml/min in temperature range from room temperature (RT) till 250 °C with heating rate 10 deg/min.

This method was used to test the thermal stability of membrane materials, because in real working conditions they often reach temperatures 100 °C and more, so good stability in this interval is required. Also amount of absorbed water can be established from TG measurements. For measurements freshly soaked membranes were cut in small pieces with total weight about 50 mg and placed in aluminium crucibles for measurements.

2.2.2. *Proton conductivity*

Both membranes were placed in water for 24 hours before measuring proton conductivity. The relative humidity in system was 100% during the measurements.

Proton conductivity was measured using Becktech conductivity cell [6]. Four electrode scheme was used (Fig. 2) to determine in-plane conductivity of membrane. During conductivity measurements at different temperatures, the maximal humidity of environment was provided with special experimental setup.

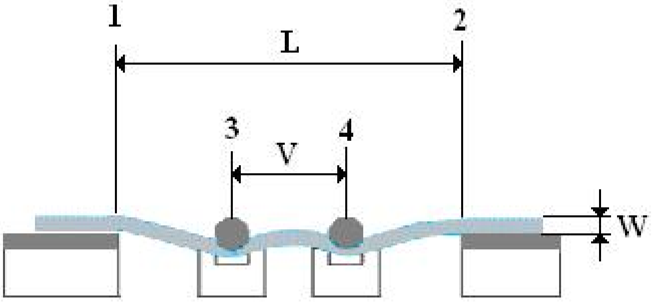

Fig. 2. Proton conductivity measurement scheme. Distances L and V are fixed, membranes width (W) is dependant on the sample; current is given through electrodes 1 and 2, voltage is measured between electrodes 3 and 4

3. RESULTS AND DISCUSSION

DTA analysis showed good thermal stability of our SPEEK membranes till temperatures around 250 °C (Fig. 3). The mass loss (room temperature – approximately 120 °C) indicates dehydration of the membrane, which is reversibly and typical for this type of membranes with bounded water inside. Polymer degradation is not observed till the end of measured interval, that indicates stability at working temperatures in polymer membrane fuel cells (typically less than 100 °C, for some polymers it could reach values of 160 °C [7] or even 200 °C [8]). Also behaviour of the curves indicates that SPEEK membrane has a possibility to work at higher temperatures than Nafion due to slower loss of bounded water.

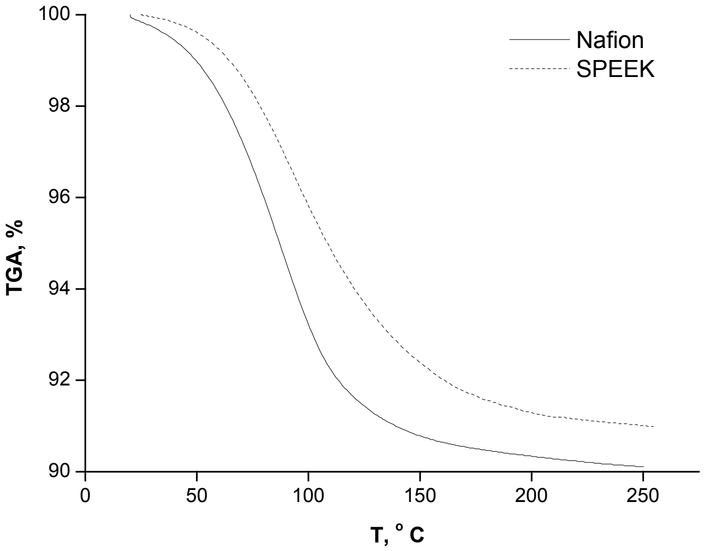

Fig. 3. Results of the thermogravimetric analysis of the Nafion and SPEEK polymers

Proton conductivity is an important factor, which determines whether the membrane is good enough to be used in fuel cells. Since for Nafion typical working temperatures are between 60 and 80°C due to water loses, last value was chosen as the limit for measurements. Results of these measurements showed that this sample has good proton conductivity starting already at low temperatures – at 40°C and reached approximately 80 mS/cm (Fig. 4). At the end of measured temperature interval proton conductivity increasement slowed down, indicating closeness to optimal working condition, were balance between conducting and evaporation processes is attained.

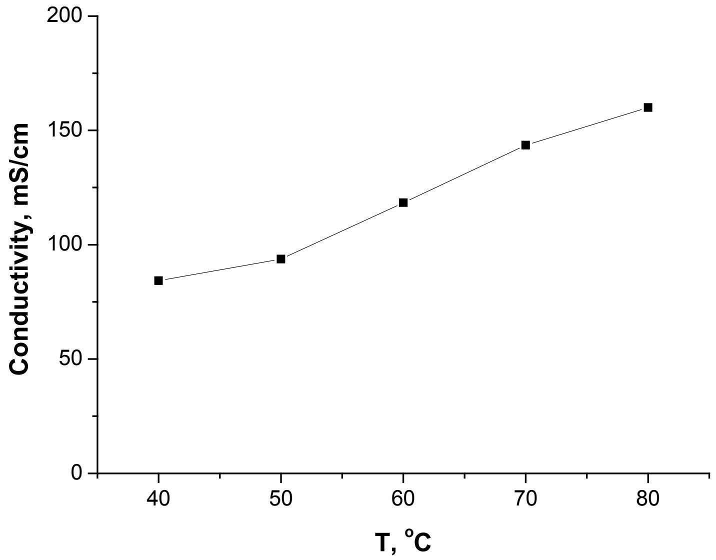

Fig. 4. Proton conductivity measurement results for commercial Nafion115 membrane

Since SPEEK samples were made from our material, we tested them for a temperature till 90°C (Fig. 5). Our membranes showed not as good results as Nafion, reaching only several mS/cm at 40°C, but at higher temperatures proton conductivity grew close to 50 mS/cm, and the tendency of the process didn‘t show any sign of growth rate slowing. This could indicate a possibility to use our membrane at higher temperatures than Nafion that could lead to better proton conductivity in case of optimal water supply.

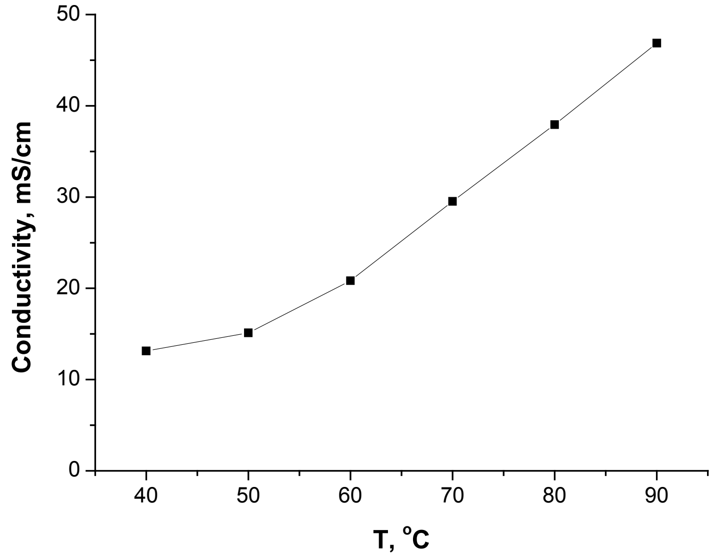

Fig. 5. Proton conductivity diagram for SPEEK membranes

All measured parameters indicate that our SPEEK membranes show promising results. Working at higher temperature range, but still in comparably low temperature diapason makes membranes from our polymer candidate for working in portable devices (such as laptop) in less friendly conditions, such as hot days or desert. At the same time these properties make it a candidate for usage in cars as alternative energy source, or in any other device, where temperatures reach values of 100°C.

For better understanding of the properties of the samples further experiments are needed, e.g. we are planning to test SPEEK membranes with Pt/Ru catalyst electrodes for applications in fuel cells.

4. CONCLUSIONS

Experimental results of new SPEEK type membranes are reported. Termogravimetric analysis showed stability of SPEEK membranes at comparably high temperatures, which enable to use membranes in fuel cells at working temperatures. Proton conductivity of our SPEEK membrane is lower than that of Nafion, but at higher temperatures these values become closer, and change of temperatures increases conductivity of a SPEEK approximately 4 times.

Further experiments are planed to compare the power characteristics for both polymers - testing their usability in fuel cells.

5. ACKNOWLEDGMENT

We would like to thank ESF (European Social Fund), National State Program in Energetic and University of Latvia for financial support in researches and preparation of patent application.

REFERENCES

1. J. Schindler, R. Wurster, M. Zerta, V. Blandow and W. Zittel. Where will the Energy for Hydrogen Production come from? Status and Alternatives. Published by EHA (European Hydrogen Association), 2006.
2. F. Barbir. PEM Fuel Cells. Theory and Practice, Elsevier Academic Press, 2005
3. S.M. Javaid Zaidi, T. Matsuura. Polymer Membranes for Fuel Cells, (Eds.) 2009, 550 p.
4. DuPont™ Nafion® PFSA Membranes N-115, N-117, N-1110. Technical sheet DuPont: dfc101.pdf
5. H. Luo, G. Vaivars, J. Kleperis. A novel double cross-linked proton conducting membrane and the methods, Latvian Patent Application P-07-145, 2007.
6. BekkTech`s procedures for performing in-plane membrane conductivity testing. Report on US DOE Contract # DE-FC36-06GO16028 (2008), 18 p.
7. Fuel cell handbook, 7th edition, By EG&G Technical Services, Inc.
8. J. Zhang et all. High temperature PEM fuel cells. Journal of Power Sources 160 (2006), p. 872–891

CYSENI 2009, May 28-29, Kaunas, Lithuania
ISSN 1822-7554, www.cyseni.com

SEARCH FOR A METAL – INSULATOR TRANSITION IN MG2NIH4 FILMS THAT COULD BE SWITCHED BY MECHANICAL SENSITIVE STACKING FAULTS

M. Lelis, D. Milcius, E. Wirth
Lithuanian Energy Institute
Centre for Hydrogen Energy Technologies
Breslaujos St. 3, Kaunas, LT-44403 – Lithuania
Phone: +370 37 401909
E-mail: martynas@hydrogen.lt

D. Noréus, K. Jansson, U. Hålenius, T. Yokosawa, T. Sato
Stockholm University
Department of Structural Chemistry, Arrhenius Laboratory
S-106 91 Stockholm, Sweden
Phone: +46 8 161253
E-mail: dag@struc.su.se

ABSTRACT

We investigated whether thin film samples of Mg_2NiH_4 could be used in a switchable mirror or window device by utilizing the high to low temperature transition. In powder samples transition between a monoclinic conducting low temperature (LT) phase to an FCC non-conducting high temperature (HT) phase have been demonstrated in a mechanical reversible conductor–insulator transition. The new thin film Mg_2NiH_4 samples were produced by reacting hydrogen with magnetron sputtered Mg_2Ni films on quartz glass or CaF_2 substrates. But we could not obtain the monoclinic low temperature phase upon cooling the samples. Instead a cubic phase, related but not identical to the cubic high temperature phase, was formed at temperatures both below and above 510 K. TEM pictures revealed the new cubic phase in the films to have the same cell parameter as the FCC high temperature phase. But the symmetry was lower with similar streaking patterns as observed for the monoclinic low temperature phase. IR-spectroscopy indicated an identical vibrational frequency for the allowed stretching mode of the tetrahedral NiH_4-complex both in film and powder samples. Band gap measurements indicated a band gap of 2.3 eV for the films but 1.1 eV for monoclinic Mg_2NiH_4 powders. The films were transparent with a yellow colour that gradually deepened into red when heating up to 600 K in hydrogen. A typical first order phase transition from a low to high temperature phase could not be observed with DSC when heating through the low- to high temperature phase transition at 510 K. A severely strained film was revealed with optical microscopy in reflected light. This observed microstrain may reflect a prevailing intrinsic structural strain. We assume that strain in the film prevents the NiH_4-complexes from fully relaxing back into an ordered arrangement as in the monoclinic structure.

Keywords: Mg2NiH4, hydrogen storage, switchable mirrors, nanomaterials

1. INTRODUCTION

Mg_2NiH_4 became a target for many studies since its discovery by Reilly and Wiswall in 1968 [1]. Mg_2NiH_4 is built by 18 electrons, tetrahedral $[Ni(0)H_4]^{4-}$ complexes (with formal zero-valent nickel) which charge is counter balanced by Mg^{2+} ions. This implies unusual and interesting structural and bonding properties and makes it at first sight an unexisting compound. The central nickel atom is in a formal zero-valent d^{10} oxidation state surrounded by the four hydride ligands. Such low oxidation states usually require good electron accepting ligands, as for example carbonyl, cyanide or phosphine groups, where suitable ligand orbitals help to relieve the high electron density on the central atom. This is conventionally referred to as electron "back- donation". In homoleptic complexes with hydrogen as ligand, this is not directly possible. In solid state Mg_2NiH_4, the easily deformable electron density of the very polarizable hydride ion H^- offers a mechanism to relieve the high electron density indirectly, by transferring it to the counter ions in the solid state lattice. Theoretical calculations of the electron structure can be used to describe how the complex needs charge compensation support from the small and strongly polarizing Mg^{2+} counter ions for stability [2, 3]. This makes Mg_2NiH_4 too stable with respect to hydrogen release for most practical applications but also opens up for possibilities to modify the bond strength and stability by manipulating the lattice and it implies that lattice defects like disorder and impurities may have profound effects on stability as well as the electric properties. In the related hydrides Li_2PdH_2 and Na_2PdH_2, this leads to metallic conductivity, when a small number of electrons are transferred to the alkali metal matrix from the linear 14 electron $[PdH_2]$-complex with formal zero-valent d^{10} palladium [4, 5]. Mg_2NiH_4 is a semi conductor with a not too wide band gap of 1.7 eV similar to silicon. Doping from impurities or non stoichiometry can give it metal like electric conductivity, and both conductivity and stability is connected to the presence of a stacking fault [6, 7]. A pressed tablet of Mg_2NiH_4 without stacking faults is black and electric conductive. If the tablet is heated the monoclinic low temperature Mg_2NiH_4 structure undergoes a low to high temperature (HT) phase transition and become cubic, as the NiH_4-complexes become disordered and start to perform a fast reorientational motion above about 510 K. When cooled to room temperature the colour is changed to yellow-brown as the reorientational motion of the NiH_4-complex is frozen. After which the electric conductivity also is lost. The monoclinic structure is recovered but in addition a large number of stacking faults is introduced into the lattice, forming domains with presumably different orientated NiH_4-complexes. This was referred to a LT-2 modification of the low temperature phase of Mg_2NiH_4. The LT-1 modification, without stacking faults, is obtained if the Mg_2Ni alloy powder is hydrided well below the low to high temperature transition at about 510 K.

In the present paper we wanted to investigate the possibility to synthesize Mg_2NiH_4 thin films and to employ the LT↔HT phase transition phenomena in switchable mirrors. However, we observed high stability of Mg_2NiH_4 thin films and incapability to perform LT↔HT phase transition, thus the goal of the research was to investigate the micro structure of new Mg_2NiH_4 samples produced by physical vapour deposition technique and to examine the structural reasons for.

2. EXPERIMENTAL METHODOLOGY

2.1. Sample preparation

The Mg-Ni alloys were deposited on quartz glass and CaF_2 substrates using a physical vapour deposition system equipped with two independent direct current (DC) magnetron sputtering sources. A vacuum system consisting of mechanical and diffusion pumps enabled a base pressure of $2x10^{-3}$ Pa. Afterwards, Ar (99.999%) gas was injected to the vacuum chamber and its flow was controlled to keep a constant pressure of 0.4 Pa. Metallic Mg (99.98%) and Ni (99.999%) disks of 100 mm diameter each were used as target materials for the magnetron sources.

The calibration procedure is analogous to one described elsewhere [8], except that the sample weight was used instead of measuring the film thickness. After the film deposition rates of separate magnetrons at various currents had been determined, the exact experimental conditions were chosen to get a Mg/Ni atom ratio slightly above 2, thus to form an Mg_2Ni alloy with a small excess of Mg atoms as an impurity.

Hydrogenation of the Mg_2Ni thin films was carried out in a stainless steel hydriding cell. First, the samples were placed inside the cell which was thoroughly flushed with pure H_2 (99.999%). Then the cell was closed and the hydrogen pressure was increased up to 500 kPa, after which the cell was placed inside an autoclave and heated to 523 K. The hydrogen pressure was recorded and at 523 K it reached 600 kPa. These conditions were kept for 6 hours. After the hydrogenation the heating was turned off and the cell was left for 16 hours to cool down. Several identical samples were produced by this procedure.

For qualitative estimation of hydrogenation kinetics as well as chromatic properties thin film samples were hydrided in a colourless transparent glass tube instead of stainless steel container. In these experiments initial H_2 pressure was 500 kPa and temperature was continuously risen from 293 K up to 593 K.

Additionally, for the thorough comparison of material performance in thin film and powder forms, the Mg_2NiH_4 powder samples were made. For this purpose Mg_2Ni alloy ingot obtained from Energenics, USA (as their HYSTOR-301 Alloy) was taken as a starting material and exposed to 5 MPa hydrogen pressure. The hydrogenation temperature was kept constant at 433 K and 673 K for LT-1 (denoted as sample A) and LT-2 (denoted as sample B) modifications, respectively. Emergence of characteristic duplet and triplet peaks around diffraction angles of 22-25° in X-ray diffraction (XRD) data confirmed the formation of the different low temperature modifications of Mg_2NiH_4. However, as starting alloy contained about 10 wt % of extra magnesium to prevent the formation of the hydrogen non-absorbing $MgNi_2$, Mg hydride was also formed. Thus, we took half of the sample B and put additional Ni into it. Obtained mixture was grinded and repeatedly hydrided. Only reflections of Mg_2NiH_4 hydride were received in sample C (sample B rehydrided with additional Ni). Intensity of the peak at 23.7° was slightly increased suggesting that there were more microtwinnings in sample C than in sample B.

2.2. Sample characterisation

Before and after the hydrogenation, the Mg-Ni-H thin films were analysed at room temperature by XRD using a conventional DRON-6 diffractometer working in a Bragg-Brentano configuration (CuKα1 radiation with a flat terminal graphite monochromator). After this initial characterisation the hydrogenated thin films were scratched from the substrate and investigated by X-ray powder diffraction with a Guinier-Hägg focusing camera of 40 mm diameter, using monochromatized CuKα1 radiation (λ=1.5405980 Å). Si (a = 5.430879 Å at 25 ºC) was added as an internal standard. The obtained photographs were measured in an LS 18 film scanner [9]. The program SCANPI [10] was used to evaluate the photographs, and the program PIRUM [11] was used to index the patterns.

Transmission electron microscope (TEM) images of powder made from film material were recorded with a JEOL JEM-2000FX electron microscope. Differential scanning calorimeter (DSC) measurements were performed with a Perkin Elmer Pyris1 apparatus. From several films a total of 1.4 mg of scratched sample was collected.

Band gap evaluation of the thin films was performed by recording unpolarized optical absorption spectra in the UV/VIS/NIR range at room temperature with a Zeiss MPM800 single beam microscope-spectrometer using Zeiss Ultrafluar 10x lenses as condenser and objective. In the spectral range 400–800 nm (25000–12500 cm^{-1}), a 75W Xenon arc lamp served as a light source and a photomultiplier as detector. In the NIR spectral region, 800–2000 nm (12500–5000 cm^{-1}), a 100 W halogen lamp and a photoconductive PbS-cell were used as light source and detector, respectively. Spectra were recorded at a spectral resolution of 5 nm and the diameter of the circular measure spot was 380 µm. Bandgap evaluation of a conventionally hydrided and finely grinded powdered Mg_2NiH_4 samples A, B and C were made by recording the optical diffuse reflectance spectra in the NIR-range (2000-16000 cm^{-1}) at room temperature at a resolution of 2 cm^{-1} during 64 cycles with a Bruker Equinox 55 Fourier transform infrared spectroscopy (FTIR) spectrometer equipped with a diffuse reflectance accessory (Harrick). Measurements were performed with a halogen light source, a LN_2-cooled InSb detector and a CaF_2 beam splitter. The same apparatus at a resolution of 4 cm^{-1} was used for the IR spectrum measurements (800-2300 cm^{-1}) of Mg_2NiH_4 thin films deposited on CaF_2 substrate.

3. RESULTS

3.1. X-ray diffraction

XRD analysis of the as deposited metallic thin film showed it consists of non-oriented hexagonal-Mg_2Ni and preferentially oriented hexagonal-Mg (Fig. 1a). The thin film composition was measured to be in agreement with the prediction by the adjustment of the magnetron sputtering rates. After the hydrogenation at 525 K and 600 kPa, the metallic thin films changed their physical appearance from shiny metals to transparent orange colour films. XRD analysis of the hydrogenated films showed diffraction peaks that could be attributed to an FCC phase with a unit cell dimension of roughly a = 6.44 Å (Fig. 1b). This is in close agreement with the cubic HT phase of Mg_2NiH_4, which Gavra et al reported already in 1979 to exist only above about 510 K [12].

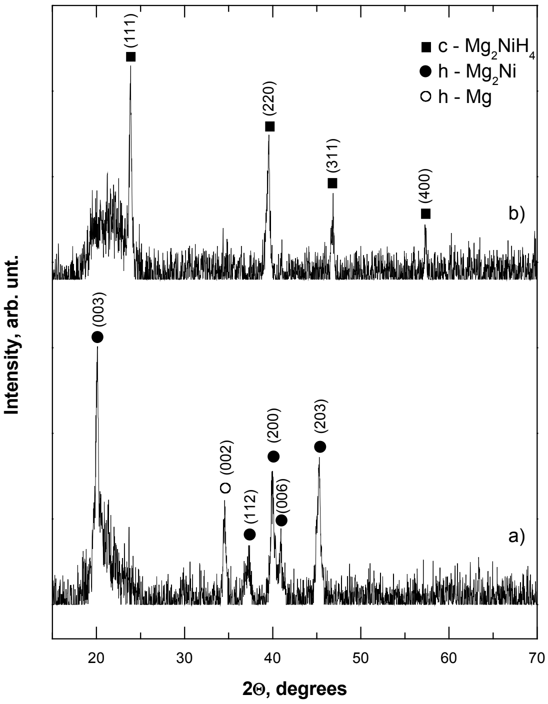

Fig. 1. X-ray diffractograms of a) as deposited and b) hydrided Mg-Ni thin films

Diffraction patterns recorded with Guinier-Hägg focusing camera (not shown here) at room temperature of Mg_2NiH_4 films scratched from the substrate confirmed the existence of only one crystallographic phase, with a unit cell parameter calibrated with Si to a = 6.508(4) Å, based on 6 observed diffraction lines. As the XRD analysis of the hydrogenated films were performed without an internal standard, we are not certain that the difference in unit cell dimension between the film and powder sample is significant.

3.2. Transmission electron microscope

A sample from the scratched film was additionally analysed by TEM. A small particle with a single domain gave a diffraction image shown in Fig. 2. The strong diffraction spots are in agreement with the FCC cell of the cubic HT phase of Mg_2NiH_4. However, in addition there are also weak peaks such as (001) and (110), which are forbidden in the cubic FCC structure, but would be allowed in the monoclinicly distorted low temperature phase of Mg_2NiH_4. A streaking phenomenon similar to what has been observed in monoclinic LT-2 Mg_2NiH_4 powder samples is also observed [13].

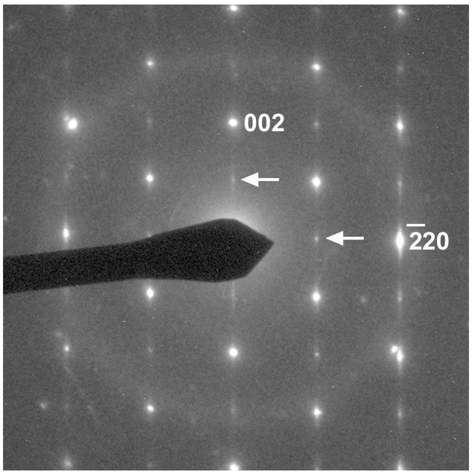

Fig. 2. TEM pattern taken from the scratched sample of Mg_2NiH_4. Main diffraction spots are indexed assuming an FCC structure, yielding the incident beam direction is [110]. But in addition weaker spots indicated by arrows, which ought to be forbidden in this symmetry, are observed

3.3. Differential scanning calorimetry (DSC)

In Mg_2NiH_4 produced from any Mg_2Ni alloy powder, the low to high temperature transition is easily observed with DSC at about 510 K. If the film of Mg_2NiH_4 is a static disordered HT-phase which is maintained at room temperature, it would be interesting to see the corresponding low- to high temperature transition by DSC. Freshly scratched Mg_2NiH_4 collected from several films was subjected to three DSC measurement cycles;

(i) First spectra was recorded as the sample was heated up to 543 K; then cooled down to 473 K and held isothermally for 10 minutes;
(ii) On the next cycle the sample was heated up to 558 K and cooled down to 453 K, where it was again kept isothermally for 10 minutes.
(iii) The sample was heated up to 558 K and then cooled down to the room temperature. The temperature scans were recorded with 10 K/min scan rates upon both heating and cooling.

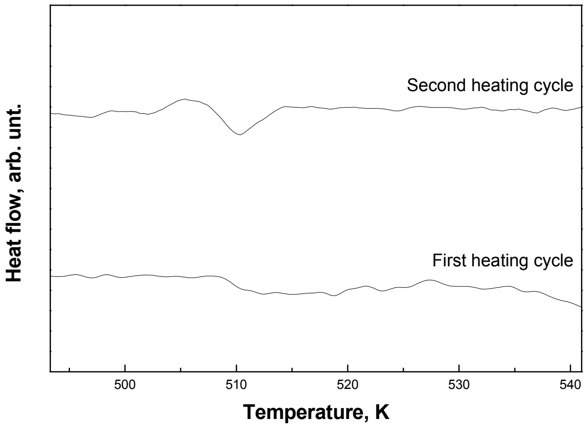

Fig. 3. Results from the DSC measurements received for the first and second heating cycles

Heat flow dependence on temperature for the first and second heating cycles is given in a Fig. 3. The curve from the third heating up is not shown as it exhibited no detectable change of the heat flow.

3.4. Band gap measurements

Theoretical calculations have shown a band gap of pure Mg_2NiH_4 to be around the value of 1.6-1.7 eV [14, 15]. However, experimental measurements of Mg_2NiH_4 thin film band gap have indicated higher values of more than 2 eV [15]. The same article suggested that the increased band gap width should depend on the MgH_2 content in the material. Thus we decided to check our thin film and powder samples for: (i) the influence from the magnesium hydride as well as (ii) the amount of the microtwinning (comparing powder samples B and C); and (iii) any differences in bandgap between powder and thin film materials.

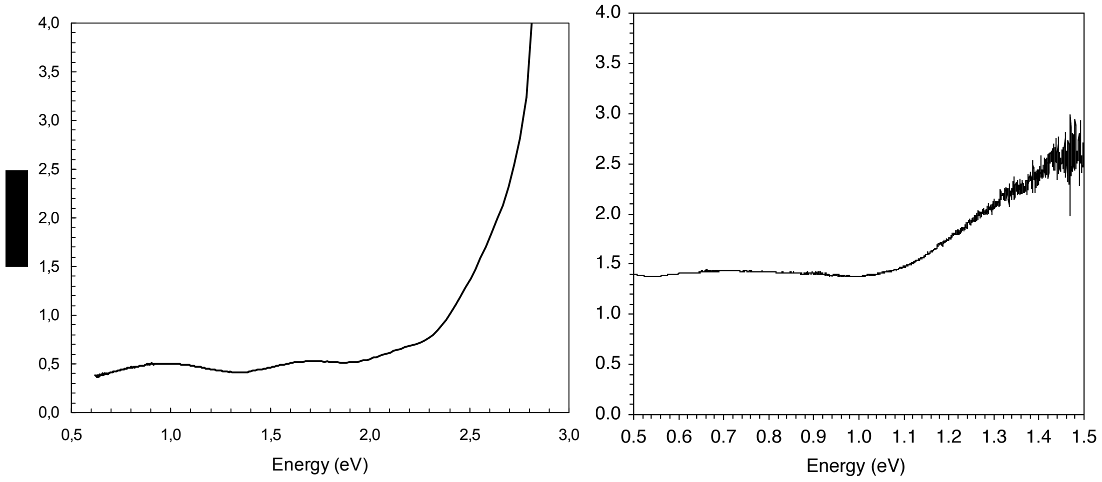

a) b)

Fig. 4. Band gap measurement results of hydrided Mg-Ni thin film (a) and hydrided Mg_2Ni powders (b)

As can be seen from Fig. 4a, the measured band gap width for the thin film reached 2.2 eV, which is considerably larger than the theoretical value. In contrast, band gap values for powder materials are much lower reaching just 1.1-1.2 eV (Fig. 4b) and virtually do not depend upon the content of magnesium hydride nor the amount of microtwinning.

3.5. IR spectrum of thin film

The FTIR measurements performed on the thin films are given in Fig. 5. The peak at 1650 cm^{-1} is in very good agreement with the reported asymmetric stretch in the tetrahedral NiH_4 complex as measured with powder samples [16–17]. Moreover, it has to be mentioned that no vibrations observed from MgH_2 (no peaks in 1100–1300 cm^{-1} region). Thus there are no signs of magnesium hydride in the FTIR spectrum.

3.6. Kinetics of the hydrogenation

As described above, we wanted to optically observe the switching of the metallic Mg_2Ni film by putting it in a transparent quartz tube under 500 kPa H_2 pressure and heating it up. Just after 2 min the film changed its colour to dark brown loosing its reflectivity (as the temperature reached 353 K). After 5 min as the sample reached 433 K the film had become orange and transparent indicating formation of the hydride. Upon further heating to 573 K it remained transparent but got a deeper reddish colour. Upon cooling down to room temperature the orange colour returned. However, during all the experiment after hydrogen adsorption film remained transparent resulting that LT↔HT phase transition does not occur and films are not suitable for switchable mirrors.

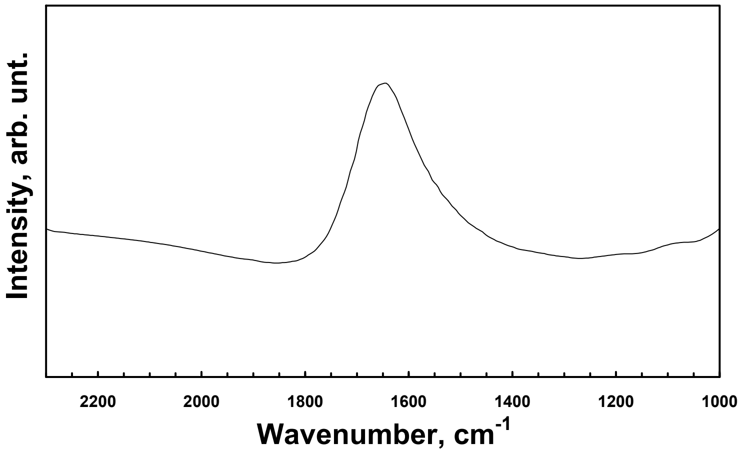

Fig. 5. FTIR measurement results of hydrided Mg_2Ni thin film on CaF_2 substrate

4. DISCUSSIONS

Examination by X-ray diffraction and TEM revealed the thin hydride films consist of a cubic Mg_2NiH_4 phase. This cubic phase is similar but not identical to the cubic FCC Mg_2NiH_4 high temperature phase. As this cubic phase existed in the Mg_2NiH_4 films at all the observed temperatures, we could not observe any drastic changes in electric properties of the films as the HT-LT transition, which is reversible in powder samples, does not occur in our films. A similar cubic phase has also been reported by groups who worked with different forms of ball milled Mg_2NiH_4 powders [18], ultra high pressure treated powders (up to 5.6 GPa) [19, 20] and thin film materials [21, 22]. Still it needs to be understood why the conventional monoclinic low temperature phases are under certain conditions not formed at ambient conditions and what is the mechanism for “locking” and maintaining this cubic phase of Mg_2NiH_4.

Rönnebro suggested that when ball milling, mechanical stress disturbs the lattice to such a degree that it is observed by X-ray diffraction to be cubic and similar to the high temperature form but not actually being it [18]. Strain is thus a likely candidate for favouring the formation of the cubic phase. The absence of a colour change of the thin film sample when heating under hydrogen atmosphere together with DSC measurements complements the information from XRD and TEM and shows that even after scratching of the film, the hydride stays in the cubic phase. Almost no change in the heat flow is observable for the first heating, but after the sample was cooled down to 473 K and reheated for the second time the phase transition peak appeared (Fig. 3), suggesting that interaction with the substrate might play an important role in maintaining the cubic phase. The DSC curves indicate that after being scratched from the substrate and heated up to 543 K the material shows same behaviour as ordinary Mg_2NiH_4 powders [23].

Moreover, FTIR suggests that there is no difference in tetrahedral $[NiH_4]$-complexes between powder and thin film material as Ni-H stretching peaks are identical. On the other hand the significant difference in the band gap reveals that there must be differences in the electron structure of monoclinic Mg_2NiH_4 powders and cubic thin film Mg_2NiH_4. In the monoclinic Mg_2NiH_4 powders, however, the band gaps show very little dependence on the amount of MgH_2 impurity and/or microtwinning. This suggests that the main difference between the phases lies in the ordering of rather similar $[NiH_4]$-complexes which corresponds to the slight distortions of the counterions network. In the cubic phases the complexes are disordered. In the cubic HT phase this disorder is dynamic but in the other cubic phases this disorder is probably static. Strain is the main culprit but there could be another explanation such as stabilization by some small amount of impurities, such as for example oxygen. These could unintentionally have been added by ball milling or during the sputtering of the films.

5. CONCLUSIONS

Thin Mg-Ni alloy films have been successfully formed by magnetron co-deposition and hydrogenated at high hydrogen pressure and temperature. XRD and TEM showed that hydrogenated film consisted of a cubic phase similar to the high temperature phase of Mg_2NiH_4. However, FTIR, TEM and partially DSC also showed that the cubic phase in the films had much in common with the monoclinic low temperature phase. The main difference was the bandgap, which would tend to be sensitive to also slight distortions of the counterions, in this type of hydride, where the stabilization of the formal zero valent NiH_4-complex is depend on the counter ion framework.

6. ACKNOWLEDGEMENT

This work has been financially supported by Lithuanian State Science And Studies Foundation project: “Development of multifunctional materials heterostructures for hydrogen fuel cells“(Contract No. C-15/2008/02, Acronym: H_2technologijos). M. Lelis activities were supported by the Nordic Energy research program project: “Nordic Centre of Excellence on Hydrogen storage Materials“(Contract No. 06-HYDRO-C15).

REFERENCES

1. J.J. Reilly, R.H.Jr. Wiswall, Inorg. Chem. 7 (1968), p. 2254.
2. U. Häussermann, H. Blomqvist, D. Noréus, Inorg. Chem. 41 (2002), p. 3684.

3. G.J. Miller, H. Deng, R. Hoffmann, Inorg. Chem., 33 (1994), p. 1330.
4. K. Kadir, M. Kritikos, D. Noréus, A. F. Andersen, J. Less-Common Met. 172-174 (1991), p. 36.
5. M. Olofsson-Mårtensson, U. Häussermann, J. Tomkinson, D. Noréus, J. Am. Chem. Soc. 122 (2000), p. 6960.
6. H. Blomqvist, D. Noréus, J. Appl. Phys. 91 (2002), p. 5141.
7. S. E. Guthrie, G. J. Thomas, D. Noréus, E. Rönnebro, Mater. Res. Soc. Symp. Proc. 513 (1998), p. 93.
8. J. Isidorsson, I.A.M.E. Giebels, M.Di Vece, R. Griessen, Solar and Switching Materials, 4458 (2001), p. 128–137.
9. K.E. Johansson, T. Palm, P.-E. Werner, J. Phys. E 13 (1980), p. 1289.
10. P.-E. Werner, L. Eriksson, S. Salomé, SCANPI, a program for evaluating Guinier photographs, Stockholm University, (1980).
11. P.-E. Werner, Ark. Kemi 31 (1969), p. 513.
12. Z. Gavra, M.H. Mintz, G. Kimmel and Z. Hadari. Inorg. Chem. 18 (1979), p. 3595.
13. D. Noréus, L. Kihlborg, J. Less-Comm. Met. 123 (1986), p. 233.
14. J. Isidorsson, I.A.M.E. Giebels, R. Griessen, M.Di Vece, Appl. Phys. Lett. 80 (2002), p. 2305.
15. W.R. Myers, L-W. Wang, T.J. Richardson and M.D. Rubin, J. of App. Phys. 91 (2002), p. 8.
16. S.F. Parker, K.P.J. Williams, T. Smith, M. Bortz, B. Bertheville, K. Yvon, Phys. Chem. Chem. Phys., 4 (2002), p. 1730–1737.
17. N. Patel, A. Kale, P. Mosaner, R. Checcheto, A. Miotello, G. Das, Ren. Energy, 33 (2008), p. 232–236.
18. E. Rönnebro, J.O. Jensen, D. Noréus, N.J. Bjerrum, J. of All. and Comp. 293–295 (1999), p. 146–149.
19. S. Yamamoto , Y. Fukai, E. Rönnebro, J. Chen, T. Sakai, J. of All. and Comp. 356–357 (2003), p. 697–700.
20. E. Rönnebro, Y. Fukai, S. Yamamoto, T. Sakai, J. of All. and Comp. 385 (2004), p. 276–282.
21. K. Tanaka, H. Tanaka, H. Kawaguchi, J. of All. and Comp. 330–332 (2002), p. 256–261.
22. Y. Suyun , O. Liuzhang, Z. Min, Rare metals 25 (2006), p. 295.
23. E. Rönnebro, D. Noréus, App. Surf. Science 228 (2004), p. 115–119.

INFLUENCE OF THE MEMBRANE UNIT LENGTH ON THE OUTPUT OF A GAS SEPARATOR IN EXTRACTION OF HYDROGEN FROM SYNTHESIS-GAS

N.V. Kolyago
A.V. Luikov Institute of Heat and Mass Transfer NAS Belarus
Belarus, 220072, Minsk, P. Brovka str., 15
Phone: +375(017) 284 12 42
E-mail: kolyago@hmti.ac.by

ABSTRACT

The influence of the membrane unit length on the output of a gas separator in extraction of hydrogen from synthesis-gas is considered. The effects of the convectional external diffusional and intramembrane resistances on the mass transfer in a gas-separating hollow-fiber and flat-frame elements with selectively-permeable membranes (all components of the mixture but with different velocities penetrate from the pressure channel through the walls of the separating element) are taken into account. The analysis of the output of a gas membrane unit is performed on the basis of the solution of the complex-conjugate problem on the mass transfer through the membrane and the mass exchange in the head channels under the specific boundary conditions on the selectively-permeable membrane. A analytic expression for membrane unit length as a function of is the purity of retentate and the hydrogen concentration in the synthesis-gas has been obtained. It has been established that excess surface area of the membrane markedly decreases the efficiency of hydrogen cleaning and the output of a membrane gas separator. The prospects of the use of various membranes for separation of hydrogen from the synthesis-gas have been assessed.

Keywords: hydrogen, mass transfer, gas separation, selectively-permeable membrane, flat-frame and hollow-fibrous elements, permeation rate, selectivity

1. INTRODUCTION

In the last 50 years there have been strong developments in technology for hydrogen separation from hydrogen-containing mixtures. Hydrogen has a number of advantages over other energy resources [1]:

- it has the highest heating capacity per mass unit (120 MJ/kg);
- it is non-toxic (by comparison, petroleum fuels are extremely toxic);
- it is less flammable than gasoline (the auto-ignition temperature of hydrogen is 500 ºC, auto-ignition temperature of gasoline is 280 ºC);
- it disperses quickly in the atmosphere (if a leak or spill does occur, the hydrogen becomes rapidly sparse and difficult to ignite, even if it does catch fire, it burns itself out very quickly);
- it stores safely (the tanks used to store hydrogen undergo demanding testing procedures, gasoline and diesel fuel tanks do not undergo stringent stress tests);
- it is an absolutely "pure" fuel (the single emission from burned hydrogen is water).

Synthesis-gas is a mixture of hydrogen and carbon monoxide predomination. Today it is one of the most widespread fuels and may be source of hydrogen-containing production. CO:H_2 ratio depends on method of synthesis-gas production and it is varying from 1:1 to 1:3 [2]. The urgency of hydrogen-containing mixtures separation problem and obtaining hydrogen for secondary usage is beyond doubt.

Today the membrane technology for hydrogen separation from synthesis-gas is the most promising. Among the advantages of the membrane method are the ecological purity of the process, reliable operation, compactness, explosion- and fire-safety, flexible characteristics of separation and their smooth regulation, independence of operation, and the mobility of the process – the possibility of continuous and periodic modes of operation [3]. This is due to the high selectivity and permeability of polymeric, carbonic and metal membranes to hydrogen and to the low cost of the membrane method of obtaining hydrogen [4]. However, not only must one solve a number of technological and instrumental problems for the membrane processes of gas separation to be commercialized, but one must also create calculation methods for these processes. Apparatus with flat-frame and hollow-fiber membrane modules are used for separation of gas mixtures [5].

To calculate modules incorporating membranes one has to solve a conjugate problem of convective mass transfer in the head channel and of mass transfer through the membrane. Such a problem for a semipermeable membrane has been posed for the first time and solved in [6, 7]. In what follows, we consider mass transfer of a binary gas mixture in the membrane element with a selectively permeable membrane (i.e. with a membrane having a nonideal selectivity $\beta \neq \infty$), since precisely this situation is realized in practice. In the separation of synthesis-gas, one is usually dealing with selectively permeable membranes; therefore, all components of the mixture but with different velocities penetrate from the head channel through the walls of the separating element. Since the driving force of component transfer is determined by the difference of the chemical potentials in head and drain channels, the permeation rate of each component varies with membrane-element length and is dependent on the thermodynamic and hydrodynamic parameters of the process. Consequently, the design of a membrane module is of fundamental importance in the development of high efficiency membrane processes.

Membrane unit length is the starting point to design membrane apparatus. Once the membrane unit length is defined, a membrane module can be designed taking into account considerations such as output, maintainability, operability, efficiency, membrane deterioration, and costs.

The aim of the present investigation is to determine the character of the dependence of the output of gas separator on the membrane unit length in separation of hydrogen from synthesis-gas, which ultimately will make it possible to develop a highly efficient membrane apparatus. The effects of the convectional external diffusional and intramembrane resistances on the mass transfer in a gas-separating hollow-fiber and flat-frame elements with selectively permeable membranes are taken into account.

2. MATHEMATICAL MODEL

The base unit of the membrane apparatus is the gas-separating module fabricated on the basis of flat-frame or hollow-fiber elements made from polymeric and carbonic membrane material. A syntethisis-gas with a hydrogen concentration c_0 enters into the head channel of the membrane element (Fig. 1). As a result of the different penetration rates of hydrogen and carbon monoxide during flow through the membrane, the composition of the mixture undergoes a change. In the head channel the fraction of the hydrogen is decreased as a result of passage through the drainage channel and the concentration of the carbon monoxide is increased. The gas mixtures from the head and drainage channels are delivered from the membrane element. The resistance of the drainage channel is not taken into account in this work.

When gas separation is implemented in practice, gas separation circuits are used, including hollow-fiber and flat-frame elements based on the membranes with different separation characterictics (Tab. 1).

The flow in the head channel is two-dimensional and symmetrical relative to the channel axis, laminar, steady, and fully developed at the entrance to the channel. The synthesis-gas is incompressible, the process is isothermal, the coefficients of viscosity and diffusion are constant. The bulk viscosity and barodiffusion are neglected. For diffusion of gases in polymers with a low critical temperature the coefficients of permeability Λ are usually independent of gas concentration in the membrane and are considered constant.

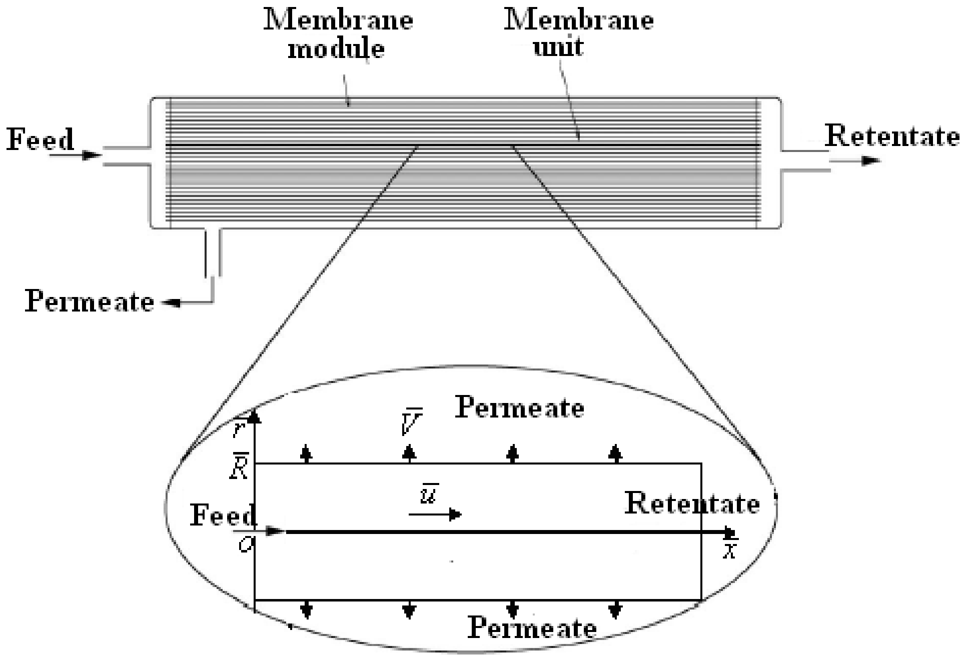

Fig. 1. Diagram of membrane separation of synthesis-gas mixture: membrane unit –cell containing a drainage and head channels, a membrane to separate the streams of feed, permeate, and retentate; membrane module – manifold assembly containing membrane unit; permeate – stream containing penetrants that leaves a membrane module; retentate – stream that has been depleted of penetrants that leaves the membrane modules without passing through the membrane to the downstream

Table 1. The physicochemical properties of a membrane

№	membrane material	type of unit	$\delta_m \cdot 10^6$, m	$\Lambda_1 \cdot 10^{15}$, mole·m/(m^2·Pa·sec)	β	references
1	cellulose acetate “Gasept”	flat-frame	0.1	11	41	[5]
2	polyimide “Du Pont”	flat-frame	0.1	6.7	74	[5]
3	kapton	flat-frame	0.2	20	39	[8]
4	polysulfone “Monsanto”	hollow-fiber	0.1	7.3	32	[5]
5	cellulose acetate “Du Pont”	hollow-fiber	1	89.4	122.4	[5]
6	phenolformaldehyde	hollow-fiber	5	705.6	32	[8]

The equations of continuity, motion, and of convective diffusion in a dimensionless form are

$$\frac{\partial u}{\partial x}+r^{-\alpha}\frac{\partial\left(r^{\alpha}\upsilon\right)}{\partial r}=0, \qquad (1)$$

where $u=\overline{u}/u_0$ is the dimensionless longitudinal projection of the velocity; $\overline{u}$ is the longitudinal projection of the velocity, m/sec; u_0 is the mean flow rate at the input of the channel, m/sec; $x=\bar{x}/L$ is the dimensionless longitudinal coordinate; $\bar{x}$ is the longitudinal coordinate, m; L=1 m is the caliber of length of the channel, m; $r=\bar{r}/R$ is the dimensionless radial coordinate; $\bar{r}$ is the radial coordinate, m; R is the radius (halfwidth) of the channel, m; α = 0 corresponds to a flat-frame unit and α = 1 corresponds to a hollow-fiber unit; $\upsilon=\bar{\upsilon}L/(u_0R)$ is the dimensionless radial projection of the velocity; $\bar{\upsilon}$ is the radial projection of the velocity, m/sec;

$$\frac{\partial p}{\partial x}=\frac{1}{\mathrm{Re}\,\varepsilon}\left[r^{-\alpha}\frac{\partial}{\partial r}\left(r^{\alpha}\frac{\partial u}{\partial r}\right)\right],\qquad \frac{\partial p}{\partial r}=0, \tag{2}$$

where $p=\bar{p}/(\rho u_0^2)$ is the dimensionless pressure; $\bar{p}$ is the pressure, Pa; ρ is the density, kg/m^3; $\mathrm{Re}=u_0R/\nu$ is Reynolds number; ν is the kinematic viscosity, m^2/sec; $\varepsilon=R/L$ is the ratio between two characteristic sizes of the channel;

$$u\frac{\partial c}{\partial x}+\upsilon\frac{\partial c}{\partial r}=\frac{1}{\mathrm{Pe}_D\varepsilon}r^{-\alpha}\frac{\partial}{\partial r}\left(r^{\alpha}\frac{\partial c}{\partial r}\right), \tag{3}$$

where c is the concentration of the hydrogen; $\mathrm{Pe}_D=u_0R/D$ is the diffusion Peclet number; D is the diffusion coefficient, m^2/sec;
at the boundary conditions
at the input to the channel (at x = 0):

$$c=c_0,\qquad p=p_0,\qquad u=\frac{\alpha+3}{2}\left(1-r^2\right), \tag{4}$$

where substript 0 is the value at the input of the channel;
at the axis (plane) of symmetry (at r = 0):

$$\frac{\partial u}{\partial r}=0,\qquad \upsilon=0,\qquad \frac{\partial c}{\partial r}=0, \tag{5}$$

on the membrane (at r = 1)

$$u=0, \tag{6}$$

$$\left.\left[\left(1-c(x,r)\right)\upsilon(x,r)+\frac{1}{\mathrm{Pe}_D\varepsilon}\frac{\partial c(x,r)}{\partial r}\right]\right|_{r=1}=\frac{\Lambda_2M_2\left(1-c_{\mathrm{w}}(x)\right)p(x)u_0}{\delta_{\mathrm{m}}\varepsilon}, \tag{7}$$

$$\upsilon(x,1)=V(x)=\left(\Lambda_1 M_1 c_{\mathrm{w}}(x)+\Lambda_2 M_2\left(1-c_{\mathrm{w}}(x)\right)\right)\frac{p(x)u_0}{\delta_{\mathrm{m}}\varepsilon}, \tag{8}$$

where $V=\bar{V}L/(u_0 R)$ is the dimensionless penetration rate through the membrane; $\bar{V}$ is the penetration rate through the membrane, m/sec; Λ is the penetrability coefficient, mole·m/(Pa·m^2·sec); M is the molar mass, kg/mole; δ_{m} – effective thickness of the membrane, m; substripts: w is the value at the wall of the channel; 1 and 2 are the hydrogen and carbon monoxid.

In solving the equations of continuity and motion (1), (2), subject to boundary conditions (4)–(6), we find the distributions of the rates and pressure in the membrane channel [6]:

$$u(x,r)=\frac{\alpha+3}{2}\left(1-(\alpha+1)\int_0^x V(x)dx\right)\left(1-r^2\right), \tag{9}$$

$$\upsilon(x,r)=\frac{(\alpha+1)(\alpha+3)}{2}V(x)\left(\frac{r}{\alpha+1}-\frac{r^3}{\alpha+3}\right), \tag{10}$$

$$p(x)=p_0-\frac{(\alpha+1)(\alpha+3)}{\mathrm{Re}\,\varepsilon}\int_0^x\left(1-(\alpha+1)\int_0^x V(x)dx\right)dx. \tag{11}$$

The checking of the model was made on the bases of experiments and on the bases of limit case (ideal agitation model, ideal displacement model) [10].

When Eqs. (1)–(3) are solved with (4)–(11), we obtained the equation for the most important characteristic of the membrane gas separation – the rate of mass transfer through the membrane V [9]:

$$\begin{aligned}
V(x)=&\frac{(\alpha+5)(\alpha+7)}{2(5\alpha+17)\mathrm{Pe}_D\varepsilon}\left(\frac{\Lambda_1 M_1 u_0}{\delta_{\mathrm{m}}\varepsilon}p(x)\frac{(5\alpha+17)\mathrm{Pe}_D\varepsilon}{(\alpha+5)(\alpha+7)}+1-\right.\\
&-\left[\left(\frac{\Lambda_1 M_1 u_0}{\delta_{\mathrm{m}}\varepsilon}p(x)\frac{(5\alpha+17)\mathrm{Pe}_D\varepsilon}{(\alpha+5)(\alpha+7)}+1\right)^2-4\frac{\Lambda_1 M_1 u_0}{\delta_{\mathrm{m}}\varepsilon}p(x)\frac{(5\alpha+17)\mathrm{Pe}_D\varepsilon}{(\alpha+5)(\alpha+7)}\left(\frac{\Lambda_2 M_2}{\Lambda_1 M_1}+1+\right.\right.\\
&+\frac{1}{(\alpha+1)^{-1}-\int_0^x V(x)dx}\left(\frac{\Lambda_2 M_2 u_0}{\delta_{\mathrm{m}}\varepsilon}\left(p_0 x-\frac{(\alpha+1)(\alpha+3)}{2\mathrm{Re}\,\varepsilon}x^2\right)-(\alpha+1)^{-1}\times\right.\\
&\left.\left.\left.\left.\times\left[\left(1+\left(\frac{\Lambda_2 M_2}{\Lambda_1 M_1}-1\right)\frac{\Lambda_1 M_1 u_0}{\delta_{\mathrm{m}}\varepsilon}p_0\frac{(5\alpha+17)\mathrm{Pe}_D\varepsilon}{(\alpha+5)(\alpha+7)}\left(c_0\left(1-\frac{\Lambda_2 M_2}{\Lambda_1 M_1}\right)+\frac{\Lambda_2 M_2}{\Lambda_1 M_1}\right)\right)(1-c_0)+c_0\frac{\Lambda_2 M_2}{\Lambda_1 M_1}\right]\right)\right)\right]^{\frac{1}{2}}\right).
\end{aligned} \tag{12}$$

3. INFLUENCE OF THE MEMBRANE UNIT LENGTH ON THE OUTPUT OF A GAS SEPARATOR

3.1. Determination of the membrane unit length

Distribution of hydrogen concentration on a wall of the head channel [9] allows to conditionally partition membrane element into three zones (Fig. 2).

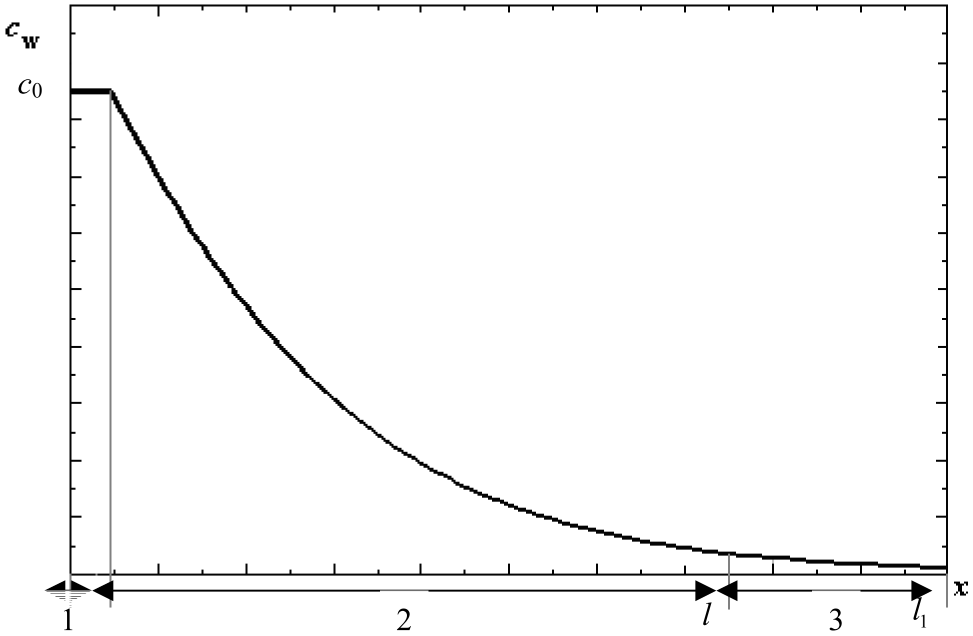

Fig. 1. Concentration of hydrogen on the membrane surface: 1 – the first zone; 2 – the second zone; 3 – the third zone

There is an area of constant hydrogen concentration in the first zone at the plane (axis) of channel symmetry. There is an area of varying concentration at the channel wall. Estimation shows that for gas mixtures with a laminar mode of flow the zone of diffusion boundary layer occupies a small portion of the membrane channel length and can be neglected [11].

There isn't area of constant hydrogen concentration in the second zone at the plane (axis) of channel symmetry. The basic part of hydrogen passes into the drainage channel, so that penetrate density increases and hydrogen concentration decreases. Therefore, depletion of hydrogen from synthesis-gas occurs and synthesis-gas purification efficiency increases.

Since the total flux depends on the partial flux, at small values of hydrogen concentration at the head channel wall hydrogen concentrations depends only slightly on the longitudinal coordinate in the third zone (the unit length with the third zone is l_1). Fine synthesis-gas cleaning and carbon monoxide permeation into the drainage channel occurs in the given zone basically. The diminution of membrane unit length by the third zoneis is necessary to obtain pure hydrogen.

Hence, working membrane unit length is the length of the second zone l.

3.2. Calculation of the membrane unit length

The membrane unit length l is determined by the penetration rate $V(x)$. It depends on the membrane selectivity β, the physical properties of synthesis-gas (c, D, M_1, M_2, ν, ρ), the physicochemical properties of a membrane (Λ_1, Λ_2), the technological parameters of the process ($\overline{p}$, u_0, T), and the geometry and dimensions of the membrane unit (α, R, δ_{m}). By employing Eq. (12) it is possible to discuss the working length of flat-frame unit and the working length of hollow-fiber unit. The work [10] seeks to develop the procedure of solution of Eq. (12).

The membrane separation of gases is characterized by small values of a transverse Peclet number. As a result the characteristic feature for membrane separating hydrogen from synthesis-gas

$$\frac{(17+5\alpha)\mathrm{Pe}_D\,\varepsilon}{(5+\alpha)(7+\alpha)}\frac{\Lambda_1 M_1 u_0}{\delta_\mathrm{m}\varepsilon}p(x)<0.15$$

for real-life membranes. Therefore, we may expand the Eq. (12) into Taylor's series. For this purpose we introduce the notation

$$\theta'(x)=V(x);$$

$$\theta(x)=\int_0^x V(x)\,dx;$$

$$\Omega_1=\frac{\Lambda_2 M_2}{\Lambda_1 M_1}+\frac{\frac{\Lambda_2 M_2 u_0}{\delta_\mathrm{m}\varepsilon}\left(p_0 x-\frac{(\alpha+1)(\alpha+3)}{2\,\mathrm{Re}\,\varepsilon}x^2\right)-(\alpha+1)^{-1}\left(1-c_0+c_0\frac{\Lambda_2 M_2}{\Lambda_1 M_1}\right)}{(\alpha+1)^{-1}-\theta(x)};$$

$$\Omega_2=\frac{(1-c_0)\left(\frac{\Lambda_2 M_2}{\Lambda_1 M_1}-1\right)\left(c_0\left(1-\frac{\Lambda_2 M_2}{\Lambda_1 M_1}\right)+\frac{\Lambda_2 M_2}{\Lambda_1 M_1}\right)}{1-(\alpha+1)\theta(x)};$$

$$\gamma=\frac{(5\alpha+17)\mathrm{Pe}_D}{(\alpha+5)(\alpha+7)}\frac{\Lambda_1 M_1 u_0 p(x)}{\delta_\mathrm{m}};$$

and pass from the variable $V(x)$ to a new variable $\theta(x)$

$$\theta'(x)=\frac{(\alpha+5)(\alpha+7)}{2(5\alpha+17)\mathrm{Pe}_D\varepsilon}\left(\gamma+1-\left[(1-\gamma)^2-4\gamma(\Omega_1-\Omega_2\gamma)\right]^{\frac{1}{2}}\right)=\frac{(\alpha+5)(\alpha+7)}{2(5\alpha+17)\mathrm{Pe}_D\varepsilon}\times$$
$$\times\left[(2+2\Omega_1)\gamma+\left(2\Omega_1+2\Omega_1^2-2\Omega_2\right)\gamma^2+\left(2\Omega_1+6\Omega_1^2+4\Omega_1^3-2\Omega_2-4\Omega_1\Omega_2\right)\gamma^3+\ldots+R_n(\gamma)\right], \tag{13}$$

where $|R_n(\gamma)|=\left\{\begin{array}{l}\gamma_0=0\\ \gamma_0+\Upsilon(\gamma-\gamma_0)=\Upsilon\gamma\\ 0<\Upsilon<1\end{array}\right\}=\dfrac{\left(1+\gamma-\sqrt{(1-\gamma)^2-4\gamma(\Omega_1-\Omega_2\gamma)}\right)\Big|_{\Upsilon\gamma}^{(n+1)}\cdot\gamma^{n+1}}{(n+1)!}$ is the Lagrange's remainder term. Within 10^{-2} inclusively (i.e. $R_n(\gamma)<10^{-2}$), number of term n equal to one. The expansion (13) is given by

$$\theta'(x)=\frac{(\alpha+5)(\alpha+7)}{2(5\alpha+17)\mathrm{Pe}_D\varepsilon}(2+2\Omega_1)\gamma=\frac{\Lambda_1 M_1 u_0}{\delta_\mathrm{m}\varepsilon}p(x)\times$$
$$\times\left(\frac{\Lambda_2 M_2}{\Lambda_1 M_1}+1+\frac{\frac{\Lambda_2 M_2 u_0}{\delta_\mathrm{m}\varepsilon}\left(p_0 x-\frac{(\alpha+1)(\alpha+3)}{2\,\mathrm{Re}\,\varepsilon}x^2\right)-(\alpha+1)^{-1}\left(1-c_0+c_0\frac{\Lambda_2 M_2}{\Lambda_1 M_1}\right)}{(\alpha+1)^{-1}-\theta(x)}\right). \tag{14}$$

The equation (14) is the ordinary nonlinear differential equation of first order in separable variables.

We integrate relation (14) with respect to the coordinate *x*. Then we obtain the equation for the process of hydrogen separation of the synthesis-gas in the gas separating element with selectively permeable membranes:

$$1+\frac{\frac{\Lambda_2 M_2 u_0}{\delta_\mathrm{m}\varepsilon}(\alpha+1)\left(\frac{\Lambda_1 M_1 u_0}{\delta_\mathrm{m}\varepsilon}\left(p_0 x-\frac{(\alpha+1)(\alpha+3)}{2\,\mathrm{Re}\,\varepsilon}x^2\right)-\theta(x)\right)}{\left(\frac{\Lambda_1 M_1 u_0}{\delta_\mathrm{m}\varepsilon}-\frac{\Lambda_2 M_2 u_0}{\delta_\mathrm{m}\varepsilon}\right)(c_0-1)}=$$

$$=\left[1+\frac{\frac{\Lambda_2 M_2 u_0}{\delta_\mathrm{m}\varepsilon}(\alpha+1)\left(p_0 x-\frac{(\alpha+1)(\alpha+3)}{2\,\mathrm{Re}\,\varepsilon}x^2\right)-(\alpha+1)\theta(x)}{c_0\left(1-\frac{\Lambda_2 M_2}{\Lambda_1 M_1}\right)}\right]^{\frac{\Lambda_2 M_2}{\Lambda_1 M_1}} \qquad (15)$$

In the case of a semipermeable membrane ($\Lambda_2 = 0$), relation (15) agrees with the solution of [7].

Accounting for the condition (15) and boundary condition (8), the concentration of hydrogen at the wall of the membrane channel becomes

$$c_\mathrm{w}(x)=\frac{-(\alpha+1)\theta(x)+\frac{\Lambda_2 M_2 u_0}{\delta_\mathrm{m}\varepsilon}(\alpha+1)\left(p_0 x-\frac{(\alpha+1)(\alpha+3)}{2\,\mathrm{Re}\,\varepsilon}x^2\right)+c_0\left(1-\frac{\Lambda_2 M_2}{\Lambda_1 M_1}\right)}{\left(1-\frac{\Lambda_2 M_2}{\Lambda_1 M_1}\right)\left(1-(\alpha+1)\theta(x)\right)}. \qquad (16)$$

Giving the hydrogen concentration on membrane surface at the downstream of the head channel with accaunt for Eq. (16), we find analytic formula for the working length of the membrane unit:

$$1+\frac{\frac{\Lambda_2 M_2}{\Lambda_1 M_1}\left(\frac{\Lambda_1 M_1 u_0}{\delta_\mathrm{m}\varepsilon}\left(p_0 l-\frac{(\alpha+1)(\alpha+3)}{2\,\mathrm{Re}\,\varepsilon}l^2\right)(\alpha+1)\left(1-c_\mathrm{w}(l)\right)-c_0+c_\mathrm{w}(l)\right)}{(c_0-1)\left(1-c_\mathrm{w}(l)\left(1-\frac{\Lambda_2 M_2}{\Lambda_1 M_1}\right)\right)}=$$

$$=\left[1-\frac{\frac{\Lambda_2 M_2 u_0}{\delta_\mathrm{m}\varepsilon}(\alpha+1)\left(p_0 l-\frac{(\alpha+1)(\alpha+3)}{2\,\mathrm{Re}\,\varepsilon}l^2\right)c_\mathrm{w}(l)+\left(c_0-c_\mathrm{w}(l)\right)}{\left(1-c_\mathrm{w}(l)\left(1-\frac{\Lambda_2 M_2}{\Lambda_1 M_1}\right)\right)c_0}\right]^{\frac{\Lambda_2 M_2}{\Lambda_1 M_1}}. \qquad (17)$$

Considering selectivity as the ratio of the resistance to mass transfer of carbone monoxid through membrane to that of hydrogen, Eq. (17) becomes

$$1+\frac{\left(\frac{\Lambda_1 M_1 u_0}{\delta_\mathrm{m}\varepsilon}\left(p_0 l-\frac{(\alpha+1)(\alpha+3)}{2\,\mathrm{Re}\,\varepsilon}l^2\right)(\alpha+1)\left(1-c_\mathrm{w}(l)\right)-c_0+c_\mathrm{w}(l)\right)}{\beta(c_0-1)\left(1-c_\mathrm{w}(l)\left(1-\beta^{-1}\right)\right)}= \qquad (18)$$

$$=\left[1-\frac{\dfrac{\Lambda_2 M_2 u_0}{\delta_{\mathrm{m}}\varepsilon}(\alpha+1)\left(p_0 l-\dfrac{(\alpha+1)(\alpha+3)}{2\,\mathrm{Re}\,\varepsilon}l^2\right)c_{\mathrm{w}}(l)+\left(c_0-c_{\mathrm{w}}(l)\right)}{\left(1-c_{\mathrm{w}}(l)\left(1-\beta^{-1}\right)\right)c_0}\right]^{\frac{1}{\beta}}.$$

3.3. The findings of investigation

The output is characterized by the membrane unit length and the process conditions (the temprature of the synthesis-gas, the pressure at the head channel, membrane characteristics, ect.). The output of gas separator and the surface area of the membrane in the module F are related by the kinetic relation

$$q_1=\int_0^F V_1(x)\,dF. \tag{19}$$

There study of membrane element is carried out with the parameters $M_1=2\cdot10^{-3}$ kg/mole; $M_2=28\cdot10^{-3}$ kg/mole; c_0= 0.2 mass fraction, T = 300 K, $\overline{p}_0$ = 1 MPa, R = 10^{-3} m, ν = $5.26\cdot10^{-6}$ m^2/s; D = $4.36\cdot10^{-7}$ m^2/s; u_0 = 0.5 m/s; $c_{\mathrm{w}}(l)=0.01c_0$. To insure that the membrane surface area of flat-frame unit and the membrane surface area of hollow-fiber unit are $2\pi Rl$, we set the width of flat-frame unit equal to πR. Having been given the hydrogen concentration on membrane surface at the downstream of the head channel corresponding to 1 per cent of the hydrogen concentration at the input of the head channel (i.e. $c_{\mathrm{w}}(l)=0.01c_0$), we calculate the major features of gas separator (the change of the output per unit length with the diminution of membrane unit length by the third zoneis is $\Delta q_1,\%$; the change of the efficiency of hydrogen recovery from synthesis-gas is $\Delta\beta,\%$; in case of l the hydrogen concentration in permeate is $c^{permeate}(l)$; in case of l_1 the hydrogen concentration in permeate is $c^{permeate}(l_1)$; the change of the efficiency of permeate cleaning is $\Delta c^{permeate},\%$; the change of separation factor). Based on data from Table 1, the findings of investigation are reproduced in the Table 2.

Table 2. The major features of membrane gas separator

№ membrane	**1**	**2**	**3**	**4**	**5**	**6**
$\Delta q_1,\%$	28.70	29.63	28.62	22.61	24.51	22.23
$\Delta\beta,\%$	-0.88	-0.82	-0.86	-7.17	-7.25	-7.67
$c^{permeate}(l)$	0.70	0.80	0.69	0.77	0.92	0.77
$c^{permeate}(l_1)$	0.62	0.74	0.61	0.71	0.90	0.72
$\Delta c^{permeate},\%$	11.36	8.12	11.70	7.02	2.66	6.77
$\Delta\varphi,\%$	19.56	23.42	19.17	16.76	22.45	16.59

From the tabular data, it has been established that excess surface area of the membrane decreases the output per unit length by 30 %, the efficiency of permeate cleaning by 12%, the separation factor by 20%, and only increases the efficiency of hydrogen recovery from synthesis-gas by 7%. The choice of optimum membranes, the construction of the membrane plant is economically justified in the analysis of the working length of gas separation unit.

Developed mathematical model can be successfully applied by developer and research activities for gas separation process modeling in semipermeable and selectively-permeable membrane elements at membrane equipment development for the purpose of technological processes optimization.

4. CONCLUSIONS

1. The analytic formulas for the working length of flowing membrane flat-frame and hollow-fiber elements for hydrogen extraction from synthesis-gas with laminar flow are founded on the basis of the created theory of baromembrane gas separation in the presence of external and intramembrane diffusion resistances, membrane selectivety.
2. It has been established that excess the length of membrane unit and, consequently, excess surface area of the membrane markedly decrease the output of membrane gas separator per unit length, the efficiency of permeate cleaning, the separation factor. Such approach ultimately will make it possible to develop a highly efficient membrane apparatus.

5. ACKNOWLEDGEMENT

This work was carried out with support by the National Academy of Sciences of Belarus through the project “Hydrogen-08”. The author is grateful to Prof. V.I. Baikov for useful discussions of results.

REFERENCES

1. Separation Technology R&D Needs for Hydrogen Production in the Chemical and Petrochemical Industries // A Chemical industry Vision 2020 Initiative to help identity future R&D needs, http://www.chemicalvision2020.org/pdfs/h2_report.pdf, 2005.
2. O.L. Amosova, O.V. Malykh, V.V. Tepljakov Integrated membrane/PSA method for hydrogen recovery from multicomponents gas mixture of biotechnology and petrochemistry // Membranes, 2008, vol. 38, № 2, p. 26–39.
3. A. Bazile, F. Galluchchi, A. Yullianelli. Researches of Institute membrane technologies (National centre of science of Italy ITM-CNR) on reception of hydrogen in membrane plants // Membranes, 2007, Vol. 34, № 2, p. 3–22.
4. M. Mundschau Hydrogen separation using dense composite membranes // Springer; 2007.
5. Yu. I. Dytnerskii, V. P. Brykov, and G. G. Kagramanov . Membrane Separation of Gases [in Russian]//Khimiya, Moskow, 1991.
6. V. I. Baikov, I. Yu. Kostareva, and N. V. Primak. Theory of membrane separation of binary gas mixtures// Journal of Engineering Physics and Thermophysics, 2004, Vol. 77, № 5, p. 999–1004.
7. N. Primak Qualitative analysis of the length of the gas separation membrane unit in separating hydrogen from synthesis-gas // Proc. of annual conference of young scientists on energy issues „CYSENI 2008“, Kaunas: LEI. 2008, p. 1–7.
8. Saufi S.M., Ismail A.F. Fabrication of carbon membranes for gas separation – a review // Carbon, 2004, Vol. 42, p. 241–259.
9. V.I. Baikov, N.V. Primak. Membrane selective separation of binary gas mixtures// Journal of Engineering Physics and Thermophysics, 2007, vol.80, № 2, p. 382-387.
10. V.I. Baikov, N.V. Primak. Rate of penetration at selective membrane gas separation // IFZh, 2008, Vol.81, № 3, p. 421–426.
11. I.Yu. Kostareva and N.V. Primak Gas separation in a flat-frame module with nonideal selectivity // Vestsi Nats. Akad. Navuk, Ser. Fiz.-Tekh. Navuk, 2005, №. 5, p. 81–85.

CYSENI 2009, May 28-29, Kaunas, Lithuania
ISSN 1822-7554, www.cyseni.com

HEAT PIPES FOR FUEL CELLS THERMAL MANAGEMENT

O.S. Filatova
A.V. Luikov Heat and Mass Transfer Institute
of the National Academy of Sciences of Belarus
P. Brovki str. 15, 220072 Minsk – Belarus
Phone: +375 17 284 2138
Email: filatova@hmti.ac.by

ABSTRACT

A question of energy production and efficient consumption is of greatest importance for world ecological and economic development strategy. Numerous difficulties concerned with decrease of fossil fuel reserves determine onrush of new technologies dealing with application of alternative renewable energy sources and systems of energy regeneration.

Fuel cells are promising energy sources due to their performance coefficient (40–60%), environmental safety and high reliability. Nowadays extensive production and wide deployment are constrained by expensive value of manufacturing technology, materials and catalysts cost, which are mostly conditioned by novelty and insufficiency of researches in the given area.

For the most efficient and steady functioning of fuel cells special conditions are necessary. It is important to ensure required temperature of incoming reagents, uniform temperature distribution on bipolar plate surface and removal of releasing heat from fuel cells stack. Heat pipes use phase change phenomenon and are able to solve these problems owing to their extremely high thermal conductivity coefficient, low thermal resistance and absence of additional energy consumption. Depending on power dissipation in variety of constructions of fuel cells different types of researched and developed heat pipes may be used (micro and miniature heat pipes (1–100 W), loop, pulsating, and sorption heat pipes (100–1000 W)).

Keywords: fuel cells thermal management, micro and miniature heat pipes, capillary structure

1. INTRODUCTION

A modern scale of production of electronic devices of different types and fields of application requires vast energy inputs. Continuous decrease of available traditional fuel resources (petroleum, coal, natural gas, etc.) leads to necessity of looking for new energy sources. As a result, technologies dealing with use of alternative energy sources, regeneration and trigeneration systems have received a wide distribution. Together with tendencies of the most effective consumption of energy resources and applying of efficient technologies numerous investigations have been directed to development of a new field, namely hydrogen energetic. Researches connected with questions of hydrogen energy devices establishments received a wide distribution. In addition, questions of hydrogen transportation and storage have been getting encouragement, as they are a necessary condition for building and successful functioning of branchy infrastructure.

Fuel cells (FC) are perspective energy sources of electrical energy of new age. They use hydrogen or hydrogenous compounds and oxygen as a fuel. FCs are electrochemical generators, and in contrast to traditional devices (vapour and gas turbines, internal combustion engines, etc.) whose functioning is based on certain thermodynamic cycles, maximum efficiency of FC is not constrained by Carnot cycle. Depending on construction, maximum performance of contemporary FC is about 40–60%. Moreover, ecological safety and high reliability are the advantages of FC (by-product of the reaction is water and harmful rejections are absent).

A wide range of FC constructions gives possibility for their use in different applications, including power stations, stationary generators, engines and mobile devices. PEMFC (proton exchange membrane fuel cell), DMFC (direct methanol fuel cell), SOFC (solid oxide fuel cell) and MCFC (molten carbonate fuel cell) had the most distribution in commercial field as most perspective FC types.

The bulk production of FCs is constrained by the high costs of fabrication technology, materials and catalysts, and this is caused mostly by the novelty of the field. Present technical difficulties can be over passed by use of new technologies, increasing of components efficiency, reduction of size and mass, as well as by preliminary modelling and optimization.

The aim of this paper is to present an overview of special conditions important for efficient and steady functioning of fuel cells, necessity of thermal regulation of fuel cells and application of different types of heat pipes for fuel cells thermal management.

2. FUEL CELLS HEAT DISSIPATION AND NECESSITY OF THERMAL REGULATION

A question of heat dissipation is of great interest for investigations. Making of certain conditions is necessary for sustainable working of FC. That is why thermal regulation of FC and FC stack is to be created. Thermal regulation system is able to maintain certain operational temperature in determined range. A right choice of temperature of reactants containing hydrogen and oxygen and coming to channels in bipolar plates and removal of heat produced during chemical reaction are needed. Specific humidity of gases is an important parameter for required humidity of membrane, and in some cases additional moisturizing is essential. Nonobservance of these conditions may cause element overheating and drying of a membrane, what may lead to FC failure. Moreover, optimal FC construction can increase total system efficiency by utilization of waste heat. Heat removal to ambience is the simplest method of heat removal, but its secondary use for power supply of other elements or in some cases for an additional energy production is more advantageous [1]. For example, there is a possibility of combined application of FC and sorption heat pumps in trigeneration system, Fig. 1. Such system is ecologically safe since environment, alternative (water pools, soil, soil waters, solar energy) and secondary energy sources can be low potential sources. Besides, an advantage of heat pump is that for coolant transport electrical energy is not necessary, since its functioning is based on adsorption and desorption phenomena. By use of low potential heat sources, electrical energy heat pump allows saving up to 30% of primary energy and reducing harmful outputs [2]. Coefficient of performance (COP) shows the ratio of heat production to the heat supplied from high potential source (FC).

For the FC thermal regulation not only the heat removal, but also the uniform temperature distribution plays an important role, as far as more effective functioning of FC requires uniform temperature of incoming reactants, which are located in channels of bipolar plates, Fig. 2.

A choice of an optimal construction of thermal regulation system depends on heat load value that is to be removed from FC stack. Taking into account system performance it is necessary to remove up to 50% of emitted energy. Heating rate Q, which is produced at FC stack functioning, can be calculated as

$$Q = P(\frac{v}{V_c} - 1)\,, \tag{1}$$

where P is electrical power of the FC stack, v – output voltage in case when all chemical energy of reaction transfers into electrical energy (v=1.25 V if water is produced in vapor form, v=1.48 V if water is produced in liguid form), V_c – voltage produced by one cell [3].

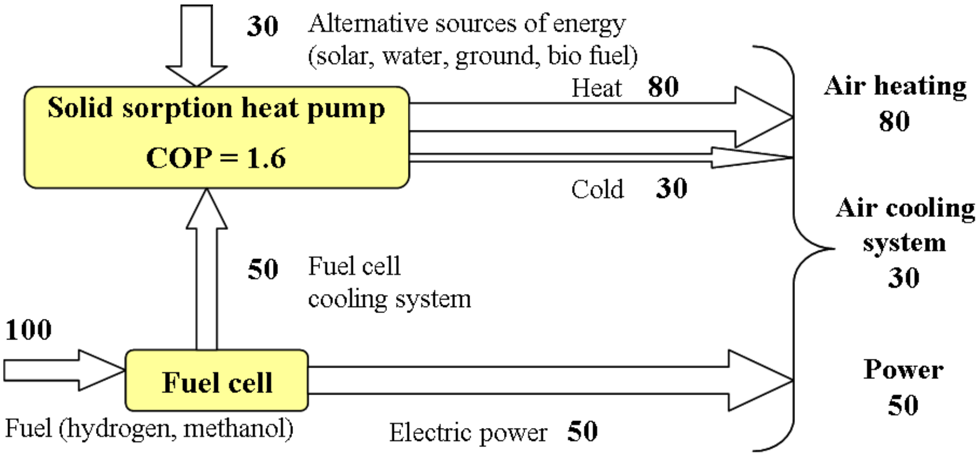

Fig. 1. System of trigeneration based on application of fuel cell and solid sorption heat pump

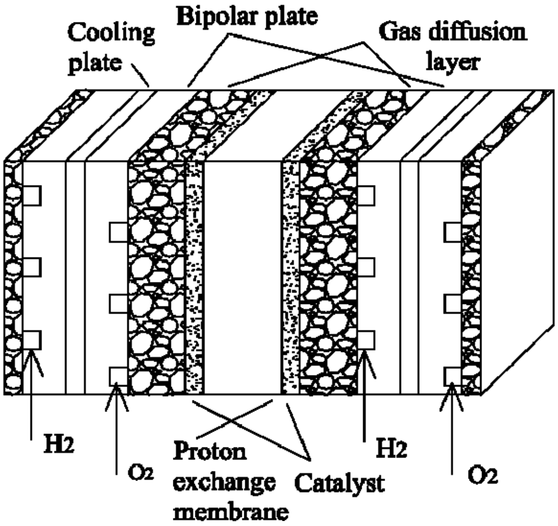

Fig. 2. Scheme of fuel cell with integrated cooling system

Operating temperatures differ greatly depending on FC type. For PEMFC and DMFC this value may reach 100 °C, for SOFC is about 1000 °C, and consequently methods of thermal regulation are distinguished sufficiently. Special peculiarities also exists for micro fuel cells since there is often no possibility to use minimized construction of thermal regulation system without qualitative changes [4].

Heat pipes (HP) and evaporation cooling systems with capillary-porous structures are suggested to use for solving these problems. HPs have extremely high coefficient of thermal conductivity, low thermal resistance, high reliability, they work without noise and independently, do not require special technical service, as well as have compact size and light weight. HPs are also able to increase a performance of a total system by use of waste heat.

The main methods of thermal control of FC system are next.

1. Natural convection is a simpliest way of cooling, it is well suited for FC of small power. A potential drawback of natural convection regime at great heat fluxes is appearance of instabilities. Such way of regulation requires a presence of free space at the cathode side, which leads to an increasing of total system volume.

2. Forced convection. In this case the system can be more compact, but sufficiently high velocity of air flow is necessary. In turn this requires an additional energy supply to the system. If there is an increasing of air flow velocity, which is a fuel cell reactant, the amount

of transferred heat flux is enlarged. But too high velocity can lead to PEM dry out. Thus reactant air supply and cooling system need to be separated.

3. Liquid cooling is necessary for high power FC. At the same time additional requirements for system cooling are necessary, namely liquid (water) temperature and presuure control. Extra channels are necessary for liquid circulation, they can be implemented into a bipolar plate and have different shapes.

4. Thermal conductivity. FC cooling by thermal spreaders allow for effective heat transfer outside the stack. Additional means may be used to remove heat from a free end of a spreader.

5. Heat transfer at phase changes. This method can be realised by using phase changes in special channels, which are the elements of HP or thermosyphons. In [5] loop thermosyphon application is described, which use microchannels with flowing boiling liquid. By means of heat pipes it is possible to provide thermal regulation of FC and incoming reactants. Several constructions of heat pipes may be used for thermal control depending on dissipated power (e.g. [6–8]).

3. APPLICATION OF DIFFERENT TYPES OF HEAT PIPES FOR FUEL CELLS THERMAL MANAGEMENT

Porous Media Laboratory of A.V. Lykov Heat and Mass Transfer Institute carry out heat pipes investigations during many years. Heat pipes for fuel cell thermal management ought to have high effective thermal conductivity and be insensitive to the gravity forces. Providing of functioning of FC at different orientations is especially important for mobile applications such as notebooks, pocket PC, mobile phones. FCs have some advantages over accumulator battery as they can work for longer time without recharge or interruption continue functioning while permanent recharging by hydrogen or methanol is provided. Moreover, FCs does not contain toxic components and do not require special utilization.

The vacant porous media for micro/miniature heat pipes is a metal sintered powder wick or a silicon/carbon porous wafer with biporous (micro/macro pores) composition, saturated with working fluid. Heat pipes fuel cell management can be performed in different ways [9]:

1) micro/mini heat pipes for fuel cells thermal management (< 10 W),
2) heat pipes for fuel cells with moderate heat dissipation (10–100 W),
3) heat pipes for portable and stationary fuel cells (> 100 W).

3.1. Micro and miniature heat pipes for fuel cells thermal management

Micro and miniature heat pipes have cylindrical, flattened or flat shape and can be embedded into bipolar plate of FC. Hydraulic diameter of micro channels for fluid flow is about 10–500 μm in micro HP and 2–4 mm in miniature HP. Smaller channels application is desirable because of higher heat transfer coefficient, and higher heat transfer surface area per unit flow volume.

The most efficient thermal management of micro and miniature fuel cells can be performed when two-phase thermal control typical for an animal body or plant leaves is realised. Thermal control realized by so called open-type micro heat pipes is feasible, if the heat loaded structures are covered with a thin porous layer, saturated with liquid [10–12]. Gas diffusion layer and gas channels of PEMFC ought to be formed by the porous structure including macro and micro pores. There is a strong interaction between basic phenomena in heat pipes. Basic equations are related to vapour flow in the micro HP channel, liquid flow in the capillary structure, interface position between the vapour and liquid (mechanical equilibrium yields interface curvature), radial heat transfer, vapour flow limit, capillary limit.

Feedbacks may cause instabilities, waves, flooding, and performance jump. Optimisation of the new copper sintered powder wick in miniature heat pipes with outer diameter 3–4 mm and length up to 200 mm was carried out in the Institute since 1997. The maximum heat transfer rate for these HPs is almost 50 W [13]. Original software was developed and used for prediction of cylindrical and flattened heat pipes (including miniature HP, Fig. 3) characteristics [10]. Heat pipe family qualified geometry is: circular tube diameter 3–25 mm, flat heat pipe thickness 2–20 mm, length 0.1–0.8 m, wall thickness 0.2–1.0 mm. Pipe material is copper of 99.95% purity, wick is formed by copper sintered powder, layer thickness is being equal to 0.2–0.8 mm. Transport capacity is about 10–500 W. Water, methanol and propane are used as working fluids.

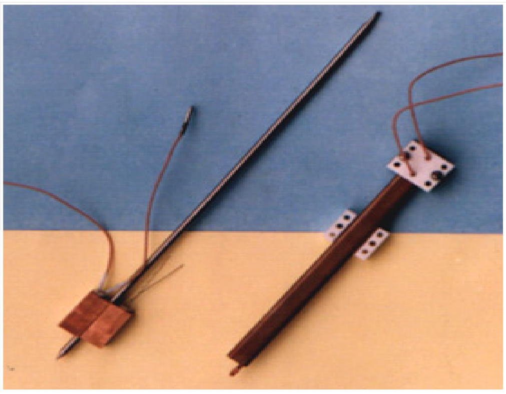

Fig. 3. Cylindrical and flattened miniature heat pipes for fuel cells thermal management

3.2. Loop heat pipes for fuel cells with moderate heat dissipation

Loop heat pipes (LHP) are an attractive alternative for heat regulation. The performance of the evaporator depends on the transport properties of the wick, i.e. permeability, thermal conductivity as well as structural characteristics of the wick, namely homogeneous or heterogeneous porous system, narrow or wide size distribution of the pores. In fuel cells and heat pipes, the flow characteristics in the porous media (gas diffusion layers or capillary wick) are useful in performance modelling. Permeability is a parameter that describes the relationship between pressure drop and mass transport through porous media. In heat pipes effective pore radius is a parameter used to describe the available pressure rise for liquid pumping [13, 14]. In the LHP there is a possibility to use an evaporator above the condenser, the vapour flows through the vapour channels towards the condenser and the liquid goes back to the evaporator due to the capillary pressure head of the porous wick.

3.3. Loop thermosyphons for portable fuel cells

Since the loop thermosyphon has larger critical heat flux than conventional thermosyphon it is convenient to use it in many different applications, for example, for fuel cells thermal control. The loop thermosyphon evaporator requires a good thermal contact with a stack, the condenser ought to be cooled by air or water. The loop thermosyphon transports thermal energy from a heat source to a sink by natural convection without any external power supply such as a pump. The thermosyphon evaporator and the condenser are installed separately, but they are connected to each other by small diameter bendable pipes. Due to the relation between momentum and energy transport theoretical analysis of the loop performance is very complicate, therefore it is necessary to solve these problems by experimental investigation before applying the loop thermosyphon to heat exchanger design.

In the loop thermosyphon the heat transfer is considered to be affected by many factors, such as type and quantity of working fluid, pipe diameter, pipe length, and ratio of cooled surface to heated surface, the length of the adiabatic zone between heated and cooled sections, heat flux and operating temperature. Evaporator and condenser of the loop thermosyphon can be made of carbon-steel, copper or aluminium. Propane, R 134a, R 600, ammonia or water can be used as working fluid. Water is the best working fluid if copper can be applied. In order to establish heat transfer correlations for the application in the design program for the loop thermosyphon heat exchanger, regression analysis could be applied to experimental data for heat transfer coefficients in evaporator and condenser.

Typical loop thermosyphon with the flat evaporator is shown on Fig. 4. This thermosyphon is capable to transport heat flux near 100 W at the temperature of the adiabatic zone equals to 100 °C. The condenser is cooled by water circulation. The thermal resistance of thermosyphon R is 0.03 K/W.

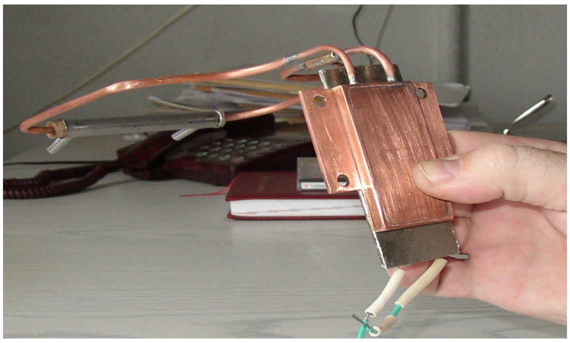

Fig. 4. Copper/water loop thermosyphon for the FC stack thermal management

3.4. Loop heat pipes with noninverted meniscus

Loop heat pipes (LHP) are more flexible to compare with loop thermosyphons due to its insincerity to the gravity field. Typical LHP for PEMFC with optimal heat flow rate 800 W at the working temperature near 80°C is shown in Fig. 5.

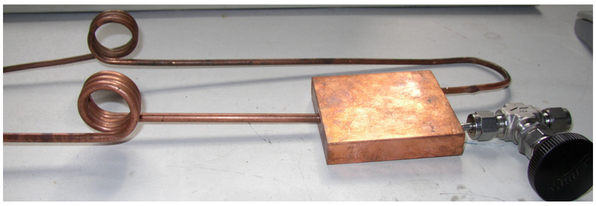

Fig. 5. LHP flat evaporator made from copper with sintered powder
porous structure and mini grooves for liquid suction

LHP with non inverted meniscus of the evaporation designed and tested. It is made from copper and has the wick performed by copper sintered powder. The working fluid is water. The typical maximum heat flow rate of such evaporator is near 1500 W, the thermal resistance of the evaporator is 0.06 K/W. The length of the evaporator is 70 mm, width is 60 mm and thickness is 12 mm. The wick porosity is more than 45% and the effective thermal conductivity of the wick is 40 W/(m·K).

3.5. Pulsating heat pipe panels

Aluminium (multi-channel) heat pipe panel (Fig. 6) with propane as a working fluid is another alternative to the conventional heat pipe for FC stack cooling [15–17]. Pulsating heat pipe (PHP) is one of several oscillatory thermal transport cycles under development that are receiving attention as a potential semi-passive, high-power, high flux heat transport device. The PHP is unique because it is capable to produce driving pressures in excess by many mechanically pumped loops. Capillary forces do not limit the PHP and it is capable to transfer high heat loads over long distances and against significant resistance (i.e. gravity, small tube diameters, etc.).

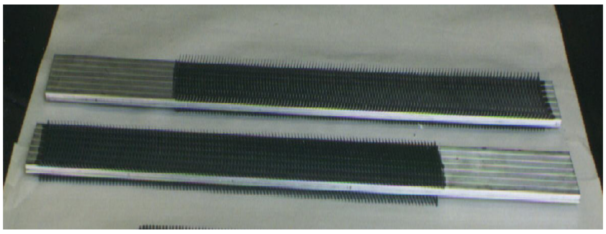

Fig. 6. Aluminum pulsating heat pipe panel with mini channels inside and mini fins on the outer surface

The main parameters of developed flat heat pipe panels are: HP width is 70 mm, HP height is 7 mm, HP length is 700 mm, evaporator length is 98 mm, condenser length is 500 mm, mass is 0.43 kg. HP thermal resistance is 0.05 K/W, evaporator heat transfer coefficient is 8500 W/(m^2·K), condenser heat transfer coefficient is 2500 W/(m^2·K). Working fluid (hydrocarbon) dynamic movement is stable with liquid filling ratio near 0.6 of the heat pipe volume.

3.6. Sorption heat pipes

The sorption heat pipe (SHP) combines enhanced heat and mass transfer in conventional heat pipes with sorption phenomena of a sorbent bed. The original design of such a sorption heat pipe was patented in USSR in 1992 [17]. Sorption heat pipe could be used as a sorption heat transfer element and be cooled and heated as a heat pipe [18].

The sorption heat pipe (Fig. 7) has a sorbent bed (adsorber/desorber and evaporator) at one end and a condenser and an evaporator at the other end. Sorption heat pipe have a sorbent bed (adsorber/desorber and evaporator) at one end and a condenser + evaporator at the other end. Traditional two-phase thermal control system for FCs is sensitive to the vehicle acceleration and vibration. Sorption heat pipe thermal control is efficient for such cases.

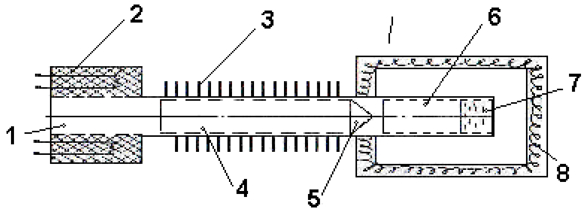

Fig. 7. Sorption heat pipe: 1 – vapor channel, 2 – sorption structure, 3 – finned surface of heat pipe evaporator/condenser, 4 – porous wick, 5 – porous valve, 6 – low temperature evaporator with porous wick, 7 – working fluid, 8 – cold box with thermal insulation

The solid sorption cooler begins to function, when cooling possibilities of the conventional heat pipe are exhausted. Sorption heat pipe cooler has some advantages comparing with conventional loop heat pipe coolers in the case, when the following is required:

- operation in large accelerations,
- higher pumping capability, require more intense heat transfer in the evaporator,
- operation of sorption heat pipe evaporator at temperature lower than the environmental one.

The heat output of SHP developed is about 1000 W (water), the thermal resistance of the evaporator is 0.03 K/W, pressure drop is 200 mbar.

4. CONCLUSIONS

Heat pipes enable to provide the required regime of FC functioning and to increase f the whole system efficiency by using waste heat. There is a possibility to ensure necessary temperature of electrodes and incoming reagents by applying different types of HPs. It is a promising way for mobile and stationary FC. Micro and miniature heat pipes can be used for FC with power of 1–100 W; loop, pulsating and sorption heat pipes are able to provide thermal management for FCs with power of 100–1000 W. Undoubtedly, the implementation of HPs into FC stacks requires a specific case study for the optimal construction of the thermal regulation system.

REFERENCES

1. Vasiliev L. L., Filatova O.S., Tsitovich A. P. The way to increase the efficiency of new power sources. Proceedings of the XII International Symposium “Heat Transfer and Renewable Sources of Energy”. Wydawnictwo Uczelniane Politechniki Szczecińskiej, Szczecin, 2008, p. 243–250.
2. Antukh A.A., Filatova O.S., Kulakov A.G., Vasiliev L.L. Solid sorption coolers for cooling in tri-generation // Int. J. of Low Carbon Technologies. Vol. 1, No. 3, July 2006, p. 262–272.
3. Larminie J., Dicks A. Fuel Cell Systems Explained. Second edition. John Wiley & Sons Ltd., England, 2003. 406 p.
4. Faghri A., Guo Z. Challenges and opportunities of thermal management issues related to fuel cell technology and modeling // Int. J. of Heat and Mass Transfer, Vol. 48, 2005, p. 3891–3920.
5. Garrity P.T., Klausner J.F., Mei R. A flow boiling microchannel evaporator plate for fuel cell thermal management // Heat Transfer Engineering, Vol. 28, No.10, 2007, p. 877–884.
6. Faghri A. Micro Heat Pipe Embedded Bipolar Plate for Fuel Cell Stacks, U.S. Patent Pub. No. 2005/0026015, 2005.
7. Faghri A. Integrated Bipolar Plate Heat Pipe for Fuel Cell Stacks, U.S. Patent Pub. No. 2005/0037253, 2005.
8. Sarraf D. B., Schwendermann J. T. Flat plate fuel cell cooler. U.S. Patent Pub. No. 6,817,097, 2004.
9. Vasiliev L.L., Filatova O.S., Kulakov A.G., Vasiliev L.L.Jr., Tsitovich A.P. Heat pipes in new power sources technologies. Abstracts of the VI Minsk International Forum “Heat and Mass Transfer”, Minsk, Belarus, May 19–23, 2008.
10. Dunn P., Reay D. A. Heat pipes. Pergamon Press, Great Britain, 1976, p. 21–25.
11. Reutsky V. G., Vasiliev L. L. Papers of Academy of Sciences, Belarus, 24, No. 11, 1033–1036.

12. Maziuk V., Kulakov A., Rabetsky M., Vasiliev L., Vukovic M. Miniature heat pipe thermal performance prediction tool – software development // Appl. Therm. Eng., 2001, 21, 559–571.
13. Vasiliev L., Atukh A., Maziuk V., Kulakov A., Rabetsky M., Vasiliev L. Jr., Min O. S. Miniature heat pipes experimental analysis and software development // Proc. of 12th Intern. Heat Pipe Conf. "Heat pipes science, technology, application" ed. By Maidanik Yu. Russian Academy of Sciences, Moscow, Russia, 2002, p. 329–335.
14. Weislogel M. M., Golliher E., McQuillen J., Bacich M. A., Davidson J. J., Sala M. A. Recent results of the micro scale pulse thermal loop // International Two-Phase Thermal Control Technology Workshop, Newton white Mansion, Mitchelville, 2002, MD, Sept. 24–26.
15. Vasilev L.L., Zhuravlyov, Shapovalov A., Litvinenko V. Vaporization heat transfer in porous wicks of evaporators // Arch. of Thermodynamics, 2004, 25, No. 3, p. 47–59.
16. Vasiliev L. L. sorption machines with a heat pipe thermal control // Proc. of Int. Sorption Heat Pipe conf., Sept. 24–27, 2002, Shanghai, China, p. 408–413.
17. Vasiliev L. L., Bogdanov V.M. Heat pipe, USSR Patent 174411, B. I., No. 24, 30.06.1992.
18. Vasiliev L., Vasiliev L. Jr. Sorption heat pipe – a new thermal control device for space and ground application // Int. J. of Heat and Mass Transfer, 2005, Vol. 48, No. 12, p. 2464–2472.

CYSENI 2009, May 28-29, Kaunas, Lithuania
ISSN 1822-7554, www.cyseni.com

EXPERIMENTAL TECHNIQUE FOR INVESTIGATION OF SODIUM BOROHYDRIDE HYDROLYSIS BY HYDROGENOMETRY

A.A. Nesteruk, V.I. Kalinin
A.V. Luikov Heat and Mass Transfer Institute of NAS of Belarus
15 P. Brovki str., Minsk, BY-220072 Belarus
Phone: +37529 860 38 80, +37517 284 23 65
E-mail: favourite2003@bk.ru

ABSTRACT

In this paper peculiarities of experimental technique for determination of borohydrides hydrolysis rates based on pressure measurements in closed vessel are studied. Impact of both directly measured experimental characteristics (temperature and pressure) along with their errors and processes in the vessel on accuracy of results obtained for water-alkali solutions of sodium borohydride with sodium hydroxide concentrations varying from 10^{-3} to 2.5 M and test temperatures from 20^{o}C to 90^{o}C is considered. Technical and methodological procedures of the technique performance are discussed. Experimental data and their errors evaluations are given. The technique for calculation of sodium borohydride conversion rate during the process of hydrolysis is outlined. It accounts for the thermal expansion of gases (such as air, hydrogen produced, water vapour) above the solution, the thermal expansion of reacting mixture, the hydrogen dissolution in alkali solution formed, the atmospheric pressure variation and moisture in the laboratory. It is shown that difference in saturated pressure values above solution and pure water almost does not have effect on the results of calculations.

Keywords: sodium borohydride, hydrolysis, experimental technique, conversion rate, hydrolysis constants

1. INTRODUCTION

For the recent decade an interest in alkali metals borohydrides hydrolysis kinetics was revived. A vast majority of published works deal with sodium borohydride hydrolysis as the most promising substance for hydrogen storage. The first wave of interest in this substance arose in late sixties and early [1–4], and by nineties activity of publishing on this topic decreased significantly. It was 60–70 years, when step-by-step kinetic hydrolysis procedures still being the last results of this kind were developed and published. Present experimental studies deal mostly with water-alkali borohydride solutions stable storage and with catalytic hydrolysis processes in these solutions. Kinetic hydrolysis procedures of the first wave works [5–12] were not checked for the new data, and we have not seen new published works on development of step-by-step kinetics. At the same time kinetic coefficients have significant variances. Adjustment and testing of these procedures was performed within relatively limited range of temperatures and water-alkali sodium borohydride solutions. The range of solution parameters used in present applied tasks is significantly larger than that in sixties-eighties. Hence there is a necessity to analyze sodium borohydride solutions hydrolysis kinetics using broadened parameters range.

To adequately investigate water-alkali sodium borohydride solutions kinetics a method that would give reproducible results with acceptable error is needed. There are two ways of $NaBH_4$ conversion rate measurement: i) iodometry and ii) two modifications of hydrogenometry [13]. The former technique based on oxidation of fixed hydrogen with iodine (that is measured by quantity of iodine involved into reaction), and the two latter ones directly measure amount of produced hydrogen: in one of them hydrogen volume (typically at atmospheric pressure) and in other hydrogen pressure is measured. Iodometry is more labour-consuming activity, requires a number of manual operations and almost unsuitable for fast processes, while both kinds of hydrogenometry are easily automated. Technique based on hydrogen volume measurement is unsuitable for high conversion rates, where hydrogen production is slow and large volumes of test solutions are needed, because for such solutions content and temperature uniformity becomes a relevant issue. The most convenient technique for performance (automation capability, reasonable experiment duration) is the one based on pressure measurements of hydrogen evolved in sealed reactor. In the paper peculiarities of this technique are described, the way of conversion rate calculation is given, effect of possible errors for parameters measured on results precision and impact of different processes during the experiment in total error is considered, a set of experimental hydrolysis constants determined by the technique performed in the range of sodium hydroxide concentrations varying between 0.001 M and 2.5 M at temperature from 20 to 90°C are given.

2. EXPERIMENTAL TECHNIQUE

Layout of the experimental setup for measurement of sodium borohydride conversion rate is shown in Fig. 1. The procedure of experiments performance is the following:

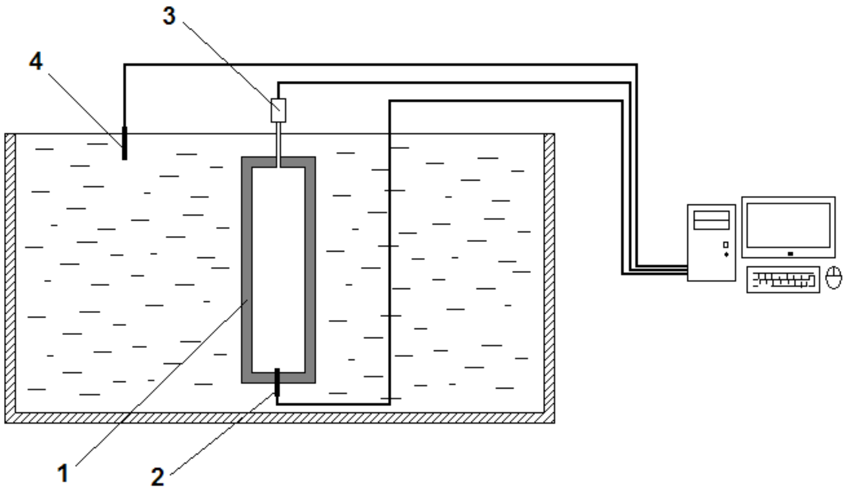

Fig. 1. Layout of the experimental setup for measurements of sodium borohydride conversion rate, where 1 – reactor, where the reaction occurs; 2 – thermocouple, measuring temperature of solution inside of the reactor; 3 – pressure gauge, measuring differential pressure inside of the reactor; 4 – computer controlled thermocouple, measuring temperature of water in thermostat

1. 0.3783 g of sodium borohydride is dissolved in 100 ml of sodium hydroxide solution (cooled down to temperature close to 0°C in case of low alkali content) of required concentration, i.e. solution with sodium borohydride concentration of 0.1 M $NaBH_4$ is prepared. Almost all the experiments with alkali solutions were performed at this borohydride concentration. The designed volume of solution is transferred into cooled reactor, after this operation the reactor is sealed.

2. Atmospheric pressure and air humidity are recorded.

3. Reactor is placed into thermostat. As reactor tightness is a critical parameter for this technique, to provide absence of leakage through the contacts between reactor and its closure reactor is turned upside down when immersed into the thermostat. In this way air layer between the closure and reactor is replaced by water with higher density.

4. During the experiment the evolution of temperature and pressure inside the reactor is recorded. In case of long experiments atmospheric pressure changes are fixed.

5. Due to hygroscopic properties of sodium borohydride powder and due to possible manufacturing impurities iodometric analysis of sodium borohydride is performed before hydrogenometry experiment starts. Therefore, the initial content of sodium borohydride in solution is precise.

6. After the experiment is finished, the rate of conversion determined by hydrogenometry is controlled by iodometric titration of the solution formed as a result of hydrolysis. It assures the absence of leakage of liquid or gases solved in it using the type of seal mentioned above.

3. CALCULATION

In this section we will discuss parameters of experiment in sealed reactor necessary to be taken into account for calculation of sodium borohydride hydrolysis rate. Hydrolysis rate is defined as the ratio of the quantity of hydrogen evolved to the highest possible quantity of hydrogen evaluated by gross process equation:

$$\mathrm{NaBH_4} + 2\mathrm{H_2O} = \mathrm{NaBO_2} + 4\mathrm{H_2}, \tag{1}$$

$$\alpha(t) = \frac{m_{\mathrm{H_2}}(t)}{m_{\mathrm{H_2}}^{\max}} \cdot 100\%, \tag{2}$$

where $\alpha(t)$ – borohydride conversion rate at time t, %;

$m_{\mathrm{H_2}}(t)$ – weight of hydrogen produced at time t, g;

$m_{\mathrm{H_2}}^{\max}$ – weight of hydrogen produced at complete hydrolysis of the initial quantity of sodium borohydride (calculated value), g.

According to the equation (1):

$$m_{\mathrm{H_2}}^{\max} = \frac{m_{\mathrm{NaBH_4}}(t_0)\beta_{pur}}{M_{\mathrm{NaBH_4}}} \cdot 8M_{\mathrm{H}}, \tag{3}$$

where $m_{\mathrm{NaBH_4}}(t_0)$ – initial weight of sodium borohydride in reactor, g;

$M_{\mathrm{NaBH_4}}$ – molar weight of sodium borohydride, $M_{\mathrm{NaBH_4}} = 37.8326$ g/mol;

M_{H} – molar weight of atomic hydrogen, M_{H} =1,00787 g/mol;

β_{pur} – purity of sodium borohydride used.

Absolute pressure in reactor is a sum of instrumental pressure and atmospheric pressure in the laboratory:

$$P_{reactor}(T,t) = P_{det}(T,t) + P_{atm}(t), \tag{4}$$

where $P_{reactor}(T,t)$ – the pressure in reactor at temperature T, K, at the moment t;

$P_{det}(t)$ – the instrumental pressure;

$P_{atm}(t)$ – the atmospheric pressure during the experiment.

On the other hand the pressure in the reactor is the sum of hydrogen pressure, air pressure inside of reactor and saturated water vapour pressure:

$$P_{reactor}(T,t) = P_{H_2}(T,t) + P_{air\ inside}(T) + P_{\mathrm{H_2O}}(T), \tag{5}$$

where $P_{air\ inside}(T)$ – the pressure of air inside of reactor for temperature T;
$P_{\mathrm{H_2O}}(T)$ – the saturated water vapour pressure for temperature T;
$P_{\mathrm{H_2}}(T,t)$ – the hydrogen pressure inside of reactor at time t for temperature T.

At the initial moment of time (reactor closure) the air humidity inside of the reactor is accepted equal to the ambient humidity, ϑ_0, this results in the following relations:

$$P_{reactor}(T_0,t_0) = P_{atm}(t_0) = P_{air\ inside}(T_0,t_0) + \vartheta_0 P_{\mathrm{H_2O}}(T_0), \tag{6}$$

$$P_{air\ inside}(T_0,t_0) = P_{atm}(t_0) - \vartheta_0 P_{\mathrm{H_2O}}(T_0). \tag{7}$$

During the experiment in closed reactor the equilibrium saturated water vapour pressure is established:

$$P_{reactor}(T,t) = P_{air\ inside}(T) + P_{\mathrm{H_2}}(T,t) + P_{\mathrm{H_2O}}(T). \tag{8}$$

Pressure of the air inside of reactor at the moment of closure will change as a function of temperature and gas volume, that gives relation:

$$P_{air\ inside}(T) = \frac{\left[P_{atm}(t_0) - \vartheta_0 P_{\mathrm{H_2O}}(T_0)\right] T V^0_{space}(T_0)}{T_0 V_{space}(T)}, \tag{9}$$

where $V_{space}(T)$ – the volume of free space inside the reactor for temperature T, the temperature expansion of the solution is taken into account.
To calculate change of solution density as a function of temperature, the properties of water were used, i.e. it was supposed that thermal expansion coefficient (not density!) does not change when NaOH and borohydride is solved in water:

$$V_{space}(T) = V_{reactor} - \frac{\rho_{\mathrm{H_2O}}(T_0)}{\rho_{\mathrm{H_2O}}(T)} V_{sol}(T_0), \tag{10}$$

where $V_{reactor}$ – the reactor volume;
$V_{sol}(T_0)$ – the initial volume of the solution poured into the reactor.

To calculate water density approximation of experimental data from [14] was used:

$$\rho_{\mathrm{H_2O}}(T) = 0.748772 + 0.00191313T - 3.6275\cdot 10^{-6} T^2, \tag{11}$$

where $\rho_{\mathrm{H_2O}}(T)$ – the water density for temperature T.
The hydrogen pressure inside of reactor, $P_{\mathrm{H_2}}(T,t)$, is calculated by measurements of the weight of the hydrogen in gas space inside the reactor, $m_{\mathrm{H_2}gas}(t)$:

$$P_{\mathrm{H_2}}(T,t) = \frac{m_{\mathrm{H_2}gas}(t) RT}{M_{\mathrm{H_2}} V_{space}(T)}. \tag{12}$$

To evaluate saturated vapour pressure above the solutions $P_{\mathrm{H_2O}}(T, c_{\mathrm{NaOH}})$ our approximation of experimental data from [15] for water and water solutions of NaOH was used:

$$\begin{aligned} P_{\mathrm{H_2O}}(T, c_{\mathrm{NaOH}}) &= 1.09659\cdot 10^{10} e^{-\frac{3678.89}{T}\left(1+\frac{65.4344}{T}\right)} \times \\ &\times \left[1 - th\left(4.0186\cdot 10^{-2}\cdot c_{\mathrm{NaOH}} + 4.0103\cdot 10^{-4} c^2_{\mathrm{NaOH}}\right)\right] \end{aligned}. \tag{13}$$

In case of slow experiments (large concentrations of NaOH) to increase the sensitivity it is necessary to deal with small free space, i.e. with relatively large volumes of solution. In these cases it is desirable to consider solubility of gases (hydrogen, nitrogen and oxygen) in liquid. For hydrogen this effect increases with its partial pressure that can achieve 10 Bar in our experiments. Nitrogen and oxygen solubility effect can be essential only in case of temperature change, because the solubility of these gases decreases remarkably with increase of temperature.

To account for solubility effects experimental data on nitrogen, oxygen and hydrogen solubility in water and water solutions of NaOH [15] were used. Approximations we used consisted of two functions product, one of them evaluating gas solubility approximately and depending on its partial pressure and water temperature, and the other being a function only of NaOH concentration, i.e., it was accepted that:

$$Sol_{gas\_\mathrm{H_2O}\_\mathrm{NaOH}}(T,P_{gas},c_{\mathrm{NaOH}}) = Sol_{gas\_\mathrm{H_2O}}(T,P_{gas})Corr_{gas}(c_{\mathrm{NaOH}}). \tag{14}$$

For hydrogen the following approximating functions were used:

$$\begin{gathered} Sol_{\mathrm{H_2}\_\mathrm{H_2O}}(T,P_{\mathrm{H_2}}) = P_{\mathrm{H_2}}\left[0.0159405+1.44812\cdot10^{-6}\left(T-332\right)^2\right] \\ Corr_{\mathrm{H_2}}(c_{\mathrm{NaOH}}) = 1-th\frac{0.31\cdot c_{\mathrm{NaOH}}}{1+0.093\cdot c_{\mathrm{NaOH}}} \end{gathered} . \tag{15}$$

Approximation for pure water $Sol_{\mathrm{H_2}\_\mathrm{H_2O}}(T,P_{\mathrm{H_2}})$ is based on the pressure data in the range from 1 to 100 atm and temperature data from 0 to 100°C. Function $Corr_{\mathrm{H_2}}(c_{\mathrm{NaOH}})$ is based on the only available set of data for 25$^{\mathrm{o}}$C [14], where the highest value for c_{NaOH} was 2 M.

Approximations for oxygen and nitrogen solubility use data for pressure at 1 atm and temperature in the range from 0 to 100$^{\mathrm{o}}$C. For oxygen function depending on concentration $Corr_{\mathrm{O_2}}(c_{\mathrm{NaOH}})$ is based on the experimental data for 15 and 25°C. Alkali concentrations in these data are not greater than 2 M. There was no available data on nitrogen solubility in NaOH solutions that is why function $Corr_{\mathrm{O_2}}(c_{\mathrm{NaOH}})$ was used for nitrogen either:

$$\begin{gathered} Sol_{\mathrm{O_2}\_\mathrm{H_2O}}(T,P_{\mathrm{O_2}}) = P_{\mathrm{O_2}}\left[1.6564\cdot10^{-2}+2.0012\cdot10^{3}e^{-0.040423\cdot T}\right] \\ Corr_{\mathrm{O_2}}(c_{\mathrm{NaOH}}) = 1-th\frac{0.4283\cdot c_{\mathrm{NaOH}}}{1+0.1576\cdot c_{\mathrm{NaOH}}} \end{gathered} , \tag{16}$$

$$\begin{gathered} Sol_{\mathrm{N_2}\_\mathrm{H_2O}}(T,P_{\mathrm{N_2}}) = P_{\mathrm{N_2}}\left[9.1325\cdot10^{-3}+1.2145\cdot10^{3}e^{-0.04155\cdot T}\right] \\ Corr_{\mathrm{N_2}}(c_{\mathrm{NaOH}}) \equiv Corr_{\mathrm{O_2}}(c_{\mathrm{NaOH}}) \end{gathered} , \tag{17}$$

Approximated data on the solubility gives volume of gas solved per unit of solution volume (calculated per standard conditions: temperature - 0°C, pressure - 760 mm Hg). Therefore the weight of gas solved m_{gas} is expressed in terms of solution volume as follows:

$$m_{gas} = \frac{P_{NC}M_{gas}}{RT_{NC}}V_{sol}(T_0)Sol_{gas\_\mathrm{H_2O}}(T,P_{gas})Corr_{gas}(c_{\mathrm{NaOH}}), \tag{18}$$

where P_{NC} and T_{NC} – the pressure and the temperature of “normal conditions”.

Initially (before hydrolysis started) there was no hydrogen in reactor, all the hydrogen produced would be contained in the gas space and in the solution:

$$m_{\mathrm{H_2}}(t) = m_{\mathrm{H_2}gas}(t) + m_{\mathrm{H_2}sol}(t), \tag{19}$$

$$m_{\mathrm{H_2}}(t_0) = m_{\mathrm{H_2}gas}(t_0) = m_{\mathrm{H_2}sol}(t_0) = 0. \tag{20}$$

The weight of nitrogen and oxygen in the reactor does not change with time, but redistributes between the gas space and solution in case of temperature changes. It was assumed that at the beginning of experiment the solution contained equilibrium quantity of nitrogen and oxygen solved at parameters $P_{atm}(t_0)$ and T_0, then:

$$m_{\mathrm{N_2}gas}(t) + m_{\mathrm{N_2}sol}(t) = const = m_{\mathrm{N_2}gas}(t_0) + m_{\mathrm{N_2}sol}(t_0), \tag{21}$$

$$m_{\mathrm{O_2}gas}(t) + m_{\mathrm{O_2}sol}(t) = const = m_{\mathrm{O_2}gas}(t_0) + m_{\mathrm{O_2}sol}(t_0). \tag{22}$$

Account for nitrogen and oxygen can have effect only in case of experiments with small volume $V_{space}(T)$ and providing that T_0 and T are essentially different. In this case the expression for $P_{air\ inside}(T)$ is modified as follows:

$$P_{air\ inside}(T) = \frac{m_{\mathrm{N_2}gas}(t) + m_{\mathrm{O_2}gas}(t)}{m_{\mathrm{N_2}gas}(t_0) + m_{\mathrm{O_2}gas}(t_0)} \cdot \frac{\left[P_{atm}(t_0) - \vartheta_0 P_{\mathrm{H_2O}}(T_0)\right] T V_{space}^0(T_0)}{T_0 V_{space}(T)}. \tag{23}$$

Hydrolysis rate calculation at time t by measured values of T and P_{det} is performed as follows:

1. $V_{space}(T)$ is calculated by formula (10):
2. The weight of nitrogen and oxygen in solution as well as the air pressure inside of reactor are calculated by the following procedures:

$$\tilde{P}_{air\ inside}(T) = \frac{\left[P_{atm}(t_0) - \vartheta_0 P_{\mathrm{H_2O}}(T_0)\right] T V_{space}^0(T_0)}{T_0 V_{space}(T)}, \tag{24}$$

$$m_{\mathrm{N_2}sol}(t) = \frac{P_{NC} M_{\mathrm{N_2}}}{R T_{NC}} V_{sol}(T_0) Sol_{\mathrm{N_2\_H_2O}}(T, 0.79\tilde{P}_{air\ inside}) Corr_{\mathrm{N_2}}(c_{\mathrm{NaOH}}), \tag{25}$$

$$m_{\mathrm{O_2}sol}(t) = \frac{P_{NC} M_{\mathrm{O_2}}}{R T_{NC}} V_{sol}(T_0) Sol_{\mathrm{O_2\_H_2O}}(T, 0.21\tilde{P}_{air\ inside}) Corr_{\mathrm{O_2}}(c_{\mathrm{NaOH}}), \tag{26}$$

$$P_{air\ inside}(T) = \frac{m_{\mathrm{N_2}gas}(t) + m_{\mathrm{O_2}gas}(t)}{m_{\mathrm{N_2}gas}(t_0) + m_{\mathrm{O_2}gas}(t_0)} \cdot \tilde{P}_{air\ inside}(T). \tag{27}$$

3. The vapour pressure is computed by the expression (13).
4. The pressure of hydrogen inside the reactor is calculated as:

$$P_{\mathrm{H_2}}(T,t) = P_{det}(T,t) + P_{atm}(t) - P_{air\ inside}(T) - P_{\mathrm{H_2O}}(T, c_{\mathrm{NaOH}}). \tag{28}$$

5. The weight of hydrogen produced is calculated as:

$$m_{\mathrm{H_2}gas}(t) = \begin{cases} 0 & P_{\mathrm{H_2}}(T,t) \le 0 \\ \dfrac{P_{\mathrm{H_2}}(T,t) M_{\mathrm{H_2}} V_{space}(T)}{RT} & P_{\mathrm{H_2}}(T,t) > 0 \end{cases} \tag{29}$$

$$m_{\mathrm{H_2}sol}(t)=\begin{cases}0 & P_{\mathrm{H_2}}(T,t)\le 0\\ \dfrac{P_{NC}M_{\mathrm{H_2}}}{RT_{NC}}V_{sol}(T_0)Sol_{\mathrm{H_2\_H_2O}}(T,P_{\mathrm{H_2}})Corr_{\mathrm{H_2}}(c_{\mathrm{NaOH}}) & P_{\mathrm{H_2}}(T,t)>0\end{cases},\tag{30}$$

$$m_{\mathrm{H_2}}(t)=m_{\mathrm{H_2}gas}(t)+m_{\mathrm{H_2}sol}(t).\tag{31}$$

6. Hydrolysis rate is calculated by formula (2).

4. RESULTS AND DISCUSSION

By the procedure given calculation of conversion rate and error evaluations are performed for three experiments with different levels of sodium hydroxide content. The experimental parameters (Table 1) as well as evolution of temperature (Fig. 2*a*) and pressure (Fig. 2*b*) during the experiments are provided below.

Table 1. Experimental parameters used for calculation of conversion rate.

c_{NaOH}, M	$m_{\mathrm{NaBH_4}}(t_0)$, g	$V_{sol}(T_0)$, l	T_0, °C	$P_{atm}(t_0)$, mm Hg	ϑ_0, %	$P_{atm}(t)$, mm Hg
0.001 M	0.1911	0.05	20	751	45	751
0.1 M	0.1877	0.05	16	737	45	737
2.5 M	0.1879	0.05	30	749	45	749

Error evaluations are performed by known instrumental errors. Thus, for the thermocouple inside of the reactor its value is ± 2°C, for the balance it is ± 0.001 g, for the reactor volume – ± 0.001 l, for the volume of solution inside the reactor – ± 0.0005 l, for the pressure sensor – ± 0.001 Bar. Atmospheric humidity for each of the experiments is 45%. For value of atmospheric pressure error is 5 mm Hg. For the concentration of sodium hydroxide the error is not greater than 1%, i.e. ± 10^{-5} M, ± 0.001 M and ± 0.025 M for 0.001 M, 0.1 M and 2.5 M NaOH respectively.

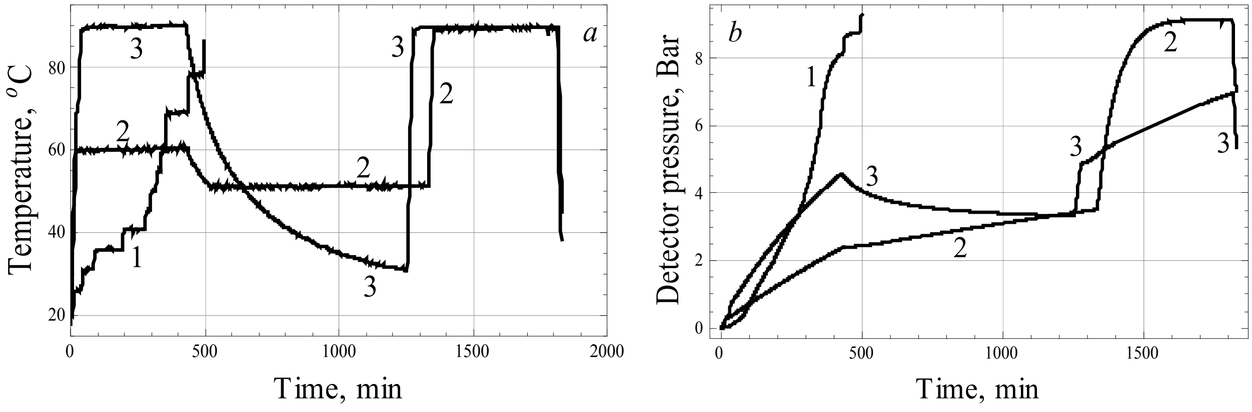

Fig. 2. Temperature (*a*) and pressure (*b*) evolution for the experiments: 1 – 0.001 M NaOH, 2 – 0.1 M NaOH; 3 – 2.5 M NaOH

In Fig. 3 (*a-c*) the plots of the conversion rate evolution during the experiments and its upper and lower limits of absolute errors are shown. Errors were calculated for each point as the sum of absolute values of errors for each parameter.

In Table 2 the highest values of errors are given for every experiment and parameter. Sum of the highest errors for parameters is not equal to the highest experimental error as maxima of parameters errors may not coincide.

The highest impact in total error is due to uncertainties of reactor and solution volume, borohydride weight and temperature inside of the reactor. To reduce impact of reactor volume error, one should increase free space volume, i.e. to use small solution volumes, however, this leads to increase of the solution volume error. Hence, solution volume (and respectively free space volume) is chosen so that error from both parameters is minimal. Issue of precise temperature measurement can be solved by substitution of the thermocouple with more precise one for the range of temperature measurements.

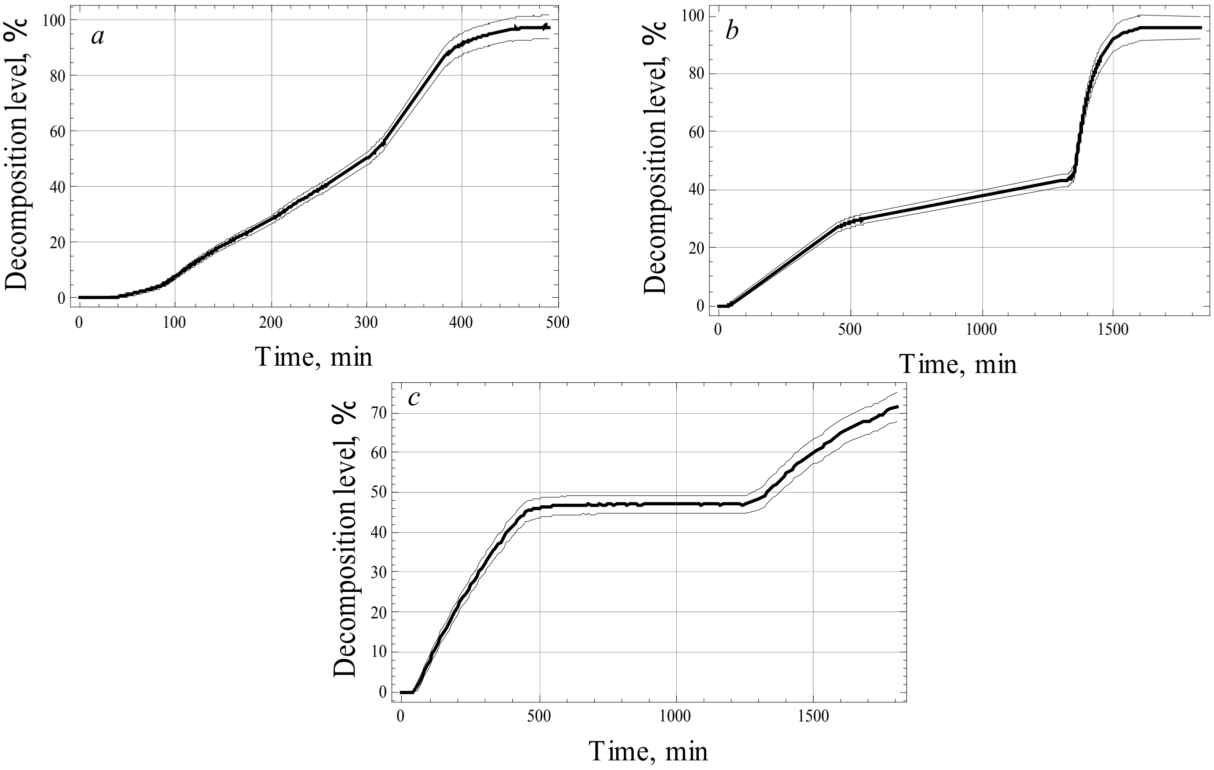

Fig. 3. Borohydride conversion rate (bold lines) and conversion rate accounting for possible errors (thin lines) for experiments with different sodium hydroxide concentration: a – 0.001 M NaOH , b – 0.1 M NaOH ; c – 2.5 M NaOH

Table 2. Maxima errors for different parameters of experiment

Parameter	Alkali concentration		
	0.001 M	0.1 M	2.5 M
Total maxima error, %	4.39	4.40	3.55
Solution volume, ±0.001 l	1.42	1.40	1.05
Volume of solution inside of the reactor, ±0.0005 l	0.72	0.71	0.54
Weight of sodium borohydride inside of the reactor, ± 0.001 g	0.52	0.56	0.38
Alkali concentration, ±1 %	0.00	0.00	0.00
Initial atmospheric pressure, ± 5 mm Hg	0.10	0.10	0.09
Initial temperature, ±2 °C	0.16	0.16	0.16
Humidity, ±10%	0.03	0.03	0.05
Atmospheric pressure during the experiment, ± 10 mm Hg	0.19	0.18	0.19
Readings of pressure sensor, ±0.001 atm	0.01	0.01	0.01
Temperature inside of the reactor during the experiment, ±2 °C	1.28	1.34	1.12

Among the processes in the reactor when it is heated, cooled down, when the pressure increases and reduces the most important are water evaporation inside of the reactor as input of evaporation can reach up to 10%, and temperature expansion of liquid inside of the reactor (effect can amount for up to 4%), which changes the free space volume.

Despite of low solubility of hydrogen in alkali solution this process becomes essential at pressure about 10 atm and its impact can reach 2% even at concentration of sodium hydroxide 0.001 M. Nitrogen and oxygen solubility, saturated vapour pressure above alkali solution comparing to water one have negligible impact in total error, however these corrections are made in our calculations to make processing of experiments with higher alkali content more precise. In program processing relative humidity and variation of atmospheric pressure in the laboratory was taken into account, although these parameters do not essentially influence on conversion rate values.

50 constants of hydrolysis rate determined by means of the technique described above for temperature range from 20°C to 90°C at 8 different levels of alkali concentration in the range between 0.001 M to 2.5 M NaOH are given in table 3 below.

Table 3. Constants of hydrolysis rate for sodium borohydride in solutions for different alkali concentrations and temperatures.

Alkali concentration, M	Temperature, °C	Constant of hydrolysis, c^{-1}	Alkali concentration, M	Temperature, °C	Constant of hydrolysis, c^{-1}
0.001	41	5.0×10^{-5}	0.1	69	4.0×10^{-5}
	50	1.1×10^{-4}		74	6.2×10^{-5}
	55	1.6×10^{-4}		78	9.4×10^{-5}
	69	4.3×10^{-4}		83	1.5×10^{-4}
	78	8.4×10^{-4}		89	6.2×10^{-5}
0.01	36	5.8×10^{-6}	0.37	90	1.28×10^{-4}
	42	9.6×10^{-6}		80	5.25×10^{-5}
	46	1.9×10^{-5}		70	2.06×10^{-5}
	51	3.2×10^{-5}		60	7.6×10^{-6}
	53	3.8×10^{-5}		50	2.45×10^{-6}
	54,5	5.1×10^{-5}		40	1.27×10^{-6}
	60	9.0×10^{-5}		30	2.95×10^{-7}
	65	1.4×10^{-4}		20	2.02×10^{-7}
	70	2.3×10^{-4}	0.5	38	7.7×10^{-7}
	74,5	3.3×10^{-4}		47	2.2×10^{-6}
	79	4.8×10^{-4}	1.0	41	8.0×10^{-7}
	84	7.0×10^{-4}		50,5	2.35×10^{-6}
	89	9.8×10^{-4}		89	7.9×10^{-5}
0.1	25	1.5×10^{-7}	1.5	30	1.75×10^{-7}
	41	2.0×10^{-6}		89	6.0×10^{-5}
	46	3.5×10^{-6}	2.5	28	4.7×10^{-8}
	51	5.1×10^{-6}		38	1.65×10^{-7}
	56	1.0×10^{-5}		47	5.5×10^{-7}
	60	1.39×10^{-5}		57	1.75×10^{-6}
	65	1.5×10^{-7}		66	4.56×10^{-6}

Constants of hydrolysis rate for sodium borohydride are determined by rate equations for gross process (1):

$$c_{\mathrm{BH}_4^-}(t)=\left(c_{\mathrm{BH}_4^-}\right)_0\exp\left(-\mathrm{k}^{\mathrm{hydr}}(T)t\right)\ , \tag{33}$$

$$\frac{dc_{\mathrm{BH}_4^-}}{dt}=-\mathrm{k}^{\mathrm{hydr}}(T)\left(c_{\mathrm{BH}_4^-}\right)_0\exp\left(-\mathrm{k}^{\mathrm{hydr}}(T)t\right)=-\mathrm{k}^{\mathrm{hydr}}(T)c_{\mathrm{BH}_4^-}\,, \tag{34}$$

$$\mathrm{k}^{\mathrm{hydr}}(T)=-\frac{1}{c_{\mathrm{BH}_4^-}}\frac{dc_{\mathrm{BH}_4^-}}{dt}\,,$$

(35),

where $c_{\mathrm{BH}_4^-}(t)$ – the concentration of sodium borohydride at time t, M;

$\left(c_{\mathrm{BH}_4^-}\right)_0$ – the initial concentration of sodium borohydride, M;

$\mathrm{k}^{\mathrm{hydr}}(T)$ – the constant of hydrolysis rate at temperature T, s^{-1}.

Concentration time derivative is determined on the sites of conversion rate curve where temperature is constant.

5. CONCLUSIONS

In this paper the technique for determination of sodium borohydride hydrolysis rate in water-alkali solutions by determination of realised hydrogen (pressure increase) during the hydrolysis into sealed vessel is presented. For experiments with alkali concentration 0.001 M, 0.1 M and 2.5 M the evaluation of maximal error for the technique was performed, and it was calculated not to exceed 4.4%. Among the most important parameters having effect on conversion rate the pressure of saturated vapour above the solution, solution temperature expansion and hydrogen dissolution are outlined. 50 constant of hydrolysis determined for 8 levels of alkali concentration at different temperatures from 20 to 90 ^{o}C are given.

REFERENCES

1. Jensen E.H. A study on sodium borohydride Copenhagen. 1954. 219 p.
2. Lyttle D.A., Jensen E.H., Struck W.A. A simple volumetric assay for sodium borohydride // *Anal. Chem.* 1952. Vol. 24, p. 1843–1844.
3. Knechtel J.R., Fraser J.L. Preparation of a Stable Borohydride Solution for Use in Atomic-absorption Studies // *Analyst*. 1978. Vol. 103, p. 104–105.
4. Davis R.E., Swein C.C. General acid catalysis of the hydrolysis of sodium borohydride // *J. Amer. Chem. Soc.* 1960. Vol. 82, p. 5949–5950.
5. Kreevoy M.M., Hutchins J.E.C. H_2BH_3 as an intermediate in tetrahydridoborate hydrolysis // *J. Amer. Chem. Soc.* 1972. Vol. 94, No. 18, p. 6371–6376.
6. Kreevoy M.M., Jacobson R.W. The rate of decomposition of $NaBH_4$ in basic aqueous solutions // *Ventron Alembic*. 1979. Vol. 15, p. 2–3.
7. Mesmer R.E., Jolly W.L. The hydrolysis of aqueous hydroborate // *Inorganic Chemistry*. 1962. Vol. 1, No. 3, p. 608–612.
8. Mochalov K.N., Shifrin Kh.V., Bogonostsev A.S. Sodium borohydride hydrolysis // *J. of Physical Chemistry*. 1963. No. 11, p. 2404–2407.

9. Khain V.S., Volkov A.A. On stability of water solutions of sodium and potassium tetraborohydrides // *J. of Applied Chemistry*. 1980. Vol. 53, No. 11, p. 2404–2406.
10. Mochalov K.N., Shifrin Kh.V., Bogonostsev A.S. Kinetics of hydrolysis of potassium borohydride // *Kinetics and Catalysis*. 1964. Vol. 5, № 1, p. 174–177.
11. Mochalov K.N., Khain B.S., Gil'manshin G.G. Overall procedure of borohydride-ion and diborane hydrolysis // *Transactions of Academy of Science of the USSR*. 1965. Vol. 162, No. 3, p. 613–616.
12. Mochalov K.N., Khain V.S., Gil'manshin G.G. Kinetic study of intermediate stages of ion BH_4^- hydrolysis // *Kinetics and Catalysis.* 1965. Vol. 6, issue 3, p. 541–543.
13. Shabunya S.I., Martynenko V.V., Kalinin V.I. et al. Differential methods for experimental study of sodium borohydride kinetically // The Third Intern. Workshop "Nonequilibrium Processes in Combustion and Plasma Based Technologies", Minsk, Belarus, August 23–28. 2008, p. 125–130.
14. Short handbook on chemistry eds. O.D. Kurilenko, 4th edition "Naukova dumka", Kiev, 1964. p. 775, 778.
15. Chemist's handbook eds. B.P. Nikol'skiy, V.3, 2nd edition, "Chimiya", Moscow, 1964. 1008 p.

CYSENI 2009, May 28-29, Kaunas, Lithuania
ISSN 1822-7554, www.cyseni.com

DOPED CERIUM OXIDE THIN FILMS FORMED BY E-BEAM DEPOSITION TECHNIQUE

D. Virbukas, O. Katkauskė, G. Laukaitis, J. Dudonis
Physics Department, Kaunas University of Technology
Studentu str. 50, LT-51368 Kaunas – Lithuania
Phone +370-37-300303
Fax: +370-37-456472
E-mail: darius.virbukas@stud.ktu.lt

ABSTRACT

One of the main challenges in today's solid oxide fuel cell (SOFC) technology is the reduction of their operating temperature. The main influence on SOFC temperature has the electrolyte and its properties. The SOFC electrolyte can be fabricated using physical vapour deposition (PVD) techniques. PVD allow control of the thin film porosity, microstructure, stoichiometry, and growth rate during deposition. It is possible to produce good quality and homogeneous electrolyte thin films. An effective method to control thin film properties is to design the microstructure of the electrolyte by controlling the process parameters using the e-beam deposition (EB) method. The large number of process parameters in the EB process: e-beam power, chamber pressure, substrate temperature, bias voltage, ingot feed rate and work piece motion, have effect on the final coating structures. In the present work, samarium doped ceria oxide (SDC) electrolyte thin films were deposited using e-beam deposition technique. Thin films were grown by evaporating $Ce_{0.85}Sm_{0.15}O_{1.925}$ ceramic nano-powders. The electron beam gun power, bias voltage and substrates types were changed in order to understand the influence on the formed thin films texture, crystallite size, porosity and microstructure. Properties of deposited films were studied by scanning electron microscopy (SEM), X-ray diffraction (XRD) and transmittance spectroscopy in a visible light wavelength region. It was determined that the electron gun power (in range from 0.12 to 0.78 kW) has influence on film crystallite size (increased from 5 to 19.2 nm) which increases as the gun power increases. The porosity decreases up to 9% by increasing bias voltage from 0 to -125 V.

Keywords: samarium doped ceria oxide (SDC), electron beam deposition, solid oxide fuel cells (SOFC), bias voltage

1. INTRODUCTION

One of the main focuses in SOFC development is to lower their operating temperatures to 500 °C so that an expensive materials could be replaced by less expensive metallic ones. Lower temperatures would also increase fuel cell lifetime because of the reduced thermal degradation and thermal cycling stress [1, 2]. In recent years doped ceria, as a potential substitute for stabilized zirconia electrolyte, has increasingly attracted more interest for its higher conductivity in the field of intermediate temperature solid oxide fuel cells [3]. CeO_2 based ceramics are one of the potential candidates to replace YSZ electrolytes in SOFC [4]. Extensive investigations on CeO_2 conductivity with respect to different types of dopants (Ca^{2+}, Sr^{2+}, Y^{3+}, La^{3+}, Gd^{3+} and Sm^{3+}) and their concentrations show that Sm^{3+} and Gd^{3+} dopants give CeO_2 the highest conductivity [5].

CeO_2 is a ceramic material that has a fluorite structure and exhibits very high stability up to its melting point. Doping of this material with divalent or trivalent cations (such as Sm_2O_3) creates oxygen vacancies within its crystal structure and increases the concentration of oxygen-ion vacancies compare to the pure cerium oxide material. Oxygen vacancies are essential for oxygen ion conduction through the material. Presence of vacancies also allows oxygen ions to be inserted in the lattice of the material in oxygen rich environment and to be extracted from it in a low oxygen environment [6]. Although the main focus on ceria based ceramics is for SOFC applications but they also could be used as catalyst, electrochemical filters for oxygen sensors, gas purification membranes, and thermal barrier coatings [7–10]. In those applications, the nanostructured CeO_2 materials attracted much attention due to their considerably small sizes and the general improvements in their physical and chemical properties with respect to their bulklike materials.

Many techniques can be employed for thin film preparation such as traditional wet chemical processing methods (tape casting, tape calendaring, screen printing, transfer printing) or vapor processing methods (chemical vapor deposition, physical vapor deposition, e-beam deposition, sputtering, plasma spray, etc.). Vapor processing methods despite being more expensive and complex provide unique possibilities to make very thin and dense films, to control their thickness, porosity, crystalline structure, grain boundary surface, refractive index and other qualities [11].

In the present study, SDC electrolyte thin films were deposited using e-beam deposition technique. The scope of this work was to investigate the effect of e-beam gun power and bias voltage, applied to the substrates during thin film deposition, on crystallite size, and porosity of SDC thin films.

2. EXPERIMENTAL

SDC thin films (2-3 μm of thickness) were deposited on two types of different substrates: optical quartz (SiO_2) and Alloy 600 (Fe–Ni–Cr). Before deposition substrates were cleaned in an ultrasonic bath (in pure acetone) and their surfaces were treated in Ar ion plasma for 7 minutes. All deposition experiments were performed at the room temperature (20 °C). Cubic phase samarium doped ceria ceramic nanopowder $(Ce_{0.85}Sm_{0.15})O_{1.925}$ (99.9% purity based on trace metal analysis, 5–10 nm particles of powder) was used as evaporation material. Before deposition SDC powder was pressed into pallets. The residual gas pressure in the vacuum chamber during deposition was 2×10^{-3} Pa. The distance between the electron gun and the substrate was fixed at 250 mm. The bias voltage (−125 to 0 V) was applied to the substrate during the deposition of SDC thin films.

The experimental measurements of the thin film thickness were performed using weight method by employing precise (10^{-9} kg) microbalances. Porosity of formed SDC thin films on optical quartz were calculated from transmittance spectra data by using Swanepoel method [12]. Transmittance measurements were performed with Spectruma 300 spectrometer in 370–800 nm wavelength range. The film structure was analyzed by X-ray diffraction (XRD) (DRON-UM1 with standard Bragg-Brentan focusing geometry with an error of 0.01°) in a 10–80° range using the Cu Kα ($\lambda = 0.154059$ nm) radiation. The crystallite size D of SDC thin films was estimated using Scherrer's equation [13]. A scanning electron microscope (SEM, JSM5600) was used to investigate the surface morphology and microstructure of the SDC thin films.

3. EXPERIMENTAL RESULTS AND DISCUSSIONS

The XRD diffraction patterns of the formed SDC thin films at different e-beam gun powers show that the positions of the Bragg peaks are typical for the cubic $(Ce_{0.85}Sm_{0.15})O_{1.925}$ (according to Crystallographica Search-Match, Version 2) (Fig. 1–2).

The XRD peaks of SDC thin films indicate sharp (111) and minor (200), (220), (311) and (222) orientations when the cubic phase SDC powder as evaporation material is used. Formed SDC thin films repeat the crystal structure of the chosen evaporated material at all electron gun powers and the dominant SDC thin films orientation keeps cubic (111) for both type of substrates. Crystallite sizes of SDC thin films vary from 5 nm to 9 nm and from 7 nm to 18 nm for optic quartz (SiO_2) and Alloy-600 (Fe-Ni-Cr) respectively by changing e-beam gun power.

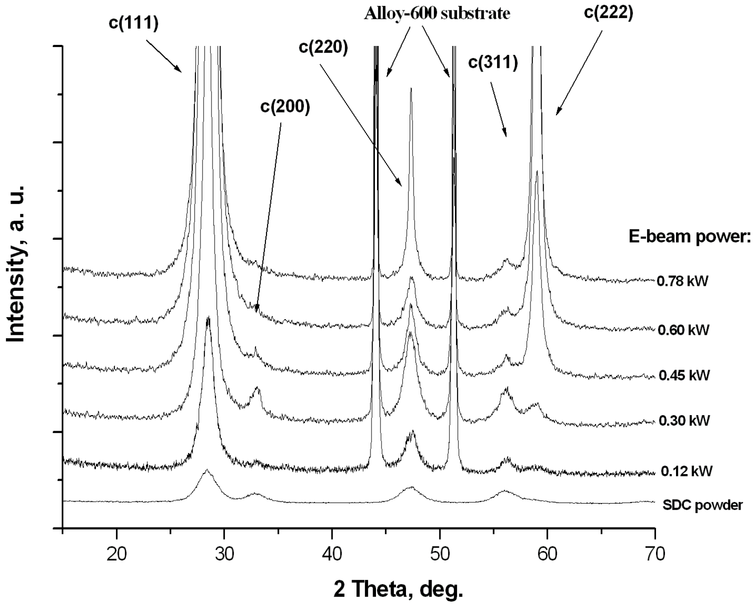

Fig. 1. XRD patterns of SDC thin films deposited on Alloy 600 (Fe-Ni-Cr) substrates at different e-beam gun powers

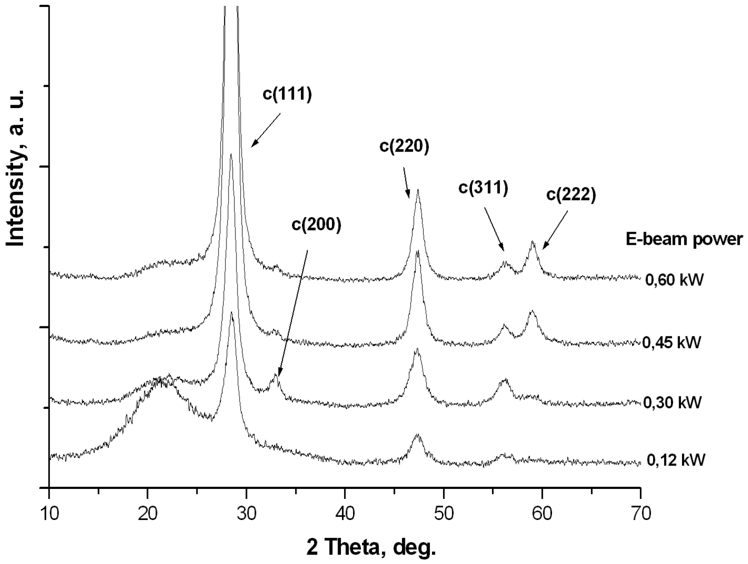

Fig. 2. XRD patterns of SDC thin films deposited on SiO_2 substrates at different e-beam gun powers

Table 1. Dependence of crystallite size on e-beam gun power for SDC thin films formed on Alloy 600 (Fe-Ni-Cr) and SiO_2 substrates

	Crystallite size, nm	
	Substrate type	
E-beam gun power, kW	**Alloy 600 (Fe-Ni-Cr)**	**Optical quartz (SiO_2)**
0.12	7.0	5.6
0.3	7.5	6.0
0.45	9.0	7.2
0.6	11.5	9.0
0.78	18.0	---

Crystallite size (Table 1) increases linearly with the increase of e-beam gun power from 0.12 kW to 0.8 kW (the growth rate increases respectively). The lowest crystallite size is found to be for the e-beam gun power equal to 0.12 kW. It could be caused that during the e-beam deposition and increasing e-beam gun power the vapor stream consists of bigger amount of atoms with the higher energy. The mobility of atoms on the surface of substrate increases too. The same effect was found in the previous work when were formed YSZ thin films [14].

The SEM measurements confirm the influence of e-beam gun power on the crystallite size, i.e. crystallite size increases by increasing the e-beam gun power [15]. Using flat substrates (Alloy 600 and SiO_2) the morphology of the surface region of thin films has a crystalline columnar texture with all columnar grains oriented in the same direction, namely perpendicular to the substrate, and with a predominantly open microporosity [16]. The microstructure consists of parallel columns with gaps in between. The average columnar diameter is close to the crystallite size obtained from XRD data. Nanocrystalline morphology and columnar growth was observed in previous works [17] and by using magnetron sputtering or pulsed laser deposition (PLD) methods, also [18, 19].

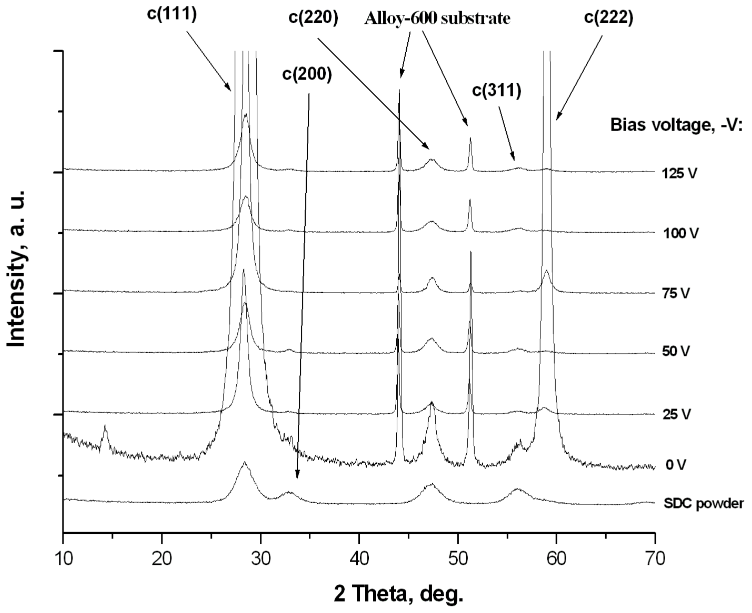

Fig. 3. XRD patterns of SDC thin films deposited on Fe-Ni-Cr (Alloy 600) at different bias voltages (substrate temperature 20ºC)

To get more dense SDC thin films were used an additional ion bombardment initiated by bias (-125 ÷ 0 V) applied to the substrate during the deposition of SDC thin films. XRD measurements show that the formed SDC thin films with applied bias repeat the crystal structure of the chosen evaporated material at all bias voltages. The dominant SDC thin films orientation keeps the same cubic (111) as it was with different e-beam gun powers (Fig. 3.).

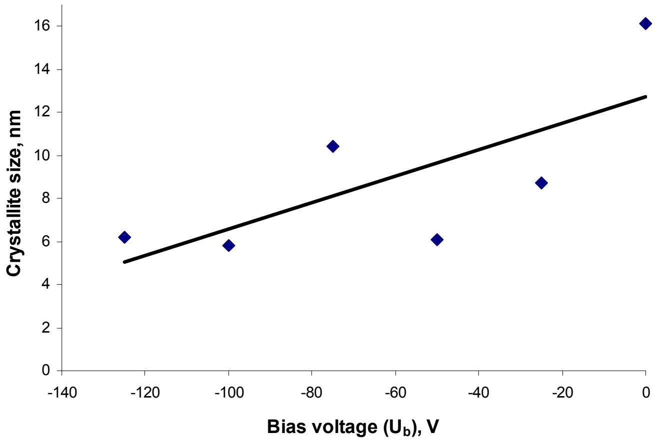

Fig. 4. Crystallite size dependence on bias voltage of SDC thin films deposited on Alloy 600 (Fe-Ni-Cr) substrate

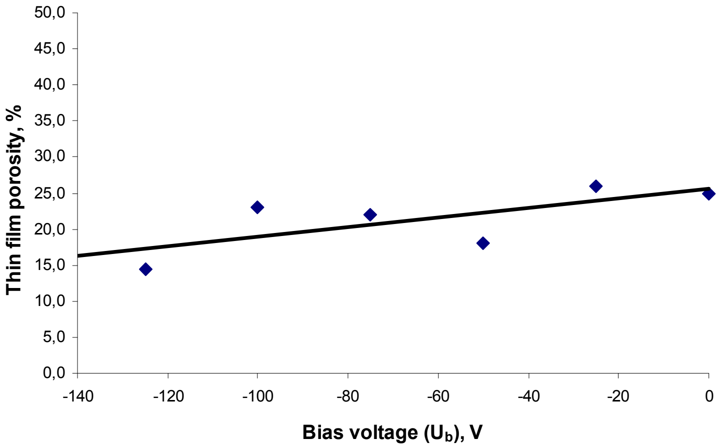

Fig. 5. Dependence of porosity on bias voltage for SDC thin films formed on SiO_2 substrates (e-beam gun power 0.3 kW)

Table 2. Dependence of SDC thin films texture coefficients *R* (normalized to different peaks intensities) on bias voltage

Bias Voltage, V	**R111**	**R200**	**R220**	**R311**	**R222**
	111/(111+200+220+311+222)				
SDC material	0.478	0.099	0.252	0.158	0.013
-0 V	0.936	0.002	0.005	0.002	0.055
-25 V	0.936	0.002	0.005	0.002	0.055
-50 V	0.841	0.021	0.071	0.023	0.044
-75 V	0.622	0.062	0.196	0.078	0.042
-100 V	0.894	0.006	0.038	0.007	0.055
-125 V	0.613	0.054	0.201	0.085	0.047

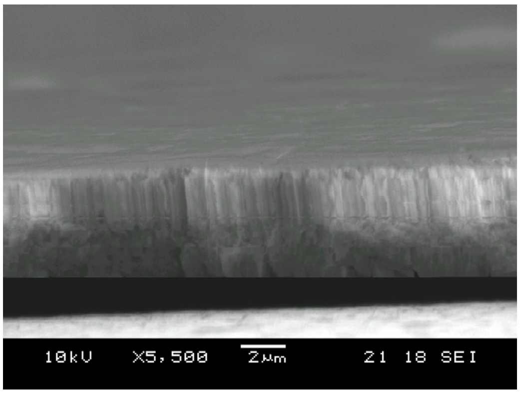

a)

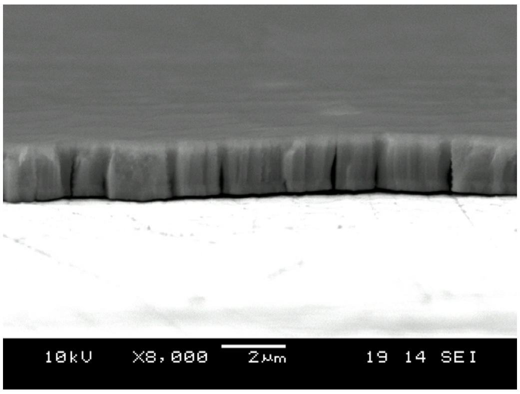

b)

Fig. 6. SEM images of the cross section of SDC thin films deposited on Alloy 600 (Fe-Ni-Cr) substrates with e-beam gun power P= 0.3 kW at applied bias voltages: a) -75V, b) -125 V

The crystallite size decreases with increasing the bias. It decreases to 6 nm (Fig. 4). It can be related to intensified ion flux to the substrate as the bias is increased. Ion bombardment can disturb the columnar growth by enhance of adatom mobility and lead to more dense thin film formation. Porosity of formed SDC thin films on optical quartz was calculated by Swanepoel method [12] from the transmittance measurements. The calculations show that it is possible to control thin film porosity by applying different bias voltage and the porosity decreases up to 9% (comparing to the porosity of SDC thin films formed without bias voltage) by increasing bias voltage to -125 V (Fig. 5). That could be seen not only from calculation but from SEM pictures, also (Fig. 6). As the substrate bias is applied a more compact and dense structure is observed (Fig. 6 b). The density of formed SDC thin layers was increased linearly by increasing bias voltage from 0 to -125 V. By applying the bias voltage is possible to control the size of compact and dense region of the formed SDC layer. The same effect of bias voltage was found in the formation of gadolinium doped cerium oxide thin films in the work [14]. The texture coefficient does not change, also (Table 2). That shows that the applied bias has influence on the crystallite size but did not change the crystallites orientation. The microscopic changes of the deposited film are seen as a function of the applied bias, providing an opportunity to control the microstructure of SDC films for different functional purposes.

4. CONCLUSIONS

E-beam gun power and applied bias to the substrate have influence on the microstructure of electron beam deposited SDC thin films. The crystallite size increases by increasing the e-beam gun power from 5 to 18 nm. Crystallite size decreases by applying the bias to substrate during thin film formation. Also, more compact and dense structure and lower porosity is observed as the substrate bias is applied. The bias does not influence the texture of formed SDC thin films. The SEM pictures are showing that applied bias interrupt columnar growth of thin film.

Acknowledgement

The work was supported by the Lithuanian State Science and Studies Foundation.

REFERENCES

1. S.P.S. Badwal, F.T. Ciacchi, D. Milosevic. Solid State Ionics, 136-137, 2000, p. 91–99.
2. C. Xia, M. Liu. Solid State Ionics, 144, 2001, p. 249–255.
3. B.Lin, W. Sun, at all. Journal of Alloys and Compounds, 465, Issues 1-2, 2008, p. 285–290.
4. F. Wang, B. Wan, S. Cheng. J Solid State Electrochemistry, 9, 2005, p. 168–173.
5. V. Kharton, F. Marques, A. Atkinson. Solid State Ionics, 174, 2004, p. 135–149.
6. M. Y. Cheng, D. H. Hwang, H. S. Sheu, B. J. Hwang. Journal of Power Sources, 175, 2008, p. 137-144.

A. Rice, A. Costa, J. Labrincha, F. Marques. Ionics, 3, 1997, p. 36-43.

7. [8] K. Muthukkumaran, P. Kuppusami, R. Srinivasan, K. Ramachandran, E. Mohandas, S. Selladurai. Ionics, 13, 2007, p. 47-50.
8. H. Hwang, J Moon, M. Awano. Journal of the European Ceramic Society, 24, 2004, p. 1325–1328.
9. Godinho, R. Goncalves, L. Santos, J. Varela, E. Longo, E. Leite, Mater. Lett., 61 (8-9), 2007, p. 1904–1907.
10. L. Pederson, P. Singh, X. Zhou. Vacuum, 80, 2006, p. 1066–1083.

A. Diaz-Parralejo, R. Caruso, A. L. Ortiz, F. Guiberteau. Thin Solid Films, 458, 2004, p. 92–97.

B. B. Patil, S. H. Pawar. Applied Surface Science, 253, 2007, p. 4994-5002.

11. G. Laukaitis, J. Dudonis, D. Milcius. Applied Surface Science, 254, 2008, p. 2980-2987.
12. G. Laukaitis, M. Jauneika, J. Dudonis, O. Katkauske, D. Milcius. Vacuum, 2009, in press.
13. G. Laukaitis, J. Dudonis, D.Virbukas, D. Milčius. Formation of samarium doped ceria oxide thin films, Lithuanian Journal of Physics, 2009, in press.
14. G. Laukaitis, J. Dudonis. Journal of Alloys and Compounds, 459, 2008, p. 320-327.
15. Jong Hoon Joo, Gyeong Man Choi. Journal of the European Ceramic Society, 27 (13-15), 2007, p. 4273-4277.
16. C.Brahim, A.Ringuedé, E. Gourba, M.Cassir, A.Billard, P.Briois. Journal of Power Sources, 156, 2006, p. 45–49.

CYSENI 2009, May 28-29, Kaunas, Lithuania
ISSN 1822-7554, www.cyseni.com

ELECTRICAL PROPERTIES OF CGO-10, 20 SOLID ELECTROLYTE CERAMICS

T. Šalkus, V. Venckutė
Faculty of Physics
Vilnius University
Saulėtekio ave. 9/3, LT-10222 Vilnius, Lithuania
Phone: 852366064
E-mail: tomas.salkus@ff.vu.lt

ABSTRACT

$Ce_{0.8}Gd_{0.2}O_{1.9}$ (CGO-20) and $Ce_{0.9}Gd_{0.1}O_{1.95}$ (CGO-10) solid electrolyte powders with different surface area (BET) were used for preparation of ceramics. The ceramic samples were studied by SEM and impedance spectroscopy. A dispersion of complex conductivity and impedance found in the spectra was attributed to the relaxation of oxygen vacancies in the bulk of ceramics. The relaxation frequency of the mobile ions increases when temperature is increased. Temperature dependences of ionic conductivity follows Arrhenius law and depends both on chemical composition of CGO and on the initial powder used.

Keywords: solid electrolyte, ionic conductivity, ceramic, impedance spectroscopy, relaxation dispersion

1. INTRODUCTION

CeO_2 is a cubic crystal with fluorite-type structure (space group $Fm\bar{3}m$) in the temperature region from 313 to 1770 K [1]. Unit cell parameter of CeO_2 is 5.4070(2) Å at 313 K and it increases with temperature (a = 5.5138(4) Å at 1770 K) [1]. At high temperatures and low oxygen partial pressures Ce^{4+} changes valence to Ce^{3+} in CeO_2. Due to this behaviour ceria is usually written as $CeO_{2-\delta}$ (where $\delta = [Ce^{3+}]/2$) [2].

CeO_2 ionic conductivity is low but it can be significantly increased by doping with three valence metal oxides such as Y_2O_3 [3–6], Gd_2O_3 [6-8], Sm_2O_3 [4, 6, 9], Sc_2O_3 [5], La_2O_3 [6]. Thus oxygen vacancies, determinant ionic transport, are created in the material. The crystal structure of $Ce_xGd_{1-x}O_2$ remains unchanged in the region $0 \leq x < 0.5$ [2]. Unit cell parameter of $Ce_{0.9}Gd_{0.1}O_{1.95}$ is 5.418 Å [10], its density determined from X-ray diffraction (d_{XRD}) – 7.12 g/cm^3 [11]; unit cell parameter of $Ce_{0.8}Gd_{0.2}O_{1.9}$ is 5.4243(6) Å, d_{XRD} = 7.24 g/cm^3 [2]. The unit cell of CGO increases with increasing amount of Gd_2O_3 dopant because of the bigger ionic radii of Ce^{4+} (0.94 Å) compared to Gd^{3+} (0.96 Å) [5]. Ionic conductivity of $Ce_{0.8}Gd_{0.2}O_{1.9}$ is 0.35 S/m at 773 K, its activation energy is 0.89 eV [2]; ionic conductivity of $Ce_{0.9}Gd_{0.1}O_{1.95}$ is 0.63 S/m at 773 K, its activation energy – 0.6 eV [11].

Due to high ionic conductivity and appearance of electronic conductivity in H_2 atmosphere [12, 13] CeO_2 doped by Gd_2O_3 or Sm_2O_3 are candidates for solid oxide fuel cell (SOFC) anodes. Therefore the understanding of the processes related to the ionic transport in the ceramics as well as the influence of the ceramic preparation on electrical properties are of great importance. In the present work $Ce_{0.8}Gd_{0.2}O_{1.9}$ (CGO-20) and $Ce_{0.9}Gd_{0.1}O_{1.95}$ (CGO-10) solid electrolyte ceramics were prepared from powders with different BET. Impedance spectroscopy technique allowed us to determine ionic conductivity of the ceramics.

2. METHODOLOGY

Powders of CGO-10 with different BET (6.44 m^2/g and 158.3 m^2/g) and CGO-20 (BET = 220 m^2/g) from company Fuel Cell Materials, USA were used for ceramics' preparation. The nanopowders were pressed at 100 MPa and the powder of CGO-10 with BET = 6.44 m^2/g was pressed at 300 MPa pressure in 8 mm die. The sintering of the ceramics was performed at 1573 K for 1 h.

The surfaces of the ceramics were observed by scanning electron microscope (SEM Leo 1530).

Impedance and conductivity spectra were recorded using coaxial line spectrometer. The block scheme of the set-up is shown in Fig. 1.

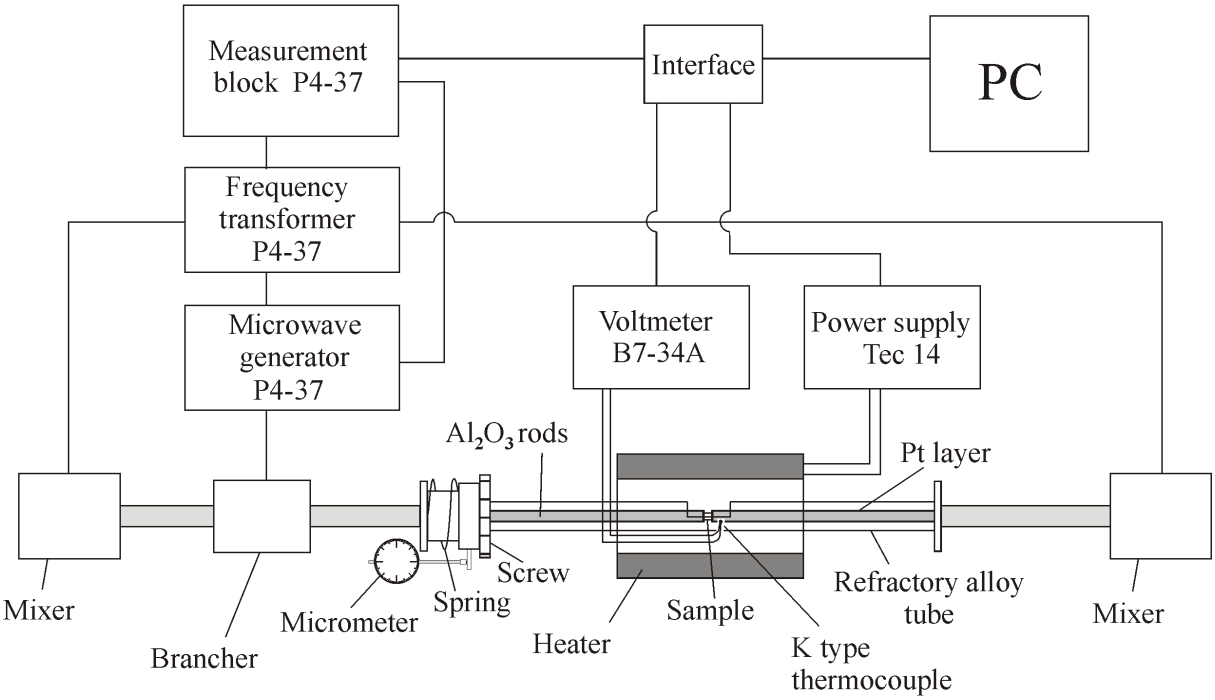

Fig. 1. Scheme of coaxial line and impedance measurement's equipment operating at frequencies 1 MHz – 1.2 GHz

An inner conductor of the coaxial line is cut into two parts. A gap between them is controlled by micrometer connected to a screw. A spring ensures proper contacts between the ends of the inner conductor's parts. The method of finding of electrical properties using this set-up is based on the measurement of complex transmission coefficient ($\widetilde{T}$). Three measurements should be performed to calibrate the set-up: one when the line is short-circuited and two with calibration samples with known electrical parameters. Impedance of the sample

$$\widetilde{Z}(f) = Z' - \mathrm{i}Z'', \tag{1}$$

specific impedance of the material

$$\widetilde{\rho} = \widetilde{Z}\frac{S}{l}, \tag{2}$$

(where *S* is the area of the electrode, *l* is the length of the sample) and complex conductivity

$$\widetilde{\sigma} = \sigma' + \mathrm{i}\sigma'' = \frac{1}{\widetilde{\rho}} \tag{3}$$

are then calculated from $\widetilde{T}$ as described in [14–16]. Impedance spectrometer based on P4-37 instrument operates in the frequency range from 1 MHz to 1.2 GHz. The measurements of electrical parameters were performed in the temperature range 500–750 K. The temperature of the sample is measured by K-type thermocouple. The experiment is fully controlled by a computer through an interface.

3. RESULTS AND DISCUSSION

A relaxational dispersion has been found in the frequency dependences of conductivity (Fig. 2) and impedance (Fig. 3). The dispersion is related to the migration of oxygen vacancies in the ceramics. The process is thermally activated and the frequency range of this dispersion shifts towards higher frequencies when temperature is increased.

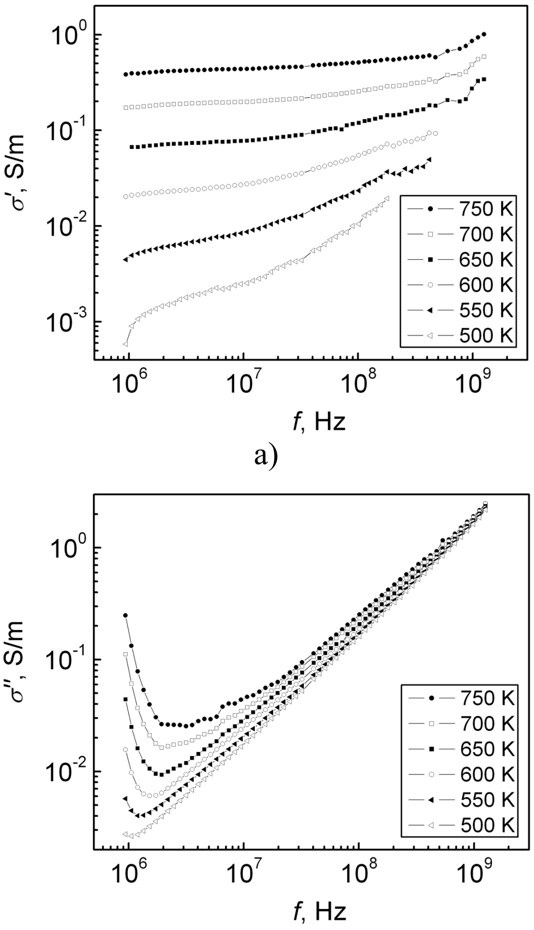

a)

b)

Fig. 2. Frequency dependences of the real (a) and imaginary (b) parts of complex conductivity of CGO-20 ceramics measured at different temperatures

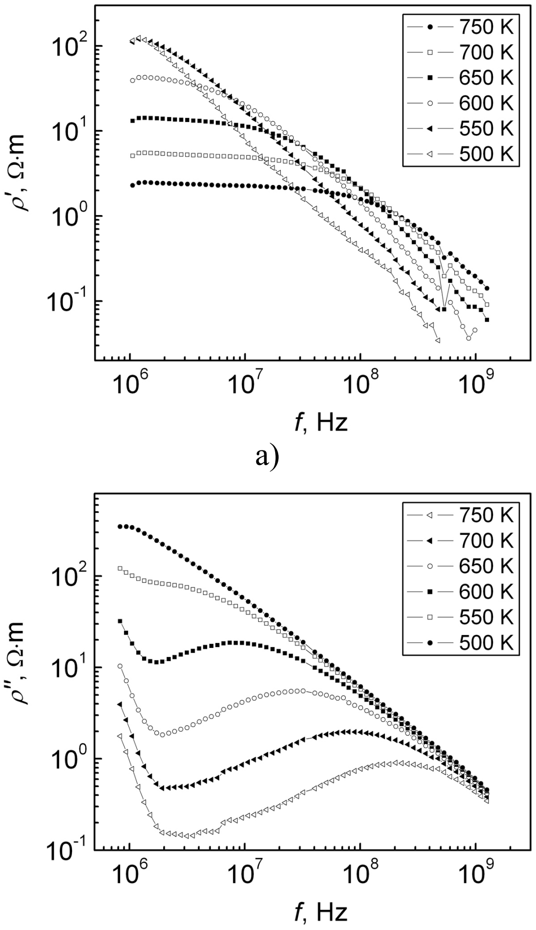

a)

b)

Fig. 3. Frequency dependences of the real (a) and imaginary (b) parts of impedance of CGO-20 ceramics measured at different temperatures

Relaxation frequencies (f_R) of oxygen vacancies have been determined from the maxima of $\rho''(f)$. At frequencies much higher than f_R dielectric permittivities of the investigated compounds can be calculated:

$$\varepsilon' = \frac{\sigma''}{2\pi f \varepsilon_0}, \tag{4}$$

where ε_0 – dielectric constant of vacuum. In our case ε' was calculated at 1 GHz frequency. The values of f_R and ε' at 700 K are presented in Table 1.

Table 1. Relaxation frequencies (f_R) and dielectric permittivities (ε') of CGO samples at 700 K

Sample	**f_R, Hz**	**ε'**
CGO-10, BET = 6.44 m^2/g	$1.5 \cdot 10^8$	36
CGO-10, BET = 158.3 m^2/g	$1.15 \cdot 10^8$	34
CGO-20, BET = 220 m^2/g	$8 \cdot 10^7$	30

Dielectric permittivity of the studied ceramics increases while temperature is increased. Such behaviour is common for most solid electrolytes.

The values of the ceramics' conductivity can be obtained from conductivity or impedance in complex plain [17]. The intersection of the semicircle in $\rho''(\rho')$ plot with the real axis corresponds to bulk ionic resistance of the ceramics (ρ) and the intersection of a curve in $\sigma''(\sigma')$ plot with the real axis corresponds to bulk ionic conductivity of the ceramics (σ). Furthermore $\sigma = \frac{1}{\rho}$. Complex impedance plots of the studied ceramics are shown in Fig. 4 and complex conductivity plots are shown in Fig. 5.

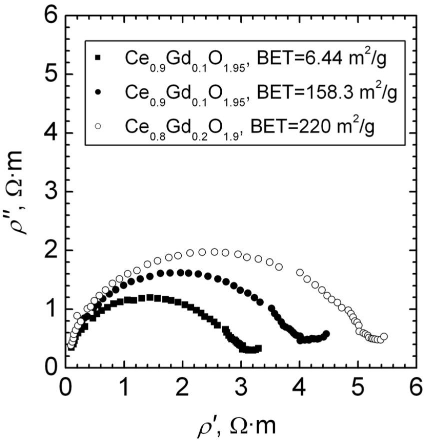

Fig. 4. Complex impedance plots of CGO ceramics measured at 700 K.

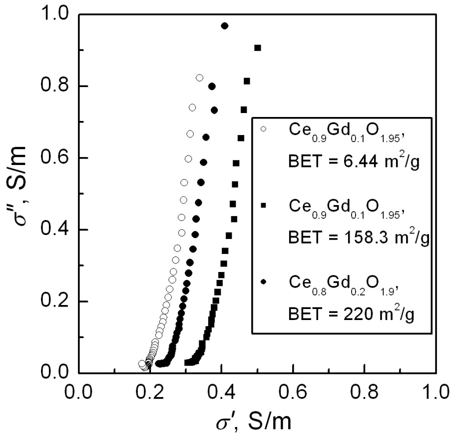

Fig. 5. Complex conductivity plots of CGO ceramics measured at 700 K.

Temperature dependences of σ are shown in Fig. 6. Ionic conductivities of CGO ceramics change with temperature according to Arrhenius law

$$\sigma = \sigma_0 \exp\frac{-\Delta E}{\mathrm{k}T}, \tag{5}$$

where T is temperature, σ_0 – preexponential factor, ΔE – activation energy of conductivity, k – Boltzmann's constant.

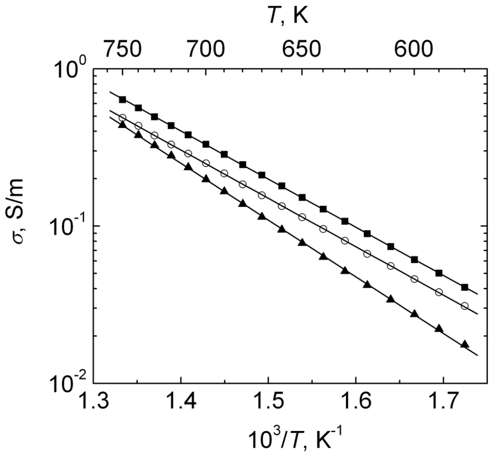

Fig. 6. Temperature dependences of bulk conductivity of CGO-10 ceramics prepared from powder with BET = 6.44 m^2/g (■), BET = 158.3 m^2/g (○) and CGO-20 (BET = 220 m^2/g) (▲)

CGO-10 ceramics prepared from powder with smaller BET shows higher ionic conductivities. This experimental result can be explained by looking at different microstructure of the obtained ceramics. The crystallites observed by SEM (Fig. 7) are bigger for ceramics, prepared from powders with bigger grains and the relative density of obtained ceramics are also higher when initial powder with BET = 6.44 m^2/g was used. However the activation energies of both studied CGO-10 ceramics are the same. Electrical parameters and densities of CGO are presented in Table 2.

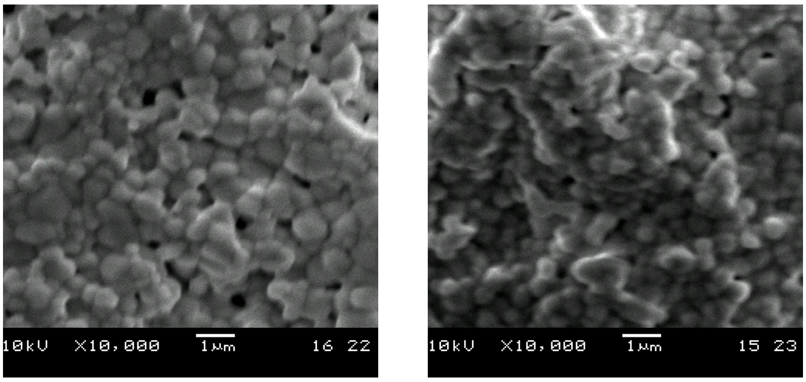

a) b)

Fig. 7. SEM images of CGO-10 ceramics prepared from powders with BET=6.44 m^2/g (a) and BET=158.3 m^2/g (b).

Table 2. Bulk ionic conductivities (σ), activation energies (ΔE) at 700 K, and relative densities (d) of CGO samples.

Sample	**σ_b, S/m**	**ΔE, eV**	***d*, %**
CGO-10, BET = 6.44 m^2/g	0.32	0.61	94
CGO-10, BET = 158.3 m^2/g	0.24	0.61	91.5
CGO-20, BET = 220 m^2/g	0.19	0.72	89.7

4. CONCLUSIONS

A relaxational dispersion has been found in conductivity and impedance spectra of CGO-10 and CGO-20 ceramics in the frequency range 1 MHz – 1.2 GHz and temperatures from 500 to 750 K. The dispersion is related to fast oxygen vacancy transport in the bulk of ceramics. Ionic conductivity of the ceramics was described by Arrhenius law. The highest ionic conductivity was found for CGO-10 sample prepared from powder with BET = 6.44 m^2/g, its $\sigma = 0.32$ S/m, $\Delta E = 0.61$ eV, $\varepsilon' = 36$ at 700 K. The conductivity of above mentioned ceramic is higher due to bigger crystallites observed by SEM.

ACKNOWLEDGEMENT

This work was supported by Lithuanian State Science and Studies Foundation.

REFERENCES

1. M. Yashima, S. Kobayashi, and T. Yasui. Crystal structure and the structural disorder of ceria from 40 to 1497 °C // Solid State Ionics, Vol. 177. 2006, p. 211–215.
2. G. Chiodelli, L. Malavasi, V. Massarotti, P. Mustarelli, and E. Quartarone. Synthesis and characterization of $Ce_{0.8}Gd_{0.2}O_{2-y}$ polycrystalline and thin film materials // Solid State Ionics, Vol. 176. 2005, p. 1505–1512.
3. P. Sarkar, P.S. Nicholson. Electric field relaxation studies in the CeO_2–Y_2O_3 system // J. Phys. Chem. Solids, Vol. 50. 1989, p. 197–206.
4. T. Inoue, T. Setoguchi, K. Eguchi, and H. Arai. Study of a solid oxide fuel cell with a ceria-based solid electrolyte // Solid State Ionics, Vol. 35. 1989, p. 285–291.
5. Y.S. Zhen, S.J. Milne, and R.J. Brook. Oxygen ion conduction in CeO_2 ceramics simultaniously doped with Gd_2O_3 and Y_2O_3 // Science of Ceramics, Vol. 14. 1988, p. 1025–1030.
6. R.-Q. Liu, Y.-H. Xie, J.-D. Wang, Z.-J. Li, and B.-H. Wang. Synthesis of ammonia at atmospheric pressure with $Ce_{0.8}M_{0.2}O_{2-\delta}$ (M = La, Y, Gd, Sm) and their proton conduction at intermediate temperature //Solid State Ionics, Vol. 177. 2006, p. 73–76.
7. C. Xia and M. Liu. Low-temperature SOFCs based on $Gd_{0.1}Ce_{0.9}O_{1.95}$ fabricated by dry pressing // Solid State Ionics, Vol. 144. 2001, p. 249–255.
8. U. Nigge, H.-D. Wiemhöfer, E.W.J. Römer, H.J.M. Bouwmeester, and T.R. Schulte. Composites of $Ce_{0.8}Gd_{0.2}O_{1.9}$ and $Gd_{0.7}Ca_{0.3}CoO_{3-\delta}$ as oxygen permeable membranes for exhaust gas sensors // Solid State Ionics, Vol. 146. 2002, p. 163–174.
9. T. Matsui, T. Kosaka, M. Inaba, A. Mineshige, and Z. Ogumi. Effects of mixed conduction on the open-circuit voltage of intermediate-temperature SOFCs based on Sm-doped ceria electrolytes // Solid State Ionics, Vol. 176. 2005, p. 663–668.
10. G. Brauer and H.Z. Gradinger. Über heterotype Mischphasen bei Seltenerdoxyden. I // Anorg. Allg. Chem., Vol. 276. 1954, p. 209.
11. C. Xia and M. Liu. Microstructures, conductivities, and electrochemical properties of $Ce_{0.9}Gd_{0.1}O_2$ and GDC–Ni anodes for low-temperature SOFCs // Solid State Ionics, Vol. 152–153. 2002, p. 423–430.
12. T. Matsui, M. Inaba, A. Mineshige, and Z. Ogumi. Electrochemical properties of ceria-based oxides for use in intermediate-temperature SOFCs // Solid State Ionics, Vol. 176. 2005, p. 647–654.

13. S.H. Chan, X.J. Chen, and K.A. Khor. A simple bilayer electrolyte model for solid oxide fuel cells // Solid State Ionics, Vol. 158. 2003, p. 29–43.
14. R. Sobiestianskas, A. Dindune, Z. Kanepe, J. Ronis, A. Kežionis, E. Kazakevičius, and A. Orliukas. Electrical properties of $Li_{1+x}Y_yTi_{2-y}(PO_4)_3$ (where x, y = 0.3; 0.4) ceramics at high frequencies // Materials Science & Engineering, Vol. B 76. 2000, p. 184–192.
15. W. Bogusz, J.R. Dygas, F. Krok, A. Kezionis, R. Sobiestianskas, E. Kazakevicius, and A. Orliukas. Electrical conductivity dispersion in co-doped NASICON samples // Phys. Stat. Sol., Vol. A 183 (2), 2001, p. 323–330.
16. A.F. Orliukas, A. Kezionis, and E. Kazakevicius. Impedance spectroscopy of solid electrolytes in the radio frequency range // Solid State Ionics, Vol. 176. 2005, p. 2037–2043.
17. J. Ross Macdonald. Impedance Spectroscopy. Emphasizing Solid Materials and Systems. John Wiley & Sons, New York Chichester Brisbane Toronto Singapore, 1987.

CYSENI 2009, May 28-29, Kaunas, Lithuania
ISSN 1822-7554, www.cyseni.com

INVESTIGATIONS OF HYDROGEN SORPTION PROPERTIES USING SIEVERT TYPE APPARATUS

L. Grinberga, E. Rancans, J. Kleperis
Institute of Solid State Physics of University of Latvia
8 Kengaraga str., Riga, LV-1063, Latvia
Phone: +371 67262145
E-mail: Liga.Grinberga@cfi.lu.lv

ABSTRACT

Gas sorption analysis is important in many fields of material science though it has a vital role in the development of energy storage materials lately. The Sievert or volumetric (manometric) method is simple enough and within scientists is accepted as an accurate technique. Apparatus PCTPro 2000 determines the amount of hydrogen gas that is sorbed in studied material by measuring pressure changes in a reservoir where the volume and the temperature is known. The sophisticated software for procedure automation of the measurements is used that ensures a safe operations and a reliable data collecting and processing. Using PCTPro 2000 equipment is possible to determine the pressure composition isotherms (PCT), gas sorption kinetics, heat-of-formation, cycle-life kinetics, cycle-life PCT and calibrate the volume. Our first measurements using hydride forming materials as Pd and $LaNi_5$ are performed to learn and investigate the operational issues and to gain experience with the new Sievert type apparatus PCTPro-2000.

Keywords: Volumetric method, hydrogen sorption, metal hydride

1. INTRODUCTION

Due to the decreasing oil reserves and inconsistent oil price there is great interest in the development and investigations of original materials for the transition to renewable energy. Comparison of the hydrogen fuel with petrol shows that an effective technique of hydrogen storage can be regarded that for competitive system the mass of hydrogen content must exceed 5%, while that of volume should exceed 60 kg/m^3 [1]. The hydrogen storage in solid materials proceeds through at least three mechanisms: adsorption, absorption and chemical reactions. Adsorption process has two forms - physisorption and chemisorption, as the case from the bond between a hydrogen molecule and material. Adsorptive processes typically require highly porous materials with a high surface area available for hydrogen sorption to occur. There is evidence of adsorption of molecular hydrogen mostly; nevertheless atomic hydrogen could be adsorbed during spill-over processes [2, 3].

There are many metals known which form hydrides, since 1889, when Graham [4] firstly reported that palladium metal could absorb a large amount of hydrogen. The character of the metal-hydrogen bond is very dependent on the properties of the metal atoms due to low electron affinity of hydrogen. Unfortunately, none of the metals fulfil the requirements for commercial use as hydrogen storage materials – high reversible storage capacity and fast kinetics at ambient temperature.

The science of gas sorption has become particularly important in the development of materials for hydrogen storage. To test the adequacy of the new materials for hydrogen economy the characterization of gas absorption, adsorption and desorption kinetics, capacity, thermodynamic properties, as well as cycling performance of reversible materials is crucial. The ability to measure the tolerance of material to air, moisture and contaminants is important as well.

Several techniques are employed for gas sorption measurements but the most common ones are gravimetric and volumetric methods. In gravimetric methods, the amount of sorbed gas is determined by measuring the apparent mass change of the sample. In volumetric methods, the amount of gas sorbed is typically determined by a change in pressure within a calibrated volume containing the sample. The PCTPro-2000 is a volumetric instrument that offers the best state-of-the-art measurements [5].

2. THEORETICAL DESCRIPTION

The major component of a Sievert type apparatus is a gas manifold with a series of tubes and valves connecting the sample chamber to one or more gas reservoirs of known volume, and pressure transducers for measuring reservoir pressure (Fig. 1).

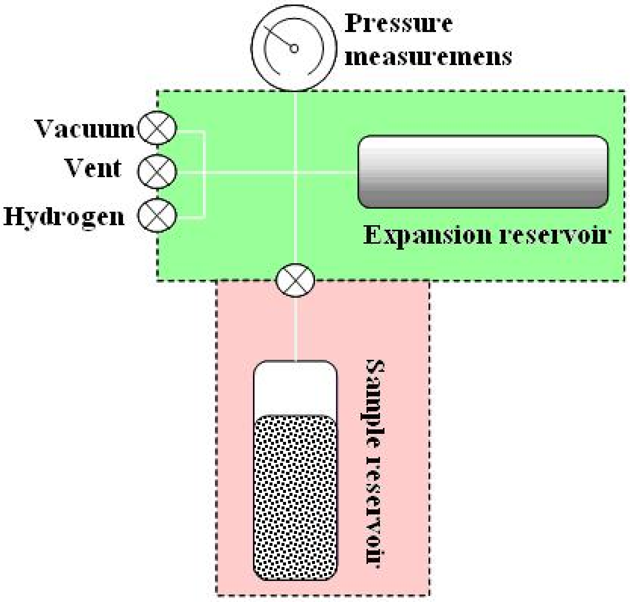

Fig. 1. Schematic of PCTPro-2000 apparatus [6]

By knowing the initial and final pressure and volume of a sample chamber the quantity Δn of gas absorbed or desorbed by the samples is calculated:

$$\Delta n = \frac{P_f (V_R + V_S) - (P_R V_R + P_S V_S)}{RT}, \tag{1}$$

where P_f, P_S, P_R – measured, sample and reservoir pressure, accordingly, V_R – reservoir volume, V_S – sample volume, R – universal gas constant and T – temperature [5].

Using a wide range of calibrated volumes, pressure and temperature measurements, it is possible to make a wide range of analyses with one device. The provided analyses of PCTPro-2000 are capacity, kinetics, pressure composition isotherm, thermodynamic and material performance measurements.

Capacity is the highest hydrogen concentration measured in the hydride phase. This value depends of pressure and temperature changes, therefore precise measurements are required. Comparatively with the gravimetric method where even small amounts of impurities in the test gas may strongly impact a result, in the volumetric method impurities possibly will impact the performance of the material, but they will not produce a significant pressure changes and wherefore will not affect the result significantly [6]. Usually the capacity is presented in both an atomic ratio, H/M (H-hydrogen, M-metal or alloy), and weight percent:

$$wt\% = \frac{H}{H+M} \cdot 100\% \,. \qquad (2)$$

Kinetics refers to measurements of gas absorption and desorption from a sample as a function of time. PCTPro – 2000 consists of five reservoirs with a range of volumes from 4 to 1200 cc that enables to use a variety of sample sizes and a sorption conditions for different type of experimental materials. Moreover, sorption reactions involve endothermic or exothermic processes and heat transfer from the sample is necessary to provide proper measurements [7].

Pressure – Composition – Temperature (PCT) measurements are one of the most reported methods to describe properties of the hydrogen storage materials in the literature as well as the most informative one. The result is a plot of the equilibrium absorbed gas concentration in the material as a function of pressure and temperature (Fig. 2).

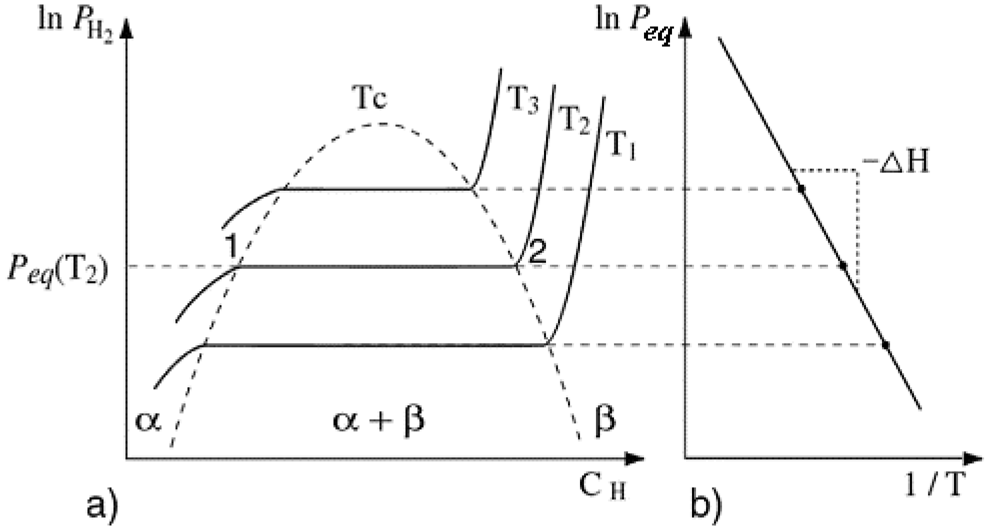

Fig. 2. a) PCT curve; b) van't Hoff plot [7]

The PCT plot is representing an equilibrium plateau providing a complete phase diagram. For metal hydride materials that reversibly react with hydrogen, on the left side of the plateau will be the solid solution α-phase, where hydrogen is randomly dissolved within the solid matrix, while on the right side of the plateau is located the β-phase, where hydrogen is in distinct structural sites and is bonded to the host solid material (Fig. 2.a)). In between there is a well-defined plateau where both phases are coexisting.

The instrument obtains PCT measurements by adding/removing hydrogen gas to/from the sample volume in a small doses and waiting for the resulting gas/solid equilibrium. During the measurements the concentration of gas sorbed and the final pressure of each dose is determined and data points are plotted as it is seen on Fig. 2 a). Each dose gives one point to form the curve thereby the more doses will be applied the more points will be measured and more information will be gathered. Well defined PCT measurements can provide detailed information on the presence of crystal structure changes, new phases and sorption kinetics as a function of gas concentration.

Using the data from PCT curves a van't Hoff plot (Fig. 2. b)) can be drawn. It provides information on the free-energy, enthalpy and entropy change in a reaction and is widely used to characterize hydrogen-storage materials. These thermodynamic properties are presented in the van't Hoff equation:

$$\ln P = \frac{\Delta H}{RT} - \frac{\Delta S}{R}, \tag{3}$$

where $\ln P$ – natural logarithm of equilibrium pressure, T – temperature in K, ΔH – enthalpy change of hydriding, ΔS – entropy change of hydriding, R – universal gas constant.

The slope of a van't Hoff plot is linearly related to the latent heat (ΔH) of a vaporizing or subliming substance. The Clausius-Clapeyron equation for enthalpy is:

$$-\Delta H = R\frac{(\ln P_2 - \ln P_1)}{\left(\frac{1}{T_2} - \frac{1}{T_1}\right)}, \tag{4}$$

where the index *2* represents the highest values, but the index *1* represents the lowest values.

The standard Gibbs free energy ΔG change is the maximum reversible work that can be obtained from a mole of ideal gas at standard temperature against the resistance of standard atmospheric pressure. Hydrogen is a very nearly ideal at moderate pressures and temperatures. An equation for Gibbs free energy can be derived as:

$$\Delta G_i = RT_i \ln\left(\frac{P}{P_i}\right), \tag{5}$$

where the index *i* stands for initial values, but P is the final pressure after temperature *T* is applied.

Now the entropy can be calculated:

$$\Delta S = \frac{\Delta H - \Delta G_i}{T} \tag{6}$$

In addition to the all measurements described above Sievert type instrument PCTPro-2000 is good for collecting important material performance data as well. For example, by making cycle life measurements it is possible to determine degradation of material by multiple absorption – desorption cycles. There can be performed also catalytic measurements by adding different impurity gases (as CO, CO_2, etc) in the sorption gas. The tolerance of the sample to poisoning can be determined. This information is very useful and important when a material potential for commercial applications is considered.

3. EXPERIMENTAL

PCTPro-2000 is a fully automated Sievert type instrument for measuring gas sorption properties of materials. There are several advanced features combined in one instrument, such as controlled gas pressure, accurate gas handling system under controlled temperature environment, 5 different calibrated volumes, automatic high and low-range pressure switching and sophisticated measurement and process controls. An experimental range of pressure lies between 0.01 and 200 bar and temperatures in a sample chamber can be set up from cryogenic to 400°C.

The standard sample holder has a small dead volume (<10 cm^3). It is designed to transfer samples without an air contact from a glove box to the instrument. The sample holder is designed for ease of handling, cleaning, loading and closing in a glove box environment. It includes a thermocouple in the centre of the sample, direct-connect access to sample for other instrumentation if necessary, and copper cladding for even temperature distribution (Fig. 3).

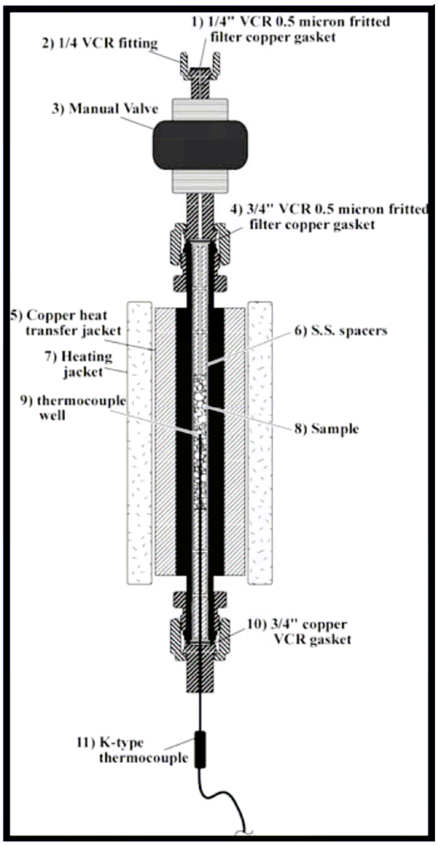

Fig. 3. Cross-section of the sample holder [8]

The hydrogen gas supply should be free of moisture and gaseous impurities, for experiments the hydrogen purity have to be not less than 99.999%. The system is automated by using pneumatic valves and controlled by software therefore a clean, compressed air is necessary. Using oil air-pumps the oil filters must be used to maintain life time of valves. For calibration of volume a helium gas must be provided while other gases to run specific material poisoning measurements can be added to the instrument.

Before starting each new sample measurement several procedures must be done to prevent leaks, dangerous mixtures of gas and air, contamination of samples, invalid measurements or damage of the equipment. Purging of gas lines when a new gas connection has been made as well as purging of system and sample volumes when a connection was open to an air is crucial. When a new sample is connected it is necessary to perform a leak check for a safety reasons and accurate measurements [8].

The PCTPro-2000 apparatus provides a volume calibration process to calibrate the empty volume of the sample holder and connecting lines up to the first valve 1 (Fig. 3) that is necessary to be able to make accurate kinetic, PCT and cycle life measurements. Furthermore, this calibration procedure can be performed in two steps to obtain the density of a sample – without and with a sample in the sample holder. The difference is the volume of the sample and density is calculated from this volume and mass of the sample. This two-step calibration process offers to measure volume expansion during gas sorption as well.

After these treatments the experimental part can be started. In the Fig. 4 a regular window of measurement types is shown.

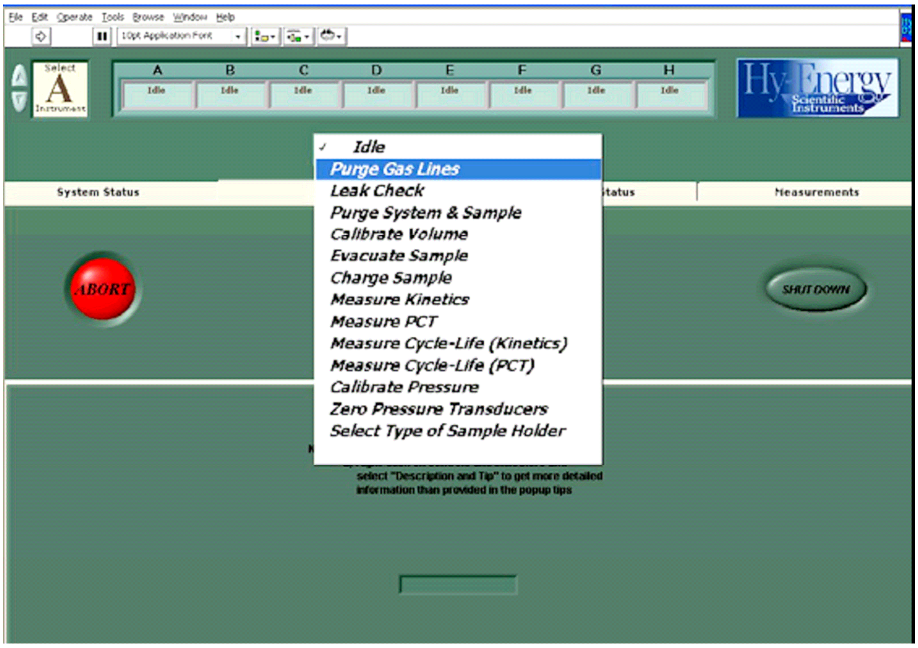

select "Description and Tip" to get more detailed information than provided in the popup tips

Fig. 4. The master control panel [8]

A typical measurement consists of several steps. The first one is a sample pre-treatment that differs from sample to sample e.g. for metal hydrides it is necessary to activate the sample by heat treatment and series of charging and discharging. Afterwards, the sample is brought to the desired temperature for main measurements. Secondly, the valve between the sample and reservoir must be closed and gas into the reservoir to bring it to the pressure of interest is introduced. When the valve is opened again the reservoir pressure change can be observed – it is so called 'dead volume' that must be deduced from the amount of gas uptake by the sample.

For full capacity and kinetics measurements the reservoir must hold significantly more gas than the uptake or release in the sample so that the pressure will not vary significantly during the measurements. By repeating the measurement at different pressures at a fixed temperature, the pressure–composition isotherm can be obtained. Gained data can be used to calculate thermodynamic properties and to estimate absorbed/desorbed amount of the hydrogen gas.

For a determination of novel material endurance, degradation and/or poisoning impact a cycle-life measurements are the most appropriate. PCTPro-2000 provides a fully automated routine that combines a series of absorption and desorption kinetics or PCT measurements. The reservoir volumes and pressures should be selected for complete absorption and desorption as is done with a full kinetics or PCT measurements. The end result is one data file with the samples concentration (or pressure) as a function of time for the entire cycling experiment for kinetics measurements. However, for PCT measurements the data set displays a sample equilibrium pressure as a function of concentration as well as the full time history for the entire cycling experiment.

4. RESULTS

PCTPro-2000 is very advanced instrument with an excellent possibilities to perform a precise and advanced measurements that allows investigating hydrogen storage materials. Although, apparatus is very well developed there must be experience gained before one can feel sure about achieved results.

For the first experiments Pd powder was chosen and sample treatment was performed as described before. Parameters used for PCT measurements are showed in Fig. 5.

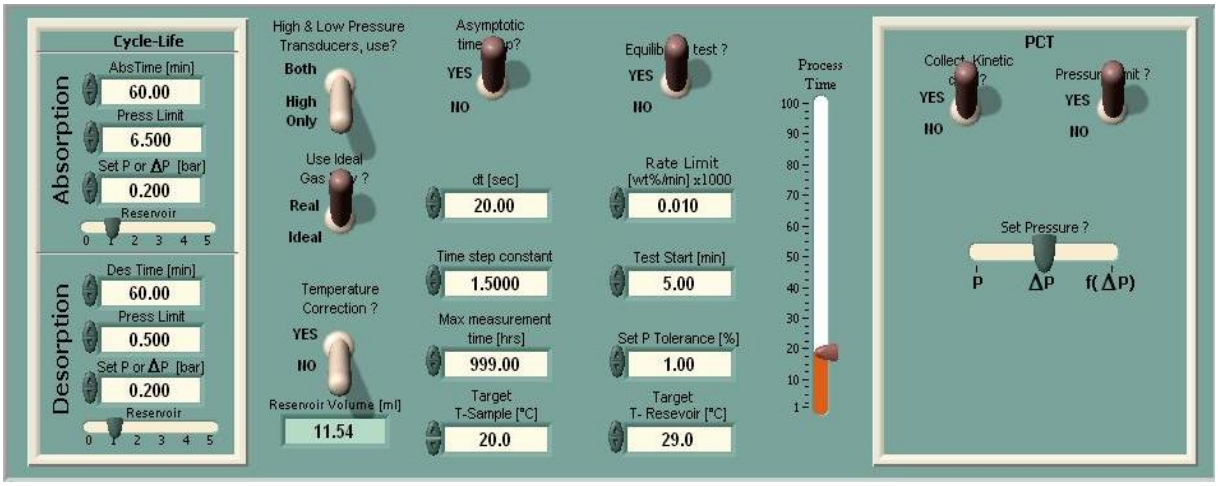

Cycle-Life

Absorption
AbsTime [min] 60.00
Press Limit 6.500
Set P or ΔP [bar] 0.200
Reservoir 1

Desorption
Des Time [min] 60.00
Press Limit 0.500
Set P or ΔP [bar] 0.200
Reservoir 1

High & Low Pressure Transducers, use? High Only
Use Ideal Gas ? Real
Temperature Correction ? NO
Reservoir Volume [ml] 11.54
Asymptotic time p? YES
dt [sec] 20.00
Time step constant 1.5000
Max measurement time [hrs] 999.00
Target T-Sample [°C] 20.0
Equilib test ? YES
Rate Limit [wt%/min] x1000 0.010
Test Start [min] 5.00
Set P Tolerance [%] 1.00
Target T- Resevoir [°C] 29.0

PCT
Collect Kinetic ? YES
Pressu mit ? YES
Set Pressure ? ΔP

Fig. 5. The parameter control panel

The dose of hydrogen that was introduced to the sample at each measurement step was 11.54 ml. Just the high pressure transducer was used and for the data calculations the real gas law was applied. To complete PCTPro-2000 data analysis specially upgraded software ‘Igor’ was purchased.

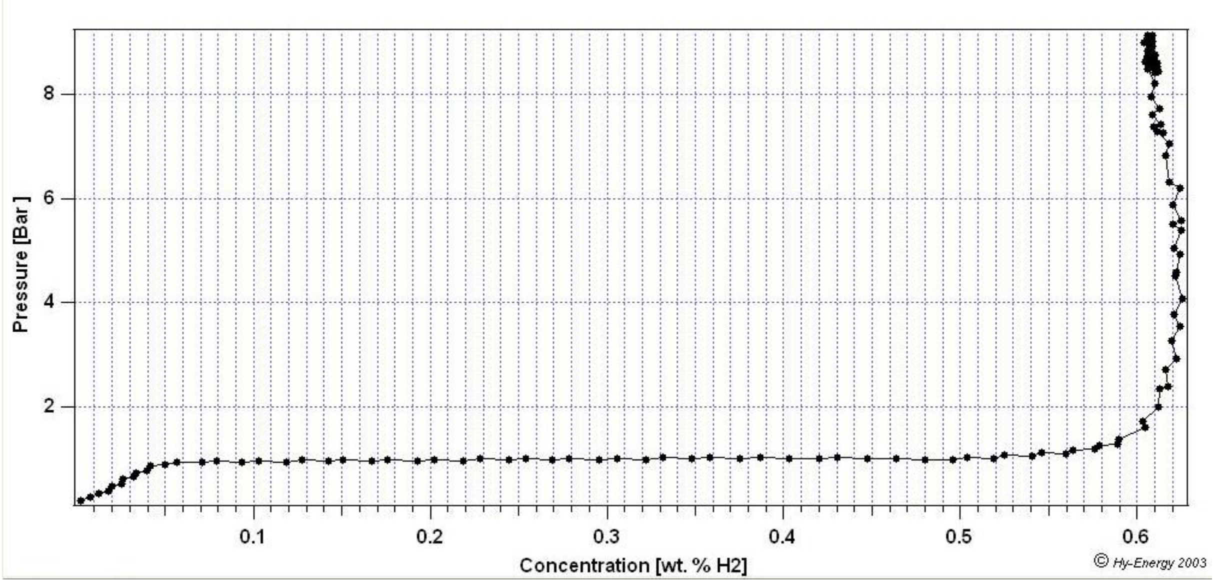

Fig. 6. Experimentally obtained PCT curve for Pd powder at 120 ^{o}C

Due to that Pd at a room temperature starts to adsorb hydrogen at a low pressure; temperature was elevated up to 120^{o}C.

The Fig.7 represents the hydrogen concentration change as a function of time. The sample is coarse grained $LaNi_5$ and during the performed measurement the maximal hydrogen concentration is not reached yet. A glitch on the data plot appears when the low pressure transducer switches to the high pressure transducer.

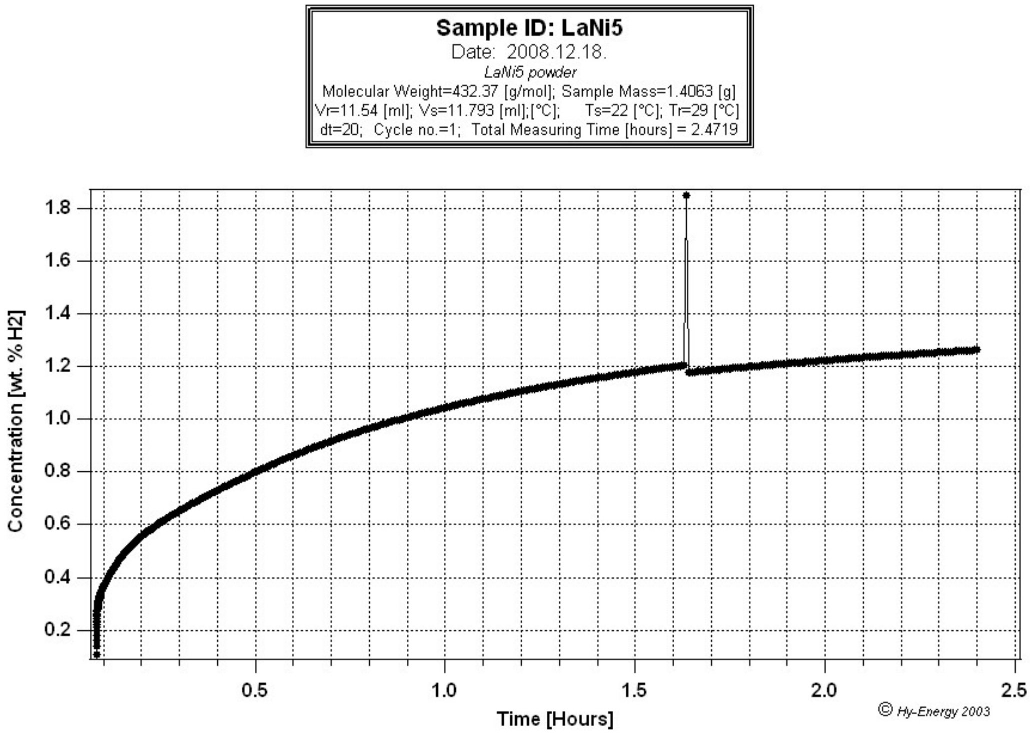

Fig. 7. Hydrogen sorption kinetics of $LaNi_5$; the incorrect point is caused by the transducer swap.

As $LaNi_5$ was not reaching the fully charged state at satisfactory rate it was considered to activate sample by several cycles of charging and discharging. The cycle life measurement plot (Fig. 8) shows three cycles where the absorption pressure is set at 20 bars for 20 min. Desorption process starts after a while due to that system has to reach vacuum and has to stabilize.

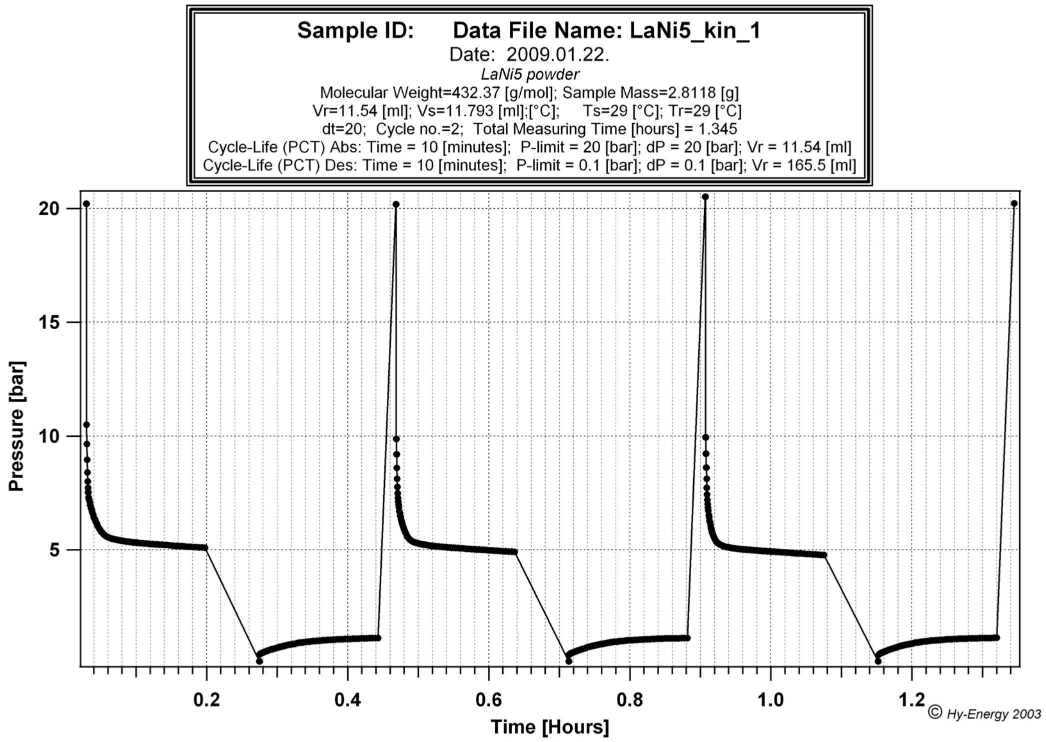

Fig. 8. Cycle life measurements of $LaNi_5$

The third cycle shows slightly larger amount of absorbed gas that indicates higher activity of sample. This experiment was prolonged for 70 hours and amount of sorbed hydrogen was increased.

In the further experiments an impact of particle dimensions and admixture of an inert material to sorbed amount of hydrogen will be investigated.

SUMMARY

Volumetric Sievert method was used to measure hydrogen absorption in metal hydrides. Specially designed apparatus PCTPro 2000 determines the amount of hydrogen gas that is sorbed into material by measuring pressure changes in a reservoir with known volume and temperature. Success of PCTPro 2000 is fully automated pressure management system with sophisticated software to ensure safe operations and a reliable data collecting and processing.

To avoid the faulty points when transducers are switching it is suggested to use only the high pressure transducer if the pressure in the experiment is set up higher than 4.7 bar. To perform correct and repeatable measurements it is crucial to activate sample properly.

Preliminary results are reported about hydrogen absorption in metals forming hydrides, such as Pd and $LaNi_5$ and determinated amounts of absorbed hydrogen in those materials were in accord with results reported in literature.

REFERENCES

1. The 2005 Progress Report for the DOE Hydrogen Program: http://www.hydrogen.energy.gov/annual_progress05.html
2. L. Can, X. Qin (eds). Spillover and migration of surface species on catalysts // Proc. of the 4th International Conference on Spillover, Dalian, China, 1997, 538 p.
3. L.Grinberga, J.Kleperis et al. Estimation of hydrogen transfer mechanisms in composite materials // Solid State Ionics, Vol. 179, Issue: 1–6, 2008, p. 42–45.
4. T.Graham // Phil. Trans Roy. Soc. 156, 415, 1866.
5. K.J. Gross. The PCTPro-2000—The Ultimate Tool for Gas Sorption Analysis // Material Matters, Vol. 2, Nr. 2, 2007, 26–28
6. K.J. Gross, The PCTPro-2000 for Gas Sorption Measurements // 'Setaram' lecture, 2008
7. K.J. Gross, K.R.Carrington, The best practices for the characterization of hydrogen storage materials // Reference guide, 2008, 177 p.
8. Hy-energy LCC/Settaram, Installation and Operational manual of PCTPro-2000 // 2007, 148 p.

CYSENI 2009, May 28-29, Kaunas, Lithuania
ISSN 1822-7554, www.cyseni.com

WIND POWER PLANTS AND ENVIRONMENTAL NOISE ASSESSMENT

A. Kanapickas, G. Macijauskienė
Department of Physics, Vytautas Magnus University
Vileikos 8, LT-44404, Kaunas, Lithuania
Phone: +37037327922
E-mail: a.kanapickas@gmf.vdu.lt

ABSTRACT

This study presents the analysis of a mechanism to provide the balance between negative noise impacts of a proposed wind noise project and the benefits that that development is expected to bring to the community. Environmental impact assessment for the noise from a proposed wind energy development requires assessment of the predicted noise level. Estimated values have to be compared with acceptability criteria on purpose to assess noise impact. Several approaches can be used for the assessment of the noise impact: assessment by comparison with background noise level and assessment with a specified criterion level. Establishment of criteria levels is based on an assumption that there may still be small proportion of the community who will experience annoyance or disturbance from the noise. On the other hand, there is no firm agreement about a level that clearly separates an acceptable from an unacceptable noise impact. Therefore, interpretations of noise exposure criterion levels need to be made for the permission to proceed with the proposed wind plant development. As a result satisfactory resolution involves not only noise impact assessment, but also negotiation process with the proponent, the community, and the government. Permission with the proposed development ends with the assurance of noise monitoring and reviewing.

Keywords: wind turbines, background noise, noise reduction, EIA

1. INTRODUCTION

Wind energy during past decade became an important part of energy developments in every country that lacks usual energy sources. In addition, wind energy expansion serves as a mean that may help to solve climate issues mankind faces at a global range. However, the government authorities responsible for installation of required capacities as well business proponents seeking for profitable contracts have to overcome challenges related to the community opposition. During last years in Lithuania it has been difficult to find a case when community complaint about wind plant related questions would be solved in a satisfactory form [1–3]. Noise impact assessment and monitoring of noise levels which do not exceed specified exposure criterion levels do little influence to public opinion.

Such disfavor may be related to several reasons. Noise from wind turbines is not studied well as, for instance, from road traffic. Some studies indicate that annoyance from wind turbine noise occurs to a higher degree at low noise levels than noise annoyance from other sources of community [4]. Annoyance also is affected by the turbines visual impact on the landscape. Due to wind turbine characteristics it is not easily masked by background noise. The last to be mentioned is the fact that the regulations on noise from wind turbines are based on different principles leading to a heterogeneous legislation in Europe.

On the other hand, the number of noise complaints about windfarms should be compared with complaint statistics for other types of noise. The results of such investigations show [5] that the total number of complaints about noise generally exceeds those from windfarms by between four and five orders of magnitude indicating that windfarm noise is a small scale problem in absolute terms. The mistrust about wind energy may be related to the insufficient social management of this important branch of energy economy.

This study does an attempt to reveal causes of public concerns and tries to find proper way to assess noise impact, which could form more acceptable community's opinion about wind energy development. The outline of present work is as follows. First of all, environment noise descriptors are presented and possible reactions to environmental noise are reviewed. Then different methods for assessment of noise impact are presented. Finally, assessment of proposed wind developments is analyzed and premises for the positive resolution between the proponent, the community, and the government are discussed.

2. REACTION TO ENVIRONMENTAL NOISE

2.1. Environmental noise descriptors

The definition of environmental noise given in the European Commission Environmental Noise Directive [6] is: „unwanted or harmful sound created by human activity outdoors, including noise emitted by means of transport and from industrial sites or industrial buildings". Quantitative descriptors for environmental noise are generally based on the A-weighted decibel scale. The A-weighting is essentially a frequency filter that has a similar response to that of human hearing. As environmental noise is rarely constant in level, this time variation must be taken into consideration to provide a representative noise descriptor. A variety of such derived noise descriptors have been developed that incorporate time averaging of the sound pressure levels or integration of the energy within a sound over a defined period. Descriptors that are used in this text are presented as follows.

Percentile Value, $L_{\mathrm{A}n}$ – the A-weighted level exceeded for a percentage of a nominated time period. The most commonly used are the $L_{\mathrm{A}10}$, the level exceeded for 10% of the time period and so representative of the higher noise levels, and the $L_{\mathrm{A}90}$, the level exceeded for 90% of the time period and considered representative of the background noise levels.

Equivalent Energy Level, L_{Aeq} – the A-weighted sound pressure level for a continuous steady sound that has the same energy as the time-varying sound over the same time period.

Maximum Noise Level, $\mathrm{L}_{\mathrm{Amax}}$ – the maximum noise level during the time period and often used as a criterion in conjunction with $\mathrm{L}_{\mathrm{Aeq}}$ or $\mathrm{L}_{\mathrm{A10}}$ to limit the highest noise levels in the noise.

Sound Exposure Level (SEL) – the noise level for a sound over a defined time period, such as 1 s, that would have the same energy as the noise from a single event like a car pass by.

Perceived Noise Level (PNL) – the level of a sound that is considered to be equally noisy. It is calculated from the one-third octave band data.

Peak Noise Level, L_{Cpeak} – the peak C-weighted sound pressure level for impulse sound such as explosive noise. Note this environmental noise descriptor is not based on the A-weighting but is based on the C frequency weighting.

A number of derived noise descriptors are used for the assessment of noise impacts. The common ones include:

$L_{\mathrm{A10,18h}}$ – the average of the hourly LA10 values between 06:00 and 24:00 and used for the assessment of noise from road traffic.

$L_{\mathrm{Aeq,Nh}}$ – average of $\mathrm{L}_{\mathrm{Aeq}}$ over a defined number of hours such as 24 h, 9 h over a night, 15 h over a day, 1 h over a day, and so on, and used for wide range of environmental noises.

LDEN – the average of $\mathrm{L}_{\mathrm{Aeq}}$ over the day with an adjustment to allow for the additional annoyance during the defined evening and night periods. The day period is 12 h and normally from 06:00 to 18:00, the evening 4 h normally from 18:00 to 22:00 with an adjustment of

+5 dB, and the night 8 h with an adjustment of +10 dB. This derived descriptor is planned to be used in implementation of the new European Commission (EC) Directive on Environmental Noise [6]. The length of each period is given in hours, but the clock times can be changed to suit the lifestyle of the country.

As there are a large variety of descriptors for environmental noise, it is vital that the descriptor used for a criterion in regulations and guidelines be clearly stated to avoid any ambiguity. These details also need to be considered when comparing noise effects research findings and noise exposure criteria from various countries to ensure the validity of the comparison. There may be particular frequency characteristics in the noise, such as high frequency bird sounds during wind farm noise field measurements. In such cases it may be necessary to incorporate criteria based on the noise levels in particular frequency bands, in addition to the overall A-weighted level. These criteria generally use the L_{eq} descriptor.

2.2. Human response to noise

Annoyance, speech interference, and sleep disturbance are considered to be the main effects of environmental noise [7]. It is only rarely that the level of environmental noise would be sufficient to produce permanent hearing damage. Important factors that lead to reactions to noise such as disturbance and annoyance include the noise level and character, the duration, the time at which it is occurring, and the activity of the person at that time. There have been extensive studies aimed at determining the relationship between some form of noise descriptor and reaction to environmental noise. These social surveys have typically led to dose–response relationships based on some form of quantitative descriptor for the noise and the percentage highly annoyed (%HA). However, the majority of these surveys have focused on reactions to transportation noise sources. An example of that dose – response relation is presented in Fig. 1 [8]. There are appropriate separate dose – response relationships for noise from aircraft, road traffic, and railways [9]. However, there is not universal acceptance of these curves. There is little done to determine such relationship for wind plan produced noise.

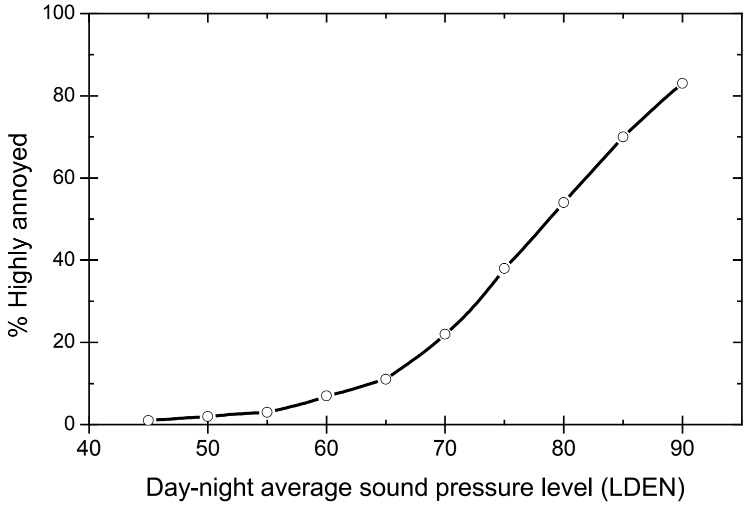

Fig. 1. Dose annoyance curve (from [8])

The most common metrics for assessing the impacts of community noise, such as LDEN, already contain a strong 10-dB penalty for nighttime noises, and community noise exposure policies typically do not include separate criteria for sleep disturbance. However, in the case of wind plants a separate analysis of the impacts of nighttime noise is required.

There have been extensive studies of sleep disturbance using subjects sleeping in their homes and sleeping under laboratory conditions. The World Health Organization (WHO) [10] has recommended that nighttime indoor sound pressure levels should not exceed approximately 45 dB L_{Amax} more than 10 to 15 times per night. It needs to be pointed out, however, that the criteria recommended by WHO are long-term targets and do not take into consideration the cost or technical feasibility of meeting their recommended ideal maximum exposure levels. WHO intended that these criteria be used as part of a noise management decision-making process, for which environmental noise impact analysis is the central issue.

Speech interference is also an important part of the overall assessment of annoyance. For specific situations where the level of environmental noise is high, speech interference is possible inside buildings. Talker-to-listener distances for just-reliable communication in noisy environment are presented in Fig. 2 [11]. It is seen that the expected voice level will increase with increasing noise level because a talker will raise his or her voice in noise, typically at the rate of 3 – 6 dB for every 10 dB increase in the A-weighted noise level above 50 dB. The cross-hatched area shows the range of permissible talker-to-listener distances under these conditions.

To authors knowledge there aren‘t established any standard test procedures to determine quantitative measures of speech interference in the case of wind plants. It should be noted, that the noise from wind installations may not reach noise levels indicated in Fig. 2, however, these procedures should be established and reliable implication should be find to ensure public confidence.

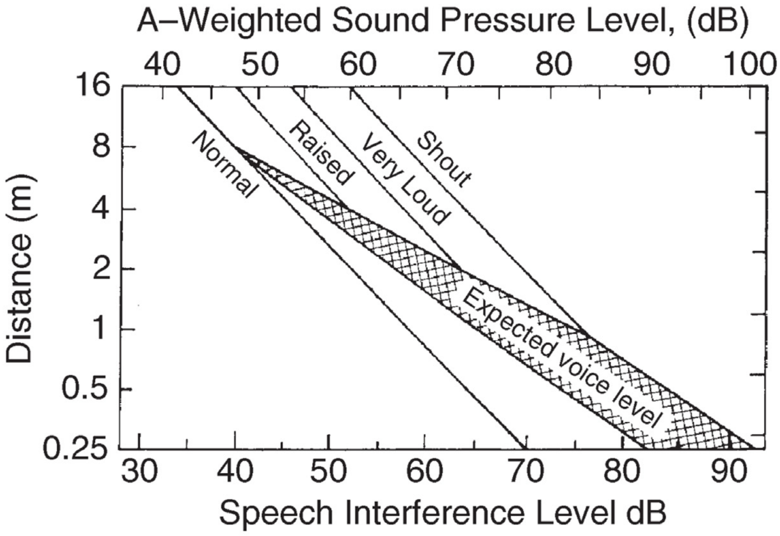

Fig. 2. Talker-to-listener distances for just-reliable communication. The curves show maximum permissible talker-to-listener distances for just-reliable speech communication. The parameter on each curve indicates the relative voice level [11]

2.3. Wind turbine noise impact assessment

2.3.1. Comparison with background noise level

The ordinary procedure authorities have to arrange in the case of complaints is the assessment of the acceptability of an environmental noise. Usually assessment of environmental noise means comparison with noise limits. However, many people feel these simple limits are insufficient to protect people from noise’s harmful effects, or even to address the annoyance level.

Therefore there are several approaches that can be used for the noise impact assessment [7]: 1) Assessment by comparison with background noise levels; 2) Assessment of environmental noise by comparison with a specified criterion level; 3) Establishing noise exposure criterion levels; 4) Interpretation and use of noise exposure criterion levels.

Comparison with background noise levels requires measurement of the noise level in the area before the proposed development, or if it is in response to a complaint, with turning off the noise considered to be offensive. If it is not possible to turn the noise source off, the background noise measurements can be made in a similar type of area. The background noise is usually measured in terms of L_{A90}, the A-weighted noise level exceeded for at least 90% of the time period. The background noise can vary during different times of the day so the measurements must be made during the time the noise may be considered to be annoying. The measurement of the background noise may need to be over a number of days in which case the 90% value of the L_{A90} can provide a good representation of the background noise level in the area.

After the background level of noise is determined, then either the noise from the existing source is measured or noise from the proposed wind plant development is predicted. This noise is generally either in terms of L_{A10}, the A-weighted noise level exceeded for 10% of the time period, or L_{Aeq}, the A-weighted equivalent noise level. Adjustments are then made to the noise level to allow for the additional annoyance because of the character of the noise. Objective and subjective methods for determining these adjustments are given in ISO 1996 [12].

Assessment of wind plant noise includes additional adjustments that are not included into standard procedure. Wind turbines generate two types of noise: aerodynamic and mechanical. A turbine's sound power is the combined power of both. Aerodynamic noise is generated by the blades passing through the air. The power of aerodynamic noise is related to the ratio of the blade tip speed to wind speed. Depending on the turbine model and the wind speed, the aerodynamic noise may seem like buzzing, whooshing, pulsing, and even sizzling. Turbines with their blades downwind of the tower are known to cause a thumping sound as each blade passes the tower. Most noise spreads perpendicular to the blades' rotation. However, since turbines rotate to face the wind, they may radiate noise in different directions each day.

The amount of annoyance that wind turbine noise is likely to cause can be related to other ambient noises. Turbine noise may be more noticeable and annoying at the cut-in wind speed less than 4 m/s than at higher wind speeds [4]. At lower speed, the wind was strong enough to turn the blades, but not strong enough to create its own noise. At higher speeds, the noise from the wind itself masked the turbine noise.

A general guide to the expected reactions to noise intrusion is given in Table 1 [10]. The concept of assessment by comparison with background noise level is easy for the community to understand.

Table 1. Reactions to different levels of noise intrusion for A-weighted sound pressure levels [10]

Noise intrusion, dB	Likely reaction
0–5	Marginal
5–15	Great concern
15–20	Serious concern
20–25	Extreme action

2.3.2. Setting noise criterion levels

Assessment by comparison with background noise levels has several disadvantages. For example, background noise may change in time, therefore, duration of monitoring has to be sufficiently long. Also each new noise source introduced when community develops have to be taken into account. These disadvantages force to improve assessment methodology. The solution can be an assessment of environmental noise by comparison with a specified criterion level. This involves defining criteria for acceptable noise levels in an area with the aim of maintaining the convenience of the environment.

A number of factors are taken into consideration by the authority when selecting these criteria. Criteria often vary for the type of area and time of day. The types of activities plus the transportation such as roadways or railways contribute to the overall ambient noise that constitutes a wind plant area. Similarly higher noise levels during the day are more acceptable than during the night when they may cause sleep disturbance.

There are several methods to specifying noise limits: specifying a single all-encompassing maximum limit; determining preexisting ambient noise levels and specifying that a new noise source may not increase the ambient noise by more than a particular amount; setting a base limit, with adjustments for district types and time of day or night; specifying maximum sound levels for each octave range.

The result of establishing noise exposure criterion levels gives a guide to reasonable criteria that the government authority can adopt. However, there is no firm agreement about a level that clearly separates an acceptable from an unacceptable noise impact. An extensive study of dose – response relationship for the environmental noises was supported by WHO [10], the result could give guidance making the decisions defining acceptable levels of noise. However, wind turbine annoyance encounters additional factors as lack of data in sufficient amount on wind turbine noises, higher degree of annoyance to wind turbine noises, visual impact of wind plants, etc [4]. This gap in establishment of regulations on noise from wind turbines has to be filled for the successful expansion of wind energy developments.

2.3.3. Application of noise exposure criterion levels

Since the consistent procedures for establishing and rating noise levels and to minimise noise levels from wind turbines are not unified and vary from country to country, general procedures designed for the management of the environmental noises are used. Following procedures are usually implemented in the current regulations for the environmental noise assessment.

First of all, all environmental noise impact analyses include comparison of the noise level at the receiver location with the applicable exposure criteria. When the noise emission level is in excess of the criterion, the first step should be to attempt to mitigate (reduce) the emission noise at the source. This means that developing quiet wind turbines, particularly, small ones, becomes increasingly important task.

Once the maximum reduction in emission noise has been achieved, other approaches to noise control should be applied to reduce the emission noise levels to meet the criteria. However, in the case of wind farms these alternatives, such as use of barriers or improving the noise reduction provided by buildings, are not generalized and often do not fit into development. The only option for the control of wind farms noise can be implemented at the land-use planning stage to minimize the occurrence of inappropriate land uses. This is very important for management of environmental noise at the community level.

3. ASSESSMENT OF WIND FARM DEVELOPMENTS

Assessment of wind farm developments can include several stages, which, properly used, can help to achieve successful implementation of these developments. The following stages can be pointed out [7]: 1) Environmental impact assessment (EIA); 2) Negotiation process; 3) Interacting with the public; 4) Monitoring and review.

The first part of the assessment is EIA. Several features of EIA procedure should be noted. Firstly, in some cases the EIA may only be assessed by the appropriate government authorities. Secondly, commonly a draft assessment is produced and released for a public comment period during which time community discussion sessions may be organized. This possibility as a part of social management is not employed at full when installing wind farm.

The basic elements of the noise assessment in an EIA include: a) Identification of all the noise-producing elements in the proposal; b) Identification of all the noise-sensitive areas that could be affected by the proposal both currently and into the future, say 15 to 20 years; c) Statement of the applicable criteria in the surrounding areas; d) Estimation of the noise emissions levels for all the noise-sensitive locations; e) Comparison with the applicable criteria and determination of any excess.

If noise emissions do not meet limiting requirements, the next steps are: a) Identification of cost-effective mitigation measures and b) Comparison of the mitigated noise emission levels with the criteria. As discussed above mitigation of wind farm noise has specific limitations that relates mainly to technological breakdown in wind farm design and to the land-use planning. The responsibility for mitigation can be a complex problem, for example, in the case, when cost effectiveness of noise mitigation measures may be beyond the current technical capabilities or may be prohibitively expensive for the proponent.

Satisfactory resolution involves the action of the three main sides: the promoter, the community, and the government authority. Undesirable noise impact for the affected part of the community has to be smaller that the economic and social benefits to the wider community. All the documents provided with the assessment and the evaluation have to be presented in a form that can be understood by the public. Since the development of the use of wind energy in the country is a strategic direction, the responsibility for convenient decisions has to be assumed not only by business promoter of wind installation, but also by the government. Community affected by the increased noise impact should receive some benefits, for example, improved noise insulation of the houses, improvements to the community infrastructure, payments, etc.

It is important to provide information in a manner that can be understood by the community that is potentially affected. Factors affecting public perceptions of wind farms and other energy innovations can be divided in three groups [13]: perceptions of physical and environmental factors; psycho-social factors; social and institutional factors. Social research linked to wind energy projects has increased in the last few years. Much work has to be done if one seeks for the increase of the social acceptance of wind energy.

When the wind energy project has been installed the noise monitoring should be ensured. The task of this examination is to make clear if the actual noise levels do not exceed estimated values and that the mitigation measures are effective.

4. CONCLUSIONS

In this work the analysis of conditions that supports successful development of wind energy projects is presented and measures that may help to overcome community opposition to wind farms currently existing in Lithuania are reviewed. It is shown that because of wind farm specific features general environment noise assessment procedure can not consider all aspects to be included in such assessment. Environmental impact assessment for the noise from a proposed wind development requires not only assessment of the predicted noise level but also establishment of acceptability criteria developed for wind farms. Interpretations of noise exposure criterion levels need to be made for the permission to proceed with the proposed wind plant development. As a result satisfactory resolution involves not only noise impact assessment, but also negotiation process with the proponent, the community, and the government. Permission with the proposed development ends with the assurance of noise monitoring and reviewing. Social management of these measures is an important task in achieving higher social acceptance of wind energy.

REFERENCES

1. Vydmantiškiai nušvilpė ministerijų metodikas dėl vėjo jėgainių // http://www.pajurionaujienos.com/?act=exp&sid=2628, (247) 2008.07.01 (accessed 2009.03.03).
2. Nepageidaujamų vėjo jėgainių kaimynystė // http://www.lsveikata.lt/index.php?page_id=57&s=4026, 43 (779), 2008.10.23-29 (accessed 2009.03.03).
3. Gyventojai stabdo vėjo energetiką // http://www.balsas.lt/naujiena/213445/gyventojai-stabdo-vejo-energetika/rubrika:naujienos-verslas-investicijos, 2008.09.15 (accessed 2009.03.03).
4. E. Pedersen, H. Halmstad. Noise annoyance from wind turbines // Swedish environmental protection agency: Report 5308, 2003, 27 p.
5. A. Moorhouse, M. Hayes, S. Hünerbein, B. Piper, M. Adams. Research into Aerodynamic Modulation of Wind Turbine Noise: Final report // University of Stanford: 2007, 57 p.
6. European Commission, EU Directive on the Assessment and Management of Environmental Noise (END) // The European Parliament and the Council of the European Union, Brussels, 2002; http://eur-lex.europa.eu/LexUriServ/LexUriServ.do?uri=OJ:L:2002:189:0012:0025:EN:PDF
7. M.A. Burges. Environmental noise impact assessment, in: Handbook of noise and vibration control, ed. Malcolm J. Crocker // Wiley, New York, 2007, p. 1501-1508.
8. L.S. Finegold, C. S. Harris, and H. E. von Gierke. Community Annoyance and Sleep Disturbance: Updated Criteria for Assessing the Impacts of General Transportation Noise on People // Noise Control Engineering Journal (42) 1, 1994, p. 25–30.
9. H.M.E. Miedema and C.G.M. Oudshoorn. Annoyance from Transportation Noise: Relationships with Exposure Metrics L_{dn} and L_{den} and Their Confidence Intervals // Environmental Health Perspectives, (109) 4, 2001.
10. World Health Organization, Guidelines for Community Noise, ed. B. Lindvall, D. Schwela, and K.T. Goh // World Health Organization: Geneva, 2000: http://www.ruidos.org/Noise/Comnoise-1.pdf
11. G.C. Tocci. Ratings and descriptors for the built acoustical environment, in: Handbook of noise and vibration control, ed. Malcolm J. Crocker // Wiley, New York, 2007, p. 1267–1282.
12. International Organization for Standardization, ISO 1996-1: 2003, Acoustics – Description, Measurement and Assessment of Environmental Noise – Part 1: Basic Quantities and Assessment Procedures // ISO, Geneva, 2003.
13. D. Bell, T. Gray, C. Haggett. The ‘social gap’ in wind farm setting decisions: explanations and policy responses // Environmental Politics 14, 460–477, 2005.

PECULIARITIES OF THE SHORT-TERM WIND POWER PREDICTION OF SEDOS WIND TURBINES

M. Marčiukaitis
Lithuanian Energy Institute
Breslaujos str. 3, Kaunas,
LT-44403 Lithuania
Phone: +370 (37) 401847;370 689 15388
E-mail: mantas@mail.lei.lt

ABSTRACT

Wind power dependence on the wind volatility is one of the most important issues compared to the traditional means of power generation. For this reason certain amount of reserve power (spinning reserve) must be constantly kept to compensate power shortage in case wind ceases. Also balancing of the whole electricity system is complicated, especially when wind power share in the system is significant. This problem is usually solved by using short-term (up to 48 hours) wind power prediction systems. With increasing wind power share in Lithuania electricity network balancing problems may arise, therefore relevance of wind power prediction is evident and it will grow in the future. In this paper short-term wind power prediction model is presented, which has been developed for Sedos wind turbines. Data from the numerical weather prediction model HIRLAM, run by Lithuanian Hydrometeorological Service, are used in this model. Influence of topography and atmospheric stability conditions on the accuracy of wind speed predictions has been estimated. It has been determined that overall mean absolute prediction error (MAE) for the prediction horizons up to 48 hours is about 10 % of wind turbines' installed power.

INTRODUCTION

Wind power share in electrical systems is increasing rapidly in most countries of the world, including Lithuania. There are 47 wind turbines (WT) installed in Lithuania with total power of about 54 MW. Most WT are installed in the western part of Lithuania (Kretingos, Skuodo, Tauragės, Mažeikių districts). In 2006 wind power comprised about 0.12%, in 2007–2008 – about 1% of country‘s gross electricity consumption.

Currently electricity generation from renewable energy sources comprises about 4.7% of all consumed electricity in Lithuania. EU directive 2001/77/EC obliges Lithuania to increase this share to 7% till 2010. The increase of electricity generation from renewable energy is mostly related with wind energy development. It is planned that total installed wind power will reach 200 MW till 2010. Wind energy development is planned in the coastal region of Lithuania, where wind power resources are estimated to be the biggest.

Wind power dependence on the wind volatility is one of the most important issues compared to the traditional means of power generation. For this reason certain amount of reserve power (spinning reserve) must be constantly kept to compensate power shortage in case wind ceases. Also balancing of the whole electricity system is complicated, especially when wind power share in the system is significant. Electrical utilities all over the world are beginning to realize the need for reliable wind power predictions, as the penetration of electricity generated by wind farms in the electrical grids is increasing. With increasing wind power share in Lithuania electricity network balancing problems may arise, therefore relevance of wind power prediction is evident and it will grow in the future. Wind power predictions are necessary for optimal dispatch and scheduling of the total power production in the electricity grid. Also the experience of other countries has shown that in the liberalized markets wind power prediction influences the price of electricity generated from wind and allows wind power to compete with traditional means of power generation.

There are many short-term wind power prediction models and systems developed and operating in other countries [1, 2]. In general, the models can be classified as either using input data from a Numerical Weather Prediction (NWP) model or not. Whether the inclusion of a NWP model data is necessary, depends on the prediction horizon required by the utility. Typically, prediction models using NWP forecasts outperform time series models after 3–6 hours look-ahead time [1]. Therefore, all models used by the utilities are based on this approach.

Basically short-term wind power prediction can be performed in two ways: by the physical and the statistical approach. The physical approach attempts to estimate local wind speed using the physical laws governing atmospheric behaviour, and then the corresponding power generated at the wind farm. The statistical models are designed to determine the relationships between a set of explanatory variables and the measured power data from the wind turbines using historical data. They usually employ recursive techniques. Both approaches can be combined together to get more accurate forecasts. Physical and statistical methods and their application are better described in [1, 3].

METHODS OF THE RESEARCH

Characteristics of the object. Sedos wind farm has been chosen for the development of short-term wind speed prediction model. Wind farm is located in Mažeikiai district and is about 50 km from the Baltic sea (Fig. 1) and consists of two ENERCON turbines – E-40 and E-48 (total installed power 1.4 MW), located few hundred meters away from each other. The hub-height of both turbines is 65 m.

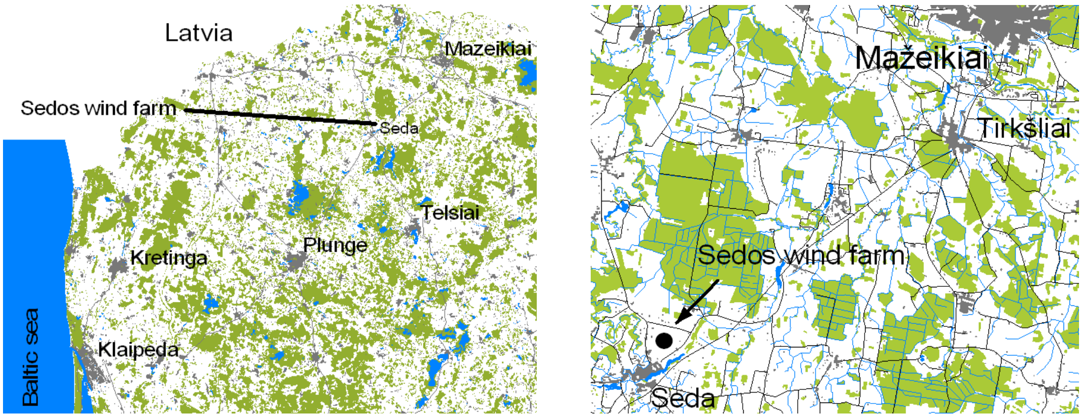

a b

Fig. 1. Location of Sedos wind farm

Wind speed and turbine power measurement data (10 min averages) were taken for the period of one month (June 2007). Measurement data were available from both turbines of the wind farm, but as their hub-height is the same, wind speed and power time series were averaged to one.

Physical method has been chosen for the analysis of short-term wind speed prediction accuracy requiring wind speed, direction, air temperature and other atmospheric parameters' data from a NWP model. These data were provided by the Lithuanian Hydrometeorological Service, where HIRLAM (High Resolution Limited Area Model) model has been used since 2006.

MATLAB software was used for the development of non-operational short-term power prediction model and for comparison of short-term wind speed prediction data and measured data and for the error calculation.

Two types of errors were used for the evaluation of wind speed prediction accuracy [4]: mean absolute error (MAE) and root mean squared error (RMSE):

$$MAE = \frac{1}{N}\sum_{1}^{N}\left|U_{meas} - U_{pred}\right|; \quad RMSE = \sqrt{\frac{1}{N}\sum_{1}^{N}(U_{meas} - U_{pred})^2}\,, \tag{1}$$

where: N – number of data values; U_{meas} – measured wind speed; U_{pred} – predicted wind speed.

Geostrophic drag law was used for the transformation of wind speed from the higher HIRLAM levels where needed:

$$G = \frac{u_*}{\kappa}\sqrt{\left[ln\left(\frac{u_*}{fz_0}\right) - A\right]^2 + B^2}\,, \tag{2}$$

where: G – geostrophic wind; u_* – friction velocity; κ – the Von Karman constant; f – Coriolis parameter; z_0 – aerodynamic roughness length; A and B – constants, set to 1.8 and 4.5, respectively.

Friction velocity u_* was calculated using Newton-Raphson method [5] and inserted into the logarithmic law for the calculation of wind speed at the hub-height:

$$u(z) = \frac{u_*}{\kappa} ln\left(\frac{z}{z_0}\right), \tag{3}$$

where z is the height above ground level.

Estimation of the influence of topography and atmospheric stability conditions on the wind profile. Influence of topography on the wind speed prediction accuracy was estimated twofold: by using WAsP estimated effective roughness length z_0 for 12 direction sectors (30° each) and by multiplying predicted wind speed with the correction coefficients estimated by WAsP thus eliminating the influence of topography on the wind flow.

Influence of atmospheric stability conditions was estimated twofold as well: by physical and statistical methods. Physical method uses the same logarithmic profile, adding a function based on Monin-Obuchov similarity theory [6, 7]:

$$u(z) = \frac{u_*}{\kappa}\left(ln\frac{z}{z_0} - \psi\left(\frac{z}{L}\right)\right), \tag{4}$$

where: ψ – function of $\frac{z}{L}$; L – Obuchov length parameter given as [6, 8]:

$$L = \frac{T_0 c_p u_*^3}{\kappa g H_0}, \tag{5}$$

where: T_0 – surface temperature; c_p – specific heat of air under constant atmospheric pressure (1004 $JK^{-1}kg^{-1}$); u_* – friction velocity; g – acceleration due to gravity; H_0 – heat flux towards the ground.

Functions for ψ have been chosen as proposed by Badger et al. [6] and Jensen et al. [9].

$$\psi\left(\frac{z}{L}\right)= \begin{cases} \left(1-16\frac{z}{L}\right)^{\frac{1}{4}}-1, & \text{when } L<0 \\ 0, & \text{when } L=\infty \\ -4{,}7\frac{z}{L}, & \text{when } L>0. \end{cases} \tag{6}$$

In neutrally stratified conditions the heat flux is zero, and wind speed at the desired height is calculated from the logarithmic profile.

The importance of atmospheric stability information was also tested statistically, using multiple regression. General expression is given as:

$$u_{corr} = a + b * u_{HIRLAM} + c * S_{HIRLAM}\ , \tag{7}$$

where: u_{corr} – corrected wind speed; u_{HIRLAM} – HIRLAM wind speed; S_{HIRLAM} – stability parameter; *a*, *b* and *c* – statistical parameters.

Atmospheric stability parameters tested are given as [6]:

wind speed gradient
$$S_u = \frac{u_h - u_l}{z_h - z_l}, \tag{8}$$

potential temperature gradient
$$S_\theta = \frac{\theta_h - \theta_l}{z_h - z_l}, \tag{9}$$

Brunt-Väisäla frequency
$$N^2 = \frac{g}{\theta_h + \theta_l}\frac{(\theta_h - \theta_l)}{z_h - z_l}, \tag{10}$$

wind speed average
$$u_z = \frac{u_l + u_h}{2}, \tag{11}$$

where: *u* – wind speed; *g* – acceleration due to gravity; indices *h* and *l* refer to “higher” and “lower” HIRLAM levels; θ – potential temperature, given as:

$$\theta = T\left(\frac{p_0}{p}\right)^{\frac{R}{c_p}}, \tag{12}$$

where: *T* and *p* – air temperature and atmospheric pressure of the air of interest; p_0 – standard pressure; *R* – universal gas constant (287 $JK^{-1}kg^{-1}$); c_p – specific heat of air.

Systematic errors of the model were eliminated using a simple linear regression:

$$u_{corr} = a + b \cdot U_{HIRLAM}\ , \tag{13}$$

where: u_{corr} – corrected wind speed; *a* and *b* – statistical parameters; U_{HIRLAM} – HIRLAM wind speed. It should be noted that this expression was used for the elimination of systematic errors when estimating the impact of topography and applying physical method for estimation of the influence of atmospheric stability conditions. Multiple regression equation was used when estimating the influence of atmospheric stability conditions statistically (Equation 7).

HIRLAM data. Data from the HIRLAM model were used for the development of the non-operational wind power prediction model. HIRLAM model is run every six hours (00, 06, 12 and 18 hour of the day). Every time predictions are generated for the horizon of 48 hours typically with a 3-hour interval. For the comparison with HIRLAM predictions, measured wind speed and power time series were adjusted and only 3-hour data were left. Average errors were calculated in every stage of the analysis.

RESULTS AND DISCUSSION

The main purpose of the wind power prediction model development was to obtain the smallest prediction errors. For this reason the influence of topography and atmospheric stability conditions on the accuracy of the predictions was evaluated. The reduction of errors indicates that the method applied was successful.

HIRLAM data analysis. HIRLAM model generates wind speed predictions in 60 vertical levels, therefore the best performing level had to be determined for the further analysis. Data from 13 lowest HIRLAM levels were used for the comparison of their prediction errors. Data from the HIRLAM point, closest to the wind farm were used.

Mean absolute error calculations were made in three cases. In the first case raw HIRLAM data were used, in the second case HIRLAM wind speed was transformed to the hub-height of wind farm's turbines (65 m) with a log-profile, and in the third case geostrophic drag law was used for HIRLAM wind speed transformation. Roughness value $z_0 = 0.1$ was used. In all three cases model output statistics (MOS) was used for the elimination of systematic errors (Equation 13). Results have shown that the smallest MAE were obtained when 30 m HIRLAM level was used (Fig. 2).

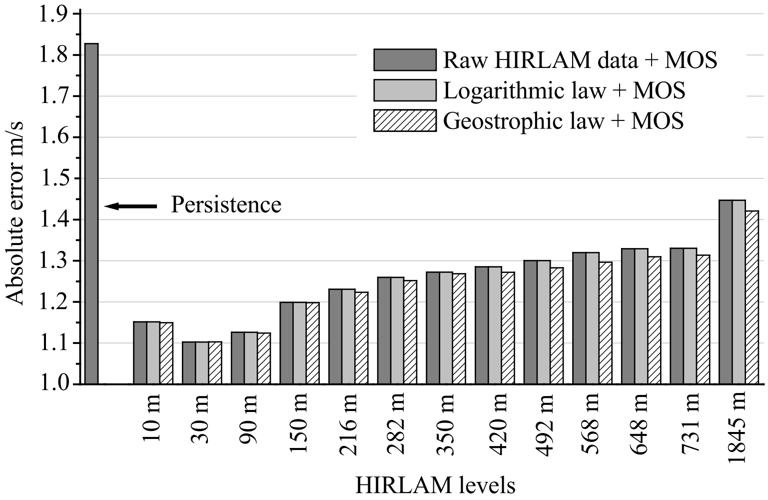

Fig. 2. Mean absolute wind speed prediction errors from different HIRLAM levels for E Sedos wind farm

Advantage of using geostrophic drag law in higher levels is evident, but the most accurate predictions are obtained using data from the 30 m level – mean absolute error is 1.1024 m/s. This error is significantly smaller than persistence mean absolute error. Data from the 30 m HIRLAM level is used for further calculations.

As it was expected, mean errors increase with height. At the height of 10 m wind speed is strongly influenced by the topography, and due to HIRLAM resolution limitations wind flows are not simulated sufficiently well. Also wind speed transformations may be an additional source for errors.

It should be noted that errors obtained using raw HIRLAM data and those transformed with logarithmic law are equal, because there is a linear relationship between wind speed at two heights. Therefore MOS, which is linear too, in both cases does all the job, and only function parameters are different.

HIRLAM model horizontal resolution is 8 km, which means that wind speed predictions are valid for an area of 64 km^2. Sedos wind farm is located in a relatively small area, therefore using data from the HIRLAM point closest to the wind farm contributes to the general prediction error. In order to eliminate this source of inaccuracy horizontal bilinear interpolation was performed which evaluates the contribution of wind speed prediction data from each of four HIRLAM points according to their distance from the wind farm. Results have shown that interpolation has reduced the mean error of the prediction by 1.4% to the value of 1.0867 m/s. Therefore interpolated prediction data are used in further analysis.

Influence of topography and atmospheric stability conditions on the accuracy of wind speed predictions. As mentioned above, values of surface roughness due to HIRLAM model resolution are calculated only every 8 km, and terrain height variation or roughness differences between grid points are "covered" under the average values, therefore smaller scale flow variations are not considered. For this purpose local scale terrain and surface roughness variation effects on the wind flow were estimated with WAsP, which evaluates wind speed and direction changes caused by local topography variation. Coefficients of wind speed changes were calculated for 12 direction sectors (30º each).

Influence of topography was evaluated by multiplying raw HIRLAM data with WAsP coefficients and by using WAsP estimated z_0 for wind speed transformation to the hub-height.

Logarithmic law is valid mostly for neutral atmosphere stratification, but in reality atmospheric conditions often are far from neutral and change the shape of the vertical wind speed profile. Therefore it may be expected that without taking into account atmospheric stability conditions an additional error will be introduced when extrapolating wind speed from one height to another [6].

The influence of atmospheric stability conditions on the accuracy of wind speed predictions was evaluated using physical and statistical method. Physical method involves introducing stability function to the logarithmic profile (Equation 4). This function contains Monin-Obuchov length L, which was calculated with the (5) formula. Statistical method uses multiple regression involving coefficients describing atmospheric stability conditions (Equation 7).

As the main purpose of the analysis is to get the smallest errors, only the combinations of the effects causing the best error improvement were selected. Calculated MAE errors were compared with those obtained without influence estimation (Table 1).

Table 1. Influence of local topography and atmospheric stability conditions on the mean absolute errors of short-term wind speed prediction

	Influence not estimated	Influence of topography	Influence of atmospheric stability conditions	
			Physical method	Statistical method
MAE m/s	1.0867	1.0843	1.0861	1.0787
Error improvement %	-	-0.22	-0.07	-0.74

Results have shown that the error improvements are small (< 1%), but any change in average error indicates that these effects influence the prediction accuracy. Analysis has shown that multiple regression method has reduced prediction errors by 0.74%, while physical method – only by 0.07%, which suggests that statistical method is more effective than the physical one. Possible reason is that atmospheric stability conditions are better described by wind speed and potential temperature gradients used in the statistical method.

In order to increase the error improvement, the evaluations of all effects were integrated in one algorithm, which makes the basis of the short-term wind power prediction model. Mean absolute errors for all horizons are given in Fig. 3.

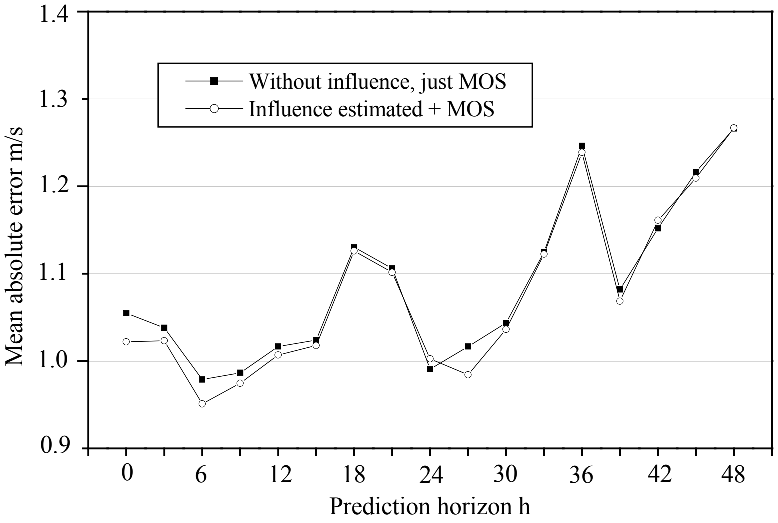

Fig. 3. Comparison of short-term wind speed mean absolute errors before and after the estimation of the general influence of topography and atmospheric stability conditions

It is seen from the Fig. 3 that estimation of the general influence of topography and atmospheric stability conditions has reduced MAE errors mostly for the horizons up to 15 hours. Mean absolute error of all prediction horizons decreased to the value of 1.0773 m/s (0.86% error improvement). It should be noted that mean prediction errors depend on the length of time series used for error calculation. The use of longer time series would lead to more reliable error estimates and smoother curves.

The importance of model output statistics. Systematic errors comprise part of short-term wind speed prediction errors, they were eliminated by MOS using simple linear regression. MOS parameters were calculated using all available measurement data and corresponding raw HIRLAM data interpolated for Sedos wind farm. Calculated MAE for all prediction horizons are given in Fig. 4.

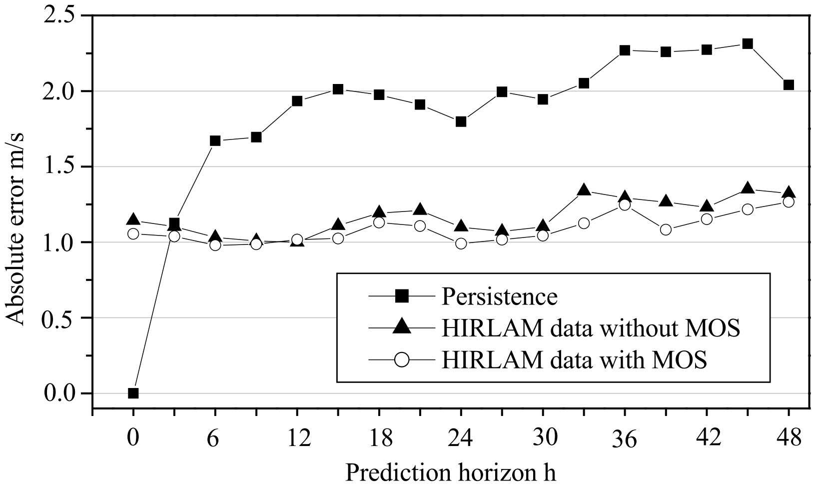

Fig. 4. Importance of MOS to mean wind speed prediction errors

After application of MOS for Sedos wind farm, mean absolute error of wind speed prediction has decreased by about 7 %, comparing with raw HIRLAM data scaled to the hub-height. Also it can be seen that model outperforms persistence only after 3 hours look-ahead time. This is typical for most wind power prediction models [1].

Conversion of the predicted wind speed to wind power. Having evaluated the influence of topography and atmospheric stability conditions on the accuracy of short-term wind speed prediction, the last stage is conversion of the predicted wind speed to wind farm power. Theoretical (manufacturer's) power curve of wind turbine may be used for this purpose, but experience has shown that prediction accuracy is better when using experimental power curve [10, 11].

Sedos wind farm consists of two Enercon wind turbines – E-40 and E-48 (600 and 800 kW, respectively). Experimental power curves were determined for both turbines according to the wind speed and turbines' power measurement data. 5th order polynomial approach was used for the approximation of the power curves:

$$y = a + b_1 x + b_2 x^2 + b_3 x^3 + b_4 x^4 + b_5 x^5 \tag{24}$$

where: y is dependent variable (WT power); x is independent variable (wind speed), a and b – statistical function parameters.

Predicted WT power was compared with measured Sedos wind farm power data, and MAE as well as RMSE errors were calculated for every prediction horizon from 0 to 48 hours. Errors are expressed in percentage of the nominal WT power (Fig. 5).

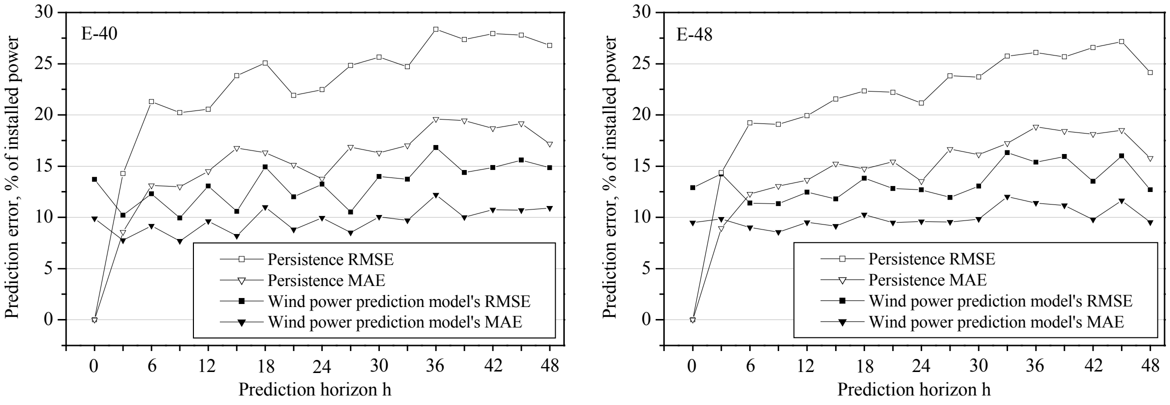

Fig. 5. Short-term wind power prediction errors for Sedos wind farm's Enercon E-40 and E-48 turbines

Results show similar error variation for both wind turbines. Wind power prediction MAE error of all horizons is 9.7% of nominal power for E-40 WT and 9.9% for E-48 WT (about 60 kW and 80 kW respectively). These results agree with the results obtained by other authors, declaring MAE errors of about 10 % [11–15]. This confirms the suitability of the developed model to the prediction of Sedos wind farm's power and suggests that model can be applied to other wind farms in Lithuania. RMSE error varies from 10 to 17% for the E-40 WT and from 11.5 to 16.5% for the E-48 WT.

It is seen in Fig. 5 that persistence MAE error is better for the horizon of 0–3 hours. This is related with the processes in the atmosphere. It takes a few days for an air system to cross the Europe, therefore wind power prediction according to the last measured value is relatively accurate for the first few hours. However, when horizon exceeds 4–6 hours, even raw HIRLAM predictions are better.

Quality of the short-term wind power prediction model is also evaluated by estimating the error improvement with respect to the persistence model [4]. In order to quantify the error improvement, the improvement score was calculated:

$$IS = \frac{MAE_{pers.} - MAE_{mod\,el}}{MAE_{pers.}} \times 100\%, \tag{25}$$

where IS is improvement score, MAE_{pers} – MAE error of the persistence, MAE_{model} – MAE error of the model. Improvement score was calculated for all prediction horizons (Fig. 6).

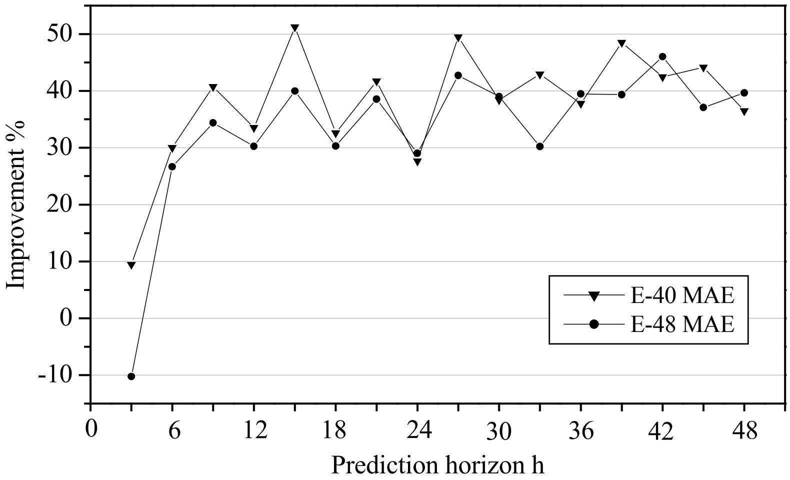

Fig. 6. Improvement of the developed short-term wind power prediction model over the persistence

Data in Fig. 6 show that mean error improvement for the first 3 hours is only 10% for E-40, and for E-48 WT there is no improvement. Similar results for this horizon were achieved by other authors [1, 3, 16]. When prediction horizon exceeds 6 hours, MAE error improvement of 28–52% over persistence is observed. This achievement is relatively low, which most likely was caused by the short time series used in the analysis. However, Madsen et al. [4] states that if prediction model is better than persistence, it can be used for wind power prediction and further improved.

Short-term wind power prediction model described in this work is designed for Sedos wind farm, but it can be adjusted for other wind farms according to their local conditions. Also this model can be further improved by using longer time series of measurement data, directional statistical parameters, by modeling WT power curves, etc.

CONCLUSIONS

1. A short-term wind speed prediction model has been developed for Lithuanian wind farms with the prediction mean absolute error of 1.077 m/s for Sedos wind farm. Such accuracy is typical for most wind speed prediction models in other countries.
2. Analysis of HIRLAM data application to short-term wind speed prediction has shown that model output statistics has the biggest influence on the reduction of mean prediction error. After the application of linear regression wind speed mean absolute errors reduced by 7% for Sedos wind farm.
3. Results of the investigation allow to state that the influence of atmospheric stability conditions is more important when predicting wind speed for Sedos wind farm than the

influence of surrounding topography. Consideration of these effects has reduced mean absolute prediction error by 0.22% and 0.74%, respectively.

4. Application of the short-term wind speed prediction model to the prediction of Sedos wind farm power has revealed that mean absolute error for E-40 turbine was 9.7% and for E-48 turbine – 9.9% of their nominal capacity. These errors are similar to the errors of wind power prediction models in other countries and thus allow to conclude that the developed model is suitable for the prediction of Sedos wind farm power and can be applied to other Lithuanian wind farms.

REFERENCES

1. Giebel, G. *The State-Of-The-Art in Short-Term Prediction of Wind Power. A Literature Overwiev*. Project ANEMOS „Development of a Next Generation Wind Resource Forecasting System for the Large-Scale Integration of Onshore and Offshore Wind Farms“. Risø National Laboratory, Roskilde, Denmark. 2003. 36 p.
2. Costa A, et al. A review on the young history of the wind power short-term prediction. Renewable and Sustainable Energy Reviews, 2007.
3. Joensen A. *Short-term wind power prediction.* PhD-Thsesis. Technical university of Denmark. 2002. 256 p.
4. Madsen, H., Pinson, P., Kariniotakis, G., Nielsen, H.A., Nielsen, T.S. Standardizing the Performance Evaluation of ShortTerm Wind Power Prediction Models. *Wind Engineering*, 2005, vol. 29, No. 6, p. 475–489.
5. Landberg, L. *Short-term Prediction of Local Wind Conditions*. PhD-Thesis. Risø-R-702(EN), Risø National Laboratory, Roskilde, Denmark. 1994.
6. Badger, J., et al. *Report on the use of stability parameters and mesoscale modelling in short-term prediction*. Risø-R-Report. Wind Energy Department, Risø National Laboratory, Technical University of Denmark. Roskilde, Denmark, 2007, 32 p.
7. Focken, U., Heineman, D. Influence of Thermal Stratification on Wind Profiles for Heights up to 140 m. In *Proceedings from European Wind Energy Conference EWEC*, Madrid, 2003.
8. Dyer, A.J. A review of flux-profile relationships. *Boundary Layer Meteorology*, 1974, No. 7, p. 363–372.
9. Jensen, N. O., Petersen, E. L., Troen I. Extrapolation of mean wind statistics with special regerd to wind energy applications. World Meteorological Organization, 1984.
10. Nielsen, H.A., et al. From wind ensembles to probabilistic information about future wind power production – results from an actual application. In *Proceedings of the 9th International Conference „Probabilistic Methods Applied to Power Systems“*, June 11–15, 2006, Stockholm, Sweden, p. 1–8.
11. Costello, R., et al. Potential Benefits of Wind Forecasting and the Application of More-Care in Ireland. In *Paper presented on the 3th MED POWER Conference*, November 4–6, 2002, Athens.
12. Giebel, G., et al. Relative Performance of different Numerical Weather Prediction Models for Short Term Prediction of Wind Energy. In *Proceedings of the European Wind Energy Conference EWEC'1999*, March 1-5, 1999, Nice, France, p. 1078–1081.
13. Dutton, A.G., et al. Load and Wind Power Forecasting Methods for the Optimal Management of Isolated Power Systems with High Wind Penetration. *Wind Engineering*, 1999, No. 23 (2), p. 69–87.
14. Giebel, G., et al. *Wind Power Prediction using Ensembles*. Risø-R Report. Risø National Laboratory, Roskilde, Denmark, 2005. 43 p.

15. Joensen, A., et al. Model Output Statistics Applied to Wind Power Prediction. In *Proceedings of the European Wind Energy Conference*, March 1–5, 1999, Nice, France, p. 1177–1180.
16. Lange, M., Focken, U. Physical approach to short-term wind power prediction. Report. Springer-Verlag, Berlin, 2006.

CYSENI 2009, May 28-29, Kaunas, Lithuania
ISSN 1822-7554, www.cyseni.com

WOOD GASIFICATION IN LATVIA: TODAY AND IN FUTURE

T. Odineca
Riga Technical University, Building Faculty, SGUTI
Azenes 16/20, Riga, LV-1048 – Latvia
Phone: 371 29597650
Email: rifat1@mail.ru

ABSTRACT

The paper analyses the possibility of using wood gasification technology in CHP plants in Latvia. According to requirements of EU directive on Renewable Energy Sources, the part of renewable sources of energy used in Latvia must be 40% in 2020. To satisfy these requirements, recently some types of energy strategies for Latvia were elaborated. During the investigation a big interest was observed in the wood gasification.

Gasification is a thermodinamical process that converts wood and woody biomass to a gaseous fuel. Gaseous fuel can be used for highly effective CHP technologies, including gas turbines.

In sustainable forestry, the cycle of carbon for trees is closed, and forests form a renewable reservoir, or sink, for carbon. It follows that using wood helps to mitigate climate change caused by greenhouse gas emissions.

Forests and timber are Latvia's main resource. Low-quality stemwood, branches and stumps that are left unutilized at logging sites form a large potential reserve of wood energy.

Today in Latvia there are no CHP plants where wood gasification would be used. This could be explained by many reasons:

- the space required for transporting and storing wood chips is greater than needed for other fuels. Therefore, wood is a local fuel which is used usually close to the source.
- the transportation and cleaning of stemwood, branches and stumps, which could be used for gasification, is expencive.
- the primary costs of gasifier, filter, and other equipments are relatively high.

However, the wood gasification can be successfully applied in Latvian CHP plants. The success depends on definite circumstances, which were analised in the paper: power of CHP plant, distance of transportation, quality and composition of fuel, etc.

Keywords: cogeneration, wood gasification

1. INTRODUCTION

Nowadays, all world's increasing interest is observed in two aspects of energy problems – energy dependence and climate change. Many investigations are being made on alternative energy sources and new technologies. To achieve the aims of European Union (EU) energy and climate policy till 2013–2020, all european countries have to concentrate on increasing both energy efficiency and renewable fuels usage [3, 6].

Since 2001 different fossil fuels usage was developed in two EU directives [5]:

- Directive 2001/77/EC on the promotion of electricity produced from renewable energy sources in the internal electricity market.
- Directive 2003/30/EC on the promotion of the use of biofuels and other renewable fuels for transport.

Both these directives define the percentage of renewable fuels usage in EU countries. The main purpose of Directive 2001/77/EC is to achieve a 12 percent share of gross renewable domestic energy consumption by 2010, and a 22.1 percent share by 2010. Directive 2003/30/EC called for an intermediate target of 2% by 31 December 2005. The target of 5.75% is to be met by 31 December 2010.

The possible principles of Energy Policy for Europe were elaborated at the Commission's green paper *A European Strategy for Sustainable, Competitive and Secure Energy* in 2006. As a result of the decision to develop a common energy policy, the first proposals, *Energy for a Changing World* were published by the European Comission, following a consultation process in 2007. Key proposals include: a minimum target of 10% for the use of biofuels by 2020; the development of a European Strategic Energy Technology Plan to develop technologies in areas including renewable energy, energy conservation, etc.

The European Commission has proposed in its Renewable Energy Roadmap21 a binding target of increasing the level of renewable energy in the EU's overall mix from less than 7% today to 20% by 2020. The targets for the member states are calculated using formula: flat rate 5.75% (one for all EU countries) + extra % (according to GDP).

In Latvia the renewable energy as a part of gross final energy consumption should be increased from 35% in 2005 to 42% in 2020 [6].

This paper observes wood gasification as a technology which can be used in cogeneration process. The aim of the paper is to summarize pros and cons of wood gasification and the possibility of its usage in Latvia as an effective way for achieving Renewable Energy Roadmap 21 aims.

2. USAGE OF WOOD GASIFICATION TECHNOLOGY IN CHP PLANTS

Cogeneration (the simultaneous production by means of a selected fuel source of both electricity and heat) is one of the most efficient methods of energy resource economy. The main indicator of CHP (combined heat and power) plant efficiency is α-ratio, which is a ratio of produced electrical and heat energy. It shows how many kWh of electrical energy can be produced on the basis of 1 kWh of heat energy.

In Table 1 there is an engineering comparison of different types of CHP technologies [1].

Table 1. Characteristics of different types of CHP technologies

Engine	Electrical efficiency, %	Total efficiency, %	α-ratio	Electrical capacity
Steam turbine	10–20	70–85	0.2–0.4	0.4–300 MW and more
Gas turbine	25–40	70–92	0.4–0.6	0.5–300 MW and more
Gas-steam combined cycle	50–55	85–90	0.8–1.1	>10 MW
Internal combustion set	28–31	80–88	0.8–1.5	From 15 kW

It is possible to use fossil or renewable fuels for different CHP technologies. One of the renewable fuels is wood. Usage of wood fuel instead of fossil fuels in cogeneration technologies reduces CO_2 emission, because CO_2 released from dead wood used in burning process is compensed by CO_2 converted from the atmosphere in wood life cycle.

The main method of wood fuel usage is direct combustion [2]. This method has low coefficient of efficiency (20–60%), causes large emissions of ashes, charcoal, and hydrocarbones. Convective and radiative heating surfaces of boilers are usually covered with solid particles' layer, therefore boilers must be stopped often for cleaning. Systems where wood fuel is burned are hard to automate. The main disadvantage of direct wood combustion is that it can be used only in steam turbines – a CHP technology with the lowest efficiency indicators.

Wood gasification (a thermodinamical process that converts wood to a gaseous fuel) does not have these disadvantages. Gas fuel can be easily transported far through pipelines or in tanks, the combustion of gas can be easily automated, the combustion gases are less toxic. Gas produced from wood can be used in highly effective CHP technologies: gas turbine, internal combustion engine or gas-steam combined cycle.

Usage of wood gasification in CHP plants helps to minimise the enviromental pollution, because during this process:

- the efficiency of energy equipment increases;
- new effective gas purification plants are used;
- renewable fuel is used.

2.1. Experience of wood gasification usage in the world

The basic principles of wood gasification were investigated and developed since the beginning of the 19 century [7]. In the 1930–40s the new generation gasifiers were developed. These were used in construction of cars and tractors, to provide internal combustion sets with gaseous fuel. In the 1950–60s new technologies based on gasification of industrial wood waste were developed. These were mostly stationary equipments constructed to produce gas for boiler houses or gas diesel engines. Interest towards gasification increased during energy crisis in the 1970s, then reduced together with oil prices in the 1980s. According to World Bank data, in 1989 only 1000–3000 gasifiers were used in the world, mainly in South America.

In the last few years interest towards renewable fuel gasification appeared again because of rapid growth of energy sources prices [3]. Gasifiers, in which wood and wood charcoal are used, are becoming a commercial product. In some countries investigations on the possibility of using other kinds of biomass as a fuel are carried out.

2.2. Technological scheme of a CHP plant with wood gasifier

As an example of a CHP plant with wood gasifier, gas-steam combined cycle CHP plant can be viewed. The equipment of the plant can be divided into 3 main blocks.

Block 1. Wood gasificationn equipment:

- fuel bunker;
- fuel drying-room;
- intermediate feeding container;
- gasifier;
- stainer;
- gas cooler;
- fine filter.

Block 2. Gas turbine equipment.

Block 3. Steam turbine equipment.

Gasifier consists of a fuel bunker, gasification camera, primary (secondary) air feeding system, kindling camera, ashes box, firebox and connecting furniture with boilers, water and air heating equipment.

Gasifier works as described below [2]:

- kindling material is placed on the grate, and the gasifier is lighted-up as a common stove. Lighting-up takes 0.5–1 hour;

- basic fuel is placed into the bunker, then it goes into the gasification camera, where it's converted into gas. Depending on the capacity of a gasifier, fuel feeding can be manual or automatic;
- gas produced in pyrolysis process goes to the firebox. Secondary air is passed into the firebox, and the mix kindles;
- combustion products are passed to the boiler, water or air heating equipment, which is connected to the gasifier.

The process is regulated by changing the passing of primary or secondary air.

Gasifiers can work using principles of direct or reversal combustion. When reversal combustion is applied, combustion products contain much less resin and acid steams.

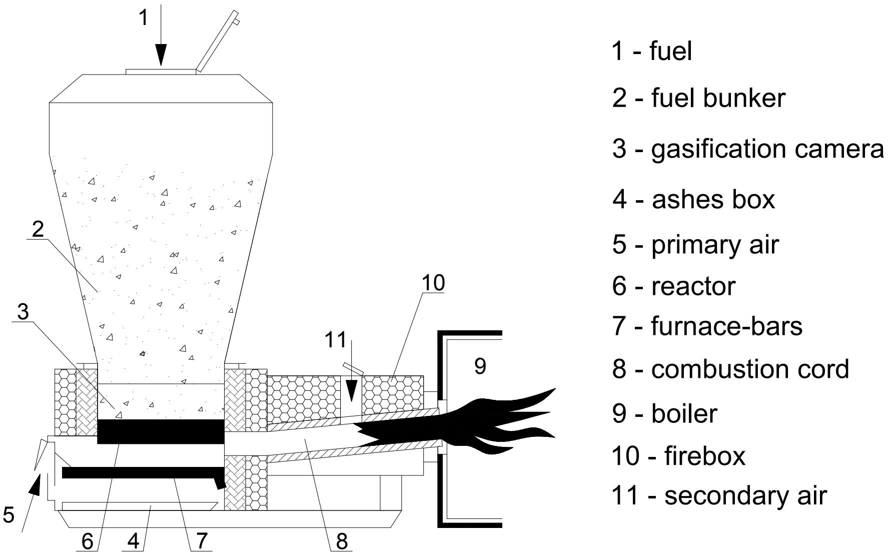

Fig. 1. Gasifier

2.3. Usage of different kinds of wood fuel in gasification process

In wood gasifiers different types of wood fuel can be used: wood waste (particles 1–200 cm sized), wood chips, chip briquettes, etc [2].

Humidity of wood fuel used in gasifiers can be different, up to 60–65%, however, it's preferred to use wood fuel with 30-35% humidity, which can be achieved by laying the wood off for 3 months. The species of wood does not have a big influence on the composition of gas, liquid and solid products.

Usage of industrial wood waste almost always is economically more attractive than the usage of forest wood waste. Ecological effect of industrial wood waste gasification is the same as of forest wood waste, only if chemically impregnated or coloured wood is not used. The last one must be treated like domestic or chemical waste depending on the handling type.

If gas is used in an internal combustion engine for the production of electrical energy, it demands special quality of gasifier and gas. Necessity of cleaning, cooling and mixing of gas makes technology rather difficult. World's experience of exploitation of this kind of systems shows, that they are sensitive towards the changes of fuel parameters, changes of the load of equipment, quality of service, and enviromental conditions.

3. POSSIBILITIES OF WOOD GASIFICATION USAGE IN LATVIA

3.1. Usage of wood fuels in CHP plants in Latvia

By 2007 there were 20 CHP plants with capacity higher than 1 MW in Latvia [4]. Total electrical capacity comprised 586.2 MW and total thermal energy – 1320.2 MW.

The main part (91%) of them used natural gas as a fuel. Other kinds of fuel were used as well – these were fuel oil (4%), woodchips and biogas (5%). Meanwhile, wood fuel is used in cogeneration process only in a few wood CHP plants with total electrical capacity of 2 MW.

In Latvia there are as well some small capacity (<1MW) CHP plants as well. By 2004 these were 12. These CHP plants have to submit the reports for common statistics only, therefore it is difficult to get precise information about their capacity x, technologies, amount of produced energy and fuel used. Mainly all small CHP plants use natural gas as a fuel, except AS „Rīgas siltums" CHP plant in Daugavgriva, where biomass is used, and SIA „Rīgas ūdens" CHP plant, where biogas is used.

Today in Latvia wood fuel is used mainly for the production of heat energy. In 2005 the proportion of wood fuel in total Latvian energy balance was 29.1% of total energy resources consumption, and 46.4% of total fuel consumption [4]. Wood is used in all kinds of heat supply systems (centralised, local and individual). The bigger part (51%) of wood fuel is used in individual heat supply systems.

The kinds of wood fuel used in Latvia today are:

- firewood;
- wood-cutting waste;
- wood-processing byproducts (woodchips, shingles, bark, wood particles, wood dust);
- special products (briquettes, pellets, charcoal);
- energetic wood plantations (meanwhile in the early phase of development).

Usage of wood fuel in cogeneration processes by applying direct wood combustion is possible in a steam turbine. Thermodinamical efficiency of this technology is 25–40%, efficiency of fuel usage is 82–85%, and α-ratio is 0.2–0.4. As it is seen, this technology can not be called effective comparing to the technologies where wood gasification is used (gas turbines, gas-steam combined cycle, internal combustion set).

3.2. Resources of wood fuels in Latvia

During the last 10 years the potential of wood resources usage in Latvia was widely researched. The results of the researches are presented in Table 2 [4].

As it is seen, the biggest amplitude in the researches is towards wood cutting waste and wood-processing byproducts. Potential and usage of cutting and wood-processing remnants must be connected with the development of technologies and wood fuel prices comparing to other energy resource prices. The growth of fossil fuel prices usually causes wider usage of low-grade wood fuel.

The lower border of potential is less than wood resource annual amount, which is used in Latvia now (not including annual amount of exported wood). The annual amount of power-generating wood used in Latvia, together with annual amount of exported wood, reaches the higher border of wood potential. This means that in order to ensure the lasting possibility of wood usage, wood cutting must not exceed wood resources' possible renewal. Therefore, it is necessary to concentrate on more complete and efficient usage of wood fuel.

The prices of firewood and woodchips can be very different depending on the region where these kinds of fuel are used. The reasons for this difference are: quality of fuel, technology of collecting the fuel, amount of used fuel, accessibility of resourses, conditions of transporting and storage.

Table 2. Wood usage potential in Latvia

Wood fuel	Potential, million m^3 per year	Potential, PJ
Firewood	1.8 - 2.4	12 - 16
Cutting waste (foliage, branches of trees, etc.)	1.8 - 2.7	12 - 18
Brushwood	0.3 - 0.75	2 - 5
Stumps	0.1 - 0.4	0.7 - 3
Yearly dead wood	0.3	1,5
Wood-processing byproducts	1.6 - 4.5	14 - 37
Secondary wood from dumping-grounds	0.3	2
Total	**6.2 - 11.4**	**44.5 - 82.5**

Recently the prices of woodchips, firewood, and saw dust are growing rather rapidly. The reasons for growth of prices are:

- rapid growth of wood-processing costs (mainly transportation and salaries);
- the amount of wood suppliers decreased. It is related especially to small wood suppliers: many of them have cut out all wood permissed by norms;
- during last 4-5 years demand of wood increased, and as a result, sometimes woodchips are transported from more than 100 km distance;
- wood waste from wood felling areas and small wood-processing production units is used rather seldom, because of high costs;
- the price of wood in Scandinavia achieved the level, when it is more profitable for Latvian wood suppliers to export wood, than to sell it in Latvia.

Today wood prices are getting close to European prices. In future in Latvia wood prices will grow together with prices of other kinds of fuel and prices of electrical energy. The prices of wood fuel in Latvia are influenced by market processes in this area in other European countries.

3.3. Potential of wood gasification in Latvia

As it was said before, the annual amount of power-generating wood used in Latvia, together with annual amount of exported wood, reaches the higher border of wood potential. According to Latvian normatives, in which speed of forest reforestration is accounted, increasing of annual wood cutting is impossible. All possible amount of wood fuel (which is not exported) is in use now – in boiler houses (for producing of heat energy) or in small CHP plants (using direct combustion technology). Therefore, there are two ways how to develop cogeneration with wood gasification technology in Latvia: reconstruction of existing boiler houses, and more complete and efficient usage of wood fuels (for example, usage of wastewood, including remnants left in forests after improvement and sanitation cutting).

Building of CHP plants with wood gasifier instead of existing common boiler houses is reasonable in case if there is a high heat demand in the surroundings, not only during the heating season, but for a whole year running. This is important for economical efficiency of a CHP plant, because cogeneration equipment will work with base heat load all year, and for the peak load during heating season peak load boilers will be used. The bigger is the base load of cogeneration equipment, the bigger the economical efficiency of a CHP plant.

If it is planned to use low-quality wood fuel or remmants of improvement and sanitation cutting for gasification, it is necessary to remember that in the composition of these kinds of fuel there are particles which quickly pollute the filters of a gasifier. Frequent change of filters causes large maintenance costs. Besides, the methods of collection, transportation and cleaning of improvement cutting remnants are not well developed in Latvia.

It is possible to compare natural gas and gas generated in a gasifier because these two fuels can be used in the same cogeneration technologies (gas turbines, gas-steam combined cycle, internal combustion set). Today in Latvia natural gas is a prefered fuel for CHP plants from both ecological and economical point of view. If natural gas is accessible in the surroudings of a newly designed CHP plant, it is cheaper to use natural gas as a fuel. Primary costs of gas CHP plant are usually less tnan costs of the one with wood gasifier, especially if new gas supplying line required for a CHP plant is not long. Relatively high primary costs of wood gasification equipments are explained by the fact, that all of them are usually imported. Capital investment can be reduced if local materials are used for building. For example, the cost of a gasifier, which was built of local materials in Asian Technical Institute (Bangkok), was 10 times less than the cost of the western analogue.

The advantage of wood fuels compared to natural gas is that wood is a renewable fuel. Besides, wood is a local resource, and natural gas is imported. Gas distribution system in Latvia does not cover large territories, including the territories with big forest density.

It is necessary to remember that CHP plants, where wood fuels will be used, should be situated as close as possible to wood logging or wood-processing territory, because transportation of wood fuels to long distances is expensive.

4. CONCLUSIONS

1. Usage of wood fuels not only helps to satisfy the demands of EU Directive 2001/77/EC and to increase the part of renewable energy in gross final energy consumption from 35% in 2005 to 42% in 2020, but also gives an opportunity to get more independence from importing of fossil fuel resources (natural gas).
2. Wood gasification technology used in cogeneration process is more effective than common combustion of wood, because generated gas can be a fuel for highly effective CHP technologies, including gas turbines, gas-steam turbines and internal combustion sets. Wood gasification is less dangerous for enviroment comparing to common combustion, because during gasification process less emissions go to the atmosphere.
3. Wood gasification can be successfully applied in Latvian CHP plants, if:
    - it is planned to reconstruct the existing boiler house where wood fuel is used;
    - there is a rather big demand of heat energy all year long in the surroudings of the designed CHP plant;
    - there are no natural gas supplying systems in the surroudings of the designed CHP plant, and building of new gas supplying line is too expensive;
    - the designed CHP plant is planned to be situated relatively close to wood cutting or wood-processing area.

REFERENCES

1. Bažbauers G., Blumberga A., Blumberga B., Sarma U., Veidenbergs I. Mazās koģenerācijas stacijas. – Rīga, 2002. – 281 p.
2. О. И. Бегунков, Н. В. Выводцев, В. В. Гурьев и др. Использование низкотоварной древесины и отходов лесопромышленного производства: Практическое руководство / Под ред. В. В. Шкутко. – Хабаровск.: Изд-во Хабар. гос. техн. ун-та, 2003. – 132 с.
3. Ekmanis Y., Zebergs V., Zeltins N., Zeberga E. Energy efficiency problems for sustainable development of the Latvian Energy Sector – Scientific Proceedings of Riga Technical University: Power and Electrical Engineering, ser.4, vol.6, 2002, p.36–43.
4. Latvijas enerģētika skaitļos. Latvijas Investīciju un Attīstības Aģentūra, 2006.
5. Enerģētikas attīstības pamatnostādnes 2007. – 2016. gadam: Latvijas Republikas Ekonomikas ministrija, 16.06.2006.
6. Directive 2001/77/EC on the promotion of electricity produced from renewable energy sources in the internal electricity market: EU directive, 2001.
7. http://www.bumprom.ru/index.php?ids=324&sub_id=10902

ENHANCED SELECTION OF BIOFUELD SMALL-SCALE COMBINED HEAT AND POWER PLANT

E. Latõšov, A. Siirde
Tallinn University of Technology
Department of thermal Engineering
Kopli 116, EE-11712 Tallinn – Estonia
Phone: +372 605 3163
E-mail: eduard.latosov@ttu.ee; asiirde@staff.ttu.ee

ABSTRACT

Present-day world energy policy is based on two main directions: energy efficiency and environmental protection. Efficient Combined Heat and Power (CHP) production is one of the energy consumption effective methods, where CHP production from the renewable fuels is preferable. The technologies for smaller CHP applications are more expensive (price per MW installed) and less efficient than those for larger CHPs, while the use of large scale CHP units is restricted with the availability of heat load (income from the heat and electricity production is restricted). This paper presents an overview of biofueld small-scale (under 10 MW_{el}) CHP selection and its capacity influence on CHP economical, efficiency and environmental figures. In this paper, the summarized effect of CHP scale factor on the project cash flow, CHP electrical efficiency and CO_2 reduction potential are discussed. The paper contains analysis of above mentioned figures calculations for CHP expansion in district heating area with 30 000 MWh annual heat demand in Estonian conditions.

Calculations show that for the time beings the only feasible is a steam turbine/engine CHP technology. ORC and biogas engine technologies are quite expensive. Without grants they are not feasible yet (IRR<0). Enactment of the regulation draft, which regulates grant payments for the renewable energy production and construction of CHP plants in Estonia will increase the attractiveness of CHP production and will have a positive effect on CHP expansion in Estonia. It is reasonable to provide calculations for the different electrical capacities, technologies and available fuels for each concrete CHP expansion project to find impacts of those components on the economical figures and CO2 savings.

1. INTRODUCTION

This paper draws on ongoing PhD thesis ‘Analysis on the technical and economic consequences of renewable energy based CHP systems in new areas with the lowered useful heat demand or after implementation of energy conservation measures in the areas with older buildings’ within the project ‘Primary Energy Efficiency’ partly financed by Nordic Energy Research, which contributes to the effort of enhancing the primary energy efficiency (PEE) and reducing CO_2 emissions in the energy sector.

The goal of PhD thesis is to create a computer program to estimate economical and technical feasibility to build a CHP plant based on renewable fuels in Nordic/Baltic Sea Region countries taking into account the local conditions. The novelty of the planed computer program is an orientation to small scale (under 10 MW_{el}) distributed CHP units, based on the existing district heating networks.

The program is targeted to heat and power engineers, enterprises with high heat/steam demand, businessman, and local government.

The program is intended to help to estimate an expediency to use one or the other CHP technology based on renewable/local biofuels taking into account local conditions as well as carry out economical calculations and make a decision to invest into new CHP units.

The goal of paper is to provide test calculations using a developed computer program for the district heating area with 30 000 MWh annual heat consumptions and compare economical feasibility for the different combinations of CHP technologies, biofuels and selected CHP electrical capacities and find the most feasible solution. The results of the calculations will show the general guidelines for the CHP expansion in basic small scale district heating areas in Estonia, whereas every single case should be calculated separately.

The paper is structured as follows. The section 2 discribes the methodology for the computer program used in the calculations. Then after an overview of the CHP location and proposed heat load graph, the paper provides an overview of the CHP technologies which can be used in CHP plants. The next section defines fuels which are mainly used in CHP plants. This section includes statistics as well as forecasts for fuels used in the economical calculations. Then state control on limit heat price, fixed electricity supply prices and supports, grant payments for expanding of CHP and usage of renewable fuels, as well as formation of electricity price and environmenthal fees are discussed. The next section provides an overview the economical calculations for different CHP technologies, fuels and grant payment possibilities. Last section provides conclusions and proposals based on calculation results and data from the previous sections.

2. METHODOLOGY

The calculations are based on a range of initial data classes:

- local climate data (temperature duration data),
- local energy prices and forecasts,
- local indexes and forecasts,
- consumer heat consumption and forecast,
- consumer electricity consumption, load duration and forecasts,
- initial financial data of the project,
- CHP technologies related data.

These data are then used in the main calculations to generate the Internal Rate of Return (IRR) and Net Present Value (NPV) for evaluating the investments. The data types and interactions between them are given in Appendix 1 as a visual structure of the computer program used in the calculations.

Evaluation of the economic and technical feasibility of the chosen small scale CHP concept is a complex of optimization processes with the aim to achieve an optimum between the CHP electrical capacity (the technical component) and one of the measures for capital budgeting (the economic component).

The proposed model is based on an assumption that the electrical capacity is the main technical component and all other technologies and economic figures are basically in correlation with the capacity.

The accuracy of the calculations results depends much on the initial data values. The data used in the calculations, such as specific investment costs for CHP plant technologies, variable and fixed operating costs for CHP plant technologies, nominal electrical efficiency of CHP plant technologies, operation margins and electrical efficiency drops for CHP plant technologies as well as statistics and forecasts for biofuel prices are based on the internal data collected by the company ÅF-Estivo, which is a leader in the energy and environmental consultancies in Estonia. The free accessed data used in the paper will be provided by the references to the base documents.

3. LOCATION DESCRIPTION

Analysis of CHP plant work is done taking into account Estonian economic, political and climatic conditions. It is assumed that district heating area annual heat consumption is 30 000 MWh, where pipe and heat dividing loses compose 15 per cent. It is assumed that hot water is prepared in local hot water preparations systems (electrical boilers, etc). It is supposed that outdoor temperature for heating period beginning/ending is 14°C and there is no district cooling.

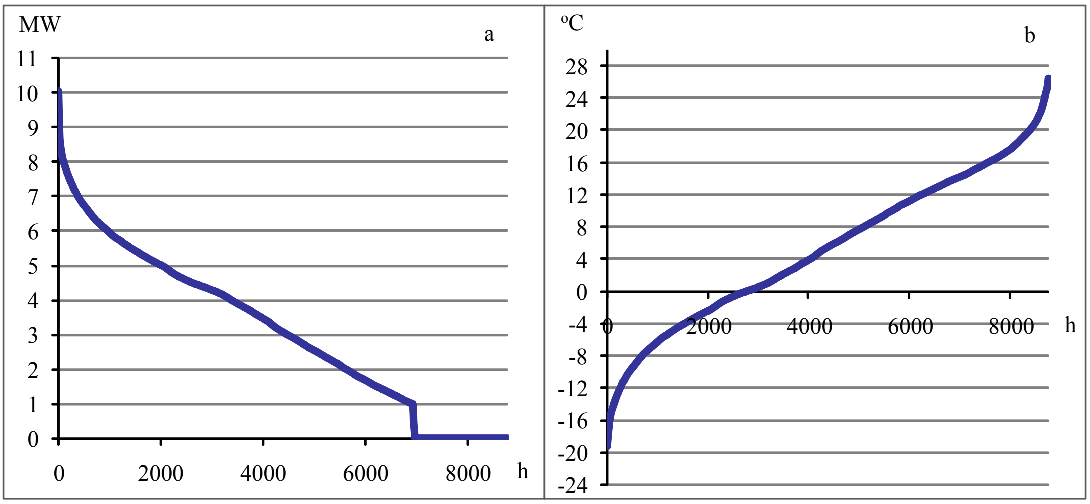

Fig. 1. a) district heating area heat load duration curve; b) temperature duration curve in CHP plant location

Heat consumption of the district heating area is described in Fig. 1. It is prepared on the basis of data purchased from Estonian Meteorological and Hydrological Institute for a few previous year average temperature durations in the Harku meteorological plant. (Fig. 1 b).

4. CHP TECHNOLOGIES

There are numerous CHP technologies that can be theoretically used for small scale systems (Fig. 2).

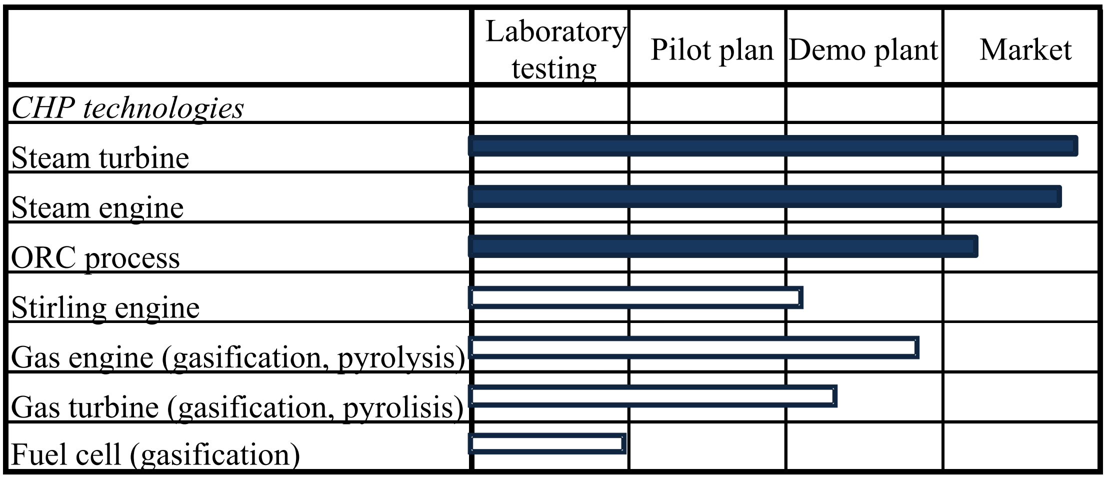

CH P

Fig. 2. Technologies used in CHP applications

It is important to consider the market ready solutions, such as a steam turbine, steam engine and ORC technology. It is reasonable to compare available data for technologies which are close to reaching the market level with market ready technologies. For example, gas engine technology based on the gasification or pyrolysis of solid biofuels. So the CHP expansion calculations are carry out with steam turbine/engine, ORC and gas engine technologies.

For CHP plant economical calculations it is important to know such CHP plant parameters as:

- efficiencies,
- price,
- operating costs.

Above mentioned parameters are collected and systemized on the basis of studies prepared by ÅF-Estivo regarding bio fuels and/or peat burning CHP plants for carrying out economical calculation.

In this paper investment means all costs before CHP plant commissioning. A value for investments used in this paper depends on CHP nominal electrical capacities and CHP technology, as shown in Fig. 3.

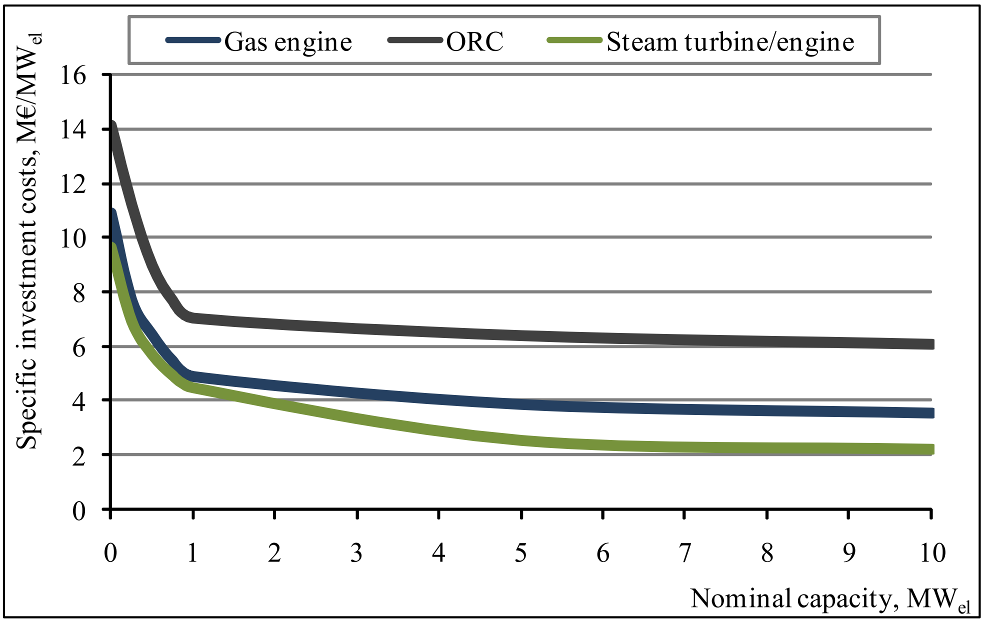

Fig. 3. Specific investment costs for CHP plant technologies

Operating costs are related to whole CHP production costs, except fuel price and capital costs. Operating costs are divided into variable and fixed operating costs. Values for operating costs used in calculations are shown in Fig. 4 and Table 1.

The interaction between CHP plant nominal electrical capacity and nominal electrical efficiency are used in the calculations for paper (Fig. 5). It is assumed that overall efficiency of CHP plants for all technologies is 85%.

The interaction between CHP plant nominal electrical capacity and nominal electrical efficiency are used in the calculations for paper (Fig. 5). It is assumed that overall efficiency of CHP plants for all technologies is 85%.

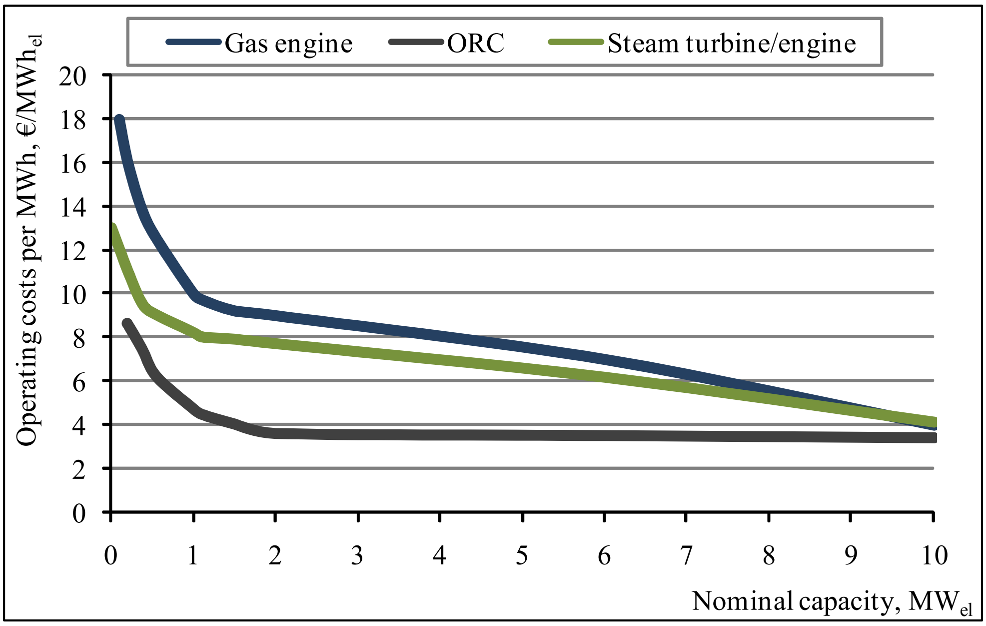

Fig. 4. Variable operating costs for CHP plant technologies

Table 1. Fixed operating costs for CHP plant technologies

Technology		
Gas engine	% of investment in CHP	3,0%
ORC	% of investment in CHP	1,5%
Steam turbine/engine	% of investment in CHP	2,0%

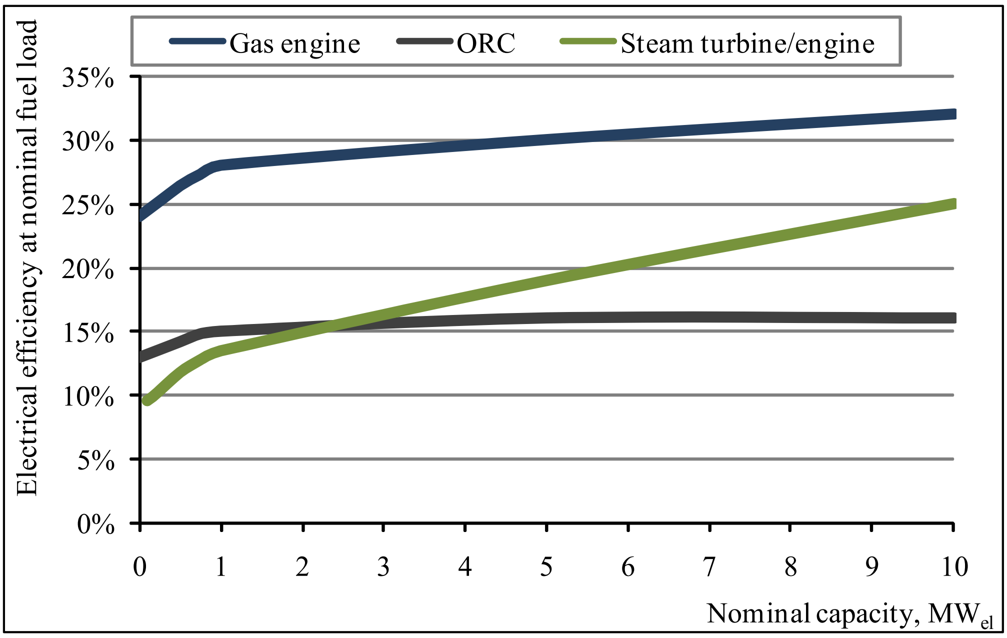

Fig. 5. Nominal electrical efficiency of CHP plant technologies

Sometimes CHP plant economical figures are calculated based on the fixed power-to-heat ratio (mainly equal to ratio at nominal electrical capacity). In the real situation CHP could work in a partial load, as an example during the summer time. Working on the partial load brings an electrical efficiency drop (power-to-heat ratio decrease) which means lower electricity production (lower income). So the CHP plant electrical efficiency drop is also included in calculations. Electrical efficiency drop as well as CHP plants operation margins are shown in Table 2.

Table 2. Operation margins and electrical efficiency drops for CHP plant technologies

	Operation margin % of CHP nominal fuel capacity		**Electrical efficiency drop** % of CHP nominal electrical efficiency	
	max	min	max	min
Technology				
Gas engine	100%	55%	100%	85%
ORC	100%	15%	100%	75%
Steam turbine/engine	100%	30%	100%	30%

5. FUELS

Definition of *biofuels* in Estonian and European Union legislation is some different. Pursuant to Directive 2003/30/EC article 2 clause 2 biofuels are in transport used liquid and gaseous fuels produced from biomass or animal fats or bio waste which are (bioethanol, biodiesel, biogas, etc). Biomass is not included into biofuels definition [1].

Pursuant to *Estonian Long-term Public Fuel and Energy Sector Development Plan until 2015* clause 1.3.2 *biofuels* explanation contains biomass (cut fuel wood, wood-processing waste and logging waste) [2].

Pursuant to Directive 2003/30/EC peat is not a renewable fuel. In Estonia peat is partly renewable (when peat annual consumption is below estimated peat annual increase).

In this paper definition *biofuels* includes biomass, biogas as well as peat.

Mainly CHP plants use non-refined biofuels, such as saw dust, wood chips, milled peat and sod peat. For the comparison reasons it is also assumed that those none-refined fuels are used for the biogas production for gas engines.

Pricing statistics for above mentioned crude biofuels is shown in Fig. 6.

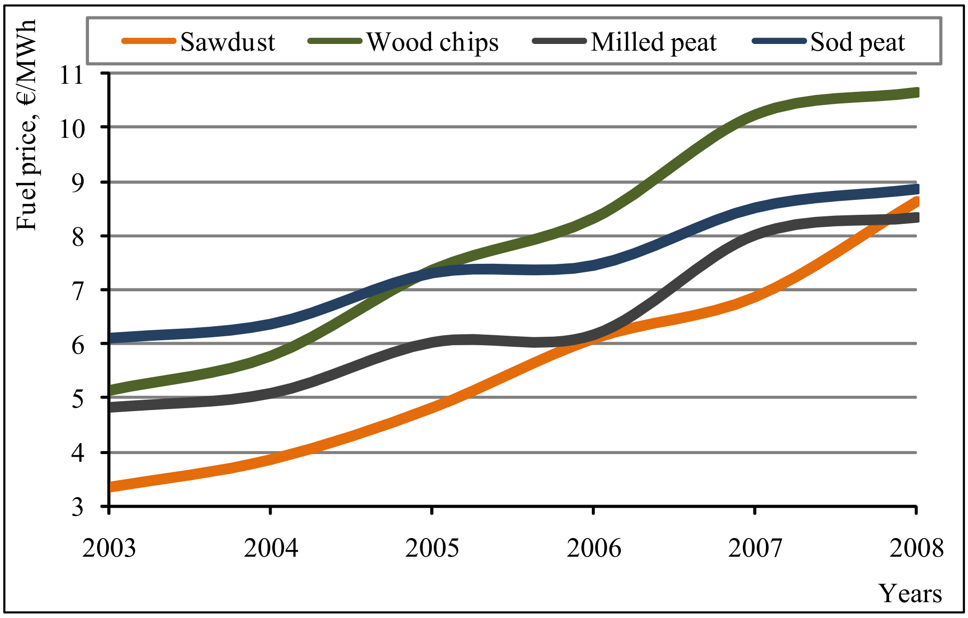

Fig. 6. Statistics for biofuels prices

Forecasts for biofuels prices, which are used in CHP plant economical calculations, are shown in Fig. 7.

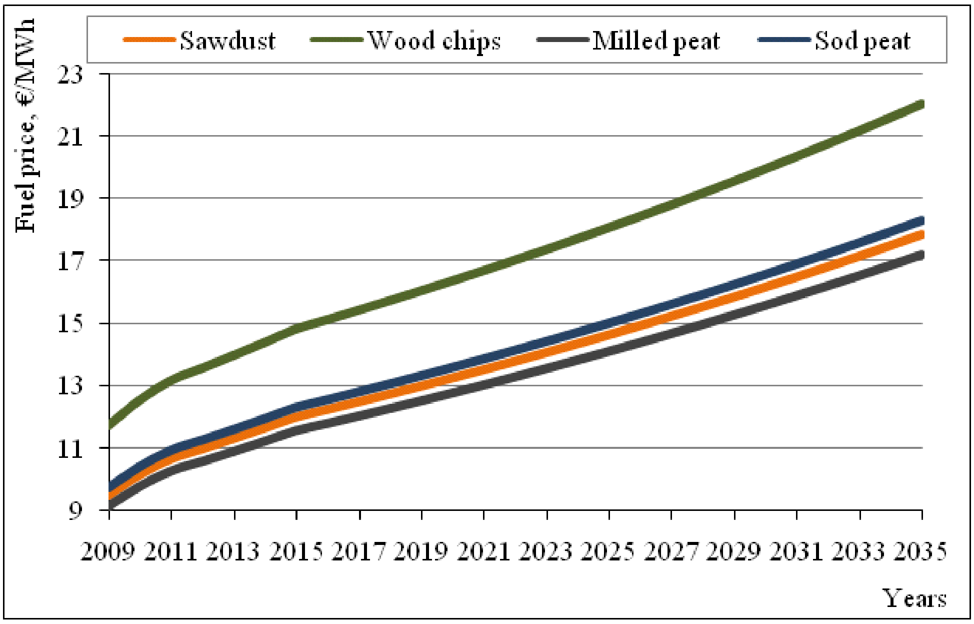

Fig. 7. Forecast for biofuels prices

6. CHP PLANT ECONOMIC CALCULATION

During planning of CHP economical operation contingencies, grant payments and obligations stated in Estonian legislation should be considered. It is important to take into account draft reports of normative documents which could have a serious effect on CHP economical feasibility after enactment.

The major factors are:

- state control on limit heat price,
- prices of fixed electricity supply and supports,
- grant payments for expanding of CHP and usage of renewable fuels, regarding to regulation draft.

Above mentioned factors are described in more detail in the following subsections.

6.1. Limit heat price calculation

Pursuant to Estonian District Heating Act heating undertakings that produce heat in the process of combined heat and power production should approve the price of heat for every district heating area. It means that during planning of CHP plant it is not correct to define income from heat sale using any heat prices. The maximum price of heat shall be set such that:

- The necessary operating expenses, including the expenses incurred upon the production, distribution and sale of heat, are covered;
- Necessary investments for the performance of operational and development obligations are made:
- Environmental requirements are met;
- Quality and safety requirements are met;
- Justified profitability is ensured [3].

6.2. Dividing of costs to heat and power production

To realize the above-mentioned procedure for the approval of maximum prices for heat a heating undertaking shall keep separate accounts for the production, distribution and sale of heat and for areas of activity not related to such activities.

Pursuant to District Heating Act combined heat and power plant should separate costs for heat and power production from one CHP facility, which vary significantly depending on CHP technology and costs separating methodology.

As an example, part of equipments in CHP plant based on steam turbine technology is used for heat or power production only. Main equipment (boiler, steam turbine, fuel handling equipment) is used both for heat and power production, which brings necessity to divide equipments depreciation between joint products.

Basically, there are some well-known methods to separate share of fuel for heat and electricity production. Instructions, prepared by Estonian Competition Authority, refer to them. Those methods distinguish between each other by fuel dividing methodology and results, which will be achieved. Unfortunately, at the moment, there is no approved general methodology for that.

In this paper heat price calculation is based on commercial, or in other words, alternative boiler house method. It means that the price of heat produced in CHP plant is equal to the price of heat produced in the heat-only plant (virtual reference heat-only plant) with the same fuel and the same heat capacity as CHP plant has. This method is also approved by the Estonian Competition Authority and is used due to its relative simplicity and clarity.

Reference heat price 40 €/MWh$_{\text{heat}}$ for wood and peat fuels for the first CHP plant operating year (2010) is taken as an average value approved in 2009 by Estonian Competition Authority for such a kind of heat only plants. Reference heat price for the other is given by:

$$P_{n+1} = (0{,}6 \times P_n \times \Delta_{fuel} + 0{,}4 \times P_n \times \Delta_{other}) + P_n \qquad (1),$$

where

P_{n+1} – heat price for the calculated year (€/MWh$_{\text{heat}}$),

P_n – heat price for the year before calculated year (€/MWh$_{\text{heat}}$),

Δ_{fuel} – proposed growth rate for calculated year fuel price,

Δ_{other} – proposed growth rate for calculated year virtual reference heat-only plant non fuel costs.

In the calculations growth rate for reference heat only plant non fuel costs is equal to CHP plant non fuel operating costs growth rate. It is assumed, that $\Delta_{other}=0{,}03$.

6.3. Grant payments for the expansion of CHP and usage of renewable fuels

For the time being there is no approved legislation, which regulates grant payments for the renewable energy production and construction of CHP plants in Estonia. There is only regulation draft, which is on the adjusting stage now [4].

Regulation draft assumes grant payments for under 2 MW$_{\text{el}}$ CHP plants up to 50% from expenses eligible for assistance.

Enactment of this regulation is an extremely important for small-scale biofueled CHP plants expansion.

In the computer program calculations it is assumed that regulation draft will be approved with no material changes and investments to CHP plant will be granted in compliance with it.

6.4. Electricity price

Regarding to *Electricity Market Act* a producer has the right to sell electricity as a fixed supply to a seller designated by the transmission network operator or to receive support from the distribution network operator for the electricity supplied and sold to the network if it is generated from a renewable energy source with a generating installation which has a net capacity not exceeding 100 MW and in efficient cogeneration regime if waste within the meaning of the Waste Act, peat or oil-shale processing retort gas is used as a source of energy.

Fixed supply price and support values are assembled in Table 3.

Table 3. Fixed supply price and support for electricity from a renewable energy source and electricity generated in efficient cogeneration regime.

	Price	**Support**
	€/MWh	**€/MWh**
Renewable electricity	73.7	53.8
Efficient cogeneration regime	51.9	32.1

It is assumed that until year 2013 CHP plant will sell electricity at fixed supply price. From year 2013 Estonia will have fully open energy market. It is predicted that in the open market conditions electricity price will grow by 3 per cent annually [5].

6.5. Environmental impact and fees

Regulation *Procedure and Methods for Determining Emissions of Pollutants from Combustion Plants into Ambient Air* regulates the determination of emissions of sulphur dioxide (SO_2), nitrogen oxides (NO_2 + NO), carbon oxide (CO), volatile organic compounds (CnHm), solid particles, and heavy metals generated by combustion plants and emitted into ambient air. Regulation describes possibilities to determinate pollutants on the basis of direct measurements and/or calculations.

In this paper the assessment of emissions of pollutants from CHP plants into ambient air is carried out on the basis of the procedure described in regulation [6].

Pollution charge rates upon emission of pollutants into ambient air used in the calculations correspond to pollution charge rates stated in the *Environmental Charges Act* (Table 4) [7].

Table 4. Pollution charge rates upon emission of pollutants into ambient air

Pollutant	Particulates[1]	SO_2	NO_x	CO	VOC[2]	Heavy metals	CO_2
Charge rate, €/t	30.4	30.4	69.7	4.4	69.7	1108.8	2.0

[1] – particulates except heavy metals and compounds of heavy metals
[2] – volatile organic compounds, except mercaptans

7. ECONOMICAL CALCULATIONS

The revenues of a CHP company are generated from the sales of heat and electricity and they must cover the costs of the company completely. For calculating project IRR and NPV values in addition to information from previous paper sections, some other parameters have to be specified:

- Project length time 25 years,
- Power plant in operation 24 years (first year - planning and construction),
- Power plant in operation from 01 January 2010,
- Project financing: bank loan or bank loan with government grant payments. Bank's interest rate is 6%. Annuity loan for 24 years,
- 1% of investments per year for power plant insurance,
- CHP plant life time is 24 years.

The results of calculations for different CHP expansion scenarios in 30 000 MWh district heating area are collected in Table 5. Table shows project IRR and NPV to specify economical feasibility of the scenario. Not feasible scenarios (IRR is below 0) have an *x* mark. Table also contains annual CO2 emission levels for different feasible scenarios (peat as a fuel) for raw CO2 saving estimation.

8. CONCLUSIONS AND PROPOSALS

Test calculations using a developed computer program for the district heating area with 30 000 MWh annual heat consumptions under the Estonian conditions are provided. Economical feasibility for the different combinations of CHP technologies, biofuels and selected CHP electrical capacities is compared.

The results of the calculations describe the general guidelines for the CHP expansion in basic small scale district heating areas in Estonia, whereas every single case should be calculated separately.

CHP expansion could be economically feasible in a small, about 30 000 MWh district heating areas in Estonian conditions.

The preferable is a classical steam turbine/engine technology, which is only feasible solution in a current market situation. ORC and biogas engine technologies are quite expensive. Without grants they are not feasible yet (IRR<0).

Enactment of the regulation draft, which regulates grant payments for the renewable energy production and construction of CHP plants in Estonia will increase the attractiveness of CHP production and will have a positive effect on CHP expansion in Estonia. The expected IRR from the steam turbine/engine CHP plant is <11% and NPV <8.4M€ depending on selected fuel and CHP plant nominal electrical capacity. Without grant payment IRR and NPV are <7% and <4..9M€, respectively.

It is preferable to use renewable fuels (wood fuels) to get higher income from the fixed supply price and support for electricity from a renewable energy source and reduce CO2 emissions. As an example CHP expansion project based on gas engine technology is feasible when in addition to grant payments the renewable biofuels are used (IRR<4 and NPV<3.5M€ depending on nominal electrical capacity).

9. REFERENCES

1. Directive 2003/30/EC. [WWW] http://ec.europa.eu/energy/res/legislation/doc/biofuels/en_final.pdf (09.03.2009)
2. Long-term Public Fuel and Energy Sector Development Plan until 2015. [WWW] http://www.legaltext.ee/et/andmebaas/paraframe.asp?loc=text&lk=et&sk=en&dok=X90006.htm&query=Estonian%20fuel%20&tyyp=X&ptyyp=I&pg=1 (09.03.2009)
3. District heating act. [WWW] http://www.legaltext.ee/text/en/X70045K2.htm (09.03.2009)

4. Meetme “Taastuvenergiaallikate laialdasem kasutamine energia tootmiseks” tingimused eelnõu seletuskiri [WWW] http://eoigus.just.ee/?act=dok&subact=1&DOK_W=229998 (09.03.2009)
5. Electricity Market Act. [WWW] https://www.riigiteataja.ee/ert/act.jsp?id=13123108 (09.03.2009)
6. Procedure and Methods for Determining Emissions of Pollutants from Combustion Plants into Ambient Air. [WWW] http://www.legaltext.ee/et/andmebaas/tekst.asp?loc=text&dok=V00076&keel=en&pg=1&ptyyp=RT&tyyp=X&query=Procedure+and+Methods+for+Determining+ (09.03.2009)
7. Environmental Charges Act. [WWW] http://www.legaltext.ee/et/andmebaas/tekst.asp?loc=text&dok=XX10001&keel=en&pg=1&ptyyp=RT&tyyp=X&query=Environmental+Charges+Act (09.03.2009)

Appendix 1. Conceptual structure of a planed computer program.

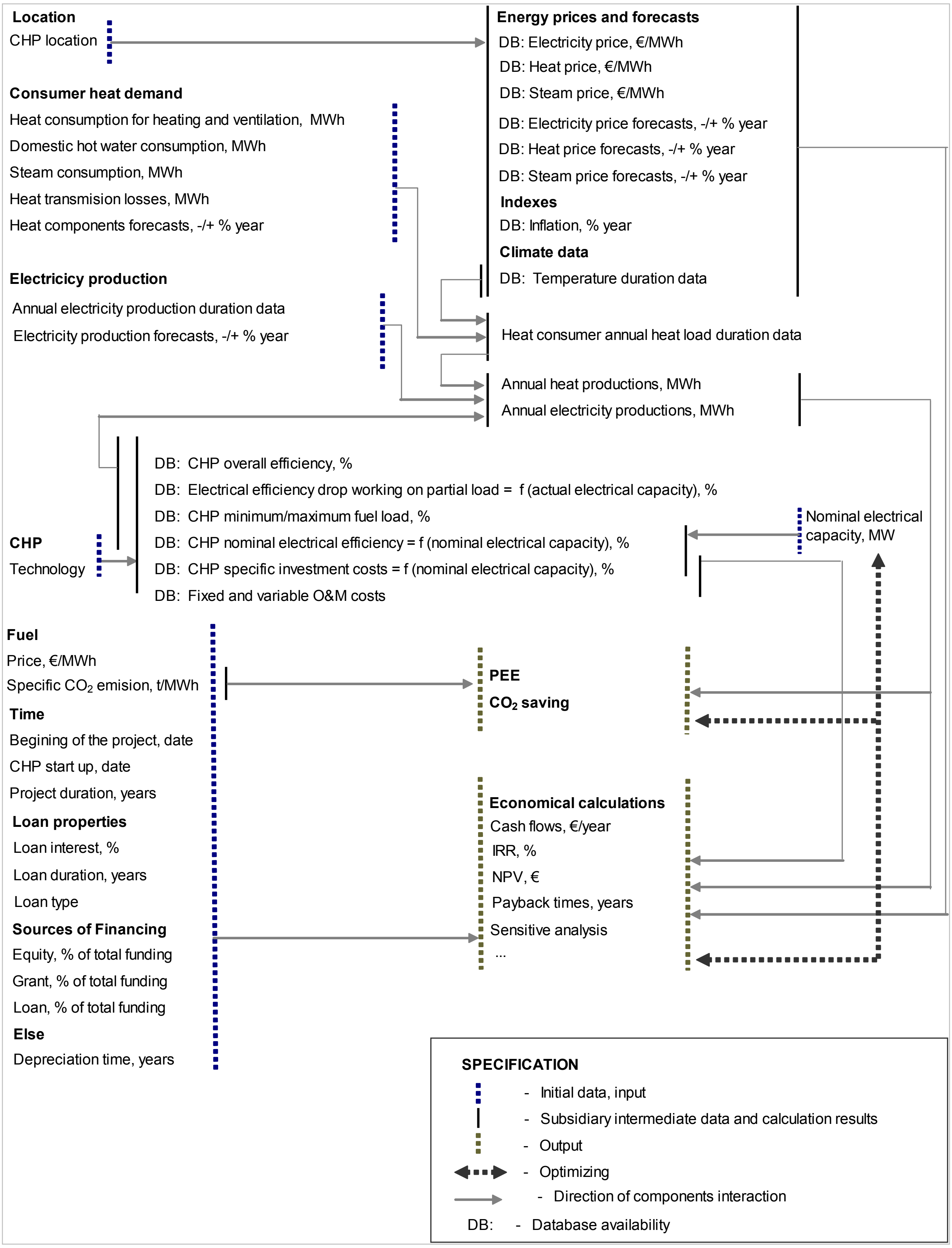

Appendix 2. Summarised results of the calculations for different CHP expansion scenarios in 30 000 MWh district heating area

El. capacity	Fuel	Technology														
		ORC					Gas engine					Steam turbine				
		With grant		Without grant		CO_2	With grant		Without grant		CO_2	With grant		Without grant		CO_2
		NPV	IRR	NPV	IRR		NPV	IRR	NPV	IRR		NPV	IRR	NPV	IRR	
MW		M€		M€		Mt	M€		M€		Mt	M€		M€		Mt
0,25	Sawdust	0,48	1,1%	x	x	13,5	x	x	x	x		4,4	11,4%	2,8	7,4%	
	Wood chips	x	x	x	x		x	x	x	x		2,5	7,3%	0,89	2,8%	
	Milled peat	x	x	x	x		x	x	x	x		3,2	8,8%	1,6	4,6%	
	Sod peat	x	x	x	x		x	x	x	x		2,3	6,7%	0,66	2,1%	17,3
0,5	Sawdust	2,4	3,1%	x	x	24,2	0,27	0,5%	x	x		7,1	11,2%	4,4	7,2%	
	Wood chips	x	x	x	x		x	x	x	x		4,1	7,3%	1,4	2,7%	
	Milled peat	0,34	0,5%	x	x		x	x	x	x		5,1	8,5%	2,4	4,3%	
	Sod peat	x	x	x	x		x	x	x	x	14,0	3,7	6,5%	0,94	1,8%	27,6
0,75	Sawdust	3,8	3,7%	x	x	31,8	1,9	2,8%	x	x		8,4	10,5%	4,9	6,4%	
	Wood chips	0,5	0,6%	x	x		0,28	0,4%	x	x		4,8	6,7%	1,3	1,9%	
	Milled peat	15,6	1,1%	x	x		x	x	x	x		6,0	7,8%	2,5	3,5%	
	Sod peat	x	x	x	x		x	x	x	x	19,9	4,2	5,8%	0,66	1,0%	34,0
1	Sawdust	4,0	3,3%	x	x	37,8	3,5	4,0%	x	x		8,2	8,7%	3,9	4,4%	
	Wood chips	0,11	0,1%	x	x		1,4	1,7%	x	x		4,1	4,9%	x	x	
	Milled peat	0,78	0,7%	x	x		x	x	x	x		5,6	6,3%	1,3	1,6%	
	Sod peat	x	x	x	x		x	x	x	x	24,9	3,6	4,3%	x	x	37,5
1,25	Sawdust	1,5	1,1%	x	x	41,4	3,2	3,1%	x	x		5,9	5,6%	0,65	0,7%	
	Wood chips	x	x	x	x		12,1	0,8%	x	x		1,7	1,8%	x	x	
	Milled peat	x	x	x	x		x	x	x	x		3,4	3,4%	x	x	
	Sod peat	x	x	x	x		x	x	x	x	29,2	1,3	1,4%	x	x	38,7
1,5	Sawdust	x	x	x	x		2,5	2,1%	x	x		2,9	2,6%	x	x	
	Wood chips	x	x	x	x		x	x	x	x		x	x	x	x	
	Milled peat	x	x	x	x		x	x	x	x		0,67	0,6%	x	x	
	Sod peat	x	x	x	x		x	x	x	x	32,7	x	x	x	x	38,3
1,75	Sawdust	x	x	x	x		1,4	1,1%	x	x		x	x	x	x	
	Wood chips	x	x	x	x		x	x	x	x		x	x	x	x	
	Milled peat	x	x	x	x		x	x	x	x		x	x	x	x	
	Sod peat	x	x	x	x		x	x	x	x	35,7	x	x	x	x	
2	Sawdust	x	x	x	x		0,03	0,02%	x	x	38,0	x	x	x	x	
	Wood chips	x	x	x	x		x	x	x	x		x	x	x	x	
	Milled peat	x	x	x	x		x	x	x	x		x	x	x	x	
	Sod peat	x	x	x	x		x	x	x	x		x	x	x	x	

CYSENI 2009, May 28-29, Kaunas, Lithuania
ISSN 1822-7554, www.cyseni.com

UTILIZATION OF SOLID BIOMASS FOR ENERGY GENERATION IN LITHUANIA

L. Zidonis, S. Sinkunas, E. Puida
Kaunas University of Technology
Department of Thermal and Nuclear Energy
K. Donelaicio 20, LT-44293 Kaunas – Lithuania
Phone: +370 687 27658
E-mail: Lukas.Zidonis@gmail.com

ABSTRACT

National Energy Efficiency Programme for 2006-2010 says that renewable energy resources would account for up to 12% in the total primary energy balance in 2010 in Lithuania. The European Union and Lithuania herewith strives to develop renewable energy systems capacity even more because of negative global economical - the big fluctuation of gas and oil prices, political - the dependence on Russian gas and oil, and environmental – unsatisfactory scales of carbon dioxide emission tendencies. These types of solid biomass were observed in the paper: a) wood and its waste; b) straw c) energy crops. The usage of the solid biomass today and in the past, the energetic characteristics, the energetical potential in Lithuania were discovered. The papers revealed that the utilization of solid biomass potential provides about 14 150 GWh per year and if utilized, this amount of energy would cover about 54% of total electrical and heat energy demand in Lithuania.

Keywords: renewable energy sources (RES), biomass and energy generation

1. INTRODUCTION

Lithuania imports all mineral primary energy sources that are used for energy generation – crude oil, natural gas and coal. Using renewable energy sources (RES) for energy generation would allow leaving exported money inside the country, create new work places, improve environment protection and increase political independence from energy resources exporters.

There are many renewable energy sources – solar, wind, geothermal hydro, biomass, etc. Since vegetables are the source of biomass that can be used for energy generation, this type of RES is one of the most viable in Lithuania because of these reasons:

- Lithuanian climate conditions are hospitable for plants to grow;
- Lithuanian territory is rich of green areas – forests, grasslands, etc;
- The agriculture is one of the main industry sectors in Lithuania and it produces big quantities of biomass waste.

This paper observes biomass types, the present situation and perspectives of solid biomass utilization for energy generation in Lithuania. Paper concentrates on solid biomass that does not require special and conditionally expensive technological processing before using it as fuel.

2. THE BIOMASS AS PRIMARY ENERGY SOURCE

Biomass as a renewable energy source refers to living and recently dead biological material that can be used as fuel. In this context, biomass refers to plant matter grown to generate energy. Biomass may also include biodegradable wastes that can be burnt as fuel. It excludes organic material which has been transformed by geological processes into substances such as coal or petroleum [1].

There are two distinctive types of biomass: a) primary – vegetative material directly used for energy generation; b) secondary – vegetative material waste from biomass that was used in other technological processes (stockbreeding, etc.).

The chemical elements constituting the biomass are presented in table 1 [2]:

Table 1. Biomass chemical elements.

No.	**Constituent**	**Quantity, %**
1	Carbon	50
2	Oxygen	43
3	Hydrogen	6
4	Nitrogen, Phosphorus, Sulphur, other	1

The main element that allows the biomass to transform to energy is carbon. This transformation is cyclic: a) carbon is rendered by combustion to carbon dioxide and vegetables – this can be organized process like burning biomass in boiler or natural and b) carbon dioxide is synthesized back to solid carbon by photosynthesis (Fig. 1).

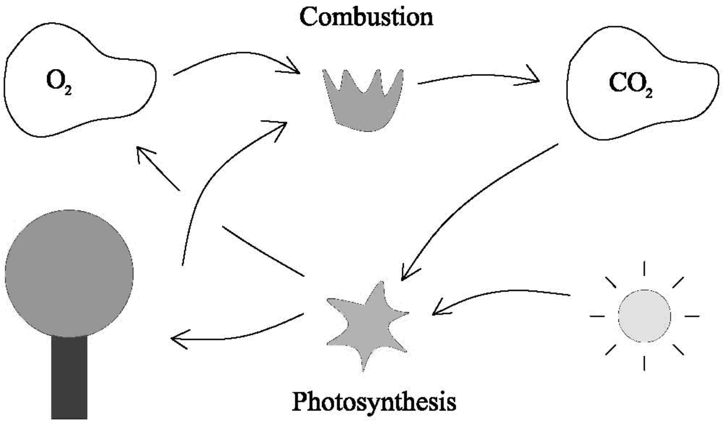

Fig. 1. The combustion – photosynthesis cycle

Biomass can be solid, liquid and gaseous consistence. The biomass fuel types by its consistence can be divided to three groups (Table 2).

Table 2. Biomass fuel types by its consistence

No.	**Biomass consistence**	**Biomass fuel types**
1	Solid	Wood: firewood, wood chips, sawdust, briquettes, pellets etc.
2		Agriculture secondary biomass: straw, shrubbery, old leafs etc.
3		Energy crops: willows, Jerusalem artichoke, etc.
4		Peat
5		Dehydrated sewage sediments
6		Waste materials (waste paper, etc.)
7	Liquid	Rape methyl ester (RME)
8		Ethanol
9		Methanol
11		Liquid fuels from wood
12	Gaseous	Biogas from slurry or manure

13		Biogas from food industry wastes
14		Biogas from fermentation of sewage sediments
15		Biogas from refuse dump
16		Biogas from wood

The solid consistence biomass main advantage if compared with other biomass types is that it can be prepared as fuel more simply, the main deficiency – the burning process automation is difficult. These peculiarities of solid biomass fuel determine that it is widely used in household energetics and if processed to small particles – even in big capacity boiler plants to produce energy for district heating or industry. The liquid consistence biomass fuel can be more suitably used in transportation sector to replace the mineral fuel; the gaseous consistence fuel commonly is made from all kinds of putrefactive waste - these types of fuels are not in the scope of this paper.

3. THE SOLID BIOMASS UTILIZATION FOR ENERGY IN LITHUANIA: SITUATION TODAY AND PERSPECTIVE FOR THE FUTURE

National Energy Efficiency Programme for 2006–2010 [3] plans that renewable energy resources would account for up to 12% in the total primary energy balance in 2010 in Lithuania. The possibilities to transform this objective into reality are discussed further.

The energy is consumed by electrical equipments and facilities (1) and for heat generation for favorable temperature to achieve in cold season (2) – this creates demand for electrical and heat types of energy. The consumed energy quantities of these types in 2007 in Lithuania are presented (Table 3) [4].

Table 3. Energy consumption in 2007 in Lithuania.

No.	Energy type	Gross energy consumption, GWh	Net energy consumption, GWh
1	Electricity	12 635.6	8 858.7
2	Heat	13 655.1	10 700.3
	TOTAL	**26 290.7**	**19 559.0**

There is no statistics for 2008 energy consumption in Lithuania, thus the following considerations and calculations in this paper were made on the presumption that the gross energy consumption in 2008 was similar to energy consumption in 2007.

3.1. Electrical energy generation

The major electrical energy producers today are nuclear plant “Ignalina”, power plant “Lietuvos elektrine“ and thermal power plants of the biggest cities (Table 4).

After shut down Ignalina nuclear power plant in 2009 12 31, the deficient energy will be imported or produced locally mainly using natural gas as primary energy source. The extra power capacity will generate power plant upgrades in Elektrenai, Kaunas and other new power plants.

The RES power plants operating at maximum capacity can generate 198 MW of electrical power. Estimating that the wind and hydro plants do not operate at full capacity constantly, the RES share in energy balance decreases - it produced about 4% of electrical energy [6] in 2008 what constituted about 505.4 GWh per year.

Table 4. The installed power capacity of Lithuanian power plants, (Source: [5], 2008).

No	Power plants	Installed power capacity, MW
1	Nuclear power plant “Ignalina”	1 300
2	“Lietuvos elektrine“ power plant	1 800
3	Thermal power plant in Vilnius	384
4	Thermal power plant in Kaunas	178
5	Thermal power plant in Mazeikiai	194
6	Thermal power plant in Klaipeda	11
7	Thermal power plant in Panevezys	35
8	Industrial power plants	75
9	Kruonio hydro accumulative plant	800
10	Biomass power plants	19
11	Hydro power plants in Kaunas	101
12	Small hydro power plants	26
13	Wind power plants	52
	Total	4 975

3.2. Heat energy generation

The key fuel used for heat energy generation is gas (Fig. 2) [7].

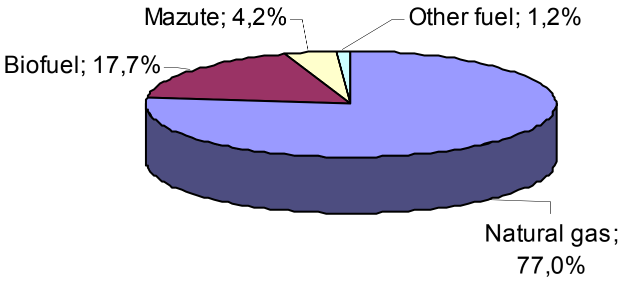

Fig. 2. Fuel input for DH production in 2008 in Lithuania

The Fig. 2 shows that biofuel used for district heat generation in 2008 was 17.7%, what constituted about 2 417.0 GWh per year.

To sum up the above data and considerations, RES used for electricity and heat energy generation constituted about 2 922,4 GWh (11.1%) in 2008 in Lithuania. To reach the strategic objective of national efficiency programme (12%), it must be produced extra 232.5 GWh (0.9%) per year of RES energy. The strategic objective of 12% needs to be reached until 2010, but the biomass share in energy balance have to increase beyond this point to catch up advanced European Union members (Fig. 3) [2]. The last EU column indicates the average renewable energy share in EU territory.

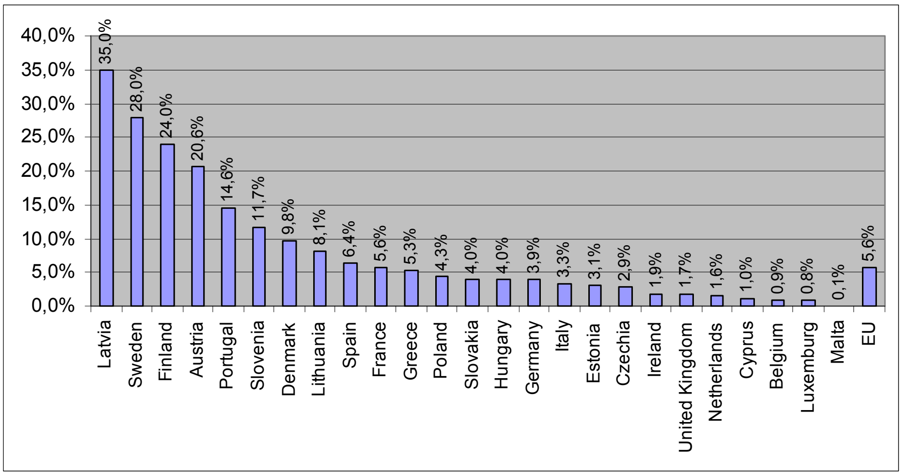

Fig. 3. Renewable energy share in EU countries in 2004

The Fig. 4 presents the biomass and wastes energy share in total RES energy balance in European Union [2].

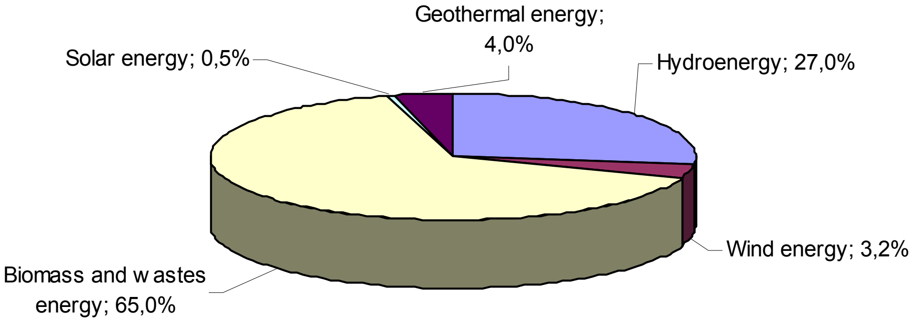

Fig. 4. The biomass energy share in RES balance in EU countries in 2003

The assumptions and calculations were made further to evaluate wood and its waste, straw and energy crops energetical potential to achieve higher RES energy share in primary energy balance.

3.3. Wood and its waste potential

The wood and its waste are used for energy generation in district heating boilers and for domestic energy demand especially in rural regions. It includes the billets prepared for burning, wood processing waste in industrial wood plants and in forests. Energetical potential of wood and its waste in 2010 in Lithuania is presented in Table 5 [8].

Table 5. Wood and its waste energetical potential in 2010 in Lithuania

No	**Wood type**	**Energetical potential in solid thous. m^3**
1	Wood billets	2 664
2	Wood processing waste in industrial wood plants	1 578
3	Wood processing waste in forests	882
	Total wood and its waste energetical potential	5124

The exploitation of this RES reached 3 602 of solid thousand m^3 in 2007 in Lithuania [4]. That means there is still energetical potential of about 1522 thousand m^3 of wood and its waste per year. This quantity could provide approximately 2 200 GWh of energy per year.

3.4. Straw potential

The straw is the waste of grain breeding process. There is no statistical information about how mach straw is reaped every year in Lithuania, but these values can be derived from information about grain yield. There were 3.9 Mton of straw grown in 2004 in Lithuania. The usage repartition of the straw is presented (Fig. 5) [9].

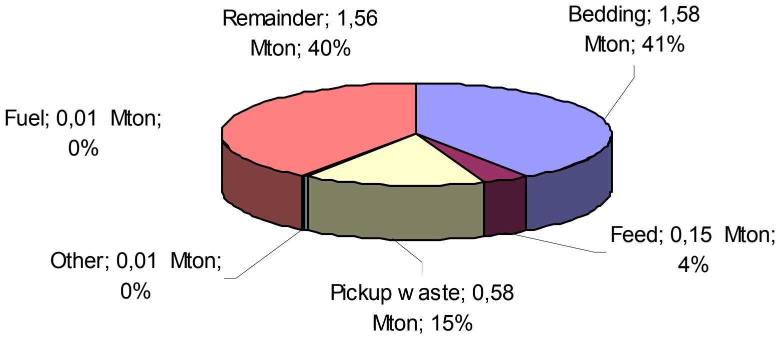

Fig. 5. The utilization of straw in Lithuania

If the assumption is made that half of all straw remainder (20% of all straw yield) could be collected and utilized for energy generation that would provide about 3 200 GWh of energy per year. To make a comparison, in Denmark, there were 2.6 megatons of total 6.5 megatons straw yield utilized for energy generation, what constituted about 40% [8].

3.5. Energy crops potential

An energy crop is a plant grown as a low cost and low maintenance harvest used to make bio fuels, or directly exploited for its energy content. Commercial energy crops are typically densely planted, high yielding crop species where the energy crops will be burnt to generate power [10].

The information sources about the unused for any purpose Lithuanian territory provide values that range from 6 000 to 8 000 kha. The information sources about energy crops fertility provide values that range from 7–15 t/ha per year of wet biomass [11]. The calorific capacity of such biomass is about 9 MJ/kg. If the assumption is made that half of unused Lithuanian territory (about 3 500 kha) could be planted with energy crops with fertility of 10 t/ha that would provide about 8 750 GWh per year. These numbers are sketchy, since where is no researches conducted to confirm that namely 3 500 kha could be planted by energy crops. On the other hand some of the land now utilized for other purposes could be used for growing energy crops.

3.5 Solid biomass energetical potential in Lithuania (summary)

Above made assumptions and calculations are summarized in Table 6.

Table 6. Energy consumption and solid biomass energetical potential in Lithuania

No	Power plants	Energy, GWh per year
	Energy consumption:	
1	Gross energy consumption in 2007 in Lithuania	26 290.7
2	Programmed RES share in 2010	3 154.9
3	Energy generated using RES in 2008 in Lithuania	2 922.4
4	The remainder of RES generated energy per year needed to achieve 12%.	232.5
	Energetical potential:	
5	Wood and its waste unutilized energetical potential	2 200
6	Straw unutilized energetical potential	3 200
7	Energetical crops unutilized energetical potential	8 750
8	Total solid biomass energetical potential	14 150

If utilized for energy generation solid biomass energetical potential is about 14 150 GWh per year. This amount of energy would cover about 54% of total electrical and heat energy demand in Lithuania.

4. CONCLUSIONS

1. Lithuania needs to generate extra 232.5 GWh per year of energy from RES to achieve strategic objective of 12% in the total primary energy balance in 2010.
2. The unused energetical potential of wood and its waste in Lithuania is about 2200 GWh per year.
3. The energetical potential of straw in Lithuania was observed – it is about 3200 GWh per year. The assumption that half of retained straw could be used for energy generation was made.
4. The potential of energetical crops in Lithuania was observed – it is about 8750 GWh per year. The assumption that half of unused territory could be used for planting energy crops was made.
5. The utilization of solid biomass potential would provide 14 150 GWh per year and this amount of energy would cover about 54% of total electrical and heat energy demand in Lithuania.

5. REFERENCES

1. http://en.wikipedia.org/wiki/Biomass
2. Stasys Kytra. Atsinaujinantys energijos šaltiniai, Technologija, Kaunas, 2006, p. 25, 222–262.
3. National Energy Strategy for 2006–2010.

4. Energy balance 2007. Lithuanian statistic department, p. 25.
5. Jeronimas Laucius. Belaukiant Visagino AE. Mintys apie Lietuvos energetiką, „Trys žvaigždutės“, Vilnius, 2008, p. 8.
6. Lietuvos energetika po 2009 metų. Valstybė. The 16th of November, 2008.
7. Lietuvos šilumos tiekėjų asociacija. Šilumos tiekimo bendrovių 2008 metų ūkinės veiklos apžvalga, Vilnius, 2008, p. 15.
8. Lietuvos atsinaujinančių energijos išteklių naudojimo skatinimo veiksmų planas 2010 – 2020 m. LITBIOMA, Vilnius, 2008, p. 57–62.
9. Genutis A. Šiaudų kuro vartojimas Lietuvoje. Institute of Agriculture Engineering of Lithuanian University of Agriculture, 2006 10 06, p. 3.
10. http://en.wikipedia.org/wiki/Energy_crop
11. Algirdas Jasinskas, Vladimiras Liubarskas. Energetiniai augalai ir jų naudojimo technologijos, Technologija, Kaunas, 2003, p. 21.

CYSENI 2009, May 28-29, Kaunas, Lithuania
ISSN 1822-7554, www.cyseni.com

FORECASTING OF ELECTRICITY DEMAND IN HOUSEHOLD SECTOR USING THE ECONOMETRIC MODEL

N. Rutkauskaitė, I. Konstantinavičiūtė, V. Radziukynas
Lithuanian Energy Institute
Breslaujos str. 3, LT-44403 Kaunas – Lithuania
Phone: +370 (37) 401939
E-mail: rutkauskaite@mail.lei.lt

ABSTRACT

Household takes a significant share in total electricity consumption. It's forecast becomes especially important.

In this paper the application of econometric forecasting methodology for electricity consumption is reviewed. Also both advantages and disadvantages of the methodology are discussed which are based on the main assumptions important for variation of electricity demand in future. This econometric model was applied to forecast the future electricity demand in Lithuanian household sector in the 15 – 25 years time horizon.

Key words: household, electricity, forecast, econometric model.

1. INTRODUCTION

Due to restructurization and liberalization process in electricity sector, forecasts become very important. While regulation of electricity sector was based on long- term experience, when planning investments, it was enough to formulate forecasts for five years or even shorter period. In case of free competition, in many countries long-term (15–25 year period) forecasts become the basis for perspective planning. Meanwhile short-term forecasts become the field of activity of companies and associations competing on the electricity market.

To prepare reliable forecasts it is necessary to have very detailed information, no matter what kind of model would be used. Forecast accuracy also depends on the structure of consumers. For example, to forecast the schedule of load, when household consumers are dominating in the structure of electricity demand, it is easier due to a big number of consumers. Unusual behaviour of one or several small consumers almost doesn't influence their general demand.

Household has a significant role in the balance of general electric energy. Its forecast of demand becomes especially important and we hope that this value will be increasing in the nearest future.

Econometric forecasting methodology of electricity demand is overviewed in the article taking into account relevant assumptions on the main factors, conditioning electricity demand, variation in the future, forecasting of household electricity demand has been carried out by applying econometric model. The econometric model has been chosen since while applying it there is no need for a big number of statistical data to forecast energy demand. Available data, which defines in detail energy expenditure and factors conditioning it in the beginning of forecasting period, is enough in order to perform further mathematical calculations.

2. THE METHODOLOGY OF ELECTRICITY DEMAND FORECASTING

At the moment, there are several different methods, which are used for forecasting. Considering stable economy growth, we can use energy demand forecasting for [1]: 1) simple extrapolation, which makes reference to the increasing of energy consumption and shows previous curve of growth, 2) various mathematical statistical methods, which enable the researcher to determine empirical data variation and to choose mathematical function, which most accurately define variation trends of empirical data. There are no doubts that until factors, influencing long-term variation tendencies of energy consumption, remain unchanged, these methods are very relevant for analysis and enable to determine perspective energy demand. However, no sudden energy consumption increase or reduction changes can be estimated by these methods. In present global economic crisis case it is very important to thoroughly investigate the fields of activity where most of energy is consumed, and those factors which condition variation of energy expenditure.

For such analysis the following may be applied: 1) comparative analysis methods, 2) imitational methods, and 3) econometrical models.

3. ECONOMETRICAL MODELS

Econometric models *are statistical models, used in econometrics, which enable to simulate, repeat, model or forecast indicators important for future economy development, which cover both national and international economic system.*

Quite often the priority is given to simple models, which are limited to the establishment of relationship between energy consumption and of state's gross domestic product (GDP).

In general case it should be analysed what factors could have more or less influence on variation of energy demand applying for this purpose more complicated models.

Important factors should be considered indicators of production scopes (in most common case, state's GDP), scopes of services provided to habitants, number of habitants, energy intensity change and income and prices elasticity.

In most common case, energy demand at any time moment may be defined as its previous value, relative variation of the activity (which may be defined as GDP of analysed economy branch or income indicator) and energy prices, consumer reaction to variation of income and prices, as well as opportunities to increase energy consumption function:

$$E_{ij}(t) = E_{ij}(t-1)[A_i(t)/A_i(t-1)]^{\alpha(ijl)};(1)$$

$$E_{ij}(t) = E_{ij}(t-1)[A_i(t)/A_i(t-1)]^{\alpha(ijl)} \times [P_{ij}(t)/P_{ij}(t-1)]^{\beta(ijl)}; \quad (2)$$

$$E_{ij}(t) = E_{ij}(t-1)[A_i(t)/A_i(t-1)]^{\alpha(ijl)} \times [P_{ij}(t)/P_{ij}(t-1)]^{\beta(ijl)} \times C_{ijl}; \quad (3)$$

there E_{ij} – index *j* – kind of fuel or energy demand in *i* branch of household; *i* – branch of household index, *i* = 1,…,m; *j* – kind of fuel (energy) index, *j* = 1,…,n); *l* – final energy consumption of equipment (processes) index, *l* = 1,…,L; *t* – time interval, *t* = 2000, 2005, 2010, 2015, …; A_i – *i*- branch of household economic activity; P_{ij} – *j*-kind of fuel (energy) price in *i* branch of household; $\alpha(ijl)$ – *j*-kind of fuel (energy),using in *i* branch of household of *l* process, elasticity of profit; $\beta(ijl)$ – *j*-kind of fuel (energy), which is used in *i* household branch of l process, elasticity of prices; C_{ijl} – energy - saving potential in *i* household branch of l process, using *j* kind of fuel (energy).

Using econometrical models it is very important to rather thoroughly and accurately define the activity trends, where energy is consumed finally, and those activity indicators, which enable to quantitatively estimate energy consumption. Depending on the fact how energy demand are forecasted, such activity indicators are used which best define factors conditioning those demand. Forecasting energy demand by applying econometric models income and prices elasticity indicators, defining consumer reaction, are very significant.

Merit of econometric models – while applying them to forecast energy demand there is no need of a number of statistical data, defining long-term dynamics of energy resources consumption. It is important to have enough data, which explicitly define energy expenditure and factors conditioning them in the beginning of the forecasted period. However, additional data is needed to define the relationship between energy expenditure and factors conditioning it, which is hard to estimate under transitional period conditions due to lack of statistical data.

Drawback of econometric models – a necessity to estimate elasticity of income and prices. Extra investigations should be carried out. For example, it is almost impossible under Lithuanian conditions to determine real elasticity values of income and prices, defining consumer reaction. Thus while preparing energy demand forecasts one has to rely on research results of other countries and only partially on the assessment of changes taking place in Lithuania.

4. MAIN ASSUMPTIONS OF ELECTRICITY FORECASTING

Main indexes, describing energy input in household sector, are given in Table 1.

Table1. General household characteristics in the period of 2000 – 2007

Index	2000	2001	2002	2003	2004	2005	2006	2007
Population, thousand	3512.1	3487	3475.6	3462.5	3445.9	3425.3	3403.3	3384.9
Number of flats, thousand	1356.2	1291.7	1295	1292	1300	1299	1299	1305
Population in dwelling	2.59	2.69	2.68	2.68	2.65	2.64	2.62	2.59
Final consumption of electricity in household, GWh	1767	1818	1812	1895	2066	2141	2350	2464.4
Input of electricity for one household inhabitant, kWh	504.93	522.22	522.33	547.29	599.55	625.05	690.51	728.1
Real disposable income (for one member Lt/month)	415	410	422	458	496	580	681	859.3

As can be seen in Fig. 1, with growth of economy and improvement of life living level, real income of inhabitants increased as well. From 2000 to 2007 real income per one economy member changed by 444.3 Lt. (107.01%). With increase of income increases number of electronic devices and their intensity, due to this additional electricity expenditure occurs in household sectors. From Fig. 1 we can see that input of electricity for one inhabitant increased by 223.17 kWh (44.2%) from 2000 till 2007.

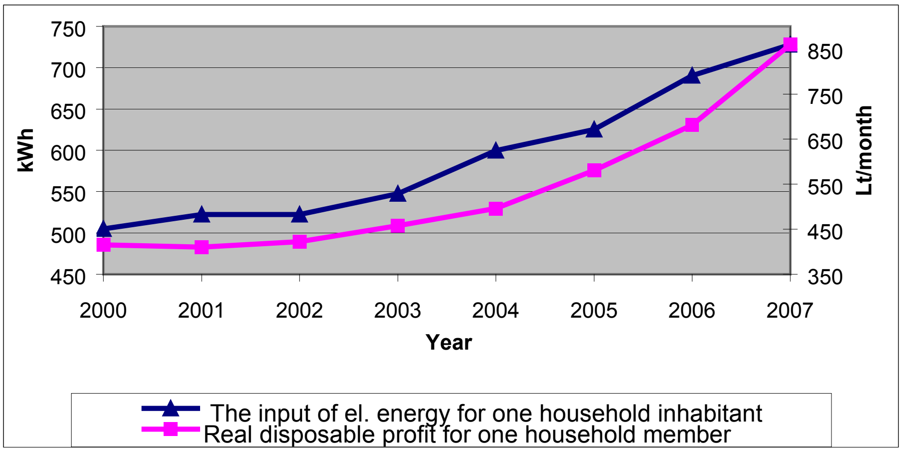

Fig. 1. The input of electricity for one household inhabitant and his disposable income

Aiming at performing forecast of electricity prices of household sector it is expedient to estimate probable variation of inhabitants'' number and GDP for the forecasted period (Fig. 2–3).

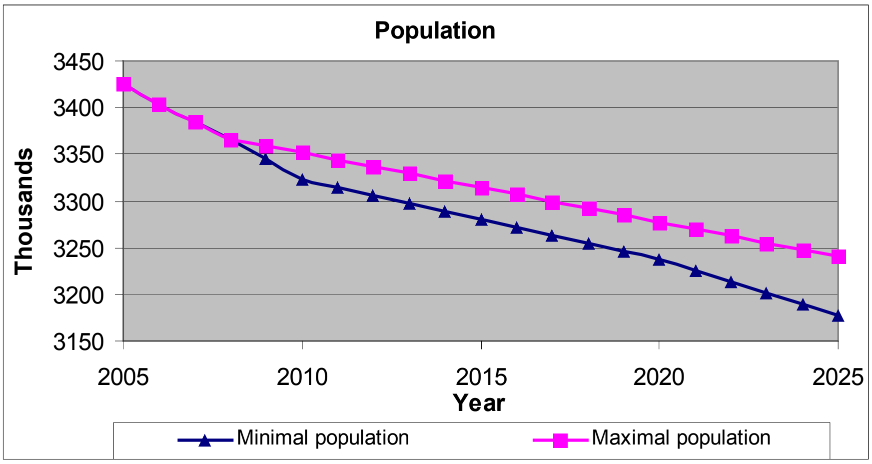

Fig. 2. Variation of population for the period of 2005–2025

Due to conditioning uncertainties two scenarios were chosen for the analysis: minimal and maximum. Factual values of inhabitants' reduction for the period 2005–2008 and variation scenarios of inhabitants' number till 2025, created by the Lithuanian Statistics Department, are given in Fig. 2 [2].

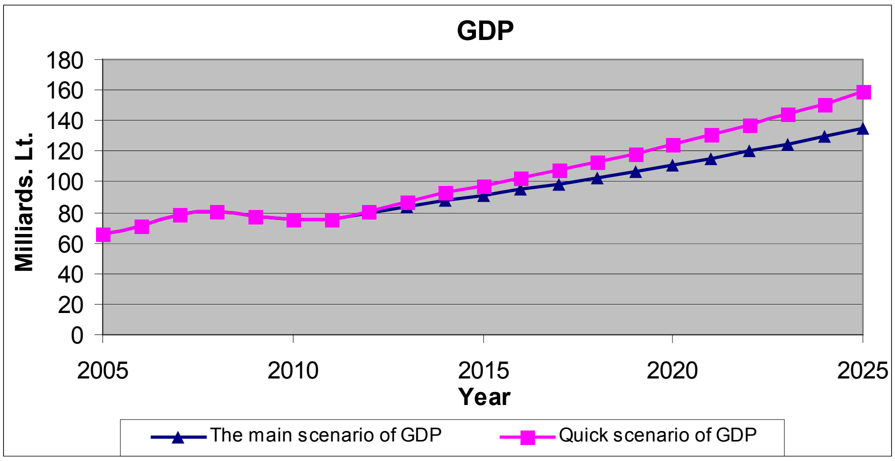

Fig. 3. Variation of gross domestic product for the period of 2005–2025

Two GDP variation scenarios are given in Fig. 3: basic GDP growth and rapid GDP growth. GDP factual values from 2005 to 2008 are also given in this figure.

GDP variation trends of 2009-2001 were estimated according EC forecasts, which confirm that in 2009 GDP will drop by 4%, whereas in 2010 – by 2.6%. These last forecasts are less optimistic than forecasts of last November, as presented by European Commission, according which it was forecasted that Lithuanian GDP in 2009 will not change, whereas in 2010 will diminish only by 1.1%.

In accordance with National Energy Strategy, in the period by 2020 rather rapid speeds of Lithuanian economy growth are foreseen – on average by 5% per year expecting that: 1) Lithuanian industry will be expanded rather quickly; 2) common economy development policy will be favourable to huge investments, devoted for economy modernization and purchasing of new technologies; 3) technical and economical assistance from EU will be significant and efficiently applied. Main scenario is based on these directions of economy development, which are foreseen in the forecasts of macroeconomic indicators of the Ministry of Finances – after 2010 – 3% (on average 3.85% during the period from 2000 to 2020). Variation forecasts of both scenarios GDP till 2025 are given in Fig. 3.

Aiming at forecasting household electricity demand it is necessary to estimate how the relationship between GDP and inhabitant number differs:

$$A(t) = GDP/\text{number of inhabitants}$$

Share of GDP per one inhabitant for the period 2005-2025 is given in Fig. 4.

From Fig. 4 it can be seen that in minimal variation scenario GDP share per one inhabitant will vary from 19360.35 Lt in 2005 to 42500.51 Lt. In 2025 variation would comprise approximately 219.5%. In maximum variation scenario GDP share per one inhabitant will vary from 19360.35 Lt. 2005 m. to 48988.29 Lt. In 2025 variation would comprise approximately 153 %.

Household electricity demand are influenced by electricity prices (2, 3). In 2005–2006 average electricity tariff for domestic consumers was equal 31 ct/kWh, whereas in 2007–2008 – 33 ct/kWh, and in 2009– 37ct/kWh. However, Ignalina NPP shutdown at the end of 2009 will greatly influence the electricity price in Lithuania. Considering the results of latest studies and expert assessments [3] forecasted increase of price may reach 60–70 ct/kWh. Thus for the forecasting of household electricity and assessment of price impact two probable price variation scenarios were created: in minimal price scenario electricity price in 2025 will account for 60 ct/kWh, whereas in maximum price scenario – 70 ct/kWh (Fig. 5).

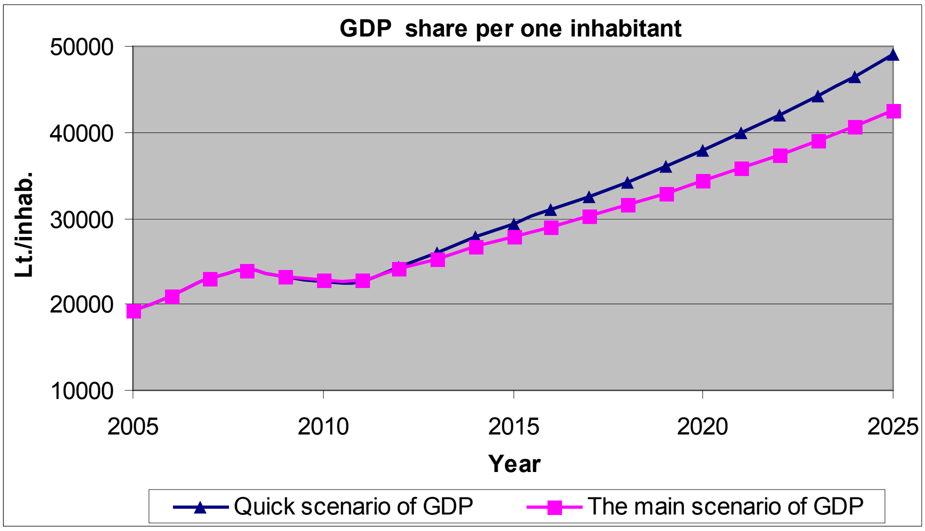

Fig . 4. GDP share per one inhabitant for the period of 2005–2025

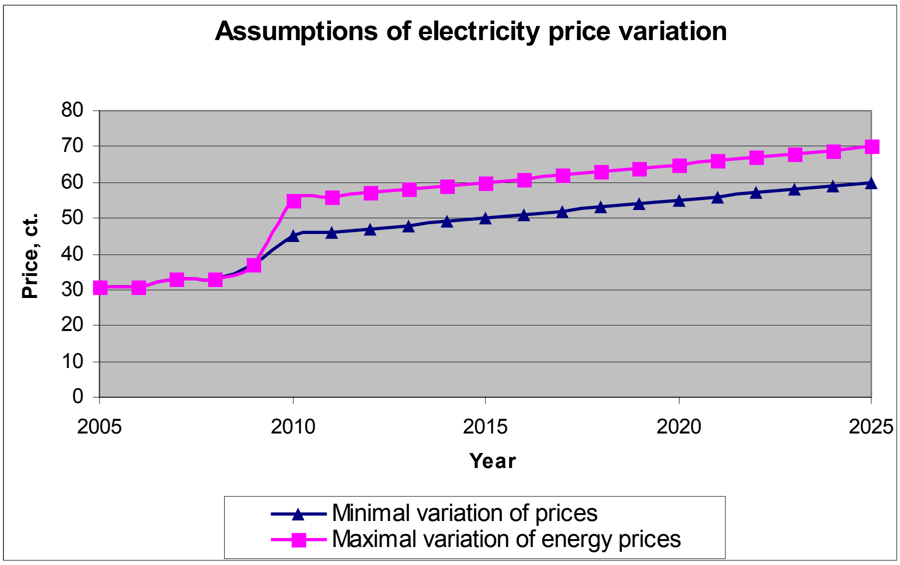

Fig.5. Assumptions of electricity price variation

Assumptions of electricity price variation are given in Fig. 5. in accordance with minimal price scenario electricity price variation would comprise approximately 93.55%, whereas in maximum price scenario – 125.8%.

5. ECONOMETRIC MODELLING

In accordance with assumptions of factors influencing household energy demand, given in section 4, and applying three variations of econometric model electricity forecast till 2025 was carried out. Applying three different models (1, 2, 3) the impact of individual factors on the value of electricity demand may be estimated.

1) Household electricity demand forecast considering only economical activity.

Forecasts of household electricity demand till 2025 taking into account only economical activity (1) results given in Fig. 6.

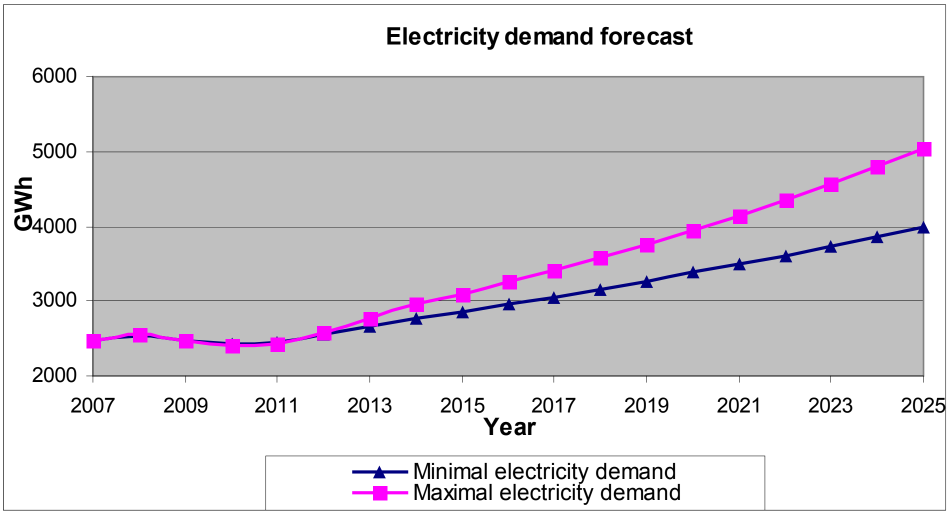

Fig.6. Electricity demand forecast for the period 2007–2025

In given Fig. 6 electricity demand in household in minimal variation scenario would vary from 2464.4 GWh in 2007 to 3996.69 GWh in 2025. According minimal forecasted increase would comprise 62.2%, whereas in maximum variation scenario electricity demand would increase from 2464.4 GWh to 5033.77 GWh. Thus increase would comprise approximately 104.3%.

2) Household electricity demand forecast considering economical activity and electricity price.

In this case forecast of household electricity demand was carried out according formula (2). Calculation results are given in Fig. 7.

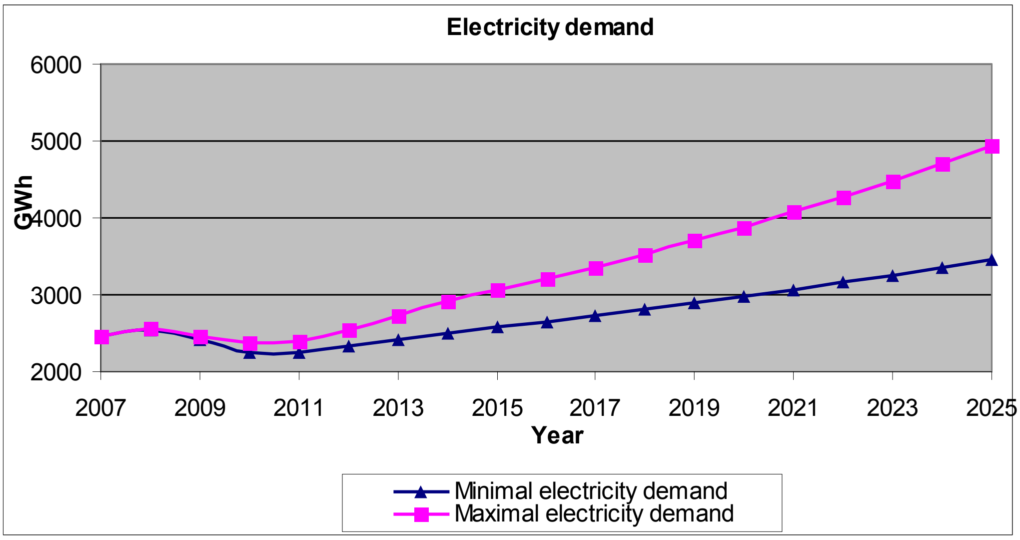

Fig.7. Electricity demand forecast for the period 2007-2025.

From Fig. 7 it can be seen that electricity demand in household in minimal variation scenario would change from 2464.4 GWh in 2007 to 3456.66 GWh. In 2025, i.e. demands would increase by 40.26%, whereas in maximum variation scenario from 2464.4 GWh to

4940.02 GWh. In this case demands would increase by 100.5%. According maximum variation scenario demands would increase almost 2 times.

3) Household electricity demands additionally considering probable saving potential.

In this case household electricity demands forecast was carried out applying formula (3). (Fig. 8).

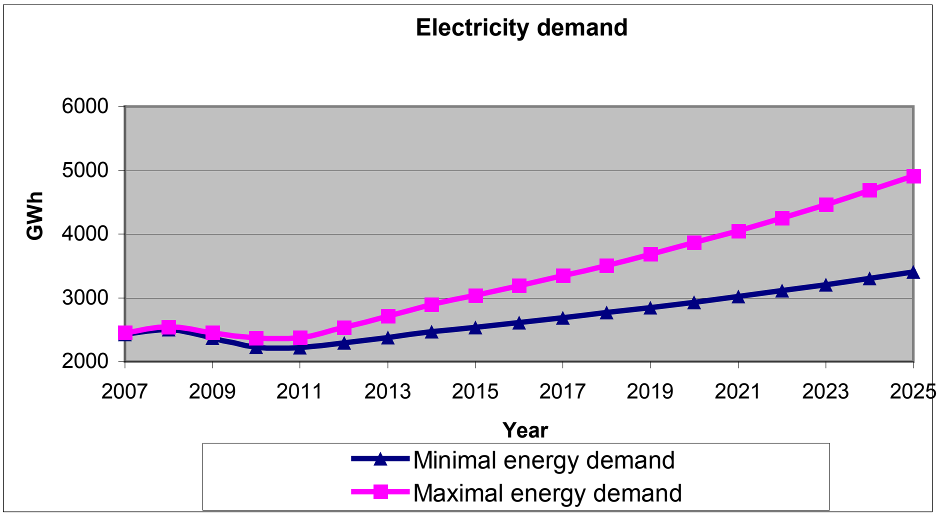

Fig.8. Forecast of electricity demand considering saving potential for the period 2007–2025

In Fig. 8 it can be seen that electricity demand in household in case of minimal variation scenario would vary from 2464.4 GWh in 2007 to 3404.81 GWh in 2025, i.e. demand would increase approximately 38.16%, whereas in maximum variation scenario from 2464.4 GWh. to 4915.32 GWh. In this case demand would increase approximately 99.45%.

Forecasted average annual electricity demand growth rates for the period 2007-2025.

Table 2. Forecasted average annual electricity demand growth rates

	(1) econometric model	(2) econometric model	(3) econometric model
MIN (%)	1.95	1.36	1.30
MAX (%)	2.89	2.82	2.80

From Table 2 it can be seen that forecasted average annual electricity demand growth rate for 2007–2025 are the biggest (2.89%) at maximum scenario when applying econometric model (1), i.e. when household electricity demand forecast has been carried out considering only economical activity, whereas the smallest (1.30%) at minimal scenario when applying econometric model (3), i.e. when household electricity demand forecast has been carried out considering economical activity, electricity price impact and saving impact.

Aiming at comparing calculation results, all analysed variants of household electricity demand forecasts are given in Fig. 9.

Applied different variations of econometric model enabled to estimate not only the impact of analysed factors, but also considering the uncertainties of influencing factors to formulate probable limits of household electricity variation forecasts. The least forecasted electricity demand in household 3404.81 GWh, at minimal scenario assumptions and estimating probable saving potential. The biggest forecasted electricity demand in household – 5033.77 GWh, at maximum scenario assumptions and connecting demand with economic activity (1). Maximum forecasted electricity value differs from the minimal one by 47.84%.

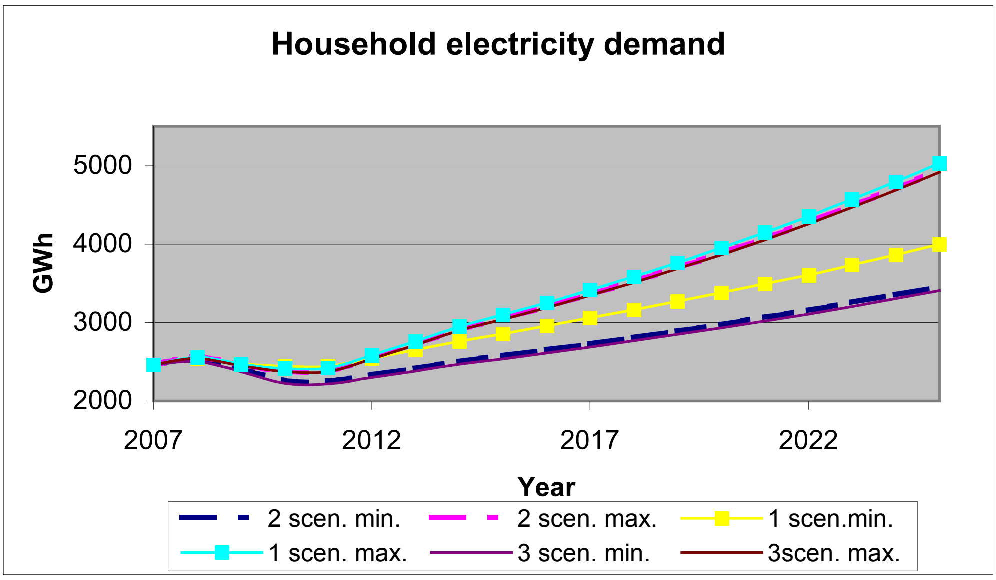

Fig. 9. Household electricity demand for the period 2007-2025.

Performed analysis reveals that most precisely electricity consumption in household is defined by econometric model, which relates electricity demand with economic activity, electricity price and considering saving potential. Applying this model it is possible in more detail to analyse the impact of various factors. However, aiming at estimating the accuracy of model it is necessary to perform model adequacy analysis by performing retrospective forecast. Adequacy of econometric forecast methods in electricity household under Lithuanian conditions will be performed in further works.

6. CONCLUSIONS

1. It is expedient to perform household electricity demand forecast by applying econometric models, which do not need many statistical data, defining long-term energy resources consumption dynamics. In these models it is important to define in detail energy expenditure and factors conditioning them.
2. Aiming at estimating the uncertainties of factors conditioning electricity demand two scenarios of main assumptions (number of inhabitants, GDP, and electricity prices) have been developed: minimal and maximal. According these assumptions and applying various variations of econometric model household electricity demand forecast by 2025 has been carried out.
3. Forecasted average annual growth rates of household electricity demand – 1.3% at minimal scenario and 2.8% at maximum scenario growth demand applying econometric model, which related electricity demand with economic activity, electricity price and probable saving potential.

Applied different variations of econometric model enabled to estimate the impact of analysed factors, but also considering the uncertainties of conditioning factors to formulate probable forecast limits of household electricity variation. The smallest forecasted electricity demand in household 3404.81 GWh at minimal scenario assumptions and considering probable saving potential. The biggest forecasted electricity demand in household

5033.77 GWh, at maximum scenario assumptions and relating demand only with economical activity. Maximum value of forecasted electricity from the minimal one differs by 47.84%.

REFERENCES

1. Miškinis V, Konstantinavičiūtė I., Norvaiša E. Energijos poreikių namų ūkio sektoriuje prognozės //Energetika 2004. Nr. 1, p. 17–24.
2. Statistikos departamentas prie Lietuvos respublikos vyriausybės [found on the 14 of January, 2009], axes to the internet: http://www.stat.gov.lt/lt/
3. Vilemas J., Miškinis V., Galinis A. Ekonomikos raidos prognozės//Nacionalinė energetikos strategija 2003, p. 13–15, Lithuanian Energy Institute.
4. Miškinis V., Navickas A. Energijos poreikių prognozavimas. Kaunas, 2004.
5. Vilemas J., Miškinis V., Galinis A. Ekonomikos raidos prognozės // Nacionalinė energetikos strategija 2003, p.13–15, Lithuanian Energy Institute.

SUSTAINABLE DEVELOPMENT EVALUATION OF LATVIAN ELECTRICAL TRANSMISION NETWORK AND GENERATION

O. Kochukovs, A. Mutule
Institute of Physical Energetics
Aizkraukles 21, LV-1006 – Latvia
Phone: +371 67558616
E-mail: amutule@edi.lv

ABSTRACT

In paper are analyzed development conditions of Latvian power system, as well as selected the optimal sustainable development methods and technologies. In the paper it is described: 1) the transmission network and generation system development model; 2) results of Latvian power system development analysis till 2050.

Research shown, that taking into account development conditions of Latvian power system, in nearest future, especially after Ignalina NPP closing, we will have base power capacity deficit. Therefore, the topical problems are related to new power plant construction, transmission network reconstruction taking into account liberalized electricity market conditions. One of possible ways of solving this problem is building modern nuclear power plants.

Keywords - Power Transmission, Power Generation, Power System planning.

1. CHARACTERISTICS OF LATVIAN POWER SYSTEM

Because of historically constructed grid of 330 kV Latvian Power system operate with Lithuanian and Estonian Power systems, and also (on a synchronous AC grid) with the United Power System of Russia and The Power System of Belarus.

The transmission system of the Baltic States is illustrated in Fig. 1, [4].

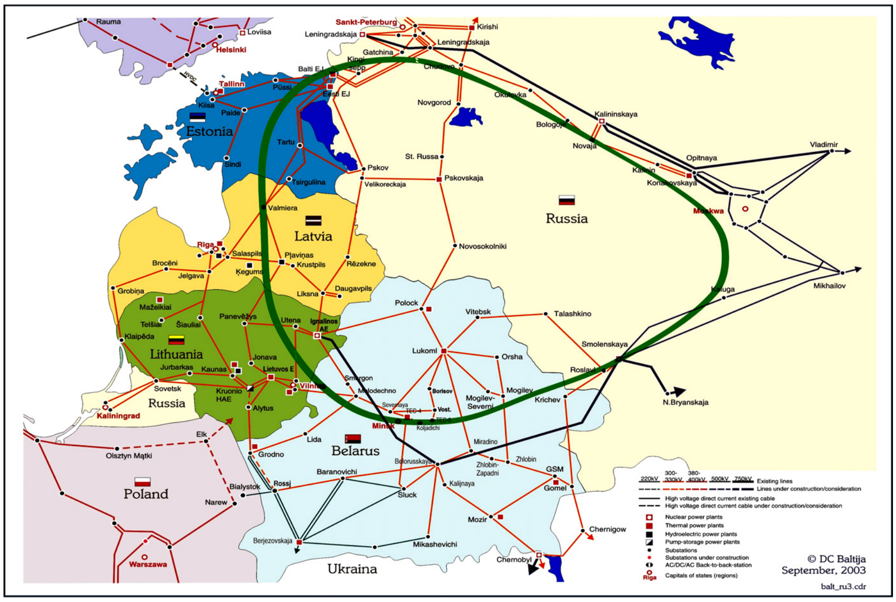

Fig. 1. Transmission network of power systems of Baltic countries and connection ties with Russia

The power systems in the three Baltic countries differ considerably. The Estonian system is purely thermal; the Latvian system is based on hydro and thermal technologies, and the Lithuanian system is dominated by nuclear power production. Table I below illustrates the installed net power capacity in the three countries, represented by diversified types of technologies.

Big differences in the power systems create potential benefits to be gained from international electricity trade between the countries, just as in the Nordic countries.

Table 1. Installed Net Capacities (MW)

	Estonia	**Latvia**	**Lithuania**	**Total**
Installed capacity	2324	2324	4609	10206
Nuclear power	0	0	1183	2366
Thermal power				
– condensing	1960	0	1732	3408
– CHP	342	744	805	1940
Hydro power	0	1553	90	1643
Wind power	22	27	52	49
HPSPP$_2$	0	0	800	800

Within the period 1997 to 2008, the power consumption in Latvia was rather stable. During the same period in Estonia and Lithuania, the tendency of a slight decrease in the power consumption is observed.

The power consumption today is considerably lower than when the Baltic countries were a part of the former Soviet Union, especially in Lithuania. In 1990, Estonia, Latvia and Lithuania consumed more than 35 TWh in total. The reason for the drop in electricity consumption after 1990 is mainly due to economic recession and restructuring of economy.

Estonia generates approx. 30% of the total power generation in the three countries. In Estonia, the power is mainly generated from oil shale. Latvia accounts for 11–18% of the power generation, which is mainly produced by hydropower and CHP plants. Lithuania accounts for the largest power generation in the three countries, i.e. 48–60%. The power generation in Lithuania is highly dependent on the country’s nuclear power plant, Ignalina. Lithuania also has several thermal oil/gas plants, including thermal combined heat and power plants.

With respect to import and export, Latvia is definitely an importer of electricity while Estonia and Lithuania are net exporters of electricity.

At present, in Baltic countries demand increment rate is 3% per year and the total balance of electric energy is positive. However, from 2010, due to liquidation initiation of Ignalina NPP, the total capacity of PP in Baltic countries would not be capable to cover the demand.

2. MODEL OF BALTIC STATES TRANSMISSION NETWORKS

Baltic States (Estonia, Lithuania, and Latvia) power system 330 kV network, taking into consideration connection ties with Russia, Belorussia and Finland, are given in Fig. 1.

Various power system transmission network model forming principles of are different. **Latvian power system.** Network of Latvian power system operated by Latvian transmission system operator (TSO) is represented by 1) 300 kV nods and lines, 2) 110 kV nodes and lines. Latvian TSO network model uses Latvian power system Dispatcher Center operational calculation program MUSTANG data base information about nods and lines. The main parameters of Latvian power system TSO network model are given in Table 2.

Lithuanian and Estonian power systems. These power system transmission networks in the model are represented only by 330 kV nodes and lines, which are formed with *LDM-TG'08 (Latvian Dynamic model – Transmission &Generation'08)*. The main parameters of Lithuanian and Estonian power system transmission network model are given in Table 2.

Table 2. Main parameters of Baltic State power system transmission network model

	Latvia		**Lithuania**	**Estonia**
	330 kV	**110 kV**	**330 kV**	**330 kV**
Number of nods	15	223	20	5
Number of lines	16	279	28	14

Russian and Belorussian power systems. Transmission networks of this power system in the model are represented by 330 kV, 500 kV, 750 kV nods and lines, which form circle Narva - St. Petersburg – Moscow – Belorussia – Ignalina and are formed with *LDM-PG'08*. The main parameters of Russian and Belorussian power system transmission network model are given in Table 3.

Table 3. The main parameters of Russian and Belorussian power system transmission network model

	Russia			**Belorussia**		
	330 kV	**500 kV**	**750 kV**	**330 kV**	**500 kV**	**750 kV**
Number of nods	11	3	8	9	0	1
Number of lines	17	2	5	8	0	2

3. BALTIC STATE GENERATION SYSTEM MODEL

Number of power plants in Baltic State generation model, taking into consideration links with Russia and Belorussia are given in Table 4

Table 4. Structure of generation system model

Country	**Number of power plants**			
	Current			**Alternative**
	Basic TPS or NPP	**CHP**	**HEP**	**Basic TPS or NPP**
Latvia	-	4	4	2
Lithuania	3	-	1	2
Estonia	2	-	-	-
Russia	7	-	-	-

Explanations:
NPP - Nuclear Power Plant
TPS - Thermal Power Station
CHP - Combined Heat -and- Power Plant
HEP - Hydroelectric Plant

As well, in the model there is a fictive energy source in Russia, which means possibility to use other Russian power plants, which are not directly shown in the model. The price of electric energy produced by all Russian power plants for Baltic States is consider as constant.

4. CONDITIONS AND MEASURES FOR DEVELOPMENT OF LATVIAN POWER SISTEM TRANSMISSION NETWORK AND POWER PLANTS

In order to perform development analysis of Latvian power system and optimization of its development task of analysis and optimization should be defined. The main components of the task are as follows: 1) conditions of development, 2) calculation regime and 3) development measures. Conditions of development are given in Table 5.

Table 5. Conditions of development

Year	Load, r.u.	Price (eur/kWh)	Cp(eur/kW)	Pns(eur/kWh)
2010	1	0, 10	4, 27	0, 14
2015	1, 1	0, 11	4, 27	0, 14
2020	1, 2	0,121	4, 27	0, 14
2030	1, 49	0,131	4, 27	0, 14
2050	2, 2	0,171	4, 27	0, 14

Explanations:
Price – average sale price
Cp – capacity max price
Pns – energy not supplied price

Development period from 2010 till 2050 is divided into 5 development steps. Our prognosis has shown that in 2031 load will be increased 1.75 times. The prognosis is based on analysis of the last five year load increase tendency. In calculations average load increase in reviewed period is 2% per year, so in 2030 load is increased 1.49 times, what shows nearly the same as our prognosis.

12 calculation regimes are reviewed in the analysis, where each regime corresponds to average load of one month. This gives an opportunity to consider output of Hydro power plants and CHP in different meteorological conditions.

Development measures are given in Table 6.

Table 6. Development measures

Nr.	Measure	Capacity, MW	K (t.eur)	Pe Eur/kWh	p%	pm %	Tbeg	Tend
1.	Shutdown NPP Ignalina	0	0	0	6	6	2010	2050
2.	Connect NPP Ign (1)	5000	0	0,04	6	6	2010	2050
3.	Connect NPP Ign (2)	5000	0	0,04	6	6	2010	2050
4.	Connect Liepaja PP	400	0	0,014	6	6	2010	2050
5.	Connect Ventspils PP	400	0	0,014	6	6	2010	2050

Explanations:
t.eur - thousand Euros
K – total capital investment
Pe – average sale price
P% – % from "K" for amortization
Pm% – % from "K" for maintenance

5 development measures are reviewed: 1) current Ignalina NPP shutting down; 2) construction of new modern Nuclear Power Plant; 3) construction of basic electric power station in Liepaja or Ventspils. Capital investment for constructing new power plants are not taken into consideration (constructing is held by independent companies). To estimate system sustainability is used only power plant electro energy price.

5. RESULTS OF LATVIAN POWER SYSTEM TRANSMISSION NETWORK AND GENERATION SYSTEM SUSTAINABILITY ANALYSIS

Forming of development scenarios. 3 development scenarios have been reviewed in order to estimate power system eligibility to generation and transmission (Table 7).

Table 7. Development scenarios

Measures	**Scenarios**		
	1	**2**	**3**
Ignalina NPP shutdown	2015	2015	2015
Ignalina NPP 1st block connect	-	2020	2020
Ignalina NPP 2d block connect	-	2020	-
Liepaja Power Plant	2020	-	2020
Ventspils Power Plant	-	-	2020

Analysis of energy and power balance for all scenarios 2010, 2015, 2020, 2030 and 2050 annual electro energy balance is calculated (Table 8).

Table 8. Annual electrical energy balance (GWh)

Year	**Country**	**Scenarios**		
		1	**2**	**3**
2010	Latvia	-1973,42	-1973,42	-1973,42
	Lithuania	1757,23	1757,23	1757,23
	Estonia	-2422,66	-2422,66	-2422,66
	Russia	2638,66	2638,66	2638,66
2015	Latvia	-2714,84	-2714,84	-2714,84
	Lithuania	-8709,86	-8709,86	-8709,86
	Estonia	9523,51	9523,51	9523,51
	Russia	1901,19	1901,19	1901,19
2020	Latvia	47,74	-6277,87	2371,64
	Lithuania	-8932,27	39307,67	29838,21
	Estonia	8967,71	-6665,62	-6665,62
	Russia	-84,18	-26364,18	-25544,23
2030	Latvia	-2102,38	-8428,00	805,9
	Lithuania	-4259,30	47549,51	32625,85
	Estonia	12203,43	-6999,77	-6999,77
	Russia	-5841,75	-32121,75	-26431,17
2050	Latvia	-7366,48	-12772,03	-3862,48
	Lithuania	10591,13	66547,45	32243,58
	Estonia	12505,33	-7817,87	-385089
	Russia	-15729,99	-45957,55	-24530,21

"-" - import

As we can see, after Ignalina NPP shutdown in 2010 till new power plant construction (Table 7) all Baltic State power systems have large energy deficit. The biggest deficit is in Latvian power system (Table 9).

Table 9. Latvian power system annual electro energy balance in relation with consumption, %

Year	**Scenarios**		
	1	**2**	**3**
2010	-27	-26	-26
2015	-33	-33	-33
2020	0	-70	26
2030	-19	-76	7
2050	-45	-78	-23

The only power system with positive energy balance is Russian power system, which will influence Baltic State power supply.

In first scenario in 2020 it is planned to run-up new power plant in Latvia. In 2020 Latvia can go without electrical energy import, but in further perspective import increases to 50%. Other Baltic State countries electrical energy deficit levels remains, but Russia's energy reserves decrease.

In the second scenario in 2020 it is planned to run-up Ignalina NPP two new blocks. Electrical energy deficit in Lithuania decreases, in Latvia increases, in Estonia remains the same.

In the third scenario in 2020 it is planned to put into operation one unit of the new Ignalina NPP and two new power plants in Latvia. In 2020–2030 there is no electro energy deficit in Latvia, and export is possible. At the same time export of electricity from Lithuania increases. Estonia have electrical energy deficit.

Baltic state power system eligibility to generation and transmission can vary in accordance with calculation regimes. Let's see how Latvian power balance is changing with regime change. Calculation results are given in Table 10.

Table 10. Latvian power system power balance for regimes (MW)

Year	**Regime**	**Scenarios**		
		1	**2**	**3**
2010	February	-48,84	-48,84	-48,84
	April	514,62	514,62	514,62
	June	-333,62	-333,62	-333,62
	August	-464,97	-464,97	-464,97
	October	-407,92	-407,92	-407,92
	December	-165,53	-165,53	-165,53
2015	February	-133,36	-133,36	-133,36
	April	433,89	433,89	433,89
	June	-403,43	-403,43	-403,43
	August	-539,70	-539,70	-539,70
	October	-497,39	-497,39	-497,39
	December	-263,85	-263,85	-263,85
2020	February	180,12	-775,54	305,77
	April	765,17	20,40	820,40
	June	-73,24	-679,34	120,66

Year	**Regime**	**Scenarios**		
		1	**2**	**3**
	August	-214,42	-804,80	-4,80
	October	-186,86	-855,58	146,28
	December	37,83	-804,71	437,83
2030	February	-70,79	-1026,45	329,21
	April	548,47	-196,30	603,70
	June	-275,68	-881,78	-81,78
	August	-431,12	-1021,50	-194,52
	October	-446,33	-1115,05	-46,33
	December	-247,30	-1089,84	152,70
2050	February	-685,1	-1640,76	-285,10
	April	17,94	-726,83	417,94
	June	-771,31	-1377,41	-371,31
	August	-961,65	-1552,03	-561,65
	October	-108,58	-1750,30	-681,58
	December	-945,37	-1345,37	-545,37

There is no electrical power deficit in Latvia in April, while the highest power deficit is in August and October. The same situation is with overload of transmission network lines. It shows that Latvian transmission network has to be strengthened.

Analysis of technical and economical criterions. Annual technical and economical criterions for 1 and 3 development scenarios (see Table 7) are given in Table 11-12.

Table 11. Annual technical and economical criterions for 1 scenario

	2010	**2015**	**2020**	**2030**
1. Annual consumption (tWh)	48,07	60,17	62,99	71,19
2. Maximum power (MW)	6293	6680	7066	8194
3. Capital investment (M. Euro)	0	0,028	0,014	0
3.1 Remainder capital (M. Euro)	0	0	0	0
4. Operation expenses (M. Euro)	45415,32	47426,22	57807,58	82663,59
4.1. Maintenance + penalties (M. Euro)	45409,79	47421,74	57803,07	82657,94
4.2. Repair expenses (M. Euro)	5,53	4,48	4,51	5,65
5. Loss expanses (M. Euro)	7,63	9,06	15,69	19,74
6. Non-delivery energy expenses (M. Euro)	153,67	165,05	180,71	206,32
7. Energy expenses for plants (M. Euro)	89,58	133,69	132,47	163,13
8. Income from sold electric energy (M. Euro)	2736,2	3424,87	3585,66	4052,36

Table 12. Annual technical and economical criterions for 3 scenario

	2010	2015	2020	2030
1. Annual consumption (tWh)	48,07	60,17	62,99	71,19
2. Maximum power (MW)	6293	6680	7066	8194
3. Capital investment (M. Euro)	0	0,028	0,042	0
3.1 Remainder capital (M. Euro)	0	0	0	0
4. Operation expenses (M. Euro)	45415,32	47426,22	248457,4	288620,6
4.1. Maintenance + penalties (M. Euro)	45409,79	47421,74	248451,9	288615,5

4.2. Repair expenses (M. Euro)	5,53	4,48	5,52	5,03
5. Loss expanses (M. Euro)	7,63	9,06	103,8	107,77
6. Non-delivery energy expenses (M. Euro)	153,22	164,88	191,19	226,29
7. Energy expenses for plants (M. Euro)	89,58	133,69	21,39	36,47
8. Income from sold electric energy (M. Euro)	2736,2	3424,87	3585,66	4052,36

Table 13. Number of overload lines

Scenario	**Regime, month**	**2010**	**2015**	**2020**	**2030**	**2050**
1.	2	5	5	17	20	29
	4	3	1	10	17	25
	6	4	2	11	14	22
	8	3	3	13	15	26
	10	3	5	15	17	28
	12	4	5	15	22	34
3.	2	5	5	46	49	57
	4	3	1	41	44	53
	6	4	2	42	46	53
	8	3	3	43	49	53
	10	3	5	48	47	59
	12	4	5	47	50	60

Risk analysis. In liberalized electricity market regimes of power plants depend on price of electricity. Development of Baltic States power system is basically influenced by price of electricity imported from Russia. Let's perform risk analysis for three different prognoses of price for imported electricity: 1st prognosis (average) – 2.5 santims (1.76 eurocents) per 10 kWh, 2d prognosis (maximum) – 3 santims (2.1 eurocents) per 10 kWh, 3d prognosis (minimum) – 2 santims (1.4 eurocents) per 10 kWh (Table 14).

Table 14. Risk matrix (billion EUR)

Prognoses	**1 scenario**	**2 scenario**	**3 scenario**
1 prognosis	0,0	35056	32380
2. prognosis	0,0	35056	32380
3. prognosis	0,0	24171	22240
Maximum risk	0,0	35056	32380

According to the Table 14 data, taking into account reviewed development conditions, optimal scenario is 1.

CONCLUSIONS

It was performed Latvian power system transmission network and generation system sustainability research in the period of 2010-2050. On the basis of the last five year load increase analysis it was decided to take 2% as average annual load increase. Development period is divided into 5 development steps: 1) from 2010, 2) from 2015, 3) from 2020, 4) from 2030 and 5) from 2050.

In order to perform research of Latvian power system development, within the framework of the project were was made: 1) Baltic State transmission network model, taking into account Russian power system 750 kV circle St. Petersburg – Moscow – Ignalina, 2) Baltic State and Russia generation system model, and 3) generation system development measures and development scenarios.

The research has been made, using software *LDM-PG'08*. Evaluating power system sustainability, most important questions are: 1) formation of development model, 2) analysis of energy and power balance, 3) calculation of annual technical and economical criterions, and 4) risk analysis.

Research has shown that current condition of Baltic State power system can't provide sustainable power system development, as well as power system operational capability in the nearest future (after Ignalina NPP shutdown). Therefore it is essential to start construction of new basic power plant in the place of Ignalina NPP, as well as in Latvia. Also, research has shown that Latvian power system transmission networks have to be reconstructed, taking into consideration regulations of liberalized electrical energy market.

REFERENCES

1. Z.Krishans, V.Neimane, G.Andersson. Dynamic Model for Planning of Reinforcement Investments in Distribution Networks // 13th Power Systems Computation Conference, Trondheim, Norway, June 28 - July 2nd, 1999. - Conference Proceedings, Vol. 2, p. 863–869.
2. Krishans Z., Oleinikova I., Mutule I. (2003) New Technologies for Long-Term Management of Power System. Latv. J. Phys. Tech. Sci **5** 10–19.
3. Merkurjevs J., Krišāns Z., Oļeiņikova I. (2007) European foundation of regional development co-financed project "Information technologies for providing sustainability of transmission networks and generation". "Energy & the World", 6 86-89.
4. Krishans Z., Oleinikova I. (2007) Energy utility management principles. (in Latvian), Riga Technical university, p. 158.

CYSENI 2009, May 28-29, Kaunas, Lithuania
ISSN 1822-7554, www.cyseni.com

THE RENOVATION PLAN DEVELOPMENT EXAMPLE FOR OLD DISTRICT HEATING NETWORK IN NARVA CITY

A. Hlebnikov, A. Siirde
Tallinn University of Technology
Department of Thermal Engineering
Kopli 116, 11712 Tallinn – Estonia
E-mail: +372 620 3908
Phone: ahleb@staff.ttu.ee

ABSTRACT

Poor condition of the old district heating networks decrease futures of centralised heating and consumers make choice for the local heating. Often the local heating is not effective solution for regional heat supply-system as in Narva city and decreases potential of combined heat and electricity power production. Narva city district heating system is based on Balti CHP, which uses oil shale as fuel. Objective estimation of district heating networks actual conditions and technical-economical argumentation for networks renovation and expansion should be carried out to increase combined heat and electricity power production and decrease fuel consumption. Main characteristic parameters of the Narva city district heating network and their difference from the optimal values are estimated and compared with the typical Swedish networks. Current comparison gives example of Narva old non-optimised district heating network economic optimisation. The optimisation purpose is to get minimal distribution costs of heat. Narva city district heating network efficiency increasing potential was found out.

Keywords: district heating network, heat losses, heat transfer coefficient, thermal insulation efficiency, friction losses, water velocities, optimal design, distribution cost, economic optimisation, energy saving

INTRODUCTION

The over-dimensioning and poor insulation of district heating (DH) networks causes high heat losses in Estonian district heating sector (average are around 18.5%), for instance, in Finnish district heating networks the heat losses are in the range of 6–7 %, whereas in Sweden – 7–9%. The technical conditions of Estonian district heating networks that are 20–40 years old are out of date.

Poor condition of old DH networks decrease futures of centralised heating and consumers make choice for the local heating. Often the local heating is not effective solution for regional heat supply-system as in Narva city and decrease potential of combined heat and electricity power production. District heating system of Narva city is based on Baltic CHP, where heat and power are produced from oil shale.

Objective estimation of district heating networks actual conditions and technical-economical argumentation for DH networks renovation should be carried out to minimise expenses of heat distribution.

Main characteristic parameters of the Narva district heating network and their difference from the optimal values are estimated and also compared with the typical networks in Sweden [1]. Current work gives the actual conditions of pipes thermal insulation in Narva. Narva city district heating network efficiency increasing potential was found out.

METHODOLOGY

The major characteristic parameter for estimating the efficiency of the district heating networks is heat loss factor q_{hlf}. The heat loss factor is a ratio between the heat loss and the quantity of heat supplied to the district-heating network. The heat loss factor does not depend only on the efficiency of the pipe insulation. It depends on the following parameters:

- The overall heat transfer coefficient K_o, in W/(m^2·K), which characterizes the efficiency of pipe insulation;
- The specific surface area of the distribution pipes A/L, in m^2/m, which characterizes the average size of the district heating pipes;
- The degree-hours number $\int \Theta d\tau$, in ^{o}C·h, which indicates the level of water distribution temperature relative to the annual average outdoor temperature;
- The specific heat supply Q/L, in MW·h/m, which characterizes the concentration of the district heating demand.

Where,

A – surface area of the distribution pipes, m^2;
L – pipes length, m;
Θ – difference between average water temperature and outdoor temperature, ^{o}C;
τ – average water temperature and outdoor temperature difference duration time, h;
Q – the annual quantity of the heat supplied to the district-heating network, MW·h.

The overall heat transfer coefficient can be calculated on the basis of design data of the district heating networks or estimated from the heat loss measurements. In the present work the overall heat transfer coefficient is calculated on the basis of the annual heat losses. The annual heat losses are calculated as difference between the heat supplied to the district heating network and the heat delivered to the consumers.

The heat loss factor is given by:

$$q_{hlf} = \frac{Q_{hlf}}{Q} = \frac{K_o \cdot A \cdot \int \Theta d\tau}{Q} = K_o \cdot \frac{(A/L) \cdot \int \Theta d\tau}{(Q/L)}, \tag{1}$$

Where,

Q_{hlf} – the annual heat losses, MW·h,

The overall heat transfer coefficient K_o is given by:

$$K_o = \frac{q_{hlf}}{\left[\dfrac{(A/L) \cdot \int \Theta \, d\tau}{(Q/L)} \right]}, \text{ W/(m}^2\text{·K)} \tag{2}$$

The average diameter of the district heating pipes d_a is given by:

$$d_a = \frac{A/L}{2 \cdot \pi}, \text{ m} \tag{3}$$

For analysing district heating network efficiency, the heat loss factor can be divided into two parts: the overall heat transfer coefficient and the distribution parameter. The distribution parameter is given by:

$$q_{dp} = \frac{q_{hlf}}{K_o} = \frac{(A/L)\cdot\int\theta\, d\tau}{(Q/L)},\ (\mathrm{m^2\cdot K})/\mathrm{W} \qquad (4)$$

The question of how to select the optimal diameter of pipes in which a fluid is transported, represents a classical optimisation problem [2–5]. Fig. 1 shows qualitatively how an economic optimum can be found for the diameter of district heating pipe. Total cost is mainly the sum of costs for pipeline installation, for heat losses, and for pumping power. Of these three cost elements, the costs of pipeline installation and heat losses increase their values strongly with diameter, while the pumping power drops rapidly ($K_{pumping} \sim D_s^5$) with diameter increasing.

Optimisation of this kind usually assumes that the flow rate is constant when the diameter is varied. This method was developed to be as simple as possible yet complete and accurate enough for design calculations.

Dynamic simulation models of district heating networks today are also very popular. One type of mathematical model involves a full physical modelling of the network [6] and in other type of model - DH network is replaced by a simplified one [7].

The water velocities and friction losses in pipes of Estonian old district heating networks as rule are much lower than optimum values. This situation exists because old networks where designed for much bigger load and take into account growing potential. In present time the heat load of consumers is 15–30% less than designed.

Pumping costs in old networks with over dimensioned pipes are much lower than in new optimised networks. At the same time heat losses in old networks with over dimensioned and badly insulated pipes are times higher. The saving in heat losses gives great increasing of total DH distribution cost.

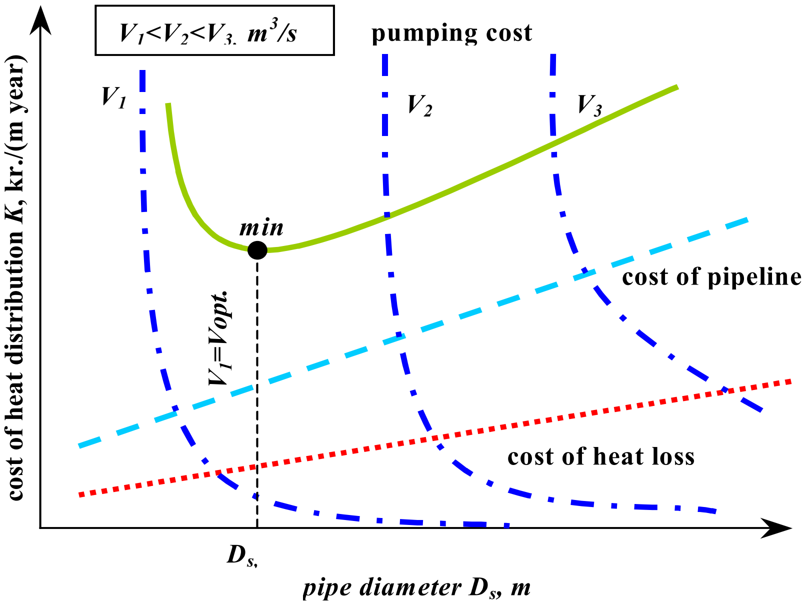

Fig. 1. Pipe diameter economic optimisation

As rule of thumb many district heating networks in Denmark and in other European countries have been designed by applying a friction loss of 100 Pa/m [2, 4, 5]. Estonian old networks are designed also by applying similar friction loss of about ~80 Pa/m [8], but real friction loss are much less. This situation exists because old networks where designed for much bigger load and take into account growing potential.

The water velocities and friction losses in pipes of Narva old district heating network are mainly lower than optimum values. The optimal values of the water velocities and friction losses for water temperature regime 110/70°C are the next: water velocity increase from 0.5 to 2.2 m/s and friction losses decrease from 110 to 50 Pa/m with pipes diameter growing from 40 to 700 mm.

RESULTS AND CONCLUSIONS

The relative heat losses in the Narva old DH network are about 18–19%. In Swedish typical networks relative heat losses are 7–9%, and there are similar heat demand concentration as in Narva: 5–7 MWh/m, but much better heat insulation of pipes: overall heat transfer coefficient is 0.9–1.1 W/(m^{2}K) (in Narva 1.8–2.0 W/(m^{2}K)), more than two times less than in Narva DH network.

Efficiency of heat insulation in Narva DH network, which is estimated by the overall heat transfer coefficient, is about 3 times less than the same value for the ordinary Swedish networks.

Total overall heat transfer coefficient before and after prospective optimisation for Narva district heating network are presented in Figure 2.

Recently, considerable tendency of the overall heat transfer coefficient reduction in the district heating networks in Narva was observed (from 2.3 W/(m^{2}K) to 1.8 W/(m^{2}K)) (Fig. 2). This reduction is caused by replacement of district heating network main sections old thermal insulation with new one (main pipelines TM1 and TM2 in 2003...2005 years) and replacement of the oldest networks parts by preinsulated pipelines with optimal diameters.

Several “wet” sections of the network can significantly increase the value of the heat transfer coefficient. Replacement of those sections will significantly decrease the overall heat transfer coefficient. Also in Tallinn district heating networks the same decreasing tendency of the overall heat transfer coefficient was observed. This reduction is caused by replacement of district heating network old sections with new pre-insulated pipes or thermal insulation renovation.

In Table 1 the major characteristic parameters found are presented for Narva old non-optimised district heating network. Also optimisation calculations for observed network where done and determined, how much that values can change in the better direction.

After optimal selection of DH network pipes diameters (new optimal average diameter will be 0.198 m), according to consumers real heat demand and total renovation of pipes (replacing by the preinsulated pipes and thermal insulation renovation), relative heat losses drastically decreases. Relative heat losses in Narva district heating network decrease from 17–18% to 7–8%.

As we can see, potential to decrease heat losses is very big. After optimisation and total renovation of old network, heat losses can decrease up to 2.85 times.

Table 1. The major characteristic parameters for the Narva district heating network before and after prospective optimisation and comparison with ordinary Swedish networks

Average year	Supplyed heat MWh	Used heat MWh	Network heat losses MWh	Network heat losses %	degree-hours 10^5 °C h	q_{hlf}	L, m	d_a, m	A/L, m^2/m	V/L, m^3/m	Q_{suppl}/L, MWh/m	Q_{used}/L, MWh/m	Q_{suppl}/V, MWh/m^3	$Q_{heat\ loss}/L$, MWh/m	K_o, $W/(m^2K)$	q_{jt}, $(m^2K)/W$
Narva old network	577 402	474 400	103 002	17.8	4.9	0.178	68 569	0.249	1.56	0.15	8.4	6.9	57.5	1.5	2.0	0.091
Narva new optimized network	510 453	474 400	36053	7.1	4.9	0.071	68569	0.198	1.24	0.06	7.4	6.9	120.9	0.5	0.7	0.082
ordinary Swedish networks				7.5-8.5	5.6	0.07-0.085			0.88-0.942	0.031-0.035	5-6		162-170	0.35-0.43	0.9-1.1	

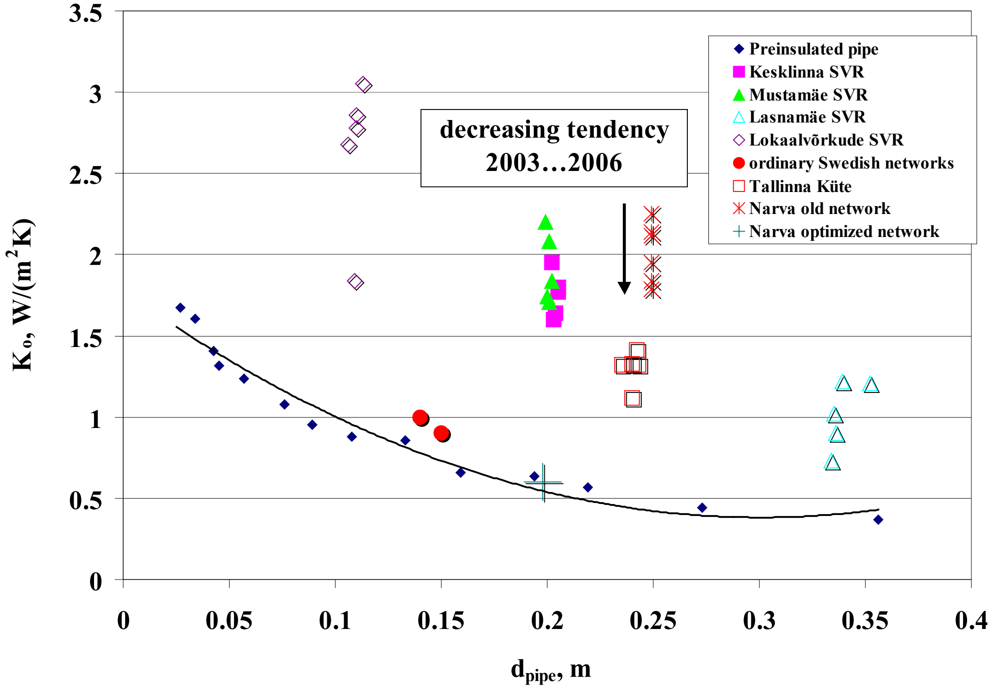

Fig. 2. Total overall heat transfer coefficient before and after prospective optimisation for Narva and Tallinn district heating networks

REFERENCES

1. Fredriksen, S., Werner, S., Fjärrvärme. Teori, teknik och funktion. Lund 1993.
2. Bøhm, B. Energy-economy of Danish District Heating Systems. A Technical and Economic Analysis. Technical University of Denmark, Copenhagen, 1988.
3. Frederiksen, S. A Thermodynamic Analysis of District Heating. Lund Institute of Technology, Lund, 1982.
4. Koskelainen, L., A Model for Optimal Design of District Heating Networks. Lappeenranta University of Technology. Lappeenranta 1978.
5. Phetteplace, G., Optimal Design of Piping Systems for District Heating. CRREL Report 95-17., U.S. Army Corps of Engineers. Cold Regions Research and Engineering Laboratory. Hanover 1995.
6. Benonysson, A., Dynamic Modelling and operational optimization of district heating systems. PhD Thesis. Laboratory of Heating and Air Conditioning, Technical University of Denmark, September 1991.
7. Larsen, H., Pallson, H., Bøhm, B., Ravn, H, Aggregated dynamic simulation model of district heating networks. Energy conversion and management, 43 (2002), Elsevier Science, Pergamon press 2002.
8. Козин, В.Е., и др., Теплоснабжение. Москва, Высшая школа, 1980.

CYSENI 2009, May 28-29, Kaunas, Lithuania
ISSN 1822-7554, www.cyseni.com

MEASURES OF ENERGY ECONOMY IN VENTILATING SYSTEMS OF PIGGERIES

A. Krēsliņš, A. Ramata
Institute of Heat, Gas and Water Technology
Riga Technical University
Kalku str. 1, LV-1658 – Latvia
E-mail: kreslins@bf.rtu.lv; Anna.Ramata@rtu.lv

ABSTRACT

The efficient and appropriate energy use determines the production costs in agriculture as well the costs of the end-product. Effective utilization of energy, sustainable agriculture and welfare of animals are interrelated activities.

The owner must provide in the livestock housing the appropriate indoor climate set by the physiological requirements of the animals. It includes optimal air exchange, temperature and relative humidity of the air, while the concentration of the gases, dusts and odours should not exceed certain limits. Thus, the indoor air parameters directly influence animal welfare and reduce or increase the productivity.

Among the most important parameters determining the microclimate of the livestock housing are air temperature and relative humidity, velocity of the air and temperature of the surfaces. The analysis of the cost-efficiency of the farm and productivity of the animal breeding includes these parameters as it is proven that the efficiency of the production could be increased by 30% in case the optimal microclimate is provided.

The study analysing the balance of the heat and moisture content in the model pig farms shows strong dependence of the energy consumption under different working conditions by the operating equipment. It has strong influence on the process of heat and mass transfer, its intensity and on the moisture exchange rate. In the project, the necessary air exchange ratio is calculated for the maximal load of shelters (m^3/h) that provides the optimal indoor climate and heat balance in the livestock housing. The heat losses through the building constructions are taken into account.

The ventilation system provides optimal indoor climate while it is also responsible for the major part of the energy loss. The energy consumption can be decreased by the optimising the specific moisture regimes in the piggeries. The regenerative heat exchangers with efficiency 50% provides appropriate heat and moisture balance and decreases energy consumption by 30–40% in comparison with the traditional ventilation systems. Energy consumption (kWh) for different ventilating systems calculated using the climatology data.

Keywords: energy efficiency and savings, piggeries.

INTRODUCTION

Effective utilization of energy, sustainable agriculture and welfare of animals are interrelated activities. At 2001 The Council of the European Union accepted Directive 2001/88/EC laying down minimum welfare standards adaptable for the intensively kept pigs. These directives provide requirements concerning breeding of pigs and their welfare. The Cabinet of Ministers of Latvia adapted a Law Nr 5 “General Requirements of Welfare for Agriculture Animals”, which was legislate in accordance with law of Animal Protection. Under the rules, in livestock housing the owner must provide optimal air exchange, ventilation, temperature, relative humidity of air, level of concentration of gases, dusts and odours, which are harmless and agree for physiology requirements of animals. One of indices of animal welfare and factors of influence to productivity is quality of air parameters.

To provide air parameters in livestock housing of pigs, workings of ventilating system was analyzed. We research, how to decrease consumption using heat- moisture balance and regenerative heat exchange apparatus for heat recovery from exhaust air. For study we employ outdoor air temperature and moisture climatology data per each month, about fluctuations of sun radiation and find more effective ventilating system, whose will have to provide an optimal heat and mass transfer.

Meteorology parameter of air – temperature, moisture content, relative humidity, velocity of air, and temperature of surfaces – determine the microclimate of livestock housing. It is one of main animal's productivity and farm cost-efficiency influence factor. There is proven that optimal microclimate in livestock housing provide output up to 30%.

Animal nature can keep even optimal temperature of body. Receive energy from food provide common energy balance of organism and it number is similar to heat energy quantity, what animal return to environment.

The microclimate of livestock housing must provide footing thermodynamic balance between animals of heat-moisture exchange with environment.

Optimal environment of piggeries on recommendations of zoo hygienists are substantially depend at physiology position of swine, age, exploitation group.

They fluctuations of temperature from 5 °C to 27 °C for finishing pigs and 22 °C to 32 °C for piglets to 3 week age, relative humidity fluctuated from 60% to 80%. Study of heat-moisture balance at model pig farms we are establish that consume of energy in various air supply schemes are depend of heat and mass transfer device working and kind, of heat transfer efficiency, intensity of moisture exchange

Many factors besides the diet including ambient temperature and air quality, housing and grouping conditions, breed or genetics line can influence the nutrient needs of pigs.

MATERIAL AND METHODS

Ventilation in livestock housing is a process for controlling several environmental factors by diluting inside air with outside air. Ventilating systems affect: air temperature, moisture level, moisture condensation on surfaces, air temperature uniformity, air speed across animals, odour and gas concentration, airborne dust and disease organism level. A ventilating system is use to control the environment. Ventilating capacity was based on the amount of air exchange rate needed to remove moisture in winter and excess heat in summer.[1]

Air meteorological parameters – temperature, moisture content, relative humidity, velocity of air, surfaces temperature – determine microclimate of livestock housing. It is one of the main effectiveness factors to influence productiveness of animal production and farm efficiency gain. The production output greater for 30 % with optimal microclimate in livestock housing. Optimal environment in piggeries by zoo hygiene recommendations are 5 °C to 27 °C for sows and growing – finishing pigs, and 22 °C to 32 °C for piglets till to three weeks age. Relative humidity is 60% to 80%.[2]

To study heat and moisture balance in standard pig barns was established energy consumption with various air supply scheme dependant of staff action of heat and mass transfer and manner: the efficiency of heat transfer and intensity of moisture transfer. Ventilating system must provide sufficient capacity for regulation the temperature in pigsty at hot summer months and minimal air flow velocity at cold winter months. For reduce energy consumption for heating and ventilation, the best solution imaginable.[3]

Combined ventilating systems provide air exchange of livestock housing completely, which integrate function of natural and mechanical ventilation systems.

---

[1] Krelins A. Gaisa kondicionesana rupnieciskajas un sabiedriskajas ekas. Riga 1975.

[2] Zalitis L., Hmelnickis A. Zoohigienas praktikums. Riga, 1971.

[3] Mechanical Ventilating Systems for Livestock Housing. Handbook 32 of Midwest Plan Service, 69 p.

Necessary ventilation ratio in winter provide, employing mechanical ventilating systems, but in summer time – combined ventilating systems. Using regenerative heat exchangers in mechanical ventilating systems, cold supply air to get warming with exhaust air. Heat exchangers can reclaim some of the heat lost with the exhaust ventilating air.

Important parameters of microclimate in piggeries are concentration of CO_2, relative humidity, and optimal temperature. Consider Latvia climate with high humidity, follow to relative humidity for providing the standards.

For calculations required air parameters of livestock shelters and analysis of operation of ventilating system, was to use standard projects of piggeries. In intensively pig-breeding animals was grouping for physiological position, exploitation and age group.

For each animal group has particular shelters, in which must provide required microclimate. Piggeries are grouping in three general groups (look Figure 1):

1. Farrowing pigs and sows (piglets from birth till to 21 day age);
2. Nursery pigs (from 21. till to 65 days age);
3. Breeding, gestation and growing/finishing pigs (from 65 till to 165 days age);

In farrowing barns must be provided two environments: one for sows, one for piglets. The environment within the nursery is similar to that within the farrowing barn for piglets. The requirements for growing barns and breeding stock housing are similar.

Far rowing pigs and sows:

In far rowing barns must be two environment zones: one for sows, one for piglets. Air temperature 18 °C–21 °C, with small areas for piglets warmed to 26 °C–32 °C by brooders, heat lamps, or flor heat.

Relative humidity 60–70%, ventilation rate 35–60 m^3/h per animal, air velocity 0.15–0.20 m/s.

Nursery pigs:

Air temperature for first week after weaning 26 °C. Lower temperature 3 °C per week to 22 °C. Provide heat lamps, or warm floors. Relative humidity 60–70%, ventilation rate 35–60 m^3/h, air velocity 0.20–0.60 m/s.

Breeding, gestation and growing/finishing pigs:

Air temperature 16–18°C, relative humidity 70–80%, ventilation rate 35–70 m^3/h, air velocity 0.20–1.00 m/s.[4].

Necessary conditions for indoor climate are shown in h-x diagram (Fig. 1).

---

[4] ASHRAE Handbook. Fundamentals, 2005.

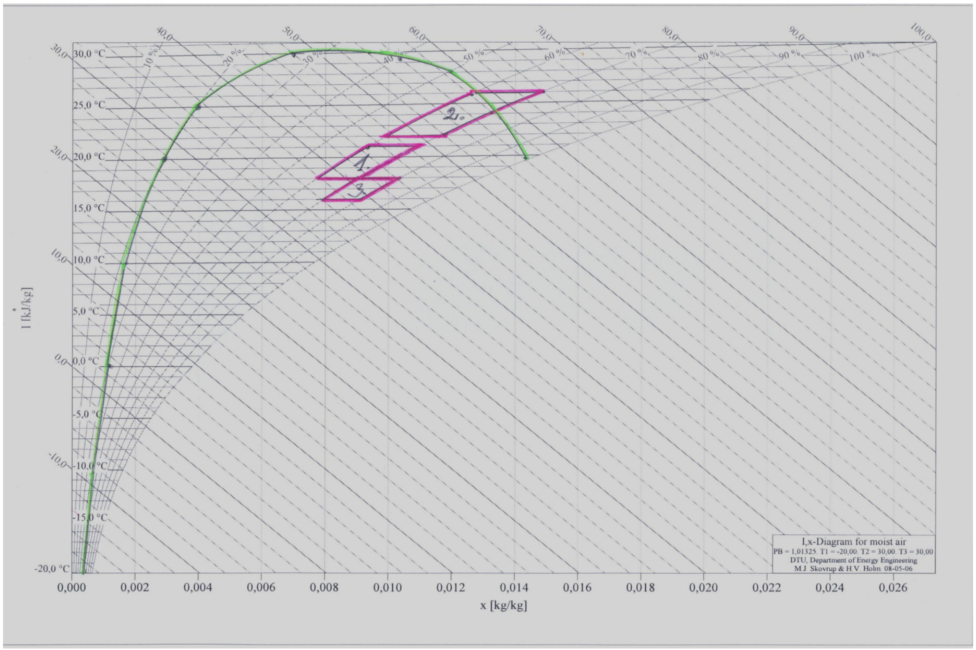

Fig. 1. Necessary conditions for indoor climate for farrowing pigs and sows (1), nursery pigs (2) and breeding, gestation and growing/finishing pigs (3)

RESULTS AND DISCUSSION

In further study process was calculate necessary ventilating ratio for maximal load of shelters (m^3/h), heat balance of livestock housing regarding zoohygiene standards and heat loses through livestock building insulation constructions.[5] Results are show in Table 1.

Table 1. Calculations of ventilating intensity in three different pigsties

Animal group	**Volume of pigsty, m^3**	**Number of pigs/ kg per pig**	**Heat Q from animal, kW**	**Heat loss ΣQ, kW**	**ΔQ, kW**	**ΔI=ΔQ/L, kJ/kg**	**Ventilating volume L, m^3/h**	**Moisture ΔG=G/L g/kg**	**Intensity of ventilating E times/h**
Pigsty for farrowing pigs and sows with piglets	4536	225/ 150	125,6	64.8	60.8	15.6	15750	3.8	3.4
Pigsty for nursery pigs	4536	1400/7–25	121.3	64.8	56.5	20.6	8575	7	1.9
Pigsty for breeding, finishing pigs	4536	1350/25-100	243.4	64.8	178.6	17.44	30712	3.9	6.8

Findings improve for research heat and moisture exchange processes in piggeries with different working aspects of ventilating systems. Our investigation compare tradition ventilating system with mechanical ventilating in which can used heat and moisture exchangers. Utilization of outflow air heat raises efficiency of ventilating system, thus reduce operational costs for preparing of supply air. In ventilating systems with direct air supply was

---

[5] ASHRAE Handbook. HVAC Applications, 2007.

utilized heat of outflow air using regenerative heat exchangers, which provide energy exchange between two airflows.[6]

Efficiency of regenerative heat exchangers are $\varepsilon = 0.6–0.75$. Both systems compare on necessary enthalpy for heating of inlet air. Acquired results for each group are demonstrated on I-x diagram.

In practise at piggeries, fresh air exchange became through inlets of building walls. It mixing with warm and moisture inside air and was bustle out with exhaust fans. Significant heat quantity comes to environment. But cold and dry inlet air in additional must to warming and to humidify, that microclimate fulfill to conditions. That livestock housing ventilating system are lower-cost, are not needful for large capital investments. But at working conditions get to energy consumption rise cost price of porky production. Inadequate microclimate conduce animals illness, lower body weight growth, inefficient nutrient disposition, what damages for farm economy.

Investigating the possibilities to decrease the energy consumption in the ventilation equipment there are considered the mechanical ventilation system with separate supply and exhaust channels where the heat exchangers and the humidity exchangers could be installed. Both systems are compared by the enthalpy necessary to heat up the outdoor air. The obtained results for each group are presented in the I-x diagrams.[7]

Pigsty for farrowing pigs and sows with piglets requires the enthalpy for heating up the outdoor air from -20 to +30 kJ/kg, humidification from 0.00025 to 0.006 kg/kg in order to reach the necessary result. In case humidification is not applied for the supply air, the humidity of the supply air is 24% what does not satisfy the requirements (Fig. 2).

The supply air is heated up by the exhaust air in the recovery (regenerative) heat exchanger. The enthalpy of the heating up of the outdoor air is from 12.5 to 30.5 kJ/kg, humidification from 0.0043 to 0.006 kg/kg (Fig. 3.).

Pigsty for nursery pigs requires the enthalpy for heating up the outdoor air from -20 to +38 kJ/kg, humidification from 0.00025 to 0.0065 kg/kg in order to reach the necessary result. In case humidification is not applied for the supply air, the humidity of the supply air is 24% what does not satisfy the requirements (Fig. 4).

The supply air is heated up by the exhaust air in the recovery (regenerative) heat exchanger. The enthalpy of the heating up of the outdoor air is from 19 to 37 kJ/kg, humidification from 0.0055 to 0.0065 kg/kg (Fig. 5).

Pigsty for breeding, gestation and growing/finishing pigs requires the enthalpy for heating up the outdoor air from -20 to +26.25 kJ/kg, humidification from 0.00025 to 0.006 kg/kg in order to reach the necessary result. In case humidification is not applied for the supply air, the humidity of the supply air is 20% what does not satisfy the requirements (Fig. 6).

The supply air is heated up by the exhaust air in the recovery (regenerative) heat exchanger. The enthalpy of the heating up of the outdoor air is from 13.25 to 26.25 kJ/kg, humidification from 0.0055 to 0.0065 kg/kg (Fig. 7).

---

[6] Yoshie R. et al. Numerical Analysis of Heat and Moisture Transfer in Desiccant Wheel for Dehumidification. Proc. CLIMA 2007, Helsinki.

[7] Влажный воздух. Справочное пособие АВОК. Москва – 2004.

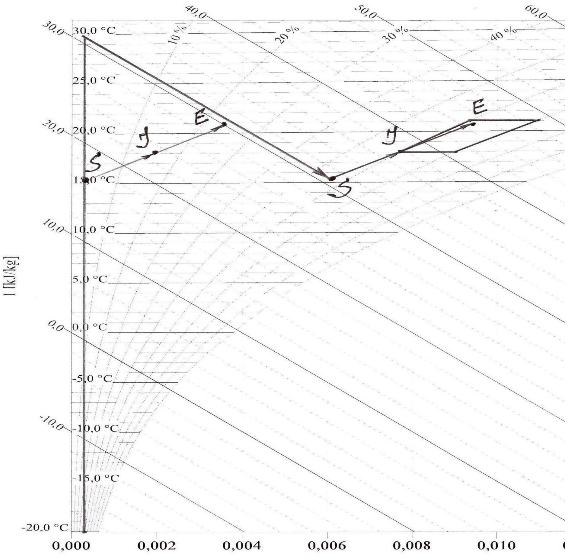

Fig. 2. Air handling process with the traditional ventilation system in the pigsty for farrowing pigs and sows with piglets

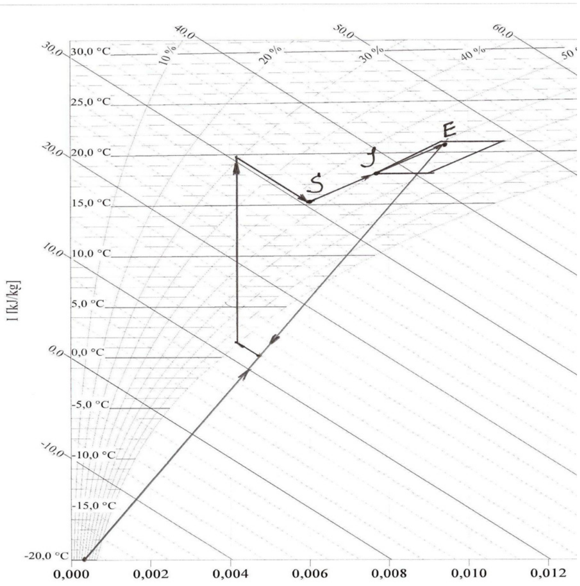

Fig. 3. Air handling process with the rotating heat exchangers in the dwelling for sows with piglets

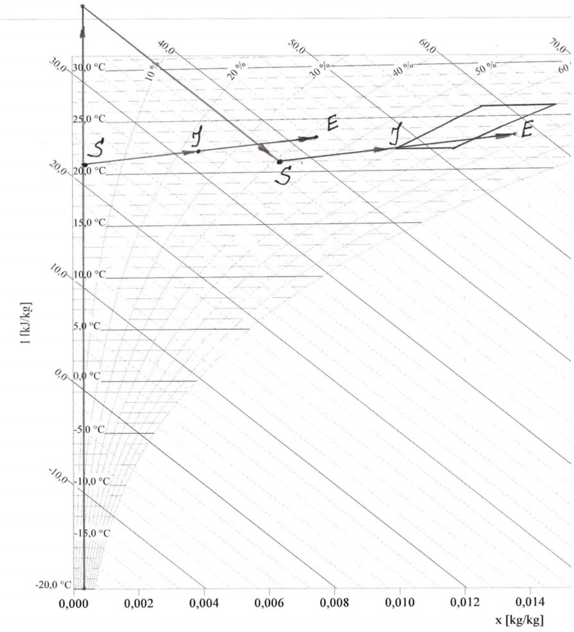

Fig. 4. Air handling process with the traditional ventilation system in the pigsty for nursery pigs

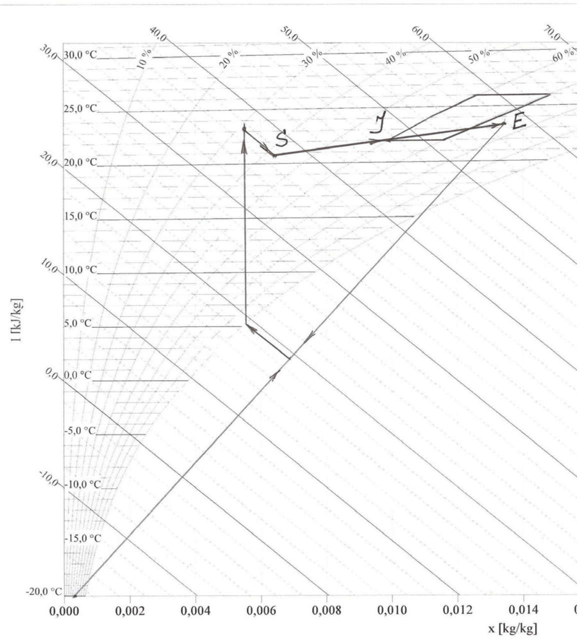

Fig. 5. Air handling process with the rotating heat exchangers in the pigsty for nursery pigs

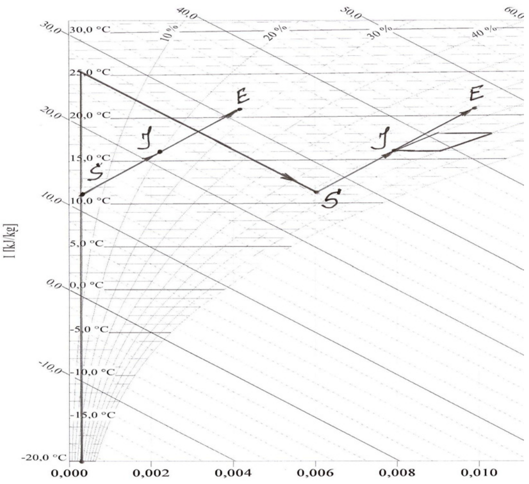

Fig. 6. Air handling process with the traditional ventilation system in the stand for feedlot stock and breeding pigs

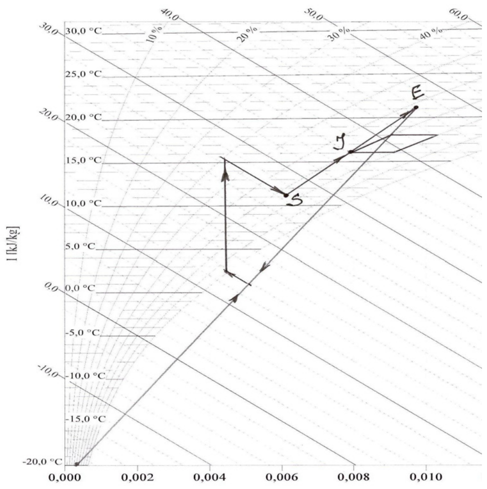

Fig. 7. Air handling process with the rotating heat exchangers in the stand for feedlot stock and breeding pigs

In the following investigation, the air exchange (kg/s) and energy consumption (kWh) for air handling are calculated for each group of animals under 3 different working conditions of the ventilation system:

1. Ventilation system with heating up and humidification of the supply air;
2. Ventilation system with heating up of the supply air;
3. Ventilation system with heat recovery (regeneration).

Calculations are carried out by taking into account the average air temperature (°C) of the five coldest days in Latvia. The calculation results are presented in Table 2.

Table 2. Calculated heat consumption in three different pigsties for three different ventilating systems

Nr	**Group**	**I vent system kW**	**II vent system kW**	**III vent system kW**
1.	Pigsty for farrowing pigs and sows with piglets	263	184	100
2.	Pigsty for nursery pigs	224	167	73
3.	Pigsty for breeding, gestation and growing/finishing pigs	460	317	133

CONCLUSIONS

1. Most of energy loses at piggeries proceed through ventilating system for achieving the indoor temperature.
2. The energy consumption in ventilating system will be much higher for achieving the specific moisture regime at piggeries.
3. Using regenerative heat exchangers with effectiveness 50% get provide heat and moisture regime, but energy consumption are reduce for 30–40% compare with tradition ventilating system.
4. This data in further possible to take for analyze different variants of ventilating systems for capital investment expedience.

REFERENCES

1. Krēsliņš A. Gaisa kondicionēšana rūpnieciskajās un sabiedriskajās ēkās. Rīga 1975.
2. Zālītis L., Hmeļņickis A. Zoohigiēnas praktikums. Rīga, 1971.
3. Mechanical Ventilating Systems for Livestock Housing. Handbook 32 of Midwest Plan Service, 69 p.
4. ASHRAE Handbook. Fundamentals, 2005.
5. ASHRAE Handbook. HVAC Applications, 2007.
6. Yoshie R. et al. Numerical Analysis of Heat and Moisture Transfer in Desiccant Wheel for Dehumidification. Proc. CLIMA 2007, Helsinki.
7. Влажный воздух. Справочное пособие АВОК. Москва – 2004.
8. www.thepigsite.com/

CYSENI 2009, May 28-29, Kaunas, Lithuania
ISSN 1822-7554, www.cyseni.com

INFLUENCE OF BUILDING SHAPE INDICATOR ON BUILDING ENERGY CONSUMPTION EFFICIENCY

R. Savickas
Department of Heating and Ventilation
Vilnius Gediminas Technical University
Saulėtekio ave. 11, LT 10223- Vilnius
Phone +370 652 27398
E-mail: svk@ap.vgtu.lt

ABSTRACT

Buildings have various shapes and building energy consumption depends upon building surface area – larger surface area – greater energy consumption. However, heating demand depends not only from building envelope surface area, insulation, inside and outside temperatures but also shape because of influence such factors as self-shading, lee and etc. This study has investigated dependence of heat energy consumption upon building shape factor, expressed by various authors given and in this investigation derived theoretical formulas. These formulas relates building surface area and its volume. 123 buildings of 11 different project types were analysed in the investigation. This article shows that in investigation mentioned theoretical formulas do not mach exactly with practical data. The main reasons can be described as follows – even building is of the same project, but its heat transfer coefficient can vary in few percents upon construction quality, also energy consumption depends upon building maintenance quality (one building after few decades of exploitation can have very leaky windows, damp roof and etc., another of the same construction year – opposite situation). Energy demand for space heating also depends upon building orientation, self-shading, window to wall ratio and so on, that compactness factor do not describes. Therefore, energy consumption of the same buildings of the same project differs in a wide range. As an example, the specific heat consumption value of a largest investigated buildings group (53 buildings) average value varies in range of about ± 15%. So building shape dependence on actual heat energy consumption can has a trend, but not with high coefficient of determination (R^2) value. For the investigated buildings energy consumption depends on derived surface to volume coefficient C_b and has a dependence of R^2=0,6727. Investigation presents the dependence equation.

Keywords (building shape, energy consumption, energy efficiency, building shape coefficient)

1. INTRODUCTION

In present days the expenses for heating of premises rises in inadequate way. There are a lot of methods and recommendations to save energy in existing or buildings under reconstruction, but many people forget that efficient building must be developed efficient by its nature almost in a building design stage. From this point of view has born such terms as “passive building”, whose main idea is to decrease energy consumption in building to a minimum value by such means as big thermal insulation and small infiltration level. So everybody agree that the main role plays thermal insulation thickness and heat losses for ventilation/infiltration but optimizing these values to the maximum logical value we come to the stage when thicker insulation layer do not plays significant role anymore and we have to turn back into another tools. So after insulation level and ventilation influence to the building as the following – third mean I describe as building shape factor and building orientation to the cardinal point, also the site selection. Most of studies only describes that building form must be simple, but do not describes the total result on energy efficiency. This investigation is concentrated to found these answers.

2. METHODOLOGY

Most of building or energy related standards and codes do not take any attention to building form, statutory acts do not regulate the shape of building, so the building form is left to be chosen free by architect desired flexibility in the design stage. P. Depecker [2] and W. Pessenlehner [5] have took attention that building form can strongly influence energy efficiency for residential buildings in Europe, but there are very limited studies investigating the impact of form to thermal performance of buildings. Optimisation of building form can be proceed by taking into consideration that energy effective building shape also decreases the building construction costs. But non of authors have provided recommendations or simple guidelines for architects to help choose energy efficient building shape which influences not only heating but also cooling load. So this research is developed to indentify the impact of building form upon heating energy, to develop simple methodology for that and compare results with energy efficiency analysis of actual buildings and actual energy consumption.

The building shape can be identified by various factors and criteria. P. Depecker [2] has introduced building shape coefficient C_f as follows:

$$C_f = \frac{S_e}{V}, \tag{1}$$

where:

C_f – building shape coefficient, m^{-1};
S_e – total building envelope area, m^2;
V – total building volume, m^3.

To reduce heating and cooling energy for building by reducing heat transmission through the envelope area S_e, building shape coefficient C_f for certain building should be as low as possible. It would be expedient to have non-dimensional coefficient, so W. Pessenlehner and A. Mahdavi [5] have introduced non-dimensional shape indicator – the relative compactness, defined as the ratio of a reference building model shape factor to the actual building shape factor:

$$RC = \frac{C_{f(ref)}}{C_f}, \tag{2}$$

where:

RC – non-dimensional shape indicator;
$C_{f(ref)}$ – reference building model shape factor;
C_f – actual building shape factor.

Above mentioned authors gives an example that if reference building has a cubical shape with width c and the actual building has a rectangular shape with length a and width b, then the RC value can be obtained assuming that both buildings have the same height

$$RC = \frac{C_{f(ref)}}{C_f} = \frac{4c^2}{2(a+b)c} = \frac{2c}{(a+b)} \tag{3}$$

The width of a reference building model in a case, then building volume remains the same for all buildings, can be eliminated and the related compactness can be expressed as a function of only the dimensions of the actual building for a rectangular building [5]:

$$RC = \frac{2\sqrt{ab}}{(a+b)} \tag{4}$$

The relative compactness of this equation is a fraction that varies from 0 to 1 and the higher is RC value the more compact is the building. Also W. Pessenlehner and A. Mahdavi have investigated buildings with different compactness value, but having the same building volume of 250 m^3 and the same height of 2.5 m. They have investigated eight different buildings types – from very long to the square shape. All these eight types they divided into 5 more types according to window to wall glazing ratio (WWR) and every type of WWR ratio to the five glazing types. Also they take into consideration the impact on energy performance of four orientation types according to site location and got results of about 8800 simulations.

Building morphology, transparency and energy performance was investigated by W. Pessenlehner and A. Mahdavi [5]. They have described buildings geometric compactness, expressed by the relation between the volume of a built form and its surface area. Compactness does not capture the specific morphology or three-dimensional architectural form and massing of a building's shape. Though it as through via self-shading could be influenced the thermal performance. Compactness does not capture the amount and distribution of the transparent components, so corresponding radiate gains and losses are not accounted. Also changing the orientation of a building does not change its compactness, but may affect thermal performance. A research was based on a modular geometry system derived based on an elementary cube (3.5×3.5×3.5 m) and to generate different building shapes, 18 such elements were used and created 54 morphological variations (Fig. 1.).

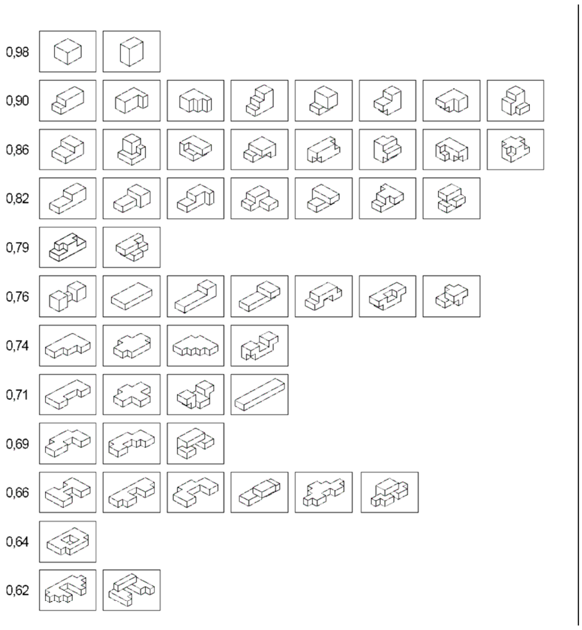

Fig. 1. Generated shapes [5]

To specify the compactness the "Relative compactness" (RC) indicator was used, derived from its volume (V) to surface (A) ratio, compared to the most compact shape with the same volume. For the sphere as reference:

$$RC = 4{,}84 \cdot V^{0{,}66} \cdot A^{-1} \tag{5}$$

For the cube as reference:

$$RC = 6 \cdot V^{0{,}66} \cdot A^{-1} \tag{6}$$

The research simulation shows many results and the most interesting is the relation between heating load and RC (Fig. 2.). The correlation coefficient is relatively high and equal to $R^2=0.88$. The most by W. Pessenlehner and A. Mahdavi given relations have linear trend. Also they make an assumption that RC is not volume dependant.

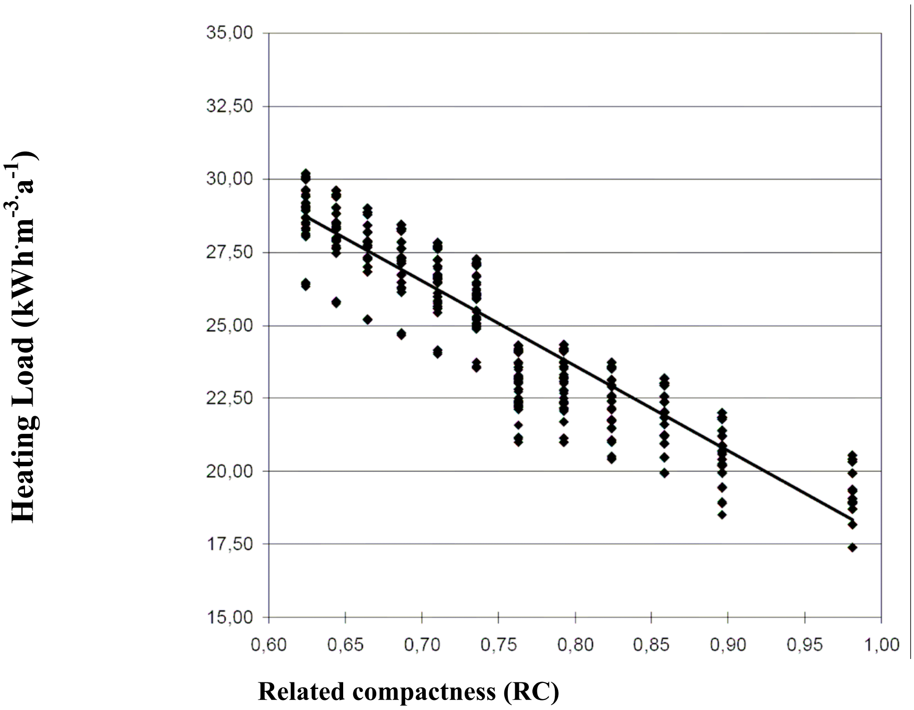

Fig. 2. Simulated heating loads as a function of RC [5]

3. RESULTS AND DISCUSSION

Since all of above authors have performed interesting investigations, it is interesting to check these results in practice for Lithuania conditions. For the investigation were taken 123 buildings. All buildings have the same public function, all of them were built before 1992 year according the same building standards and codes and have the similar structure of walls and windows, all of them are located in Vilnius, so these buildings perfectly are suitable for the building shape indicator investigation upon heat energy efficiency.

These 123 buildings were built according to 11 different project types. The distribution of the number of buildings within project types is presented in a Table 1.

Table 1. The distribution of the number of project types

No.	Project type	Number of project types
1.	Project type No.1	9
2.	Project type No.2	19
3.	Project type No.3	13
4.	Project type No.4	9
5.	Project type No.5	3
6.	Project type No.6	4
7.	Project type No.7	2
8.	Project type No.8	53
9.	Project type No.9	1
10.	Project type No.10	9
11.	Project type No.11	1
	TOTAL:	**123**

During the investigation was collected the data of heat energy consumption during the last five 2003–2007 years. Buildings have different heating area, also outside temperature during every month and year differ. In a reason to compare these buildings we have to eliminate these factors, so heat energy is compared by specific heat energy value, derived dividing heat energy consumption by building area and degree-days. Theoretically these specific heat energy consumption values of certain building has to correspond in 100%, but practically they differ, so for the investigation are taken average values of specific heat energy values for every of five project types.

According to W. Pessenlehner and A. Mahdavi "Relative compactness" calculation formulas were calculated RC values, derived from its volume (V) to surface (A) ratio, compared to the most compact shape for every different project types. The results are presented in a Table 2.

Table 2. RC values for the reference as sphere and as cube

No.	Project type	**RC** for the sphere as reference	**RC** for the cube as reference
1.	Project type No.1	0,74	0,91
2.	Project type No.2	0,57	0,70
3.	Project type No.3	0,65	0,80
4.	Project type No.4	0,38	0,47
5.	Project type No.5	0,52	0,64
6.	Project type No.6	0,50	0,62
7.	Project type No.7	0,77	0,96
8.	Project type No.8	0,88	1,09
9.	Project type No.9	0,55	0,68
10.	Project type No.10	0,58	0,71
11.	Project type No.11	0,67	0,83

According to all above mentioned authors heat energy consumption decreases increasing RC value. Relation between RC for the sphere as reference and specific heat consumption value is shown in Fig. 3 and relation between RC for the cube as reference and specific heat consumption value is shown in Fig. 4.

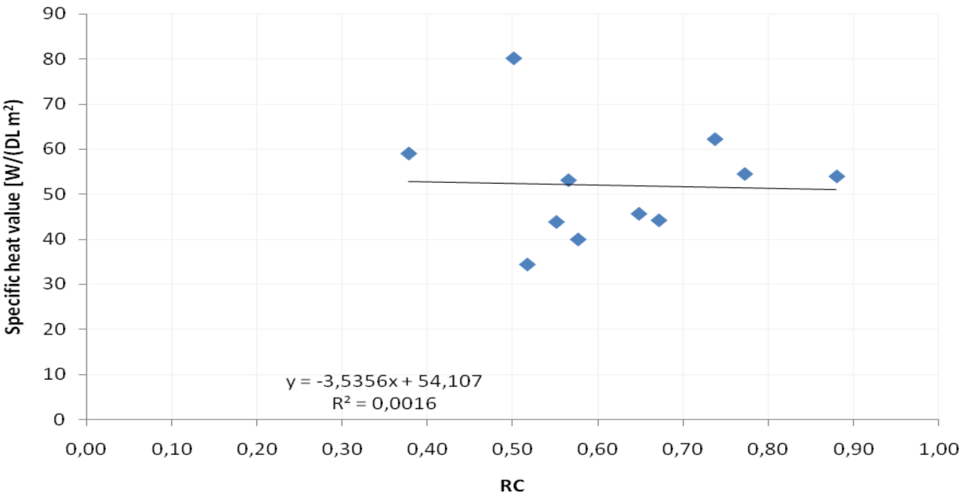

Fig. 3. Relation between RC for the sphere as reference and specific heat consumption value

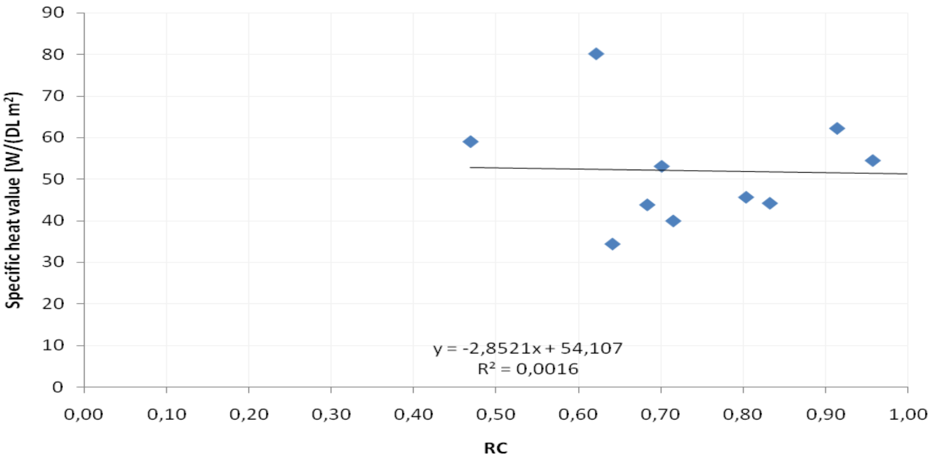

Fig. 4. Relation between RC for the cube as reference and specific heat consumption value

Neither Fig. 3. or Fig. 4. shows relation between RC and heat consumption, (R^2 value for sphere equal to R^2=0,0016 and for cube R^2=0,0016). That means that the methodology of all above mentioned authors can not be applied in practice in Lithuania, because the methodology is not grounded by experimental data. One of the reasons can be the fact that all calculations they have performed for the same building height and volume.

All above mentioned authors have performed a hard work and a lot of calculations but the principles they applied do not correspond to Lithuania conditions and also can be practiced hardly because of such shortcomings as the same building height. Practically for the designers in a building design stage is desirable that the building shape factor would be dimensionless and applied for all types of buildings, for different heights and etc. So I think we have to go to the basis and to develop another different but simple methodology. The ideal form in a nature is sphere, because it takes the smallest surface among all surfaces enclosing a given volume and it encloses the largest volume among all closed surfaces with a given surface area. For this reason the sphere commonly appears in nature - for instance bubbles and small water drops are roughly spherical, because the surface tension locally minimizes surface area. These factors tend me to develop non-dimensional shape coefficient, showing the relation of actual building to ideal theoretical form – sphere. By all means talking, larger is surface area, larger must be energy consumption and that must be seen from data trend. If the actual data would not show the dependence that means that exist other factors, which influence dependence upon energy more than shape. So will be used relation of sphere surface area (A_s) to it's volume (V_s) value or shape coefficient C_s in comparison with reference building shape coefficient C_b. Analysing the relation of ideal form - sphere surface to it's volume is seen that it is not constant and increasing the volume of sphere C_s value approaches to zero (Table 3).

Table 3. Sphere surface area (A_s), it's volume (V_s) and A_s/V_s values

Name	**Values**							
Sphere volume V_s	1	3	30	112	300	3.000	30.000	150.000
Sphere surface area A_s	5	10	47	112	217	1.006	4.669	13.652
C_s	4.84	3.35	1.56	1.00	0.72	0.34	0.16	0.09

So the non-dimensional shape coefficient for every reference building must to show the relation of sphere C_s to reference building C_b assuming that the volume of reference building and sphere are the same:

$$SC = \frac{C_s}{C_b}, \tag{7}$$

where:

SC – non-dimensional shape coefficient;
C_s – sphere shape coefficient;
C_b – actual building shape coefficient.

The surface area A_s of a sphere of radius r is:

$$A_s = 4\pi r^2. \tag{8}$$

It's volume V_s is:

$$V_s = \frac{4}{3}\pi r^3. \tag{9}$$

So the shape coefficient C_s can be described as follows:

$$C_s = \frac{A_s}{V_s} = \frac{4\pi r^2}{\frac{4}{3}\pi r^3} = \frac{3}{r}. \tag{10}$$

That equation has the only variable – diameter r. So (7) equation we can update to:

$$SC = \frac{C_s}{C_b} = \frac{{}^{3}\!/_{r}}{C_b} = \frac{3}{C_b r}. \tag{11}$$

Calculating the shape coefficient of real building we'll have it's dimensions so and the volume. The volume of sphere V_s will be the same as buildings volume V_b and in (11) Equation we can instead of sphere diameter to write Equation of sphere diameter calculation according to sphere (or building) volume:

$$SC = \frac{3}{C_b r} = \frac{3}{C_b\left(V_s \frac{3}{4\pi}\right)^{\frac{1}{3}}} = \frac{3}{\frac{A_b}{V_b}\left(V_s \frac{3}{4\pi}\right)^{\frac{1}{3}}} = \frac{3V_b}{A_b\left(V_b \frac{3}{4\pi}\right)^{\frac{1}{3}}} \tag{12}$$

Relation between SC for the sphere as reference and specific heat consumption value is shown in Fig. 5

Fig. 5. does not shows any relation between SC and heat consumption (R^2=0,0038). That means that compactness relation of reference building cannot be compared with sphere compactness relation.

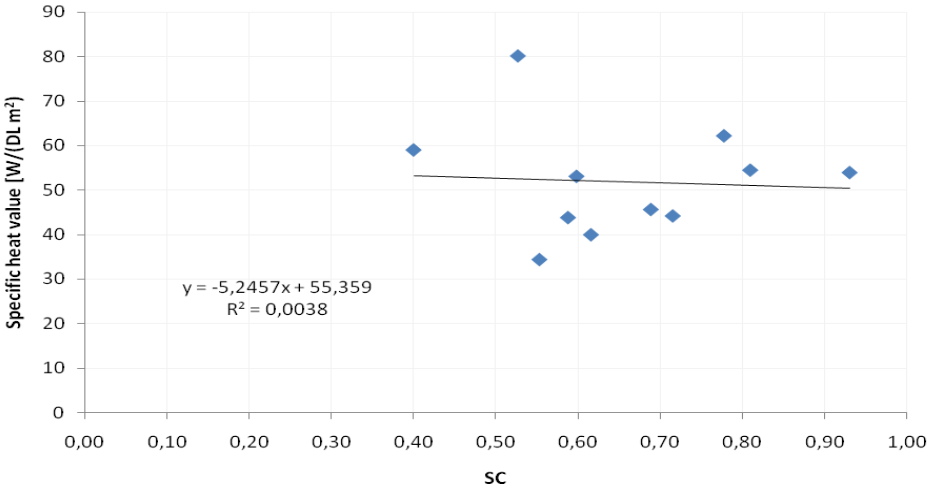

Fig. 5. Relation between SC for the sphere as reference and specific heat consumption value

Nonetheless the energy consumption dependence upon origin C_b value, shown in Fig.6, shows dependence, which is much stronger (R^2=0,6727), but do not a lot. The dependence upon energy consumption is expressed by (13) equation:

$$y = 64{,}572x + 25{,}643 \tag{13}$$

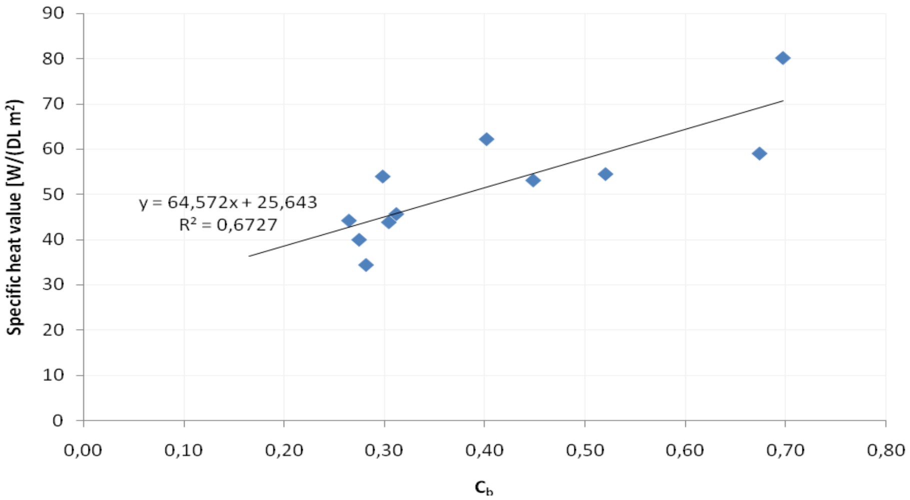

Fig. 6. Heat consumption dependence onC_b

This investigation shows that above mentioned theoretical formulas do not mach exactly with practical data. The main reasons can be described as follows – even building is of the same project, but it's heat transfer coefficient can vary in few percents upon construction quality. Later energy consumption depends upon building maintenance quality, because one building after few decades of exploitation can have very leaky windows, damp roof and etc., another of the same construction year – opposite situation. Also heat energy depends upon site orientation, self-shading, window to wall ratio and so on, that is not described by compactness factor. So energy consumption of the same buildings of the same project differs in a wide range. As an example the specific heat consumption value of a largest investigated buildings group (53 buildings) average 54.0 W/DL value varies in 46.8–62.9 limits or about ± 15%. So building shape dependence on energy consumption in principle must have trend, but not with high R^2 value. For the investigated buildings energy consumption dependence upon surface to volume (size) and shape coefficient C_b has R^2=0.6727 and the dependence can be expressed by (13) Equation.

4. CONCLUSIONS

This study has investigated dependence of total energy consumption upon building shape factor, expressed by various authors given theoretical formulas. These dependence formulas are related with building surface area and volume. Nonetheless, this investigation shows that:

1. Theoretical building compactness formulas do not mach exactly with practical data and cannot be grounded by practical data - R^2 value for sphere equal to R^2=0.0016 and for cube R^2=0.0016. Should be noticed that during calculations were eliminated influencing factors due to different outside and inside temperatures, heating periods, heating area, hot water but factors due to different volume of buildings remains. In further research should be taken special attention to volume of building.
2. Derived related compactness SC does not shows any relation between compactness and heat consumption (R^2=0.0038).
3. The main reasons of that are that even average specific heat consumption 54.,0 W/DL value of largest investigated building group varies in 46,8-62,9 limits or about ± 15%.
4. The absence of practical substantiation does not let to call in question theoretical formulas, because they are grounded by theoretical experiments.
5. Investigated buildings have a simple surface to volume (size) and shape coefficient C_b dependence of R^2=0.6727 upon energy consumption and the dependence can be expressed by (13) equation. (See comment 8)

REFERENCES

1. K. Ouertani. Impact of shape on building energy use in Tunisia // “Cenergypt”, Tunisia Polytechnic school, Tunisia, La Marsa 2078. 2005, p. 1–8.
2. P. Depecker, C. Menezo, J. Virgone, S. Lepers. Design of buildings shape and energetic consumption // Building and environment, 2005, Vol. 30, No.2, p. 201–222.
3. H. Jedrzejuk, W. Marks. Optimization of shape and functional structure of buildings as well as heat source utilization. Basic theory // Building and environment, 2002, Vol. 37, p. 1379–1383.
4. W. Marks. Multi-criteria optimization of shape of energy-saving buildings // Building and environment, 1997, Vol. 32, No. 4, p. 331–339.
5. W. Pessenlehner, A. Mahdavi. Building morphology, transparency, and energy performance // Eight international IBPSA Conference Proceedings, Eindhoven, Netherlands, 2003.
6. D. R. Prestemon. Building energy-efficient new houses // Iowa State University of science and technology, 1992, p. 1–3.
7. F. Gordon. Feasibility study of renewable energy and energy efficiency options for a 79-unit condominium development in south Boston // 79-unit condominium development in south Boston, Boston. 2005-05-31, p. 13–18.

CYSENI 2009, May 28-29, Kaunas, Lithuania
ISSN 1822-7554, www.cyseni.com

LIFE CYCLE MODEL FOR THE EVALUATION OF ENERGY EFFICIENCY IN BUILDINGS UNDER RENOVATION

L. Užšilaitytė
Vilnius Gediminas Technical University
Department of Heating and Ventilation
Saulėtekio ave. 11, LT-10223 Vilnius-40, Lithuania
E-mail: Lina.Uzsilaityte@ap.vgtu.lt

ABSTRACT

Building is a complicated system, consuming big amount of energy, making significant impact on environment and social welfare. The main function of the building is to provide people with conditions to live, work, study and relax. Building demands permanent flow of energy to function. Thus it becomes a polluting object. Therefore the reduction and optimisation of energy demand is a very important issue allowing solving global and political problems such as climate change, energy independence and social welfare.

Although scope of the new buildings construction increases as well as the energy performance requirements for the newly constructed buildings, there are much more old buildings which require renovation. Here the problem is faced – what criteria should be used to evaluate benefits of the renovation and assess reasonable scope of the renovation. To follow only economical criteria while evaluating benefits of the renovation is not sufficient. Systemic, sustainable standpoint is necessary to gain maximal benefit for both: building owner and society.

In the paper life cycle model for the evaluation of energy efficiency in the buildings under renovation taking into account building rehabilitation, energy, environmental and economical aspects during the whole building lifetime is proposed.

Keywords: life cycle assessment, buildings, energy efficiency

1. INTRODUCTION

Sustainable development means that the needs of the present generation should be met without compromising the ability of future generations to meet their own needs. Unsustainable use of energy causes climate change, depletes natural resources, threaten public health. EU Sustainable development strategy calls to respect the limits of the planet's natural resources and ensure a high level of protection and improvement of the quality of the environment, to prevent and reduce environmental pollution and promote sustainable consumption and production, to promote integration of economic, social and environmental considerations etc. One of the objectives is to improve management and avoid overexploitation of natural resources, while avoiding the generation of waste and enhancing efficient use of natural resources by applying the concept of life-cycle thinking and promoting reuse and recycling etc. [1]

The building stock is a complex system, consuming 40% of final energy both in Lithuania and European Union [2, 3] and thus making a significant impact on the environment and social welfare. Although a question is posed what is more reasonable to demolish old buildings and to build the new ones or to renovate them, results of the research show that renovation of the buildings is more acceptable alternative both in respect of energy and environment [4, 5, 6].

The main function of the building is to enable people to live, work, learn and relax. In order for the building to function, it requires continuous energy flow. Thus the building becomes the source of pollution. Although no pollution can occur at the building site, it occurs at the objects that produce energy for the building. Reduction and optimization of energy demand of the buildings is a major issue, which also helps solving such global and political problems as climate change, energy independence, and social welfare.

Although the scope of construction of the new buildings increases and energy efficiency requirements for buildings become tighter, there are much more old buildings to be renovated. In Lithuania 89% of buildings were built before 1990 [7]. Therefore the largest energy saving potential exists in these buildings. Here the problem is faced – what criteria to use for evaluation of the benefits and scope of the building renovation. Rely solely on traditional economic criteria in assessing benefits of the building renovation is not sufficient, because the renovation has also an impact on energy, environment and social aspects. An integrated, systematic, sustainable development approach allowing to evaluate not only the immediate costs and benefits, but also the impact of renovation on building physical state, economic costs, energy consumption and pollution emissions during the building life cycle, is needed.

In practice economical criteria (payback time, internal rate of return, net present value, cost of conserved energy) prevails for evaluation of the building renovation projects which are calculated during standard energy audits. In Article [8] two-factor (energy efficiency and improvement of physical state of a building) approach for evaluation of the renovation projects, where benefits of the building rehabilitation in renovation projects are evaluated is proposed. Multi-criteria decision making methods [9] are used for evaluation of building renovation projects, which allow using variety of different criteria describing the project. Life cycle analysis is more widely applied, but mostly for new buildings or for general evaluation or evaluation of recycling potential without emphasis on the building renovation stage [10, 11, 12 and 13].

Goal of this paper is to propose life cycle model for the evaluation of energy efficiency in buildings under renovation, taking into account building rehabilitation, energy, environmental and economical aspects during the whole building lifetime. With the view of this goal the impact of energy efficiency increase in buildings on energy, economy, environment and society and concerns of different stakeholders of the process is analysed and criteria for the evaluation of energy efficiency in buildings under renovation allowing to look at renovation from the point of view of sustainable development and to make evaluation in terms of life cycle are identified.

2. ENERGY EFFICIENCY BENEFITS, OBJECTIVES OF THE STAKEHOLDERS AND EVALUATION CRITERIA

Energy efficiency benefits may be considered in several aspects – the energy, economical, environmental, and social. While increasing energy efficiency, energy demand and negative impact on the environment is reduced. The main economic effect of the implementation of energy efficiency measures is reduced energy costs and the possibility of savings to use for the increase of comfort. In addition, costs of environmental damage are reduced. While renovating buildings, repair costs are reduced, the building becomes more valuable. Inadequate thermal comfort conditions in depreciated buildings have negative social effects – decreased working capacity, increased morbidity and mortality. While improving the thermal comfort conditions, the costs incurred by the state for institutionalization, medicines because of the loss or reduction of working capacity are reduced. Energy efficiency programs also have a positive impact on employment. [14, 15, 16]

Increase of energy efficiency in buildings is related with many stakeholders – building owners and users, utilities, financial companies, governments etc. Stakeholders can be divided according to their objectives as their objectives determine criteria for the selection of energy efficiency measures. Benefits and costs of energy efficiency are not allocated equally to different stakeholders. Benefits to one stakeholder can become costs to the other. For example decrease of end-user energy consumption will decrease income for energy companies [15]. This is one of the conflicts while evaluating energy efficiency measures.

Energy end-user can be a building owner, resident, tenant, renter, or seller. It determines the objectives for implementation of energy efficiency measures. The main factors determining decision to invest into energy efficiency are high energy prices, thermal comfort problems and deterioration of the building. Probably the most important restrictive factor is ability to invest, which usually is limited whereas more efficient solutions are usually more expensive and have long payback time.

Energy company may be interested in increase of energy efficiency at the energy end-user if it has lack of generating capacities, what allows decreasing investment into new capacities. In this case it may start demand side management activities. If the company had overcapacity, it will face decrease of income, what usually is not the interest of the company.

Energy service company is interested in more energy efficiency projects as it is related with their income. The main factor determining the choice of energy efficiency measures is profitability and the shortest payback time of the project. However this stakeholder is important as it may encourage investments into energy efficiency.

Financial company is interested to invest, but invest into big projects with low risk. The main criteria to choose the project are profitability, payback time and degree of the risk.

Factors determining the choice of the government depend on the policy of the government. If it implements sustainable development policy and energy, environmental, social problems seek to be solved, energy efficiency measures will be evaluated according to the criteria in line with the sustainable development concept. Also abilities of the government to invest are important.

While summarising benefits of the energy efficiency and objectives of different stakeholders, the main criteria determining the choice of energy efficiency measures are increase of thermal comfort, decrease of energy consumption, decrease of emissions, decrease of building deterioration and increase of property value and cost-efficiency of the project.

3. LIFE CYCLE MODEL OF THE BUILDING

3.1. Requirements and maintenance of the buildings

The purpose of the buildings is multifunctional. They have to satisfy human (functionality, safety, health, comfort), economical (economy of investments, construction and lifetime), cultural (lifestyle, building traditions, business culture, aesthetics, architectural styles and trends, image), ecological (economy of raw materials, energy, environmental burdens and waste, biodiversity) requirements [17, 18]. According to the Council directive 89/106/EEC and it implementing Law on Construction of the Republic of Lithuania, buildings have to comply with 6 essential requirements: mechanical resistance and stability, safety in case of fire, hygiene, health and environment, safety in use, protection against noise and energy economy and heat retention [19].

Although life time of the building usually is considered up to 100 years, buildings older than couple hundred of years exist. Appropriate and timely maintenance and reconstruction is required to ensure that building complies with the above mentioned 6 essential requirements.

In this paper building is divided into passive and active technical systems. The passive technical system is a structural part of the building, protecting interior of the building from the impact of exterior environment. These are envelopes, retaining and bearing constructions, which do not directly consume energy. The active technical system is engineering systems creating appropriate microclimate and ensuring technological processes in the building, which require energy for operation.

3.2. Life cycle of the building

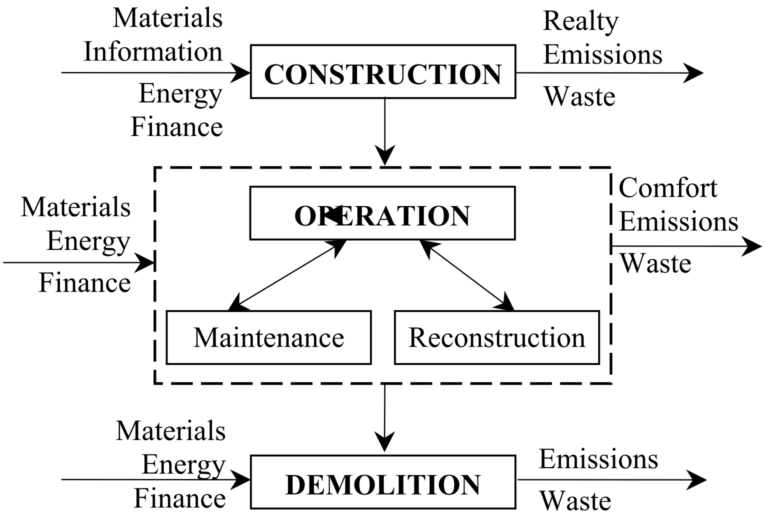

Fig. 1. Life cycle of the building

With a view of long-term sustainable use of the building, it is reasonable to analyse it with regard of its life cycle. It allows instead of solving local problems to evaluate entirety and to avoid situation when one solved problem creates the new one. The main phases of the building life cycle are construction, operation, which includes maintenance and reconstruction, and demolition (see Fig. 1). In each phase input and output flows take place – information, materials, energy, finance, emissions, waste, comfort, realty, which can be evaluated quantitatively and qualitatively.

Evaluation criteria presented in chapter 2 of this paper include technological, energy, environmental and economical aspects. Therefore it is proposed to divide life cycle of the building into technological, energy, environmental and economical sub-cycles later joining the results of the evaluation for decision making.

3.2.1. Technological model of the building life cycle

Technological life cycle of the building encompasses change of the building value as a physical unit. Building is composed of different parts and elements, which deteriorate physically and morally with time. Due to deterioration value of the building decreases as well as comfort and energy consumption increases. It is considered that the building is physically deteriorated when its resistance and stability is decreased, heat and noise conduction is increased, hydro insulation worsen due to natural factors and processes in the building. Moral deterioration of the building is related with the technological development [20].

To compose a technological model of the building, life cycle parts and elements of the building, their lifetimes and trends of the deterioration have to be identified [21].

Lifetime of the building is a period of time during which the building, which is normally exploited taking into account construction products, local and climate conditions, complies with the essential requirements for the buildings [22]. Parts and elements of the building also have their lifetimes.

Deterioration trends of the building, its elements and parts can be expressed as a mathematical function. Precise function can be found using data of statistical observations or after visual estimation of the building state. In this paper graphical [23] and analytical [21] functions, which express residual value of the building (the opposite value of deterioration) are used.

In Fig. 2 technological life cycle model of the building is presented. Thin lines show change of the residual value of the building parts (construction and engineering systems), assuming that those parts or their elements are replaced after the end of their economical lifetime (period after which the part or element can be still used, but its reliability is not ensured). Walls, windows and electricity system lines overlap because of the assumed the same their economical lifetime. The bold line shows change of the residual value of the building. Residual value of the building is calculated as the weighted average of the residual values of the building parts. Weight coefficients are estimated according to the cost share of certain part of the building in total building construction costs.

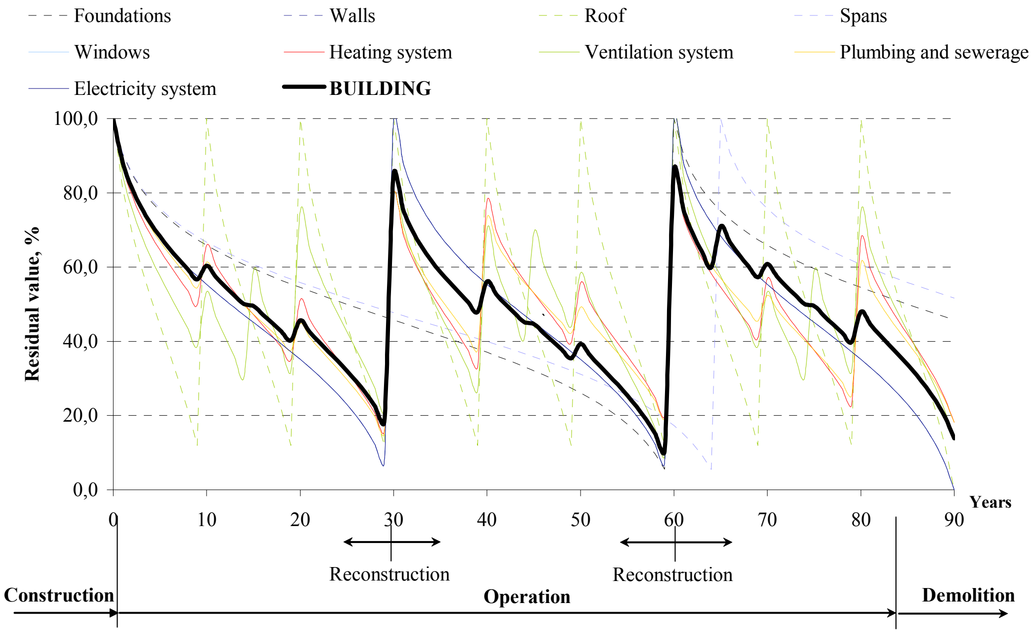

Fig. 2. Technological model of the building life cycle

If the dates of the reconstructions and repairs are known, the real residual value of the building, scope and impact of the renovation on the residual value of the building can be estimated. While using this model it is possible to estimate the deterioration of the building at any time of its operation and to estimate, how the planned renovation activities will change its value.

3.2.2. Energy model of the building life cycle

Energy life cycle of the building shows the change of energy consumption during building lifetime taking into account all flows of energy.

Building has to be designed ensuring efficient and saving use of energy. However it is insufficient to judge energy efficiency only according to the consumption of heat and electricity. The real energy efficiency of the building has to be expressed in primary energy, i. e. amount energy value of the fuel required to produce necessary amount of heat and electricity consumed.

Implementation of the energy efficiency measures allows reducing operational use of energy in engineering systems. However energy is required to create and install these measures (embodied energy). The more performance of the building is improved the more energy is consumed to implement this. This is especially relevant issue in case of low-energy or passive buildings [13].

Total energy consumption (TE, MWh) during building life cycle includes primary energy consumption for installation of passive and active technical systems of the building and their maintenance, reconstruction and demolition (EE, MWh) and operational primary energy consumption (OE, MWh) in active technical system:

$$TE_n = \sum_{i=1}^{n} EE_i + \sum_{i=1}^{n} OE_i \tag{1}$$

Where: n – age of the building, years; i – calculating year.

Embodied energy amounts primary energy consumption for construction, maintenance, reconstruction and demolition of the building:

$$EE_i = EE_i^c + EE_i^m + EE_i^r + EE_i^d \tag{2}$$

Where: EE_i^c – primary energy consumed during construction of the building for manufacturing, transportation and installation of the parts and elements of the building, MWh. This is a unitary value having a value in the year when the building is constructed; EE_i^m – primary energy consumption during maintenance of the building, MWh. This is an iterative value, which can be precisely calculated registering all elements replaced and installed and primary energy consumed during each repair; EE_i^m – primary energy consumption during reconstruction of the building for production, transportation and installation of the building elements and parts, MWh. This is an iterative value occurring in certain intervals; EE_i^d – primary energy consumption for demolition of the building, MWh. This is a unitary value occurring in the year when building is demolished.

Calculation of the embodied energy consumption often is a challenging task, as usually required data is not available, especially in the building maintenance phase. However only through such calculations it is possible to obtain real results of the building life cycle.

Operational energy consumption amounts energy value of the fuel consumed in a building and energy value of the fuel used for the production of heat and electricity supplied via networks:

$$OE_i = OE_i^f + OE_i^{el} \cdot \eta_{el} + OE_i^h \cdot \eta_h \cdot \gamma_{in} \,. \tag{3}$$

Where: OE_i^f – fuel consumption in building, MWh; OE_i^{el} – consumption of electricity supplied from the grid for lighting, operation of equipment and technological processes, MWh; η_{el} – coefficient, evaluating electricity generation efficiency, allowing to recalculate electricity consumption into primary energy; OE_i^h – district heating consumption in building, MWh; η_h – coefficient, evaluating efficiency of district heating generation and supply, allowing to recalculate consumed heat into primary energy; γ_{in} – coefficient, evaluating insulation deterioration, allowing to estimate increase of the heat consumption because of the worsen thermal characteristics of heat insulation.

Fig. 3 presents change of energy consumption during building life cycle. Sum of “operational energy” and “embodied energy” show total primary energy consumption of the building, which is periodically modernised, assuming that after each reconstruction operational energy consumption will decrease due to technological progress. “Status quo” line indicates the total energy consumption if the building was not modernised. The difference between status quo and sum of operational and embodied energy is equal to the saved energy.

Fig. 4 shows change of the embodied energy consumption. Rapid increase of the embodied energy consumption shows amount of primary energy consumed during reconstructions of the building.

Using energy life cycle model for evaluation of the building renovation impact of different renovation alternatives on energy consumption of the building life cycle can be estimated. Energy consumption in each year of the building lifetime can be calculated. Different tasks can be solved – minimization of operational energy consumption; minimisation of embodied energy consumption; optimisation of total energy consumption; estimation how different solutions for reduction of operational or embodied energy consumption affects total energy consumption after the renovation etc.

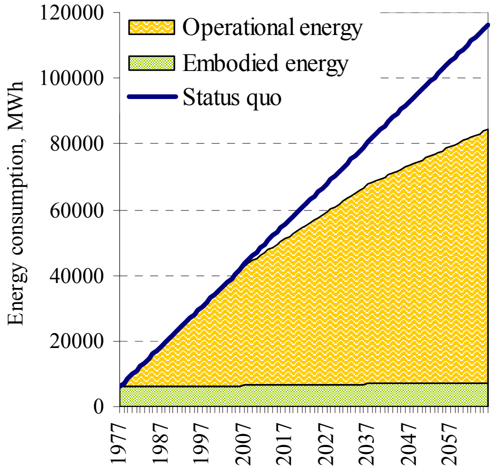

Fig. 3. Energy consumption of the building

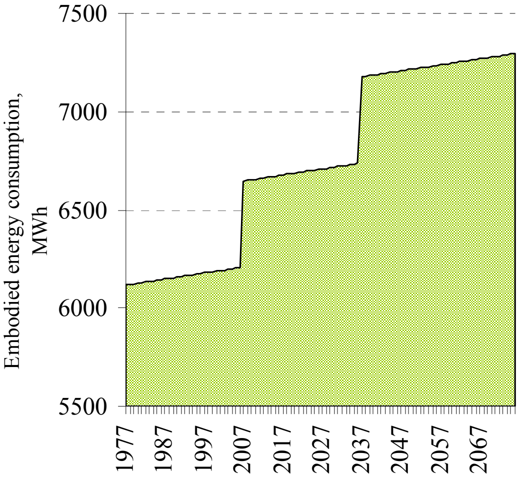

Fig. 4. Embodied energy consumption of the building

3.2.3. *Environmental model of the building life cycle*

Energy sector poses the biggest impact on climate change, what is one of the most relevant topics at the moment. Greenhouse gases became a commodity, in certain cases necessity for energy and industrial activities. Therefore it is reasonable to evaluate environmental benefits of the energy efficiency measures.

Likewise energy consumption, greenhouse gases emissions expressed in equivalent of carbon dioxide during building life cycle is calculated. Total greenhouse gases emissions (TG) during building life cycle amount emissions related to embodied energy (EG) and emissions related to operational energy (OG) consumption:

$$TG_n = \sum_{i=1}^{n} EG_i + \sum_{i=1}^{n} OG_i \; . \tag{4}$$

Embodied greenhouse gases emissions occur during construction, maintenance, reconstruction and demolition of the building:

$$EG_i = EG_i^c + EG_i^m + EG_i^r + EG_i^d \; . \tag{5}$$

Where: EG^c – emissions due to construction of the building, tCO_{2eq}; EG_i^m – emissions due to maintenance of the building, tCO_{2eq}; EG_i^r – emissions due to reconstruction of the building, tCO_{2eq}; EG^d – emissions due to demolition of the building, tCO_{2eq}.

Operational greenhouse gases emissions occur during operation of the engineering systems of the building:

$$OG_i = OE_i^f \cdot \tau_f + OE_i^{el} \cdot \eta_{el} \cdot \tau_{el} + OE_i^h \cdot \eta_h \cdot \gamma_{in} \cdot \tau_h \,. \tag{6}$$

Where: τ_f - fuel pollution coefficient, tCO_{2eq}/MWh; τ_{el} - pollution coefficient of electricity supplied from the grid, tCO_{2eq}/MWh; τ_h – pollution coefficient of district heating production and supply, tCO_{2eq}/MWh.

Using environmental model of the building life cycle emissions in all phases of the building life cycle can be calculated and different optimisation tasks to minimise emissions can be solved.

3.2.4. *Economical model of the building life cycle*

The renovation project to be implemented has to be financially attractive for the user. Technological solutions influence results of the energy model and results of energy model influence results of the environmental model. Results of those 3 models can be evaluated economically (see Fig. 5).

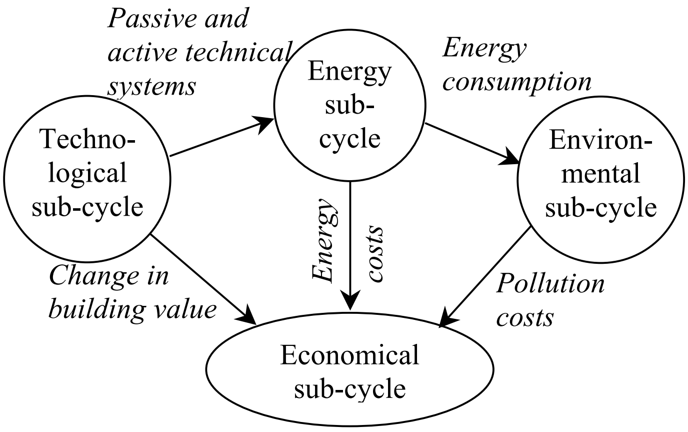

Fig. 5. Combination of different sub-cycles

Change of the building value depends on the renovation of its physical state up to legal requirements and modernisation level. The more modern is building the greater is its value. Value of the building can be calculated as the difference between its primary value and expenses necessary for reduction of deterioration consequences [20].

Economical evaluation of the energy model results is performed calculating investments into renovation and expenses required for operation of the building after renovation. Life cycle costing method allows comprehensive evaluation of the initial investments and operational expenses. Even if the initial investments are higher, total costs during the life cycle (LCC) of the considered energy saving measures package can be lower, when the operational expenses are evaluated. Also LCC evaluates the change of the value of money in long-term perspective, while including discount factor into calculations. [24]

Costs of the greenhouse gases emissions, avoided because of the implemented energy efficiency measures, can be estimated calculating externalities or using carbon dioxide price depending on the case under consideration. It is proposed to include avoided emissions costs into the life cycle costing calculation formula for the evaluation of total economical benefits of the energy and environmental solutions of the building renovation:

$$LCC = I + E \cdot \frac{(1+d)^n - 1}{d \cdot (1+d)^n} - A \cdot \frac{(1+d)^n - 1}{d \cdot (1+d)^n} \,. \tag{7}$$

Where: n – calculating period, years; d – discount factor; I – investments into renovation measures, LTL; E – operational expenses required for maintenance of the building after renovation, LTL; A – avoided emissions costs, LTL.

The proposed formula allows comprehensive evaluation of the costs and benefits of the building renovation in terms of its life cycle.

3.2.5. Decision making

Before starting building renovation, different alternatives should be considered – different levels of building insulation and modernisation levels of engineering systems may be investigated. Each alternative under consideration will give different technological, energy, environmental and economical effect (see Fig. 6).

For example five alternatives for one building renovation may be considered, assuming that each subsequent alternative is more energy efficient in terms of building operational energy consumption. But it doesn't necessarily will give the positive effects in each sub-cycle of the building. Technological benefits may stop increasing after certain rehabilitation level of the building. Total energy consumption instead of decreasing may start increasing after particular increase of the building thermal characteristics etc. The same applies to environmental and economical benefits.

Decision maker may prioritise different criteria and search for the optimal combination of the results. While integrating results of the individual calculations for alternatives to be considered using the proposed life cycle model, it is possible to find the optimal combination of the criteria values, allowing satisfying the interests of decision makers.

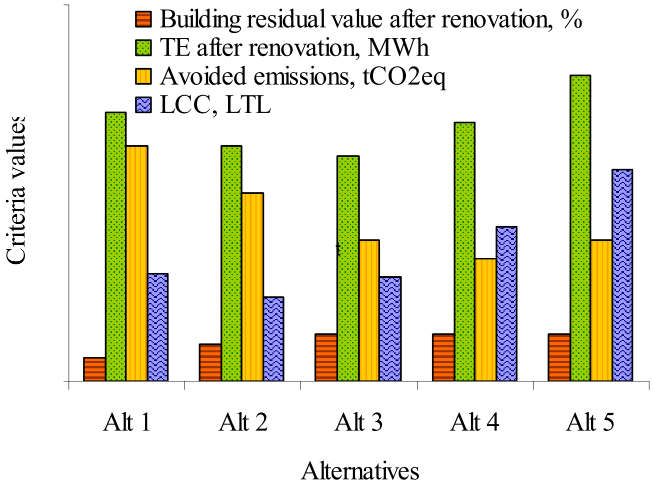

Fig. 6. Alternatives under consideration

4. CONCLUSIONS

1. The proposed life cycle model evaluates all life cycle phases of the building and impacts of the building renovation on the technological, energy, environmental and economical aspects.

2. The building renovation alternatives can be comprehensively evaluated using the proposed model. Model allows to fully assess the associated consequences of the building renovation – how value of the building is changing while reducing its physical deterioration and increasing its modernity; how the decrease of operational energy consumption affects the embodied energy and total energy consumption (it checks if minimization of the operational energy consumption does not increase total energy consumption, etc.); how energy-related decisions affect greenhouse gases emissions. The model allows to perform optimization of the investment and maintenance costs and to include avoided pollution costs into calculations.

3. The proposed model can be used to solve optimization task to find an optimal combination of technological, energy, environmental and economical values for building renovation.

4. The technological model can be used to find the most optimal frequency of renovation taking into account energy, environmental and economical criteria.

5. The energy model can be used to find the optimal combination between embodied and operational energy consumption of the building; to assess how technological development affects embodied energy consumption and estimate the embodied energy saving potentials; to consider efficiency of engineering systems including energy supply systems.

6. The environmental model can be used for different emissions optimisation tasks.

REFERENCES

1. Council of the European Union. Renewed EU sustainable development strategy // Available from internet < register.consilium.europa > [cited 04 03 2009].
2. Department of Statistics under the Government of the Republic of Lithuania. Energy balance 2007 // Department of Statistics under the Government of the Republic of Lithuania, Vilnius. 2007, 52 p.
3. Statistical Office of the European Communities (Eurostat) // Available from internet < epp.eurostat.ec.europa.eu > [cited 04 03 2009].
4. B. Dong; Ch. Kennedy, K. Pressnail. Comparing life cycle implications of building retrofit and replacement options // Canadian Journal of Civil Engineering, Vol. 32, 2005, p. 1051–1063.
5. M. Erlandsson, P. Levin. Environmental assessment of rebuilding and possible performance improvements effect on a national scale // Building and Environment, Vol. 40, 2005, p. 1459–1471.
6. A. Power. Does demolition or refurbishment of old and inefficient homes help to increase our environmental, social and economic viability? // Energy Policy, Vol. 36, 2008, p. 4487–4501.
7. Nacionalinė žemės tarnyba prie Žemės ūkio ministerijos, valstybės įmonė Registrų centras. Lietuvos Respublikos nekilnojamojo turto registre įregistruotų statinių apskaitos duomenys 2008 m. sausio 1 d. // Available from internet < www.nzt.lt > [cited 04 03 2009].
8. V. Martinaitis, E. Kazakevičius, A. Vitkauskas. A two-factor method for appraising building renovation and energy efficiency improvement projects // Energy Policy, Vol. 35, 2007, p. 192–201.
9. A. Kaklauskas, E. K. Zavadskas, S. Raslanas. Multivariant design and multiple criteria analysis of building refurbishments // Energy and Buildings, Vol. 37, 2005, p. 361–372.
10. A. P. Arena, C. de Rosa. Life cycle assessment of energy and environmental implications of the implementation of conservation technologies in school buildings in Mendoza – Argentina // Building and Environment, Vol. 38, 2003, p. 359–368.
11. B. De Meester, J. Dewulf, S. Verbeke, A. Janssens, H. Van Langenhove. Exergetic life-cycle assessment (ELCA) for resource consumption evaluation in the built environment // Building and Environment, Vol. 44, 2009, p. 11–17.
12. Ch. Scheuer, G. A. Keoleian, P. Reppe. Life cycle energy and environmental performance of a new university building: modelling challenges and design implications // Energy and Buildings, Vol. 35, 2003, p. 1049-1064.
13. C. Thormark. The effect of material choice on the total energy need and recycling potential of a building // Building and Environment, Vol. 41, 2006, p. 1019–1026.
14. J. P. Clinch, J. D. Healy. Cost-benefit analysis of domestic energy efficiency // Energy Policy, Vol. 29, 2001, p. 113–124.
15. C. W. Gellings. Efficient use and conservation of energy // In Energy Sciences, Engineering and Technology Resources, from Encyclopedia of Life Support Systems (EOLSS), Developed under the Auspices of the UNESCO, Eolss Publishers, Oxford, UK.

16. Ch. Goodacre, S. Sharples, P. Smith. Integrating energy efficiency with the social agenda in sustainability // Energy and Buildings, Vol. 34, 2002, p. 53–61.
17. A. Sarja, E. Vesikari. Durability Design of Concrete Structures // RILEM Report of TC 130-CSL, RILEM Report Series 14, E&FN Spon. Chapman & Hall, London, 1996, p. 151.
18. A. Sarja. Development towards practical instructions of life cycle design in Finland // Proceedings of the RILEM/CIB/ISO International Symposium, Integrated Life-Cycle Design of Materials and Structures, ILCDES 2000, Helsinki, 2000.
19. Lietuvos Respublikos Seimas. Lietuvos Respublikos statybos įstatymas // Valstybės žinios, Nr. 101-3597, Vilnius: Valstybės žinios, 2001.
20. N. Lepkova, T. Vilutienė. Pastatų ūkio valdymas. Teorija ir praktika // Vilnius: Technika, 2008, 325 p.
21. V. Martinaitis, A. Rogoža. Statinio gyvavimo ciklo technologinis modelis // Statyba, T. VII, Nr. 1, 2001, p. 73–77.
22. Lietuvos Respublikos aplinkos ministras. Statybos techninis reglamentas STR 1.12.05:2002 Statinio naudojimo paskirtis ir gyvavimo trukmė // Valstybės žinios, Nr. 109-4837, 2002.
23. Правила оценки физического износа жилых зданий. ВСН 53-86(р) // Госгражданстрой, Москва, 1988, 71 с.
24. S. K. Fuller, S. R. Petersen. Life-cycle costing manual for the Federal energy management program. NIST Handbook 135 // Available from internet < www.bfrl.nist.gov > [cited 04 03 2009].

CYSENI 2009, May 28-29, Kaunas, Lithuania
ISSN 1822-7554, www.cyseni.com

REGIONAL POSSIBILITIES TO COVER HEAT AND ELECTRICITY GENERATION DEMAND USING BIOMASS FROM FOREST CUTTING RESIDUES

E.F. Dzenajavičienė
Lithuanian Energy Institute
Breslaujos str. 3, LT-44403 Kaunas – Lithuania
Phone+370 37 401935
E-mail: farida@mail.lei.lt

ABSTRACT

Complicated processes in energy sector – such as growing prices for imported natural gas, closure of Ignalina Nuclear Power Plant (NPP) – as well as the requirements of the new EU Directive on the promotion of the use of energy from renewable sources define the important role for the increase of the use of renewable energy sources as one of the most effective measures for mitigation of the consequences of above mentioned processes. Existing energy policy documents – Energy strategy, etc., – define strategic goals as well as tasks and available resources on national level only. Energy planning, however, is not implemented on regional – counties and municipal – levels and there is no statistic information published on the energy demand forecasts and local energy resources in the regions. The paper provides information on current situation of the use of biomass fuel by regions, as well as assessment of thermal energy and power generation possibilities from forestry biomass to cover energy demand in household and services sectors in Lithuania's counties.

Keywords: regional development, forestry biomass, solid biofuel, heat and electricity demand

1. INTRODUCTION

Complicated economic processes are currently undergoing in Lithuanian energy sector, such as: changes in the prices of imported natural gas, unclear coverage of electricity demand after closure of Ignalina NPP. This causes current growth of heat and electricity prices, which has direct impact on economic development and social security of population. Use of renewable energy sources (RES) is considered as one of most efficient mitigation measures for above problems. Here we should mention National Energy Strategy and the Directive of the European Parliament and of the Council on the Promotion of the Use of Energy from Renewable Sources, which aims to establish an overall binding EU target target of 20% share of renewable energy sources in energy consumption by 2020, which for Lithuania is 23% of primary energy [1].

2. REGIONAL STRATEGIC PLANNING FOR COVERING ENERGY NEEDS

The main political goal of regional policy is reduction of regional disparities in output, unemployment and income, a contribution to national cohesion. In no country, though, is the reduction of interregional disparities seen as the only or even the primary objective of regional policies [2]. The times when economic growth was taken for granted, and when regional policy was concerned simply with where to direct it, are gone. Regional policy is now expected to promote growth throughout the entire country by encouraging competitiveness and regional self-sufficiency [3].

The objectives of regional strategic energy planning usually are as follows:

- Provide an integrated approach to meeting the energy needs and supporting future prosperity of the regions;

- Ensure that adequate supplies of electricity, heat and transportation fuels to meet the region's needs and that those supplies are reliable and competitively priced;
- Ensure fair distribution of energy costs, balancing the diverse needs, cost causation and usage characteristics of all customer classes.
- Create an enduring framework for regional energy planning and implementation that incorporates the diverse interests and capabilities of key stakeholders in the region;
- Strongly encourage the development of clean, safe energy and environmentally benign resources.
- Look forward toward preparing the region for the potential transition from a fossil-fuel economy to new alternative supply sources and technologies [4].

Though Lithuania is a small country and politicians often suppose that regional development is not this important, and often emphasize single region attitude toward Lithuania in EU regional policy, however regional statistics shows significant growth of difference in Gross Domestic Product (GDP), wages between the most and the least developed regions. Fig. 1 shows that the difference in GDP per capita between Vilnius and Tauragė residents has grown from 15.6 to 31.4 thousand Litas during four years.

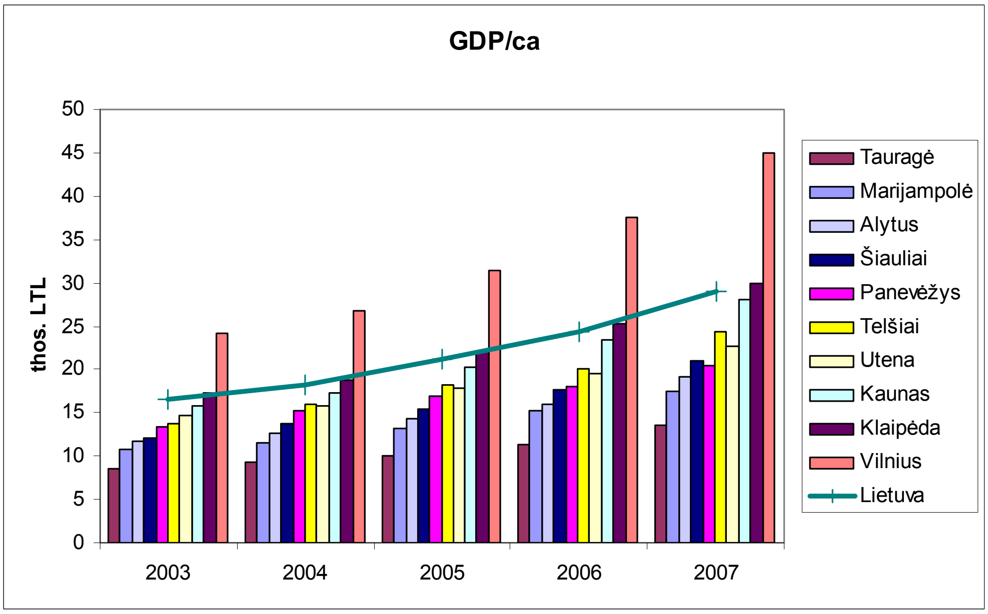

Fig. 1. Growth of GDP per capita by Lithuanian counties, in LTL [5]

The growth of the use of renewable energy sources, and first of all biofuel, during recent years is not so much related to sustainable regional development, but rather to strict environmental requirements – prohibition to burn heavy oil fuel with high sulphur content – and high prices for oil products. These were the reasons for increasing growth rates for the use of biofuel

The use of renewable energy sources provide economic, as well as non-economic benefit for the users of such fuel, which can be seen in Fig. 2.

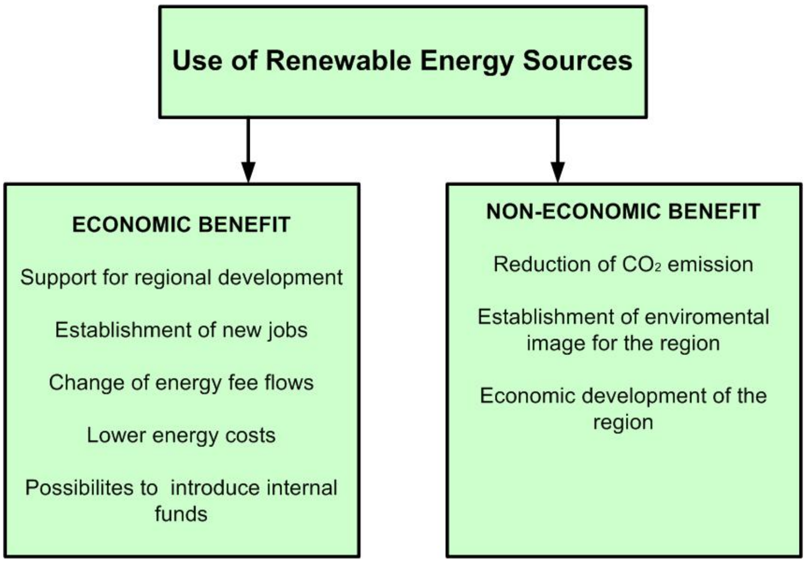

Fig. 2. Economic and non-economic benefit from the use of RES in regional development [6]

The use of solid biofuel has grown from 2% in year 2000 till 16% in 2007 in district heating systems (DHS), as well as in local boiler-houses in Lithuania. However, assessment of this use by counties or municipalities disclose significant differences among various regions. The largest share of such installations is in Vilnius county, including the biggest biofuel CHP plant in Vilnius City. There are 2–3 times more boiler-houses burning biofuel in Klaipėda, Kaunas, Panevėžys, Telšiai and Utena counties than in Šiauliai, Marijampolė or Alytus (Fig. 3).

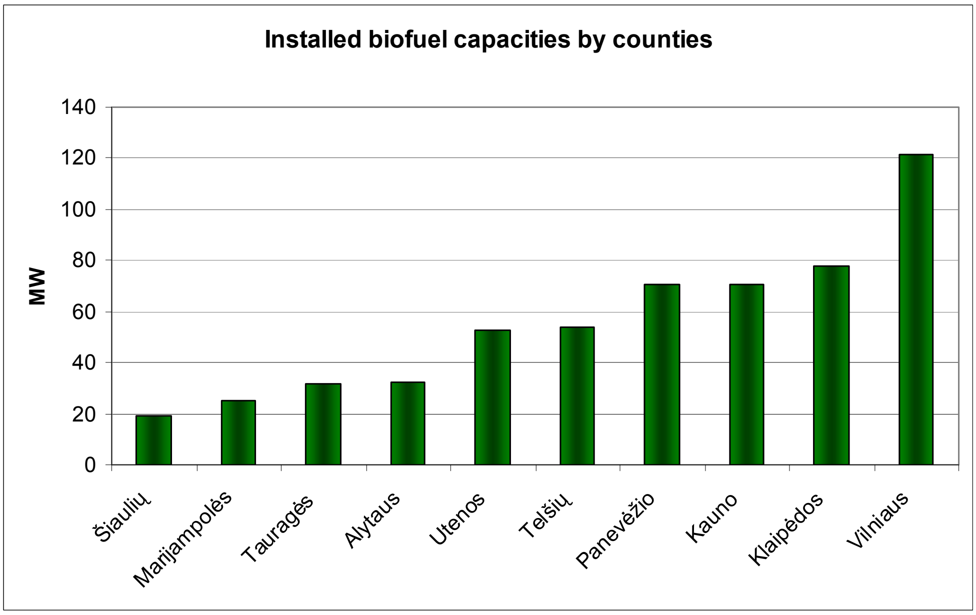

Fig. 3. Distribution of solid biofuel incineration capacities by counties [7]

Differences in separate municipalities are even higher. Here Vilnius and Klaipėda municipalities are obvious leaders. Only one DHS in Akmenė municipality has no biofuel installations at all. The capacities vary significantly and can‘t be somehow related to available biofuel resources or availability of natural gas. In some cases we can see the tendency to install biofuel boiler-houses in DHS, which after prohibition of heavy oil fuel with high sulphur content had to be renovated for incineration of other liquid fuel – oil-shale oil or light fuel oil (Fig. 4).

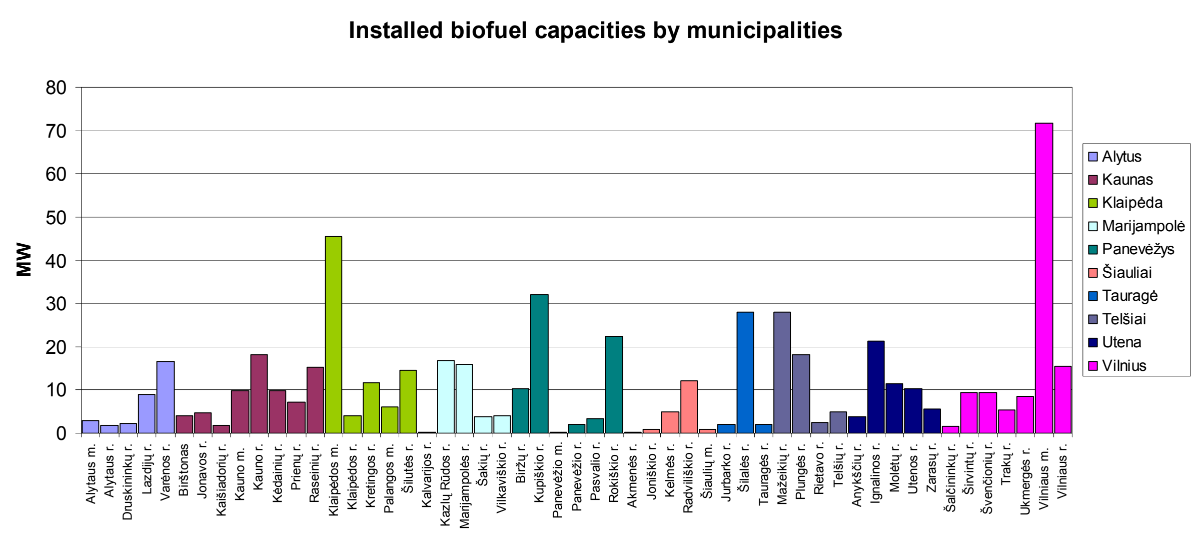

Fig. 4. Distribution of solid biofuel incineration capacities by municipalities [7]

3. FORESTRY BIOMASS POTENTIAL FOR REGIONAL HEAT AND ELECTRICITY DEMAND

3.1. Forestry biomass potential by counties

Biomass fuel and especially wood biomass is and will be in future the main renewable energy source for heat and power generation in Lithuania. It can be used as single fuel or in fuel mixes with coal, peat, agriculture biomass, etc. Currently approximately 500 MW capacity for incineration of wood fuel is installed in Lithuania. Unfortunately, according to some experts, all easily accesible wood resources are already used: over 700 ktoe of wood fuel out of 900 ktoe [8]. With the aim to keep the existing rate of the use and growth of the use of biofuel, we should estimate possibilities to use forest felling waste. Production of such fuel started just several years ago and is not widely developed all over the country: more in the south-east, where highest biofuel capacities are installed. Though it should be mentioned that Vilnius CHP plant with capacity 60 MW brings fuel from different and distant locations. As permission on construction of every new boiler-house or CHP plant needs assessment of fuel availability [9], the most convenient way is to use regional basis, since forrest cutting residues are indigenuous and bulky fuel, and transportation is cheaper in smaller distances. On the basis of data provided by the experts from State Forest Management and Inventory Institute the following forestry residues biomass potential is presented in Table 1 [10].

Table 1. Potential of forest felling residues for energy generation in 2007

Counties	Mass, thos. tons			Energy value, MWh		
	Young trees	Branches	Stumps	Young trees	Branches	Stumps
Alytus	6894	77593	47411	19303	217260	132751
Kaunas	15539	99505	87818	43509	278614	245890
Klaipėda	5633	32882	25103	15772	92070	70288
Marijampolė	5210	42587	36298	14588	119244	101634

Panevėžys	13005	89476	74433	36414	250533	208412
Šiauliai	10950	84511	71933	30660	236631	201412
Tauragė	6865	62896	56860	19222	176109	159208
Telšiai	5914	40559	32799	16559	113565	91837
Utena	7462	85841	72118	20891	240355	201930
Vilnius	11486	143834	105407	32161	402735	295140
Total in Lithuania:	***88957***	***759686***	***610179***	***249080***	***2127121***	***1708501***

Table 1 provides technical potential of forestry biomass, which can be taken from the forest, in mass and energy values. The highest potential comes from all types of cuttings. Presented potential exclude the forestry residuals used in the forest for technological needs and those to be left in the forest for preservation of biodiversity.

3.2. Theoretical assessment of energy demand at regional level

However, more complicated task is to define energy demand on regional level and define, which share of energy could be covered from existing biomass potential. Regional energy statistics in fact does not exist in Lithuania. Some information is available in data basis of the Lithuanian District Heating Association, however there is no information on a big number of small municipal energy producers.

Annual heat and electricity consumption in household and tertiary sectors was estimated on the basis of national statistics on energy demand in household and tertiary sectors and population in the counties. The latest available statistcs is for year 2007 [11, 12]. The outcome of this estimation is presented in Table 2.

Table 2. Population, heat and electricity demand in household and tertiary sectors by counties

Counties	Population	Population, % share of total in Lithuania	Heat demand in household and tertiary sector, GWh	Electricity demand in household and tertiary sector, GWh
Alytus	177040	5,26%	435,96	289,31
Kaunas	673706	20,01%	1658,99	1100,95
Klaipėda	378843	11,25%	932,89	619,09
Marijampolė	181219	5,38%	446,25	296,14
Panevėžys	284235	8,44%	699,92	464,49
Šiauliai	349876	10,39%	861,56	571,76
Tauragė	127378	3,78%	313,67	208,16
Telšiai	173383	5,15%	426,95	283,34
Utena	172580	5,13%	424,98	282,03
Vilnius	848097	25,19%	2088,43	1385,94
TOTAL:	***3366357***	***100,00%***	***8289,60***	***5501,21***

In the above estimation uniform energy demand is assumed per capita all over the country.

Two economic activity sectors – household and tertiary were selected as they form the vital interest of municipal energy sector, i.e. energy supply to population and public sector – educational, health protection, social, administrational and other buidings.

For more realistic assessment stumps were not included into total biomass potential, taking just residues from planned fellings and thinning. The following assumptions were made for the estimating the covering of regional demand:

- Fuel is wood chips with moisture content appr. 40%;

- Efficiency of heat boiler 0.85;
- Efficiency of condensing power plant 0.33;
- Efficiency of CHP plant 0.85;
- Heat/power generation ratio in CHP plant 0.67/0.33;
- Average heat supply losses in networks 18%;
- Average power supply losses in grids 12%.

Using above assumptions estimation of the heat and electricity output was performed, using most common technologies in Lithuanian energy sector (Table 3).

Table 3. Power and heat demand in household and tertiary sectors, which might be covered with forestry biomass by counties

Counties	Biomass fuel potential, GWh	Heat output in boiler-house, GWh	Electricity output in condensing power plant, GWh	Heat output in CHP plant, GWh	Electricity output in CHP plant, GWh
Alytus	237	165	69	110	58
Kaunas	322	225	94	150	80
Klaipėda	108	75	31	50	27
Marijampolė	134	93	39	62	33
Panevėžys	287	200	83	134	71
Šiauliai	267	186	78	125	66
Tauragė	195	136	57	91	48
Telšiai	130	91	38	61	32
Utena	261	182	76	122	64
Vilnius	435	303	126	203	107
TOTAL:	***2376***	***1656***	***690***	***1110***	***587***

The highest heat output is in boiler-houses, which is the most convenient practice in Lithuanian heat sector. However, use of forest biomass fuel in small-scale CHP plants is also an efficient possibility to reduce heat generation costs in small towns if appropriate electricity feeding tariffs are applied. This will also open wider possibilities for co-generation in a whole, since the future of this efficient technology is not optimistic even after closure of Ignalina NPP, if the new NPP will be constructed.

Having evaluated heat and electricity output, it is possible to define the share of heat and electricity demand, which could be covered using residual wood from forest cuttings. (Fig. 5 and Fig. 6).

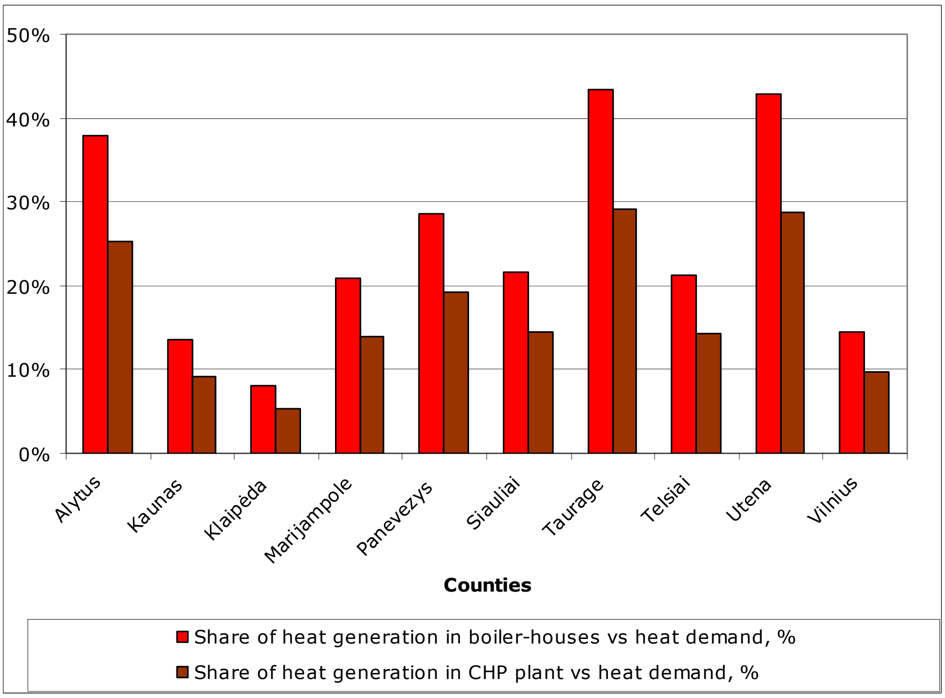

Fig. 5. Share of heat demand, which could be covered with forestry biomass burning in boiler-houses and CHP plants

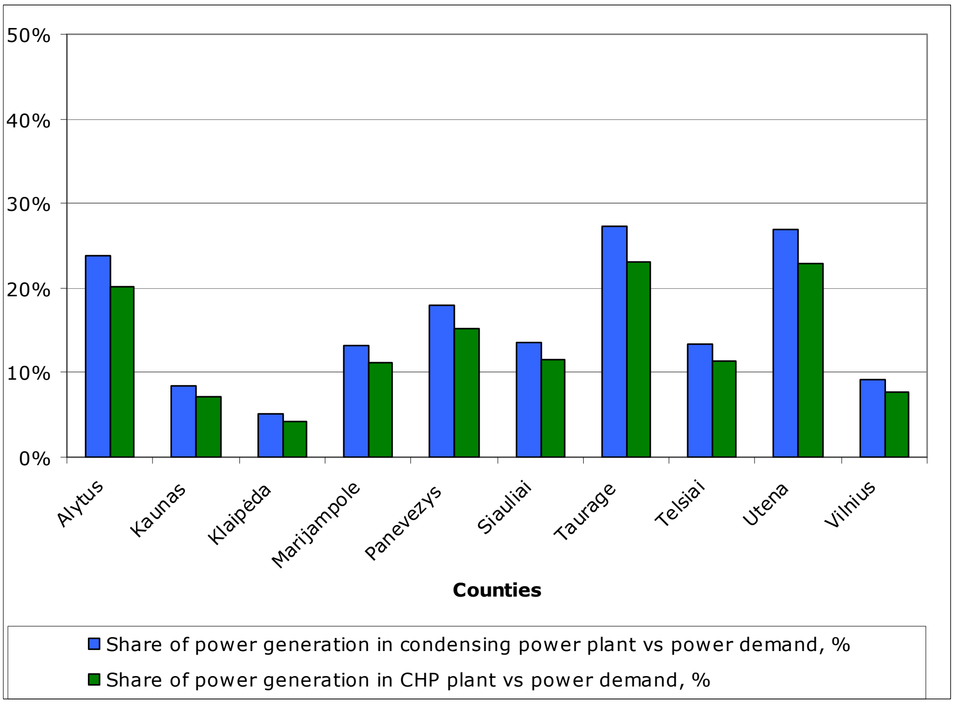

Fig. 6. Share of power demand, which could be covered with forestry biomass using it in condensing power and CHP plants

Here we must bear in mind that this demand will be covered in case all technical potential of forest cutting and thinning residues will be used as fuel. Economic potential will always be lower, but in present conditions of high natural gas prices, economic potential for forestry biomass will also stay higher.

3.3. Environmental aspect in using forest biomass fuel

Renewable energy sources have been identified to play an important role in mitigating climate change. The main reason is that carbon dioxide emission is avoided when fossil fuels are replaced. Generally, biofuel itself is considered as neutral regarding CO_2 emissions. However, certain share of fossil fuels is used in biofuel production, storage, ash recirculation and forest fertilisation chain [13]. Greenhouse gas emissions from combustion of biofuels were found to be in the range of 3–20 kg CO_2 eq/MWh_{chip}. According to Finnish scientists, who are among world leaders in production and use of biofuel, the emissions from collecting, chipping and transporting the residues are 4.3–7.5 kg CO_2 eq/MWh_{chip}. Significant amounts of greenhouse gas emissions may be released during chip storage, especially if rapid decaying takes place in the fuel heap. Monthly CO_2 emissions during storage of chip could be 5–10 kg CO_2 eq/MWh_{chip}. The emissions of the ash recirculation process were calculated to be about 0.2 kg CO_2 eq/MWh_{chip}. The nutrient loss compensation with fertilisation, if the whole nitrogen content in the fuel would be refunded to the forest site, was calculated to cause emissions in the range of 7 kg CO_2 eq/MWh_{chip}. With above assumptions on CO_2 emissions it was possible to estimate the average CO_2 emissions input from the use of forest biofuel (Fig. 7) and to compare this with current emissions from natural gas and heavy fuel oil (Table 4).

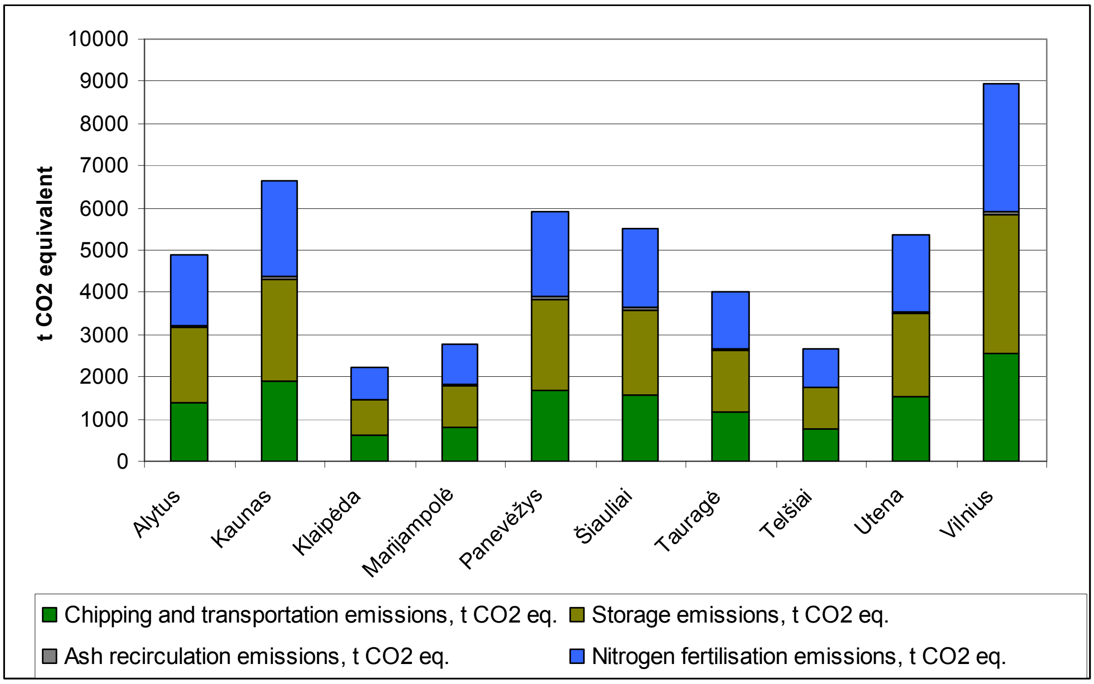

Fig. 7. CO_2 emissions from the use of estimated potential of forestry biomass

Total estimated amount of CO_2 equivalent from biomass use is approximately 49,000 tons. To have the better view of the total emissions we have compared this to the CO_2 emissions produced from incineration of the same amount of natural gas and heavy oil fuels, which currently makes the largest share of fossil fuel in Lithuania‘s fuel-energy balance. Conversion factor for incineration of natural gas fuel is 0.185 t CO_2 eq./MWh and for heavy oil fuel it is 0,268 t CO_2 eq./MWh [14].

Table 4. Comparison of CO_2 emissions from the use of forestry biomass and natural gas

Country	Total biofuel potential, MWh	Total emissions from biomass fuel, t CO_2 eq.	Total emissions from natural gas fuel, t CO_2 eq.	Total emissions from heavy fuel oil, t CO_2 eq.
Alytus	236563	4873	43764	63399
Kaunas	322123	6636	59593	86329
Klaipėda	107842	2222	19951	28902
Marijampolė	133832	2757	24759	35867
Panevėžys	286947	5911	53085	76902
Šiauliai	267291	5506	49449	71634
Tauragė	195331	4024	36136	52349
Telšiai	130124	2681	24073	34873
Utena	261246	5382	48331	70014
Vilnius	434896	8959	80456	116552
Total in Lithuania:	***2376195***	***48950***	***439596***	***636820***

Use of the same amount of natural gas fuel gives nearly 9 time higher greenhouse gas emissions and the same amount of heavy oil fuel gives 13 times higher emissions. This explains why renewable energy sources have been identified to play an important role in mitigating climate change.

4. CONCLUSIONS

1. Since easily accesible wood biomass resources are nearly fully used in Lithuania, attention should be directed towards wider use of forest cutting residues with the aim to maintain existing use and growth rates of biofuel. This is also important to reach the targets, set by national and EU strategies.
2. Technical potential of forest cutting biomass, available for energy generation in Lithuania is approximately 250.000 MWh from young trees thinning and management, approximately 2.127,000 MWh from branches and tops from all types of cuttings and about 1.700,000 of stumps from clear-cuttings.
3. Approximately 1.656 GWh of heat could be produced in boiler-houses, 690 GWh electricity could be produced in condensing power plants, or 1110 GWh of heat and 587 GWh of electricity could be produced in combined heat and power (CHP) plants using only forestry waste from forest thinning and all types of cuttings;
4. At least about 5% of heat and electricity could be covered from forest biomass fuel in counties with high population rate and low afforestation (like Klaipėda) and up to 40% of heat and nearly 30% of electricity demand in relatively less populated counties (like Tauragė). This demand comes from two socially important sectors – household and tertiary.
5. Use of forest biomass fuel in small-scale CHP plants is also an efficient possibility to reduce heat generation costs in small towns.
6. Even though production of biofuel in the forest is responsible for certain amount of greenhouse gas emissions, CO_2 emissions from incineration of the same amount of natural gas fuel are 9 times higher and even 13 times higher using heavy oil fuel.

REFERENCES

1. 2008/0016(COD) Directive of the European Parliament and of the Council on the promotion of the use of energy from renewable sources amending and subsequently repealing Directive 2001/77/EC and 2003/30/EC.
2. Third Informal Meeting of OECD Ministers Responsible for Regional Policy", *Schriften zur Regionalpolitik und Raumplanung*, No. 25, OECD and Government of Austria, Federal Chancdlery, Vienna, 1994.
3. Rémy Prud'homme. New Goals for Regional Policy // Journal "OECD Observer", Vol. a, 1995.
4. Energy 2030. The San Diego Regional Energy Strategy. // Creating a more Secure Energy Future for the San Diego Region, San Diego Regional Energy Office, 2003.
5. Statistical Yearbooks of Lithuania 2004 – 2008, Department of Statistics, 2004–2008.
6. Case Study – Lithuania // „Strategic Assessment Framework for Implementation of Rational Energy – Local Planning" (SAFIRE-LP), Project Report, LEI, June 2004.
7. V. Stasiūnas. Lithuanian heat sector – current situation and barriers for development // Presentation at the conference „The most expensive heating season. Reasons and solutions", Vilnius, October 22, 2008 (in Lithuanian).
8. N. Pedišius. The use of biofuel for energy generation in Lithuania // Presentation at the seminar „Incineration of biomass and other fuel mixes", LEI, Kaunas, September 30, 2008 (in Lithuanian).
9. The Decree of the Government of Lithuanian Republic "On adopting of the Main Development Trends of Heat Sector", No 307, from March 22, 2004.
10. E.F. Dzenajavičienė, S. Vrubliauskas, G. Mozgeris, V.V. Buivydaitė, D. Tiškutė-Memgaudienė, M. Lynikas, M. Palicinas. Modelling of biomass resources suitable for fuel at regional level // Energetika, Nr. 3, 2008.
11. Lithuanian energy 2007, ISSN 1822-5268, Lithuanian energy institute, 2008 (in Lithuanian).
12. Lithuanian counties 2007, ISSN 1648-0260, Statistics department, 2008 (in Lithuanian).
13. M.Wihersaari. Greehouse gass emissions from final harvest fuel chip production in Finland // Biomass and Bioenergy, Elsevier, Vol. 28 (2005), p. 435–443.
14. Carbon Trust resources: Greenhouse Gas Conversion Factors [Interactive website]. Reference [2009-03-05], available on Internet: http://www.carbontrust.co.uk/resource/conversion_factors/default.htm

CYSENI 2009, May 28-29, Kaunas, Lithuania
ISSN 1822-7554, www.cyseni.com

ANALYSIS OF ENERGY ACCOUNTING METHODS OF SUSTAINABLE ENERGY ECONOMY

K. Biekša, A. Klevienė
Lithuanian Energy Institute
Laboratory of Regional Energy Development
Breslaujos str. 3, LT-44403 Kaunas – Lithuania
Phone: +370 680 16985, +370 37 401982
E-mail: bieksa@mail.lei.lt, audrone@mail.lei.lt

ABSTRACT

The earth's environmental assets are now insufficient to sustain our present patterns of economic activities. We've entered the era in which global prosperity increasingly depends on using resources more efficiently and distributing them more equitably, and on reducing consumption levels overall. The exhaustible resources are in the certain limits and they cannot be regenerated as renewable resources. We need better understanding of no economic and nonmaterial values. The main factors of energy economy growth ignore the environmental costs of economic activities. Existing accounting models should be grounded on constructive methodology of economy theory and models, but at the same time should be well-approved by indicators, factors and indexes of sustainable development concepts. The new kinds of accounting are named as "environmental accounting", "green accounting", "ecological footprint" and etc. They provide basis to include such accountings into all kinds of energy costs. Sustainable development paradigm extends accounting elements from pure economical to environmental and nature's sources. It's become true to evaluate and account all possible sources and cost, what are necessary for actual energy economy and will be necessary for future generations. Using concepts and ideas of sustainable development the development of energy economy, its variations, possibilities, limitations and actuality of implementation will be examined. The major attention of the article will be focused on identification of methodological problems of sustainable development of energy economy and investigation of possibilities to use green accounting models of sustainable development of energy economy.

Keywords: sustainable development, accounting models, green accounting, environmental accounting, ecological footprint, renewable recourses, RES (renewable energy resources)

1. INTRODUCTION

The culture of sustainable development is characterized as an attempt to give the same meaning to the economical, environment protection and social priorities, at the same time emphasizing the responsibility for future generations of decisions made, in our country is being formed not as quickly as it is wished. National development strategy, the persistent structure of energy management institutions and the finance accounting system gives a priority to the economical growth and the management of the economy, while the environment protection and the sustainable development tasks are left aside as needful, but not of a primary importance [3].

The "environment accounting", "green accounting" standards are being used in the world more and more often, while the accounting systems and tools, evaluated by the attitude of the environment, in our country are not being discussed comprehensively, so the advantage is left to the direct production costs method. That is why the natural resources are being irreversibly used and not left to the future generations. Energy system in Lithuania is being developed with not enough attention given to the principals of sustainable development; the preference is being given to the traditional types of fuel, such as nuclear, oil, gas. The National economy very much depends on the world oil and gas resources, which are sinking

[3]. The prices are rising not only of the resource limits but also that supply of resources significantly depends from a political situation, so the hardly foreseen negative outcome is possible for the present and future generations.

2. PRINCIPLES OF SUSTAINABLE DEVELOPMENT

The Brundtland Commission Report, better known as "*Our Common Future*", has popularised the notion of sustainable development in the following way "…development that meets the needs of the present without compromising the ability of future generations to meet their own needs". The expression 'sustainable development' has first appeared in the 1980´s – first in the World Conservation Strategy of 1980 (IUCN, WWF and UNEP) and then in the Brundtland Report of 1987 – the real debate has started with the Club of Rome Report "Limits to growth" in 1972. Today, after more than twenty-five years, there are still discussions about the sense, limitations and possibilities of this phenomenon. Studying article of A. Wijkman [4] concerned the phenomenon of sustainable development was found out that we are studying some theoretically and methodologically uncertain thing. The problem seems as non-harmonized with surround (nature and society) human being. If to accept dialectical attitude that human being is the development, so at first approach, the problem is non-harmonised human development. It is necessary to emphasize the necessity of harmonisation of human being. The first philosophical question is – should human take care about harmonisation of human being with environment, or not? The answer should be positive in every day's behaviour. Every day each of us are defining tasks of harmonization with surroundings. The problem is appearing in a higher level of human organization – State development level. It became obvious, that human knowledge about development laws and mechanisms of nature and society are not sufficient for safe use them in practice. A time when we have invested every tree, brook, hill and creature with its own guardian spirit has passed, nowadays we allow proceed development without concern for the feelings of natural objects [9]. In effect, nature became no longer spirit, but natural resources. Natural resources eventually became the domain of economy, under the heading of land. For too long, we have been looking at the environment and its resources through the wrong end of the telescope. By turning the telescope around and looking through the proper end, the importance of the natural world is suddenly and rightly magnified [8].

We can see the fact that natural environment encompasses the economy. The economy is an open system within the ecosphere, importing useful resources from the natural world and exporting wastes back to it. Human beings appropriate the resources provided by the ecosphere and turn them into food or artifacts using labour and capital [8]. This produces wastes (pollution) that the environment can absorb. The environment also provides services that we must have and cannot supply. All economic activity is thus enabled by the natural environment. All economic production is actually consumption of natural resources [12].

Sustainability requires non-decreasing levels of capital stock over time, non-decreasing per capita capital stock [7]. Indicators of sustainability could be based on the value of total assets every period. For a proper measure of sustainability, all assets should be included in such indicators: manufactured capital, natural capital and human capital [7]. The recognition of the importance of natural capital has led to the expansion of the asset boundary to include this asset. Economic sustainability can be defined as strong or weak, reflecting controversy over the degree to which one form of capital can substitute for another [7].

Weak sustainability requires only that the combined *value* of all assets remain constant [7]. This means that it is possible to substitute one form of capital for another, so natural capital can be depleted or the environment degraded as long as there are compensating investments in other types of capital. *Strong sustainability* is based on the concept that natural capital is a complement to manufactured capital, rather than a substitute [7]. Renewable resources can be exploited only at the natural rate of net growth. The use of non-renewable resources should be minimized and used only at the rate for which renewable substitutes are available. Emissions of waste should not exceed the assimilative capacity of the environment. The indicator of sustainability requires that all natural capital is measured in physical units [7].

The economic growth suggests that the scarcest factor now is natural capital or natural resources, which with human economic activity are continuing to draw down. So the first our priority should be to stop its further depletion as soon as possible. However essentially it is easier to prepare asset accounts first. The cost of depletion was initially measured as the value (net price) of extraction of non-renewable resources, and, for renewable resources, the value of the volume of harvest above sustainable yield [7]. Another method is the net present value (NPV) method which shows the discounted sum of its future income stream [7]. The income stream is calculated as the net price of resources minus the marginal costs of extraction of resources [7]. In practice, net price is often calculated as price minus the average costs of extraction because information about marginal costs is unavailable. The most widely available accounts are for energy and air emissions, especially emissions linked to the use of fossil fuels. Energy accounts have been constructed by many countries since the dramatic oil price increases in the 1970s, and, since many air pollutants are linked to energy use, it is relatively simple to extend the accounts to include these pollutants [7]. Trans-boundary flows of atmospheric pollutants that cause acid rain has been a major policy concern throughout Europe for more than two decades. More recently, the concern with climate change has made tracking greenhouse gas emissions a priority. Accounts are also constructed for other air pollutants, water pollutants, solid waste, and other forms of environmental degradation such as soil erosion [7].

3. ACCOUNTING PRICNIPLES OF ENERGY IN LITHUANIA

Our first mission is to review accounting principles used in energy sector of Lithuania before the investigation of environmental accounts. The electricity prices in Lithuania are under the control of the National Control Commission for Prices and Energy. Electricity generation and supply were determined as competitive activities, prices of generation and supply were not regulated and set by the market, except if some generators or suppliers dominate in the market – in the current case some price regulation mechanism was to be developed and applied by the Regulator – National Control Commission. The National Control Commission for Prices and Energy (Regulator) controls the price cap for energy as follow [6]:

- Price cap of transmission and distribution services shall be determined for 3 years
- Purchasing price for electricity produced from local fuel, renewable energy sources or waste shall be approved by Regulator.
- The purchasing price may be defined in accordance with level of voltage and time of connection.
- Price cap for the appropriate activity in the electricity sector must be established for all providers of such service if they have authorizations or licenses.
- Electricity prices sold by producers and independent suppliers as well as for the capacity reserve are not regulated, except if the producers and independent suppliers have more than 25% of market share.
- The price cap of public service tariffs shall be set each year by Regulator shall publish tariffs for transmission and distribution services.

The Commission is also responsible for supervision of the non-discriminatory access to the grid, it sets the transmission and distribution tariffs using the incentive price regulation - price cap formulas.

The prices for energy in Lithuania nowadays are very rapidly approaching the international level. Heat prices have risen sharply for the 2008–2009 heating season, mainly due to the dramatic increase of the natural gas price. Average price for district heating amounts to approximately 45 € per MWh. Import prices for natural gas have increased more than five times, from 85 USdollars/1000m^3 in 2004, to 500 USdollars/1000m^3 in 2008. The gas prices increase approaching for about 67% according to company "Lietuvos Dujos", which signed a new gas agreement with Russian company "Gazprom" in January 2008. Electricity prices for final consumer depend on the size of the consumer, one or two stages (day and night) tariffs are used, electrical or natural gas stoves are used, and the price can range from 4 €cents per kWh to 11 €cents per kWh [1].

The National Control Commission for Prices and Energy has set the following prices from different energy production sources. (Commission decision No.7 of 2002-02-11 (News., 2002, No.16-648)): average production price 2002 – 2004 m. 9 ct/kWh; average action price 2002 m. – 7,45 ct/kWh; price of energy produces in Ignalina NPP – 7,54 ct/kWh; price of energy produces in Vilniaus CHP – 9,86 ct/kWh; price of energy produces in Lithuanian power station – 13,92 ct/kWh; price for wind energy – 22 ct/kWh; price for hydro energy – 20 ct/kWh; for facilities generating electricity from biofuel – 22 ct/kWh.

4. ACCOUNTING OF WIND ENERGY PRICE

Wind and other renewable energy sources (RES) are free resources, however, the systems used to capture the energy from the wind and to convert it into electricity are not free. Wind power and other RES production require large capital outlays up-front, but do not incur fuel costs over the life of the plant. Wind and other RES producers also incur significant costs due to transmission infrastructure and regulatory frameworks that have been developed to suit the special characteristics of the fuels from which electricity has traditionally been produced – such as coal, gas, nuclear and in some extent hydropower. The many benefits of wind power and other RES accrue to producers, utilities and society. Governments can help to spur RES development by revising regulations and providing financial incentives to RES power producers.

Capital costs for wind plants installations, which include the purchase of the turbine itself, construction of roads and foundations, connecting to the grid and installation, account for about 75% of the total cost of energy. This is in contrast to fossil fuel-powered generation, which typically has lower up-front capital costs, but incurs fuel costs over the life of the system. Today, however, it looks that other external environmental costs are not included in the accounting of wind energy price [1].

Economists are willing to argue that the price for users of renewable energy resources, such as wind energy, will increase. Comparing traditional energy production methods with wind energy the increase in energy price is estimated by the overvalued price for wind energy which is supported by the Government. Difference in price in Lithuanian cents is 13.5 cents/kWh (where 8.5 cents/kWh is an average cost of energy production in the power system minus 22 cents/kWh supporting price for wind energy). The increase is also occurring by the need to keep the reserve of power. The data of this investigation is presented in Table 1.

The wind energy supporters say that wind energy is an attractive source of power for utility or small scale, for distributed power generation applications. Wind energy is clean and inexhaustible fuel. Wind power produces no emissions and is not depleted over time.

Table 1. Increase of energy price

Development trend	Perspective capacity, MW	Perspective generation, MWh	Increase of energy price in million Litas		
			Due to increased feed-in tariff	Due to the fact to keep 50% of the reserve of power.	In Total
1	80	0,144	19,44	3,56	23
2	170	0,306	41,31	7,57	48,88
3	500	0,900	121,5	22,26	143,76

Source: V.Katinas. The presentation of schema of zones for building of wind generator in Lithuania"//Wind energy seminar. Vilnius, 2003.

A single 1MW wind turbine running for one year can displace over 1500 tons of CO_2, 6.5 tons of SO_2, 3.2 tons of NO_x, and 27 kg of mercury. Wind plants can provide a steady flow of income to landowners who lease their land for wind development, while increasing property tax revenues for local communities. Wind applications can take many forms, including large wind farms, distributed generation, and single end-use systems. Wind energy reduces dependence on conventional fuels that are the subject of price stability. Wind energy expenditures are not used to obtain fuels from abroad, keeping funds closer to home, and lessening dependence on foreign governments that supply these fuels

The levelized cost of energy, commonly expressed in €cents/kWh, is the annual cost of recovering the total capital costs plus the recurring costs such as operations and maintenance and royalty payments divided by annual expected output. Cost varies due to differences in scale, quality and type of resource, and cost of financing. The comparison of the cost of wind energy to other types of energy generation costs for different fuels are presented in Figure 1 below.

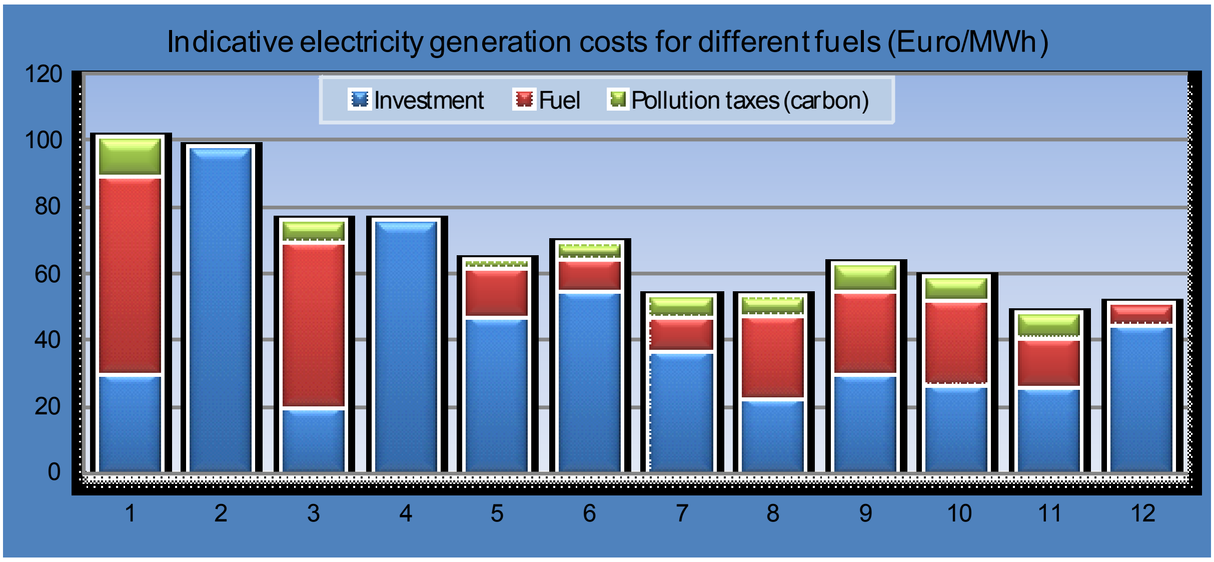

Fig. 1. Indicative electricity generation costs for different fuels
Source: Dresdner Kleinwort Equity Research // Feasibility study of constructing of a new nuclear power plant, 2006

Data in Fig. 1 are taken from the study "Feasibility study of constructing a new nuclear plant in Lithuania" which was done in 2006. On the *x* axis the following types of electricity generation are presented:

1. Open cycle gas turbine (OCGT);

2. Offshore wind generators;
3. Open cycle gas turbine (OCGT) + carbon capture and storage (CCS);
4. Onshore wind generators;
5. Coal pulverised fuel (pf) + carbon capture and storage (CCS);
6. Coal fuelled Integrated Gasification Combined Cycle (IGCC) + CCS;
7. Coal fuelled Integrated Gasification Combined Cycle (IGCC);
8. Combine cycle gas turbine (CCGT);
9. Coal pulverised fuel;
10. Coal fluidized bed;
11. Brown coal lignite supercritical;
12. Nuclear energy (average).

It shows that nuclear technology offers a relatively stable and predictable initial cost base compare to other energy production methods. From the figure above it's clear to see that onshore wind energy costs consist only from investment costs meanwhile the rest of energy production methods need to include other type of costs. Cost of emission of carbon dioxide as environmental cost was included as environmental cost for energy production. However other types of environmental costs were not included.

5. ANALYSIS OF ENVIRONMENTAL ACCOUNTING MODELS

Environmental accounting is an attempt to identify and bring to light the utilized resources and cost imposed on the ecosystem by companies' activities. It is also a system of accounting designed to record the benefits and costs rendered by the environment to a business corporation and costs and benefits tended to the environment by the same business corporation. The main problem in environmental accounting is that there is lack of standard definitions of environmental costs. Environmental cost should be a part of an integrated system of material and money flow throughout a corporation, and not a separate type of cost altogether. Doing environmental accounting is simply doing better; more comprehensive management accounting that reveals hidden costs. During the past decade for many companies it has become increasingly sensible to introduce systems for managing environmental information. The first environmental accounts (EA) were constructed by Norwegian government in the 1970s and were only slowly adopted by other countries [15]. In the early 1990's, the World Bank conducted a review of EA, providing a compendium of which countries had compiled environmental accounts, the methods that had been used to construct EA [15]. Since that time, EA have increasingly been recognized as a useful economic tool, resulting in a great deal of activity in both developed and developing countries [7].

5.1. Green accounting trends in Europe

The Net National Product (NNP) of an open economy consists of consumption plus net investment (investment minus depreciation) plus net exports (exports minus imports). In the last 50 years the resulting indices NNP and particularly Gross National Product (GNP), have come to be regarded not simply as tools for economic management but also as indicators of economic performance and economic wellbeing, and of a country's "income". GNP measures economic activity in terms of the amount of final demand satisfied by economic output. The use of this figure as a measure of wellbeing is based on the assumption that wellbeing is proportionate to consumption of produced goods.

However, economic activity has many negative external effects. These can often be described as environmental externalities; a major example is the pollution into air, water and soil caused by production. Some of the damage caused by this pollution is reflected in reduced output, as in the case of reduced agricultural output due to polluted soils and water supplies. This damage is thus reflected in the national accounts, since output figures are lower than they would otherwise have been. Similarly, environmental damage directly affects human welfare and this loss is not reflected in the national accounts. Examples of this loss of welfare are the increase of costs for mitigation of discomfort of breathing polluted air. This defensive expenditure does not contribute to welfare, but because it is final expenditure, it is counted as part of GNP. Finally, while estimates are made of the depreciation of manmade capital stocks, depreciation of natural capital stocks is not accounted for. The framework of Green National Accounting firstly shows the fact that the environmental damage caused by production and consumption has a negative effect on human wellbeing, and secondly that under the current System of National Accounting (SNA) the depletion of natural resource stocks is not counted as depreciation in calculating Net National Product [15].

A major issue in the development of Green National Accounts has been the identification of factors that should be corrected for in adjusting Net National Product. These include environmental services, environmental damages, defensive expenditures and resource depletion.

The direct contribution of *environmental services* to human welfare is not reflected in produced output. Thus, the suggestion that the value of these services should be included in GNP reflects the desire that GNP should be a measure of total welfare generated in the current period, including the welfare generated by environmental assets.

Environmental damages should be deducted from GNP, in order that net welfare derived from the economy and the environment should be accurately measured.

Defensive expenditures should be deducted from NNP since they constitute not a net contribution to welfare but the avoidance of a decrease in welfare.

The value of overall productive capital is reduced when stocks of productive natural capital is *depleted*. The decrease in value of the asset is measured by the "resource rents" on the decrease in the resource stock, which is equal to the level of extraction in the case of non-renewable resources. This amount should be deducted in the calculation of NNP as representing part of the depreciation of the overall capital stock.

Two broad methods have been used to value degradation: *cost-based methods* and *damage-based methods*.

Cost-based methods – counts how much would it cost to avoid the generation of residuals by changing production and consumption patterns.

Damage-based method – calculates what is the value of the damage caused by current levels of residual generation.

The EC-funded GREENSTAMP project methodology is based on a requirement for strong environmental sustainability. According to this approach, the appropriate way in which “demand” of for society’s is measured, is expressed by respecting environmental standards compatible with preserving the ecological base required for sustainability. The methodology estimates sustainable national income, using an empirically calibrated multi-sector equilibrium model of a national economy to estimate economic output that is consistent with respecting environmental sustainability standards. It therefore provides policymakers with information on the costs to be borne by society in meeting given standards of environmental protection. The major disadvantage with this approach is that the complexity of a real national economy is so great that the inaccuracies associated with attempting to model an economy are at least as great as those associated with the damage-based method [7].

The EC-funded GARP project is an example of an empirical study that gathers the type of information that could be used to estimate a Green NNP, or could be provided as satellite accounts to be interpreted alongside with standard national accounts. The aim of the GARP welfare-based approach is to develop a practically measurable estimate of the net welfare that an economy generates. The core objective is to provide a scientifically robust method for the calculation of damages to human health, crops and materials. Thus, information is delivered to policy makers in the form of both physical and monetary impact estimates. Problems with this approach include the fact that this type of income in general does not measure sustainability even in theory, and that observable prices in any case would not allow us to do so. It is unlikely to be feasible to provide a single indicator that measures both current welfare and long-term sustainability [7].

5.2. "Ecological footprint"[1]

The **ecological footprint** is a measure of human demand on the Earth's ecosystems. It compares human demand with planet Earth's ecological capacity to regenerate. It represents the amount of biologically productive land and sea area needed to regenerate the resources a human population consumes and to absorb and render harmless the corresponding waste. However footprint method essentially accounts the use of the planet's renewable resources (its 'interest' rather than its "capital"). Non-renewable resources are accounted for only by their impact on, or use of, renewable, bio productive capacity. The footprint does not attempt to include the social or economic dimensions of sustainability. The footprint is not possible to forecast from data of bio capacity and eco-efficiency, although it is possible to make assumptions about future consumption and thus create informative, but speculative, scenarios. Today humanity uses the equivalent of 1.3 planets to provide the resources we use and absorb our waste. This means it now takes the Earth one year and four months to regenerate what we use in a year. Moderate UN scenarios suggest that if current population and consumption trends continue, by the mid 2030s we will need the equivalent of two Earths to support us. Turning resources into waste faster than waste can be turned back into resources puts us in global ecological overshoot, depleting the resources on which human life and biodiversity depend.

Footprint values at the end of a survey are categorized for carbon, food, housing, and goods and services. The approach can also be applied to an activity such as the manufacturing of a product and energy sector as well. Energy resource accounting is similar to life cycle analysis wherein the consumption of energy, biomass, water and other resources are converted into a normalized measure of land area called "global hectares" (gha).

Per capita ecological footprint is a mean of comparing human's consumption with nature's ability to provide for this consumption. The tool can inform policy makers to what extent we use more or less than is available within its territory. The footprint can also be a useful tool to educate people about carrying capacity and over-consumption, with the aim of altering personal behaviour. Ecological footprints may be used to argue that many current humans behaviour are not sustainable.

Nowadays the total world ecological footprint is 2.7 global hectares per capita and the ecological reserve, or bio capacity - the amount of land available for production, is in deficit at 0.6 global hectares per capita. According data of 2005 presented in global footprint network, the U.S. footprint per capita was 9.4 gha, Switzerland footprint was 5.0 gha per person, while in China was 2.1 gha per person. Lithuania footprint per capita is about 3.2 gha, Latvia footprint is 3.5 gha, Estonia – 6.5 gha, Belarus – 3.8 gha, Belgium – 5.1 gha.

Ecological footprint can be used as an indicator of environmental sustainability to measure and manage the use of resources throughout the economy. It can be used to explore the sustainability of energy services and industry sector. The fossil fuel footprint is typically

---

[1] Internet sources: http://lt.wikipedia.org and etc.

accounted for in terms of its carbon dioxide emissions although it is also possible to assess ecological footprints of energy use in terms of the land area required to sustainable derive bio fuel alternatives and also to assess the biological area necessary to produce a substitute.

One of the obstacles of use of footprint model in energy sector is that footprint treats nuclear power the same as it treats coal power. A life cycle analysis is centred around estimated carbon dioxide where emissions from Nuclear energy is at rate of 3.10-5.05 g/kWh (Torness Nuclear Power Station in Sweden). This compares to emission rate of 11 g/kWh for hydroelectric power, 700 g/kWh for coal, 900 g/kWh for oil and 400 g/kWh for natural gas generation. Nuclear power produced the smallest amount of CO_2 of any of electricity sources. Claims exist not only for CO_2 emission values but for fossil fuel waste value as well. According data of the World Health Organization 3 million people died worldwide by outdoor air pollution annually from vehicles and industrial emissions, and 1.6 million indoors through using solid fuel. In the U.S. alone, fossil fuel waste kills 20,000 people each year. A coal power plant releases 100 times as much radiation as a nuclear power plant of the same capacity.

6. CONCLUSIONS

Energy is a substantial factor influencing the future development of our society. Strongly increased demand, volatile prices with a tendency to rise over the next years, severe impacts on the environment, energy security and others are a high priority on the political agenda. Energy consumption is closely linked to individual behaviour, development and dissemination of new technologies requires the acceptance of the public. Thus in order to turn towards sustainable development it is essential to understand people's knowledge, attitudes and perceptions of energy matters in general and of energy technologies in particular. However the culture of sustainable development in Lithuania is only in the beginning stage of forming and a major part of national economy activity is still grounded on economic priorities. The development of energy economy could be changed easily from material patterns to social oriented and environmental friendly if we will use appropriate energy accounting methods. Environmental accounting, green accounting, ecological footprints are just approaching the initial stage of implementation. Sustainable energy accounting methods are still in the development stage, and their concepts, tools, processes and the potential benefits are not clearly recognized. International organizations such as the United Nations and the European Union perform important role in international exchange of information and experience, and establishment of guidelines and standards. Close collaboration of academic, research institutions and environmental organizations are necessary for further development of sustainable energy accounting methods.

7. REFERENCES

1. F. Juška. Renewables and their use in Lithuania // Vilnius, Division of Energy Development, Ministry of Economy, 2003.
2. S. Paulauskas. Savivaldos dialektika //Klaipėda, Klaipėdos universiteto leidykla. ISBN 9986-505-8-8, 1999, p. 251
3. S.Paulauskas. Preface. Innovations net "Susatainabilty culture" // Klaipėda, Strategic self-management, ISSN 1648-5815, 2005 Nr. 1(2), p. 15.
4. A.Wijkman. Sustainable development – challenges and prospects // Stockholm, Bilaga 1, FRN-Report, 1998:12.

5. Ž. Stasiškienė. Environmental Accounting in Lithuanian Industry: Analysis Necessity, Possibilities and Perspectives // Environmental research, engineering and management, 2001 No 2 (16), p. 25–31.
6. Kainodaros principų, taikomų energetikos sektoriuje, analizė ir jų tobulinimo rekomendacijos // Vilnius, LR Ūkio ministerija, 2008.
7. Gleann-Marie Lange. Policy application of environmental accounting// The world bank environmental department, 2003, p. 66.
8. G. Heal. Valuing Ecosystem Services //*Ecosystems* , 2000, N. 3: p. 24–30.
9. D. Jamieson. Sustainability and beyond // *Ecological Economics*, 1998, N 24, p. 183–192.
10. I. Moffatt. Ecological footprints and sustainable development // *Ecological Economics*, 2000, N 32, p. 359–362.
11. W.E. Rees. Eco-footprint analysis: merits and brickbat // *Ecological Economics*, 2000, N 32, p. 371–374.
12. E. Masoodoch, L. Garwin. Costing the Earth: when ecology meets economics // Nature, 395(1998:6701), p. 426–430.
13. Mäler Karl-Göran, Growth and Environment// The Beijer international institute of ecological environment, Stockholm, 1993, pp. 229-241.
14. D. Fullerton and R. Stavins. How economists see the environment // Nature 395(1998:6701), p. 433–434.
15. Dale Jorgenson & J. Steven Landefeld & William D. Nordause. Principles of National accounting for nonmarket accounts // A New Architecture for the U.S. National Accounts, 200, p. 143–160.

CYSENI 2009, May 28-29, Kaunas, Lithuania
ISSN 1822-7554, www.cyseni.com

MATHEMATICAL MODELLING OF SECURITY OF ENERGY SUPPLY DISTURBANCE SCENARIOS

L. Martisauskas, J. Augutis
Lithuanian Energy Institute
Laboratory of Nuclear Installation Safety
Breslaujos str. 3, LT-44403 Kaunas – Lithuania
Phone: +370 37 401938, +370 37 401973
E-mail: linasm@mail.lei.lt, juozas@mail.lei.lt

J. Augutis
Vytautas Magnus University
K. Donelaicio str. 58, LT-44248 Kaunas – Lithuania
Phone: +370 37 203775
E-mail: j.augutis@adm.vdu.lt

ABSTRACT

Security of energy supply is extremely important for each country energy development. It depends not only on energy production and infrastructure but also on technical, economical, political and environmental impact. Energy security covers many fields, whereas threats to energy system can be various and consequences have impact to all areas of country's economy.

Mathematical model for consequence scenarios of energy supply potential disturbances, such as technical failure of energy system, natural disasters and catastrophes, terrorism acts, reduction of energy supply, economical blockades, economical and political crisis, etc. is analysed in the paper. Consequences of disturbances used in methodology are technical, economical and socio-political. Development of the model is based on mathematical methods (Markov chains and processes) analysing consequence scenarios of disturbances, performing probabilistic and frequency analysis. In the paper, developed mathematical model of energy system disturbance consequence analysis is presented.

Keywords: security of energy supply, disturbances of energy supply, mathematical modelling.

1. INTRODUCTION

Energy supply is essential for the functioning of modern economies. However, the uneven distribution of energy supply among countries and critical need for energy has led to significant vulnerabilities.

The importance of energy security supply and conception of energy supply security is determined in the previous papers (Augutis et al., 2008)[1–5]. The International Energy Agency describes the conception "energy supply security" as a reliable possibility to obtain a proper quantity of energy for reasonable price. The description of energy security according to the World Energy Council is the following: it is the protection of citizens, society, economics and state against threats, arising to reliable fuel and energy supply.

Energy security covers many fields, whereas threats to energy system may be various and consequences have impact to all areas of country's economy. The main aim of this paper is to present mathematical model of security of energy supply. This model allows assessment of energy security level according to the consequences of potential energy disturbance.

2. METHODOLOGY OF ENERGY SUPPLY DISTURBANCE CONSEQUENCE SCENARIOS

2.1. Mathematical approach

Take a system that at any point in time may be described by one of N different states $S_1,S_2,...,S_N$. Moments of time when states are changed mark $t=1,2,...,N$, and state at time moment t mark q_t. To describe fully in probabilistic way a given system need to know the current state (in time t) and all theretofore states. In the case of first-order Markov chain, this probabilistic description is simplified to the current and prior states:

$$P\left[q_t = S_j \middle| q_{t-1} = S_i, q_{t-2} = S_k, \ldots\right] = P\left[q_t = S_j \middle| q_{t-1} = S_i\right] \tag{1}$$

The chosen processes of the right part of Equation (1) are independent in time and obtain the state transition probabilities (coefficients):

$$a_{ij} = P\left[q_t = S_j \middle| q_{t-1} = S_i\right],\ 1 \le i, j \le N\,.$$

These coefficients have the following characteristics: $a_{ij} \ge 0$, $\forall i, j$; $\sum_{j=1}^{N} a_{ij} = 1$, $\forall i$.

To develop the mathematical model for consequence scenarios of energy supply potential disturbances, the Markov chain and process model is used for the basic mathematical apparatus. In this model the transition probabilities depend only on the current system state [10].

The case is analysed when country‘s energy system is disturbed (disturbance may be external, internal or both). Disturbance is treated as initiating event leading to different consequences. Consequences of disturbance used in the model are technical, economical and socio-political. Energy disturbance may have consequences, but some of them may not cause any affects (for example, if a disturbance was short-term or one type of fuel can be easily substitute for another one). Therefore, the consequences are divided into points from 0 to 5 (0– no consequences, 1 – very light consequences, 2 – light consequences, 3 – medium consequences, 4 – heavy consequences, 5 – very heavy consequences). These points of the consequences are treated as states (S) of the model. Consequences caused by disturbance, according to its type, are treated as factors (V) of the model. There are three factors of the model: technical, economical and socio-political.

Each factor consists of states and has transition from one factor states to another one. Factors of model: V_1 – technical, V_2 – economical and V_3 – socio-political. States of model: $S_0 = 0$ (no consequences), $S_1 = 1$ (very light consequences), $S_2 = 2$ (light consequences), $S_3 = 3$ (medium consequences), $S_4 = 4$ (heavy consequences) and $S_5 = 5$ (very heavy consequences). Connection of the model factors and states is shown in Table 1.

Table 1. Connection of the model factors and states

Factors / **States**	**Technical** V_1	**Economical** V_2	**Socio-political** V_3
0 point (no)	$P(V_1(0))=\pi_0$	$P(V_2(0))$	$P(V_3(0))$
1 point (very light)	$P(V_1(1))=\pi_1$	$P(V_2(1))$	$P(V_3(1))$
2 points (light)	$P(V_1(2))=\pi_2$	$P(V_2(2))$	$P(V_3(2))$
3 points (medium)	$P(V_1(3))=\pi_3$	$P(V_2(3))$	$P(V_3(3))$
4 points (heavy)	$P(V_1(4))=\pi_4$	$P(V_2(4))$	$P(V_3(4))$
5 points (very heavy)	$P(V_1(5))=\pi_5$	$P(V_2(5))$	$P(V_3(5))$

Energy disturbances are various and may cause consequences of different type and severity. Disturbance may cause technical consequences and they have any other consequences, such as economical. However, it may be that technical consequences are low but economical can be very severe, etc.

Definition of the probability vector of the initial states (technical) is needed: $\pi=\left(\pi_0 \quad \cdots \quad \pi_5\right)^T$.

Also, state transition probabilities from one state of consequences to other should be defined, i.e. matrixes of state transition probabilities:

$$A^{(t)}=\begin{pmatrix} a_{00}^{(t)} & a_{01}^{(t)} & \cdots & a_{0j}^{(t)} & \cdots & a_{05}^{(t)} \\ a_{10}^{(t)} & a_{11}^{(t)} & \cdots & a_{1j}^{(t)} & \cdots & a_{15}^{(t)} \\ \vdots & \vdots & \vdots & \vdots & \vdots & \vdots \\ a_{i0}^{(t)} & a_{i1}^{(t)} & \cdots & a_{ij}^{(t)} & \cdots & a_{i5}^{(t)} \\ \vdots & \vdots & \vdots & \vdots & \vdots & \vdots \\ a_{50}^{(t)} & a_{51}^{(t)} & \cdots & a_{5j}^{(t)} & \cdots & a_{55}^{(t)} \end{pmatrix}, \text{ where } a_{ij}^{(t)}=P\left[q_{t+1}=S_j \middle| q_t=S_i\right].$$

Denotations of $P(V_j(i))$ are: P – probability, V – factor, j – index of factor, i – index of the state. In the case when transition from any state is possible to any other state, $a_{ij}^{(t)}>0$ for all i and j. In other cases, $a_{ij}^{(t)}=0$ for one or more i and j pairs.

Model factors are different and not recurring, so transition from one factor to other is defined by the separate matrix of state transition probabilities. For instance, the transition from the technical factor to the economical has different transition probabilities comparing to the transition from the economical factor to the socio-political. Therefore, number of matrixes of transition probabilities is $T-1$. In this case, number of matrixes of state transition probabilities depends only on the number of the model factors. Dimension of matrixes of state transition probabilities depends on the number of states.

To simulate a scenario, i.e. to determine severity of disturbance consequences and estimate probabilities of the model factor states and probability of the scenario, calculation of such probabilities is needed:

$$P\left(V_j(i)\right),\ i=1,2,...,N,\ j=1,2,...,T.$$

Characteristics of Markov chain and processes are used, where transition probabilities depend only on the current system state. Using this characteristic, an equation is obtained:

$$P\left(V_{t+1}(j)\right)=\sum_{i=1}^{N}P\left(V_t(j)\right)\cdot P\left(V_t(i)\rightarrow V_{t+1}(j)\right)=\sum_{i=1}^{N}P\left(V_t(j)\right)\cdot P\left(V_{t+1}(j)\middle|V_t(i)\right) \tag{2}$$

$$j=1,2,...,N\,,\ t=1,2,...,T-1\,.$$

Probabilities of economical factor states are calculated by equation:

$$P\left(V_2(j)\right)=\sum_{i=0}^{5}P\left(V_1(i)\right)\cdot P\left(V_2(j)\middle|V_1(i)\right)=\sum_{i=0}^{5}\pi_i\cdot a_{ij}^{(1)}\,,\ j=0,1,...,5\,. \tag{3}$$

Probabilities of socio-political factor states are:

$$P\left(V_3(j)\right)=\sum_{i=0}^{5}P\left(V_2(i)\right)\cdot P\left(V_3(j)\middle|V_2(i)\right)=\sum_{i=0}^{5}P\left(V_2(i)\right)\cdot a_{ij}^{(2)}\,,\ j=0,1,...,5\,. \tag{4}$$

Simulation of disturbance scenarios is based on Equations (2)–(4) .

Implementation of these equations is based on the modified forward and Viterbi algorithms [10].

Modified forward algorithm.

1. Initialisation:

$$\alpha_1(i)=\pi_i\,,\quad 0\le i\le 5\,.$$

2. Induction:

$$\alpha_{t+1}(j)=\sum_{i=0}^{5}\alpha_t(i)\,a_{ij}^{(t)}\,,\ 1\le t\le 2\,,\ 0\le j\le 5\,.$$

Modified Viterbi algorithm.

1. Initialisation:

$$\delta_1(i)=\pi_i\,,\ \psi_1(i)=0\,,\ 0\le i\le 5\,.$$

2. Recursion:

$$\delta_t(j)=\max_{0\le i\le 5}\left[\delta_{t-1}(i)\,a_{ij}^{(t-1)}\right],\ 2\le t\le 3\,,\ 0\le j\le 5\,,$$

$$\psi_1(i)=\arg\max_{0\le i\le 5}\left[\delta_{t-1}(i)\,a_{ij}^{(t-1)}\right],\ 2\le t\le 3\,,\ 0\le j\le 5\,.$$

3. Termination:

$$P^*=\max_{0\le i\le 5}\left[\delta_3(i)\right],\ q_T{}^*=\arg\max_{0\le i\le 5}\left[\delta_3(i)\right],\ 0\le i\le 5\,.$$

4. Optimal state sequence backtracking:

$$q_t^*=\psi_{t+1}\left(q_{t+1}^*\right),\quad t=2,1\,.$$

5. Calculation of probability of optimal state sequence:

$$P=\prod_{t=1}^{3}\delta_t\left(q_t^*\right).$$

The most probable scenario is obtained from factor states, where probabilities are maximal. Probability of the most probable scenario is obtained from product of maximal probabilities of each factor.

2.2. Parameters of model

The parameters used to describe the model are:

1. N - number of model states. In general, states are connected so from any state is transition to any other (or to the same state). Separate states denote $S = S_1, S_2, \dots, S_N$, and state at time moment t - q_t.

2. T – number of model factors. Separate factors denote $V = V_1, V_2, \dots, V_T$.

3. State transition probabilities $A^{(t)} = \left\{a_{ij}^{(t)}\right\}$, $t = 1, 2, \dots, T-1$, where

$$a_{ij}^{(t)} = P\left[q_{t+1} = S_j \middle| q_t = S_i\right],\ 1 \le i, j \le N.$$

In the case, when transition from any state is possible to any other state, $a_{ij}^{(t)} > 0$ for all i and j. In other cases, $a_{ij}^{(t)} = 0$ for one or more i and j pairs.

Number of model factors is T, so number of matrixes of state transition probabilities is $T-1$.

4. Distribution of initial (technical) states $\pi = \{\pi_i\}$, where $\pi_i = P[q_1 = S_i]$, $1 \le i \le N$.

3. DISTURBANCES OF ENERGY SYSTEM

3.1. Types of disturbance

Disturbances of energy system are natural or external events connected to the human being activity, which may disturb energy system or some elements of the system work. Frequency assessment of initial events is based on event database as well as on general databases and assessments of expert.

Disturbances of energy systems are divided into short-term and long-term according to their impact to the energy system. There is no strict limit, which disturbances are considered as short-term or long-term. Therefore, this was refused in the paper.

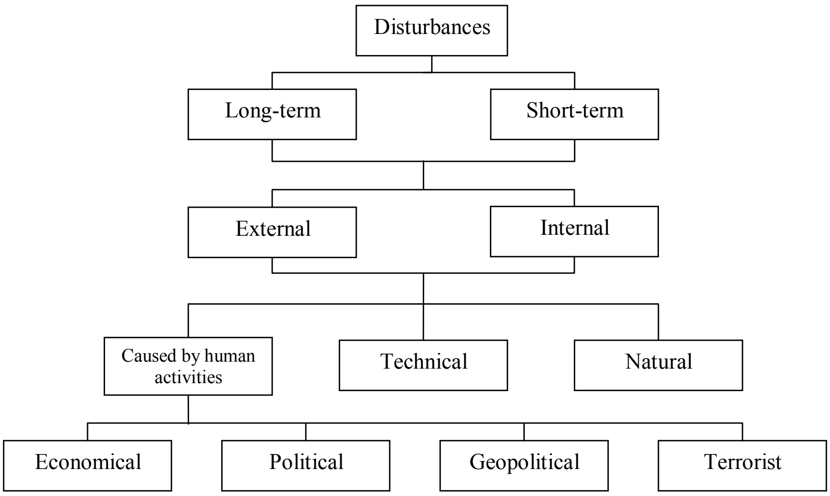

Fig. 1. Scheme of disturbances

Disturbances may be external and internal. Some of them come from outside of energy system (external) and some of them inside (internal). For example, the gas supply disturbance for Lithuania is an external disturbance, but high failure of gas transmission network is an internal disturbance. Both external and internal disturbances may be caused by human activities or arise from natural phenomena impact. Technical system accidents and failures are the biggest part of disturbances. Disturbances caused by human activities may occur for economical, political, geopolitical, terrorist and other activities. The scheme of disturbances is presented in Fig. 1.

Natural events:

- external event occurring in the air (extreme wind, tornado, showers, extreme fluctuation of temperature, drought, lightning, fogs, meteorites etc.);
- the external event occurring on the ground and under the ground (earthquake, movement of ground, volcanic eruption, subsidence of ground, erosion of coast, etc.);
- external fires (fires of the woods, fires of peat, etc.).

External events, connected to human activity:

- explosions (explosions of gas, fuel, ammunition, chemical substances, etc.);
- transport accidents (aircraft crash, accident of automobile and water transport, failure on railways, etc.);
- failures related to transportation of a dangerous cargo (accidents in transportation of explosive, poisonous, toxic, radioactive, easily inflammable and other cargoes);
- emergency events on industrial and military objects (explosions, wreck of technical constructions, outflow of toxic and poisonous substances, explosions of the ammunition, the non-authorized firing of rockets, disruption of gas and oil pipelines, etc.);
- demonstrations and acts of terrorism.

Analysis of external events impact to energy system starts with determination of external event rate, the maximum possible damage of the event to energy system is defined.

3.2. Parameters of disturbance

All values of parameters of disturbance are related to points of consequence states (from 0 to 5 points). The basic scenario shows a current situation of energy sector when primary energy supply disturbances do not exist till 2025, fuel and primary energy sources are supplied as it was predicted by demand for electric energy and heat production; also prices of primary energy resources change by average high forecasts of fuel prices.

Parameters of disturbance:

1) Fuel type of restricted supply – φ. For instance, oil products (fuel oil), gas, nuclear fuel etc.

Denote φ_1 – gas, φ_2 – oil, φ_3 – nuclear fuel, φ_4 – electricity, φ_5 – other. Ranking of fuel type to its importance and defining probabilities of not supplying each fuel type are necessary.

2) Part of energy supply deviation of basic supply scenario - δ.

It is primary energy supply amount reduction in percent of basic supply scenario. Each type of primary energy supply reduction is from 0% to 100% for basic scenario supply amounts in appropriate period. The percent of supply deviation is higher, possible disturbance has more severe consequences and probabilities of higher deviation should be less.

3) Duration of primary energy resources or fuel supply – t, $0 < t < \infty$. This parameter shows duration of energy supply termination. Probability of long-term disturbances is very low, so maximum duration has been chosen 2.5 years.

4) Price deviation of fuel or primary energy resources from predicted price projected in basic scenario – σ. In scenario of this disturbance is committed period of predictable price increase. The maximum price deviation has been chosen 50 %.

All values of disturbance parameters are shown in Table 2.

Table 2. Values of disturbance parameters.

Point	**Fuel type, φ**	**Supply deviation in percent, δ**	**Duration of supply deviation (years), t**	**Price deviation in percent, σ**
0	None	0 %	0	0%
1	Gas	20 %	0.5	10%
2	Electricity	40 %	1	20%
3	Oil	60 %	1.5	30%
4	Nuclear fuel	80 %	2	40%
5	Other	100 %	2.5	50%

A set of various disturbances is obtained from different values of disturbance parameters. To simulate scenarios of disturbances, probabilities of values occurrence is needed. These probabilities should be assessed by experts and/or obtained from statistical data. The probability matrix of disturbance parameters is obtained.

Table 3. Probability matrix of disturbance parameters.

Point **Parameter**	**0**	**1**	**2**	**3**	**4**	**5**
Fuel type of restricted supply, φ	P_{φ_0}	P_{φ_1}	P_{φ_2}	P_{φ_3}	P_{φ_4}	P_{φ_5}
Part of energy supply deviation of basic supply scenario, δ	P_{δ_0}	P_{δ_1}	P_{δ_2}	P_{δ_3}	P_{δ_4}	P_{δ_5}
Duration of primary energy resources or fuel supply, t	P_{t_0}	P_{t_1}	P_{t_2}	P_{t_3}	P_{t_4}	P_{t_5}
Price deviation of fuel or primary energy resources from predicted price projected in basic scenario, σ	P_{σ_0}	P_{σ_1}	P_{σ_2}	P_{σ_3}	P_{σ_4}	P_{σ_5}

where $\sum_{i=0}^{5} P_{\varphi_i} = 1$, $\sum_{i=0}^{5} P_{\delta_i} = 1$, $\sum_{i=0}^{5} P_{t_i} = 1$, $\sum_{i=0}^{5} P_{\sigma_i} = 1$.

Evaluation of country‘s general functioning of energy system should use this matrix, where probabilities of this matrix should be obtained from evaluation of experts and/or statistical data.

Energy disturbance is a function of parameters: $D(\varphi, \delta, t, \sigma)$. Probability of disturbance occurrence is obtained from multiplication of appropriate probabilities of disturbance parameters: $P_{Disturbance} = P_{\varphi_i} \cdot P_{\delta_i} \cdot P_{t_i} \cdot P_{\sigma_i}$, $i = 0, 1, \ldots, 5$.

4. PROBABILITIES OF INITIAL STATES AND MATRIXES OF TRANSITION PROBABILITIES

Consequences of disturbance used in the model are technical, economical and socio-political. Severity of consequences depends on parameters of disturbance. Technical consequences come first so they depend on parameters of disturbance. Technical consequences make economical ones. One of parameter of disturbance is price deviation of fuel or primary energy resources from predicted price projected in basic scenario and this parameter directly influences economical consequences. Duration has impact too. Thus, economical consequences depend not only on technical consequences, but on some parameters of disturbance. The same procedure is with socio-political consequences. Probabilities of initial states and transition probabilities are obtained from functions:

$$P(V_1) = F(\varphi, \delta, t, \sigma),$$

$$P(V_2) = F\left(\varphi, \delta, t, \sigma, A^{(1)}\right),$$

$$P(V_3) = F\left(\varphi, \delta, t, \sigma, A^{(2)}\right),$$

where, $F(\cdot)$ – function, $A^{(1)}$ – transition matrix from technical to economical factor, $A^{(2)}$ – transition matrix from economical to socio-political factor.

Binomial distribution is used to evaluate initial and transition probabilities:

$$b(m|n,p) = P\{X = m|n,p\} = C_n^m p^m q^{n-m}, \text{ where } C_n^m = \frac{n!}{m!(n-m)!},\ q = 1-p,\ m = 0,1,2,...,n.$$

5. DEMONSTRATIONAL CALCULATIONS AND RESULTS

Scenarios can be simulated using the developed model: possibility to obtain most severe scenarios, to assess their probabilities and disturbance occurrence probabilities. The developed model manages with defining severity of consequences and assessing such probabilities.

Calculations where made just to demonstrate how assessment of security of energy system of particular country can be performed when assesment of experts and/or statistical data are available. The set of statistical data should include data of disturbances have been occurred in the particular country (data of disturbance duration, fuel type, etc). Probability matrix of disturbance parameters should be filled with probabilities. Then calculations can be made. But to get these probabilities from statistical data is difficult, so assesment of experts is more accessible.

Demonstrational calculations are based on conservative assumptions. Probabilities of disturbance occurrence and not occurrence are equal. Probabilities of disturbance parameters are defined considering severity of disturbance.

According to Wilks statistics [11], 100 scenarios of energy disturbances were simulated. Results from calculations are defined. States of consequence severity are shown in Table 4.

Table 4. Frequency of states.

States	Technical	Economical	Socio-political
0	**95**	**96**	**92**
1	4	3	8
2	1	1	0
3	0	0	0
4	0	0	0
5	0	0	0

Distributions of consequence states according to their severity are shown in Figs 2–4.

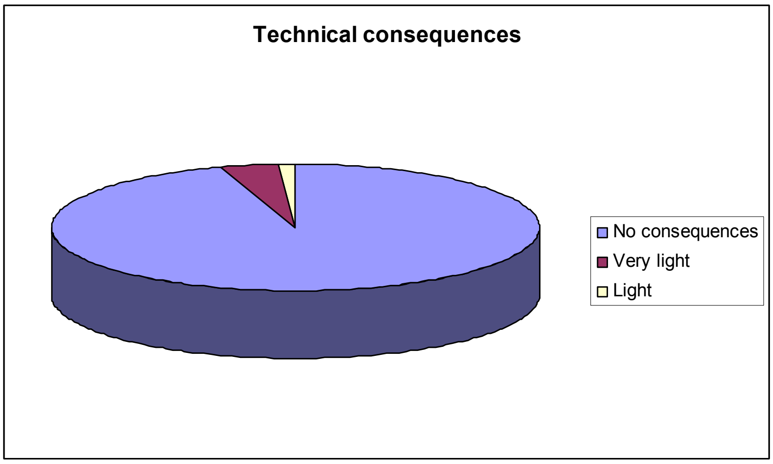

Fig. 2. Distribution of technical consequences

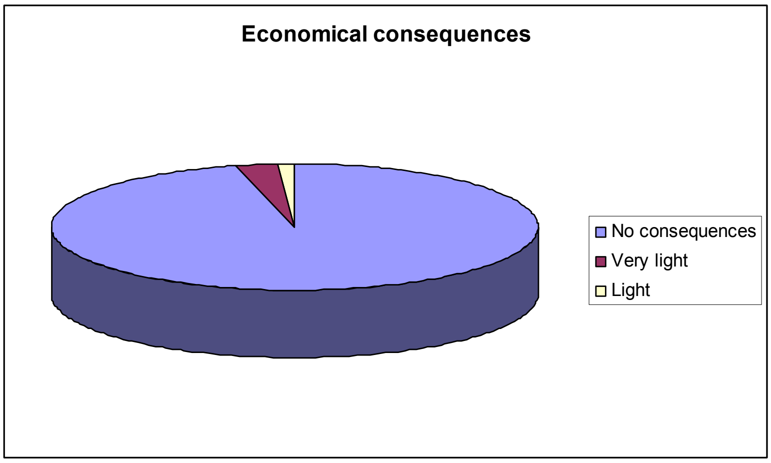

Fig. 3. Distribution of economical consequences

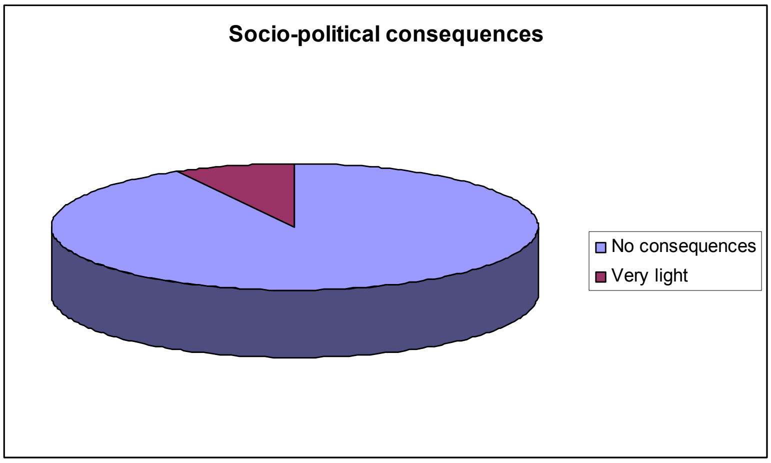

Fig. 4. Distribution of socio-political consequences

The most probable scenario is that potential disturbance has no consequences or there is no any disturbance occurred, as it is shown in the charts. From 100 simulated scenarios disturbance occur 59 time and not occur 41 time (this is from conservative assumptions). But probabilities of disturbance occurrence are very low in comparison with probability of not occurrence.

The most severe scenario is defined from obtained results. In this case, it is the scenario 28 (*S28*).

Scenario S28.

In this scenario, the disturbance has occured: gas termination for 2.5 years. It caused 50% gas price increase and part of gas supply deviation of basic supply scenario was 30%. Consequences of such disturbance would be technical, economical and socio-political. As seen from calculations, these consequences wouldn‘t be severe and the maximum probability is that consequences would be light. But probability of such disturbance occurrence is very low ($2.56 \cdot 10^{-5}$). Distribution of consequence states is shown in Table 5.

Table 5. Distribution of consequence states.

Consequences States	**Technical**	**Economical**	**Socio-political**
0	0.064313	0.201376	0.193455
1	0.235119	0.259375	**0.232658**
2	**0.343825**	**0.266119**	0.225924
3	0.251396	0.15708	0.184258
4	0.091907	0.092201	0.121954
5	0.01344	0.02385	0.041751

As seen from table, the most probable technical, economical, socio-political consequences of disturbance would be light (2 points of severity), light (2 points of severity) and very light (1 point of severity) respectively.

Not only particular scenarios development could be obtained from results, but assessment of general country‘s energy system security level in appropriate period could be made.

6. CONCLUSIONS

The mathematical model of energy supply disturbance consequence scenarios is presented in the article. The following conclusions of the article can be drawn:

The mathematical model is developed:

1) To obtain occurrence probability of each energy disturbance.
2) To obtain severity of each energy disturbance.
3) To assess probabilities of consequence states corresponding to each disturbance.
4) To determine the most severe and easiest scenarios and to assess their probabilities.
5) To assess the most probable scenario according to distributions of consequence states.

REFERENCES

1. Augutis J., Krikštolaitis R., Matuzienė V., Pečiulytė S. Mathematical simulation of energy supply disturbances // Safety, reliability and risk analysis: theory, methods and applications: proceedings of the European safety and reliability conference (ESREL 2008), Valencia, Spain, September 22-25, 2008. London: CRC Press Taylor & Francis Group, 2009. Vol. 1. ISBN 978-0-415-48513-5, p. 2575–2580.

2. Augutis J., Matuzienė V., Krikštolaitis R., Ušpuras E. Analysis of energy supply disturbances in Lithuania // Risk analysis VI: sixth international conference on computer simulation risk analysis and hazard mitigation, Greece, May 5–7, 2008. Southampton, Boston: Wit Press, 2008. ISBN 978-1-84564-104-7, p. 299–308. [Conference proceedings citation index].
3. Augutis J., Matuzienė V., Krikštolaitis R. Analysis of energy supply disturbances and energy security of supply in Lithuania // International conference on probabilistic safety assessment and management (PSAM9), Hong Kong, China, May 18–23, 2008. China, 2008. ISBN 978-988-99791-5-7, p. 1–8.
4. Matuzienė V., Augutis J. Safety and Security of Energy Supply in Lithuania // Strategic Insights. 2008. Vol. VII, Iss. 1. (http://www.ccc.nps.navy.mil/si/)
5. Augutis J., Matuzienė V., Krikštolaitis R., Pečiulytė S., Norvaiša E. Energijos tiekimo saugumo vertinimo metodų analizė // Energetika. ISSN 0235-7208. 2008. T. 54, Nr. 4 , p. 1–9. [INSPEC, Index Copernicus].
6. Augutis J., Ušpuras E. Technologijų rizika: monografija. Kaunas: Lietuvos energetikos institutas, Vytauto Didžiojo universitetas, 2006. ISBN 9986-492-89-0
7. Kubilius J. Tikimybių teorija ir matematinė statistika. Vilniaus universiteto leidykla, 1996. p. 230–253.
8. Kruopis J. Matematinė statistika. Mokslo ir enciklopedijų leidykla, 1993, p. 52–53. ISBN 5-420-01015-1.
9. Bagdonavičius V., Kruopis J. Matematinė statistika, I dalis. TEV leidykla, 2007, p. 45–46 ISBN 978-9955-511-76-2.
10. Rabiner L., Juang B. An introduction to hidden Markov models. IEEE ASSP Magazine, p. 4–16, Jan. 1986.
11. Kloos M., Hofer E. SUSA Version 3.2. User‘s guide and tutorial. GRS, Garching, 1999.

CYSENI 2009, May 28-29, Kaunas, Lithuania
ISSN 1822-7554, www.cyseni.com

THE ENERGY CHARTER TREATY: IMPLICATIONS FOR LITHUANIAN ENERGY SECURITY

I. Martinkutė, LL.M.
Law firm "Smaliukas, Juodka, Beniušis & partners"
Konstitucijos ave. 7, LT-09308 Vilnius – Lithuania
Phone: +37068526252
Email: inga@smaliukas.lt

ABSTRACT

The Energy Charter Treaty was negotiated, signed and came into force at record speed immediately after the collapse of the USSR. High hopes were associated with this multilateral treaty covering legal obligations on energy trade, transit, investment and dispute resolution. 15 years later all states within geographical Europe have to face the increasing tensions in the energy sector and political speculations over the subject. Whether the Energy Charter failed in a sense that its drafting was inadequate even from the very beginning or today's economical, political and technological situation changed so dramatically that it was impossible to predict such a turn?
Lithuania is a member of the Energy Charted Treaty since its creation. The article analyses the historical background of the treaty and the current membership benefits, as well as discuses the drawbacks of legal regulation and its limitations. The article investigates the future prospects of the Energy Charter Treaty and in particular its ability to provide energy security for Lithuania.

1. INTRODUCTION

The aim of this article is to highlight the implications of the Energy Charter Treaty (hereinafter – the Treaty) for the energy security of Lithuania. In order to achieve this it is necessary at least briefly discuss the historical background and the development of the Treaty as well as current geopolitical situation in the region. The article focuses on topical Treaty provisions and does not cover the ongoing negotiations concerning the Transit Protocol.

2. METODOLOGY

It is understood that social sience methodology is very different from the sientific methods, because of several reasons. First, social sience is about ideas, that can explain past or current status of the affairs or can can influence the changes in the future social behaviour. Secondly, no experiments are possible in law or to a very limited extent, because it is not ethical to experiment with human beings.

Thus, legal methods employed in writing this article include linguistic, formal logic, teleological, systemic, historical and comparative. Linguistic and formal logic method is used to reveal the content and structure of the legal norms used in the Treaty. Teleological method of interpretation was used to disclose the true aim of the legal norm and the intentions of the drafters of the Treaty, when it was signed. The systemic method of interpretation is used for the proper understanding of The Treaty's place within Lithuanian, European and international legal system and in particular to understand the relations between separate legal norms within the Treaty. Historical method is used to compare the development of the Treaty application and geopolitical situation. The comparatice method is used to compare the legal regulation of trade, transit and investment in different legal systems.

3. HISTORICAL BACKGROUND

The collapse of the Soviet Union offered vast posibilities for East – West cooperation. Mutual interests fuelled this process: Eastern Europe was rich in natural resources, but needed investments. Western Europe was keen to diversify its energy supplies and had available funds [1]. The initial conference that took place in 1991 produced the European Energy Charter which declared political intents of the parties and provided basic principles for the future cooperation [2]. It has to be mentioned that the Charter itself is not a legally binding document, it is only a declaration. After three years the Energy Charter Treaty was signed in 1994, which is legally binding document. The name of the Treaty derived from its predecesor -the European Energy Charter. Most of the principles of the European Energy Charter proceeded into the binding Treaty and were expanded and developed. The aim of the Treaty was to strengthen the rule of law on energy issues, thus minimising the risks associated with energy related investments and trade [3]. It has to be noted that the Treaty is the only one multilateral treaty devoted to the energy sector. It comes as no surprise, because energy issues are so sensitive to the national interests of the states, that previously no one was willing or able to surrender part of the sovereignty in fovour of some treaty.

Lithuania, being one of the first states that reinstated its independence from the Soviet Union, participated in the negotiations from the very begining and signed the Treaty on 5th April, 1998. However, virtually no Lithuanian internal documents survived evidencing Lithuanian participation in drafting and negotiating the Treaty. The Treaty came into force in April 1998 and was ratified by the Lithuanian Parliament on 23rd June, 1998 without any discussions. It rises a retorical question whether the content and nature of the Treaty was fully understood. After the ratification the Treaty became fully and directlly applicable in the territory of Lithuania and in relations between the contracting states.

4. THE STRUCTURE OF THE TREATY AND CURRENT STATUS

The structure of the Treaty consists of five main areas: energy trade, energy transit, investment into energy sector, energy efficiency and mandatory resolution of disputes arising from the abovementioned areas. Each of them have different scope, different levels of binding nature and will be discussed in more detail below.

4.1. Trade

Initially Treaty provisions on trade were based on the General Agreement on Trade and Tariffs (GATT). The Treaty makes refference to World Trade Organisation (WTO) rules even though the later is not specifically aimed at energy, but by refference WTO rules become mandatory for energy trade. It means *inter alia* that the Most Favoured Nation clause is applied wchich require to treat all foreign national and copmanies on the equal grounds, i.e. if favourable or special conditions are offered to the national or company of one country, then all others could require the same. Moreover, WTO rules mean national treatment for the energy products if they crossed the border legally, .i.e. contracting states cannot discriminate the energy products on the basis of their origin. Additionally, under the WTO rules quantitative restrictions for the energy materials and products have to be eliminated, i.e. import or export quotas have to be abolished. In 1998 the Trade Amendment to the Treaty was adopted and offered the same trade regime not only for energy materials and products, but also to energy – related equipment. Furthermore, the Trade Amendment provides mechanism for future stand-still on customs duties and charges, i.e. possible future prohibition to increase customs duties and charges for energy materials and products moving between the member states. However, the Trade Amendment is not in force yet, because it needs at least 35 ratifications and at the moment only 33 member states ratified it. It has to be noted that disputes over trade have their own dispute settlement mechanism provided by the annex D to the Treaty and is based on WTO dispute settlement procedure.

4.2. Transit

The essental part between energy exploration, explatation and consumption is energy transit. Its importance was well understood by the drafters of the Treaty, but regretfully only „soft law“ obligations were negotiated.

The transit is defined in the Article 7(10) of the Treaty by three categories: the carriage of energy materials and products originating in one contracting state, destined to the second contracting state and carried through a third contracting state.

First of all the Treaty oblige contracting parties only to facilitate the transit on a non-discriminatory and reasonable basis. Secondly the article 7(4) of the Treaty provides the obligation not to place obstacles for the new capacities.

The Treaty failed to make transit a mandatory right and obligation between the contracting states. How did it happen? It has to be said that negotiations between Russia and Western Europe was not an easy task even after the collapse of the Soviet Union. The progress of negotiations was well behind the schedulle. Negotiators were afraid, that even those provisions of the Treaty that were agreed, could fail to be signed because there were too many issues were agreement could not be reached before the provisional date of signing. Thus, crucial decision was made to leave the unsolved issues for the later negotiations and additional protocols and to include into a Treaty at least those provisions that were agreed. Therefore, detailed regulation of transit obligations was thought to be left for the additional Transit Protocol. The negotiations over additional Transit Protocol started in 2000. Considerable progress was made on definition for available capacity, principles of transit tariffication, transparent and non-discriminatory congestion management rules, the provisions for new capacity creation [4]. Unfortunately the initial contradictions between the EU and Russia could not be resolved and application of the Transit Protocol inside the EU is still unclear. Further negotiations are in a deadlock at the moment without any prospects to be finished in the nearest future.

In the context of the Treaty transit provisions it is interesting to examine the case of abrupt closure of Druzhba oil pipeline branch to Lithuania. and to analyse whether Lithuania has a valid claim against Russia? The transit provisions were drafted with the interim state in mind, but in Druzhba case it was the originating state that closed the pipeline on a dubious “technical” reasons immediatelly after unsucsessfull Lukoil attempt to buy Mazheikiai oil refinery [5]. The help was offered to fix the pipeline, but the response came that it may be too costly to do so. The interesting thing is that most of the pipeline’s branch goes through the teritory of Belarus and only the tiny part of the branch is situated in Russia. Thus, it is difficult to see how and why a reconstruction of a tiny part of Russian pipeline could be too complicated and not make sense. The Article 7(1) of the Treaty clearlly obliges the contracting states to take the necessary measures to facilitate the transit of energy materials and products in consistance with the principle of freedom of transit and without distinction as to the origin, destination or ownership of energy material or products and without imposing any unreasonable delays, restrictions or charges. Had the case been pursued by Lithuania from the very beginning I would argue that Lithuania had a good chance to claim that oil transit was discriminated on the basis of destination, i.e. Lithuania.

Two years later in the end of 2008 the Russian ambasador to Lithuania stated that Druzhba could be reopened if Lithuanian companies invested milions of litas into reconstruction [6]. The message was met coldly by the Lithuanian governement and general public.

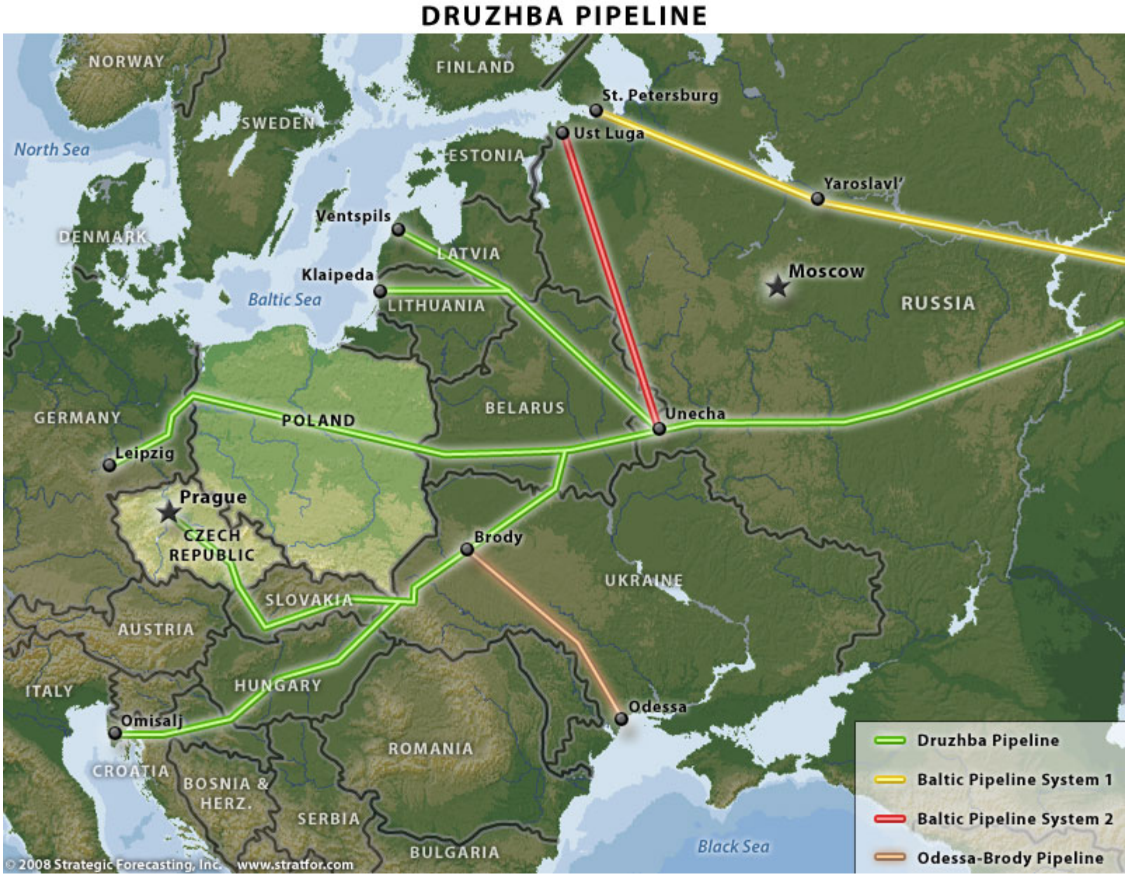

The Article 7(7) of the Treaty provides that in case of dispute first of all contractual dispute resolution remedies should be invoked and if that fails the Secretary – General of the Charter Conference should appoint the conciliator who shall seek the agreement and if that fails shall issue a recommendation. The Rules for Conciliation of Transit Disputes were adopted by the Charter Conference in December 1998 but were never used despite annual Russia – Ukraine or Russia - Belarus transit disputes. However vague the transit dispute settlement mechanism is, it has to be initiated by the the member states. At the current state of affairs it seems that member states are lacking the trust in the Energy Charter Treaty and in the Secretary – General to do so. It seems that Russia and Ukrane and Belarus do not trust the dispute settlement procedure provided by the Treaty.

4.3. Investment

The Treaty defines in the broadest way the deffinition of the investment as any kind of assets, including tangible and intangible, movable and immovable property and any property rights, companies or enterprises, shares, stocks, bonds, any form of equity or debt, money, intelectual property, returns and any contractual or legal rights. The Treaty provides that the abovementioned assets and energy related investment as business should bear no discrimination, and should enjoy national or most favoured nation‘s treatment, whichever is the most favourable.

Furthermore, the member states of the Treaty undertakes not to nationalise or expropriate the abovementioned investments, except for the public purpose in a non-discriminatory manier and under the due process of law and accompanied by the prompt, adequate and effective compensation.

However, the article 18 of the Treaty reafirms sovereign rights over natural resources, which means that only the state can decide on how, when and if it is going to explore and exploit natural resources. The Treaty does not guarantee the investors automatic rigth to investment in the energy sector. The Article 10 (5) of the Treaty obliges the member states only to endevour, i.e. to make best efforts to limit the exceptions to the national and most favoured nations treatment, plus progressively remove existing restrictions. Even though the imposed obligation is soft it is argued that adoption of new restrictions would be violation of the Treaty [7].

It has to be mentioned that initially the Treaty provisons were supposed to proted so called Western investments into the wild, politically and legally unstabe East. But currently the opposite could be observed. For example, Russian state companies aquired considerable stakes in Lithuanian energy companies, thus Russian investments should be protected applying the same standarts. Various regulatory interferance with the business of theose companies, such as mandatory tariff, could be regarded as the damage to the investment and lead to the investment claims.

After the restoration of independence Lithuania was very eager to prove that it is a secure destination for the foreign investments and concluded nearlly all posible bilateral investment protection treaties and the Energy Charter Treaty on the top. The abovementioned treaties provide a high standar which Lithuania finds difficult to follow. Once the investment is made it becomes almost untouchable and any damage which can by attributable to the govement has to be compensated by the government. As a result Lithuania experienced a handfull of investment disputes with foreign nationals and companies solved by international arbitration or by Iternational Centre for Settlement of Investment Disputes. The mechanics of those case are very different and most of them are based on contractual claims, but in general investors were quite succesfull in defending their interests. Only after several bitter cases Lithuanian government became aware of the heavy burden it had put on itself. Even if there were some lonely voices to nationalise Mazeikiu oil refinery after Yukos bankruptcy or LEO LT after some elements were declared anticonstitutional, the Lithuanian government is more self restrainant now, because it is aware that nationalisation is a strait case to the international investment claim by the investor. Nevertheless, more and more investment disputes should reach courts or arbitration panels in the future, because the increasing amount of the investments and especially bearing in mind new energy projects being developed at the moment, such as nuclear power plant, power bridges to Sweden and Poland, LNG terminal, etc.

The investment provisions of the Treaty only indirectly contribute to the energy security of Lithuania in a way that it encourages investment into this sector by providing assurances to the private investors. Consequently, investments make the research technological developlemtn as well as allow construction of newer more efficient energy production plants or infrastructure or allows diversification of energy sources.

4.4. Environment

The Treaty as well provides „soft“ provisions on the environmental aspects and energy efficiency. That means the contracting states do not undertake to achieve specific results, but only undertake to make best efforts. The wording of “best efforts obligation” is ussually used when no contracting party is really willin to be bound by any obligations. Consecuently, the article 19 of the Treaty vaguely obliges contracting states to minimize harmful environmental impacts, but imposes a condition for the said goal: in an economically efficient and cost-effective manner. Practically it means that it will be very hard to prove any breach of such a broad duty with such a broad exception.

Furthermore in the same vague maner the Treaty obliges to take precautionary measures to minimize environmental degradation and to take particular attention to improve energy efficiency, to develope and use renewable energy sources, to promote the use of cleaner fuels and technologies [8].

The Energy Charter Protocol on Energy Efficiency and Related Environmental Aspects (PEEREA) was negotiated, opened for signature and entered into force at the same time as the Treaty. PEEREA builds up on the Treaty provisions but is getting nowhere near the "result obligation" and obliges the contracting states only to formulate and implement energy efficiency strategies and policies, to create appropriate legal, regulatory and institutional frameworks to develop, implement and update energy efficiency programmes.

The observation of the abovementioned environmental provisions is supervised through regular and in-depth energy efficiency reviews [9]. The former are based on a review format agreed by the working group on Energy Efficiency and Related Environmental Aspects, which is the institutional body in the Energy Charter, and covers general issues such as energy efficiency legislation, policies and programmes, quantitative data on energy and energy efficiency. On the contrary, in-depth energy efficiency reviews are undertaken of countries that volunteer to host such an exercise and it covers broad economic and energy context of the country, patterns of energy use, energy efficiency policies and institutional frameworks and conclude with specific recommendations [10]. It has to be mentioned that a decade ago a Lithuanian review was carried out, but no public information on this review coud be found.

The Lithuanian energy efficiency problems in the context of the Treaty were analysed in previous academic works [11] and current status is even more acute. It is needless to say that enhanced energy efficiency will work only for the benefit of Lithuanian energy security, because every bit saved, means Lithuania will need to buy less from Russia.

To conclude the environmental chapter it has to be said that it was nice to include some environmental provisions into the Treaty but kind of naïve to achieve substancial comitments, because the environmental aspect is very complicated and perhaps the United Nations forum is better suited for such an owerhelming task.

4.5. Dispute resolution

The Treaty provides separate and compulsory dispute resolution mechanisms for state to state disputes and for investor – state disputes. So far there were no state to state dispute settlements according to the article 27 of the Treaty, but several investor – state disputes were resolved in accordance with the article 26 of the Treaty, which provides that the investor may choose one of the forums: the Iternational Centre for Settlement of Investment Disputes (ICSID), UNCITRAL arbitration or Arbitration Institute of the Stockholm Chamber of Commerce. Each of them will be discussed briefly below.

ICSID is an autonomous international institution established under the Convention on the Settlement of Investment Disputes between States and Nationals of Other States (the ICSID or the Washington Convention) with over one hundred and forty member States [12]. Although Russian Federation together with Moldova and Canada signed the Convention, but they refused to ratify it. Therefore, it is not mandatory to settle the claims against those states through ICSID Convention, but they may agree to use the ICSID Additional Facility Rules.

The Arbitration Rules of the United Nations Commission on International Trade Law (UNCITRAL) are specially designed for ad hoc arbitrations proceedings.

Arbitration Institute of the Stockholm Chamber of Commerce was established in 1917 as a separate institution and has a reputation as a neutral center for the resolution of the East-West trade disputes [13].

The effect of obligatory dispute resolution mechanism combined with material obligations of member states could be ground-braking, because the compulsory arbitration leads to the enforceable arbitral award, which does not depend on political situation, or political weigth of claimant or defendant.

On the other hand, it is still heavily influenced by the politics [14]. For example, the Treaty is provisionally applicable to the Russian Federation. It is held by the majority of legal authorities that provisional application of the Treaty means that practically all Treaty provisions are applicable as if the Treaty had been ratified and fully in force. That means investment claims can be brought against the Russian Federation. My guess is that Yukos case is just a pionier for the future investment cases. It has to be said that since the Treaty came into force a handfull of investment cases were already based on it. Even though the Treaty is too abstract and general on transit and environment issues, it is fairly practical for the investment protection purposes.

5. DRAWBACKS AND LIMITATIONS

At the moment when the enthusiasm of 1990 has evaporated and Russia is playing hard its energy card the Treaty sometimes looks inadequate for up today challenges, i.e. gas blackouts and pipeline closures. Thus it is questionable whether the Treaty was inadequeate and inapropriate from the very beginning? [15]

The answer would probably be - no. It was a right move to try to bring East and West more closer toghether. The Treaty is still provisionally applicable, even if Russia refuses to ratify it.

The second reason for negative answer would be the very nature of the sector. The international energy regulation is a developing area of law with no customs and established practices. It is very different from other international treaties which only codifies international law. The Energy Charter Treaty was doomed to be outdated the very moment it was signed, because it became immediatelly outdated, but not because it was badly drafted, but because the political and economical situation changes so fastly nowadays. Furthermore, even at the time of drafting and now it is still a unique multilateral investment protection treaty with strong dispute resolution teeth?

Finally, even if the Treaty provides the tools, it has to be used by the parties to the Treaty themselfes and they are not willing to do so, nobody can force them.

6. FUTURE PROSPECTS AND CONCLUSIONS

With the transit and environmental provisions being too “soft” to enforce, with the negotiation on the Transit Protocol stalled and entry into force of Trade Amendment laging the future of the Energy Charter Treaty is unclear.

The only “hard” obligations provided by the Treaty are concerned with the investment protection. Thus the only thing that we may predict that the number of litigation will be increasing over the coming years. And the trend might be quite unexpected. Since the investment oportunities eastwards for the coming decade looks to be very risky, we might encounter investments going westwards with accompanying arbitrations.

As for the energy security, the Treaty is only a small stone in the road and has little space to stretch its musculs. Thus, more should and could be achieved through joint European external actions and negotiations. The Treaty is limited in its scope and clumsy forum for negotiations, but probably better than nothing, if you know how and when to use it.

REFERENCES

1. The Energy Charter Treaty and related documents. A legal framework for international cooperation. Brussels. Energy Charter Secretariat. 2004, p. 13.
2. M. Roggenkamp, C.Redgwell, I. del Guayo, A.Ronne. Energy Law in Europe. National, EU and International Regulation. 2nd edition. Oxford University Press 2007, p. 148.
3. The Energy Charter Treaty and related documents. A legal framework for international cooperation. Energy Charter Secretariat, 2004, p. 14.
4. http://www.encharter.org/fileadmin/user_upload/Staff_presentations/Trade_and_Transit/Charter_and_Intl_Energy_Trade.pdf
5. V. Socor, Russian oil pipeline shutoff to Lithuania: wider ramifications, http://www.jamestown.org/single/?no_cache=1&tx_ttnews%5Btt_news%5D=32789
6. http://www.balsas.lt:80/print/216298
7. M. Roggenkamp, C.Redgwell, I. del Guayo, A.Ronne. Energy Law in Europe. National, EU and International Regulation. 2nd edition. Oxford University Press 2007, p. 151.
8. http://www.encharter.org/fileadmin/user_upload/Staff_presentations/Trade_and_Transit/Charter_and_Intl_Energy_Trade.pdf
9. http://www.encharter.org/index.php?id=42&L=0
10. Ibid.
11. Burba A., Bachanovas P. Energetikos chartijos sutartis ir energijos efektyvumo politikos problemos Lietuvoje // Energetika. ISSN 0235-7208. 2000. – Nr. 3. – P. 57–62.
12. http://icsid.worldbank.org/ICSID/FrontServlet?requestType=CasesRH&actionVal=Show Home&pageName=AboutICSID_Home
13. http://www.sccinstitute.com/uk/About/
14. А. Белый, После бума, http://www.globalaffairs.ru/numbers/36/11230.html
15. A.V. Belyi, S. Nappert, A New Energy Charter: Myth or Reality? Transnational Dispute Management, 2009.

EVALUATION OF ENVIRONMENTAL SUSTAINABILITY OF A BIO-FUEL ENERGY SOURCE

M.G. Gnoni, G. Lettera,
Department of Innovation Engineering, University of Salento
via per Monteroni, 73100 Lecce – Italy
Phone: +39 (0)832 297322
E-mail: mariagrazia.gnoni@unile.it
gianni.lettera@cerpi.it

ABSTRACT

According to European laws (see the Directive 2003/30/EC), a growing interest is spreading out in the field of bio-fuel diffusion in several countries, such as Italy. Several issues are contributing to this phenomenon such as the widespread attention for environmental protection issues and diversification of energy supply sources. Thus, the bio-fuel valorisation for energy production has been connected to a high level of sustainability due to the traditional perception of renewable resources. Therefore, a critical issue deals with the analysis of the actual level of sustainability of the whole bio-fuel supply chain process. Bio-fuels energy sources applied in the field of heating and electricity generation are potentially carbon dioxide neutral: this is clearly correct for the source process, but it has to be verified in the overall industrial process involved in energy generation. In traditional bio-fuel supply chains, a relevant contribution to the "consumption" of the sustainability level depends on the fossil fuel demand requested from transportation activities of raw materials – such as the bio-fuel – to energy valorisation process. Logistic activities could determine a significant contribution in the overall net carbon addition analysis mainly due to the countries of origin of the bio-fuels (South America, Africa, etc.). The paper aims to investigate how activities in the bio-fuel supply chain could contribute to define the overall sustainability level of a bio-fuel energy source through the application of a life cycle approach, i.e. from bio-fuel production to energy valorisation. This analysis could support the strategic planning about the use of renewable and alternative renewable resources: it has to be evaluated the whole supply chain sustainability according to both logistic issue as well as technological choices. The proposed approach – based on an index method - could be effective both for evaluating actual sustainability assessment of such an industrial production and for developing efficiently agro-energetic districts to support more effective environmental strategies.

Keywords: bio-fuel, sustainability indexes, life cycle approach

1. INTRODUCTION

A sustainable energy strategy, based on the promotion of renewable energy sources, has been the basis of several European Legislations in recent years. In 2006, the European Commision has published a Green Paper regarding the development of sustainble strategies in the field of energy policies, aiming to highlight future energy supply challenges and their effects on the environment [1]. This strategy has been confirmed in December 2008 with the adoption of Europe's Climate and Energy Package which is usually summarized by the so called "20-20-20 strategy"[2]. This approach has defined binding targets for each Member State in order to reach European targets within the 2020 year: the general purpose is both to cut greenhouse gas emissions by a target value and to establish a fixed percentage (i.e. 20%) of renewable energy production and to increase of 20% the energy efficiency level.

The recent directive includes also a target in transportation activities: each Member State will have to increase (i.e. up to 10%) the use of renewable energy in this sector. The directive analyzes the open issue of sustainability of bio-fuels production: it promotes the application of the so called “second generation bio-fuels”, which do not compete with food or feed production unlike traditional – i.e. "first-generation" – ones.

According to this European policy, growing interest is spreading out regarding renewable energies in several European countries, such as Italy. Economical and environmental benefits of renewable industry are widely proved; otherwise, few criticalities could belong to different points of view such as the increasing prices and the actual sustainability level of the renewable sources. Bio-fuels production and its supply chain require new analysis models for an effective assessment of its sustainability level. A multidisciplinary approach is required due to the high level of complexity of these issues in terms of ecological aspects, social aspects, data availability, etc.

The paper proposes an approach to evaluate the actual sustainability level of the whole supply chain of a bio-fuel energy source based on index method: the proposed model is focused on environmental aspects based on a life cycle approach. Economical aspects could be easily integrated in the model; otherwise, social aspects require a deeper investigation. The potentiality of the proposed method has been investigated in an application regarding the impact of logistic activities on the overall sustainability level of a bio-fuel energy source.

2. BIO-FUEL SUSTAINABILITY ISSUES: A BRIEF STATE OF THE ART

In recent years, bio-fuels have reached an increasing attention from scientific comunity and business practices. Usually, bio-fuel production derives from renewable feedstocks that can be grown by farmers in several countries; their application aims both to reduce greenhouse emissions and the global petroleum dependency of a country. Usually, the bio-fuel production process requires a significant availability of resources in terms of both cultivable land and water; this phenomenon has contribute recently to increase food prices. A recent study proposed by OECD/FAO [3] has highlighted that expected food prices will rise from 20% to 50% by the 2016; this tendency could influence bio-fuel diffusion as a energy source.

Few studies have been dedicated to evaluate how different bio-fuels could contribute to reduce greenhouse-gas emissions and actual benefits of these applications in energy generation. In [4], the authors evaluate the total primary energy inputs and total greenhouse gas emissions associated with the production of biodiesel from oilseed rape provided by a regional supply chain and production facilities in the North East of England. This study analyses total greenhouse gas emissions reduction for the bio-fuel production: it shows a positive net primary energy level and a net emissions savings (in terms of CO_2). Moreover, authors propose a comparison of different bio-fuels scenarios: the application of the rape meal oil as an animal feed, its direct application in combustion for electricity generation, and finally, the application of conventional ultra low sulphur diesel derived from crude oil.

A critical point regards how a bio-fuel is effectively sustainable focusing on different aspects. An effective assessment of the bio-fuel potentiality requires an approach from “well-to-wheels” for an evaluation of the whole production process [3]. A study commissioned by the Swiss government [5] supplies a detailed assessment of the environmental costs and benefits of different types of transportation activities of such a bio-fuel. Authors compare gasoline, diesel and natural gas with other 26 bio-fuels produced from different crops used in Switzerland according to on a life cycle approach. Total environmental impacts of each fuel have been assessed by the definition of a single indicator which supplies information about different impacts of analyzed fuels: it allows comparing different impacts to legislative targets. A comparison with gasoline supply chain process is proposed in terms of greenhouse-gas emissions for each fuel.

In [6], authors propose a review of potential impacts due to a large-scale bio-energy crop application for heating, and power generation in a UK context by evaluating environmental implications across Europe and other agricultural regions.

3. THE PROPOSED APPROACH FOR EVALUATING BIOFUEL SUSTAINABILITY

In traditional bio-fuel supply chains, a relevant contribution in the consumption of sustainability level could be derived from the production process and the transportation activities of the renewable energy source; the main cause is that the bio-fuel is usually not produced in the nation (for example South America) where the combustion plant is located (for example Italy). The proposed method aims to evaluate the contribution of the different processes in the bio-fuel supply chain through a life cycle approach. The aim is to evaluate the actual sustainability level of a bio-fuel supply chain, focusing on environmental aspects. The contribution to sustainability consumption of all levels of bio-fuel supply chain has to be evaluated: the main focus is on logistics activities which represent usually the highest impact in the lifecycle of a bio-fuel. This is mainly due to the country of origin of bio-fuels which are currently produced far from places where they are burned in a power plant. Moreover, logistics design represents an activity which could be affected directly by the management of a power plant: it could represent a key factor that could contribute to improve the overall renewability of an installation.

The proposed model is based on an index method for evaluating the renewability and sustainability level of a specific power plant or a supply chain which supplies bio-fuel for combustion process. The overall level of renewability of the specific installation or process depends both on bio-fuel type (such as jatropha oil, rapeseed oil, etc.), combustion process-type and logistic activities for supplying the bio-fuel from its country of production to the power plant. The sustainability level assessment is focused on evaluation of CO_2 emissions; the model is modular, thus, other emissions levels could be evaluated but they could not affect the overall model validity.

Following, the model is described in detail. At first, a typical bio-fuel energy source supply chain is analyzed aiming to assess the overall life cycle of a bio-fuel; the environmental impact analysis – based on CO_2 emission level – has been carried out according to a reference unit (the so called *functional unit*) which aims to define impact levels in a unified point of view. Therefore, this normalized analysis allows more effective comparison of all levels of the supply chain highlighting critical level according to an environmental point of view: this information could supply such a point of intervention for improving the overall sustainability of a specific supply chain.

Fig. 1. A typical bio-fuel supply chain scheme

A typical bio-fuel supply chain organization is depicted in Figure 1; each level is described as follows:

- “Farming” phase: this represents the first activity for producing the bio-fuel; it consists of plant cultivation for producing seeds. It varies highly depending on bio-fuel type: this is due to both intrinsic parameters such as plant type, and operational issues geographical area, agronomic techniques, etc.;

- "Oil Mill" phase: this phase could be developed using chemical or mechanical treatment. The first is characterized by a higher impact due to materials applied for chemical extraction. In the proposed supply chain model, refining activities are not considered.
- "Power Plant" phase: this is the valorization activity of the bio-fuel. Overall impact depends on the combustion technology process; in the proposed model this impact has been evaluated according to guidelines supplied by specific Best Available Technologies (BAT) defined for the specific sector.
- "Logistics" phase: each production level in the supply chain is connected by two main transportation activities: the first provides crude oil to mill plants starting from farming areas; the second starts from production countries to valorization countries (i.e. power plant location) and it supplies raw material to energy valorization.

The model has been tested in a case study regarding a specific bio-fuel: the Jatropha crude oil. Jatropha Curcas origins from tropical areas in America, but is now produced in many tropical and sub tropical regions throughout Africa and Asia. Due to its toxicity, Jatropha oil is not fit for nutritional consumption: it is traditionally used for soap production and medical applications. Jatropha potential for producing energy has been recently analyzed due to the increasing attention required for strategic planning of huge plantation areas in Asia, Africa and America [7].

Thus, the operational scenario has been defined for the supply chain process of the specific bio-fuel, i.e. the Jatropha crude oil; main hypothesis applied are synthesized in Table 1. The functional unit has been defined as the unitary output obtained from the combustion plant, i.e. one MWhe.

Table 1. Main hypothesis of the normalized scenario

SCENARIO PARAMETERS	**VALUE**
Functional Unit	1 MWhe
Combustion efficiency	50%
Fuel type	Jatropha crude oil
Heating Value	38.200 [kJ/kg]
Oil extraction technique	Cold-press process
Oil extraction efficiency	30%

After the characterization of the bio-fuel supply chain scenario, the approach proposes the evaluation of an index, called *Gross Renewability Index* (GRI) introduced in equation (1):

$$\mathrm{GRI} = \frac{\mathrm{CO_2\ emitted\ from\ combustion}}{\mathrm{CO_2\ fixed\ by\ photosyntesis}} \tag{1}$$

The GRI calculation aims to assess how the bio-fuel is renewable according to its intrinsic characteristics; this rough evaluation is based only on primary processes in the supply chain, such as combustion and photosynthesis process. The combustion process contributes to increase CO_2 emissions; otherwise, the photosynthesis process has a positive impact by capturing the CO_2. Service processes, such as logistics, bio-fuel transformation, are not yet evaluated by the GRI; thus, this index does not consider the contribution of the specific supply chain of the bio-fuel but it represents the gross potential sustainability level of the specific bio-fuel. The GRI allows a classification of bio-fuels according to potential sustainability level of the renewable energy source; it depends on bio-fuels type and combustion technology, effects due to the design of a specific supply chain such as transportation type, extraction technologies have not yet been evaluated. Moreover, combustion process could influence slightly the index evaluation: this depends on the introduction of the well known Best Available Technologies (BAT) which supplies target levels of emissions for these types of installations [8]. The GRI calculation for the case study analyzed is reported in Table 2.

Moreover, The GRI calculation could represent quantitatively the "bonus" of renewability supplied by the specific bio-fuel; this represents the sustainability level available for consumption by the operational supply chain. From a life cycle point of view, the design of the "optimal" supply chain of energy source depends on both the level of GRI index and on the supply chain structure in terms of service processes, transportation types and plant locations.

Table 2. The GRI calculation for the case study (i.e. Jatropha crude oil)

SCENARIO DATA	**VALUE**	**DESCRIPTION**
Oil quantity [Kg]	189	Quantity of oil needed to produce 1 MWhe
Combustion yield: [kg CO_2×kg oil]	2,482	The reference is Council Directive 96/61/EC of 24 September 1996 concerning Integrated Pollution Prevention and Control (IPPC). It refers to a generic bio-fuel.
Emission from combustion process [kg CO_2]	528,26	Emissions referred to 1 MWhe (the functional unit)
Photosyntesis yield: [kg CO_2 x kg oil]	2,504	To produce a mol of J. curcas oil, 57 mol of CO_2 are needed in the photosynthesis process; a mmol of J. curcas oil therefore weighs about 0.888 g. [6]
CO_2 adsorbed by photosynthesis process [kg CO_2]	533,74	CO2 captured, referred to 1 MWhe (functional unit)
	GRI	**0.988**

Each level of the supply chain will contribute to reduce the GRI consumption; finally, the overall calculation of CO_2 emissions could be positive or negative according to the initial GRI value and the supply chain structure. This evaluation is supplied by the *Supply Chain Index* (SCI), defined in equation (2):

$$SCI = \sum_i^n \frac{(\mathrm{CO_2\ emitted})_i}{\mathrm{CO_2\ fixed\ by\ Photosyntesis}}, \tag{2}$$

where *i* represents the *i-th* process in the specific supply chain structure. The SCI supports the evaluation of emissions due to the whole bio-fuel supply chain according to the *Net Renewability Index* (NRI), introduced in equation (3):

$$\mathrm{NRI} = \mathrm{SCI} - (1 - \mathrm{GRI}) \tag{3}$$

The NRI allows to evaluate the actual sustainability level of the renewable energy production chain.
In brief:

- if NRI>0 : the overall supply chain process is carbon positive;

- if NRI=0 : the overall supply chain process is carbon neutral;
- if NRI<0 : the overall supply chain process is carbon negative.

The proposed index method could be applied for both ex-ante and ex-post analysis aiming to assess effectively the renewability of a bio-fuel supply chain; the model support public authority and/or plant manager to assess more renewable bio-fuel supply chain. The aim is to reduce the NRI value: after the bio-fuel type evaluation carried by the GRI evaluation, indexes (SCI and NRI) supplies information about critical processes which contribute mainly to reduce the overall renewability of a bio-fuel. In a design phase (i.e. ex-ante analysis), indexes could contribute to evaluate alternative supply chain structures (such as technological processes, transportation types, etc.) for reducing renewability consumption of a bio-fuel, and, consequently, to improve its environmental sustainability. In an ex-post analysis, indexes could highlight critical processes in the supply chain, which have to be controlled more strictly for controlling the overall sustainability of the energy production.

4. AN APPLICATION OF THE SUSTAINABILITY ANALYSIS OF LOGISTICS ACTIVITY IN BIO-FUEL SUPPLY CHAIN

The proposed approach has been applied for evaluating, in the case study proposed previously, the impact of logistics activity in the bio-fuel supply chain. Usually, optimization of transportation activities from cultivation areas to mill plant represents a low impact in the overall supply chain. On the other hand, logistics from country of origin to combustion plant is usually complex: intermodal transportation could contribute to increase renewability of the overall supply chain structure; otherwise, distances between production countries of bio-fuel and plant location are usually high. Plant managers could define new operational strategies for reducing the overall impact of these activities; these are not strictly connected to technological investments but they affect mainly the operational management of installations.

An application is proposed aiming to evaluate impact of logistics activities in bio-fuel supply chain. An operational index, called *Logistic Index* (LI), has been defined by equation (4):

$$LI = \sum_i^k \frac{(CO2\ emitted)_i}{CO2\ fixed\ by\ Photosyntesis}, \tag{4}$$

where i represents the *i-th* transportation resource type applied in the specific supply chain. In the case study proposed, three types of transports have been evaluated: freight rail, lorry and freight ship; detailed information are reported in Table 3.

Table 3. Unitary emission data for the different transpostaton types evaluated

TRANSPORT TYPE*	**UNITARY RESOURCE CONSUMPTION** [Kg CO2 x tonn x km**]	**NOTES**
Freight Rail	0.0374	Data regards European railways-
Lorry	0.147	Lorry unitary capacity is [16–32] t. The lorry type is Euro 5
Freight ship	0.0104	transoceanic freight ship/tkm

**Source: Database Ecoinvent v.2.*
*** Source: Ecoindicator99. It represents the standard unit for the transportation processes.*

According to an ex-ante analysis, a first type of result provided by the proposed model could be obtained by setting a target level of NRI. In this application, the NRI target level has been set by equation (5):

$$(1 - GRI) = LI \tag{5}$$

In this case, authors propose to make available for all logistic activities the overall level of renewability (such as the "bonus") expressed by a function of GRI.

In a design phase, the proposed model could be applied to select the "optimal" logistic scenario, which allows obtaining a "carbon neutral" process: the procedure consists of evaluating emission data of such a transportation activity; thus, this value has to be compared to the LI value obtained by the equation (5). Obtained results represent the "optimal distance" (expressed in km) which optimizes the sustainability level of the whole bio-fuel supply chain. Potential results obtained are reported for the case study in Table 4. Emission data about the three freight transportation types have been reported from the Ecoinvent Database developed by Swiss Centre for Life Cycle Inventories [9].

Table 4. Case study analysis for Jatropha crude oil

SCENARIO PARAMETERS	VALUES
LI evaluated in the case study*	**0.012**
Freight Rail [km]	388
Lorry [km]	99
Freight ship [km]	1397

** Value has been defined by equation (5)*

Further results could be both the selection of optimal logistics scenario in terms of sustainability level such as the LI value, and the evaluation of critical transportation activities in terms of environmental impact in a specific supply chain.

These results represent a target limit: higher values could determine a process not "carbon neutral" that is less environmental sustainable. It has to be noted that this evaluation does not represent the actual values because CO_2 emissions originated from other processes in the supply chain have been neglected in this case study.

Carbon neutral condition sets previously (see equation (5)) could be modified by the introduction of a target level defined by Competent Authorities or Regulators as *Weighted Renewability Index* (WRI); this is reported in equation (6):

$$WRI = k(1 - GRI), \tag{6}$$

where k >0 and it represents the weighted factor posed by regional and or national authorities. This factor could be established by a benchmarking activity carried out between different renewables installations or by comparing them with traditional fossil power plant. Thus, condition defined in equation (5), has to be modified in equation (7):

$$WRI = LI. \tag{7}$$

The introduction of the WRI index enables to evaluate actual limits, in terms of kilometers: this weighted value could be applied in planning and authorization phase of bio-fuel installations for improving its sustainability. The weight parameter derives from a strategic decision carried out by the Competent Authorities that could apply the index calculation for evaluating actual renewable installation projects.

5. CONCLUSION

The proposed method introduces indexes with the aim to assess renewability and sustainability level of a specific power plant which uses bio-fuel for combustion process; the method is based on the life cycle approach. Results supplied by the method could support competent authorities and plant manager to carry out ex-ante or ex-post analysis in the field of renewable energy sources. The first one allows evaluating "optimal" supply chain structure in terms of environmental impact; the second one provides information about critical process phases aiming to highlight critical phase in a sustainability point of view. An application is proposed for evaluating the impact of logistic activities on environmental sustainability of a bio-fuel supply chain. Usually, logistics represents a critical activity in a bio-fuel supply chain. The proposed index method represents an effective tool for designing and managing these typesf installations in a effective way by evaluating alternative logistics scenario from an environmental sustainability point of view.

REFERENCES

1. European Commission, "A European strategy for sustainable, competitive and secure energy", 2006, N°105. Available at: http://ec.europa.eu/energy/strategies/2006/2006_03_green_paper_energy_en.htm
2. European Commission, European Parliament legislative resolution of 17 December 2008 on the proposal for a directive of the European Parliament and of the Council on the promotion of the use of energy from renewable sources (COM(2008)0019 – C6-0046/2008 – 2008/0016(COD).
3. Doornbosch R., Steenblik R. "Biofuels: is the cure worse than the disease?", Organisation for Economic Co-operation and Development (OECD), 2007, SG/SD/RT, N°3.
4. Mortimer N.D., Elsayed, M.A. "North east biofuel supply chain carbon intensity assessment", North Energy Associates Ltd, 2006. Available at: www.northenergy.co.uk
5. Zah R., Böni H., Gauch M., Hischier R., Lehmann M., Wäger P., "Life Cycle Assessment of Energy Products: Environmental Assessment of Bio-fuels", Report by Swiss Federal Istitute of Materials Science and Technology Research (EMPA) Switzerland, 2007.
6. Rowe R.L., Street N.R., Taylor G., "Identifying potential environmental impacts of large-scale deployment of dedicated bioenergy crops in the UK" Renewable and Sustainable Energy Reviews 13 (2009), p. 271–290.
7. Jongschaap R.E.E., Corrè W.J., Bindabran P.S., Brandenburg W.A., "Claims and facts on Jatropha curcas", report 158, presented to IFAD International Consultation on Pro-poor Jatropha Development, Rome, April 2008; Available at: www.jatropha.wur.nl
8. Council Directive 96/61/EC of 24 September 1996 concerning Integrated Pollution Prevention and Control (IPPC). Available at: http://eur-lex.europa.eu/LexUriServ/LexUriServ.do?uri=OJ:L:2008:024:0008:01:IT:HTML
9. Swiss Centre for Life Cycle Inventories, The ecoinvent v2 database, http://www.ecoinvent.ch/

CYSENI 2009, May 28-29, Kaunas, Lithuania
ISSN 1822-7554, www.cyseni.com

THE INFLUENCE OF FLOW PULSATIONS ON METROLOGICAL CHARACTERISTICS OF WATER METERS

I. Briliūtė
Laboratory of Heat-Equipment Research and Testing
Lithuanian Energy Institute
Breslaujos str. 3, LT-44403 Kaunas – Lithuania
Phone: +370 37 401849
E-mail: ingab@mail.lei.lt

ABSTRACT

Energy saving is one of the most important task nowadays. Therefore, an investigation of small water meters and heat meters has been started. It aims to identify the impact of various disturbances on meters metrological characteristics. During the first stage it was investigated what impact has the installation condition on metrological characteristics of water meters. The second stage of studies shows what impact on water meter accuracy has flow pulsations and media temperature. There were investigated various construction types of water meters. The investigation was done in few pulsating regimes, when flow periodically stopped at one, half and 0.2 dm^3. The influence of pulsating flow on water meter accuracy was evaluated by counting relative measurement error. The experiments show that metrological characteristics of some construction types meter become worse with flow pulsation. The measurement error for single-jet vane wheel meter increased on 5–16%. Meanwhile, volumetric meters are not so sensitive for this disturbance. The media temperature influence on meter accuracy was also investigated. This investigation shows the difference of media temperature can move both upward and downward the measurement error curve. When the media temperature is less than 20 °C for volumetric water meters, the measurement error increased to positive values. In opposite case, the measurement error increased to negative values.

Keywords: water meter, flow pulsation, error, vane wheel meter, volumetric meter

1. INTRODUCTION

It is very important to save all our nature resources: water, gas, electricity and so on. The purpose of this investigation is to identify the influence of various disturbances (flow pulsations and media temperature) on water meter accuracy. In current article the performance of utility water meters of different construction (single-jet vane wheel meter, concentric multi-jet vane wheel meter, volumetric meter with ring piston and turbine meter) with nominal capacity of 1.5 m^3/h is investigated. The investigation revealed that bigger flow pulsations determine bigger measurement error and it could be one of many reasons for unbalance between water supply and consumption.

2. METERS UNDER INVESTIGATION AND MEASUREMENT PROGRAMME

All meters, which are used for custody transfer, water meters as well, shall fulfil metrological and technical requirements. All these requirements are presented in international, national standards and technical regulations of measurement instruments. According to international ISO 4064-1:2005 standard water meters metrological characteristics are defined as:

- permanent flow rate Q_3, where are shown what numerical values of permanent flow rate, expressed in cubic meters per hour (m^3/h), could be $Q_3 = 1.0; 1.6; 2.5; 4.0; 6.3$, etc. For the transition period of 5 years these values also could be $Q_3 = 1.5; 3.5; 6$, etc.;

- measuring range for the flow rate is defined by the permanent and minimum flow rates ratio $Q_3 / Q_1 = 10;12.5;16;20;25$ etc, for transitional period it could be $Q_3 / Q_1 = 15;35;60;212$;
- the relationship between permanent flow rate (Q_3) and overload flow rate (Q_4) is defined by: $Q_4 / Q_3 = 1.25$;
- the relationship between transitional flow rate (Q_2) and minimum flow rate (Q_1) is $Q_2 / Q_1 = 1.6$. For the transition period of 5 years, the following values will be permitted: $Q_2 / Q_1 = 1.5;2.5;4;6.3$;
- maximum permissible error (MPE) lower flow range – the maximum permissible error, positive or negative, on volumes delivered at flow rates between the minimum flow rate (Q_1 included) and the transitional flow rate (Q_2 excluded) is 5 % for water having any temperature;
- MPE upper flow range – the maximum permissible error, positive or negative, on volumes delivered at flow rates between the transitional flow rate (Q_2 included) and the overload flow rate (Q_4 included) is: 2% for water having a temperature < 30 ºC and 3 % for water having a temperature > 30 ºC [1].

The metrological characteristics of investigated meters are showed in Table 1. These characteristics show that these meters fulfilled transition period requirements and can be installed for this period.

Table 1. Metrological characteristics of investigated water meters

Type of water meter	**Q_3, m^3/h**	**Q_3/Q_1**	**Q_2/Q_1**
Concentric multi-jet vane wheel, single-jet vane wheel	1.5	25	2.5
Volumetric, turbine	1.5	100	1.5

The influence of the flow pulsations on the water meter measurements accuracy was investigated using test equipment, which is described in [2]. All requirements dealing with flow pressure and temperature stability, determined in normative documents (OIML R 49-2:2004 [3] and ISO 4064-3:2005 [4]), were fulfilled. For determination of the relative error of indication the so-called “collection” method, in which the quantity water through the water meter is collected in collecting vessel and its quantity is determined by weighing (ISO 4185:1980 [5]), was applied. Thus, the relative error of indication in a single run was defined as

$$\delta = \frac{(V_2 - V_1) - V_{ref}}{V_{ref}} \cdot 100$$

here: δ – relative error of indication, %; V_1, V_2 – indication of the meter at the beginning and at the end of the measurement, l; V_{ref} – reference volume, i.e. volume that passed the meter during the measurement, l.

For better illustration of results it was calculated additional error caused by the pulsating flow, as the difference between the relative errors determined at pulsating and reference flows.

During the test, all meters were connected to the standard ½” pipe by the same brass nipples featuring 40 mm and 14 mm inner diameter that normally comes with water meters in a default set. For the evaluation of influence of pulsating flow on the measurement accuracy, all the meters were mounted in the horizontal pipe, the indicating devices turned upward (thus enabling reading from above), standard gaskets were mounted upstream and downstream the meters.

For the sake of reliability of the results, each measurement was repeated five times. Figures show the average measuring error in five runs.

The current presentation investigates the performance of a "velocity" and "volume" utility water meters during various flow pulsating regimes, these being:

- reference regime, when water flows continuously, without pulsating;
- 1st pulsating regime, when flow periodically stopped at one dm^3;
- 2nd pulsating regime, when flow periodically stopped at half dm^3;
- 3rd pulsating regime when flow periodically stopped at 0.2 dm^3;
- temperature test for investigation the temperature influence on meters accuracy in different temperature values (10…30) ºC.

3. RESULTS OF INVESTIGATION

First of all, there was done reference measurement for better evaluation of influence upon various flow pulsating regimes. The references error curve is shown in Fig. 1.

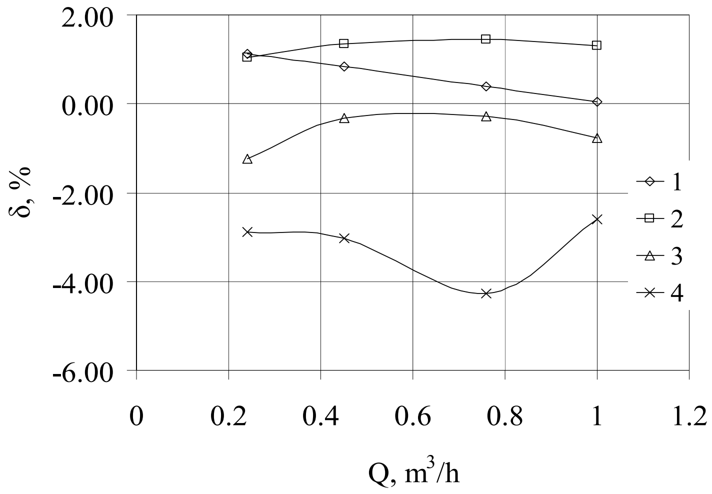

Fig. 1. The relative error variation in reference flow: 1 – volumetric water meter; 2 – turbine water meter; 3 – concentric multi-jet vane wheel water meter; 4 – single-jet vane wheel water meter.

During test flow pulsations were realized by turning the tap on/off. After each turning the tap off waited while stops the meter vane wheel. In this way, tests simulate very small water consumption in night time. In all regimes, the water amount passed through the meter was the same 10 dm^3. So, there was different quantity of meters stops in various flow pulsation regimes. In each regime additional errors were calculated for better illustration of this effect. The results are shown in Figures 2, 3 and 4 respectively for 1st, 2nd and 3rd flow pulsation regimes when water temperature was kept 20 ºC ± 5 ºC.

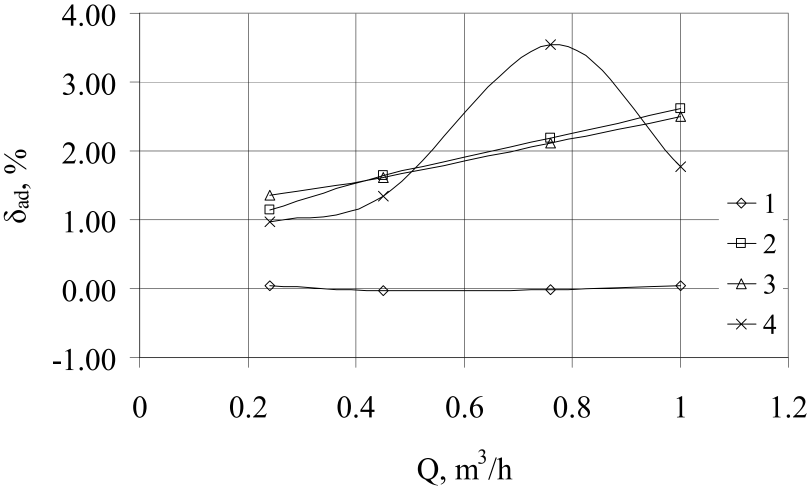

Fig. 2. The additional error variation for 1st pulsating flow regime: 1 – volumetric meter; 2 – turbine meter; 3 – concentric multi-jet vane wheel meter; 4 – single-jet vane wheel meter

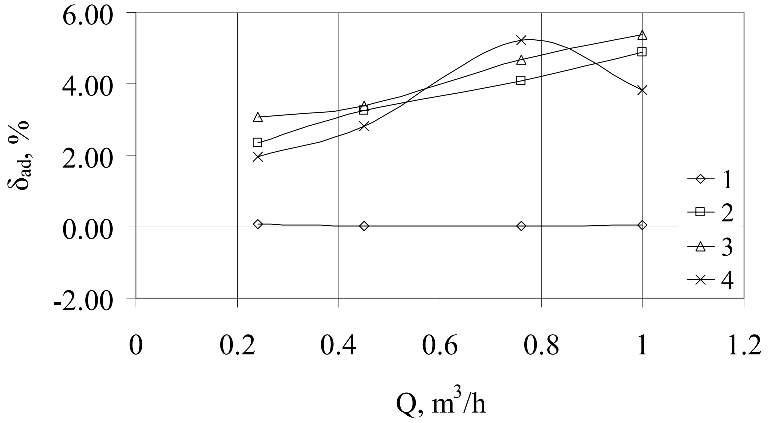

Fig. 3. The additional error variation for 2nd pulsating flow regime: 1 – volumetric meter; 2 – turbine meter; 3 – concentric multi-jet vane wheel meter; 4 – single-jet vane wheel meter

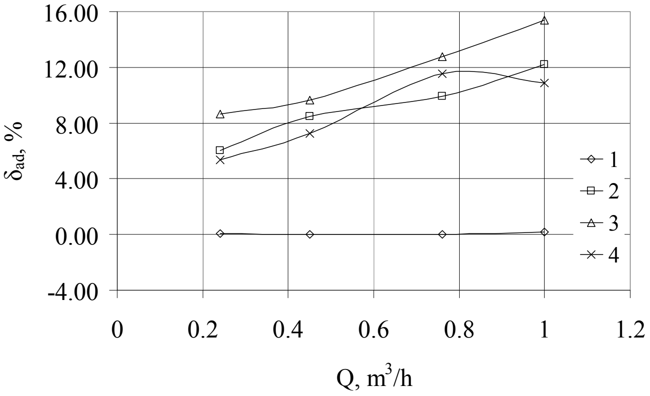

Fig. 4. The additional error variation for 3rd pulsating flow regime: 1 – volumetric meter; 2 – turbine meter; 3 – concentric multi-jet vane wheel meter; 4 – single-jet vane wheel meter

As you can see from results, the influence of flow pulsation is largest in the 3rd flow pulsation regime, when flow is stopped at 0.2 dm^3. In all cases, vane wheel and turbine meters are more under influence of flow pulsation than volumetric meter. From Figures 2–4 you can see more or less linear error dependence on flow rate: the smaller flow rate the smaller measurement error. So, in 1st flow pulsation regime the relative error for vane wheel and turbine meter is 1–2.5% depending from flow rate. In case of 2nd and 3rd regimes this error increases up to 2–5.5 % and 5.5–15.5%. At the same time, volumetric meter's accuracy remains stable and the influence of flow pulsation for it is not practically noticeable.

The purpose of temperature test was to investigate the impact of temperature on different construction meters accuracy. The test was done at one flow rate value $Q = 1.5$ m^3/h and the results are shown in Fig. 5.

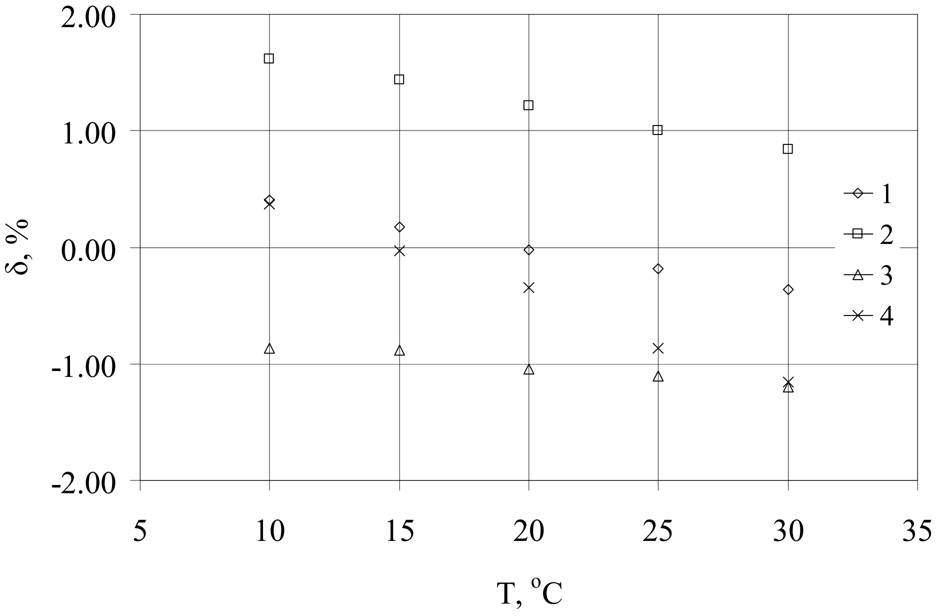

Fig. 5. The error variation under temperature: 1 – volumetric meter; 2 – turbine meter; 3 – concentric multi-jet vane wheel meter; 4 – single-jet vane wheel meter

In all cases, the relative error curve has displacement movement downward when water temperature is rising. The value of displacement fluctuates for different construction types of meter. As you can see, the single-jet vane wheel meter is most sensible for this effect, its error displacement is 1.5%, and the least sensible – concentric multi-jet meter, its displacement is 0.33%.

4. CONCLUSIONS

Flow pulsations have marked influence on small water meters readings in all measuring range and could be one of the reasons of unbalance between water supply and usage. Also one of these reasons for hot water meters can be water temperature.

The most sensible in flow pulsations are vane wheel and turbine meters, their measurement error can increase up to 1–16% in all measuring range. That means, if we often use small amount of water, meters register more water, than it really passes through water meter. In other way, volumetric meter is not sensible in flow pulsation, and its accuracy practically remains the same as in reference conditions.

The influence of temperature is most noticeable for single-jet vane wheel meters and relative error displacement of which is 1.5 %, and the least noticeable for concentric multi-jet vane wheel meters – 0.33%. Anyway, for all meters there are tendency of movement measurement error curve to negative values from error curve at reference temperature. It means all meters register less water than it really passes.

REFERENCES

1. ISO 4064-1:2005 Measurement of water flow in fully charged closed conduits – Meters for cold potable water and hot water – Part 1: Specifications, p. 12–14.
2. I. Briliute, A. Bonckus, G. Zygmantas Influence of installation effects on the performance of residential water-meters. Environmental engineering conference selected papers and proceedings. Vilnius, Technika 2008, p. 787.
3. OIML R 49-2:2004(E) Water meters intended for the metering of cold potable water – Part 2: Test methods.
4. ISO 4064-3:2005 Measurement of water flow in fully charged closed conduits – Meters for cold potable water and hot water – Part 3: Test methods and equipment.
5. ISO 4185-1980(E) Measurements of liquid flow in closed conduits – Weighing method.

CYSENI 2009, May 28-29, Kaunas, Lithuania
ISSN 1822-7554, www.cyseni.com

EVAPORATION OF WATER DROPLETS IN A HIGH TEMPERATURE GAS FLOW

A.A. Brin
A. V. Luikov Heat and Mass Transfer Institute
National Academy of Sciences of Belarus
P. Brovki St. 15, 220072 Minsk – Belarus
Phone: +375 17 2842222
E-mail: brin@hmti.ac.by

ABSTRACT

Evaporation of water droplets in a high temperature gas environment is widely used in various applications, in particular, for cooling down of industrial furnaces and chemical reactors. For the simulation of evaporation of water droplets in a high temperature gas environment the two-dimensional mathematical model was developed. The system of 3 ordinary differential equations includes the equations for changing of droplet radiuses, velocities and temperatures. For the case of the ensemble of droplets, there is an influence of evaporating droplets on the gas flow properties. To include these effects into the model it is necessary to use additional equations for changing of gas flow temperature and water vapor density in air. This system was solved numerically by the Runge-Kutta adaptive method of 4th order. The mathematical model takes into account the process of preliminary heating of droplets and effect of thermal radiation on droplet evaporation. Also, it proposes the procedure of finding the unknown temperature of boundary layer between liquid and gas phases. For the high heat and mass flows it operates with corrected heat and mass transfer coefficients.

Keywords: evaporation, droplets, high temperature, gas flow

1. MATHEMATICAL MODEL

The literature review showed that general mechanisms of the evaporation processes has been investigated and described in numerous literature sources, but qualitatively the influence of many parameters on processes of heat and mass transfer can be studied only with methods of mathematical simulation.

One of the simplest models, describing droplet evaporation, is so called D-square law [1], which states that the square of droplet diameter is a linear function of time. For practical engineering applications it would be useful to develop a model which would combine simplicity of a d-square law and accuracy of the parabolic approximation of the temperature profile inside the droplet. Such simple model of heating and evaporation of non-isothermal droplets is suggested in [2]. The rigorous numerical solution is compared with predictions of isothermal model based on d-square law and model based on parabolic approximation. This comparison showed the applicability of parabolic approximation to modeling of the heating and evaporation of droplets in realistic diesel engines.

A generalized treatment of heat and mass transport between an ensemble of particles and a surrounding continuum is presented in [3]. The conditions for which particles can be treated as isolated and correction factors are presented from which multiple particle mass transfer rates can be calculated from single isolated particle mass transfer rates.

The theoretical model, presented in [4], involves the calculation of velocity, size, and surface properties of an evaporating droplet along its trajectory in a laminar hot air flow. The time-dependent Lagrangian equations for the droplet position, velocity, and size are solved numerically. The thin-skin model is based on the assumption of high liquid Lewis number and high droplet evaporation rate. Under these conditions, the authors assume that the droplet surface temperature and its concentration distributions remain constant.

In [5] the authors numerically investigate the droplet vaporization in a high-temperature environment for a n-hexane droplet evaporating into nitrogen. The model accounts for transients in both the liquid and the gas phase; gas phase transport and thermodynamic properties are varying with temperature, pressure and composition.

The quasi-stationary evaporation of a spherical droplet suspended in a non-equilibrium vapor-gas mixture is investigated in [6]. The isothermal and non-isothermal heat and mass transfer in a surrounding gas are described on the basis of the Boltzmann equation solution by the integral-moment method. The kinetic coefficients are calculated at arbitrary Knudsen numbers and any accommodation coefficients.

The physical basis of evaporation process consists of differential-thin layer (boundary layer), which directly borders the surface of the evaporating water, air practically saturated with water vapor. Vapor pressure near the boundary layer of water droplet very insignificantly (0.2–0.7%) differs from the saturation vapor, corresponding to the surface temperature of liquid. Usually one can neglect this difference and consider that on a liquid-air interface the water vapors are saturated, and the intensity of water evaporation is proportional to the difference of densities of saturated vapor on the water surface and vapor in the air layer near the interface. Saturation of surface layer can be explained by small velocity of removal of vapor molecules and large velocity of emitting of water molecules. If the air beyond this layer is not saturated with vapor, than we have mass flux, directed from the evaporation surface to the ambient.

Consider a droplet at low initial temperature that is entered to a gaseous cross flow at high temperature. Initially, almost all heat supplied to the droplet serves to raise the droplet temperature. As the droplet temperature rises, vapor will form at the droplet surface and has two main effects: a large portion of heat transferred to droplet is used to vaporize the droplet; the outward flow of vapor impedes the rate of heat transfer to droplet. Eventually, a stage is reached where all heat transferred to droplet is used as the heat of vaporization and the droplet temperature will stabilize at a steady-state temperature (adiabatic saturation temperature).

The droplet evaporation rate in the hot gas is limited by the heat transport from the gas to the droplets. Therefore, it depends on the following parameters: temperature difference between gas phase and liquid, thermal conductivity of the gas, evaporation enthalpy of liquid, heat exchange surface. At steady-state period, the droplet diameter d at any instant may be related to its initial diameter D_0 by D-square law [1]:

$$D_0^2 - D^2 = B \cdot \tau .$$

It is clear that the larger B the shorter the time it takes for the droplet to vaporize completely. Also this time can be described by the following equation:

$$\tau = \frac{\rho_d \Delta h}{8\lambda_a(T_a)\left(T_a - T_d\right)} D_0^2 . \tag{1}$$

Droplet evaporation time for different initial gas temperatures, calculated using the formula (1), is shown in Fig. 1. For calculations we use such initial conditions: droplet diameter $D_0 = 200$ µm and droplet temperature $T_d = 20\ ^0$C.

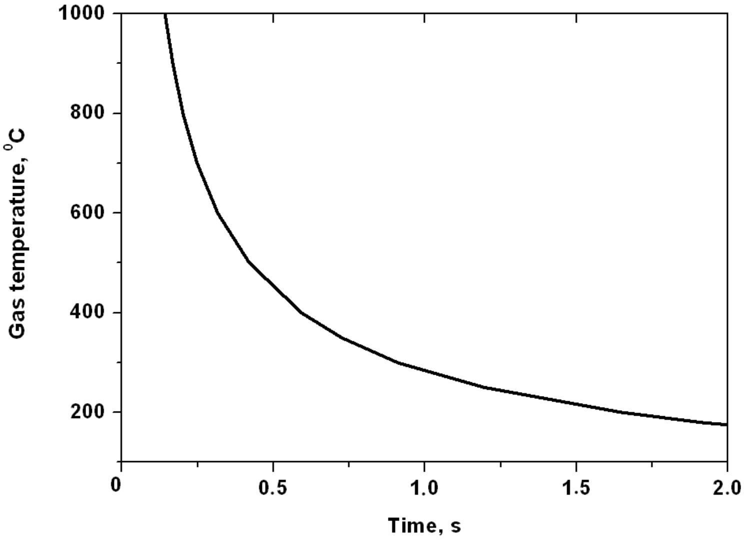

Fig. 1. Droplet evaporation time versus gas temperature

It is seen from Fig. 1 that there is the inverse relationship between droplet evaporation time and gas temperature. Clearly, the higher initial gas temperature, the smaller the evaporation time. For the initial temperature T_a = 1000 ^{0}C and droplet diameter D_0 = 200 µm, the droplet evaporation time τ = 142 ms.

Consider a droplet at low initial temperature that is entered to a gaseous cross flow at high temperature (Fig. 2). Initially, almost all heat supplied to the droplet serves to raise the droplet temperature. As the droplet temperature rises, vapor will form at the droplet surface and has two main effects: a large portion of heat transferred to droplet is used to vaporize the droplet; the outward flow of vapor impedes the rate of heat transfer to droplet. Eventually, a stage is reached where all heat transferred to droplet is used as the heat of vaporization and the droplet temperature will stabilize at a steady-state temperature (adiabatic saturation temperature).

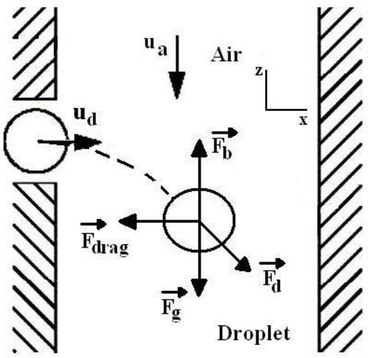

Fig. 2. Droplet moving in air cross flow.

The system of ODE for droplet velocities and trajectories can be expressed as [7]:

$$\rho_d V_d \frac{du_x}{dt} = -\frac{1}{2}\rho_a u_x |\vec{u}| S_d C_D, \tag{2}$$

$$\rho_d V_d \frac{du_z}{dt} = -\frac{1}{2}\rho_a (u_z - u_a)|\vec{u}| S_d C_D + \left(\rho_a - \rho_d\right) V_d g, \tag{3}$$

$$\frac{dx}{dt} = u_x, \tag{4}$$

$$\frac{dz}{dt} = u_z. \tag{5}$$

Droplet evaporation equation based on law of the conservation of energy is:

$$\frac{dD}{dt} = -\frac{2\beta\rho_s(T_d)}{\rho_d}. \tag{6}$$

The equation for changing of droplet temperature can be expressed as:

$$\frac{dT_d}{dt} = \frac{3\left[\alpha\left(T_a - T_d\right) - \beta\left(\Delta h - c_w T_d\right)\rho_s + \varepsilon\sigma\left(T_a^4 - T_d^4\right)\right]}{c_w \rho_d R_d}. \tag{7}$$

1.1. Ensemble of droplets

For the case of the ensemble of droplets, there is an influence of evaporating droplets on the gas flow properties. To include these effects in our model we need to use additional equations for changing of gas flow temperature and water vapor density in air:

$$\frac{dT_a}{dt} = \frac{2\pi D\, N_d\, \alpha}{\rho_a c_a}\left(T_a - T_d\right), \tag{8}$$

$$\frac{d\rho}{dt} = 2\pi D\, N_d\, \beta\left(\rho_s(T_d) - \rho(T_a)\right). \tag{9}$$

N_d is the number of droplets per unit volume and it can be defined as:

$$N_d = \frac{6Q_w}{\pi D^3 \rho_d u_d S}. \tag{10}$$

Also, it is worth to mention that we have a new parameter - water vapor density in air. So we have to make some changes in the equations for changing of droplet size and temperature:

$$\frac{dD}{dt} = -\frac{2\beta(\rho_s(T_d) - \rho(T_a))}{\rho_d}, \tag{11}$$

$$\frac{dT_d}{dt} = \frac{3\left[\alpha\left(T_a - T_d\right) - \beta\left(\Delta h - c_w T_d\right)\left(\rho_s(T_d) - \rho(T_a)\right) + \varepsilon\sigma\left(T_a^4 - T_d^4\right)\right]}{c_w \rho_d R_d}. \tag{12}$$

1.2. Boundary layer temperature

The temperature inside the boundary layer T_r between gas flow and droplet surface is unknown (Fig. 3). It was suggested the next procedure of definition the temperature T_r. Temperature at the left side of boundary layer is equal to the temperature of gas flow T_a, temperature at the right side is equal to the temperature of droplet surface T_s, which changes with time from the initial temperature of droplet T_d to the final temperature T_f, when the droplet evaporates completely.

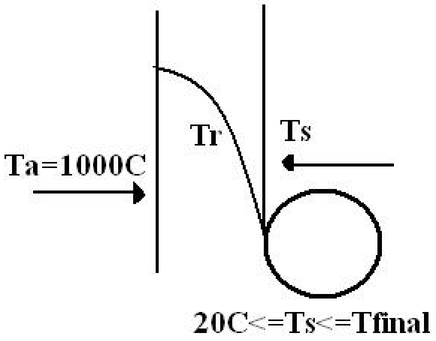

Fig. 3. Definition of the temperature inside the boundary layer

For definition of the unknown temperature T_r was suggested the following interpolation function:

$$T_r = T_s + K(T_a - T_s), \tag{13}$$

where *K* is the arbitrary coefficient in range [0, 1]:
K= 0 => T_r=T_s – boundary layer temperature is equal to the temperature of droplet surface;
K= 1/3 => T_r=T_s+(1/3)(T_a+T_s) – so called “one third rule”;
K= 1/2 => T_r= (T_a+T_s)/2 - so called “film model” [8];
K= 1 => T_r=T_a – boundary layer temperature is equal to the temperature of gas flow.

2. NUMERICAL RESULTS

For the following initial conditions D_0 = 200 µm, T_d=20 ^{0}C, T_a=1000 ^{0}C, u_a=10 m/s, u_x=20 m/s some numerical results are shown in Fig. 4-6. Dimensionless droplet diameter versus the evaporation time is shown in Fig. 4. The scale is an initial droplet diameter D_0 = 200 µm.

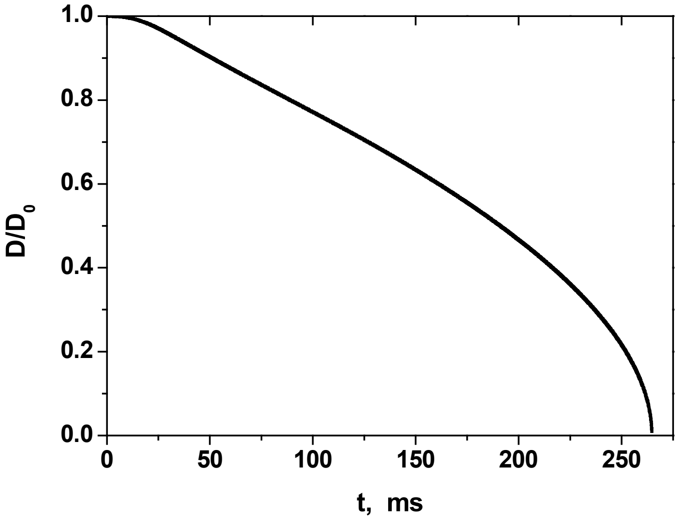

Fig. 4. Dimensionless droplet diameter versus time.

Changing of surface droplet temperature versus time is shown in Fig. 5.

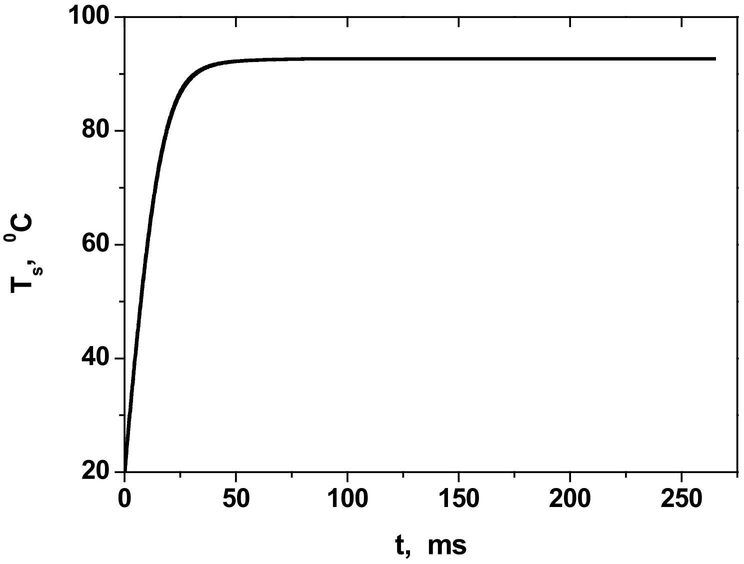

Fig. 5. Surface droplet temperature versus time

It is shown from Fig. 5 that the droplet reaches the saturation temperature very fast and then evaporates at this temperature.

It was investigated the influence of thermal radiation on droplet evaporation (third term in the right hand of the equation (12)). For the following initial conditions T_d=20 ^{0}C, T_a= 1000 ^{0}C and D_0 = 50 μm the contribution of the radiation flux is about 0.3 % in comparison with heat flux and for initial diameter D_0 = 200 μm – is about 1 %. These results are in good agreement with results from [9].

It was carried out a parametrical study of the parameter K, introduced in formula (13). For three different coefficients K the dependence of droplet size on evaporation time is shown in Fig. 6. Initial droplet diameter D_0 = 200 μm.

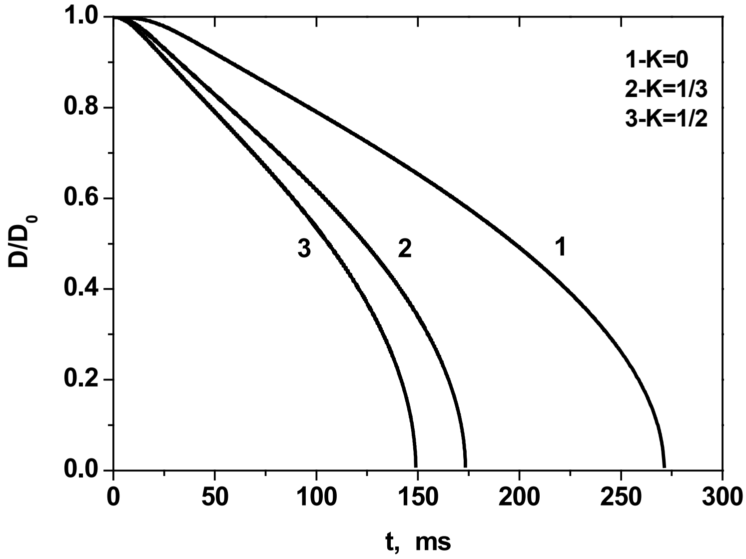

Fig. 6. Droplet evaporation for different K numbers

All previous results were obtained for single water droplet evaporation in a high temperature gas flow. The results for evaporation of an ensemble of water droplets are shown in Fig. 7 and 8. Changing of air temperature for two different initial droplet diameters along the channel axis are shown in Fig. 7.

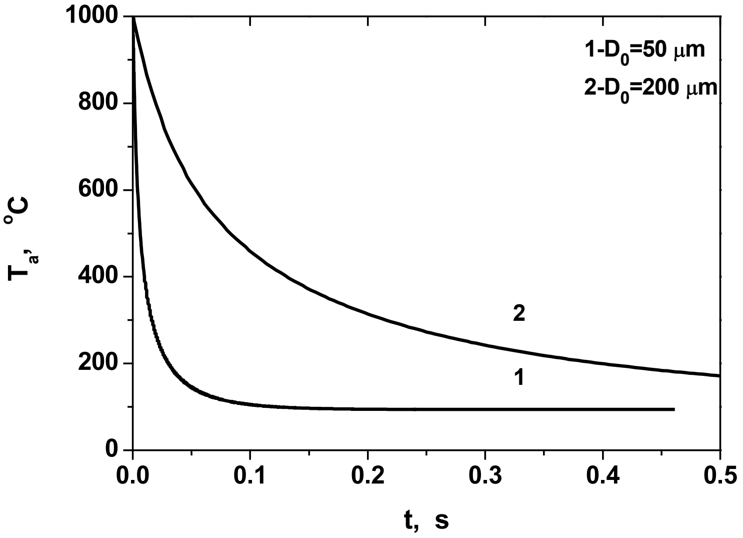

Fig. 7. Air temperature versus time along the channel axis

It is shown in Fig. 7 that the smaller droplets cool down the hot gas flow better than the larger ones. For example, after 100 ms the smaller droplets cool down the air till the stationary temperature of 95 ^{0}C and larger ones – only to 430 ^{0}C.

The influence of parameter *K* on the gas flow temperature is shown in Fig. 8. Simulation is carried out for equal mass flow rates of water and air $Q_w/Q_a = 1$ (there is a lack of water, so the air does not reach the stationary temperature, but droplets evaporate completely) and D_0 = 200 μm.

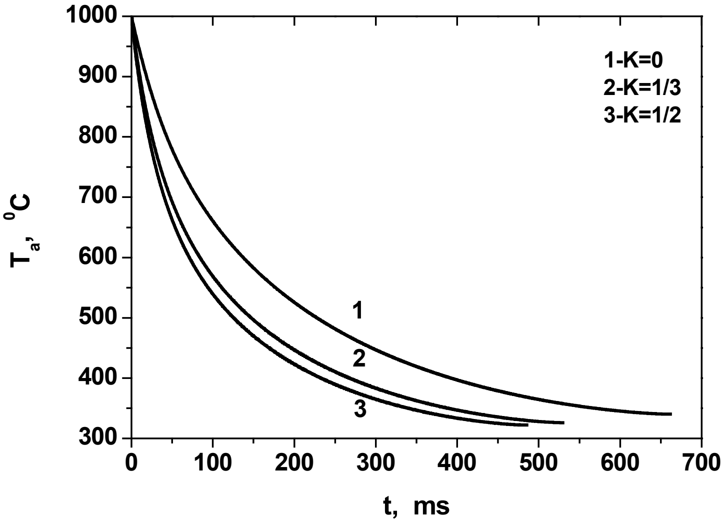

Fig. 8. Air temperature versus time for different *K* numbers

It is shown, that there is a discrepancy between results obtained for different *K* numbers. It is clear, that only the experiment can show which value of the parameter *K* should be chosen for current conditions of calculation.

3. CONCLUSIONS

The new mathematical model of water droplet evaporation in a high temperature gas flows is developed. For the high heat and mass flows it operates with corrected heat and mass transfer coefficients. Also it proposes the procedure of finding the unknown temperature of boundary layer between liquid and gas phases.

It was shown that the contribution of the thermal radiation does not exceed 1.0% in comparison with convection for all investigated initial droplets diameters.

The influence of the parameter *K* on the evaporation processes was investigated. It is shown that there is a discrepancy between results obtained for different numbers *K*.

The numerical simulation of the evaporation of water droplets ensemble was carried out.

4. NOMENCLATURE

B – steady state evaporation constant; C_D – drag coefficient; c – cpecific heat, J/(kg·K); D – diameter, m; g – free fall acceleration, m/s^2; N – number of droplets, m^{-3}; Q – mass flow rate, kg/s; R – radius, m; S – area, m^2; T – temperature, ^{o}C; t – time, s; u – velocity, m/s; V – volume, m^3; α - heat transfer coefficient, W/(m^2·K); β - mass transfer coefficient, m/s; ε – absorption capacity; Δh – evaporation enthalpy, J/kg; λ – thermal conductivity, W/(m·K); ρ – density, kg/m^3; τ – evaporation time, s; σ – Stefan-Boltzmann's constant, W/(m^2·K^4); 0 – initial; a – air; d – droplet; f – final; r – for boundary layer; s – saturated; x – radial coordinate; z – axial coordinate.

REFERENCES

1. C.K. Law. Recent advances in droplet vaporization and combustion. Prog. Energy Combust. Sci. 1982. Vol. 8, p. 171–201.
2. L.A. Dombrovsky, S.S. Sazhin. A Simplified non-isothermal model for droplet heating and evaporation. Int. Comm. Heat Mass Transfer. 2003. Vol. 30, No. 6, p. 787–796.
3. A.K. Ray, E.J. Davis. Heat and mass transfer with multiple particle interactions Part I. Droplet evaporation. Chem. Eng. Comm. 1980. Vol. 6, p. 61–79.
4. S.K. Aggarwal, G. Chen. Vaporization behavior of fuel droplets in a hot air stream. Int. J. Heat Mass Transfer. 1991. Vol. 34, No. 10, p. 2669–2673.
5. H. Jia, G. Gogos. Investigation of liquid droplet evaporation in subcritical and supercritical gaseous environments. J. Thermophys. Heat Transfer. 1992. Vol. 6, No. 4, p. 738–745.
6. V. Chernyak. The kinetic theory of droplet evaporation. J. Aerosol Sci. 1995. Vol. 26, No. 6, p. 873–885.
7. S.P. Fisenko, A.A. Brin. Simulation of a cross-flow cooling tower performance. Int. J. Heat Mass Transfer. Vol. 50, 2007, p. 3216–3223.
8. M. Renksizbulut, R. Nafziger, X. Li. A mass transfer correlation for droplet evaporation in high-temperature flows. Chem. Eng. Sci. 1991. Vol. 46, No. 9, p. 2351–2358.
9. C.C. Tseng, R. Viskanta. Enhancement of water droplet evaporation by radiation absorption. Fire Safety Journal. 2006. Vol. 41, p. 236–247.

CYSENI 2009, May 28-29, Kaunas, Lithuania
ISSN 1822-7554, www.cyseni.com

RESEARCH OF MEDIUM CONDITIONS’ AND FLOW PERTURBATIONS’ INFLUENCE ON REPRODUCED AIR VELOCITY VALUES

A. Bertašienė
Lithuanian Energy Institute
Laboratory of Heat Equipment Research and Testing
Breslaujos str. 3, LT – 44403Kaunas – Lithuania
Phone: 370 37 401865
E-mail: agne@mail.lei.lt

ABSTRACT

Laboratory of Heat Equipment Research and Testing in 2008 participated in EURAMET M.FF-K3 comparison. There was a dispersion of results, particularly in the range of low air velocity, among the national laboratories. Static Pitot tube with the amplificator and thermal anemometer for the comparison of air velocity values were used. Every laboratory had chosen its own method and facility for reproducing the reference velocity value.

The conclusion was made that different conditions of air velocity reproduction initiate the appearance of different longitudinal static pressure gradient in surroundings of installation of measurement instrument under comparison. It urgently influenced the readings of static Pitot tube with amplificator, since the amplificator generated the flow separation behind it. As to strong dependence of separated flow on flow conditions, the static pressure in separation region also strongly varies. Therefore, this comparison disclosed the quite different flow conditions during the reproduction of air velocity values and its transferring to measurement instrument under calibration. Fortunately, in the case of conventional static Pitot tube such effects are insignificant for the absence of flow separation and measurement of total and static pressure in the close vicinity of both holes to each other.

Sure enough, the results of comparison of thermal anemometer are less scattered because such factors as flow turbulence, orientation of sensor to flow direction, variation of air temperature and sedimentation on hot sensor had more or less denominated influence. It seems that similar influenced factors can only be displayed in the case of conventional static Pitot tube.

To confirm such propositions, static Pitot tube with the amplificator and thermal anemometer were investigated under different arrangement conditions and levels of turbulence.

The results and conclusions obtained during the research enable improve and harmonize the conditions of reproduction of air velocity values on international level.

Keywords: air velocity, laser Doppler anemometer, key comparison, static Pitot tube

1. INTRODUCTION

Fluid flow analysis remains of great interest. Velocity measurements become significant because of practical demand [1–3] for getting information about consistent patterns of local or mean velocity distribution. Knowledge of air velocity is essential in meteorological observations, testing and surveillance of windmills, indoor climatic investigations, emission measurement and optimisation of ventilation systems. Various kind of anemometers are being used for all kind of purposes, such as waranty measurements on ships (determination of the influence of wind velocity on the average ship velocity), human comfort measurements (air conditioning systems), and suction of dangerous gases (lead fumes at shooting lanes).

It is competently known that air velocity measurements in the channels using various kinds of measurement instruments (MI) for fully developed turbulent flow or for flow in entrance part of measurement channel is not complicated because velocity values are high enough and stable.The latter situation is converse than for air velocity measurements lower than 0.5 m/s and especially for velocity values lower than 0.1 m/s. Velocity in this region is very sensitive because of transitional flow instabilities and higher turbulence degree. Very important and essential point of velocities reproduction is uncertainty value and compatibility of reproduced values with the results of other national laboratories. By experience, it is common that standard velocity values are reproduced by different methods, in different conditions and facilities of different construction. It could be done in free stream formed by convergent nozzles, travelling linearly the meter with a constant velocity in the long channel or rotating the meter with a constant angular velocity in non turbulent environment as well as placing it in the entrance region of the channel warranting low inlet flow turbulence.

The latter method raises more substantially an issue regarding the transitional flow regime in the channels influence on the measured low velocity values under which the flow regime is approaching the transitional one. This is the reason why declared reproducible low velocity values almost always are limited by 0.2 m/s. But in practice, there is a great need to measure 0.05 m/s and lower with a well known uncertainty.

Recently air velocity values in standard facilities have been basically measured using wave measurement methods that are mostly realized by laser anemometers (LDA) but in practice the main MI are based on differential pressure measurement and the lowest values of them are limited by the resolution of differential pressure gauge. Therefore thermal anemometers (TA) are widely used especially for low velocities.

2. ANALYSIS OF PREVIOUS COMPARISONS

As it was mentioned above, the measurement traceability remains a very important aspect not only on regional level. The comparisons inside of regional metrology organizations as well as among them realized by the key comparisons play essential role in assurance of measurement traceability in the whole world. So it is very important to analyse the previous comparisons and compare with the last one.

Intercomparison project „Euromet-388“ [4] was based on 3 anemometers calibration in the range 0.2–20 m/s. Air velocity measurements have been made in wind tunnels of different cross sections, by different methods (the impact of the blockage area is different on the reading of the anemometer due to the ventilator (flowrate) control system of the wind tunnel, active or passive) and completely of different principles (rotating arm, carriage in tank, towed carriage, pipes, wind tunnels). The urge came forward to improve the method of investigation and to repeat the intercomparison tests because the transfer meters used at that time showed insufficient stability and calibration results showed deviations up to 10%. Furthermore, it became clear that significant differences exist between the definition of the reference velocity at the position of the transfer standard. Anemometer constant was calculated over a wide range and decreased considerably at low air velocities where the scatter between the laboratories increased as well. The scatter is an indication to the sensitivity of the anemometer to small influences of the flow conditions and to the kind of facility used. The scatter over the whole range (differences between the laboratories) was also more intense for the anemometers of smaller diameters. This confirms the fact that blockage effect was not properly analysed and evaluated. No trend can be seen from all the influencing factors to the value of anemometers but the differences between laboratories seemed relatively too big.

In 2002 Euromet TC – F project No 827, „LDA-based intercomparison of anemometers“, the aim of which was to accomplish appropriate pre-conditions for a detailed analysis of future calibration results in order to decrease the deviations between calibration laboratories and to reduce the calibration uncertainties for different types of anemometers was initiated [5]. The common use of LDA systems, such as velocity standards, in different calibration facilities ensures ideal conditions to realize low uncertainties for the representation of the flow velocity over a wide velocity range in each facility. Anemometers with minimal blockage effects (static Pitot tube (SPT) for higher velocities and hot wire anemometer (HWA) for lower velocities) were calibrated in each calibration laboratory (PTB, Germany; CETIAT, France; INTA, Spain and UCL, Belgium) in open wind tunnels with an closed measurement chambers such as in Fig. 1 or closed loop tunnels. All the laboratories detailed different working procedures so as to clarify the processes of calibration and simplify the analysis of comparison results. Intercomparison results showed a high level of facilities compatibility but some differences emerged that could be due to tunnels turbulences and stabilities, differencies among the calibration procedures and constructions of the facilities, different parameters of environment in the tunnel and indoors. SPT results deviation (Fig. 2) is obvious for lower than 5 m/s velocities as SPT usually is available for velocity measurement higher than 3 m/s. It is due to differential pressure measurement difficulties. TA results are in good agreement among the laboratories with several points that are out of acceptance criteria [5].

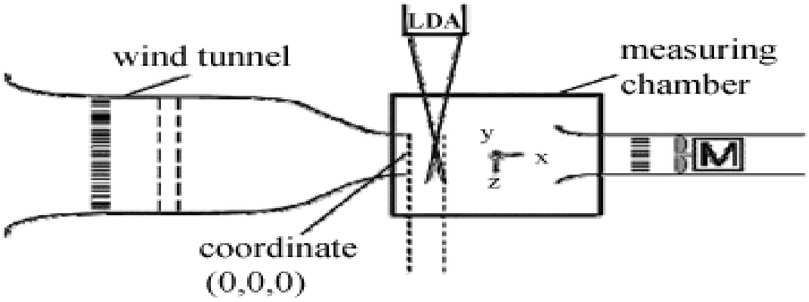

Fig. 1. Open air velocity channel in wind tunnel with closed chamber for calibration [5]

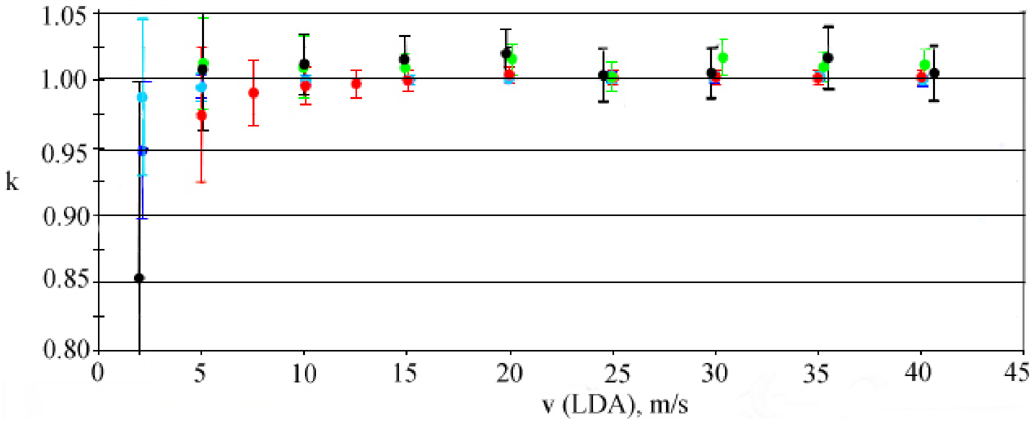

Fig. 2. SPT results of all project participants: PTB (blue and light blue dots), CETIAT (red dots), INTA (black dots) and UCL (green dots) [5]

After result summarisation it could be decided that wind tunnel Reynolds numbers should also be taken into account while comparing the results in order to define flow regime. And even seeding product (size, material) used for LDA measurements could influence velocity value deviations [5].

Finally, as an extension of EURAMET project No 388 Euramet project No 514 (M.FF-K3) was proposed for comparison of anemometer in test facilities using as transfer standards TA and SPT with amplifier. The results of this comparison are discussed in the current paper.

3. EXPERIMENTAL METHODOLOGY

Measurements for M.FF-K3 comparison and further investigations were performed in open (by removing D-C tube of measurement channel (MC), Fig. 3) and closed loop channel of the aerodynamic test facility depicted in [1]. In the case of open channel, air flowed into the room and measurements were performed at a distance ½ D (D – MC cross-section diameter) from the outlet or in the channel at a proper distance. Measurement cross-sections B was located at the dimensionless distance x/D = 3 from the inlet into MC.

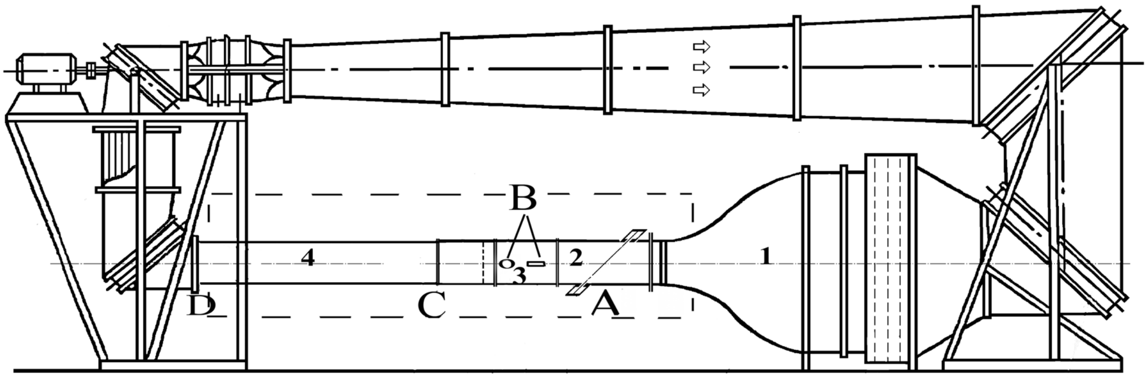

Fig. 3. Aerodynamic facility with MC (dashed area): 1 – convergent nozzle (CN) with the ratio of their inlet and outlet diameters 1650/400 mm; 2 – constant D=400 mm MC with ultrasonic (UA) anemometer (A plane); 3 – places for MI installation and LDA measurement (planes B); 4 – part of the channel (C-D) for closing loop

UA, LDA were used to evaluate mean and local velocity values, respectively. Velocity distribution in the channel cross-section was measured by LDA.

LDA revealed the possibility to measure a wide range of velocities using seeding particles injected into the air flow to measure velocity. The basic configuration of the LDA used in the research made-up by Intelligent Laser Applications GmbH company with participation of PTB (Germany) consists of [2]:

- a continuous wave 150 *mW* semiconductor laser with a *532 nm* wavelength;
- transmitting optics, including a beam splitter – Bragg cell and a focusing lens (focal distance in this case is 250 mm and diameter of a lens is 50 mm);
- traversing system of 600 mm length to change measurement point position automatically.

SPT with an amplifier, a development of NMi-VSL (The Netherlands), was used for comparison (Fig. 4, a)). The amplifier induces a larger pressure difference between the static and total pressure. The SPT was accompanied by two micromanometers and a comparator to add the two (dynamically out of phase) signals of the micromanometers. In this way the reading of the pressure difference becomes higher with factor 2, which make the readings at lower velocities easier. SPT shown on Fig. 4b with changeable amplifier having form of disk with different diameter was also investigated installing it at the outlet of MC.

TA during comparison was Testo 425 with wire sensor placed into protective tube having slots. For further investigation, after comparison for result interpretation, TA with hot wire sensor and analogue SPT (Fig.4, b)) in different channels or in the same channel but of different installation were used.

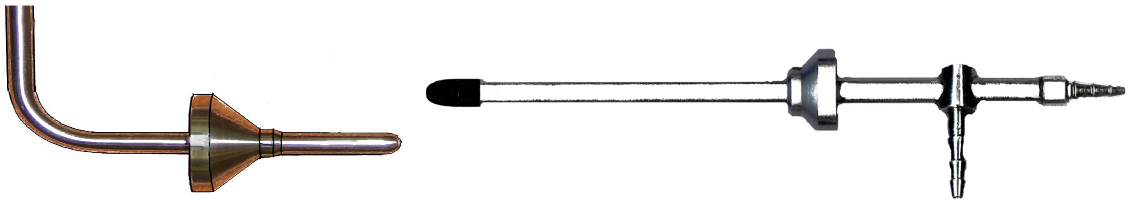

a) b)

Fig. 4. a) SPT with conical amplifier: NMi-VSL one; b) analogous to the one used in key comparison used in additional investigation

For further analysis ejector was also used realising scheme in Fig. 5 where measurements of velocity with LDA at the distances x/D = 3 and x/D = 1 (counterchanging UA measurement plane with the one for LDA) were performed. The main goal of ejector – reduction of flow instabilities produced by ventiliators at low air velocities.

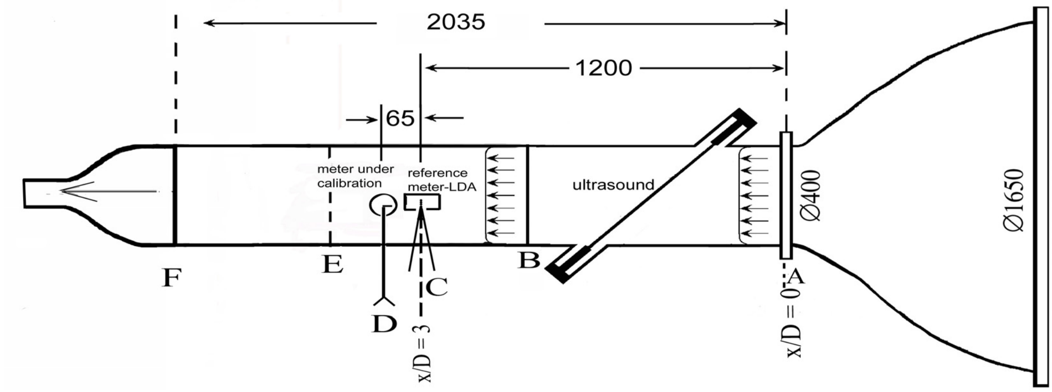

Fig. 5. Measurement channel with air ejector instead of ventilator

Several measurements were done using flow generation critical nozzles (CrN) facility, i.e. measurement section joined to the critical nozzles to get stable air flow rate (Fig. 6) [6].

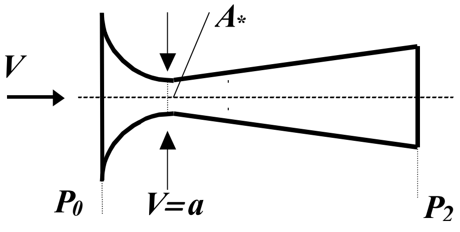

Fig. 6. a) Scheme of CrN. ***V*, *a*** – air and sound velocity, respectively; A_* – CrN inlet cross section area; P_0 and P_2 – pressure values before and after nozzle

Fig. 6. b) set of them in the laboratory

4. ANALYSIS OF COMPARISON AND SUBSEQUENT EXPERIMENTAL RESULTS

Measurements during comparison were done in different construction of the channel, wind tunnels with undisclosed measurement schemes and means of reproduction of reference velocity values. Making conclusions about the results it is quite difficult to decide whether results deviation is due to the environment influence, MI capabilities, different measurement principle or even construction of the channel. There is no relation between the type of instaliation and the results [7], but further analysis reveals other facts that are discussed further in the paper.

Analysing the results (Fig. 7.) of final report one can see at least 2 groups with approximate results, excluding UME, Turkey. The dispersion of the results becomes clearly larger at low air velocity in the range (1–0.2 m/s).

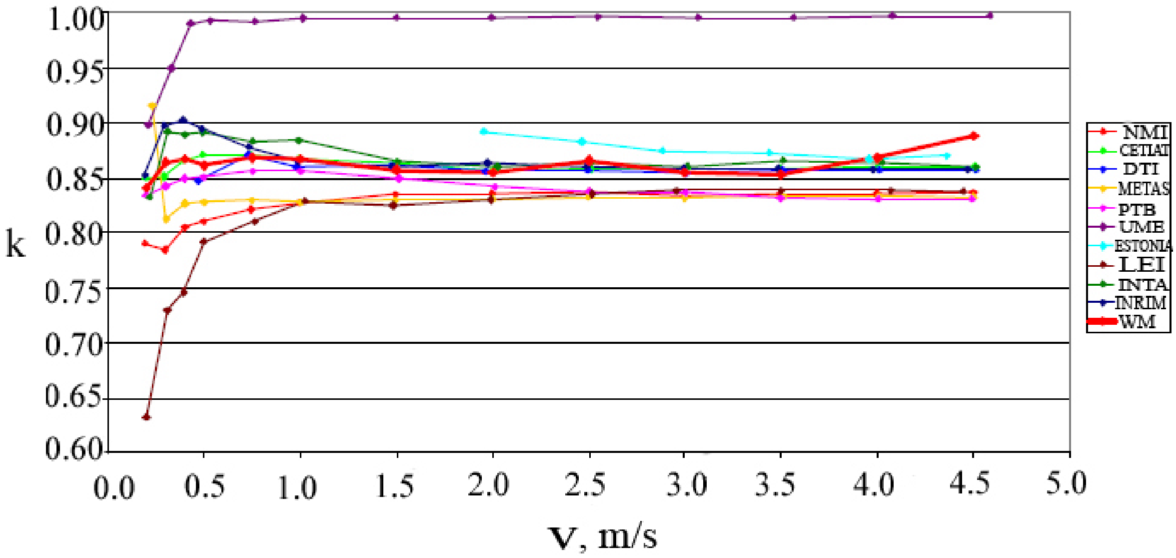

Fig. 7. Comparison participants' data including the weighted mean (WM), correction constant (k) calculated from SPT values

In our case, results agree best with one curve of NMi. But in general there is a dispersion of low velocities values. The same situation but with some different tendency also exists in METAS, INTA, INRIM results.

From the theory, correction constant, k, for conventional SPT is 1 for all the range from 2(3) m/s up to 50–60 m/s, though previous comparison (Euramet 827) showed this constant variance from 0.975 up to 1.025 in velocity range 5–40 m/s (Fig. 2) [5] and its sharp decrease up to 0.85 at the velocities less than 5.0 m/s. But depending on the capabilities to measure differential pressure low velocity value range could be extended and as it is obvious with quite larger dispersion of the measurement results.

SPT with amplifier operation at low velocities is disputable because of additional separation region behind the amplifier impact on measurement results. The flow in separation region is very sensitive to flow regime, flow turbulence level and blockage effects. The last ones are mostly determined the longitudinal pressure gradient in the region of SPT installation and differential pressure measurement.

As it could be expected, the comparison results of HWA measurements (Fig. 8) show the same tendencies of HWA readings of all participants and the uniform dispersion of the results in the whole range of velocities. It means that TA is MI being very sensitive to local flow parameters, such as flow regime ant turbulence level as well as ambient conditions. Essential for TA sensor is turbulence degree and flow stability. It is difficult now to say whether low velocity values are affected by turbulence degree, transitional region instabilities or it is a reaction of factors complex influencing velocity value.

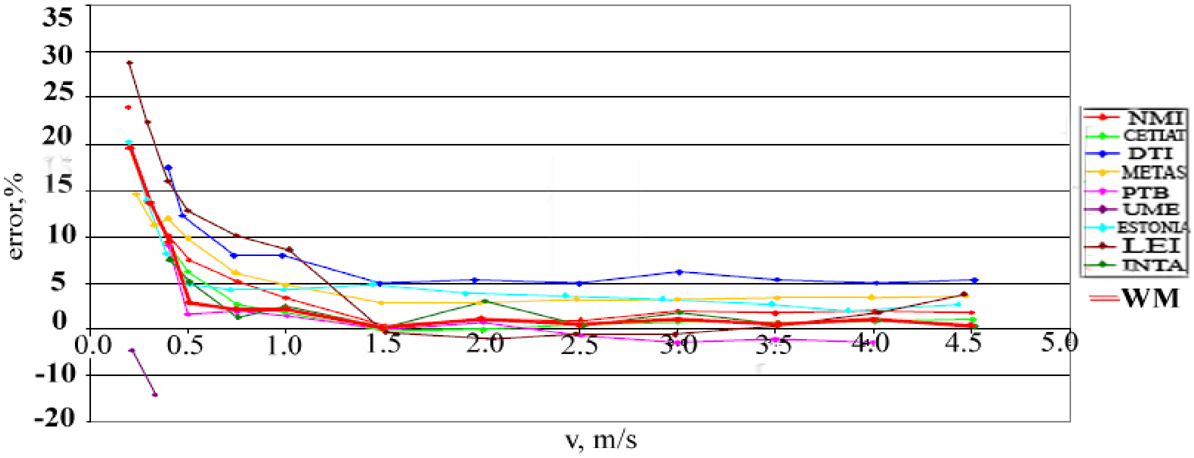

Fig. 8. TA key comparison results' errors of different laboratories [7]

To analyse possible influences discussed above, the additional research was done. First of all, analogue SPT with conical amplifier was installed in the channel as during key comparison, later measurements were repeated in closed circulation loop and one more time measurements were performed at the plane D (Fig. 3), when CD channel part was removed. Data compared with the ones from key comparison are depicted in Fig. 9, where one can see a tendency of SPT correction constant, k, like WM in Fig. 7.

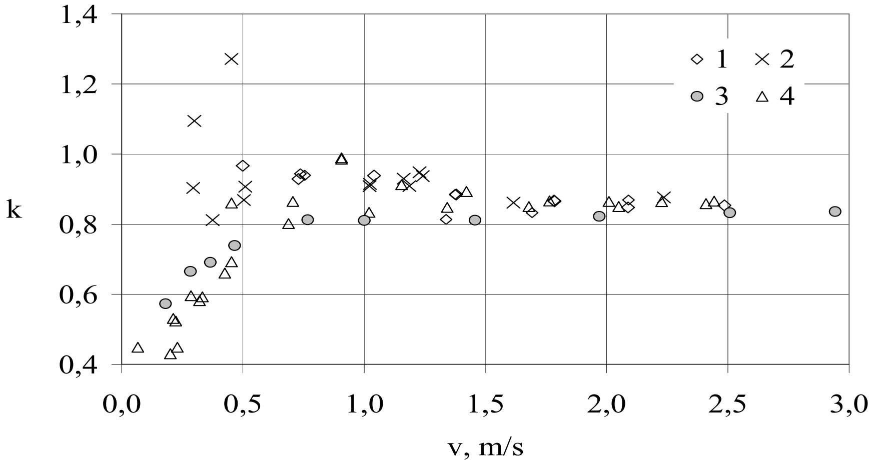

Fig. 9. SPT correction constant using different installations: 1 – Fig. 3. at plane B; 2 – the same channel as in comparison; 3 – key comparison results; 4 – closed loop channel

Comparison results deviation obviously could be clarified only by the influence of flow over MI on separation region structure that determines static pressure changes. With Re and turbulence level increase, this region size is decreasing but vorticity inside it is increasing. Using conventional SPT for measurements static and total (static and dynamic) pressure are fixed at the same cross-section. The difference of them is proportional to velocity value and is defined as [8, p. 91]:

$$v = k\sqrt{\frac{2\Delta p}{\rho}}; \tag{1}$$

here k – the corection constant of SPT; Δp – differential pressure; ρ – air density.

For ideal case $k = 1$. For SPT with an amplifier static pressure is measured at different cross-section after the obstacle (amplifier) where separation region is formed. In this case Bernouli equation is in the form:

$$z_1 + \frac{p_1}{g\rho} + \frac{v_1^2}{2g} = z_2 + \frac{p_2}{g\rho} + \frac{v_2^2}{2g} + h_v, \tag{2}$$

here h – the hydraulic loss due to obstacle (amplifier); z – the position height.

Assuming that $\bar{v}_1 \cong \bar{v}_2$, (2) relation comes into form:

$$\frac{p_1}{g\rho} - h_v = \frac{p_2}{g\rho}. \tag{3}$$

The latter equation means that differential pressure increase is influenced by hydraulic loss in the separation region, where the flow is dependent on flow regime (Re), turbulence level (Tu), longitudinal static pressure gradient which could be affected by limited channel dimensions, geometry or aerodynamic facility construction.

Flow separation phenomenon role for differential pressure increase is depicted in Fig. 10. Here are the results of SPT with conical amplifier and various dimensions of discs that were fixed instead of the amplifier. In comparison SPT without the discs and amplifier was also used. One can see the optimal height of the obstacle where static pressure reaches minimum values and SPT correction constant is close to 0.82–0.83. With the decrease of obstacle dimensions separation phenomenon influence is weakening ank $k \to 1$. Longitudinal static pressure gradient that certainly is affected by limited channel dimensions herewith limits the trace after an obstacle free development.

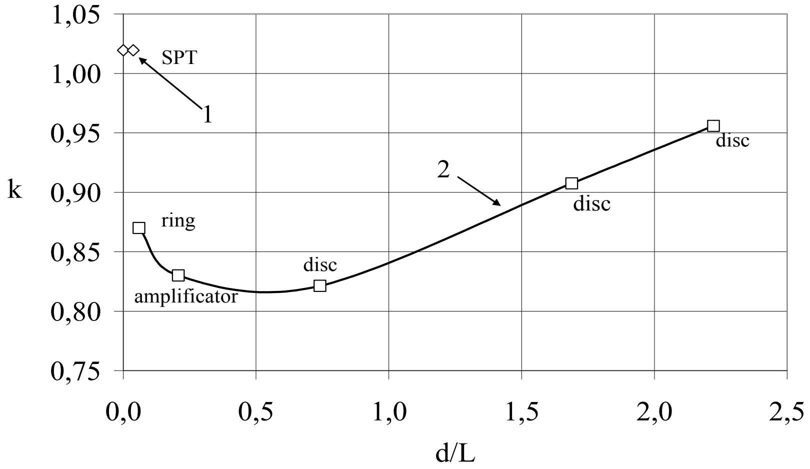

Fig. 10. Correction constant for SPT having obstacles (discs) of different diameters: d – diameter of obstacle; L – distance from SPT nose

This consistent pattern of coefficient is estimated for velocity range 2–30 m/s. Lower velocity region is not reached because of complicated low differencial pressure measurements.

As the measurements showed, turbulence degree is increasing with velocity decrease (Fig. 11). It is very likely that this tendency is the outcome of transitional from turbulent to laminar flow regime pecularities. As it is well known from investigations, *Re* number decrease and Tu level increase influence to separation region dimensions is opposite. And this comparison with such kind of SPT shows the complicated phenomenon of low Re and separation influence on the static pressure readings.

Experiments show that constant *k* values for low *Re* number could be reached with Tu increase or SPT installation in the plane of MC where separation region is under strong influence of stable suction (negative pressure) of fan (Fig. 9). Ejector usage instead of fan for low velocities showed stable velocity value reproducibility and stable Tu degree for all velocity range (0.04–0.35 m/s) (Fig. 12), while using fan Tu degree is drastically increasing for the same range.

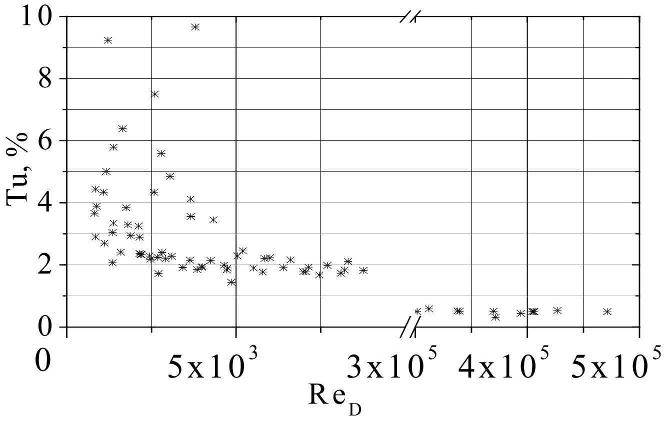

Fig. 11. Tu in dependence of Re_D at the entrance region of MC at x/D=3

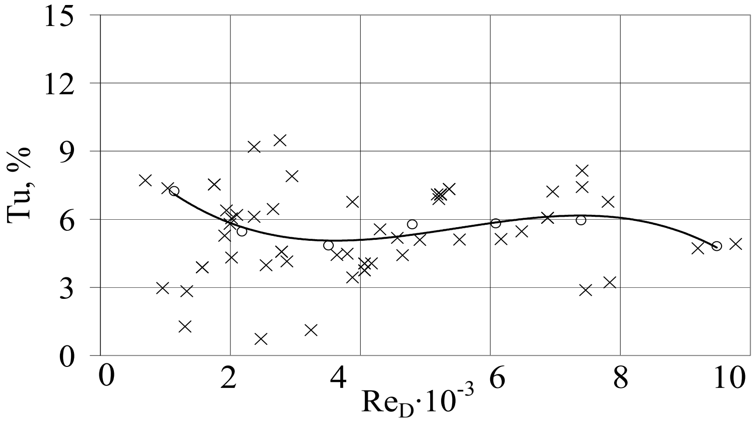

Fig. 12. Tu in dependece of Re$_D$ at the entrance region of MC at x/D=1, when ejector used for flow generation: crosses – random and dots – mean values with approximate curve

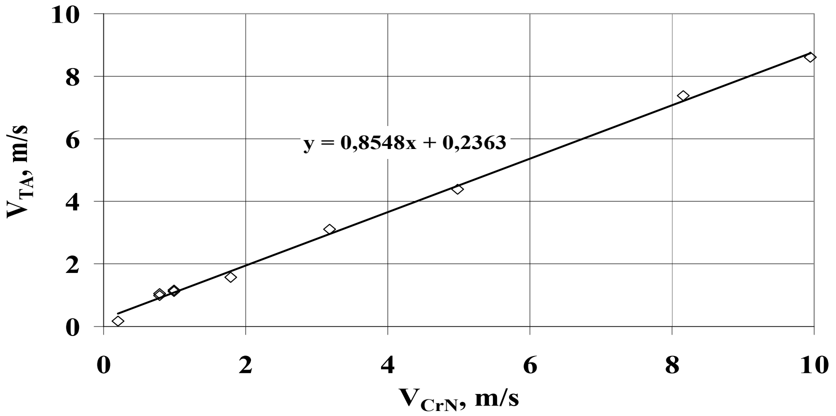

Fig. 13. Comparison of velocity valuse measured by TA and calculated according to CrN readings

Another experiment for air velocity stabilization was made with a use of CrN. As SPT with amplifier was installed in 100 mm diameter channel connected to the CrN facility the results show that *k* decreases almost linearly with velocity. But TA readings in the same facility show good correlation of local velocity values to the ones calculated from CrN readings that are stable (Fig. 13). That means for low velocity values (0.05–0.5 m/s) reproduction is expedient to use CrN and for higher velocities – aerodynamic test facility.

5. CONCLUSIONS

1. Air velocity value reproduction and calibration should be performed at the same conditions in order to get reliable compatibility.
2. Longitudinal static pressure gradient that is conditioned by measurement channel construction, its limited dimensions and flow regime and turbulence level is an influencing factor but not essential for conventional measurement instruments, however, is crucial for SPT with amplifier that evokes flow separation and for explanation of correction constant variation, pressure losses during the flow around amplifier should be taken into account.

3. Air velocity value reproduction uncertainty is influenced by flow instabilities for low Re. Measurement channel construction and MI installation should be carrefully selected to reproduce stable values.
4. One of the simplest way for air velocity value reproduction is to do it in free stream formed by convergent nozzles chamber that is limited from ambient conditions.

REFERENCES

1. A. Daugelė, V. Ilgarubis, V. Janušas. National standard of air velocity unit. Velocity value reproduction methods // Measurements. ISSN 1392-1223. 2002. No.3 (23), p. 13–20.
2. A. Bertašienė, A. Daugelė, V. Janušas. Investigation of practical application of laser Doppler anemometer // Measurements. ISSN 1392-1223. 2006. – Nr.2 (38), p. 5–10.
3. A. Pedišius, V. Janušas, A. Bertašienė. Low air velocity measurement characteristics' variation due to flow regime // International Journal of Fluid and Thermal Engineering. 2008. ISSN: 2070-3759, Vol. 1, No. 1, p. 25–29.
4. H. Lerch. Intercomparison of anemometers. Euromet project 388. Final report. 1999. p. 48.
5. J.R. Sánchez, H. Müller, I. Care, Y. Cordier-Duperray, J.M. Seynhaeve. Air velocity Sensors' Calibration Intercomparison using LDA as standards. Conference Proceedings, 12th International Symposium on Applications of Laser Techniques to Fluid Mechanics. July 2004, Lisbon, Portugal, CD-ROM, Session 22-5. 2005, p. 12.
6. ISO 9300: 1990 Measurement of gas flow by means of critical flow Venturi nozzles.
7. Euromet Key Comparison M.FF-K3 – Draft A – February 2008. NMi. P. 31.
8. N. Liutikas. J. Gudzinskas. Thermalhydromechanics (Lithuanian version). 2001. ISBN 9955-09-050-2, p. 377.

EXPERIMENTAL INVESTIGATION AND MODELING OF SHEAR STRESS AT INTERFACE OF TWO PHASE FLOW

M. Valinčius, S. Gasiūnas
Lithuanian Energy Institute,
Laboratory of Nuclear Installation Safety
Breslaujos str. 3, LT-44403 Kaunas – Lithuania
Phone: +370 37 401922
E-mail: valinc@mail.lei.lt

ABSTRACT

Shear stress at the interface is one of the most important parameters when talking about two phase stratified flow stability. In this article, measurements of pressure drop together with calculations of shear stresses at the interface of two-phase air-water and steam-water flow are presented. Experiments were performed in rectangular channel with dimensions W=20 mm, H=100 mm, L=1200 mm (length of test section was 0.84m). Thickness of water layer was 25 mm, at which void fraction was α=0.75. There were 3 flow regimes tested at atmospheric pressure: 1) air single phase flow; 2) air-water flow; 3) steam-water flow without condensation (steam and water were almost at saturation temperature). Modeling of corresponding tests was performed using best estimate code RELAP5. The results were compared with each other and verification of RELAP5 modeling results was performed.

Keywords: RELAP5, modelling, two-phase, interface, shear

1. INTRODUCTION

Two phase flow is a very important process from scientific and practical viewpoint. Phases can exist in non-equilibrium with each other, therefore, heat, momentum and mass transfers between phases, complicate the problem.

In Lithuanian Energy Institute a study of two phase flow in rectangular channel is in progress [1, 2]. This study is part of a major research program, wherein a thermal-hydraulic system based on condensation implosion should be developed and its operation should be substantiated. The current task is to identify parameters of interfacial instabilities which can cause condensation to accelerate itself. Positive feedback mechanism can take place when steam flow starts generating waves at the interface and thus, direct contact condensation area and water turbulence are also increasing.

Interfacial shear stress is one of the most important parameters when evaluating instabilities of two–phase stratified flow [3, 4]. In this paper experimental investigation results of two phase flow and interfacial shear are presented in comparison with results of modeling using RELAP5 mod3.3 code [5]. This work will allow to compare results with two phase condensable flow and identify condensation effect on interfacial stability.

2. THE EXPERIMENTS

2.1. Experimental Setup

Experimental setup is presented in Fig. 1. The main part is rectangular channel (1). There were transparent windows in sidewalls of the channel for visual observations.

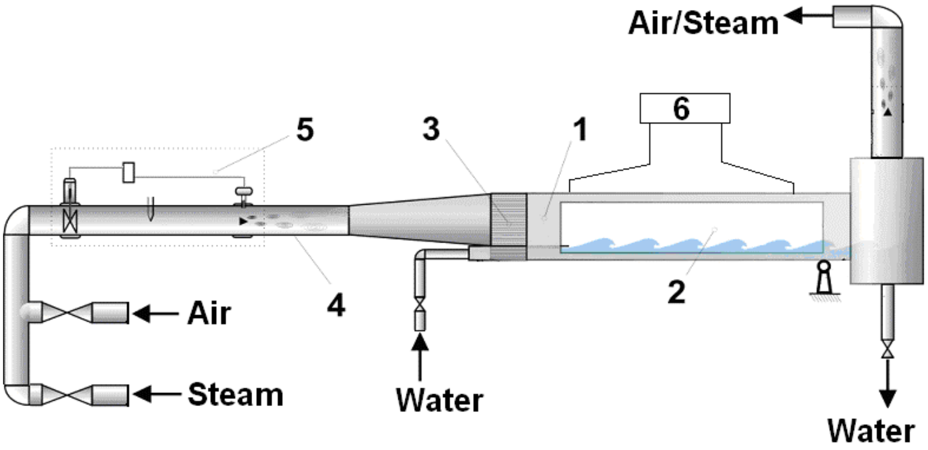

Fig. 1. Experimental setup: 1 – rectangular channel; 2 – windows; 3 – gas flow equalizer; 4 – inlet pipe; 5 – flow control-measurement; 6 – differential pressure transmitter

Configuration of channel test section:
1) length: $L = 0.843$ m;
2) height: $h = 0.1$ m (0.075 m for gas phase and 0.025 for liquid phase);
3) width $W = 0.02$ m;
4) cross-sectional area $A = 0.002$ m^2;
5) equivalent hydraulic diameter $D_{ek} = 0.032$ m.

The channel was isolated to minimize heat losses through walls, which is important when operating with steam. The experiments can be performed with either air or steam. More detail description of experimental facility is presented in paper [2].

2.2. The process

The experiments were performed with two types of gas phase media – steam and air. The liquid phase was always water. During experiments the water was stationary (no water flow).

There were 3 types of experiments:

Single phase Air flow.

In this case solid plate was inserted into the channel. It was attached to the bottom of the channel and was 0.025 m in height, to maintain the same cross-sectional gas flow area as in other two cases. Air temperature was 291 K and pressure was atmospheric.

Two phase air-water flow.

Experiments with air-water flow were performed at atmospheric conditions, water and air temperatures were the same $T_w = T_a = \sim 291$ K. The water was stationary and air velocity varied from 4 to 10 m/s. At higher air velocities it was still possible to operate, but it was difficult to visually integrate in real-time and to monitor water level in the channel. Especially at the end of the channel, where waves were quite big.

Two phase steam-water flow without condensation at the interface.

Experiments with steam-water were performed also with stationary water at atmospheric pressure, steam temperature was $T_s = 376$–381 K, water temperature was $T_w = 372$ K. Steam velocities varied from 4 to 13 m/s.

Before performing the two-phase flow experiments, the channel is set to horizontal position and filled with water up to level of 25 mm. Then gas is started to introduce at specific velocity. If operating with steam, the flow was maintained for some time to heat up the channel and to reach stationary initial conditions.

Because of friction and interfacial drag, the water is dragged to the end of the channel. Water level becomes higher there, and the channel must be inclined to maintain uniform liquid depth in the entire channel. The higher gas velocity is, the bigger drag effect it generates and the bigger inclination angle is needed to compensate that. By doing this, cross sectional area for gas flow can be equalized and friction can be calculated.

2.3. Pressure drop measurement

The pressure drop along test section was measured using differential pressure transmitter Fuji-electric FCX-A/C II. The results are presented in Fig. 2. As we can see, the results differs a lot between air and steam. This was expected, because air density is about 2 times higher than steam density. Gas phase with higher density causes higher friction and, therefore, higher drag force and pressure drop.

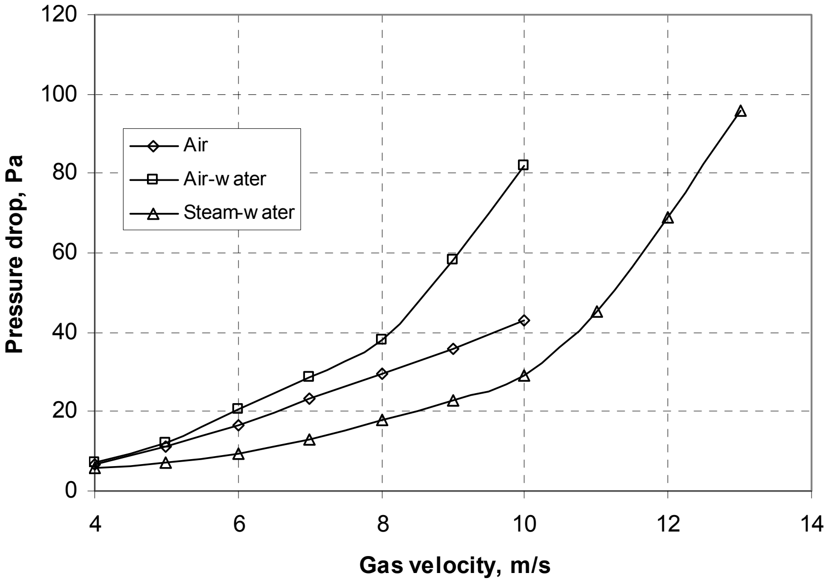

Fig. 2. Experimental results. Pressure drop vs. gas velocity

The difference between single phase air and air-water flow can be interpreted as additional pressure drop only because of disturbances on the interface, which increased roughness. Even though interfacial area is relatively small compared with walls area, the difference is quite significant. As we can see the shape of curves is more or less quadratic function. However, these are not infinite curves and are limited by flow regime transition. As we can see, there's a change in curve behavior at 10 m/s for steam-water flow and at 8 m/s for air-water flow. This might be because of formation of braking waves and entrainment of water into gas phase, which causes higher pressure losses. Also it must be mentioned, that exceeding these velocities, waves are quite big, and causes pressure measurement pulsate over time, which affects accuracy of measured value. Additional effects and interfacial interactions will be evaluated in the future, by employing investigation of interface curvature parameters.

As for steam-water flow, there is also influence of condensate droplets on channel walls, which causes additional pressure losses because of generated roughness. Some water droplets on channel walls are also present in air-water flow, especially at higher air velocities, when breaking waves appear.

3. MODELLING

A developed and verified model of the single experimental facility enables us to simulate the process in different scale or other conditions.

Lithuanian Energy Institute has a strong background of RELAP5 usage for modelling complex systems. The code has been developed for more than 30 years and is one of the most reliable system codes to model thermal-hydraulic processes in nuclear reactors. Every best estimate code (and RELAP5 is one of these) should be applied only under conditions that has been verified by experimental data. If there is no validation against the experiments – it must be done so. Two-phase system modelling using RELAP5 needs to be tested if this code is suitable for this case. Interface shear because of the difference of gas and liquid velocities is the source Kelvin-Helmholtz instabilities. It is therefore important to identify RELAP5 ability to calculate this shear. The main difference between our tests and modeling is that RELAP5 uses a circular pipe model, while in our case it's a rectangular channel. To get the correct results, this should be taken into account, as the shape of crossectional area is very important for two phase stratified flow. This is because shear stresses acting on larger (smaller) interfacial area cause larger(smaller) drag force, and, therefore, pressure drop.

In this chapter modelling results in comparison with experimental data are presented.

3.1. Model description

The scheme of the model is presented in Fig. 3. The main component is the channel, which is modeled as a pipe component in RELAP5. It is assumed that there are no heat losses through the walls of the channel and the walls do not interact at all in heat transfer.

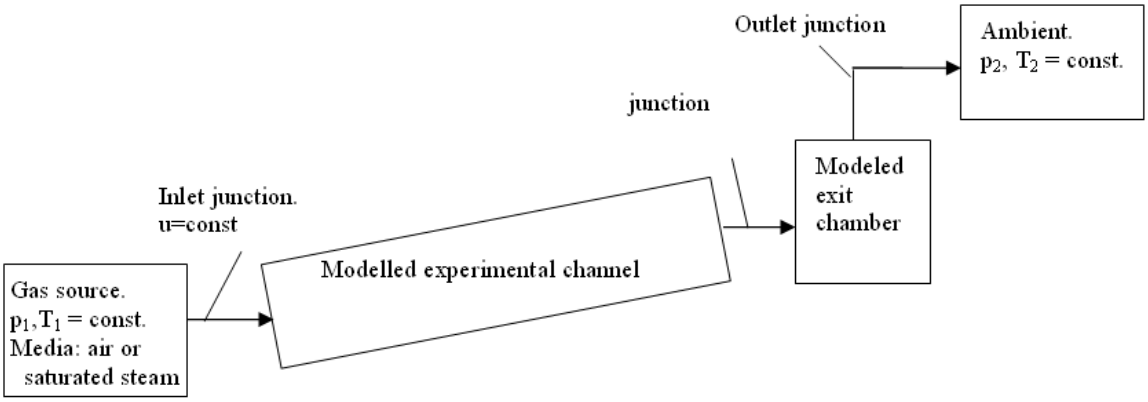

Fig. 3. Simplified RELAP5 model scheme of the experimental facility

Air or steam (depending on test case) is entering from gas source into the main channel by given velocity through inlet junction. The channel is inclined by some specific angle, so that void fraction is maintained uniform in the entire channel. Gas separation – exit chamber is modeled to keep water in the channel, as it acts for this purpose in experimental facility (see Fig. 1). Exit chamber is connected to the ambient and there's a freeflow through outlet junction. All conditions for calculations were the same as described in section 2.2.

The RELAP5 hydrodynamic model is a one-dimensional, transient, two-fluid model for flow of a two-phase steam-water mixture that can contain noncondensable components in the steam phase and/or a soluble component in the water phase. For described problems calculations were performed using nonhomogeneous 6-equations model was used, which solves conservation of mass, energy and momentum differential equations for each phase.

3.2. Modelled pressure drop

Modeling results in comparison with experimental data are presented in Fig. 4, Fig. 5 and Fig. 6. The main problem about getting results with the same conditions was that at higher velocities the water level could not be maintained. The water was blown out of the channel no matter what inclination angle was used. Despite code modification to correct interfacial area of stratified liquid in rectangular channel, the result was the same.

It was found out that interface friction strongly depends on hydraulic diameter, which is input parameter for calculations. The smaller hydraulic diameter is – the higher friction is calculated (at least for the conditions of our tests). In fact, friction can be "regulated" only by this changing parameter. However, it also affects more correlations, and needs more investigation. Therefore, when modeling non-circular pipes, this parameter must be used with caution. In this case, ordinary equivalent hydraulic diameter was used.

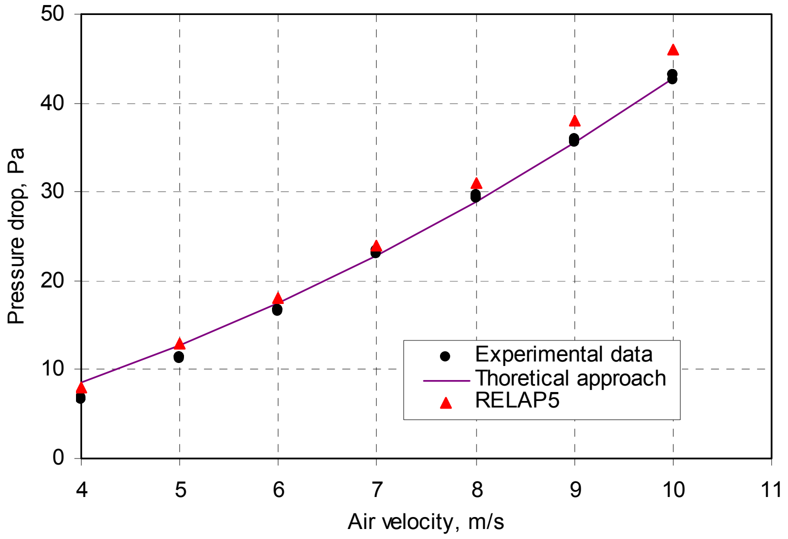

Fig. 4. Modelling and experimental results for single phase air flow (pressure drop vs. gas velocity). Theoretical approach is described in section 4 of this paper

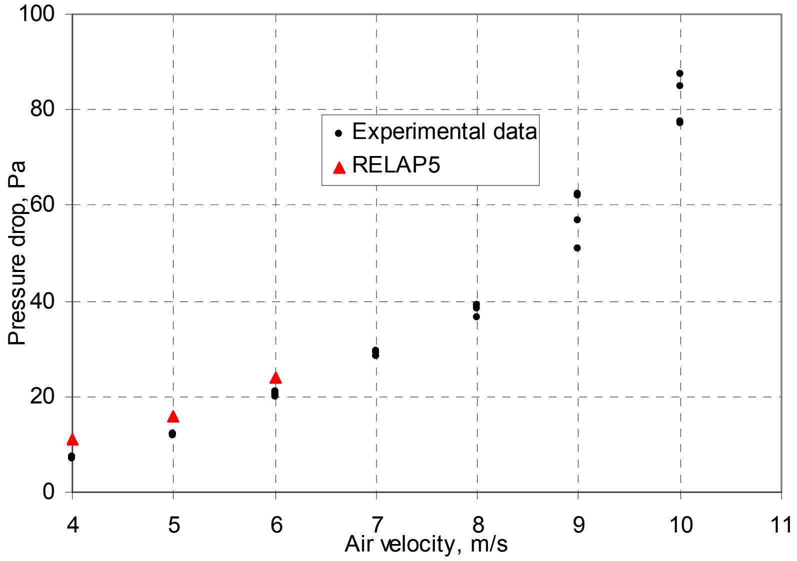

Fig. 5. Modelling and experimental results for air-water flow (pressure drop vs. gas velocity)

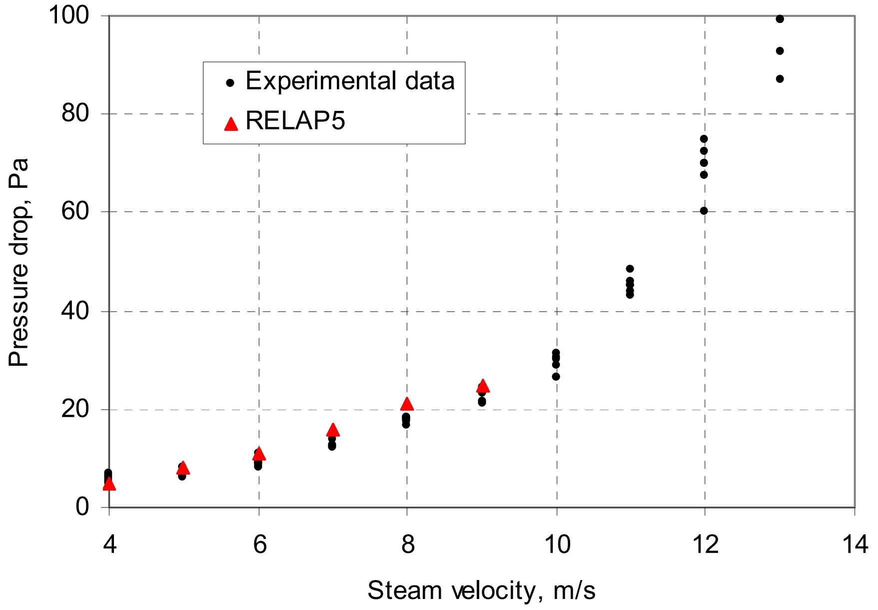

Fig. 6. Modelling and experimental results for steam-water flow (pressure drop vs. gas velocity)

As we can see, the agreement between modeled and measured pressure drop is reasonable.

4. INTERFACIAL SHEAR

As it was mentioned in previous section, pressure drop in cases without condensation occurs because wall friction and friction at the interface. The case performed with single-phase air flow gave the information about wall friction. Theoretical approach was used to check the results and it showed good agreement with experimental data (see fig. 4).

Theoretical calculation of frictional pressure drop was calculated by:

$$\Delta p = f_g \frac{L}{D_{ek}} \frac{\rho_g \cdot u_g^2}{2}; \tag{1}$$

here f_g – Darcy's friction coefficient; L – length; D_{ek} – equivalent hydraulic diameter; u_g – gas velocity; ρ_g – gas density; and:

$$f_g = C_g \cdot \mathrm{Re}_g^{-n} \tag{2}$$

where $C_g = 0.3164$ and $n = 0.25$ constants given by Blasius H. [6].

There were 3 different approaches employed to evaluate interfacial shear. Each of them is described below. The results of all these approaches are presented in Fig. 8 and Fig. 9.

1. Measured pressure drop approach

Interfacial shear was calculated from measured pressure drop and theoretical calculation of wall friction. Equations were used from Taitel, Y. & Dukler, A [7]:

Wall-gas and interfacial shear stresses:

$$\tau_{wg} = f_g \frac{\rho_g u_g^2}{2}; \tag{3}$$

$$\tau_i = f_i \rho_g \frac{(u_g - u_l)^2}{2}. \tag{4}$$

Note that in this case *f* stands for Fanning friction factor, while for single phase flow we used Darcy friction factor ($f_{Darcy} = 4 f_{Fanning}$).

Frictional pressure drop is then given by:

$$\Delta p = L\frac{\tau_{wg} S_g}{A_g} + L\frac{\tau_i S_i}{A_g}. \tag{5}$$

The only unknown variable in eq. (5) is τ_i, since we have Δp from experiments and the theoretical value of τ_{wg}.

Shear stresses calculated by theoretical evaluation of wall friction are shifted upwards, because water/condensate droplets' on channel walls influence to wall friction was not taken into account. As a result, the real interfacial friction is lower than calculated, because underestimated wall friction leads to overestimated interfacial friction. These results will be updated in near future.

2. Measured channel inclination angle approach

Another approach was employed to verify the results. This was derived from two fluid model momentum equation for liquid phase. Equations for both phases without mass transfer (i.e. without transport of momentum together with transported mass) are as follows:

$$\frac{\partial}{\partial t}(\rho_g A_g u_g) = \frac{\partial}{\partial x}(\rho_g A_g u_g^2) - \rho_g A_g g \sin\alpha - \tau_{wg} S_g - \tau_i S_i - \frac{\partial p A_g}{dx}; \tag{6}$$

$$\frac{\partial}{\partial t}(\rho_l A_l u_l) = \frac{\partial}{\partial x}(\rho_l A_l u_l^2) - \rho_l A_l g \sin\alpha - \tau_{wl} S_l + \tau_i S_i - \frac{\partial p A_l}{dx}. \tag{7}$$

Assuming uniform liquid velocity, density, cross-sectional area of liquid phase, neglecting pressure drop along the channel and shear stresses of liquid to walls (as liquid is not flowing):

$$\tau_i \approx \rho_L g \frac{A_L}{S_i} \sin\alpha. \tag{8}$$

Inclination angle α, needed to maintain uniform liquid depth was measured experimentally. The results are presented in Fig. 7.

The main advantage of this method is that interfacial shear can be extracted directly from measurement. The main disadvantage is accuracy of measured angle. In Fig. 7, dashed lines shows uncertainty ranges for measured values. The uncertainty range is the sum of angle physical measurement error and visual observation error.

The angle was calculated by measuring Δh (height difference) of lowered channel inlet. The distance between lowering and fixed points was 2.1 m. Therefore, as measurement error for Δh was ±0.1 mm, angle physical measurement error is:

$$\Delta = arctg\frac{\Delta(h)}{L} = arctg\frac{0.0001}{2.1} = \pm 0{,}00273^o$$

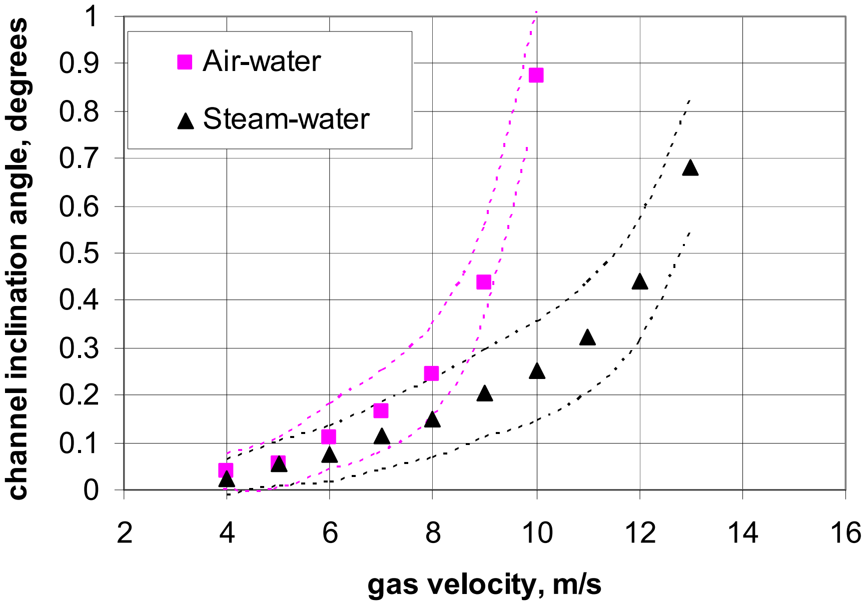

Fig. 7. Inclination angle needed to maintain uniform liquid depth along the channel

Much more uncertain is visual observation error. It is almost impossible to define uncertainty range, because it depends on the subject and needs tests to verify the range. However, this was chosen as linear increase of error between the following:

- At gas velocity of 4 m/s (it doesn't matter if it is steam or air), for length of test section (0.84 m), uniform water level of 0.025 m is set with an error of ±0.5 mm.
- At maximum gas velocity (that is 10 m/s for air and 13 m/s for steam) observation error is ±2 mm along the test section.

The total angle measurement errors for each case, according to these assumptions, are given in Fig. 7.

3. RELAP5 calculations

According to manual [5], RELAP5 uses equation (2) (also with C_g = 0.3164 and n = 0.25) to calculate interfacial friction. As we can see, there's a "jump" in values at gas velocities, which limited modelling the same flow configurations as during the experiments, even though flow regime calculated was still horizontal stratified, interfacial friction was overestimated. Water blow-out occured because of high interface friction in the model.

Analyzing the results (Fig. 8, Fig. 9), it has come to conclusions, that at current stage for air-water flow, both methods 1 and 2 are reasonable, but not RELAP5. To use RELAP5 for this case, overestimated interfacial friction needs to be analyzed in all range of air velocities. For steam-water flow all methods shows good agreement up to u_g = 8 m/s. Exceeding this velocity, RELAP5 experiences a "blow-out" problem. Underestimated theoretical wall friction causes interfacial shear to shift upwards and the effect of underestimated wall friction is increasing. For these reasons, evaluation of wall friction should be updated and RELAP5 calculation of friction should be analyzed for steam velocities higher than 8 m/s.

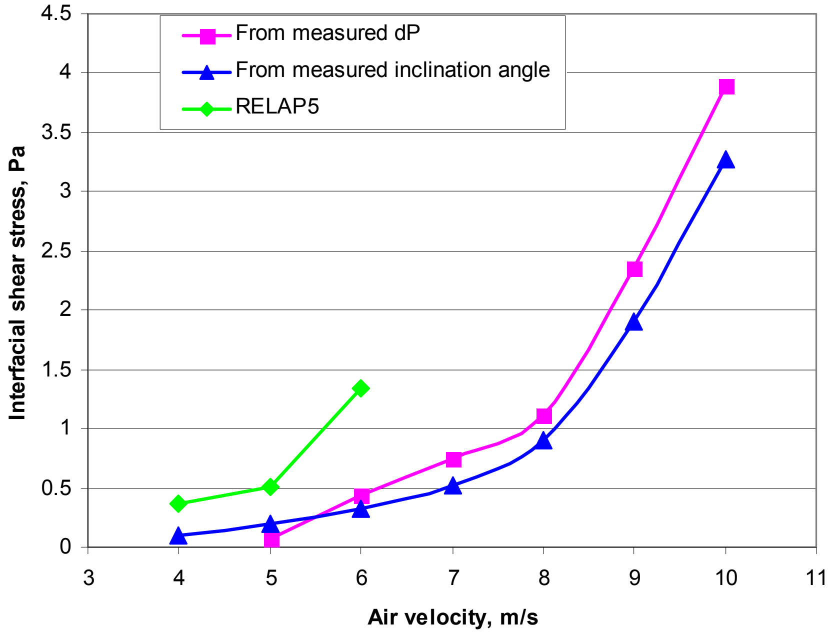

Fig. 8. Calculated shear stresses at the interface for air-water flow

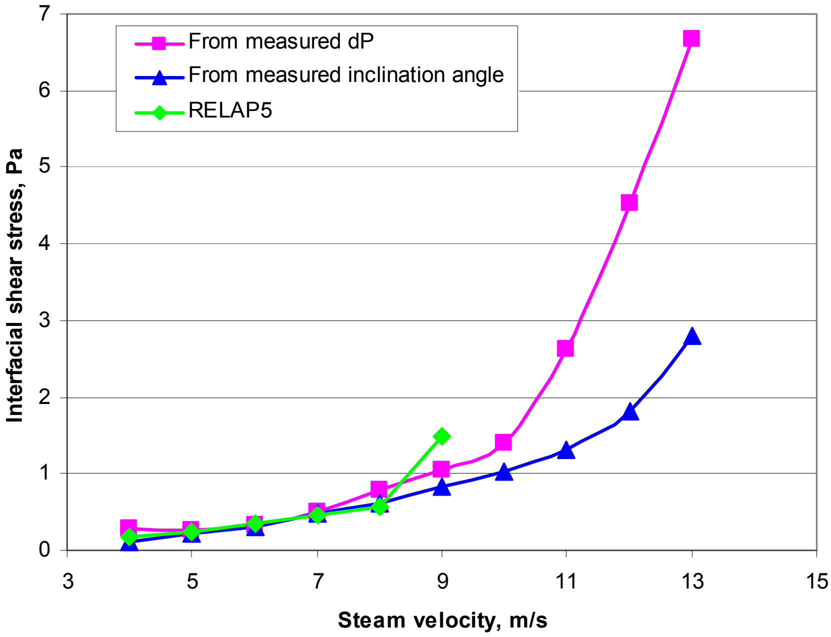

Fig. 9. Calculated shear stresses at the interface for steam-water flow

5. CONCLUDING REMARKS

Experimental investigation of two phase flow in horizontal rectangular channel and interfacial shear was performed. Theoretical approach and modeling results corresponds to the experimental data quite good for single phase flow. This shows that RELAP5 is capable to solve this kind of process.

For more reasonable results RELAP5 was modified to use real interfacial area of stratified liquid in rectangular channel instead of calculated for circular pipe, which is the only option.

Two phase flow modeling caused problems, because water depth could not be maintained at higher gas velocities. Upper gas velocity limits for modeling the same flow configuration as during the experiments were 6 m/s for air-water flow and 9 m/s for steam-water flow. This was because of overestimated interfacial shear.

It was found out that modeled interfacial friction strongly depends on hydraulic diameter, which is input parameter in the input deck. For the case studied, ordinary hydraulic diameter calculation was used ($D_{ek} = 4 \cdot A/S$) .

Further work will consider evaluation of interfacial friction in condensable two phase flow and influence of condensation to interface stability.

6. NOMENCLATURE

Δp – pressure drop, Pa;
L – length, m;
A – area, m^2;
S – wetted perimeter, m;
D_{ek} – equivalent hydraulic diameter, m;
ρ – density, kg/m^3;
τ – shear stress, Pa;
f – friction coefficient;
Re – Reynold's number;
u – velocity, m/s;
T – temperature, K;

Subscripts:
g – gas;
s – steam;
a – air;
i – interface;
wg – wall-gas.

7. REFERENCES

1. Valinčius M., Šeporaitis M., Gasiūnas S., Pabarčius R. Modeling of steam-water flow in nearly horizontal channel using RELAP5 code and verification // 11th international conference on multiphase flow in industrial plants (MFIP2008), Palermo, Italy, September 7-10, 2008. ISBN 88-88198-13-X, p. 471-478. RELAP5/MOD3.3 code manual.
2. Gasiūnas S., Šeporaitis M. Investigation of condensing two-phase co-current flow in a short rectangular channel by alternation of steam and water velocities // 11th international conference on multiphase flow in industrial plants (MFIP2008), Palermo, Italy, September 7-10, 2008. ISBN 88-88198-13-X, p. 807–814.
3. Kang H. C. & Kim M. H. The relation between the interfacial shear stress and the wave motion in a stratified flow // Int. J. Multiphase Flow, ISSN 0301-9322, 1993, No. 1, p. 35–49.

4. Brauner N. & Maron D. M. The role of interfacial shear modelling in predicting the stability of stratified two-phase flow // Chemical Engineering Science, ISSN 0009-2509, 1993, No. 16, p. 2867–2879.
5. RELAP5/MOD3.3 code manual.
6. Blasius H. Das Ähnlichkeitsgesetz bei Reibungvorgängen in Flüssigkeiten, Forchg. Arb. Ing.-Wes., 131, Berlin, 1913.
7. Taitel, Y. & Dukler, A. A theoretical approach to the Lockhart-Martinelli correlation for stratified flow // Int. J. Multiphase Flow, ISSN 0301-9322, 1976, No. 2, p. 591–595.

HEAT TRANSFER BETWEEN IN-LINE TUBE BUNDLE AND DOWNWARD DIRECTED FOAM FLOW

J. Gylys, T. Zdankus, M. Gylys
Kaunas University of Technology
Energy Technology Institute
K. Donelaicio str. 20–212 LK, LT–44239 Kaunas – Lithuania
Phone: +370 37 300444
E-mail: jonas.gylys@ktu.lt

R. Maladauskas
Kaunas University of Technology
Department of Thermal and Nuclear Energy
K. Donelaicio str. 20, LT–44239 Kaunas – Lithuania
Phone: +370 37 300445
E-mail: R.Maladauskas@lelektrine.lt

ABSTRACT

An experimental investigation of heat transfer from tube bundle to the two–phase foam system was performed. The experimental set–up consisted of the foam generator; experimental channel; tube bundle; measurement instrumentation and auxiliary equipment. Statically stable gas–liquid foam flow was used as a coolant. In–line tube bundle was used for investigation. Spacing between the centres of the tubes across and along the in–line tube bundle was equal to 0.03 m. The laminar foam flow moved vertically downward and crossed tube bundle. During an experimental investigation it was determined dependence of heat transfer intensity on flow parameters: flow velocity and volumetric void fraction of foam. Apart of this, influence of tube position of the bundle on heat transfer intensity was investigated. Experimental results were summarized by criterion equation, which is suitable for the design and calculation of foam apparatus.

Keywords: gas–liquid foam, foam flow, heat transfer, in–line tube bundle

1. INTRODUCTION

Heat transfer of different tube bundles to single–phase fluids was investigated enough [1, 2], but there practically aren't data of tube bundles heat transfer to two–phase foam flow. In our previous works heat transfer of a single cylindrical surface – tube and of tube line to upward aqueous foam flow was investigated [3]. It was noticed that heat transfer coefficient of alone tube (external diameter of which was equal to 0.014 m) to aqueous foam flow (flow velocity was equal to 0.4 m/s) varied from 350 to 682 W/(m^2K) under an influence of the foam volumetric void fraction [3]. In comparison with single–phase fluid flow the value of heat transfer coefficient of alone tube to air flow was equal to 16 W/(m^2K) and that to the water flow was equal to 3963 W/(m^2K) under the same flow velocity of coolant. For comparison a density of the same coolants is equal: 1.2 kg/m^3 for air, 3.2÷5.2 kg/m^3 for foam [3] and 998.2 kg/m^3 for water.

Usage of two–phase coolants, such as aqueous foam, could significantly reduce material and energy expenditures, simultaneously sustaining proper heat transfer intensity on heated surfaces. Comparing with single–phase coolant, the two–phase foam coolant has additional possibility to change the intensity of heat transfer by changing volumetric void fraction of foam. Small density and mentioned properties of foam type coolant enables to create compact, light and economic heat exchanger with simple and safe operation using two–phase foam flow.

Characteristics of one type of aqueous foam, namely statically stable foam, demonstrate its perfect availability for heat transfer process [3]. It appears that investigated by us statically stable foam keeps its initial structure and bubbles' dimensions within broad limits of time intervals, from several minutes to days, even after termination of the foam generation. Thus, this type of coolant was used as heat transfer working fluid in our investigation.

Presently the experimental set–up design was changed and foam flow moved downward without any turning. During an experimental investigation it was determined dependence of heat transfer intensity on flow parameters: flow velocity, volumetric void fraction and liquid drainage from foam. Apart of this, influence of tube position in the bundle on heat transfer was investigated. The results of investigation were compared with the results of our previous researches and influence of foam flow turning on heat transfer intensity of different tubes of the bundle was determinated.

Results of investigation were generalized using relationship between Nusselt and Reynolds numbers and volumetric void fraction of foam. The obtained generalized equation can be used for the designing of foam heat exchangers and calculating of heat transfer intensity of the in–line tube bundle.

2. EXPERIMENTAL SET–UP

Experimental set–up (Fig. 1) consisted of the following main parts: vertical experimental channel, in–line tube bundle, gas and liquid control valves, gas and liquid flow meters, liquid storage reservoir, liquid level control reservoir, air fan, electric current transformer and stabilizer. Cross section of the experimental channel had dimensions 0.14 x 0.14 m^2; height of it was 1.8 m. Walls of the channel were made from the transparent material in order to observe foam flow visually.

Statically stable foam – one type of aqueous foam – was used as coolant for our experiments. Statically stable foam flow was generated from the detergents water solution. Concentration of the detergents was kept constant at 0.5 % in all experiments. Foam–able liquid was supplied from the reservoir onto the special perforated plate. Foam flow was generated during gas and liquid contact. Foam flow parameters control was fulfilled using gas and liquid valves.

Perforated plate for foam generation was installed at the upside of the experimental channel and was made from stainless steel plate with a thickness of 2 mm; orifices were located in a staggered order; their diameter equal 1 mm; spacing between the centres of the holes equal 5 mm.

In–line tube bundle was used during experimental investigation. This bundle of the tubes consisted of six rows with five tubes in each. Spacing between centres of the tubes across and along the tube bundle was equal to 0.03 m (s_1=s_2=0.03 m). All tubes had an external diameter of 0.02 m. Schematic view of the experimental section with tube bundle is presented in Fig. 2. One tube – calorimeter was heated electrically. This tube was made of copper and had an external diameter of 0.02 m also. The ends of the heated tube was sealed and insulated to prevent heat loss through them. During the experiments calorimeter was placed instead of one of the bundle's tube. An electric current value of heated tube was measured by an ammeter and voltage by a voltmeter. Temperature of the calorimeter surface was measured by eight calibrated thermocouples: six of them were placed around the central part of the tube and two of them were placed in both sides of the tube at a distance of 50 mm from the central part. Temperature of the foam flow was measured by two calibrated thermocouples: one in front of the bundle and one behind it.

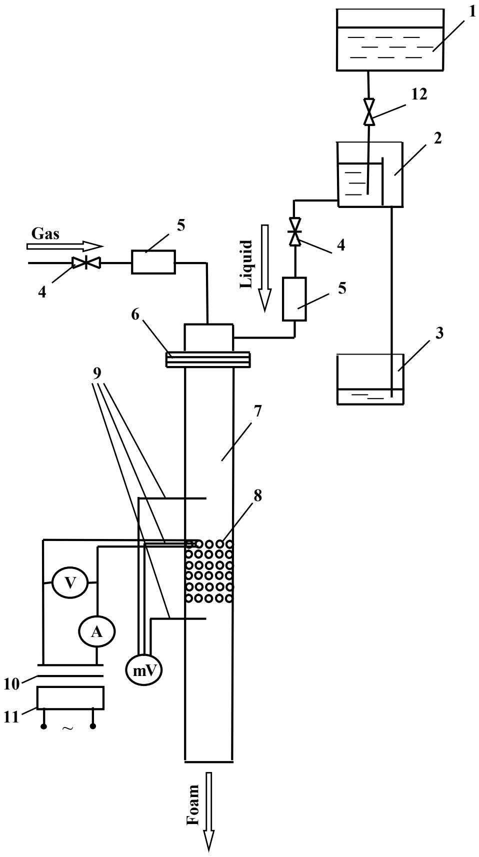

Fig. 1. Experimental set–up scheme: 1–liquid reservoir; 2–liquid level control reservoir; 3–liquid receiver; 4–gas and liquid control valves; 5–flow meters; 6–foam generation plate; 7–experimental channel; 8–tube bundle; 9–thermocouples; 10–transformer; 11–stabilizer; 12–valve

Measurement accuracies for flows, temperatures and heat fluxes were of range correspondingly 1.5%, 0.15÷0.20% and 0.6÷6.0%.

During the experimental investigation a relationship was obtained between an average heat transfer coefficient h from one side and foam flow volumetric void fraction β and gas flow Reynolds number Re_g from the other side:

$$Nu_f = f\left(\beta, Re_g\right). \tag{1}$$

Nusselt number was computed by formula

$$Nu_f = \frac{hd}{\lambda_f}. \tag{2}$$

Here λ_f is the thermal conductivity of the statically stable foam flow, W/(m·K), computed by the equation

$$\lambda_f = \beta\lambda_g + \left(1-\beta\right)\lambda_l. \tag{3}$$

An average heat transfer coefficient we calculated as

$$h = \frac{\overline{\overline{q_w}}}{\Delta T}. \tag{4}$$

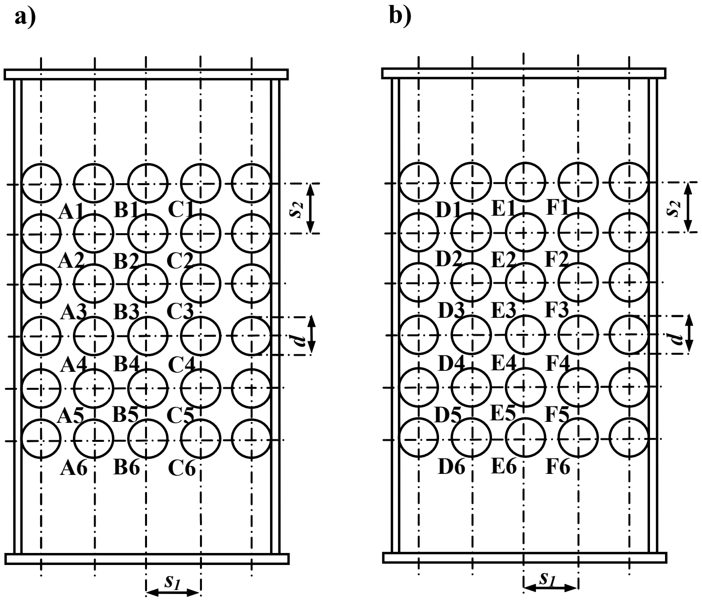

Fig. 2. In–line tube bundle in downward (a) and downward after turning (b) foam flow

Gas Reynolds number of foam flow we computed by formula

$$Re_g = \frac{G_g d}{A \nu_g}. \tag{5}$$

Foam flow volumetric void fraction we expressed by the equation

$$\beta = \frac{G_g}{G_g + G_l}. \tag{6}$$

Experiments we performed within limits of Reynolds number range for gas (Re_g): 190÷410 (laminar flow regime) and foam volumetric void fraction (β): 0.996÷0.998. Gas velocity for foam flow was changed from 0.14 to 0.30 m/s.

3. RESULTS

Heat transfer intensity of the tubes located at the different places across the experimental channel is influenced by the distribution of the local flow velocity and the local void fraction of foam across the channel. Maximum value of the foam flow local velocity is in the centre of the channel and decreases approaching to the walls of the channel. Change of the foam local void fraction is different. Foam is dryer in the centre of the channel and it is wetter near the channels walls. Comparison of heat transfer intensity (Nu_f) of the first line tubes A1, B1 and C1 to the downward foam flow is shown in Fig. 3. Side tubes A and C were located at the same distance from the vertical axis of the experimental channel, therefore the foam local void fraction and foam flow local velocity had correspondingly the same values near the side tubes A and C and the heat transfer intensity of those tubes was identical. So, some points overlap. Also an average heat transfer intensity of side tubes (A&C) was calculated for the better experimental results analysis.

Increasing foam flow gas Reynolds number (Re_g) from 190 to 410, heat transfer intensity (Nu_f) of the middle tube B1 increases by 1.9 times (from 675 to 1262) for foam volumetric void fraction β=0.996, and by 1.9 times (from 571 to 1070) for β=0.997, and twice (from 369 to 729) for *β*=0.998. An average heat transfer intensity of the first side tubes (A1&C1) for the same Re_g increases by 1.9 times (from 648 to 1207) for foam volumetric void fraction *β*=0.996, and twice (from 495 to 996) for *β*=0.997, and by 1.8 (from 362 to 668) for *β*=0.998. Heat transfer of the tube B1 is better than that of the A1&C1 on average by 5 % for *β*=0.996, by 8 % for *β*=0.997 and for *β*=0.998.

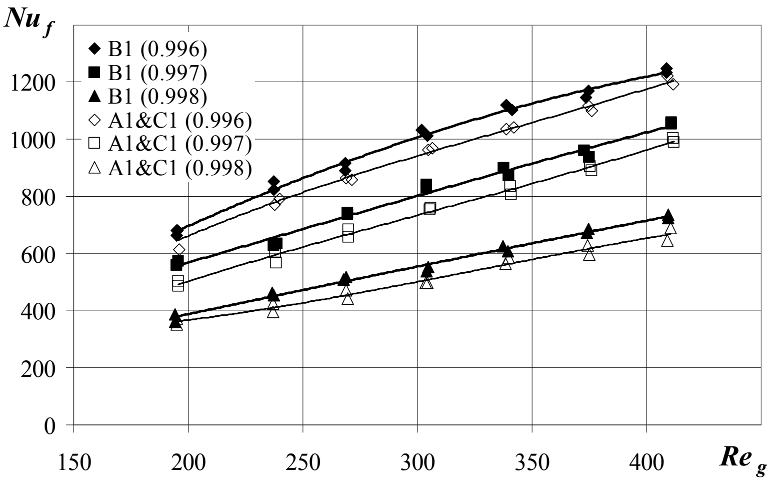

Fig. 3. Heat transfer intensity of the tubes A1, B1 and C1 to downward foam flow, *β*=0.996, 0.997 and 0.998

Comparison of heat transfer intensity (Nu_f) of the third line tubes A3, B3 and C3 to the downward foam flow is shown in Fig. 4. By increasing of foam flow gas Reynolds number (Re_g) from 190 to 410, heat transfer intensity (Nu_f) of the tube B3 to downward foam flow increases by 1.6 times (from 567 to 880) for foam with volumetric void fraction *β*=0.996; by 1.6 times (from 476 to 785) for *β*=0.997, and by 1.7 times (from 285 to 498) for *β*=0.998. The heat transfer intensity of the tube B3 is on average by 1.9 times higher to the wettest foam flow (*β*=0.996) in comparison with the driest foam flow (*β*=0.998).

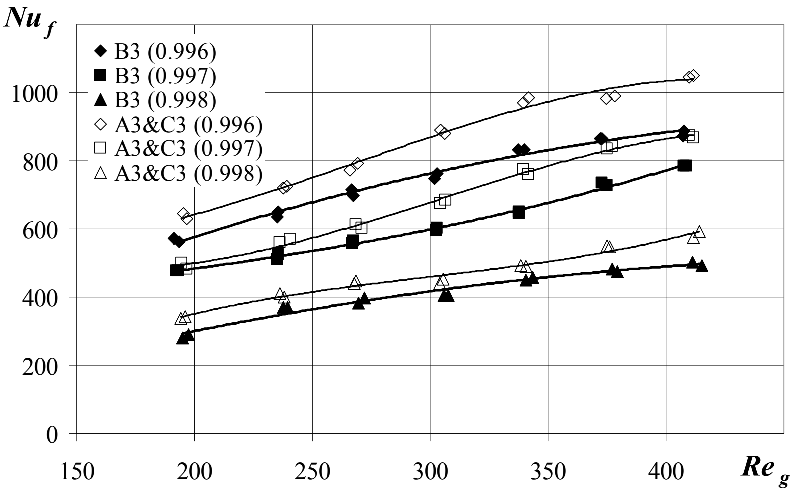

Fig. 4. Heat transfer intensity of the tubes A3, B3 and C3 to downward foam flow, *β*=0.996, 0.997 and 0.998

The Nu_f of the third tubes A3 and C3 grows by 1.6 times (from 637 to 1047) for β=0.996; by 1.8 times (from 491 to 871) for β=0.997, and by 1.7 times (from 340 to 584) for β=0.998 (Re_g =190÷410). The heat transfer intensity of the side–tubes (A3 and C3) is on average by 1.8 times greater to the wettest foam flow in comparison with the driest foam flow.

Foam structure changes, while foam passes the tube bundle. The large bubbles of foam are divided into smaller bubbles, some of foam bubbles collapse. So, the local void fraction and the intensity of the liquid drainage process are not the same along the experimental channel. The cross–sectional distribution of foam local void fraction increases. Therefore an average heat transfer intensity of the third side–tubes A3 and C3 (A3&C3) is higher than that of the third middle–tube (B3) by 15% for β=0.996; by 12% for β=0.997, and by 13% for β=0.998 (Re_g =190÷410).

For single–phase flow case the heat transfer intensity of the frontal (first line) tubes of in–line tube bundles is equal to about 60% of the third line tubes heat transfer intensity, heat transfer intensity of the second line tubes is equal to about 90% of the third line tubes heat transfer intensity, and the heat transfer intensity of the fourth and further line tubes is almost the same like that of the third line tubes [1]. Flow velocity distribution in the cross–section of the channel is the main factor, which makes different heat transfer intensity of the middle and side tubes. Situation is different in the case of two–phase foam coolant. The peculiarities of the foam [4, 5] plays significant role in that case and the heat transfer intensity of the first line tubes is better than that of the third line tubes.

In our previous works we investigated heat transfer process between the same inline tube bundle and downward after 180 degree turning foam flow [6, 7]. In that case foam flow was generated at the channel bottom [6]; foam flow moved vertically upward and then after the 180–degree turning moved vertically downward crossing the tube bundle.

An average heat transfer rate of middle–column tubes (B and E) was calculated in order to analyse the influence of foam flow turning on the heat transfer intensity of the tubes in the middle–column of the bundle. An average heat transfer intensity of the middle–column tubes (B) to downward foam flow and an average heat transfer intensity of the middle–column tubes (E) to downward after 180–degree and R=0.17 m radius foam flow turning is presented in Fig. 5.

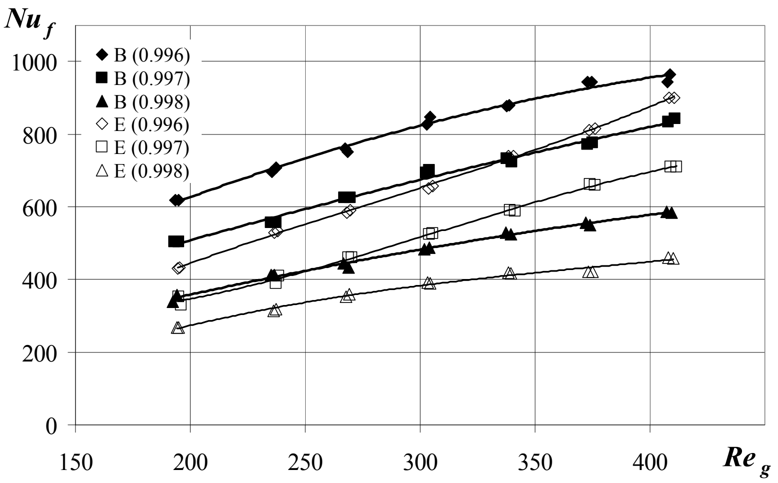

Fig. 5. An average heat transfer intensity of the tubes B to downward foam flow and an average heat transfer intensity of the tubes E to downward after 180–degree turning foam flow, β=0.996, 0.997 and 0.998

Foam is wetter and local velocity of foam is higher in the centre of the channel cross–section in the case of foam flow without the turning. Therefore an average heat transfer intensity of the middle–column tubes B is higher than that of the middle–column tubes E (downward after 180 – degree turning foam flow) on average by 22% for β=0.996; by 28% for β=0.997, and by 27% for β=0.998 (Re_g=190÷410).

Experimental results of investigation of heat transfer from the in–line tube bundle to downward and downward after 180–degree turning foam flow were generalized by criterion equation (7) using dependence between Nusselt number Nu_f and gas Reynolds Re_g number. This dependence within the interval $190 < Re_g < 410$ for the in–line tube bundle in downward and downward after 180–degree turning foam flow with the volumetric void fraction β=0.996, 0.997, and 0.998 can be expressed as follows:

$$Nu_f = c\beta^n Re_g^m \qquad (7)$$

For the entire middle–column (B) in the downward foam flow on average c=3.4, n=–500, m=41.4(β–1.018). For the entire middle–column (E) in the downward after 180 – degree turning foam flow on average c=16.1, n=518, m=140.7(1.003–β).

4. CONCLUSIONS

Heat transfer of in–line tube bundle to vertical downward laminar foam flow was investigated experimentally.

The experimental investigation showed that heat transfer intensity of the frontal tubes to foam flow is higher than that of the further tubes and is different in comparison with the single–phase flow case.

Foam is wetter and local velocity of foam is higher in the centre of the cross–section of the channel in the case of downward foam flow without turning. Therefore heat transfer intensity of the middle–column tubes to downward foam flow is higher than that of the middle–column tubes to downward after 180 – degree turning foam flow.

Criterion equation (7) may be applied for calculation and design of the statically stable foam heat exchangers with in–line tube bundles.

NOMENCLATURE

A – cross section area of experimental channel, m^2; c, m, n – coefficients; d – outside diameter of tube, m; G – volumetric flow rate, m^3/s; h – average coefficient of heat transfer, W/(m^2·K); Nu – Nusselt number; q – heat flux density, W/m^2; Re – Reynolds number; $\overline{T}$ – average temperature, K; β – volumetric void fraction; λ – thermal conductivity, W/(m·K); ν – kinematic viscosity, m^2/s. Indexes: f –foam; g – gas; l – liquid; w – wall of heated tube.

REFERENCES

1. A. Zukauskas. Convectional Heat Transfer in Heat Exchangers // Moscow, Nauka, 1982, p. 245–268.
2. T. Kuppan. Heat Exchanger Design Handbook // New York: Marcel Dekker, 2000, p. 229–303.
3. J. Gylys. Hydrodynamics and Heat Transfer Under the Cellular Foam Systems // Kaunas, Technologija, 1998, p. 50–314.
4. B. Fournel, H. Lemonnier, J. Pouvreau. Foam Drainage Characterization by Using Impedance Methods // Proceedings of the 3rd Int. Symp. on Two–Phase Flow Modelling and Experimentation, Pisa, Italy, 2004, p. 1–7.
5. V. Tichomirov. Foams. Theory and Practice of Foam Generation and Destruction // Moscow, Chimija, 1983, p. 11–106.

6. J. Gylys, T. Zdankus, S. Sinkunas, V. Giedraitis. Study of In–line Tube Bundle Cooling in Vertical Foam Flow, WSEAS Transactions on Heat and Mass Transfer, Iss. 6, Vol. 1, 2006, p. 632–637.
7. J. Gylys. S. Sinkunas. T. Zdankus. V. Giedraitis. A. Balcius. Foam flow turn influence on the in–line tube bundle heat transfer intensity // Computational Methods and Experimental Measurements XIII, Prague, Czech Republic, 2007, p. 457–464.

CYSENI 2009, May 28-29, Kaunas, Lithuania
ISSN 1822-7554, www.cyseni.com

MODELLING OF MIXED CONVECTION IN AN INCLINED FLAT CHANNEL

G. Drumstas
Lithuanian Energy Institute
Breslaujos str. 3, LT-44403 Kaunas – Lithuania
Phone: +370 37 401889
E-mail: d.giedrius@mail.lei.lt

ABSTRACT

In this paper we present the results on numerical investigation of the local opposing mixed convection heat transfer in an inclined (inclination angle $\varphi = 60^{o}$ from horizontal position) flat channel with symmetrical heating in the laminar-turbulent transition region. Numerical two-dimensional investigations using FLUENT 6.3 code have been performed under steady (quasi-steady) flow conditions in airflow of 0.4 MPa pressure at the Reynolds numbers of $2.4{\cdot}10^{3}$, $3.1{\cdot}10^{3}$, $4.7{\cdot}10^{3}$ and Grashof numbers $6.8{\cdot}10^{5}$, $6{\cdot}10^{5}$, $5{\cdot}10^{5}$ accordingly. Modelling results demonstrate that chequerwise circular flow takes place near the heated walls. This makes velocity profiles asymmetrical and causes the pulsations of the wall temperature. Wall temperature has sinusoid character. The results of numerical modelling have been compared with experimental ones and show rather good agreement. Modelling and experimental results show higher heat transfer from the bottom wall in comparision to upper wall heat transfer.

Keywords: opposing mixed convection, inclined flat channel, transition region, numerical modelling

1. INTRODUCTION

For modern nuclear and thermal energy technologies, computer, chemistry and other technologies reliability requirements are very important. So, designers of such technologies must have the detailed information about the processes including thermal ones that very often are defining the reliability and operation lifetime of the equipment.

Heat and momentum transfer in single-phase flows in case of complex processes under effect of buoyancy has not been investigated in details. Due to the importance of the problem for engineering applications a lot of researchers concentrated their attention to the turbulent mixed convection heat transfer investigations in vertical circular tubes. Wide investigations on this problem for turbulent flow in the vertical and horizontal channels were performed at the High Temperature Institute in Moscow [1], at the Manchester University [2, 3] and at the Lithuanian Energy Institute [4–6]. At the Lithuanian energy institute also investigations of the turbulent mixed convection in the inclined flat channels with one side heating (under effect of stable and unstable air density stratification) have been performed [7–9]. It was revealed that heat transfer is closely related to the channel inclination angle in case of the stable density stratification but heat transfer practically does not depend on the channel inclination angle in case of the unstable air density stratification.

Investigations of heat transfer in the laminar-turbulent transition region under the effect of buoyancy are rather limited. The flow character in pipes in a laminar-turbulent transition region was investigated in [1, 10–12]. In paper [13] the results on numerical investigation of the local opposing mixed convection heat transfer in a vertical flat channel with symmetrical heating for laminar and vortex airflow (at p = 0.1; 0.2 and 0.4 MPa and *Re* numbers from 1500 up to 4310, with Gr_q number variation from $1.65{\cdot}10^{5}$ to $3.1{\cdot}10^{9}$) were presented. The new correlations were suggested for determination of the non-dimensional distance at which the flow stability is lost in the flat channel with opposing flows. In other paper [14] the detailed results on experimental and numerical investigation of the local opposing mixed convection heat transfer in a vertical flat channel with symmetrical heating ($q_{w1} \approx q_{w2} \approx$ const) in the laminar-turbulent transition region were presented. It was shown that as the influence of the buoyancy becomes stronger the circulating flows appear along the channel. These flows cause asymmetry of velocity profiles and increase in heat transfer up to $Re \approx 8 \cdot 10^3$, when p = 0.4 MPa. The experiments were performed in airflow of different pressures (0.1, 0.2 and 0.4 MPa) in the range of Re from $2 \cdot 10^3$ to $5 \cdot 10^4$ and Gr_q up to $1.5 \cdot 10^{10}$. In the newest paper [15] originated from Lithuanian Energy Institute the results on experimental investigations of the local opposing mixed convection heat transfer in the same vertical flat channel with symmetrical heating in the laminar-turbulent transition region at higher air pressures (0.7, 0.8 and 1.0 MPa) when buoyancy effect is prevailing in the range of Re from $2 \cdot 10^3$ to $4 \cdot 10^4$, and Gr_q up to $1.0 \cdot 10^{11}$ was presented. The experimental data show similar tendencies in the heat transfer at higher air pressures (0.7 – 1.0 MPa) as it was revealed at smaller air pressures (0.2–0.4 MPa). But at higher air pressures the transition from the vortical flow regime to the turbulent one does not causes such drastic decrease in heat transfer as it was noticed at smaller air pressures (for p = 0.2 MPa at $Re \approx 4000$, for p = 0.4 MPa at $Re \approx 8000$). The recent review of the mixed convection in the channels including transition region was presented in [16].

In this paper the results on numerical investigations of the local opposing mixed convection heat transfer in the laminar-turbulent transition region in the same flat channel but with inclination angle $\varphi = 60^o$ from horizontal position is presented. Numerical two-dimensional simulations were performed for the same channel and for the same conditions as in experiments using FLUENT code. Simulations were performed at air pressure p = 0.4 MPa with symmetrical heating at the Reynolds numbers of $2.4 \cdot 10^3$, $3.1 \cdot 10^3$, $4.7 \cdot 10^3$ and Grashof numbers $6.8 \cdot 10^5$, $6 \cdot 10^5$, $5 \cdot 10^5$ accordingly.

2. METHODOLOGY

In this paper results on two-dimensional numerical modelling of opposing mixed convection in inclined flat channel (height – 0.0408 m, length – 6 m, hydrodynamic unheated length – 2.5 m, heated (calorimeter) length 3.5 m) with two sides symmetrical heating ($q_{w1} = q_{w2}$ = const) are presented for steady state flow conditions in airflow. The modelling has been carried out using FLUENT code. It is a contemporary computational fluid dynamics code, which is used for modelling the fluid flow and heat transfer in complex two-dimensional or three-dimensional systems [17]. This code solves the main flow and energy equations. In this case a control volume based technique is used which is based on division of the domain into discrete control volumes using a computational grid (which at the same time describes channel geometry).

The steady state mean flow equations to be solved in the two dimensional problem are:

conservation of mass (continuity),

$$\frac{\partial(\rho u_x)}{\partial x} + \frac{\partial(\rho u_y)}{\partial y} = 0 \tag{1}$$

conservation of the u_x and u_y momentum,

$$\rho u_x \frac{\partial u_x}{\partial x} + \rho u_y \frac{\partial u_x}{\partial y} = -\frac{\partial p}{\partial x} + 2\frac{\partial}{\partial x}\left(\mu \frac{\partial u_x}{\partial x}\right) + \frac{\partial}{\partial y}\left(\mu \left(\frac{\partial u_x}{\partial y} + \frac{\partial u_y}{\partial x}\right)\right) + \rho g sin\varphi \tag{2}$$

$$\rho u_x \frac{\partial u_y}{\partial x} + \rho u_y \frac{\partial u_y}{\partial y} = -\frac{\partial p}{\partial y} + 2\frac{\partial}{\partial y}\left(\mu \frac{\partial u_y}{\partial y}\right) + \frac{\partial}{\partial x}\left(\mu\left(\frac{\partial u_x}{\partial y} + \frac{\partial u_y}{\partial x}\right)\right) + \rho g cos\varphi \tag{3}$$

and energy equation.

$$\rho u_x \frac{\partial i}{\partial x} + \rho u_y \frac{\partial i}{\partial y} = \frac{\partial}{\partial x}\left(\frac{\mu}{\Pr}\frac{\partial i}{\partial x}\right) + \frac{\partial}{\partial y}\left(\frac{\mu}{\Pr}\frac{\partial i}{\partial y}\right) \tag{4}$$

Boundary conditions are:

- At the inlet to the experimental setup longitudinal air velocity u_x is equal to inlet velocity u_{in}, transversal velocity $u_y = 0$. Air enthalpy i at the inlet to the calorimeter is equal to the inlet air enthalpy i_{in}.
- On the walls ($y = 0$ and $y = h$) longitudinal u_x and transversal u_y velocities are equal to 0. Heat flux on the calorimeter walls are $q_{w1} = q_{w2} =$ const.

In the course of modelling process, it is very important to create the proper grid, since in most cases it defines the accuracy of the modelling and the stability of the solution. The grids 30 x 2200, 50 x 6000 and 60 x 7500 were tested in [18] and finally the grid 60 x 7500 was selected, because the tests show good agreement of results for last two grids. In this paper else more higher grid 70 x 7500 was used (Fig. 1).

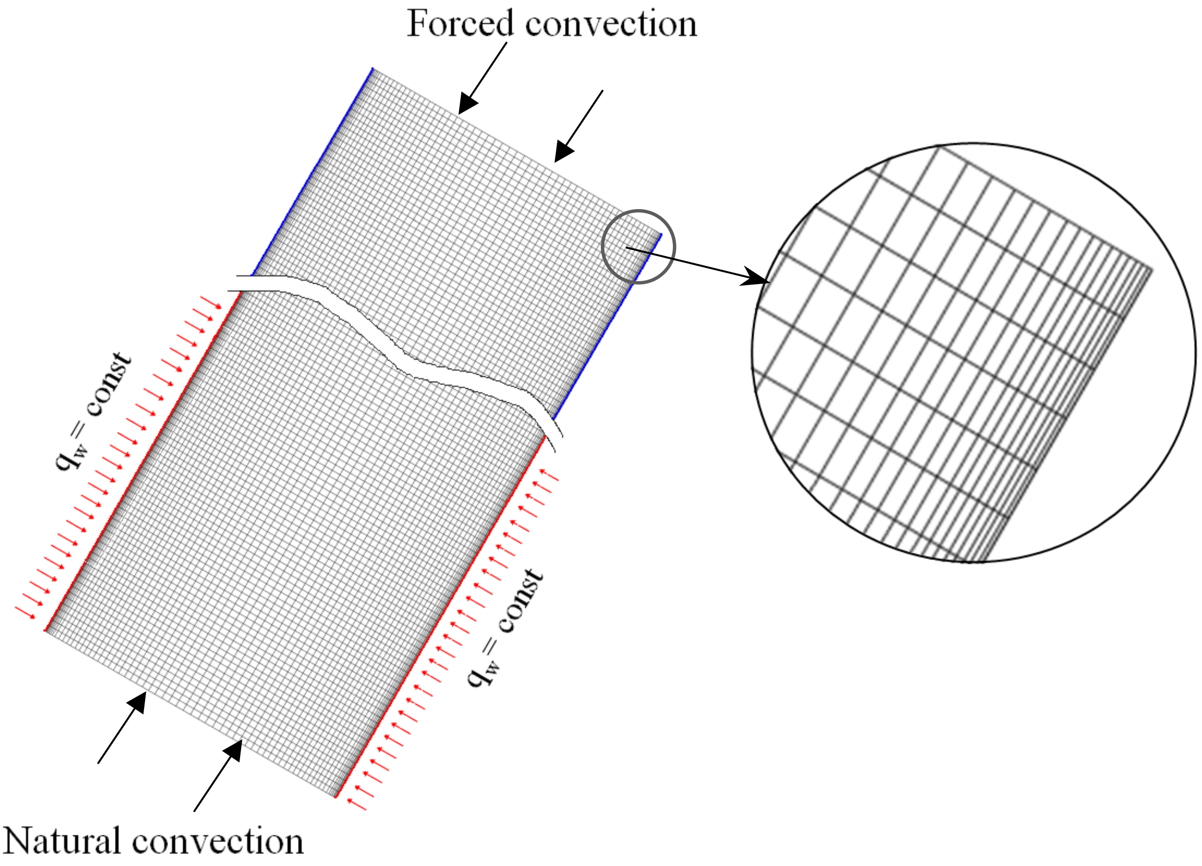

Fig. 1. Computational domain and partial view of the grid

3. RESULTS

The velocity profiles for various *Re* numbers ($2.4 \cdot 10^3$, $3.1 \cdot 10^3$ and $4.7 \cdot 10^3$) are illustrated in Figure 2. As we can see from this figure the flow in the central part of the channel is downward oriented at any time (the direction of forced flow) but the velocity profiles are always asymmetric. At $x/d_e = 1.9$ (Figure 2a, curve 1) the backward flow near the left wall occupies a larger part of the cross-section than that near the right one, and the maximum velocity is at $y/h \approx 0.6$. At $x/d_e = 3.9$ (Figure 2a, curve 2) the backward flow near the right wall occupies a larger part of the cross-section than near the left one, and the maximum velocity is at $y/h \approx 0.4$. At $x/d_e = 22.3$ (Figure 2a, curve 3) the flow near both channel walls is also oriented upwards, but in comparison with $x/d_e = 3.9$, the backward flow occupies smaller part of the cross-section near the both walls. It is also seen that maximum velocity of the flow has moved to the central position $y/h \approx 0.5$. At the next x/d_e ($x/d_e = 30.4$) (Figure 2a, curve 4) the velocity profile is very similar to the previos one and at the highest x/d_e ($x/d_e = 42$) the backward flow near the right wall becomes weaker. The maximum velocity of the flow is at $y/h \approx 0.5$ for $x/d_e = 30.4$ and at $y/h \approx 0.6$ for $x/d_e = 42$.

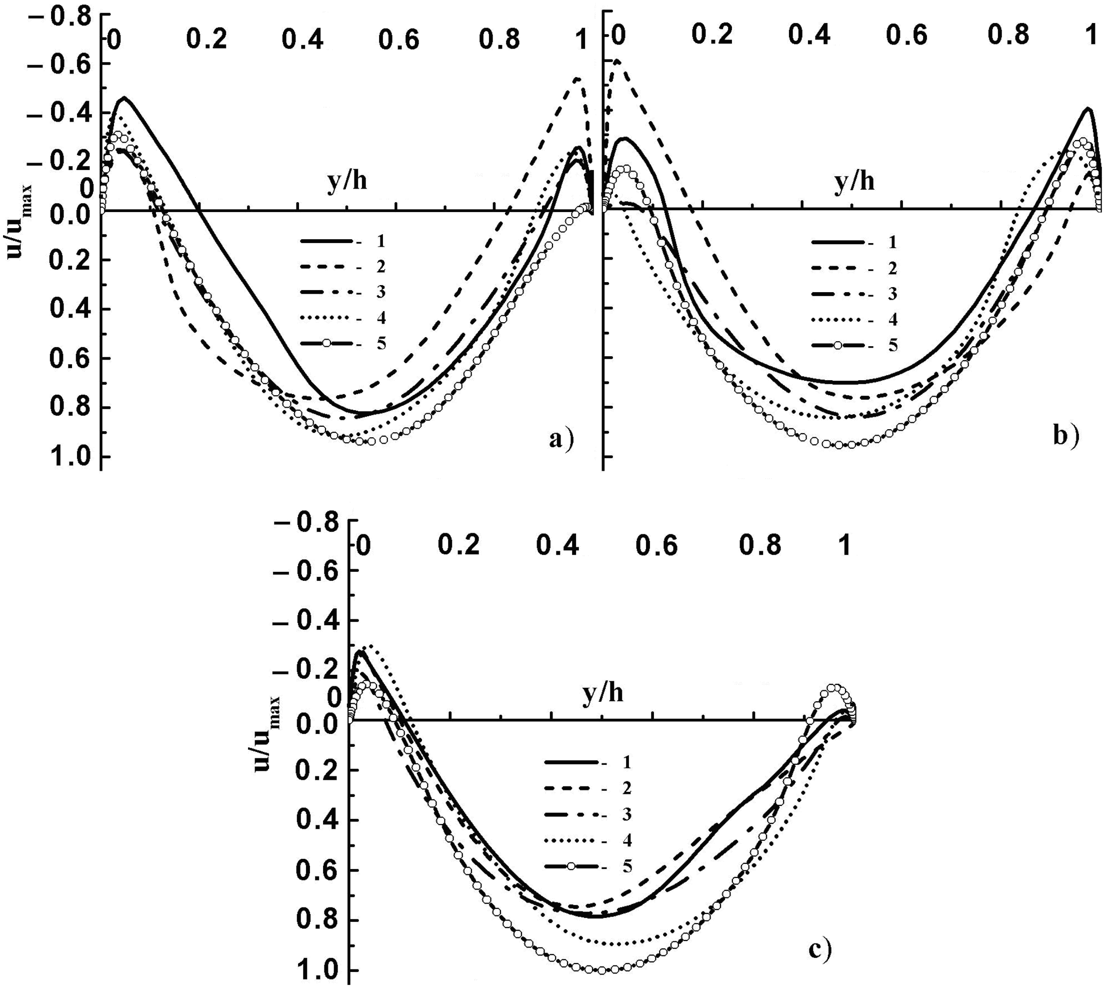

Fig. 2. The dynamics of velocity profiles depending on *Re* number and x/d_e. a) $Re_{in} = 2445$; b) $Re_{in} = 3153$; c) $Re_{in} = 4727$. 1 – $x/d_e = 1.9$; 2 – 3.9; 3 – 22.3; 4 – 30.4; 5 – 42. Upper wall is at $y/h = 0$ value and bottom wall is at $y/h = 1$value

There are two main differences in velocity profiles for higher *Re* number (Figure 2b). At $x/d_e = 3.9$ (Figure 2b, curve 2) the backward flow near the left wall occupies a larger part of the cross-section than near the right one, and at $x/d_e = 1.9$ (Figure 2b, curve 1) the velocity profile is more fulfilled than for $Re_{in} = 2.4 \cdot 10^3$ and therefore the relative velocity is smaller.

In case of the highest *Re* number (Figure 2c) the backward flow near the both walls becomes weaker in all cross-sections.

There are no clear differences observed between the flows at upper and bottom walls.

As it can be seen from Figure 3 the vortices exist near channel walls in all analysed cases ($Re_{in} = 2.4 \cdot 10^3$, $3.1 \cdot 10^3$ and $4.7 \cdot 10^3$). The chequerwise circular flow takes place at the walls (a little bit smaller vortexes are observed in Figure 3c in case of the highest *Re* number). As a result, the velocity profile becomes distorted and the flow in the centre of the channel gains sinusoid character. So as a result of vortex formation, the heat transfer is increasing also. The scales of vortexes are of the same order on both walls. As it was already indicated earlier vortical structure of the flow was revealed also in the case of vertical flat channel based on the numerical modelling results [14].

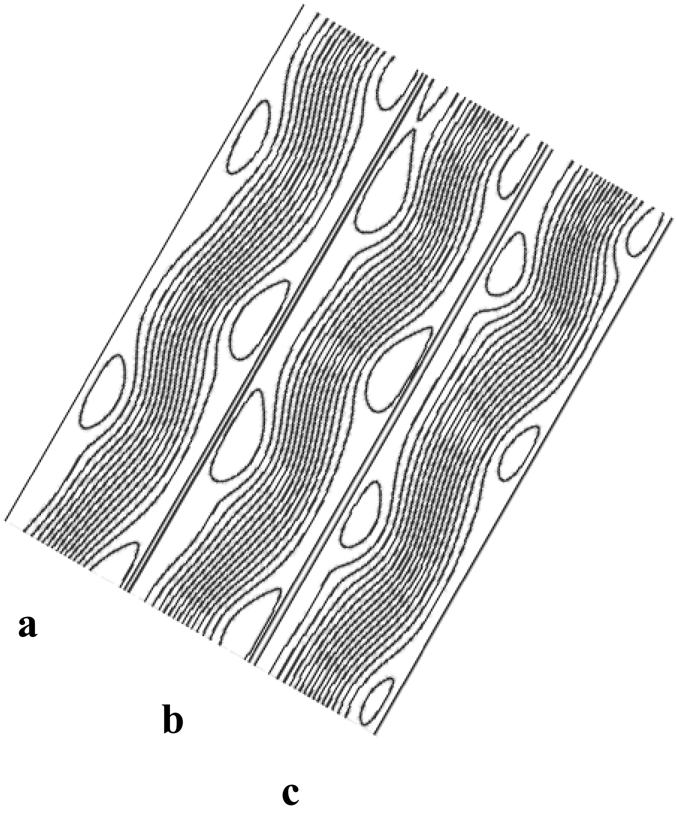

Fig. 3. Flow structure in the stabilized region ($x/d_e = 42$) of the channel for a) $Re_{in} = 2.4 \cdot 10^3$, b) $Re_{in} = 3.1 \cdot 10^3$, c) $Re_{in} = 4.7 \cdot 10^3$

The appearance of the circular flows near the walls of the channel greatly influences the distribution of temperature on channels walls. The modelling for steady conditions show that changes of temperature on the channels walls have sinusoid character (Figure 4). Experimental data don't show such variation because of the rather large thermal conductivity of the foil.

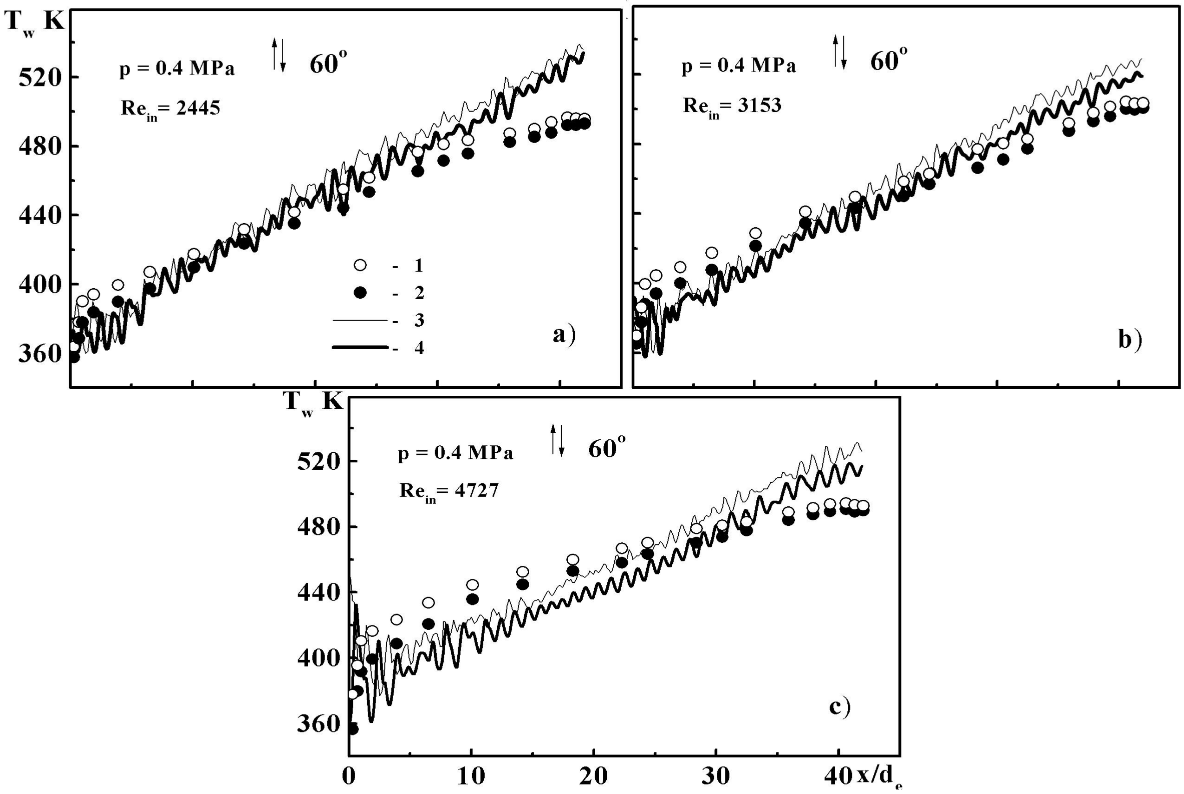

Fig. 4. Variation of wall temperature along the channel. a) $Re_{in} = 2445$; b) $Re_{in} = 3153$; c) $Re_{in} = 4727$. 1 – experimental data (upper wall); 2 – experimental data (bottom wall); 3 – numerical modelling results (upper wall); 4 – numerical modelling results (bottom wall)

The comparison of the averaged wall temperature (T_w) modelling results with the experimental data [19] is presented in Figure 5. It is evident that modelling gives the results close to the experimental data except for the highest *Re* number where modelling results shows smaller wall temperature till $x/d_e < 20$ (Fig. 5c). For the smallest *Re* number better correlation of data is observed till $x/d_e \leq 35$ (Fig. 5a). With further increase of x/d_e the modelling results give higher wall temperatures than experiment. This is most likely determined by the small structures of the flow at such *Re* numbers, which are not covered by the present laminar numerical model. For $Re_{in} = 3.1\cdot10^3$ at $x/d_e < 20$ experimental surface temperature (T_w) are higher then numerical ones but from $x/d_e > 30$ the situation is opposite. At the very beginning of the heating modelling shows a sharp decrease of wall temperature in all analysed cases. This phenomenon is related with formation of larger scale vortexes in this region. Therefore at the beginning of the heating section heat transfer is more intensive as we can see from Figure 6.

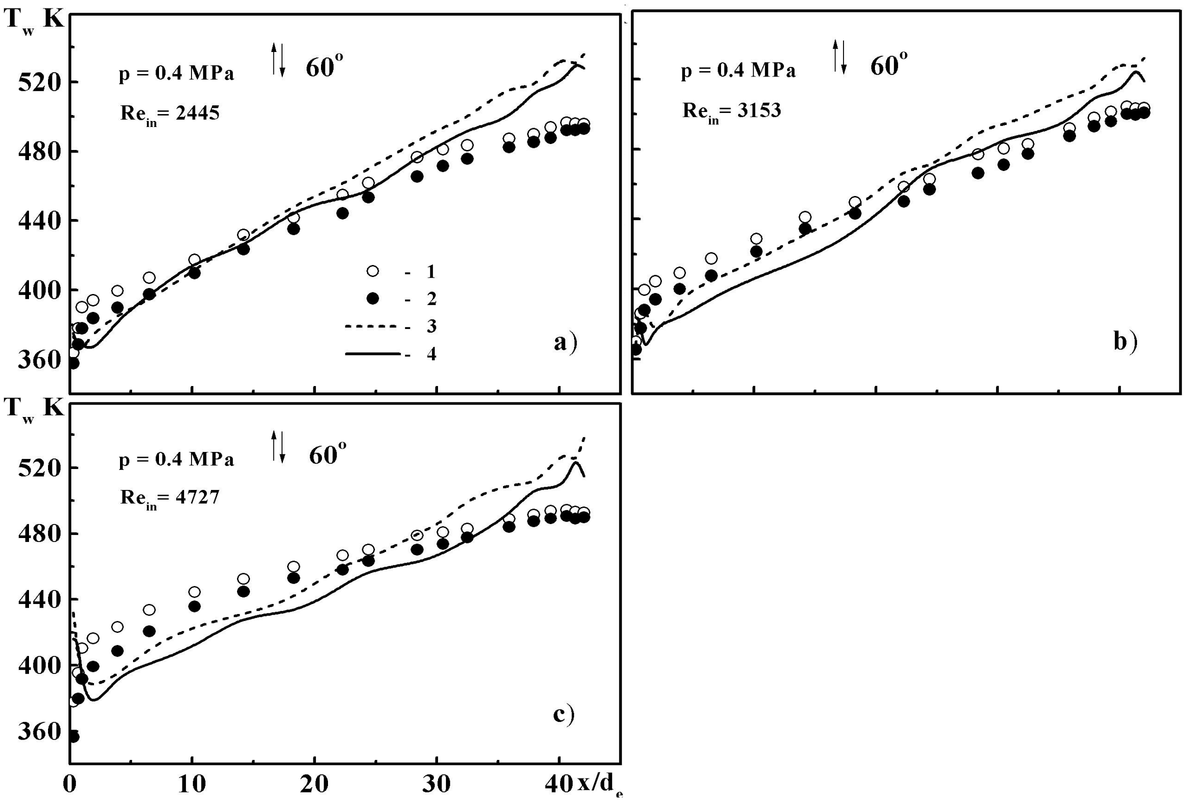

Fig. 5. Variation of averaged wall temperature along the channel. a) Re_{in} = 2445; b) Re_{in} = 3153; c) Re_{in} = 4727. 1 – experimental data (upper wall); 2 – experimental data (bottom wall); 3 – numerical modelling results (upper wall); 4 – numerical modelling results (bottom wall)

Figure 6 demonstrates clear difference between intensity of heat transfer from upper (stable air density stratification) and bottom (unstable air density stratification) walls. This difference is decreasing with increasing of x/d_e, but for all x/d_e heat transfer from bottom wall is higher then from upper wall.

The correlation between numerical simulation results and experimental data isn't so good for all *Re* numbers and the difference is about 20% for stabilized region and about 30% at the beginning of heating.

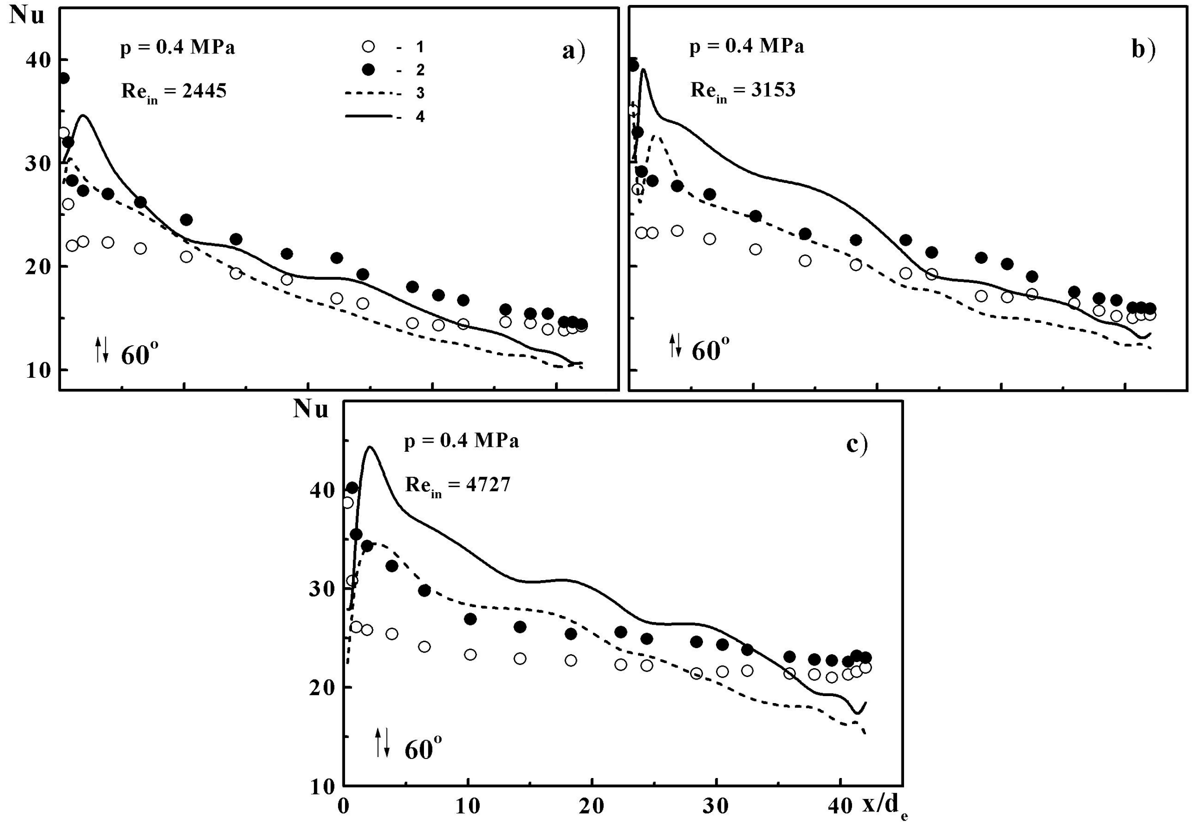

Fig. 6. Variation of heat transfer along the channel. a) Re_{in} = 2445; b) Re_{in} = 3153; c) Re_{in} = 4727. 1 – experimental data (upper wall); 2 – experimental data (bottom wall); 3 – numerical modelling results (upper wall); 4 – numerical modelling results (bottom wall)

CONCLUSIONS

Analysis of the numerical modelling data on opposing mixed convection in transition region in an inclined flat channel (inclination angle $\varphi = 60^{o}$ from horizontal position) with symmetrical heating leads to the following conclusions:

1. Modelling results demonstrate the vortex structure of the flow after its separation from the walls. Such structure of the flow causes significant variation of the wall temperature along the channel.
2. Modelling and experimental results show higher heat transfer from the bottom wall (unstable air density stratification) in comparison to upper wall (stable air density stratification) heat transfer.

REFERENCES

1. B.S. Petukhov, A.F. Polyakov and B.K. Strigin. Heat Transfer Investigations in Tubes Under Viscous-Gravitational Flow // Energija, Moscow, Vol. 1, 1968.
2. J.D. Jackson, M.A. Cotton and B.P. Axell. Studies of Mixed Convection in Vertical Tubes. Review // Int. J. Heat Fluid Flow, Vol. 10, No. 1, 1988, p. 2–15.
3. J.D. Jackson. Influences of Buoyancy on Velocity, Turbulence and Heat Transfer in Ascending and Descending Flows in Vertical Passages // Proceedings of 4th Baltic Heat Transfer Conference. Advances in Heat Transfer Engineering, Kaunas, Lithuania, August 25–27, 2003, p. 57–78.

4. J. Vilemas, P. Poškas. and V. Kaupas. Local Heat Transfer in a Vertical Gas-Cooled Tube with Turbulent Mixed Convection and Different Heat Fluxes // Int. J. Heat Mass Transfer, Vol. 35, No. 10, 1992, p. 2421–2428.
5. J. Vilemas and P. Poškas. Effect of body forces on turbulent heat transfer in channels // LEI-Bigell House, Kaunas-New York, 1999.
6. P. Poškas and R. Poškas. Turbulent Opposing Mixed Convection Heat Transfer in a Vertical Flat Channel with One Side Heating // Int. J. Heat Transfer Engineering, Vol. 25, No. 2, 2004, p. 17–23.
7. P. Poškas and R. Poškas. Local Turbulent Opposing Mixed Convection Heat Transfer in Inclined Flat Channel for Stably Stratified Airflow // Int. J. Heat and Mass Transfer, Vol. 46, No. 21, 2003, p. 4023–4032.
8. P. Poškas, R. Poškas and D. Sabanskis. Local Turbulent Opposing Mixed Convection Heat Transfer in Inclined Flat Channel for Unstably Stratified Airflow // Int. J. Heat and Mass Transfer, Vol. 48, No. 5, 2005, p. 956–964.
9. P. Poškas, R. Poškas and D. Sabanskis. Comparison of the Turbulent Opposing Mixed Convection Heat Transfer in Inclined Flat Channel for Stably and Unstably Stratified Airflows // Proceedings of 6th World Conference Experimental Heat Transfer, Fluid Mechanics, and Thermodynamics, Matsushima, Miyagi, Japan, April 17–21, 2005 (Published on CD-ROM).
10. G.F. Scheele, E.M. Rosen and T.J. Hanratty. Effects of Natural Convection on Transition to Turbulence in Vertical Pipes // Can. J. Chem. Eng, Vol. 38, 1960, p. 67-73.
11. G.F. Scheele and T.J. Hanratty. Effects of Natural Convection Instabilities on Rates of Heat Transfer at Low Reynolds Numbers // AIChE J., Vol. 9, No. 2, 1963, p. 183–185.
12. B.S. Petukhov, A.F. Polyakov and B.K. Strigin. Heat Transfer Investigations in Tubes Under Viscous-Gravitational Flow // Energija, Moscow, Vol. 1, 1968.
13. P. Poškas, R. Poškas and A. Sirvydas. Modelling of the Opposing Mixed Convection Heat Transfer in a Vertical Flat Channel in the Regions of a Laminar and Vortex Flow // Proceedings of 4th. Int. Heat Transfer Conference, Fluid Mechanics and Thermodynamics, Cairo, Egypt, September 19–22, 2005 (Published on CD-ROM).
14. P. Poškas, R. Poškas and A. Sirvydas. Opposing Mixed Convection Heat Transfer in the Vertical Flat Channel in a Laminar-Turbulent Transition Region // Proceedings of 13th. Int. Heat Transfer Conference, Sydney, Australia, August 13–18, 2006 (Published on CD-ROM).
15. P. Poškas, R. Poškas and A. Sirvydas. Opposing Mixed Convection Heat Transfer in the Vertical Flat Channel in a Laminar-Turbulent Transition Region Under Prevailing Effect of Buoyancy // Proceedings of 5th European Thermal-Sciences Conference, Eindhoven, the Netherlands, May 18–22, 2008 (Published on CD-ROM).
16. P. Poškas, R. Poškas. Mixed Convection in the Channel Flows, Heat Transfer Research // Vol. 40, No. 1, 2009, p. 31–56.
17. Fluent, Inc., 2005. FLUENT User's Guide.
18. A. Sirvydas, R. Poškas. Numerical Investigations of Opposing Mixed Convection Heat Transfer in Vertical Flat Channel // 2. Vortex Flow in Case of Symmetrical Heating, Power Engineering, No. 1, 2006, p. 9–15.
19. R. Poškas, P. Poškas and G. Drumstas. Opposing Mixed Convection Heat Transfer in an Inclined Flat Channel in a Laminar-Turbulent Transition Region // Proceedings of 7th World Conference on Experimental Heat Transfer, Fluid Mechanics and Thermodynamics, Krakow, Poland, June 28–July 3, 2009 (presented for publication).

NOMENCLATURE

b	channel width (m)
c_p	specific heat (J/(kg K))
d_e	equivalent diameter of the channel $[d_e = 2hb/(h+b)]$(m)
Gr_q	Grashof number defined by the heat flux specified on the surface $[Gr_q = g\cdot\beta\cdot d_e^4\cdot q_w/\nu^2\cdot\lambda]$
g	acceleration due to gravity (m/s^2)
h	channel height (m)
i	enthalpy (J/kg)
p	pressure (Pa)
q	heat flux density (W/m^2)
Re	Reynolds number $[Re = ud_e/\nu]$
T	temperature (K)
u	local flow velocity (m/s)
x	axial coordinate measured from start of heating (m)
y	transverse coordinate

Special characters

α	heat transfer coefficient $[\alpha = q_w/(T_w - T_f)]$ (W/(m^2 K))
β	volumetric expansion coefficient (1/K)
φ	inclination angle (degree)
λ	thermal conductivity (W/(m K))
ν	kinematics viscosity (m^2/s)
μ	dynamic viscosity (Pa s)
ρ	density (kg/m^3)

Subscripts

in	at the inlet
f	in the flow
w	at the wall
x	axial coordinate
y	transverse coordinate
1	first wall
2	second wall

CYSENI 2009, May 28-29, Kaunas, Lithuania
ISSN 1822-7554, www.cyseni.com

MODELING OF TURBULENT VORTEX FLOW IN A CHANNEL

I.M. Kuzmenko, D.V. Panasyuk
NTUU "Kyiv Politechnic Institute"
Politekhnichna str. 6, 03056 – Ukraine
Phone: +038 0683757943
E-mail: kin@aprodos.ntu-kpi.kiev.ua

ABSTRACT

The parameters of turbulent flow in a tube are experimentally and mathematically analyzed. Experimental stand is described, experiment performance methodic is elaborated, the results are obtained. The mathematic vortex flow model, which based upon vortex flow physics snapshot, is suggested. The model verification based on experimental data is conducted. The work allows us to take into account the influence of vortex structures in a flow upon energy transfer in heat engineering.

Keywords: turbulence, vortex, channel, experiment, viscosity, velocity, imitating, model

1. INTRODUCTION

The processes of energy transfer in the form of heat and mass are widely spread in engineering. In particular, in devices of chemistry, oil-processing, energetic field for gases desorption, rectification, cooling, humidification, etc. Their calculation methodics is frequently built upon experimental study of heat and mass-exchange, dynamic operating mode of such devices. Specifically, along with the transfer to turbulent mode vortexes are formed, which change velocities' epure and lead to redistribution of energy flow. This, in its turn, affects energy transfer in the form of heat and mass. Mathematically it is expressed in the following way. The equation of energy transfer takes into account vortex pulsations through a^m - temperature conductivity coefficient, which accounts turbulent (vortex) pulsations.

$$\frac{D\overline{T}}{Dt} = a\,div\left[\left(1+\frac{\varepsilon_q}{a}\right)grad\overline{T}\right], \text{ where } \overline{T} = \frac{1}{t_0}\int_0^{t_0} T dt. \quad (1)$$

Similar coefficient is present in the calculation of processes in the air or gas and even in mass transfer calculation.

Thus, the task to study the parameters of vortex (turbulent) flow and coefficients mathematic definition is of necessity.

However, all the models from the simplest one to contemporary have one essential drawback. They are not closed [1–2]. All turbulence models present a system with a greater number of unknowns than equations.

In relation to this, the aim of the work is to define local pressures and evaluate local velocities and turbulent exchange coefficient. Further, on, vortex flow static mathematic model is suggested and imitating modeling of velocities' field depending on basic parameters is carried out. So it paper describe next tasks:

1) experimental stand with sensor to evaluate dynamic pressure local values has been mounted;
2) experimental results processing methodics has been elaborated;

3) turbulent longitudinal velocity have been determined;
4) the model of vortex flow in tube has been formulated using Monte-Carlo method [3–5];
5) on the basis of experimental results mathematic model has been verified.

This will allow us to estimate and take into consideration the contribution of flow's vortex (turbulent) energy in the energy transfer in the form of heat and mass in calculations.

2. EXPERIMENT'S METHODICS

According to the study tasks, experimental stand, shown on Fig. 1, is developed and created. The main element of this stand is the working area with high-precision sensor of full pressure, photo of which can be seen on Fig. 2. The receiver of full pressure is metallic needle ∅0.8/0.7 mm connected to micro manometer with the reclined tube MMH. On the other input of micro manometer static pressure from the working area is delivered through the tube ∅2.5. The working material in the installation is the air, which is delivered by electric compressor (not shown on Fig. 2) into the working area through turbulence creating grid. The distance from the grid to the place of measurement constitutes around 10 diameters. This and the significant velocity of the flow, which corresponds to the value of Reynolds Figure $\mathrm{Re} = 2Ur/\nu = 2\cdot 25\cdot 1,5\cdot 10^{-2}/15\cdot 10^{-6} = 5\cdot 10^{4}$, allows approaching air motion mode as turbulent.

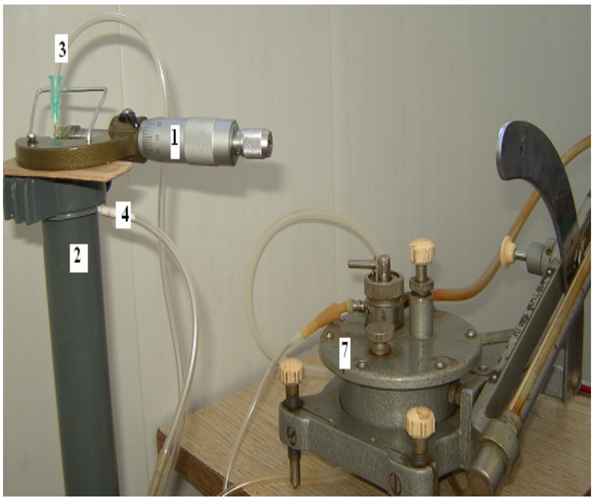

Fig. 1. Experimental stand (1 – portable sensor, 2 – working area, 3, 4 – full and static pressure measurement, 5 – micro manometer)

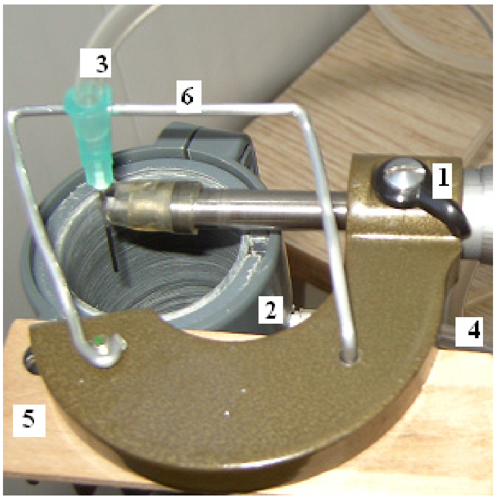

Fig. 2. Portable full pressure measuring sensor (1 – micrometer 0.01–25 mm, 2 – working area, 3 – sensor needle, 4 – static pressure sensor, 5 – sensor fixation, 6 – guide way frame)

Full pressure sensor's needle is perpendicularly soldered to the roller, placed on he micro manometer gudgeon's edge. Its movement consists in rotation of micro meter's head with the step that is, for example, 0.5 mm-topple. Thanks to this rotating movement of micro meter's head is transformed into the translational movement of the needle. Sensor fixation and guide way frame provide free and targeted needle's movement in vertical position only along the defined working area's parameter.

2.1 Methodic of Experiment running

Before running the main studies' series, a series of test studies were conducted: measurement devices were adjusted and the boundaries of mode parameters changes were specified. Drawbacks detected in the course of testing were removed.

The adjustment of measurement devices included pressure sensor graduation. For this, by means of micrometer rotation sensor needle was set in extreme position, close against the working area wall. Then the compressor was started and according to micro manometer data the dynamic pressure measurement was conducted. Sensor translational movement along the working area diameter allowed to evaluate maximum dynamic pressure and, consequently, maximum velocity. As far as maximum velocity corresponds to the centre of the working area, pressure sensor step was verified and adjusted. To reach working mode the stand was warmed up during 10–15 minutes.

During the running of experiments, the following was evaluated:

- sensor needle placement in relation to the centre of the working area according to micrometer data where the division value is 0.01 mm;
- dynamic pressure value with the help of micro manometer with reclined scale of MMH. The measurement was conducted with reclining coefficient being k = 0.3 – that is, one graduation of MMH corresponded to 0.3 mm of water column (3 Pa);

2.2 Methodics of Results processing

The velocity of flow was defined by means of Bernuli equation based on measured pressure value p on the working area [6]:

$$p_{st} + g \cdot \Delta z \cdot \rho + \frac{\rho \cdot u^2}{2} = const = p\,. \tag{2}$$

Where ρ – density of air, $p = p_{st} + p_{dyn}$ – full pressure, as a sum dynamic and static ones. Proceeding from the data that $\Delta z = 0$, from (2) local flow velocity was deducted:

$$u = \sqrt{\frac{2 \cdot (p - p_{st})}{\rho}}$$

2.3 Experimental uncertainties

2.3.1. Relative inaccuracy of distance measurement

Absolute inaccuracy of distance measurement is defined by the precision of micrometer and constitutes one graduation of scale ΔH =0.01 mm. Minimum distance value measured is the distance to the centre in the flow core, i.e. H =2 mm. In such a way, $\delta H = 100 \cdot 0.01/2 = 0.5\%$.

2.3.2. Relative inaccuracy of velocity measurement

Absolute inaccuracy of dynamic pressure evaluation is defined by MMH accuracy and constitutes 0.5 mm of water column. Minimum dynamic pressure value is p=66 mm of water column (к=0.3). As far as the density was defined with the help of tables, absolute inaccuracy does not exceed $\delta\rho = 0.01\%$. In studies air density makes 1.15 kg/m^3, that is

$$\delta U = 100\sqrt{\sum\left(\frac{\partial \ln f}{\partial x_i}\Delta x_i\right)^2} = 100\sqrt{\left(\frac{\Delta p}{p}\right)^2 + \left(\frac{\Delta \rho}{\rho}\right)^2} = 100\sqrt{\left(\frac{0,5}{65}\right)^2 + \left(\frac{0,01}{1,15}\right)^2} = 1,2$$

3. RESULTS AND DISCUSSION

Fig. 3 is a plot of dependence of turbulent flow velocity upon transverse coordinate. Basing upon the data provided by Fig. 3 the methodics of dynamic pressure sensor adjustment within the boundaries of movement limits comes to light.

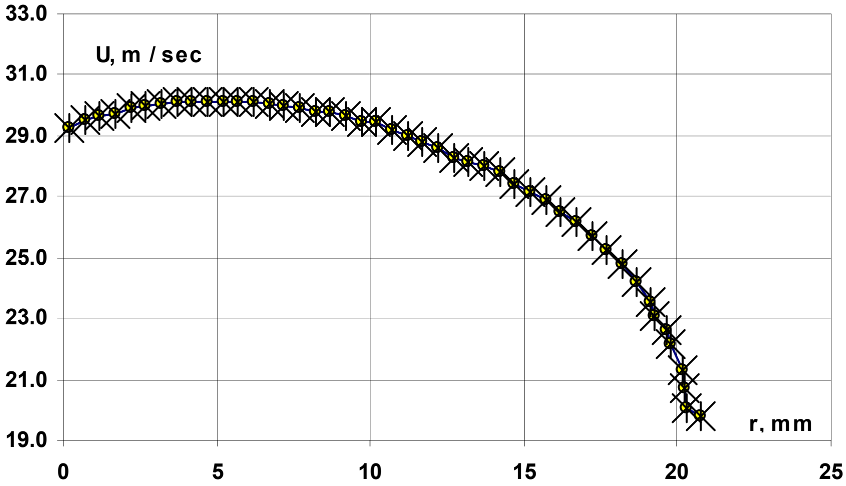

Fig. 3. Dependence of turbulent flow velocity upon distance

In accordance with [1], velocity increase in the centre is preconditioned by the augmentation of pulsation constituent of vortexes (of each one separately and of all of them taken together), which exist in turbulent flow. These results compared with Nikuradse's data [6] to verify the model. The deviation of results does not exceed 7% (except boundary layer) that demonstrates the reliability of the results.

4. MATHEMATIC MODEL DESCRIPTION

For the model formation let us assume that the flow is moving in round tube (fig. 4). Let us write down the equation of movement in cylindrical coordinates

$$(\frac{\partial}{\partial \tau} + U\cdot\frac{\partial}{\partial z} + U\cdot\frac{\partial}{\partial r})U = g - \frac{1}{\rho}\cdot\frac{\partial p}{\partial z} + \nu\cdot(\frac{\partial^2 U}{\partial r^2} + \frac{1}{r}\cdot\frac{\partial U}{\partial r})$$

Let us assume the following:

- we consider velocity U in the direction of z – axis to be dominating in comparison with velocities in other directions. Thus we do not take into account flow velocity in the direction of other coordinates $U_r \to 0$,
- we consider flow movement in the direction of z invariable, i.e. $\frac{\partial U}{\partial z} \to 0$,
- we neglect mass force because of its smallness $g = mg = \rho dF / dzg$. Thus, we receive

$$\left(\frac{\partial}{\partial\tau}+U\cdot\frac{\partial}{\partial z}\right)U=-\frac{1}{\rho}\cdot\frac{\partial p}{\partial z}+\nu\cdot\left(\frac{\partial^2 U}{\partial r^2}+\frac{1}{r}\cdot\frac{\partial U}{\partial r}\right) \tag{4}$$

Let's assume that pressure in the flow is not stationary and its fluctuation is described by a Monte-Carlo method of statistical experiments:

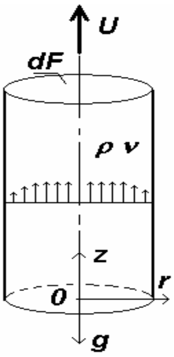

Fig. 4. Velocities profile in round tube cut

$$\frac{\partial p}{\partial z}=const+k\frac{\rho U^2}{2}\sin(c\pi\tau),$$

where c – random numbers, $\frac{\rho U^2}{2}$ – flow kinetic energy, τ – time, $const$ – flow motive force as pressure drop at the input–output. As far as we set flow speed at the input then $const=0$.

Thus we deduce that the flow pressure pulsation amplitude is preconditioned by its kinetic energy. On the basis of experimental research the proportionality factor value is set as $k=-0.2$; random numbers shape local pulsation in vortexes and the pulsations' frequency is increasing with time.

Equations (4) and (5) were solved with initial data being the following - the flow speed change at the initial moment is absent $(\partial U/\partial\tau)_{\tau=0}=0$ and the boundary conditions are:

1) the speed at the centre of the tube is set maximum, when $(\partial U/\partial r)_{r=0}=0$;

2) the vortex flow speed in the boundary layer near the wall is defined by a variable value $U=0{,}6\cdot U|_{r=0}+\cos(c\pi\tau)$, where first summand indicates 40% decrease of the speed in the boundary layer near the wall compared to one in the centre of the flow. This assumption is based on experimental studies [4]. The second summand indicates pulsation presence within the limits of boundary layer. For numerical solution of the problem, we use resulting difference method. For that we input uniform rectangular grid with the steps Δr and $\Delta\tau$ in directions r, τ. Having substituted fractional derivative, let us write down the equation in algebraic form and using the explicit method we shall receive formula for function values calculation.

5. MATHEMATIC MODEL VERIFICATION

In order to verify the model let us define the influence of tube's radius local value r and modeling time on vortex flow velocities' distribution $U=f(r,t)$ with different grid step.

In order to define on the radius the influence of the step we model the air vortex flow ($\nu=15\ 10^{-6}$ м^2/с ρ=1.15 kg/m^3) in tube of radius R = 0.015 m, and modeling time does not exceed t = 0.5 s, and initial velocity constitutes $U|_{t=0}=31$ m/s. That is, we conduct mathematic modeling of the experiment.

As a result, we receive two-dimensional matrixes of velocities distribution in the channel. To analyze the stability of the solution received, let us analyze the influence of the grid step on the received velocities distribution.

Further let us define the value of velocity increase with the change of radius in different moments of time $t = 0.46\ldots0.5$ sec with an interval being 0.01 sec., i. e.

$$\frac{\Delta U}{\Delta R} = \left| \frac{U_{R=7.5} - U_{R=3.75}}{7.5 - 3.75} \right| .$$

As shown on Fig. 5, the decrease of division step to 0.278 mm or 64 points, as shown in Table 1, is a sufficient condition for the received solution to be stable.

Table 1. Amount of division points and step of grid.

Amount of points, N	8	16	32	64	128	256
Step of grid, $\Delta R = R/(N-1)$	2.143	1	0.484	0.278	0.118	0.059

Thus, we conduct further modeling with the step that is not less than 0.278 mm. In reality the step of grid was 0.1 mm.

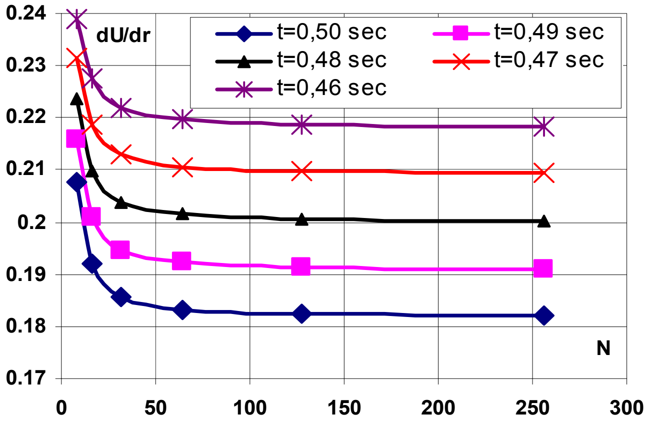

Fig. 5. The evaluation of received decision accuracy as the relation of velocity's fluctuation to transversal coordinate's motion depending on the number of points in different moments of time (after 0.46–0.5 sec)

Mathematic modeling results' processing were realized through the following methodics.

The average experimental velocity that was shown in Fig. 3 was compared with mathematic modeling results' processing was realized through the following methodics. The average velocity

$$U_{sr} = \frac{1}{t}\int_0^t U_r dt = \frac{\sum_1^N U_r}{N} ,$$

where U_r stands for local velocity at a certain moment of time with invariable radius value and N for a number of time points at which the value is fixed.

Fig. 6 shows velocity value in the channel on the basis of experimental studies and calculated from the model. It can be seen that the main discrepancy (up to 20% with r = 0.003 m) between data exists in wall-adjacent area.

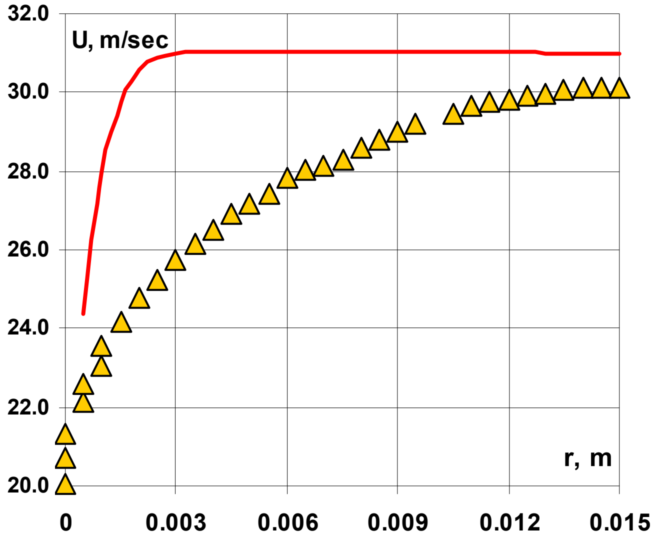

Fig. 6. The comparison of average velocity values of experimentally obtained (point) and calculated (line).

The discrepancy between measured and calculated values relay on a structure of the flow stream. It changes under the influence of friction force. Therefore, discrepancy at Fig. 6 is explaining in next way. Measured value obtained at stabilized turbulent flow, and calculated value – at the initial segment of the flow.

CONCLUSIONS

As the result of the work, the experimental stand was mounted, the sensor of which is moved by micrometer screw across the flow and defined dynamic pressure local value. Methodics of study results processing was elaborated.

Suggested mathematic model adequately reflects local velocities distribution in the centre of the vortex flow, which is confirmed by experimental study.

Given work allows further consideration of flow's vortex structure influence upon energy transfer in the form of heat and mass.

REFERENCES

1. I.A. Belov, S.A. Isaev „Modeling of turbulent flows" – Saint-Petersburg. Baltic State University publishing house, 2001. – p. 108.
2. P.G. Frick „Turbulence: models and approaches", course of lectures - Perm: Perm State Technical University, 1999 – p. 132.
3. Kuzmenko I.N., Nogin N.V., Molodid A.K., Smakovsky D.S. „Modeling of turbulent flow by means of statistic nests"/ works of Eastern-Ukrainian University of Dahl № 2, 2007 – p. 45–51.
4. Y.N. Denisov, V. S. Slobodyanjuk "Monte-Carlo Study of turbulence structure" / Vestnik KRSU , № 2, 2002. – p. 35–41.
5. R.J. Fateman Symbolic computation of turbulence and energy dissipation in the Taylor model// Int J Modern Physics 1998, Vol. 9, No 3, p. 509–525.
6. Dr. Hermann Schlichting "Grenzschicht-Theorie" – Verlag G. Braun. Karlsruhe, 1973 – 713 p.

CASE STUDY OF VENTILATION SYSTEM DEVELOPMENT OF ARCHIVE PREMISES

A. Krūmiņš, U. Pelīte, E. Dzelzītis, A. Lešinskis, A. Brahmanis
Riga Technical University, Latvia
Institute of Heat, Gas and Water Technology
Riga Technical University
Āzenes 16-20, LV 1010, Rīga, Latvia
Phone: +371 29178589
E-mail: andrisk@lafivents.lv

ABSTRACT

This paper describes the ventilation, the air conditioning and its control system's development for the archive premises in Riga, Latvia. The archive premises are located in two floors, one of them is in the basement. The ventilation and the air-conditioning system in the archive premises is developed according to the standard DIN 1946/4. The air handling unit's technical data, energy consumption, and sequence of operation and control systems development is analysed according to the average meteorological year of Latvia. The main objective for the HVAC and control designers was to maintain 18°C of indoor temperature and 50% of indoor air humidity all year round using two air handling units in sequence.

The results of the achieved climate are analysed with the trendlogs, which are saved by the control system. Paper results can be used for ventilation and air conditioning development for other archive premises.

Keywords: ventilation, simulation, Simulink, BACnet, archive, humidity, control

1. INTRODUCTION

The owner of the building, one of Ministry`s of the Republic of Latvia, renovated the archive premises in 2006. In a year of operation it was noticed that it is impossible to maintain the necessary climate in the archive premises with the existing ventilation system solution. The specialists of Riga Technical University were invited to expertise the ventilation system and give a solution for system improvement. After visiting the building site (Fig.1) it was stated that the temperature and the humidity of the room was not within the range of recommended for archive premises – 18ºC and 50% RH [6], but closer to the office environment – 21ºC with a very high room humidity dependency from the outside air humidity (Fig. 2).

2. RECOMMENDATIONS FOR MICROCLIMATE IN ARCHIVES

Most of artifacts and documents last for centuries longer if the humidity stays between 30 and 60% rh, and if that humidity swings gradually between those extremes over a period of weeks rather than over a period of minutes or hours.

Moisture content in documents steadily rises rather than returning to dry levels.

Air pressures must be maintained so that the humid air does not enter the wall cavities. That requires the maintaining of positive internal pressure in the humid season and a neutral pressure during the cold weather.

Indoor air CO_2 level based ventilation control is recommended [2, 5, 7].

Fig. 1. Archive room with movable bookshelves

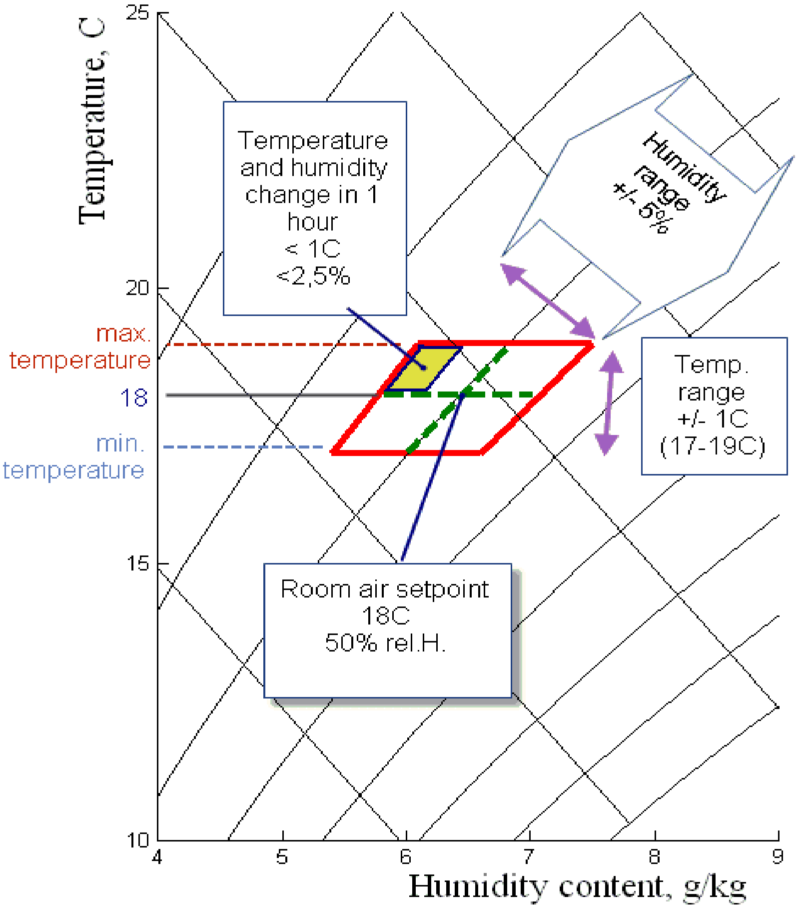

Fig. 2 Indoor air microclimate target zone of archive premises

The previous ventilation system consisted of the air handling unit No 1 (Fig. 5) and the air dehumidifiers which were installed in the archive premises. The air was distributed equally between the first floor of the archive and the basement floor. The hypothesis of the study is the following: if an archive has two different loads in zones it is impossible to reach the necessary climate without a centralised regulation of the air volume between zones. Dehumidification shall be done centrally. Only the optimal control strategy gives a possibility to reach comfort in both archive floors. We made a decision to uninstall the local dehumidifiers, to add an AHU2 and variable air volume boxes to the ventilation system and rebuild the whole climate control system.

The objective is to develop a ventilation system and its control strategy for two air handling units serving two different load zones at the same time.

3. CLIMATE IN LATVIA

Latvia is located in the moderate climatic zone. Its temperature, moist climate is caused by the Atlantic air masses, influenced by the Baltic Sea and the gulf of Riga. The outside air very rarely corresponds to the necessary supply of air parameters (Fig. 3). The rest of the time the air should be heated and humidified/dehumidified to achieve the necessary air temperature and humidity in the archive premises [3].

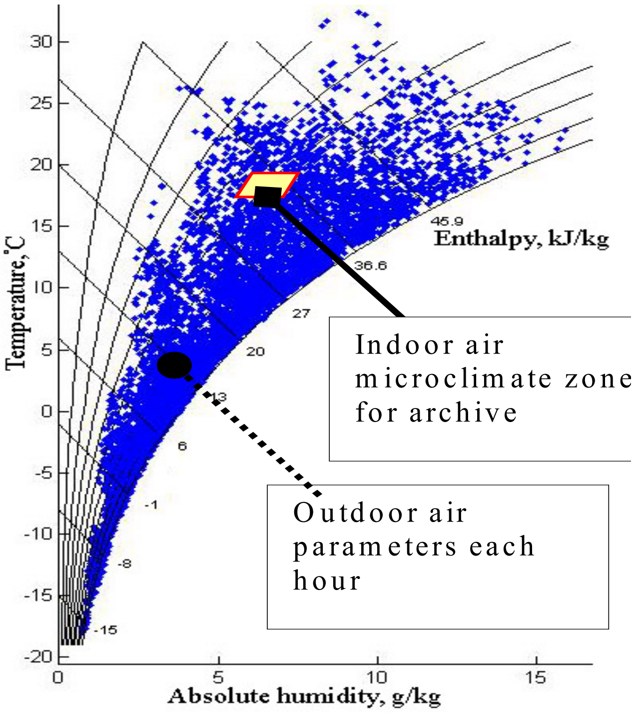

Fig. 3. Average Latvian meteorological year

4. METHODS

The research is done with a analytical decision for optimal climate achievement in archive premises. We had an opportunity to rebuild the existing ventilation and control system of the archive premises. The control system saves the trendlogs of the ventilation system work conditions and the achieved temperature and humidity in premises. The trendlogs were saved as csv format files. Using Matlab Excel link results were imported in Matlab as mat format files. Regulation parameters of air handling units were analysed and corrected with Simulink simulation software [4].

5. DIVIDING THE ROOM INTO TWO ZONES

Both floors have the same area ~100 m², the entrance is located on the first floor. There is no an operable window near the staircase. The entrance door is well sealed with rubber strips. In the case of fire emergency, at first, a gas distinguishing system will start to work, and then,- a separate exhaust system will start to remove the gas from the room.

The structure of the building contains ~600 mm thick brick walls with painted plaster. The basement ceiling is under the ground level. The outside climate impact is very low and with a low speed, according the big mass of the room enclosure.

Documents will be stored in the movable racks and the space from the racks to the ceiling will be 20 cm, therefore the air volume in the room is small in comparison with the room volume, see picture 1.

Both floors have to supply the same room air microclimate parameters, maintained by one air conditioning equipment, using the existing air ducts as it is impossible to rebuild the air duct system from the technical room to the archive premises.

The total recirculated air exchange can be reached from 2.5–5 times per hour, or 10 times in one separate floor. The outside air exchange is constant at 0.5 times per hour.

6. AIR DISTRIBUTION

The common air distribution is organized in the following way (Fig. 4):

- Basement - the air supply provided trough the air ducts under the ceiling equally distributed in 3 rows along the room. Exhaust is placed in one corner, near the main duct entrance in the room;
- Floor I – the same way as in the basement, but some amount of the air can flow freely via the staircases' opening from the basement.

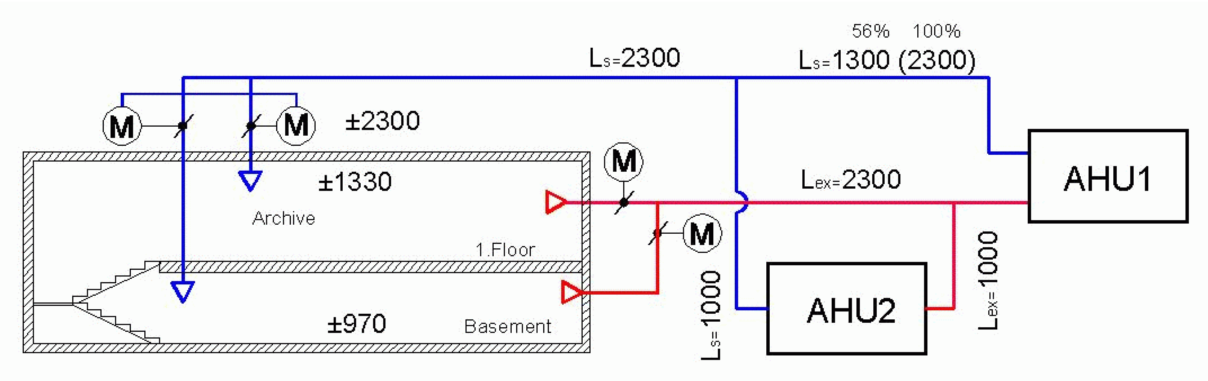

Fig. 4. Archive section

7. AIR HANDLING UNITS

Two air handling units were installed, each of them has separate functions. The air handling unit for function I consists of the following main elements (Fig. 5):

- Supply air water heating coil – to heat the supply air to the room temperature;
- Steam humidifier in air duct – to rise the supply air humidity without changing the air temperature;
- Recirculation section;
- Supply air water cooling coil – to cool the supply air to the room temperature;
- Supply and exhaust fans.

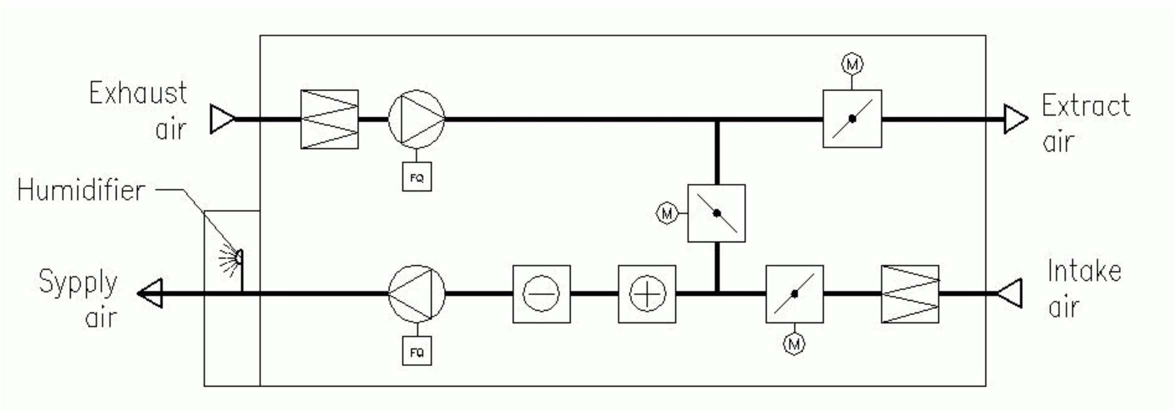

Fig. 5. Air handling unit 1 functional scheme

Air handling unit for function II consists of the following main elements (Fig.6):

- Centralised cooling coil – to lower the supply air temperature to the setpoint;
- Plate heat exchanger for heat recovery from recirculation air at dehumidification process;
- Dehumidification with compressor evaporator and condenser – to lover the supply air humidity to setpoint;
- Supply fan.

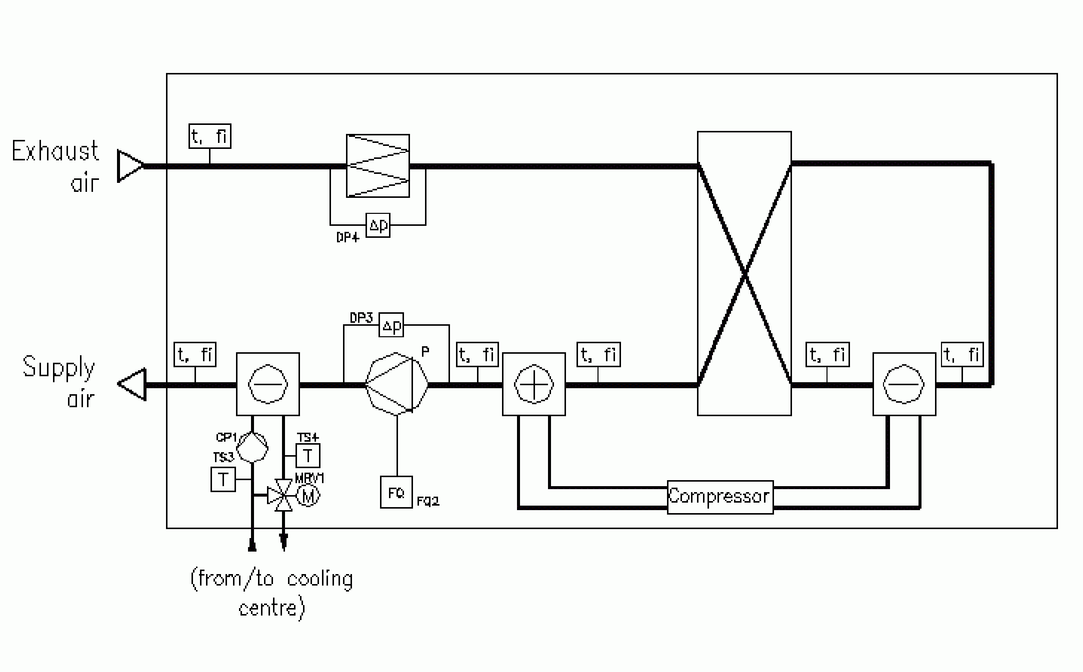

Fig. 6. Air handling unit 2 functional scheme

8. LOAD CALCULATIONS

The transmission heat losses depending of outdoor air temperature, are calculated using the equation:

$$Q = \frac{A}{R}(T_{in} - T_{out}), \tag{1}$$

where Q – heat losses, W, A – construction area, m², R – construction thermal resistance, W/ m²/K, T_{in} – indoor air temperature, °C, T_{out} – outdoor air temperature, °C [1].

The heat energy needed to warm fresh and recirculation air:

$$q = m_{da}(h_2 - h_1) \, . \tag{2}$$

Where h1 and h2 – before and after coils air enthalpies [3].

The quantity of the outdoor air, kg/h that is necessary for the room air humidification/dehumidification:

$$\Sigma m_w = m_{da}(x_2 - x_1) \, , \tag{3}$$

where: Σm_w the total of all moisture loads on the space arising from transfers through boundaries and from human, m_{da} – air mass kg/s, x_2 – exhaust air absolute humidity g/kg, x_1 – supply air humidity g/kg.

Both air handling units should work together in order to maintain the necessary microclimate. The second air handling unit works only for the dehumidification by constant supply air temperature after the dehumidification process.

Dehumidification power of AHU2:

$$\Sigma m_{wAHU1} = m_{da}(x_2 - x_1) \, , \tag{4}$$

where m_{da} – Air handling unit nr.2 air mass kg/s, x_1 – Air handling unit nr.2 supply air absolute humidity.

The necessary humidity setpoint of Air handling unit Nr.1:

$$x_1 = x_2 - \frac{\Sigma m_w - \Sigma m_{wAHU1}}{m_{daAHU2}} \, . \tag{5}$$

The necessary air handling unit parameters where chosen according the formulas given above.

9. AIR HANDLING UNIT PARAMETERS FOR CALCULATIONS

Air handling units parameters are shown in Table 1.

Table 1. Air handling unit parameters

Description	**AHU I**	**AHU II**
Electrical power of supply / exhaust fans, kW	0.35	0.37/0.37
Electrical power of compressor, kW	0.6	–
Total pressure supply / exhaust fans, Pa	564	300/300
Air flow of supply / exhaust fans, m^3/h	1000/1000	1300/1300
Temperature / humidity efficiency of heat exchanger	0.6	0.6
Nominal heating power of heat pump, kW	2.52	–
Nominal heating power of water heating coil, kW	–	13
Nominal cooling power of DX cooling coil, kW	3.48	–
Nominal cooling power of water cooling coil, kW	4.10	7.7

10. MEASUREMENTS

Fig. 7 and Fig. 8 show the temperature and the humidity measurements in the archive premises after the renovation of the ventilation system according to our requirements in winter time. It was noticed that we should pay more attention to the optimal regulation of the air handling units.

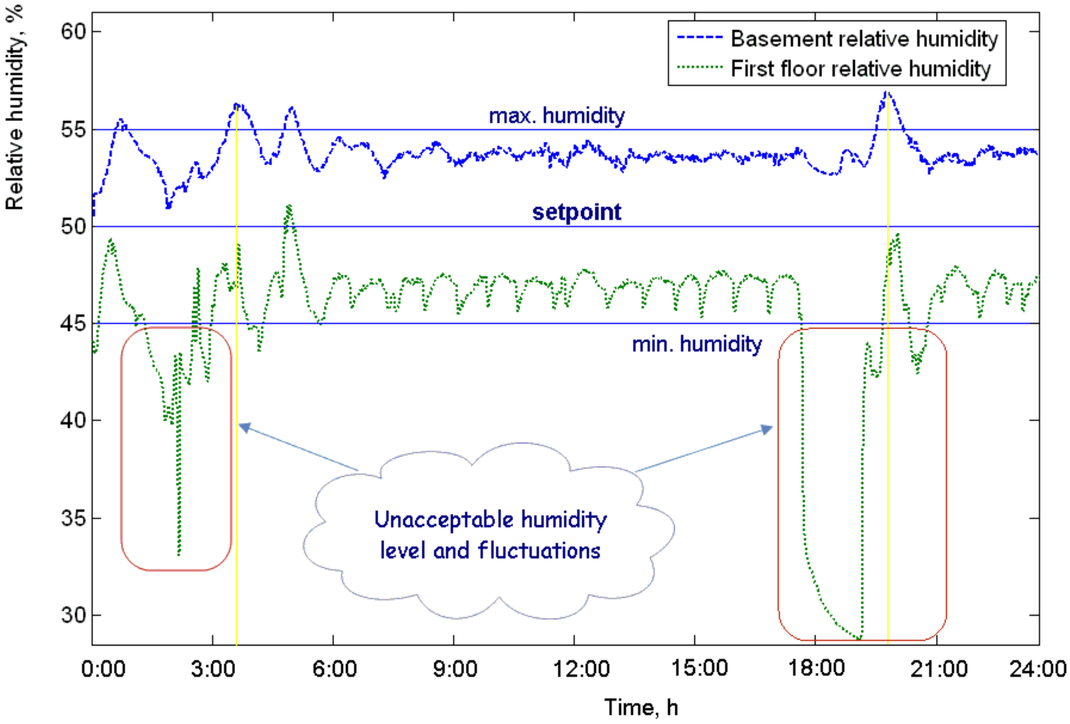

Fig. 7. RH level trendlogs

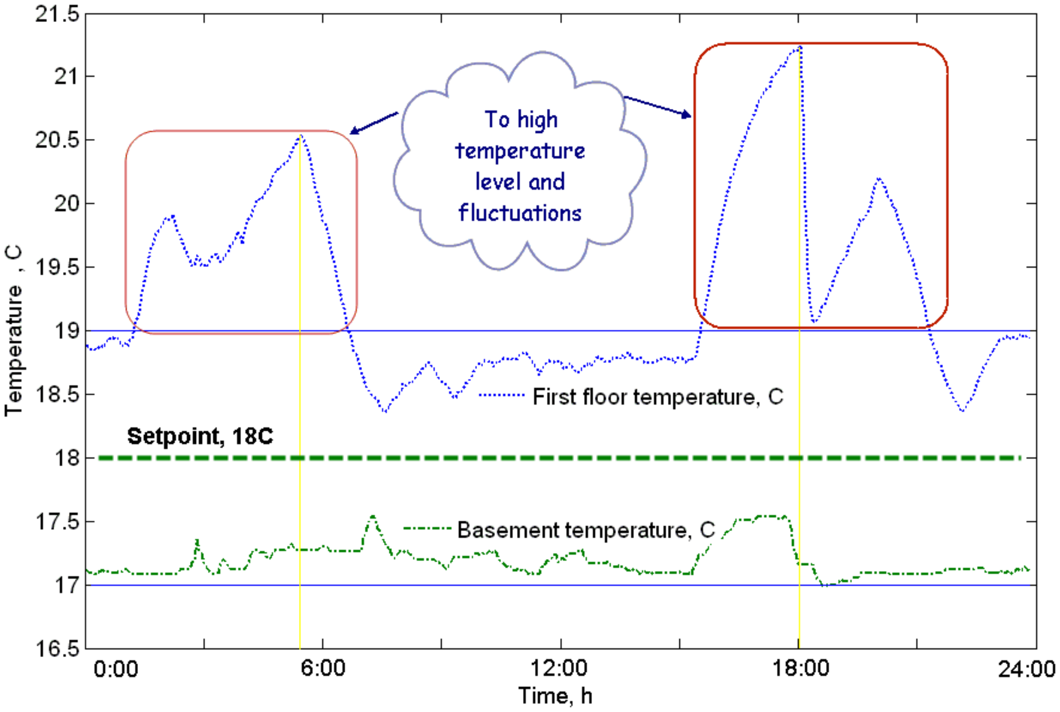

Fig. 8. Air temperature trendlogs

11. OPTIMAL CONTROL STRATEGY

The air handling unit AHU1 and air handling unit AHU2 should work with common control strategy. Several factors were taken into account for the development of the control system:

a) AHU2 is equipped with a factory installed control system and provided with BACnet communication module over Ethernet network. BACnet communication module transfers AHU2 data points to BACnet language;

b) AHU1 control system is developed with freely programmable controllers. The main controller exchange data with AHU2 control system through BACnet communication standard;

c) AHU1 control system reads data from the archive premises (temperature and relative humidity). In the case of dehumidification demand, AHU1 control system turns on AHU2;

d) The necessary room temperature and relative humidity setpoint is the same for AHU1 and AHU2;

e) Visualisation software with data storing module gives an opportunity to adjust the parameters (minimum / maximum supply air parameters; regulation rates of each section) according to the temperature and humidity measurements.

During a low outside air humidity AHU2 is turned off, AHU1 is working with 100% air volume.

Table 2. Operation scenarios for AHU 1 and AHU 2

SCENARIO	**AHU 1**	**AHU 2**
Humidification / ventilation demand	on – constant air volume (100%)	Off
Dehumidification demand	on – constant air volume (50%)	On – constant air volume (100%)

The local personal was instructed to minimise the temperature and humidity loads in the archive premises (no more than 2 persons are allowed to stay in archive). The trendlogs of the air handling unit sections' behaviour and achieved parameters were uploaded in Simulink simulation software, using Matlab Excel link module [4]. The analysis of archive parameters were done along with the analysing of each air handling unit section behaviour and supply air parameters. Several assumptions where made:

a) minimum supply air temperature was restricted to 17°C;

b) maximum supply air temperature was restricted to 19.5°C;

c) regulation parameters of the air handling unit sections were minimised to achieve very slow change of feedback;

d) control of AHU2 was done according to the change of humidity content, not relative humidity;

e) the air distribution between the floors was regulated according to the temperatures and humidity parameters on each floor. The average temperature and humidity calculation is very important for the behaviour of the air handling units' control system.

The achieved temperature and humidity parameters are showed in Fig. 9 and Fig. 10.

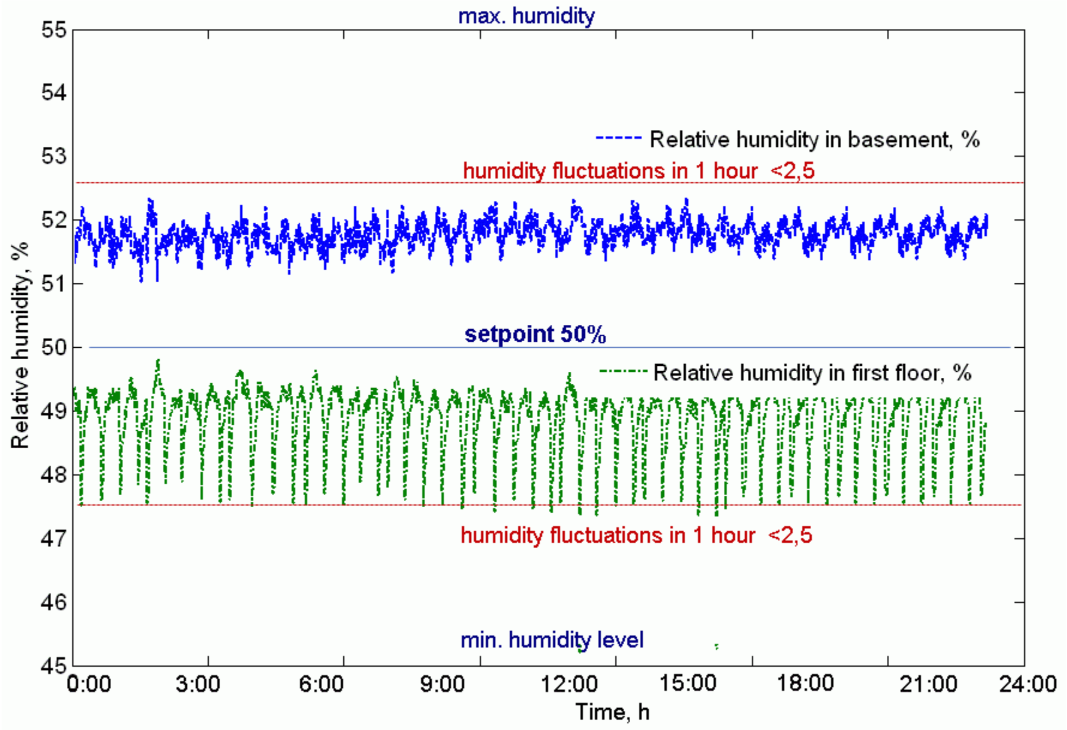

Fig. 9. RH level trendlogs after optimisation

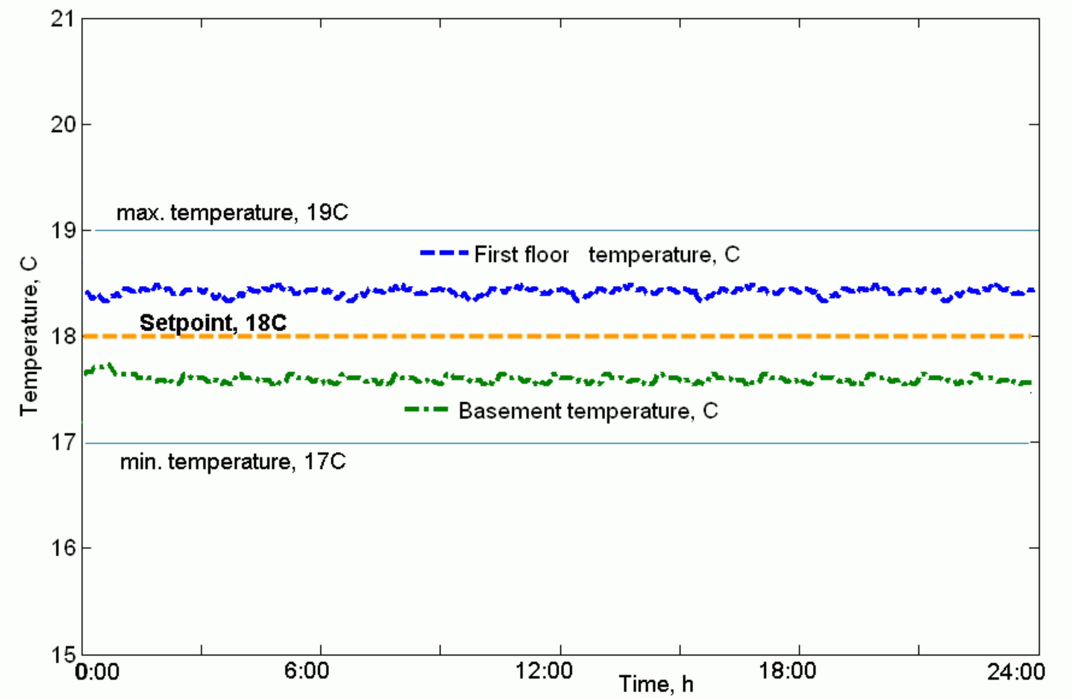

Fig. 10. Air temperature trendlogs after optimisation

12. DISCUSSION

The climate maintenance of archive premises is a very complex assignment and it requires a correct mechanical and control system's development. The optimal control strategy is very important, using 2 air handling units and variable volume valves. The found solution is optimal for the climate data of Latvia, as well as the centralised air conditioning allows to avoid a simultaneous work of the cooling/heating or humidification/dehumidification equipment.

13. CONCLUSIONS

The developed solution could be used for ventilation system development in other archive premises. We are currently working on a Simulation model the ventilation system for those archive premises to achieve the maximum energy efficiency of both air handling units. Our aim is to regulate the necessary air volume according to the requirements of loads.

14. REFERENCES

1. American Society of Heating, Refrigerating and Air-Conditioning Engineers. ASHRAE Handbook: Fundamentals. – Atlanta: ASHRAE, 1989. – 400 p.
2. Lewis G. Harriman III, G.W. Brundrett, R. Kittler. Humidity Control Design Guide For Commercial and Industrial Buildings, - Atlanta: ASHRAE, 2001. – 180 p.
3. A. Krumins. Optimization of the control of ventilation systems, doctoral thesis, Riga, 2008. – 113 p.
4. MATLAB, SIMULINK, The MathWorks, Inc., 2007
5. Recknagel E. Taschenbuch für heizung und klimatechnik einschliesslich warmwasser - und kältetechnik. - München: Oldenbourg, 2004. – 2036 p.
6. VDI 2089-1:2006-09, Technische Gebäudeausrüstung von Schwimbädern – Hallenbäder.
7. ISO 11799:2006 Information and documentation – Document storage requirements for archive and library materials.

CYSENI 2009, May 28-29, Kaunas, Lithuania
ISSN 1822-7554, www.cyseni.com

COMPARATIVE ANALYSIS OF THE EFFICIENCY OF GUIDE ELEMENTS USED FOR HEAT TRANSFER ENHANCEMENT IN AIR LAMINAR FLOW AROUND A CYLINDER

T.A. Baranova, Yu.V. Zhukova
A.V. Luikov Heat and Mass Transfer Institute
National Academy of Sciences of Belarus
P. Brovka Str. 15, Minsk, 220072 – Belarus
Phone: +375 17 2842387
E-mail: baranova@hmti.ac.by

S.A. Isaev
St. Petersburg State University of Civil Aviation
Pilotov Str. 38, 196210 – Russia
Email: Isaev3612@yandex.ru

ABSTRACT

The article presents the results on numerical simulation of air laminar flow around a heated circular cylinder equipped with guide elements. By the guide elements were understood straight and arc-shaped plates installed at an angle to the incoming flow in the rear part of the cylinder with objectives to enhance heat transfer due to the variation of the flow structure. The plates were equidistant at 0.16*d* from the cylinder surface. The length of the plates was varied from 0.05*d* to 0.5*d*. The temperature drop between the medium and the heated cylinder was 25°C. Numerical simulation was performed on a multiblock grid of a non-commercial code VP 2/3. For the verification of the model presented in this article aerodynamic characteristics and heat transfer of a single cylinder were calculated. The values obtained are in fair agreement with the available experimental data. Comparative analysis of total drag, Strouhal number, mean heat transfer, and a local Nusselt number distribution is made depending on the type of the guide elements used. It is shown that the plates with the length of 0.2-0.3*d* are considered to be optimal.

Keywords: circular cylinder, laminar flow, guide plates, Nusselt number

1. INTRODUCTION

Heat exchange facilities have found wide use in different branches of industry. As energy powers and the production volume are increasing, the mass and the overall dimensions of such facilities grow as well. The available methods of enhancing heat transfer can decrease the overall dimensions and metal consumption of heat exchange apparatus by a factor of 1.5–2 and more in comparison with the identical commercial devices with the same heat and pumping power of heat carriers. One of the promising directions in this field of research is the use of locally controlled flow separation [1, 2]. The flow separation arranged in certain bounded regions can much enhance heat transfer when small energy consumptions are spent for realizing such flow.

The present work deals with an approach adopted to control heat transfer at a surface of a cylinder considered as a single element of a tubular heat exchanger. The flow behaviour is affected by arc-shaped and straight plates that form a space near the cylinder surface (Fig. 1).

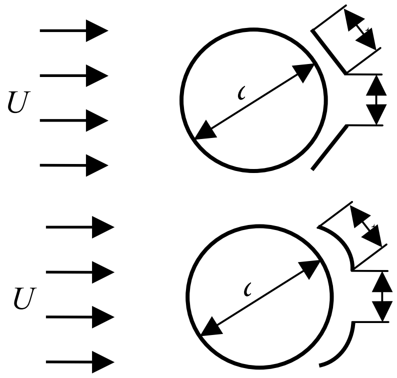

Fig. 1.Test object

2. STATEMENT OF THE PROBLEM

The work considers unsteady laminar crossflow around a cylinder with plates at the Reynolds number $\mathrm{Re} = 186$. The temperature drop between the incoming flow and the cylinder surface was 25°C. The plate length-to-circular cylinder diameter ratio was varied over the range $L/d = 0.05 \div 0.4$. The plates were installed at a distance of 0.16*d* from the cylinder surface. A gap size between them was not varied and was $l = 0.3D$. Such parameters were chosen with regard to the investigations performed earlier [3].

Numerical simulation has been performed using a code VP2/3 specially developed for solving thermal physics and aerodynamics problems. Equations are solved in dimensionless form: coordinates have a dimension of a characteristic scale *d* (cylinder diameter), velocity – of a velocity *U*, pressure – of doubled velocity head ρU^2, time – of a characteristic time scale. External boundaries of a computational domain are at a sufficient distance from the surface of a test object. Incoming flow parameters are assigned at the entrance boundary of such a domain, whereas soft boundary conditions – at the exit boundaries. Attachment conditions are realized at the streamlined surfaces of the test object. Isothermal boundary conditions are predetermined at the cylinder surface and zero temperature gradient – at the surface of guide plates.

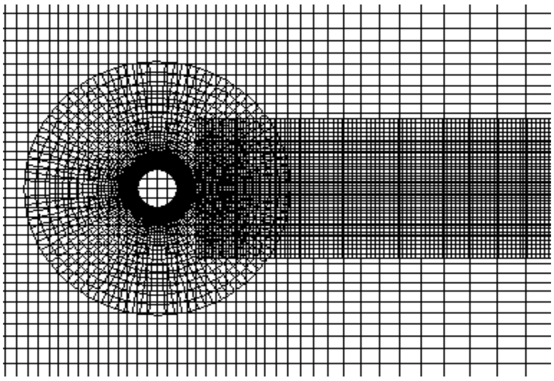

Fig. 2. Computational domain section

Computations were made on a multiblock grid (Fig. 2) comprising an outer rectangular grid, polar grids to describe a domain near the cylinder, grids around the plates and an additional grid to describe a near wake region.

2.1. Verification of computational algorithm

Computation of crossflow around a single cylinder was tested. The obtained results on aerodynamic characteristics and heat transfer of a single cylinder were compared with the experimental data presented elsewhere in [4–6]. It is found that the computed drag of a single cylinder $C_x = 1.445$ agrees fairly (within ~ 3%) with the experimental value of C_x ~1.4 [4, p. 31].

From [6], when a single cylinder is streamlined over the Reynolds number range $10^2 < \mathrm{Re} < 10^7$, the Strouhal number and the value of total drag are related by:

$$C_x = -2.2 + \frac{2.5}{\mathrm{Sh} + 0.53}. \tag{1}$$

Thus, the calculated Strouhal number Sh = 0.1559 is close to Sh = 0.166 obtained experimentally in [5]. The discrepancy is 6.5%.

A value of total heat flux from a single cylinder in laminar flow within the Reynolds number range $10^2 < \mathrm{Re} < 10^5$ can be estimated by the formula as given in [5]:

$$\mathrm{Nu} = 0.35 + 0.5\,\mathrm{Re}^{1/2}. \tag{2}$$

The value of the Nusselt number Nu = 7.631 obtained during numerical simulation agrees within 6 % with the Nusselt number Nu = 7.169 found by formula (2).

3. RESULTS AND DISCUSSION

The shape of plates differently affected the flow structure behind the rear part of the cylinder. Arc-shaped plates form a constant-size channel for medium flow, whereas straight plates – the confuser-diffuser configuration. In the confuser region of the cylinder rear part the flow accelerates, the pressure drops and the boundary layer thickness decreases. In the confuser region the flow velocity decreases, the pressure increases and, accordingly, the boundary layer thickness grows, thus causing the flow to separate. It should be noted that arc-shaped plates are more streamlined as against the straight ones. On the outer side of straight plates additional vortices are formed and reduce the drag. This is typical of straight plates with L=0.3d, 0.4d (Fig. 3). For arc-shaped and straight plates with L < 0.2d their shape does not exert any substantial influence on the drag change.

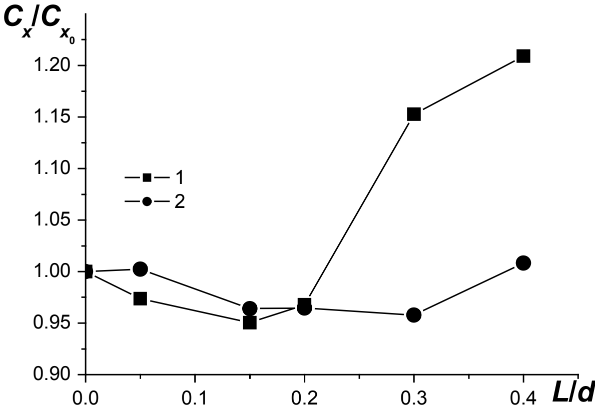

Fig. 3. Total drag vs. length and shape of plates: 1 – arc-shaped plates, 2 – straight plates

Fig. 4 illustrates the fact described above. Straight plates with L=0.3d, 0.4d are characterized by the growth of separation frequency of vortices in comparison with arc-shaped ones. This shows that smaller vortex structures are formed. As the length of straight plates is decreased, the separation frequency of vortices reduces as well. So, the size of separating vortices grows. For arc-shaped plates the separation frequency of vortices is lower than that for a single cylinder, except the plates with *L*=0.2*d*. As shown in [7], installing the plates with *L*=0.2*d*, when the flow interacts with the plate edge, additional vortices are formed and influence the growth of the Strouhal number.

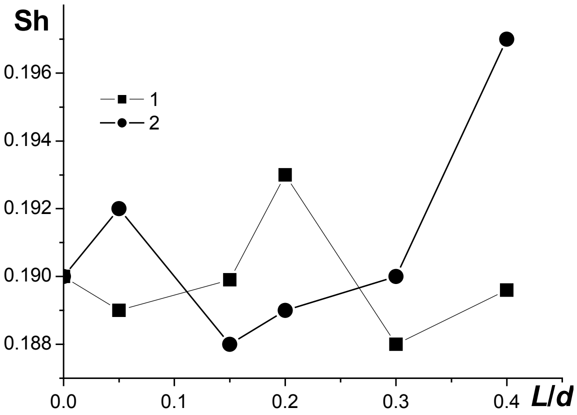

Fig. 4. Strouhal number as a function of length and shape of plates: 1 – arc-shaped plates, 2 – straight plates

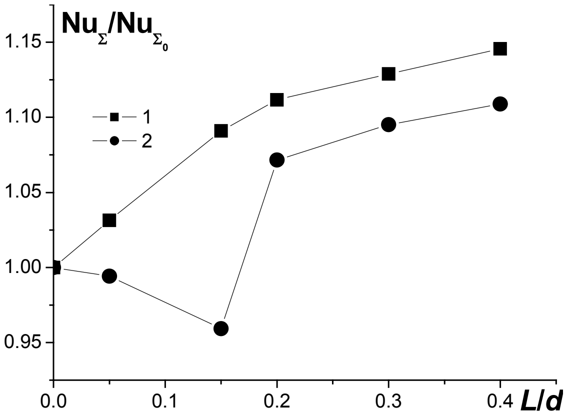

Fig. 5. Relative total Nusselt number $\mathrm{Nu}_{\Sigma}/\mathrm{Nu}_{\Sigma_0}$ as a function of length and shape of plates: 1 – arc-shaped plates, 2 – straight plates

For illustration, Fig. 5 plots the Nusselt number $\mathrm{Nu}_{\Sigma}=\frac{1}{S}\int_S \mathrm{Nu}\,dS$ based on Nu_{Σ_0} for a single cylinder as a function of length and shape of plates. Fig. 5 shows that heat transfer of a cylinder with straight plates is lower than that of a cylinder with arc-shaped ones despite a more small-scale and intense vortex system (Fig. 4). Hence, the system of vortices with straight plates located, is formed far from the cylinder surface than in the case of arc-shaped plates and, accordingly, affects to a lesser extent heat transfer of the cylinder rear part.

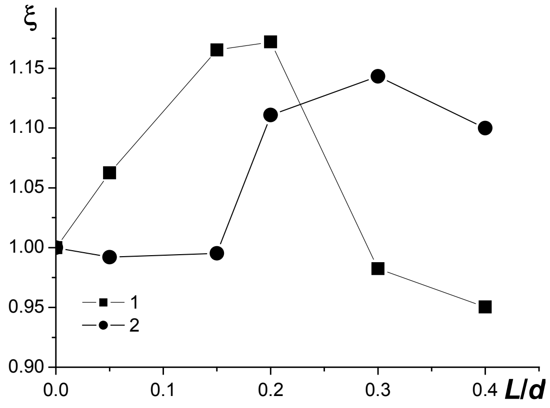

Fig. 6. Thermal-hydrodynamic efficiency ξ as a function of length and shape of plates: 1 – arc-shaped plates, 2 – straight plates

Figure 6 plots the thermal-hydraulic efficiency $\xi = \dfrac{Nu_\Sigma / Nu_{\Sigma_0}}{C_x / C_{x0}}$ as a function of length and shape of plates. The analysis shows that the most effective length of arc-shaped plates is $L<0.2d$ and that of straight plates – $L=0.2d$–$0.4d$. The thermal-hydraulic efficiency of straight plates is increased due to a drag reduction (Fig. 2) and that of arc-shaped plates – due to heat transfer enhancement (Fig. 5).

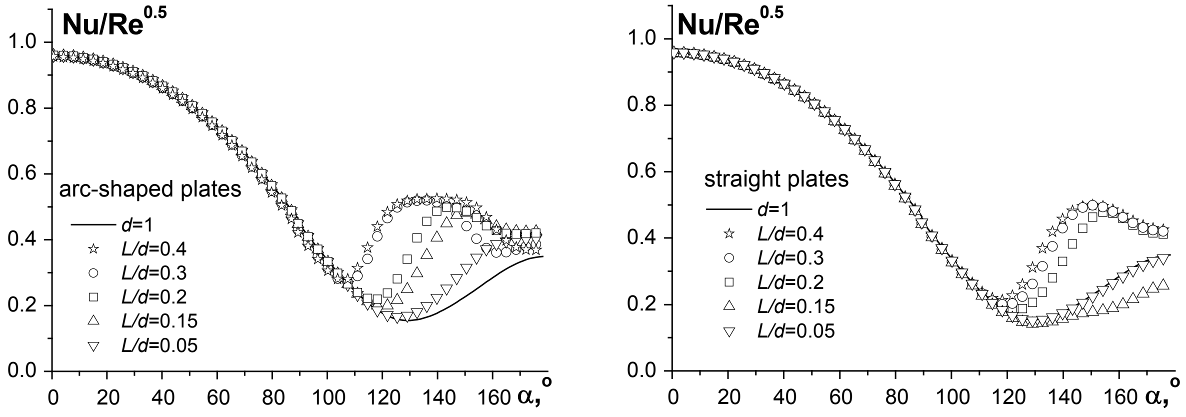

Fig. 6. Local Nusselt number as a function of plate length

To understand heat transfer between a streamlined body and a flow the behaviour of local heat transfer should be studied. The comparison of local Nu number distributions over the cylinder surface depending on the length and shape of plates (Fig. 6) makes a conclusion that the installation of straight plates delays the flow separation and thus causes the drag reduction. The vortex system formed behind the cylinder with straight plates influences weakly the cylinder rear part, thus providing the heat transfer decrease. The formation of additional small vortices in the channel between the cylinder surface and the inner surface of plates augments heat transfer of the cylinder rear part.

4. CONCLUSION

The installation of plates significantly changes frequency, with which the vortex system is formed behind a test object. Straight plates with $L=0.3d$, $0.4d$ form a smaller vortex structure but their location does not much affect heat transfer enhancement. From this point of view arc-shaped plates with L=0.15d, 0.2d are more preferable.

The work was financially supported by the Belarusian and Russian Foundations of Fundamental Research on Projects No. T08R-101, 08-08-90001, 08-08-90400, 08-01-00059.

REFERENCES

1. S.A. Isaev, X.-Ю. Niemann. Control of a near wake behind a circular cylinder due to injection of low-pressure jets. // JEPTER, 2000. Vol. 74, No 5. P. 36–38.
2. S.A. Isaev, V.L. Zhdanov, P.A. Baranov, V.B. Kharchenko. Numerical simulation of laminar and turbulent flow around circular cylinder with inner streams and contour windows // Minsk, 2002. (Preprint / HMTI NAS Belarus, No 3).
3. Yu.V. Zhukova, V.L. Zhdanov. Use of cylinder guide elements for aerodynamic characteristics control and heat transfer enhancement. Laminar flow // Minsk, 2006. (Preprint / HMTI NAS Belarus, No 1).
4. H. Schlichting. Boundary Layer Theory. Moscow: Nauka, 1969.
5. A. Zukauskas. Convective Heat Transfer in Heat Exchangers. Moscow: Nauka, 1982.
6. O. Mitrofanova, O. Gladkova. Effects reducing the hydraulic drag of channels with enhancing facilities // In Scientific Session of Moscow Engineering Physical Institute, 2001. Vol. 8, p. 69–70.
7. Yu. Zhukova, V. Zhdanov, S. Isaev. Guide Element Control of Cylinder Drag and Heat Transfer// Turbulence, Heat and Mass Transfer 5, Dubrovnik, Croatia, 2006, p. 751–754.

POLYISOPRENE-NANOSTRUCTURED CARBON BLACK FUNCTIONAL COMPOSITE FOR PRESSURE SENSORS

J. Zavickis, M. Knite, V. Teteris,
Riga Technical University
Institute of Technical Physics
Azenes str. 14-322, LV-1048 – Latvia
Phone: +371 29794188
E-mail: juriszavickis@inbox.ru

G. Malefan
University of Toulon and the Var France
Institute of Sciences and Engineering for Toulon and the Var
G. Pompidou Avenue – BP 56
83162 LA VALETTE cedex – France
Email: gmalefan@gmail.com

ABSTRACT

Broad use of compressive and strain sensors requires new materials to be designed for particular application. Usually pressure and strain sensors are a form of rigid structures making them difficult to integrate into the structure being monitored. Recent research has approved polyisoprene-nanostructured carbon black composite (PNCBC) to be a prospective material for developing super elastic mechano-electrical sensors. At certain concentrations of conductive filler PNCBC shows remarkable reversible tenso and piezorezistive effect. This is explained by sharp change of tunnelling currents between filler particles, caused by mechanical deformation. Proper use of this property of PNCBC could lead to mass production of cheap, variable size, completely flexible sensors with wide range of application. In this work we have investigated the effect of filler concentration and vulcanization pressure on the final sensor properties of PNCBC. To investigate the process of development of the percolative filler network we although present an original attempt to make an in-situ investigation of composites electrical properties during vulcanization. The dependence of piezoresistive effect on the curing time is although investigated. We believe that our research will lead to a new kind of functional sensor composite material, which could be used for intelligent sensing of ambient conditions for robotics and other smart structures.

Key words: Composite, piezoresistivity, sensor, carbon black, polyisoprene

1. INTRODUCTION

Broad use of compressive and strain sensors requires new materials to be designed for particular application. Usually pressure and strain sensor are rigid structures leading to difficulties to integrate the sensor into structure being monitored. Previously attempts were made to design a flexible pressure and strain sensors made of filled polymer or elastomer but very often they exhibited the lack of reversibility and linearity [1]. More recent works claimed polyisoprene-nanostructured carbon black composite (PNCBC) to be a prospective material for current needs [2, 3]. Our previous research proved that at certain concentrations of specific conductive filler PNCBC shows remarkable reversible tenso and piezorezistive effect [4, 5]. The phenomenal properties are achieved thanks to nano sized insulating gaps between conductive filler particle agglomerates [6]. The changing conductivity of PNCBC in this way is explained by the existence of tunnelling currents over these gaps. The smallest external load on material causes the polymer matrix to deform and changes the intensity of tunnelling, thus changing PNCBCs electrical resistivity. As the filler particles are comparatively small and highly structured, they adhere very strongly to the elastomer matrix and provide the complete reversibility of the change of these properties. To investigate the development of the percolative filler network we present an original attempt to make an in-situ investigation of composites electrical properties during its vulcanization. We are although have investigated the effect of filler concentration and vulcanization parameters - like pressure and curing rate on the final sensing properties of PNCBC. The main goal of this article is to develop current prospective composite technology and lead to mass production of cheap, variable size, completely flexible sensors with wide range of applications.

2. METHODOLOGY

PNCBC was made when concentration close to that of a percolation threshold of conductive high structure carbon black Degussa Printex XE2 and necessary curing agents were added to polyisoprene Thick Pale Creppe natural rubber matrix. The mixing of filler and matrix was done using cold rolls, but the methods used can be slightly different, including Banbury mixer and wet mixing into $CHCl_3$ solution. It depends mainly on the final product it is necessary to obtain. PNCBC samples were made by vulcanizing prepared raw rubber mixture into hot stainless steel mould. To obtain good electrical connection with samples, clean sandpapered brass foil mould inserts were used on both sides of the samples. The previous research approved them to be the most suitable for this need because brass forms permanent electro-conductive bond with the PNCBC during vulcanization. Modified teflon and polyimide film moulding was used instead of steel mould to make in-situ resistivity measurements, in such way electrically insolating the sample from press metal plates and avoiding short circuit (see Figure 1).

The initial electrical resistivity of all samples was measured using Meterman 27XT digital multimeter. For in-situ resistivity measurements the J type thermocouple was used to determine the effective temperature of the system. The Agilent 34970A digital multimeter with integrated 20 multi-channel switches was used to measure electrical resistivity of the samples. The piezoresistive properties of PNCBC samples were determined using Zwick/Roell Z2.5 universal materials testing machine, equipped with HBM 1kN load cell and HBM Spider8 data acquisition module. This allowed the measurements of mechanical and electrical properties to be taken simultaneously. This testing was done using variable external operational pressure from 0 to 1 bar, with speed of $1x10^{-2}$ $bar \cdot s^{-1}$. The deformation of the samples was so small, that it was a limited factor to measure.

3. RESULTS AND DISCUSSION

3.1. The “in-situ” resistivity measurements of PNCBC during curing phase

The “in-situ”” measurements of PNCBC electrical resistance during vulcanization phase were made by using custom made teflon frame and polyimide film to form an isolative mould and specially prepared flat sample as all this is shown on Fig. 1.

To provide optimal processing parameters, first the optimal curing time of the composite was ensured using MonsantoRheometer100 rubber rheometer. The press was thermostated at optimal curing temperature. The raw PNCBC sample was inserted between hot plates and held compressed at 30 bar for 40 minutes. The thermocouple was positioned near the sample to measure its actual temperature. The brass foil extensions were soldered to measurement circuit with data logger and the change of samples electrical resistivity was logged. Both measurements were plotted as shown in Fig. 2.

Fig. 1. The picture of "in-situ" electrical measurement sample inserted into teflon mould between two polyimide films

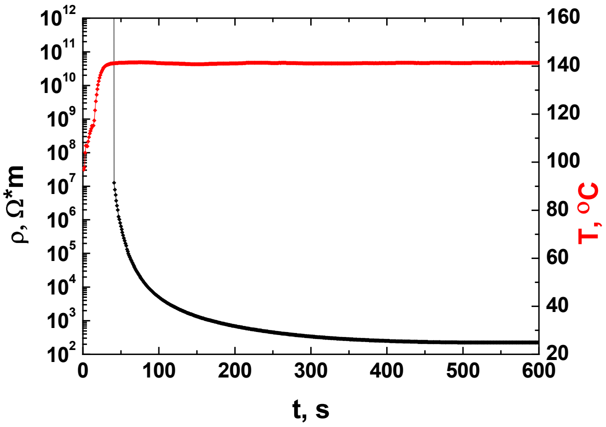

.

Fig. 2. "In-situ" measurement of PNCBC resistivity during vulcanization. The change of specific electrical resistivity (black) and temperature (red) as a function of time for sample with 9 mass parts of carbon

3.2. Dependance of piezoresistivity on PNCBC curing pressure

PNCBC samples with 8, 9, 10 and 11 mass parts of conductive filler were made at different vulcanization pressures to determine if there is a dependence of piezoresistive properties on mould pressure and filler concentration. Approximately 1 mm thick flat sticks of PNCBC were made as shown in Fig. 3.

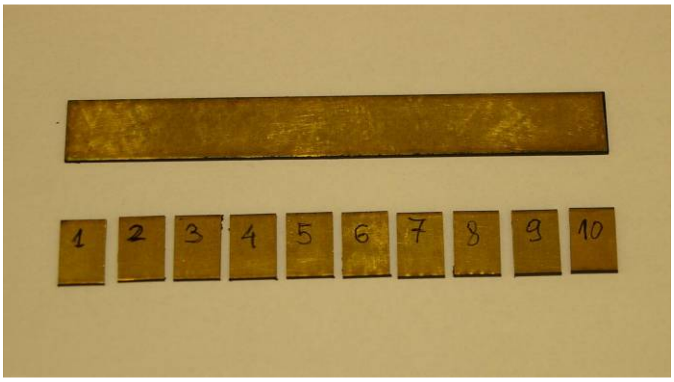

Fig. 3. PNCBC sample stick and separate samples, numbered according to their origin in stick

These sticks were cut into equal pieces with dimensions of 10x15 mm using diamond disk cutter to avoid unnecessary squeezing of PNCBC. For each curing conditions 10 to 12 parallel samples were made and numbered according to their origin in stick. The comparison of the initial electrical resistivity of these samples is shown in Fig. 4.

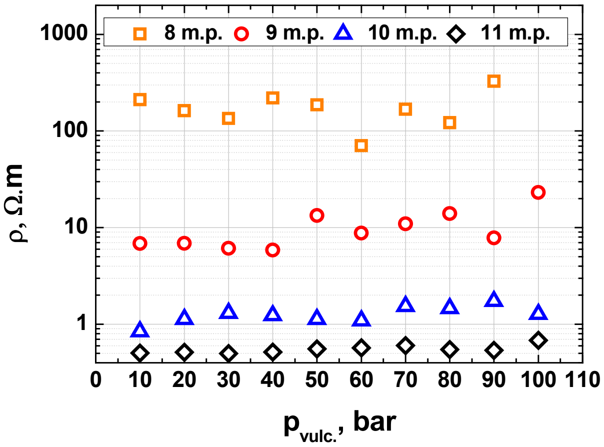

Fig. 4. The average specific electrical resistivity of PNCBC samples with 8, 9, 10 and 11 mass parts (m.p.) of conductive filler versus different vulcanization pressures used

The piezorezistive behaviour of these PNCBC samples has been determined and the results for samples with 9 mass parts of carbon are shown in Figures 5 as an example. The curves shown here are corresponding to the compression phase of testing. The piezoresistive behaviour showed very small or no hysteresis at all so the release phase could be excluded from the graph. The piezoresistive effect for all current samples and operative pressures appears to be quasi linear and could be described by effective coefficient of piezoresistance - $\overline{\Pi}$, where

$$\frac{\Delta\rho}{\rho_0} = \overline{\Pi} \cdot \Delta p_{oper.} \qquad (1)$$

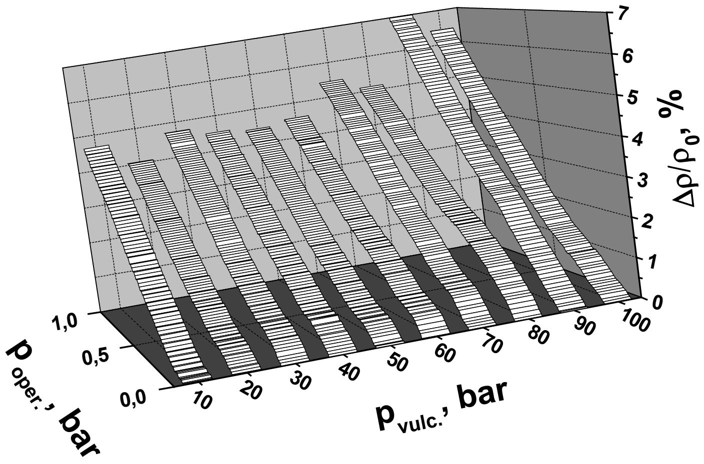

Fig. 5. The piezoresistive behaviour of PNCBC samples with 10 mass parts of conductive filler vulcanized at ten different pressures

The values of piezoresistive coefficient for samples made under conventional curing pressure (30 bar) appears to be in the range of $1{,}9\cdot10^{-6}$ to $2{,}9\cdot10^{-7}$ $\mathrm{Pa}^{\mathbf{-1}}$ (Tab.1).

W_{carbon}, **mass parts**	8	9	10	11
Table 1. The piezoresistive coefficient values of PNCBC samples with 8, 9, 10 and 11 mass parts of carbon, vulcanized under pressure of 30 bar. **$\overline{\Pi}$, Pa^{-1}**	$1.9\cdot10^{-6}$	$6.9\cdot10^{-7}$	$4.7\cdot10^{-7}$	$2.9\cdot10^{-7}$

3.3. Dependance of piesoresistivity on PNCBC curing time

Disk shape PNCBC samples 18mm in diameter with 9 and 10 mass parts were made using different curing times in range from 1 to 40 minutes. 40 minutes corresponds to previously determined time necessary for complete vulcanization of PNCBC and 1 minute was the smallest possible time to obtain the desired shape of the sample. The piezoresistive properties of samples were determined and evaluated as shown in Figs. 6 and 7.

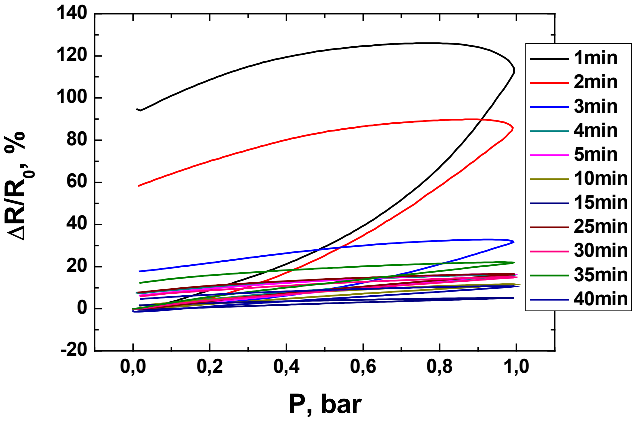

Fig. 6. The piezoresistance of PNCBC samples with 9 mass parts of carbon black which are made using different curing times from 1 to 40 minutes

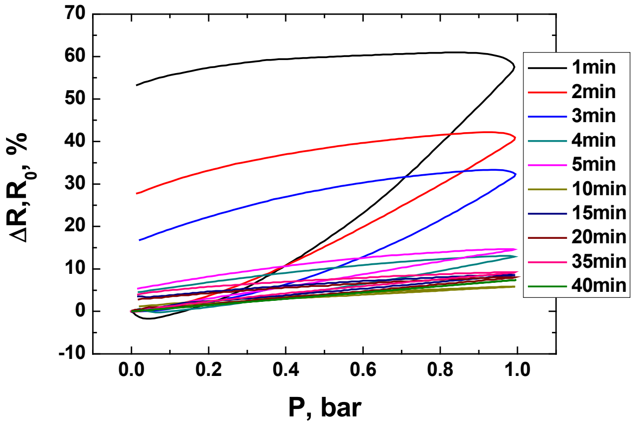

Fig. 7. The piezoresistance of PNCBC samples with 10 mass parts of carbon black which are made using different curing times from 1 to 40 minutes.

4. CONCLUSIONS

The results of “in-situ” measurements shown are clearly evident that conductive structure of PNCBC forms exactly during vulcanization phase.

The drop of initial electrical resistivity towards the increase of filler concentration is clear evidence of the percolation threshold reached and exceeded. There is although a small rise of initial electrical resistance with increasing vulcanization pressure. This can be explained by decreased mobility of filler particles, during the formation of the percolative network under higher pressure.

The results of piezoresistance measurements shown cleared out – the less the concentration of filler in vicinity of percolation threshold, the greater the piezoresistive effect. On other hand, samples with less filler concentrations exhibited large dispersion of effective piezoresistance. This can be attributed to weakly developed percolative structure due to the smaller concentration of filler.

Results provide that vulcanization time makes noticeable effect on the piezoresistive properties of PNCBC. Samples with 9 and 10 mass parts of carbon were made by using different reduced curing times. Piezoresistivity measurement results of these samples shows that partially vulcanized PNCBC samples exhibit comparatively larger piezoresistivity but on other hand, the hysteresis become very noticeable. This leads to conclude that the time of vulcanization more than 12% from time necessary to perform complete vulcanization is enough to provide useful properties of PNCBC.

ACKNOWLEDGEMENT

This work has been partly supported by the European Social Fund within the National Programme „Support for the carrying out doctoral study programm’s and post-doctoral researches” project „Support for the development of doctoral studies at Riga Technical University”, as well as by national programme “Material Science”.

REFERENCES

1. Flandin, L., Brechet, Y., Cavaille, J.-Y., “Electrically conductive polymer nanocomposites as deformation sensors”, Compos. Sci. Technol., Vol. 61, 2001, p. 895–901.
2. Ali, M.H., Abo-Hashem, A., “Percolation concept and the electrical conductivity of carbon black-polymer composites. 3: Crystallisable chloroprene rubber mixed with FEF carbon black”, J. Mater. Proc. Tech., Vol. 68, 1997, p. 168-171.
3. Job, A.E., Oliveira, F.A., Alves, N., Giacometti, J.A., Mattoso, L.H.C., “Conductive composites of natural rubber and carbon black for pressure sensors”, Synthetic Met., Vol. 135-136, 2003, p. 99–100.
4. Knite, M., Teteris, V., Polyakov, B., Erts, D,. Electric and elastic properties of conductive polymeric nanocomposites on macro- and nanoscales, Materials Science & Engineering C, V19, Iss.1-2, 2002, p. 15–19.
5. Knite, M., Teteris, V., Ķiploka, A., Kaupuzs. J., “Polyisoprene-carbon black nanocomposites as tensile strain and pressure sensor materials”, Sensor. Actuator., Vol. 110, 2004, p. 142–149.
6. Balberg, I., “A comprehensive picture of the electrical phenomena in carbon black–polymer composites”, Carbon, Vol. 40, 2002, p. 139–143.

CYSENI 2009, May 28-29, Kaunas, Lithuania
ISSN 1822-7554, www.cyseni.com

CARBON NANOMATERIALS FORMATION BY METHANE DECOMPOSITION IN HIGH-VOLTAGE DISCHARGE

K.O. Borisevich, A.V. Krauklis
A. V. Luikov Heat and Mass Transfer Institute
P. Brovki Str. 15, 220072 – Belarus
Phone: +375172841251, +375296381399
E-mail: Borisevich-kir@yandex.ru

ABSTRACT

The object of recent research is process of carbon nanomaterials formation by methane decomposition in plasma of high-voltage discharge. The main goals of research are to study mechanism of nanostructures (nanotubes and nanofibers) formation and to find out fundamental regularities of the process taking into account basic operating parameters, such as surface temperatures of reactor, composition of gaseous phase and of products of decomposition, power of discharge, etc.
As a result of study carried out, the most probable mechanism of nanostructures formation was determined and its surface nature was proven. Evaluation of process productivity and analysis of product morphology was performed. Additionally data about influence of different conditions of the process on final product containing nanotubes and nanofibres were obtained.
The results of research can be applied both for optimization of the processes of carbon nanomaterials production in electrical discharge and for development and creation of more powerful and efficient plasma-chemical systems.

1. INTRODUCTION

There are numerous methods for carbon nanomaterials (CNM) production, among them the following ones are the most commonly used: graphite electrode scattering in electric arc [1], graphite laser ablation [2], and chemical deposition process in gaseous phase [3, 4]. Most methods for carbon nanostructures production require special conditions for synthesis: low pressures, catalyst, high temperatures, resulting in energy consumption increase and process effectiveness decrease.

In the present work materials of investigation of CNM formation of methane decomposition products in cold plasma are performed. During the process growth of structured carbon materials occurred on metal surface in the absence of specially prepared catalyst at atmospheric pressure.

2. EXPERIMENTAL SETUP

A setup for carbon nanomaterials production in electric arc plasma at atmospheric pressure was developed to perform an (the) experimental research. The basic scheme of experimental setup is given in Fig. 1.

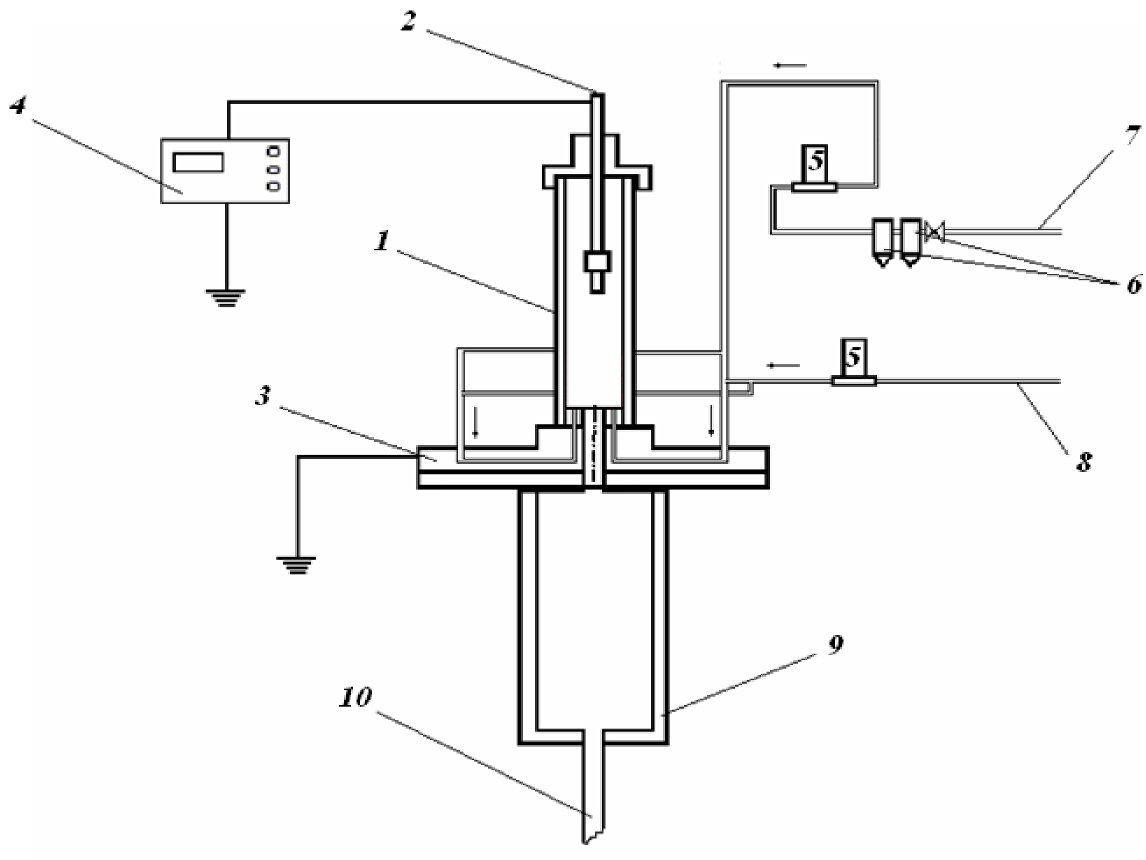

Fig. 1. Experimental setup: 1 – quartz tube; 2 – cathode; 3 – anode; 4 – high voltage power supply; 5 – flow controllers; 6 – filters; 7 – air supply line; 8 – (gaseous) hydrocarbons supply line; 9 – carbon nanomaterial deposition chamber; 10 – exhaust

A method of reverse vortex flow was used in plasma-chemical reaction construction (Fig. 2) for gas-dynamic stabilization of high voltage discharge at atmospheric pressure and for thermo-isolation of reaction site. The plasma-chemical reactor consists of hermetic cylinder quartz tube 2 (with inner diameter – 35 mm), where reverse vortex flow is set up and discharge burns, and of lower metal part, where anode 4 and swirler 8 are located. The vortex is performed due to tangential disposition of test supply connecting pipes.

Removable cathode 1 is made of high-melting metal (zirconium, hafnium, iron-titanium alloy), its length being 35 mm and diameter 5.7 mm. Cathode holder is a stick of stainless steel and has a shape of a cylinder with 4 mm by diameter and 220 mm by length, and is connected with cathode by collet. Anode has demountable central unit that allows variation of gas mixture exit channel length.

Plasma-chemical reactor construction provides vertical cathode moving without reaction site depressurization. Precise interval for inter-electrode distance is between 0 and 90 mm. Cathode movement is necessary for contact ignition of discharge and for management by energy parameters of CNM formation process.

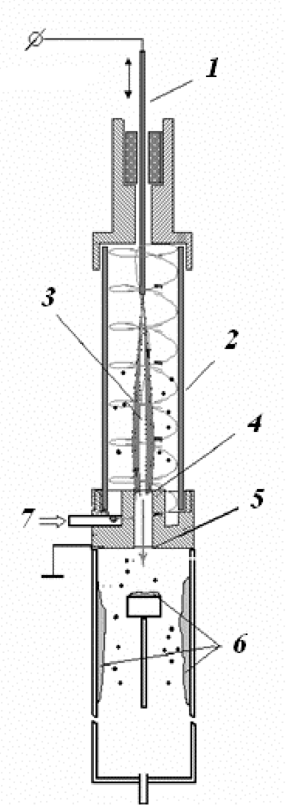

Fig. 2. Reactor scheme: 1 – removable cathode; 2 – quartz tube; 3 – discharge zone; 4 – anode; 5 – anode part exit; 6 – deposit; 7 – tangential blowing of gaseous mixture (swirler)

Due to gas-dynamic stabilization relative stability of discharge burning and at the same time heat isolation of discharge location is provided, i.e. heat is kept in gaseous flow. Cooling of exit gaseous flow is directly behind the anode in metal unit of reactor body. In the upper part of cooling zone a substrate for carbon nanomaterials deposition was set up.

CNM formation is performed as a persistent sequence of two stages: 1) methane partial oxidation process in the air and 2) pyrolysis of non-decomposed hydrocarbons on metal particles. Process products are carbon oxide (18–20%), as well as hydrogen (30–40%), that due to its strong reducing properties is able to gasify soot-like by-products, and, thus to increase portion of useful product; physico-chemical transformations occur at ambient pressure.

3. RESULTS AND DISCUSSION

One of the critical factors in carbon nanomaterials formation process is temperature. Gas flow temperature is determined by electric discharge energy. Varying discharge parameters (current, voltage) one can manage integral temperature of gas flow. Temperature of gaseous flow was measured by chromel-copel thermocouple. Position of temperature measurement points is shown in the Fig. 3.

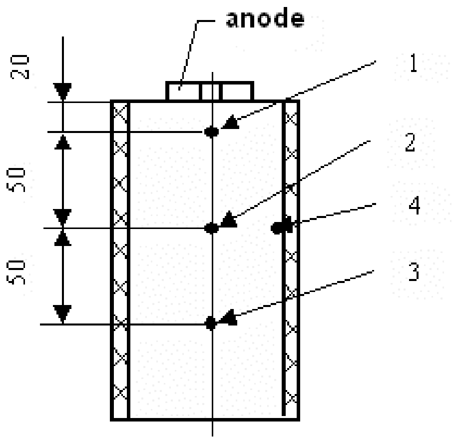

Fig. 3. Temperature measurement in CNM deposition chamber. Numbers correspond to the numbers of thermocouples.

Discharge capacity varied in the range from 0.1 to 0.5 kW. Mixture of methane with air ($0.31CH_4 + 0.54N_2 + 0.15O_2$) was used as a test mixture. Plots of gas temperature vs. time at various points of reactor for different discharge capacities are performed in Fig. 4 and 5.

As it can be seen from the relations given the highest temperature value in supposed area of carbon nanomaterials synthesis is 1000°C. This value is limited by discharge power supply capacity. It should be noted that time before reactor achieved quasi-stationary state is 30–50 min according to discharge capacity.

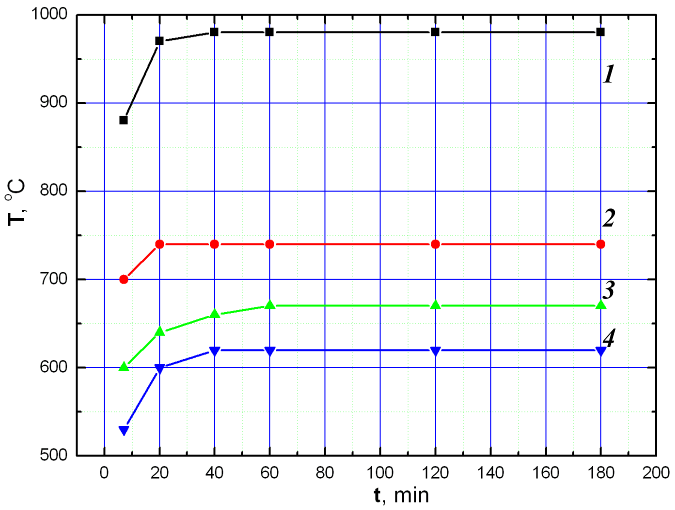

Fig. 4. Temperature changing with time in different points of reactor (see fig. 3). Power of discharge – 450 W.

After each experiment carbon nanomaterial (deposit) was taken off the chamber surface, was purified and analyzed. Finished product was a black-gray powder with bulk density 0.21 g/cm^3. Carbon nanostructures content in product was determined by transmission and scanning electron microscopy (TEM and SEM). In the Fig. 6 (a, b) pictures of materials are performed. Analysis SEM was performed in laboratory of hydrogen power engineering of “Institute of heat and mass transfer named by A.V. Lykov of NAS of Belarus” on microscope Supra 55.

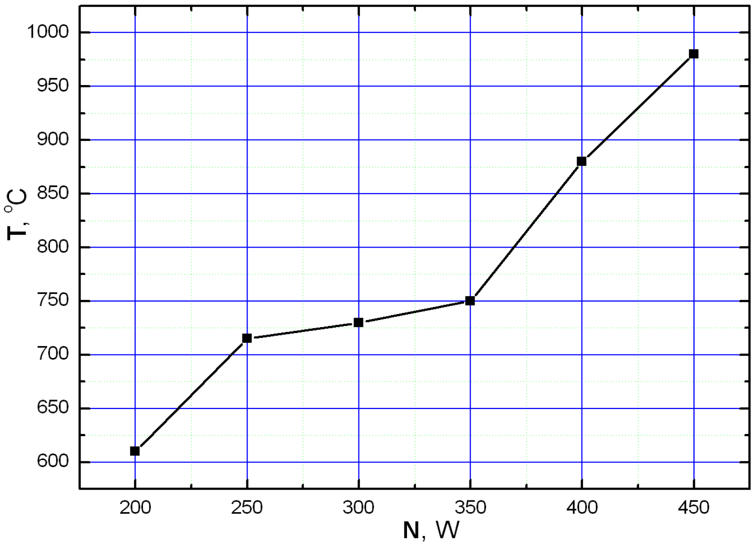

Fig. 5. Temperature of gaseous flow at the anode part exit vs. discharge capacity

Analysis of numerous pictures showed that the deposit contained up to 40–50% of structured carbon and up to 30% of amorphous one. The rest of the material was graphite (~15%), particles of metal and their oxides (~5%). After special acid and thermal treatment to remove amorphous carbon and metal particles structured carbon content in such material achieved 70–80%. Some of carbon structures are fibers with typical diameters not less than 300 nm of different length and shape. Additionally, material contains structures of diameters 50–70 nm and length up to 1 µm, and they can be considered as multi-wall carbon nanotubes.

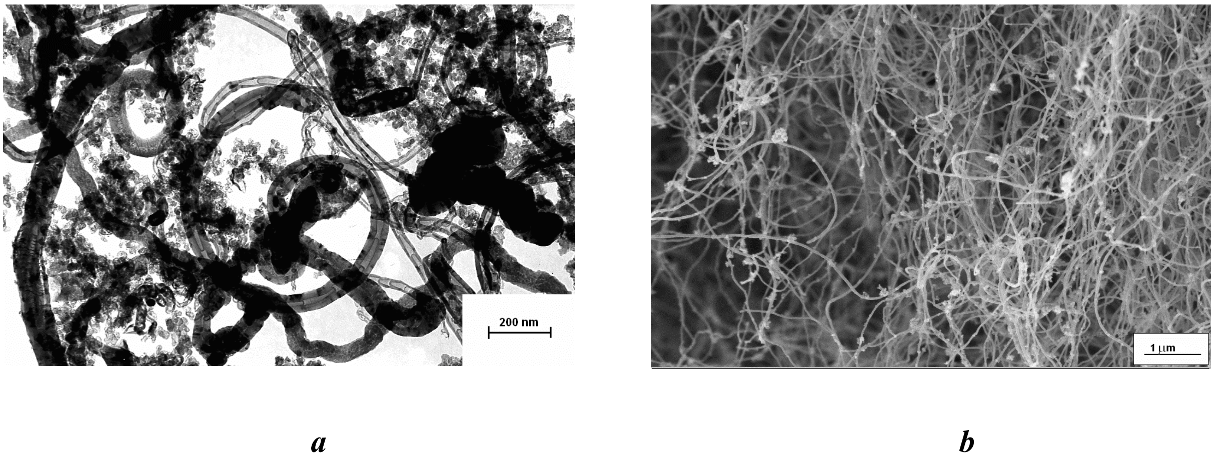

Fig. 6. Images of CNM, formed on metal surface of deposition chamber: *a* – obtained by transmission electron microscopy (TEM); *b* –by scanning electron microscopy (SEM)

Influence of clusters formed as a result of metal evaporation off the cathode surface on carbon nanostructures formation process was found out during comparing experiments on cathodes of invar and graphite. In Fig. 7 (a, b) pictures of transmission electron microscopy (TEM) for two samples of carbon material obtained at the same conditions in discharge system with different cathodes are performed. It can be seen on the pictures that formation of

CNM was in both cases, so it can be concluded that metal clusters in gas flow do not cause significant effect on the process of carbon structures formation.

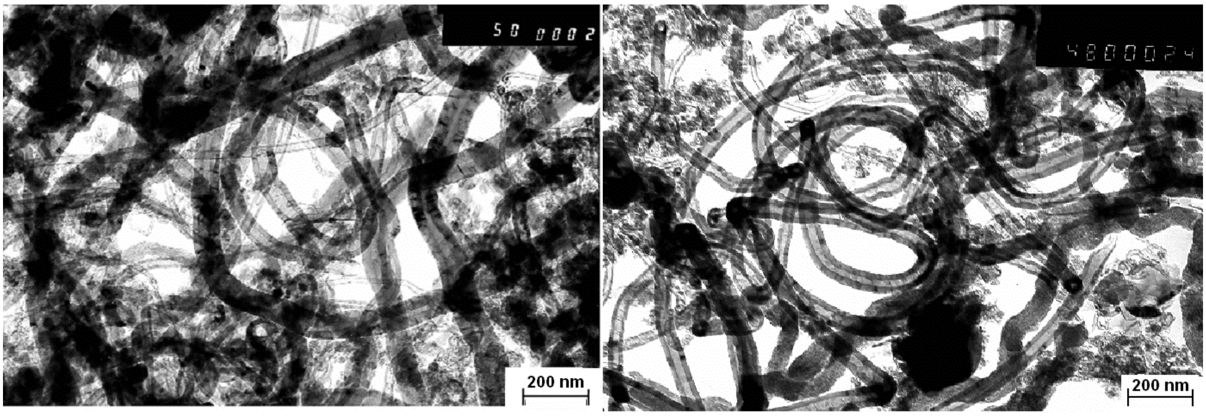

a ***b***

Fig. 7. TEM-image of CNM formed: *a* – in case invar cathode is used, *b* – in case graphite cathode is used

To find out material surface influence on CNM yield, two semi-cylinders of nickel and molybdenum foil were placed inside of reactor, on which deposition took place. Mixture of methane (200 l/hr) and air (456 l/hr) was used as a working mixture. Discharge capacity was 380 W, average temperature of deposition surface achieved 780 °C. Specific value of CNM collected off the nickel foil surface was $16 \cdot 10^{-5}$ g/(mm^2·hr), but there was no material on molybdenum foil.

Temperature of deposition surface plays an important role for consideration of heterogeneous nature of carbon nanostructures formation; it also has an influence on hydrocarbon decomposition rate and diffusion of carbon in metal. In paper [5] in case of iron catalyst effect of ordered carbon structures has a threshold nature and occurs at temperature greater than 680 °C. It was found out in our investigations that carbon structures formation takes place at surface temperature not less than 500 °C, in this case, as it is shown in Fig. 8, the higher the temperature, the greater CNM yield is observed as well. CNM yield is the amount of deposit formed per unit of deposition surface during unit of time (g/mm^2·hr).

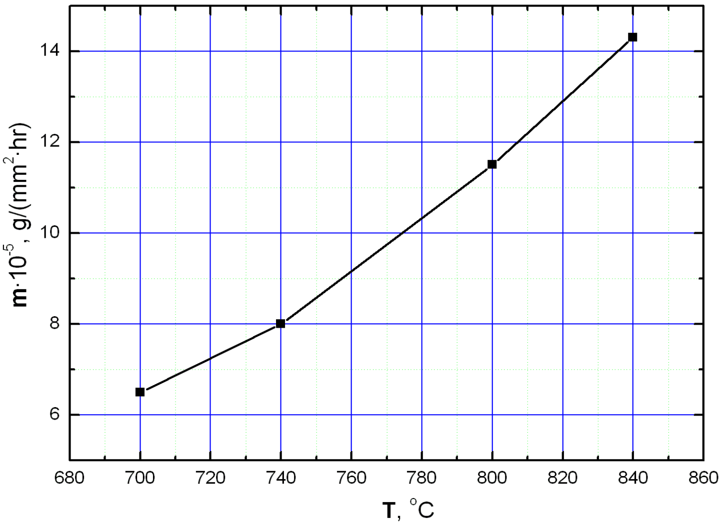

Fig. 8. CNM yield vs. surface temperature

During the investigation an important role of temperature gradient presence between gas flow and material collection surface was determined. If surface temperature is close to flow temperature or equal to it, then CNM formation does not take place. It can be demonstrated by Fig. 9, 10. In position **A** foil surface bears against quartz tube surface, in configuration **B** foil is bent as “accordion”. At the same discharge gas flow parameters in the former case CNM is formed, and in the latter it does not occur. Probably, it is connected with thermal diffusion processes determining the rate of gaseous hydrocarbon supply to the metal surface. For the case A relation of specific yield of CNM with temperature difference between the centre of the flow and the wall was plotted. Both temperatures were measured by thermocouples during the experiment. As it is shown in Fig. 7, specific yield of CNM increases with temperature gradient between gas flow and wall increase.

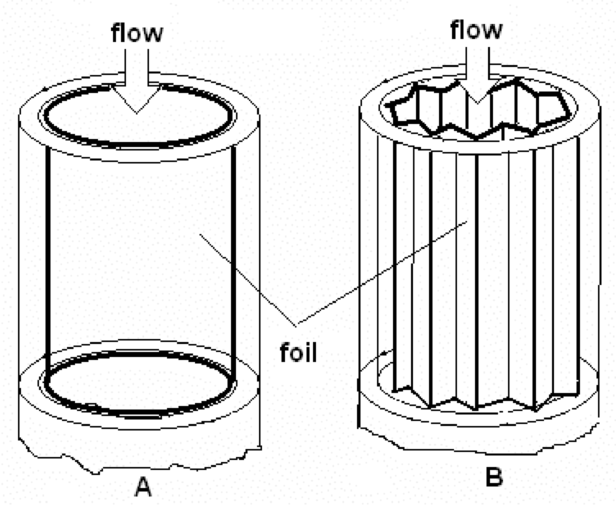

Fig. 9. Shape of CNM collection surfaces

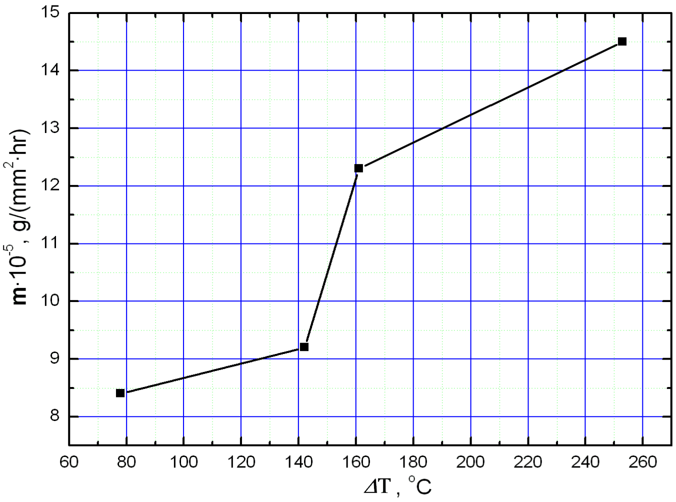

Fig. 10. CNM yield vs. temperature gradient between gas flow and surface

It can be concluded that ordered carbon structures formation takes place on metal surface, containing iron and nickel that this is in accordance with hypothesis of CNM formation by carbide cycle [6].

4. CONCLUSIONS

Thus, experimental research performed show that CNM formation in case of treatment of methane-air mixture by plasma of high voltage discharge at atmospheric pressure occurs on metal surface and is similar to processes of hydrocarbon catalytic decomposition by mechanism of carbide cycle. It determines dependence of CNM yield on deposition surface material, its temperature and the temperature gradient between gas flow and deposition surface.

Analysis of dependences obtained showed the increase of CNM yield with the growth of deposition surface temperature and temperature gradient between gas flow and deposition surface. If the temperature of the deposition surface is less than 500°C and there is no temperature gradient between gas flow and deposition surface, CNM formation does not occur, since in these conditions disable the pyrolysis of hydrocarbons on the metal particle as a catalyst and further carbon diffusion through the volume of the metal particle.

It was determined that material of cathode does not influence carbon nanostructures formation and that fact discard the possibility of carbon structuring in the whole volume of deposition chamber and confirm the surface formation mechanism.

At optimal conditions of the research the maximum productivity was up to 10 g/hr of CNM with average content of structured carbon is about 50% – nanotubes and nanofibers with diameters 50–300 nm and length up to 1 µm.

It should be noted,that almost all of the gaseous or liquid hydrocarbons can be used as row materials for such process.

REFERENCES

1. Cadek M., Murphy R., McCarthy B., Drury A., Lahr B., and Barklie R.C., Optimisation of the arc-discharge production of multi-walled carbon nanotubes // Carbon. 2002. Vol. 40. 2002. P. 923–928.

2. Arepalli S., Nikolaev P., Holmes W., and Bradley S. Files, Production and measurements of individual single-wall nanotubes and small ropes of carbon // Appl. Phys. Let. 2001. Vol. 78, No. 10. P. 1–3.
3. P. Chen, X. Wu, J. Lin , H. Li, and K.L. Tan, Comparative studies on the structure and electronic properties of carbon nanotubes prepared by the catalytic pyrolysis of CH_4 and disproportionation of CO // Carbon. 2000. Vol. 38, P. 139–143.
4. Kiselev N. A., Hutchison J. L., Moravsky A.P., Rakova E.V., Dreval E.V., Hetherington C.J. D, Zakharov D.N., Sloan J., and Loutfy R.O., Carbon micro-and nanotubes synthesized by PE-CVD technique:Tube structure and catalytic particles crystallography // Carbon. 2004. Vol. 42. P. 149–161.
5. Kukovitsky E.F., L'vov S.G., Sainov N.A., Shustov V.A. CVD growth of carbon nanotube films on nickel substrates // Applied Surface Science. 2003. Vol. 215. P. 201–208.
6. Ermakova M.A., Ermakov D.Yu., Chuvilin A.L. and Kuvshinov G.G. Decomposition of Methane over Iron Catalysts at the Range of Moderate Temperatures: The Influence of Structure of the Catalytic Systems and the Reaction Conditions on the Yield of Carbon and Morphology of Carbon Filaments // Journal of Catalysis. 2001. Vol. 201. P. 183–197.

CYSENI 2009, May 28-29, Kaunas, Lithuania
ISSN 1822-7554, www.cyseni.com

LASER STRUCTURING OF FLEXIBLE THIN-FILM SOLAR CELLS

P. Gečys, M. Gedvilas
Institute of Physics
Savanoriu Ave. 231, LT-02300 Vilnius – Lithuania
Phone: (+370) 60004346
E-mail: p.gecys@ar.fi.lt

ABSTRACT

Permanent growth of the thin-film electronics market stimulates the development of versatile technologies for patterning thin-film materials on rigid and flexible substrates. Interest in complex multilayered Cu(InGa)Se_2 (CIGS) Solar cells has increased recently because of low production costs. Laser structuring is an important step to preserve high efficiency of photovoltaic devices on large areas. We used laser with the picosecond pulse duration in selective ablation of the complex thin-films structures deposited on polymers. Here we discuss our new results in structuring of multilayer films used in production of the CIGS solar cells. The high-repetition-rate laser with pulse duration of 10 ps was applied in the experiments. Non-linear crystals were used for conversion of the wavelength generated by the laser. The shape of ablated features was controlled by the scanning electronic microscope (SEM) with the energy dispersion spectrometer (EDS).
Layer-by-layer removal of the material was performed when UV laser radiation was applied. Well-defined shapes of isolating trenches and conductor lines were produced by laser ablation with the picosecond pulse duration in thin film structures of the Cu(InGa)Se_2 Solar cells in order to increase their electric efficiency. Four regimes of CIGS thin film laser structuring were selected for: the ITO upper layer removal, the Mo back-contact exposure, the polyimide substrate exposure and the CIGS Solar cell cutting. The use of UV laser radiation with fluences close to the ablation threshold made it possible to minimize the surface contamination and the recast ridge formation during the ablation process.

Keywords: Flexible solar cells, laser structuring, CIGS

1 INTRODUCTION

A permanent growth of the thin-film electronics market stimulates the development of versatile technologies for patterning thin-film materials on rigid and flexible substrates. Utilization of laser radiation provides diversity of processing means for structuring deposited films. Interest in complex multilayered Cu (InGa) Se_2 (CIGS) solar cells has increased recently because of low production costs [1]. Efficiency of the thin-film solar cells with a large active area might be increased if small segments are connected in series in order to reduce photocurrent in thin films and resistance losses. Selective removal of the films in multilayer structures of modern Solar cells is crucial for performance of the devices. Lasers are usually used to scribe the separation lines (P1, P2, P3) for interconnection of elements by selective ablation of conducting and semi-conducting layers as shown in Fig. 1. Accuracy in the ablation depth and the high scribing speed are required for efficient and cost-effective production of Solar cells of this type. High repetition rate lasers with a short pulse duration offer new possibilities for high efficiency structuring of conducting, semi-conducting and isolating films. Various laser sources were tested in selective ablation of thin films [2–6]. The main limiting factor for laser processing of the multilayer $CuInSe_2$ structures is deposition of molybdenum on walls of channels scribed in the films, and the phase transition of semi-conducting $CuInSe_2$ to metallic state close to the ablation area due to the thermal effect [4]. Both effects shunt the photo-electric device and decrease its conversion efficiency.

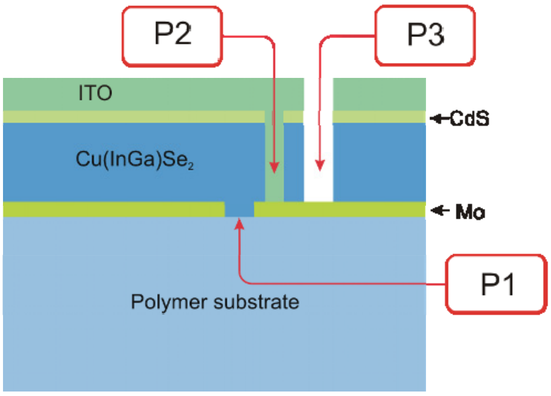

Fig. 1. Schematic cross-section of a CIGS thin film solar cell. P1, P2 and P3 indicate areas removed by laser ablation in films

Thermal degradation of the CIGS solar cells starts at temperatures above 350 °C due to diffusion of the buffer layer metal (Cd, Zn) into the absorber layer [7]. Use of nanosecond lasers is related to a high heat affected zone and nanosecond lasers are undesirable in manufacturing of this type of photovoltaic elements. Femtosecond pulses are capable of ablating the films completely and selectively enough but their use is limited because of complexity in maintenance. According to the results of theoretical modeling, the processing without damage is possible with picosecond laser pulses [5].

Our goal was to develop the flexible and rapid laser technology for precise structuring of the CIGS solar cells compatible with the roll-to-roll production line. We used the laser with the picosecond pulse duration in shaping the simple thin-films structures deposited on polymer substrates [10]. The experiments revealed potential of picosecond lasers in selective structuring of the thin films when the wavelength of laser radiation was adjusted depending on optical properties both of the film and the substrate. We present our new results in application of laser structuring of multilayered CIGS Solar cells.

2 EXPERIMENTAL

The films of metals and the whole structure of the CIGS solar cell deposited on the polymer substrates were used in the experiments. Polyimide (PI) film with the thickness of 25 µm was used as a substrate for deposition of molybdenum (0.5 µm) and the complete multilayer structure of Mo/$CuIn_xGa_{(1-x)}Se_2$/CdS/ZnO/ITO. The thickness of the films was 0.5 µm for the Mo back-contact, 1 µm for $CuIn_xGa_{(1-x)}Se_2$ absorber layer, ~10 nm for both CdS and ZnO buffer layers each and 0.5 µm for the top contact of the indium-tin oxide (ITO). All samples on polymer substrates were provided by Solarion AG, Germany.

We used lasers with the picosecond pulse duration in shaping the thin-films structures deposited on polymers. Set-up for the laser processing experiments is shown in Fig. 2.

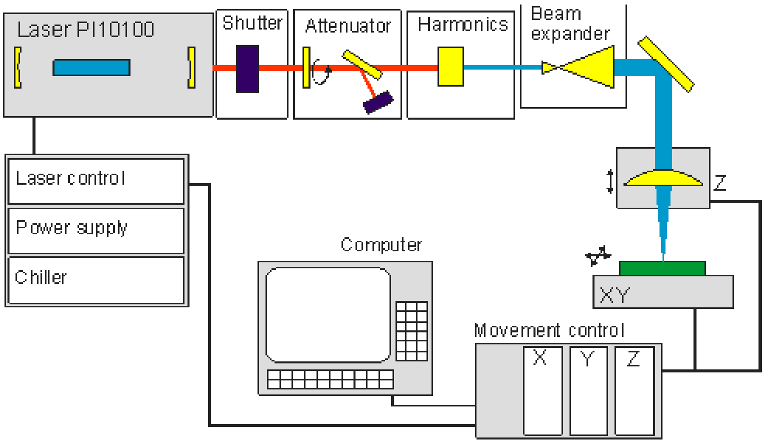

Fig. 2. Experimental complex for laser structuring of the thin films

The picosecond laser PL10100 made by Ekspla UAB was used in the ablation experiments. The pulse duration was typically of 10 ps at 1064 nm. Pulse energy could be varied from 0 up to 200 µJ at repetition rate of 50 kHz, and up to 100 µJ at repetition rate of 100 kHz. The maximum laser power was 10 W at 1064 nm. Attenuator made of Pockels cell and polarizer was used for fast shuttering and pulse energy control of laser beam. Nonlinear crystals were used for the wavelength conversion to UV radiation. The beam expander stretched the beam, which was focused with the f = 50 mm focusing lens. Positioning of the samples under the laser beam was performed with the XY stages Aerotech ALS1000.

The laser spot overlap along a scanning line was controlled by the translation speed at a constant pulse repetition rate. Various combinations of pulse energy, beam overlap and wavelength were used for etching the films. Optimal regimes for laser processing were estimated depending on the wavelength (1064 nm, 355 nm). The beam overlap played an important role in the processing selectivity because the ablation threshold was sensitive to accumulation of the irradiation dose. The laser processing parameters for selective removal of every layer were estimated.

The quality of processing was evaluated with an optical microscope and atomic force microscope (AFM) CP-II (Veeco). Profiles of the laser ablated holes and trenches and chemical composition of the resulting surfaces were controlled with the scanning electron microscope (SEM) EVO 50 XVP (Zeiss) with the X-ray energy dispersion spectrometer (EDS).

3 RESULTS

3.1 Estimation of the energy density for selective film removal

Series of samples were prepared by ablating craters and trenches in the thin films with picosecond lasers, varying the wavelength of radiation (1064 nm, 355 nm). In case of 1064 nm wavelength, craters were made with a single laser pulse or burst of pulses, consisting of 10, 100 or 1000. Experiments were repeated at least 10 times, and laser pulse energy was changed between series of experiments. When energy density (fluence) exceeded a certain value depending on material properties, material was evaporated and removed. Experiments were performed on the molybdenum film and the polyimide substrate. We used a standard method to estimate the ablation threshold [11]. The diameter of craters D etched by laser radiation were measured. The dependence of D^2 from laser energy density F in logarithmic scale was estimated and laser fluence value which corresponds to $D^2=0$ was considered as the ablation threshold of material. The results of evaluations are shown in Table 1.

Table 1. Single pulse and multi-pulse (10, 100, 1000) ablation thresholds of molybdenum film and polyimide. Laser: PL10100, 10 ps, 1064 nm. Numbers 1, 10, 100, 1000 are for the number of laser pulses to ablate a crater

	Ablation threshold F_{th}, J/cm^2			
Laser pulses	1	10	100	1000
Molybdenum	-	5.89	0.9	0.14
Polyimide	1.59	-	0.44	0.13

The molybdenum ablation threshold felt down with an increase of the number of pulses applied to irradiation. The variation can be expressed by an accumulation parameter [12] with a typical value for bulk metals of $\xi = 0.9–0.7$. Evaluation of the accumulation parameter was performed for the molybdenum film and polyimide. Results are shown in Fig. 3. Our value for the molybdenum film is quite low ($\xi = 0.19$), probably because of limited heat dissipation in the thin film.

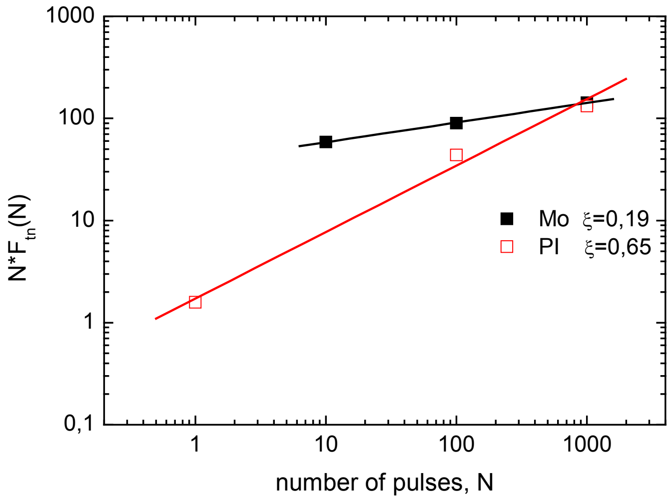

Fig. 3. Relation between the number of laser pulses N used to ablate a crater and the multi-pulse ablation threshold of molybdenum film and the polyimide substrate

Polyimide experienced less variation in its absorption properties. Its ablation threshold also fell down with a number of laser pulses applied, but the effect was less noticeable. Ablation properties of both materials became closer in the multi-pulse regime, making selective removal more complicated. Therefore, we limited overlap of laser pulses in the scribing regime when trenches were produced in the films.

3.2 Formation of the Molybdenum backcontact

The backcontact is made of the metal film, preferable molybdenum, directly deposited on the substrate. Structuring of the backcontact should be the first laser process in a production line. A homogeneous film of the metal is divided into stripes by local removal of the film and forming isolation trenches in it. Good isolation between the nearby contact lines and the diminishing effect on the substrate are the main requirements at this stage.

As the ablation thresholds of molybdenum and polyimide were close to each other at high beam overlap, we limited the experiments to a high translation speed when only a few laser pulses affected the same area of the film. Using the infrared 1064 nm laser radiation, the molybdenum film was removed from the substrate. The metal was not evaporated but formed ridges from melt on rims of the processed trenches (Fig. 4a).

Similar experiments were performed using laser radiation converted to ultraviolet (UV) at the 355 nm wavelength. Removal of the metal film by evaporation from the polymer substrate with a low melting temperature, tended to damage the substrate by the high intensive center of the laser spot. The main difference of the processing quality using the UV radiation was clean edges of trenches without appreciable melt formation (Fig. 4b).

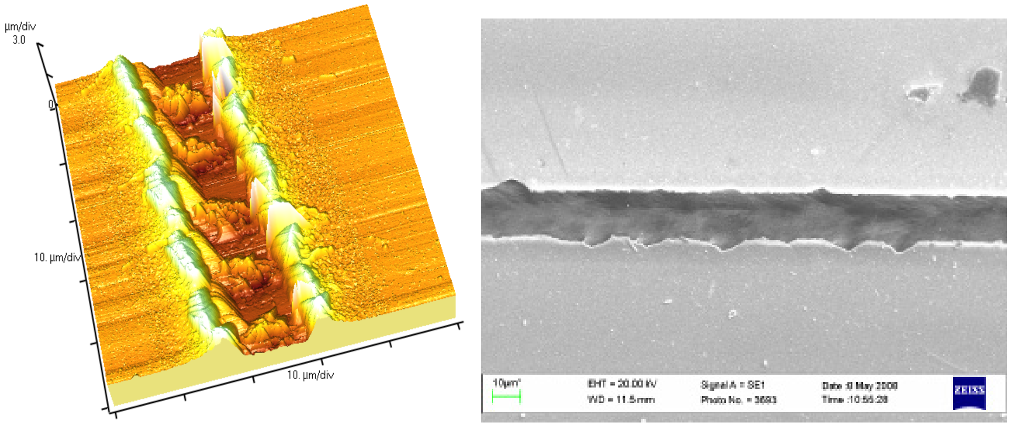

a) b)

Fig. 4. Pictures of trenches ablated with a laser: a) AFM picture (laser: λ=1064 nm, 2.4 W, 50 kHz, translation speed 600 mm/s); b) SEM picture (laser: λ=355 nm, 2.35 W, 100 kHz; translation speed 600 mm/s)

3.3 Exposition of the backcontact

The semiconducting and solar light absorbing layer of $CuIn_xGa_{(1-x)}Se_2$ deposited on the backcontact should also be structured making parallel trenches in it. We used a complete structure of layers in our experiments instead of a semiproduct to evaluate the processing regimes. The goal at this stage was to remove all the top layers, including CIGS and to expose the molybdenum backcontact.

The UV laser radiation (355 nm) was applied at this stage of investigations. It was used to ablate selectively trenches in layers of the CIGS solar cell structure. We estimated the following regimes for selective removal of films:

- to evaporate the upper electro-conducting layer of ITO;
- to remove the semiconducting film and expose the molybdenum backcontact;
- to make an isolation trench by laser ablation of all films down to the polyimide substrate;
- to cut a complete structure of the CIGS solar cell together with the substrate.

The process parameters of the regimes are presented in Table 2.

Table 2. Regimes of selective removal of layers and cutting the CIGS multilayer structure in solar cell formation. (Laser PL10100: P= 2.35 W, λ=355 nm, 100 kHz).

Regime	Scanning speed, mm/s	Process
#1	900	Removal of the ITO film
#2	380	Exposition of the Mo back-contact
#3	150	Isolation trench until polyimide
#4	35	Cutting of the CIGS multilayer

SEM pictures of trenches ablated in CIGS structure at different regimes (Table 2) and distribution of main chemical components in the cross-section of trenches are shown in Fig. 5.

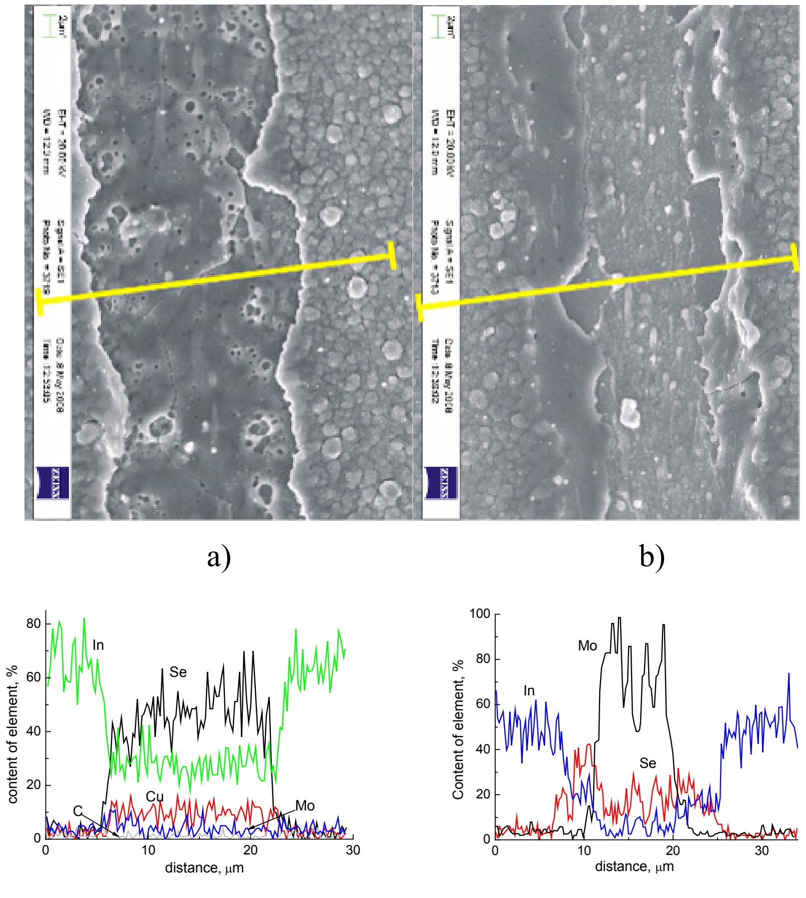

a) b)

c) d)

Fig. 5. SEM picture of a trench ablated in: a) the ITO/ZnO top layer to expose the absorber film (translation speed 900 mm/s); b) down to the Mo layer to expose the backcontact (translation speed 380 mm/s). Laser: 2.35 W, λ=355 nm, 100 kHz. EDS cross-section of a trench ablated in: c) the ITO/ZnO top layer to expose the absorber film (translation speed 900 mm/s); d) down to the Mo layer to expose the backcontact (translation speed 380 mm/s)

The top layer of ITO and thin buffer layers of ZnO and CdS were removed at regime #1 cleanly (Fig. 5a). The Se and Cu signals were detected with the EDS at the bottom of trench with a synchronous decrease in the concentration of In. Those elements construct the absorber layer. Molybdenum and carbon were found at the background level.

The 355 nm radiation was badly absorbed by ITO and thermal exfoliation prevailed [8]. The surface of the CIGS layer shows some marks of melting in the central part of the trench. As the properties of the surface of CIGS strongly depend on the bulk stoichiometry [13], heating might affect electrical properties of CIGS and special experiments are intended.

When the translation speed was reduced to 380 mm/s keeping all other processing parameters the same (Fig. 5b) the laser was able to evaporate CIGS film and expose the Mo backcontact. The high signal of Mo atoms was detected with the EDS in the central part of the trench. The trenches had inclined walls. This is a consequence of the Gaussian spatial distribution of energy in the laser beam. Slopes of the trenches were formed of a partially removed layer and in case of Fig. 5b. included $CuIn_xGa_{(1-x)}Se_2$ as quite strong signals of Se were detected with EDS. The trenches were narrow enough to ensure dense dislocation of separation lines between elements in solar cells. The upper layer of the top contact was not affected outside of the irradiation area.

4 CONCLUSIONS

Laser direct write with the picosecond pulse duration was applied in structuring the thin-films deposited on the polyimide substrate. The wavelength of laser radiation was adjusted depending on optical properties both of the film and the substrate. Absorption of laser radiation by the film material was essential to initiate its controllable removal.

- A narrow processing window of laser fluence and pulse overlap was estimated with both 1064 nm and 355 nm wavelength of laser radiation to remove the molybdenum backcontact off the substrate. The ablation thresholds of Mo and polyimide became closer due to the defect accumulation which increased with the beam overlap.
- The selective removal of ITO, CIGS and Mo layers was achieved with the 355 nm irradiation without significant damage to the underneath layers.
- Scribing the thin film layers with the Gaussian beam profile caused damage in the center of laser machined trench. To avoid damage and increase process productivity it is necessary to convert it to a flat top profile beam.
- The EDS analysis showed no residues of molybdenum projected onto the walls of ablated trench due to melt extrusion. Processing with picosecond lasers should not cause short-cut formation and degradation of photo-electrical properties of the solar cells but verification is required.

REFERENCES

1. N.G. Dhere, Solar Energy Materials and Solar Cells, 91, 1376 (2007).
2. R. Tanaka, T. Takaoka, H. Mizukami, T. Arai, Y. Iwai, Proc. SPIE 5063, 370 (2003).
3. D. Ashkenasi, A. Rosenfeld, *Proc. SPIE* 4637, 169 (2002).
4. J. Hermann, M. Benfarah, et al., J. Phys. D, 39, 453 (2006).
5. A.D. Compaan, I. Matulionis, S. Nakade, Optics and Lasers Engineering 34, 15 (2000).
6. C. Molpeceres, S. Lauzurica, J.L. Ocana, J.J. Gandia, L. Urbina, J. Carabe, J. Micromech. Microeng. 15, 1271 (2005).
7. S. Kijima, T. Nakada, Jap. Appl. Phys. Express, 1, 075002 (2008).
8. G. Račiukaitis, M. Brikas, M. Gedvilas, T. Rakickas, Appl. Surface Science, 253, 6584 (2007).
9. G. Račiukaitis, M. Brikas, M. Gedvilas, G. Darčianovas, J. Laser Micro/Nanoengineering, 2(1), 1 (2007).

10. G. Račiukaitis, M. Brikas, G. Darčianovas, D. Ruthe, K. Zimmer, Proc. of SPIE 6732, 67320C (2007).
11. J.M. Liu, *Opt. Lett.*, **7**, 196 (1982).
12. Y. Jee, M.F. Becker and R.M. Walser, J. Opt. Soc. Am. B, 5, 648 (1988).
13. A. Rockett, Thin Solid Films 361-2, 330 (2000).

6. C. Molpeceres, S. Lauzurica, J.L. Ocana, J.J. Gandia, L. Urbina, J. Carabe, J. Micromech. Microeng. 15, 1271 (2005).
7. S. Kijima, T. Nakada, Jap. Appl. Phys. Express, 1, 075002 (2008).
8. G. Račiukaitis, M. Brikas, M. Gedvilas, T. Rakickas, Appl. Surface Science, 253, 6584 (2007).
9. G. Račiukaitis, M. Brikas, M. Gedvilas, G. Darčianovas, J. Laser Micro/Nanoengineering, 2(1), 1 (2007).
10. G. Račiukaitis, M. Brikas, G. Darčianovas, D. Ruthe, K. Zimmer, Proc. of SPIE 6732, 67320C (2007).
11. J.M. Liu, *Opt. Lett.*, **7**, 196 (1982).
12. Y. Jee, M.F. Becker and R.M. Walser, J. Opt. Soc. Am. B, 5, 648 (1988).
13. A. Rockett, Thin Solid Films 361-2, 330 (2000).

CYSENI 2009, May 28-29, Kaunas, Lithuania
ISSN 1822-7554, www.cyseni.com

FAST RESPONSE TIME PHOTOEMISSION MEASUREMENTS OF GAS TEMPERATURE BEHIND THE SHOCK WAVES

Y.A. Baranyshyn, O.G. Penyazkov
A. V.Luikov Heat and Mass Transfer Institute
P. Brovka str. 15, 220072 – Belarus
Phone: 375 17 284 23 87
E-mail: baranishin-83@mail.ru

K.N. Kasparov, L.I. Belaziorava
B.I. Stepanov Institute of Physics
Independence av. 68, 220072 – Belarus
Phone: 375 17 284 17 55

ABSTRACT

There are some objective difficulties in measurements of a gas temperature with a a fast respons time, especially, when chemical reactions occur between the different gas compounds. A photoemission method for gas temperature detection with 1 μs time resolution is presented in this report. The technique is applied for temperature measurements in reaction flows behind reflected shock waves. The object of research was the luminescence of reaction methane/hydrogen/air mixtures behind shock waves reflected from plain and conical walls. Initial post-shock conditions were determined on the basis of incident shock wave velocity measurements from the 1-D shock relations assuming vibrational equilibrium and frozen chemistry. Of the course of the studies the temperature histories were dermined during strong auto-ignitions of investigated gas mixtures. Results were compared with theoretical values of Chapman-Juguet temperature of combustion products $T_{C\text{-}J}$. It was demonstrated that theoretically and experimentally determined temperatures are in good agreement.

Keywords: gas temperature measurement, combustion, methane/hydrogen/air mixtures, shock tube

1. INTRODUCTION

There are some difficulties in temperature measurements of hot gases with a high time resolution, especially, when fast chemical reactions occur between different gas components. Usually, if we want to use some optical technique for those measurements it is necessary to know the emissivity of an object. In most cases, the emissivity is unknown or changes at conditions of the experiment. Besides, the emissivity itself depends on temperature. A method of temperature measurement with the 1 μs time resolution is presented in this report.

As follows from the Einstein law for the photoeffect, the photoelectron energy distribution depends on the quantum energy of electromagnetic radiation. The quantum energy rising of monochromatic radiation increases the maximum and most probable velocities in the Maxwell photoelectron distribution in the vicinity to the photocathode. Using different methods, one can detect and measure this changing of energy distribution, for example, in the photoelectric device it can be made by measuring photocurrent cutoff voltages for normalized monochromatic light fluxes or for heat fluxes at constant temperature [1]. Light fluxes are normalized to the photocurrent I_0=const, when a retarding voltage at control electrode is zero $U_r = 0$.

The quantity of electrons of different energies in an electron spectrum emitted under radiation of any wavelength does not depend on the light flux value. That is why, the ratio $m=I_0/I$ of non-modulated (upper) and modulated (low) currents of the photomultiplier within the linearity of its characteristic is the value characterizing the given temperature T. When temperatures are identified through this value, one can deal with non-normalized light fluxes. It much simplifies measurements, as the measurement of an object spectrum is reduced to obtaining the ratio of m(T). The monochromatism of the light flux should be known a priori. The temperature is identified by the previous calibration – by the dependence of the retarding voltage U_r (or the photocurrent I at a constant retarding voltage) on a temperature T: $U_r = f(T)_{|Io=const}$ or $I = f(T)_{|Io=const,\ Ur = const}$, or by the relation m = f(T).

Two properties of this method make it very useful. At first, there is no necessity to use some disperse or focusing optics. This causes the greatest possible optical efficiency of the photoemission device. This permits one to measure the radiation of low luminous objects. The second property is the simplicity of photoelectron modulation at frequencies of 1 MHz and more. This allows performing measurements in fast phenomena and emissivity of the object does not affect the results of measurements [1, 2]. For instance, when the rate of temperature changing is 10^8 K/s.

The photoemission method can be applied for temperature measurements of hot gases or plasma, only if its line or band spectrum is similar to a continuous spectrum. Such conditions are satisfied at high pressures or at high density of spectrum lines in the spectrum interval, in which the temperature is measured. In other words, the luminous radiation should be thermal and locally equilibrium in nature. For example, this method can be applied for temperature measurements of particles in the heated gas flow. The radiation of an ensemble of heated particles in the shock tube theoretically approximates the radiation of an absolutely black body. So, we can apply this method for temperature measurement in the shock tube and also during the chemical processes, when there the local equilibrium conditions are reached.

2. MEASUREMENT TECHNIQUE

A sensor is a photomultiplier (PMT). Modulating rectangular pulses are applied to a control electrode of the PMT. In Fig. 1 the schematic of the photoemission pyrometer is presented. Radiation from object 1 through collimator 2 illuminates photocathode 3 of photomultiplier 4. The light flux can be decreased by neutral filter 5. A signal from the PMT anode through amplifier 6 comes to an input of digital oscillograph 7. For photoelectron modulation, generator 9 permanently supplies rectangular pulses of an oscillation period duration of 1 μs to control electrode 8. The display of computer 10 shows a video pulse U(t). The temperature can be obtained via registering the modulated photocurrent and current ratios of m(t). By using available calibration curve T(m) the temperature T(t) one can be obtained.

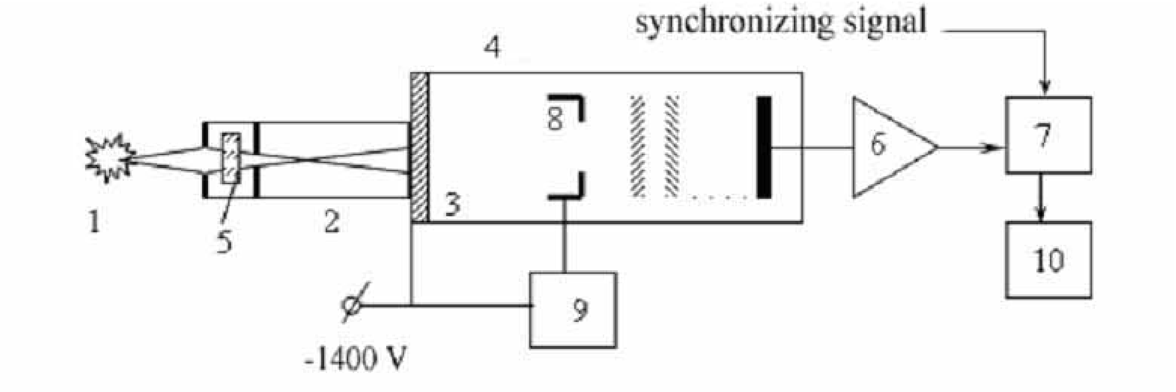

Fig. 1. Schematic of the pyrometer: 1 – object of radiation, 2 – collimator, 3 – photocathode, 4 – photomultiplier, 5 - neutral filter, 6 – amplifier, 7 – digital oscillograph, 9 – generator of rectangular pulses, 10 - display of computer

The pyrometr calibration was performed using the temperature lamps. A result was approximated by the function T = $A_1\exp(A_2m)+A_3\exp(A_4m)$, where coefficients A_1, A_2, A_3, A_4 was calculated by the least-squares method. So we used the calibration curve as continuois function, which treats the pyrometer signal. The calibration setup (a) and calibration curve (b) of the pulse photoelectron pyrometer are presented in Fig. 2.

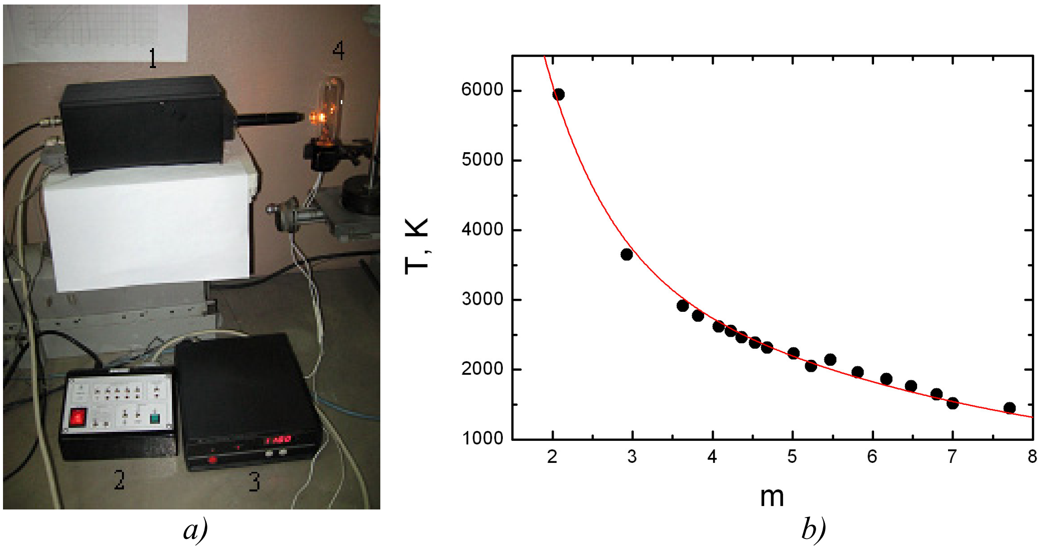

a) *b)*

Fig. 2. The calibration setup (a) and calibration curve (b) of the pulse photoelectron pyrometer: 1 – the pulse photoelectron pyrometer, 2 – a control panel, 3 – a high voltage power supply, 4 – a temperature lamp

3. EXPERIMENTAL

The object of research was the luminescence of methane/hydrogen/air mixtures at auto-ignitions behind reflected shock waves. The stainless steel shock tube 76 mm in diameter and 8.5 m long with a reflected plane and conical walls was applied for these studies (Fig. 3).

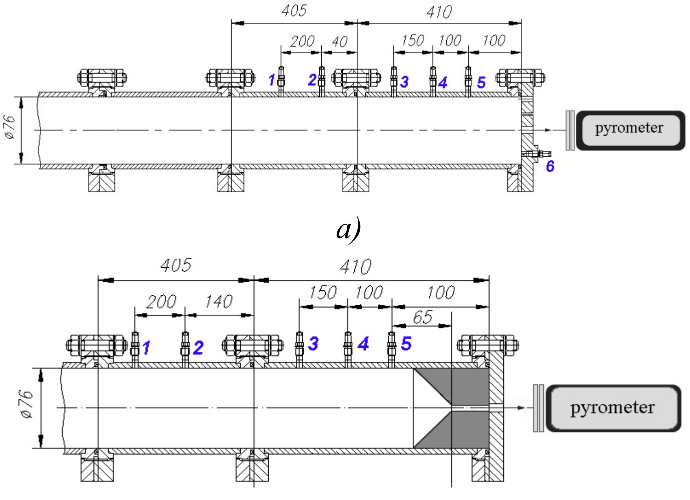

a)

b)

Fig. 3. Schematic of the test section for auto-ignition studies in methane/air (a) and hydrogen/air (b) mixtures in a 76-mm shock tube: 1-6 – high-frequency pressure transducers

High-frequency pressure sensors were used for pressure monitoring along the tube. To detect the luminescence the 8 mm quartz rods were mounted into the end wall, from which the radiation impinges on the registering PMT tube. Post-shock conditions were determind from incident shock wave velocity measurements by the 1-D shock relations, assuming vibrational equilibrium and frozen chemistry [3, 4].

Owing to the nonuniformity of a gas its temperature was not constant in time and in different cross-sections of the shock tube. The result is averaged over temperature along an observation path because the photoemission pyrometer detects the luminescence coming from different locations along the tube. An error of the temperature measuring using pulse photoelectron pyrometer is 5%.

For auto-ignitions of methane/air mixtures all luminosity records were obtained at identical experimental post-shock conditions. During the first 6 µs from the moment of ignition we registered the low luminescence that was 5–6 times higher than a dark current. Then the flash of main luminescence follows, for which one luminosity peak increases more than 20 times and reaches a maximum value. The duration of this second phase is 6–8 µs. In the third phase the light flux decreases quickly 2–3 times in the one- or two-stage process with the duration of each stage of about 30–50 µs. Then the light flux slowly decreases 5–7 times at 1 µs. The explosion of a rich methane/air mixture differs only by the last phase. The light flux increases during 600 µs after detonation. For a rich mixture (Fig. 4) the signal of pressure and luminescence (a) and measured temperature and luminescence (b) are presented. The measured average temperature behind formed C-J detonation is about 2600 K. The theoretical predicted one $T_{C\text{-}J}$ = 2700 K. So, the experimental results and predictions are in good agreement.

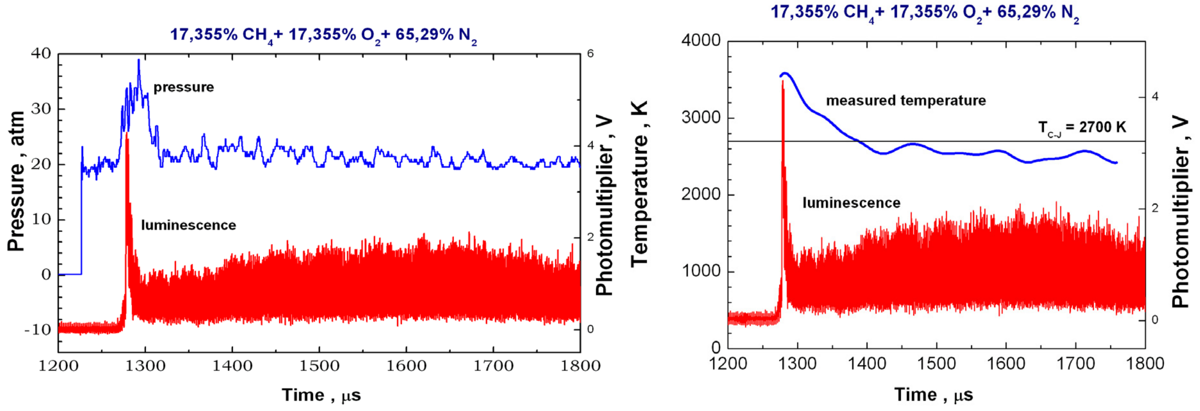

a) *b)*

Fig. 4. Signal of pressure (from the sensor in the reflected wall) and luminescence (a) and measured temperature and luminescence (b) at auto-ignition of a rich methane/air mixture $17.355\%CH_4+17.355\%O_2+65.29\%N_2$ behind the reflected shock wave

The similar experiments in stoichiometric hydrogen/air mixtures were performed at shock wave reflection from a conical cavity. The studies were performed for strong auto-ignitions when the detonation was instantaneously formed in the localized focusing area in the vicinity of the cavity apex [5, 6]. Fig. 5 shows the results of pressure and luminescence observations (a) and corresponding temperature measuring (b). The first temperature spike ≈ 3400 K exceeds the equilibrium C-J temperature because of the significant local primary gas compression. The next detonation expansion results in the visible gas cooling due to rarefaction of combustion products. The subsequent reflection and converging of bow shocks from the side wall of the tube results in the secondary axial gas compression and occurrence of the second temperature spike ≈ 3600 K. It should be noted that the photocurrent between two spikes is low, so it is impossible to perform correct temperature measurement. When steady state detonation is already propagated in the post-shock flow behind the incident shock wave at 600–900 μs, the measured temperature 2900–3040 K corresponds well to the calculated equilibrium $T_{C\text{-}J} = 2917$ K.

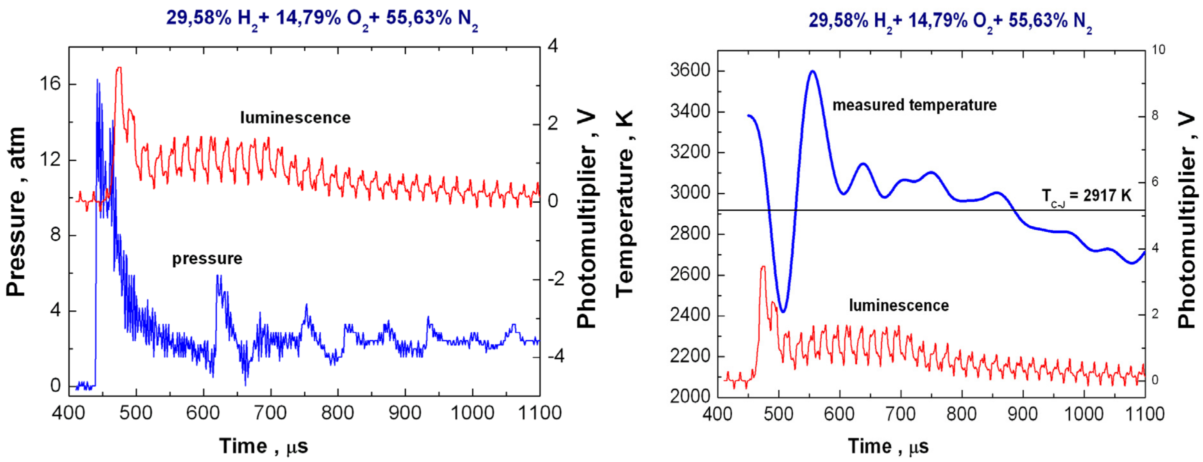

a) *b)*

Fig. 5. Pressure (from the sensor in the reflected wall) and luminescence (a) and measured temperature and luminescence (b) at auto-ignition of a stoichiometric hydrogen/air mixture behind the shock wave reflected from a cone

4. CONCLUSION

The photoemission method for temperature measurement with a 1 μs time resolution was described. The technique was applied for recording current gas temperatures in reacting flows behind the shock waves reflected from plane and conical walls. It is shown that calculated and experimental temperatures are in good agreement.

ACKNOWLEDGMENTS

This project was sponsored by State Research Programs “Hydrogen” and “Nanotechnologies and Nanomaterials”.

REFERENCES

1. K.N. Kasparov. Heated body temperature measurement by spectrometry of photoelectrons // Measurement Science and Technology. 1998, v. 9, p. 1388.
2. K.N. Kasparov. A photoemission method of temperature measurement. Two methods of a procedural error determining // Measurement Technique. 2004, v. 8, p. 62.
3. A.G. Gaydon, I.R. Hurle. The shock tube in high-temperature chemical physics. 1963.
4. R.I. Soloukhin, Shock waves and detonations in gases. 1963.
5. O.V. Achasov, S.A. Labuda, O.G. Penyazkov. Shock wave and jets initiation of gaseous detonation // Archivum Combustionis. 1995, v. 15, № 3-4, p.253-274.
6. O.G. Penyazkov, K.A. Ragotner, K.L. Sevruk, V.E. Tangirala, A.J. Dean, B. Varatharajan. Autoignition of propane/air mixture at shock wave focusing in three-dimensional ducts // In: Pulse and Continuous Detonation Propulsion, Pulse and continuous detonation propulsion. 2006, p. 43–60.

REALIZATION AND ANALYSIS OF INORGANIC METAL OXIDES PLASMA MELTING AND FIBRILLATION PROCESS

M. Milieška, R. Kėželis, V. Valinčius
Laboratory of Plasma Processing
Lithuanian Energy Institute
Breslaujos str. 3, LT-44403 Kaunas – Lithuania
Phone: +370 37 401 895
E-mail: milieska@mail.lei.lt

ABSTRACT

The presented new plasma technology for production of fiber from inorganic metal oxides overtakes traditional sustaining technologies due to simplicity of processing and quality of obtained product. This paper contains the description of uniflow plasma chemical reactor designed for melting and fibrillation of ceramic materials, the analysis of its optimal exploitation conditions at atmospheric pressure and characterization of final product obtained during the realization of the plasma fibrillation process.

An air was used as plasma forming gas and propane-butane as additional supporting gas. The power of plasma torch was in range of 66–68 kW, temperature and velocity of gas leaving the reactor was 2316–2516 K and 500–530 m/s, respectively. Mineral fiber was manufactured from different dolomite and quartz sand mixtures. The amount of dolomite in the mixtures varied from 25% to 35%. The structure and morphology of mineral fiber was examined by scanning electron microscopy (SEM). The process of fiber formation was analyzed by visualization using a CCD camera.

Fibers have been formed by kinetic energy of the flow. The mechanism of fiber formation is explained. Mineral fiber produced employing plasma fibrillation process is resistant to high temperatures (up to 1300°C), the diameter of the fiber filament doesn't exceed 2–5 µm. It is more suitable for production of high temperature or noise isolators, catalysts or filters.

INTRODUCTION

Mineral fiber is a general name for many kinds of inorganic insulation materials made of inorganic metal oxides. There are generally three categories of mineral fiber according to maximum temperature endurance. These are glass wool (from 230°C to 250°C), stone wool (from 700°C to 850°C) and ceramic fiber (up to 1200°C) [1].

Ceramic fiber made of inorganic metal oxides because of their light weight, thermal shock resistance, and strength are useful in a number of industries as high temperature and noise insulators, filters and catalysts. Materials used for manufacturing high temperature mineral fiber must be resistant to high temperatures and fire, display low thermal conductivity and chemical stability. The product must be relatively cheap and environmentally friendly such that it would be affordable by the average industry. Such properties display raw materials like quartz, dolomite, zeolite, granite, basalt, limestone, etc.

There exist several production methods for manufacturing of mineral fibers, with a wide variation of quality and quantity of the final product. The most commonly used mineral wool production process is the fibrillation of molten bulk on rapidly rotating spinning discs. The molten substances enter through a siphon neck into a homogenization reservoir, pass a weir and directing channel and under gravity falls onto a rotating disc of the spinning machine. After this the mineral wool reaches the conveyor belt of the secondary mineral wool layer where it is thermally treated and finalized to selected density, thickness and size [1].

This method requires quite complex equipment and uninterrupted fabrication technologies. Upcoming demands for high quality and new functionality products often means that traditional production methods are finding it increasingly difficult to produce refractory or compact fiber for wide range applications. On-stream technological process is required for these purposes. So, traditional technologies are unusable for high temperature resistance fiber production [2].

METHODOLOGY

In Laboratory of Plasma Processing of Lithuanian Energy Institute a specific plasmachemical jet reactor (Fig. 1) with linear step formed DC plasma torch (PT) 66–68 kW of power capacity for melting and fibrillation of inorganic metal oxides at atmospheric pressure was designed. An air was used as plasma forming gas and a propane-butane – as additional supporting gas to increase heat flux from plasma flow to dispersed particles. The propane-butane gas also improves a balance of oxygen-nitrogen mixture in plasma simultaneously increasing the temperature inside the reactor.

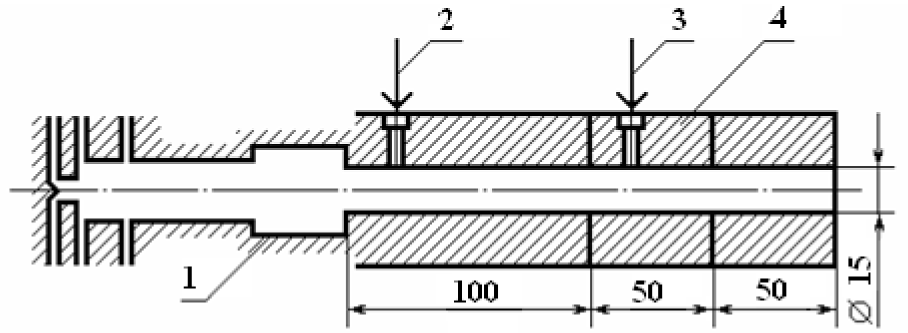

Fig. 1. Schematic presentation of uniflow plasmachemical reactor: 1 – plasma torch, 2 – injection place of raw material, 3 – additional gas feeding, 4 – transformable reactor sections

The uniflow plasma chemical reactor connected to plasma torch consists of four sections 0.015 m diameter and 0.05 m length made of stainless steel and cooled by water. Such design enables to change the length of the reactor, if needed. If it is necessary the diameter of outlet exhaust can be reduced from 0.015 m to 0.007 m. As the diameter of outlet exhaust is smaller, the velocity of plasma and dispersive particles leaving the reactor is higher. In some cases it exceeds the velocity of sound [3].

RESULTS AND DISCUSSION

The types of dolomite and quartz sand mixtures were prepared for melting and conversion into fiber (Table 1). These materials were selected because of their comparatively high melting temperature, suitable viscosity, low cost and prevalence. The dolomite amount in the mixtures varied between 25–35%. Composition of mixtures and range of basic parameters in plasmachemical reactor are presented in Table 1.

Table 1. Composition of experimental feeds and plasma jet reactor regimes

No.	Dolomite, %	Quartz sand, %	PT power, kW	Air flow rate, g/s	Propane-butane flow rate, g/s	Exhaust gas temperature, K	Flow velocity, m/s
1.	25	75	66.2	23.245	0.985	2316	507
2.	30	70	68.5	22.726	1.049	2454	522
3.	35	65	67.9	22.608	1.151	2516	533

The table above shows that three different mixtures of dolomite and quartz sand were melted and converted into fiber at similar conditions. Therefore it is possible to analyze the structural and morphological differences of the mineral fibers obtained (Fig. 2).

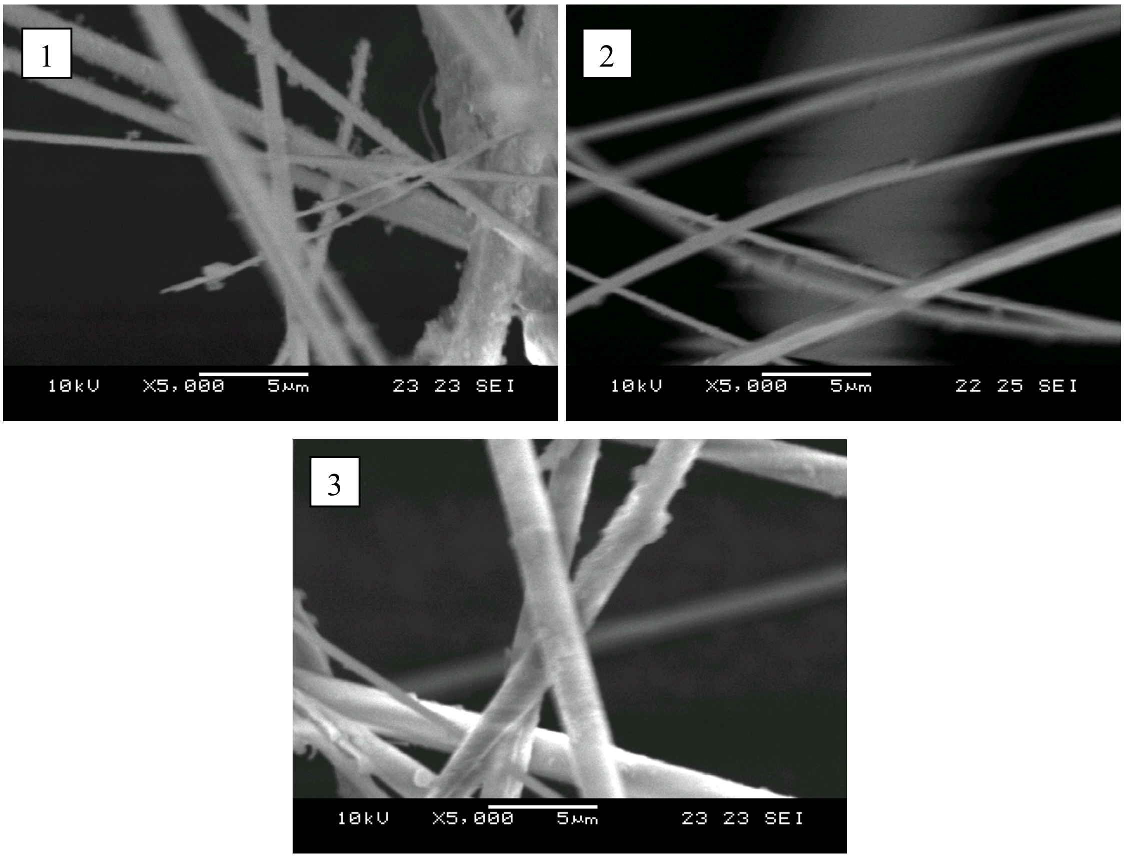

Fig. 2. Mineral fiber of dolomite and quartz sand mixture. The number of sample correspond the regime in Table 1

As it can be seen in Fig. 2 despite the temperature plasma flow of the leaving the reactor filaments of comparatively higher diameter in the bulk has been observed. The average diameter of filament was approximately 300 nm – 5 µm and the average length was about 10 cm. As the plasma torch applied voltage arc current and plasma forming gas flow rate was almost constant, the diameter of filament decreases with the increase of melting temperature of the mixture. So, the thinner fiber has been obtained in the case when the quantity of quartz sand in the mixture is bigger. The possible explanation of this fact seems to be the difference of a density behavior of melted mixture of different composition at the same temperature. While the melting temperature of pure dolomite is 2670 K and 2000 K of quartz sand [4] the melting temperature of dolomite and quartz sand mixture is in range of 1250–2400 K.

While the temperature of entering the reactor plasma flow is about 3500 K and decreases along the length of the reactor, the difference between the entering and leaving the reactor flow temperatures is about 1000 K. This temperature drop is influenced by the heat transfer between the dispersed particles, plasma flow and reactor walls. When the particles of dolomite and quartz sand mixture enters the reactor, the temperature of the flow is sufficient for melting all of those particles. When the melt flow comes to the outlet of the reactor, the temperature of the flow decreases, so its viscosity increases. The best conditions for fiber production are achieved when the melt viscosity is about 5 Pas [5]. The viscosity of the mixture with 35% of dolomite is higher than the mixture with 25% of dolomite because the melting temperature of dolomite is higher than quartz sand melting temperature. So, it influences the quality of produced fiber.

The dispersed particles start to mix with turbulent plasma flow when they enter the reactor. The smallest particles sublimate or evaporate immediately because the flow temperature is very high. Bigger particles stick to the reactor walls and flows out of the reactor as a melt. Plasma flow kinetic energy drags little drops out of the melt, stretches them and forms a fiber. The biggest particles do not melt completely and goes out of the reactor as granules. Fig. 3 shows the pictures obtained by Redlake MotionPro X4 high speed camera during the experiment of the regime No 2 (Table 1).

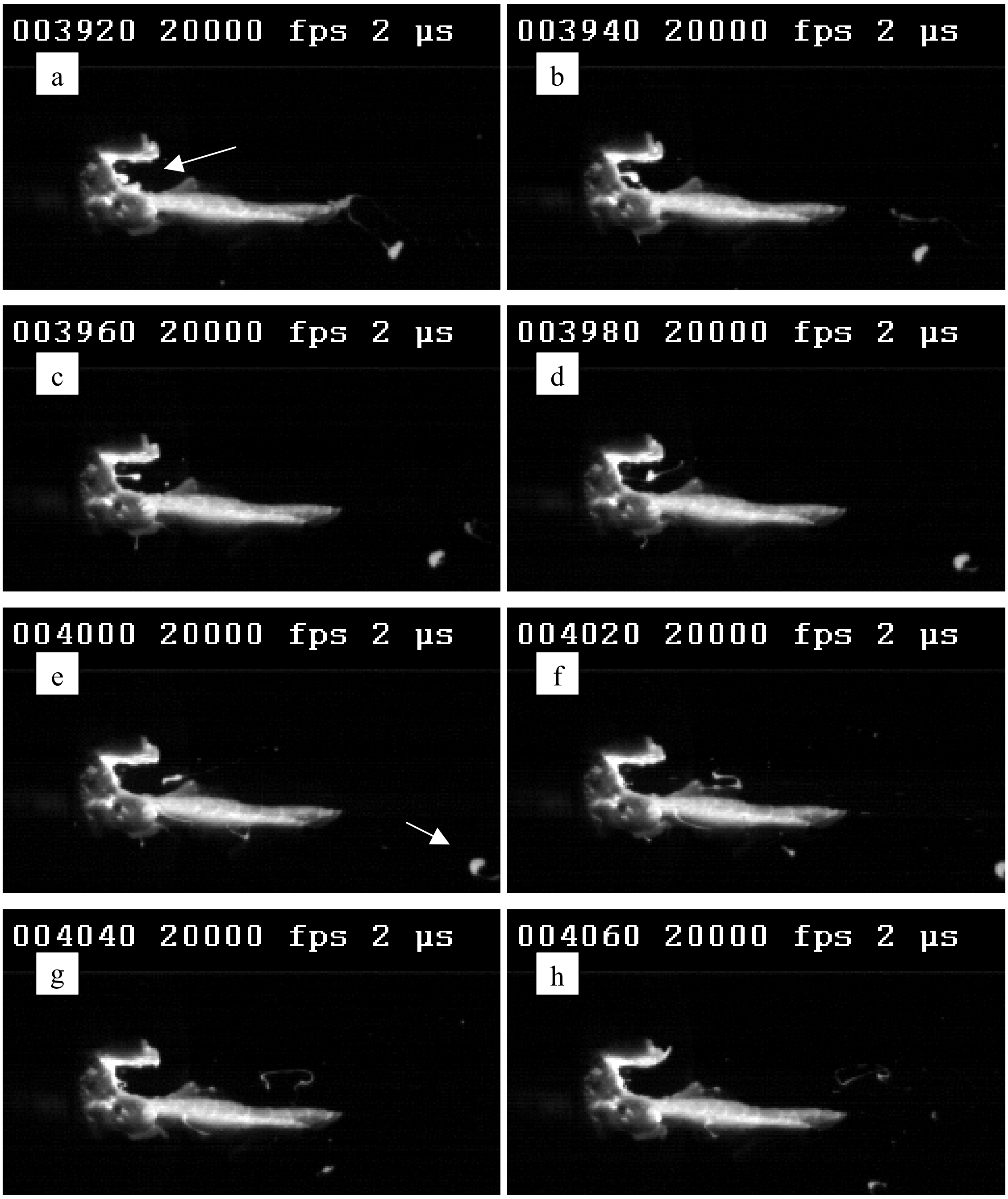

Fig. 3. The behavior of single fiber filament captured by high speed camera

In the marked place in Fig. 3a the stream of hot melt appears. The viscosity of the melt is high enough for drawing filaments. However a part of the melted stream chills and solidifies, especially near the cold wall zone and on the border with plasma jet. Other part of the stream is heated by plasma flow and keeps its temperature higher than melting temperature. This stream is increasing in volume because the velocity of melted substance leaving the reactor decreases. Therefore there appears partly melted structures volume and mass of which increases during the soldering process. They don't solidify fully because the temperature of the melt is high enough. In this reason certain partly melted small pieces may separate and get blown out of the vents at any moment. Then the kinetic energy of the plasma flow drives the melted domain and drags a fiber filament.

The time of forming of single filament of fiber is possible to estimate from Fig. 3. It depends mainly on the size of partly solidificated domain, viscosity and gas flow velocity. In the presented case the time required for the formation of fiber is in the order of 7 ms.

White spots in the segments of Fig. 3 (marked in Fig. 3e) – not fully melted particles and separated from the main layer particles turned into granules. Those granules moves with high velocity (~520 m/s) cool off and pollute the fiber collected on the mesh by sticking to it. To prevent that pollution the method of redirection of the fiber and granules to different sides must be employed. It has been found that granules separated from the fiber became hollow; therefore they could be used as high temperature material for specific application [6].

CONCLUSIONS

1. The amount of dolomite in the mixtures with quartz sand influences the shape and size of fiber filaments. The average diameter of produced fiber filaments increases increasing the amount of dolomite in the mixtures.
2. It has been found that there exists a possibility to form fibers employing kinetic energy of plasma flow. It drives the melted domains and drags fiber filaments.
3. The duration of formation of single fiber filament depend on the size of separated domain, viscosity of the mixture and gas flow velocity. In the presented case the time of prompt fiber filament formation is about 7 ms.

ACKNOWLEDGEMENTS

The authors acknowledge the Agency for International Science and Technology Development Programmes in Lithuania for financial support.

REFERENCES

1. M. Hocevar, B. Sirok, B. Blagojevic. Mineral Wool Production Monitoring Using Neural Networks // International Journal of Information Technology 2005, Vol. 11, Issue 9, p. 64–72.
2. V. Valinčius, R. Kėželis, P. Valatkevičius, M. Milieška. Melting and conversion into fibre dolomite and quartz sand mixtures by means of plasma spraying // Proceedings of 10th International conference on "Gas discharge plasmas and their technological applications". Russia: Tomsk. 2007, p. 441–444.
3. M. Milieška, R. Kėželis, R. Kalpokaitė-Dičkuvienė, J. Čėsnienė, K. Brinkienė, V. Mėčius. Application of plasma technology for nanofibre formation from oil refinery waste (zeolite) // Energetika. 2008, Nr. 4, p. 54–58. (in Lithuanian).

4. M. Milieška, V. Valinčius, R. Kėželis. Synthesis of high temperature mineral fiber in atmospheric pressure plasma jet // Proc. Of annual conference of young scientists on energy issues “CYSENI 2008”, Kaunas: LEI. 2008, p. 16–22.
5. K. Strazdas, P. Eidukevičius. Mineral and glass fiber. Vilnius. 1985, 19 p. (in Lithuanian).
6. R. Kėželis, V. Mėčius, L. Pranevičius. Al_2O_3 fibre synthesis by plasma technology // Energetika. 2003, Nr. 1, p. 46–50. (in Lithuanian).

CYSENI 2009, May 28-29, Kaunas, Lithuania
ISSN 1822-7554, www.cyseni.com

RESEARCH OF GLYCEROL COMBUSTION

K. Zakarauskas
Laboratory of Combustion Processes
Lithuanian Energy Institute
Breslaujos str. 3, LT-44403 Kaunas – Lithuania
Phone: (+370 37) 401877
E-mail: zakarauskas@mail.lei.lt

ABSTRACT

In the production of biodiesel derived glycerol fraction processing leads to expensive distillation method, where it is purified to the commercial glycerin. Pure glycerin is used in various industries: food, beverages, cosmetics, paper, pharmaceutical, tobacco industry, etc. The increase in biodiesel production volume increases glycerol supply. Such situation makes to look for rational and effective ways to use the phase of glycerol, one of most attractive ways would be for energy purposes. In this paper a possibility to burn glycerol which is formed in the bio-diesel production process is analyzed. A survey of sprinkled-off glycerol characteristics has been performed and optimum conditions for glycerol ejection have been established (glycerol temperature and pressure). Experimentation of technical glycerol combustion has been performed in a heated combustion chamber where glycerol is gasified and, after feeding-up required quantum of oxygen, high-level combustion is attained. After the experimentation of technical glycerol combustion, the emissions of main pollutants have been established: O_2, CO, CO_2, NO, NO_2, SO_2, solid particles and acrolein. In order to remove solid particles from combustion products a cyclone and a fiberglass filter sleeve have been engineered and produced, also theirs efficiency has been established. Heated glycerol is cracked into a carcinogen – acrolein (C_3H_4O). Therefore, further experimentation has been performed in order to estimate the remaining concentration of acrolein in the combustion products. The article includes glycerol combustion characteristics, test results and analysis.

Keywords: glycerol, glycerin, combustion, acrolein

1. INTRODUCTION

Biodiesel is an appealing alternative to diesel, which is promoted by the European Union legislation. In the process of biodiesel production a by-product is produced – glycerol. Producing one ton of biodiesel about 10% of glycerol is generated [1], and it constitutes ~ 6% [2] of biodiesel cost.

In order to implement the provisions of 2003/30/EC [3], Lithuania has undertaken that biofuels shall constitute 5.75% of total quantity of fuels used for transportation until the year 2010. Implementing the requirements of the laws of the Republic of Lithuania regulating biofuels and bio-oils, the production volume must be increased until 2010: 40 thousand tons of biodysel must be produced per year, so it constitute about 4 thousand tons of glycerol per year. According to Lithuanian press information, it is planned to construct a few new biodiesel production plants and their total annual production capacity should amount to ~270 thousand tons of biodiesel per year. Then glycerol production would amount to ~27 thousand tons per year.

At present, glycerol is used mostly in cosmetic industry, pharmacy, in the industries of alimentary products, beverages, paper, tobacco and other industrial fields, but when the oversupply of glycerol will be produced, new appliance methods and markets will be needed. Traditional methods of glycerol fraction utilization may be described as expensive distillation method: glycerol fraction segregated producing biodiesel has about 60% of glycerin, and the purity of glycerin used in cosmetic industry must be 99.98%.

Therefore, more effective and rational methods of glycerol fraction utilization and usage are needed, wherein one of the most appealing glycerol disposition methods would be its usage in energetic industry. Thus, in this paper work a possibility to burn glycerol which is formed in the biodiesel production process is analyzed.

2. METHODOLOGY

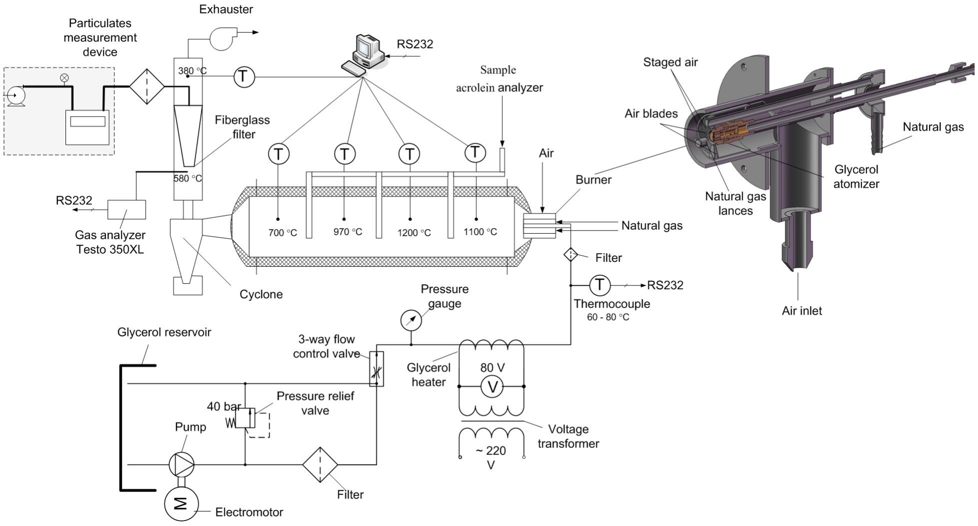

Fig. 1. Experimental setup for Glycerol Combustion

Glycerol combustion experimentation has been performed in the organic fuel combustion stand (1 Fig.), in the Lithuanian Energetic Institute, Laboratory of Combustion Processes. Glycerol was pumped up from the glycerol tank and supplied trough the electric heat echanger (wherein heated up to 60–85 ^{o}C) to the nozzle. A steady pressure of 40 bar was kept in the feeding system using protective valve. The quantity of glycerol was adjusted using throttle-valve and maintaining proper pressure. Glycerol has to pass two filters before the nozzle: (the diameter of filtering net Ø 700 µm) and thin cleaning filter (Ø 140 µm). When glycerol is fed to the nozzle, it flows to the distributor, passes through three tangentially mounted runners and gets into the twisting chamber. Twisted glycerol is ejected through outflow slot. Compressed air, which is fed into the burner, is regulated by needle-valve and controlled by flow measurement diaphragm differential manometer.

The adiabatic temperature of glycerol is 100–250^{o}C lower than adiabatic temperature of other ordinary liquid fuels.

In order to secure a steady glycerol combustion during the experimentation, the glycerol was supplied to the heated combustion chamber, where the temperature was reached up to 1000^{o} C using the natural gas. When this temperature is reached, the gas is turned off. Glycerol fraction, supplied into the heated combustion chamber, is gasified, and because of the flow distribution created by the burner an ignitable mixture of glycerol gas and air is produced, which is easily ignited.

Four termopores are installed in the combustion chamber. The indications from these termopores are collected using TC-08 (Pico) system and saved to the computer. In the chamber of fume analysis, a special fume analyzing equipment is installed: fume analyzer Testo 350 XL and the solid particles measurement device. The analyzer was used to measure O_2, CO, CO_2, NO, NO_2, SO_2 gas emissions. The concentration of fumes are solid particles was determined via weight method in accordance with the LAND 28-98/M-08 regulation [4].

In order to establish acrolein level, gas samples have been taken from three places in the combustion chamber. Acrolein was absorbed from combustion products using commercial

XAD®2 sorbents, and its concentration established using gas chromatograph Varian GC-3800. The concentration of acrolein have been measured using standard VDI 3862/5 [5] prepared by the German Association of Engineers.

The experiments were performed using a low purity fraction of glycerol, which was taken from one of the major Lithuanian biodiesel plant JSC „Rapsoila“. The parameters of glycerol are presented in Table 1.

Table 1. Parameters of glycerol

Quality indicators	Value
Molecular formula of glycerol 80-85% max9% max0,5% max9% max1,5% $C_3H_8O_3 + H_2O + CHOH + NaPO_4 + CH_3ROOH$	
Sulphur, mg/kg, not higher then	381
Flash point in open cup, °C, not lower than	109
Kinematic viscosity at 80 °C, mm^2/s, not higher than	15,2
Density, at 15 °C, kg/m^3	1260
Heat of combustion, MJ/kg, not higher than	12.2

3. RESULTS AND DISCUSSION

First of all, the purpose of glycerol fraction combustion research was to establish appropriate conditions and quality of combustion. According to the experimental resultsin all the interval of different load, the air overplus coefficient (behind the boiler) was from 1,68 to 1,52. Such a huge air overplus coefficient arises because of bad intermixture of air and fuel: in order to achieve the same boiler efficiency, when burning only glycerol (which has a low calorific value), the quantity of supplied fuel to the furnace has to be a few times higher. The quantity of air remains unchanged, because oxygen is present in the molecule of glycerol. In order to reach good glycerol combustion, the furnace of boiler must be bigger or the quantity of air supplied for combustion, must be increased. During the experimentations, in all the interval of different load NO_x (67÷90 mg/m^3), CO (73÷110 mg/m^3) and SO_2 (~0 mg/m^3) concentrations in emitted fumes from water heating boiler did not exceed the norms admissible under the requirements of LAND 43-2001. The experimental results of glycerol combustion in the Table 2.

Table 2 The experimental results of glycerol fraction combustion

Indicators	**Measure units**	**Bias**	**Mode**					
			Without filter sleeve			With filter sleeve		
Heat power	kW	±2	45			45		
Glycerol supply	kg/h	±2	13			13		
Air supply	m^3	±1	46			46		
Oxygen content in flue gases	%	±0,5	1.6	1.9	2	1.6	1.6	1.9
Air excess coefficient	–	±0,02	1.09	1.1	1.13	1.09	1.09	1.1
Carbon monoxide emission	mg/m^3	±20	90	73	110	80	90	73
Nitrogen oxide emission	mg/m^3	±14	87	88	88	90	87	88
Particulate emission	g/m^3	±25%	14,5	11,9	9,6	0,35	0,26	0,27

In the combustion products of glycerol there was a high concentration of solid particles, in average it constituted ~14,5 g/m^3. In order to remove solid particles from combustion products a cyclone was used and tested, but the measurements of solid particles indicated, that even cyclone was installed, the quantity of solid particles, produced in combustion process remained the same. Thus, it may be maintained that the diameter of the salts produced is <2µm [6,7].

Also, the efficiency of salt elimination was tested using a fiberglass filter sleeve. Thus, after fiberglass filter sleeve was installed, glycerol combustion experiments were repeated. The results of combustion and ratios of combustion quality (using this fiberglass filter sleeve and without it) are provided in the Table 2.

According to the results presented in the above mentioned Table 2, the quantity of solid particles has decreased by ~98% when fiberglass filter sleeve was installed and during all experiment it did not exceed 350 mg/m^3 (measured by standard 3% oxygen quantity). According to the regulation LAND 43-2001 (on emitted pollutants from fuel burning devices), the concentration of emitted solid particles from liquid fuel combustion devices may not exceed 250 mg/m^3. Thus, glycerol, which contains 9% of sodium salts (according to weight), may not be combusted separately based on the conditions of performed experiments. But if glycerol fraction would be mixed with other fuels, containing low quantity of solid particles, and fumes would be cleaned using the filter sleeve, then combustion would fully correspond to the requirements of LAND 43-2001.

In various sources of literature there is one fact stated: if glycerol is heated up to 280°C, it cracks into a carcinogen – acrolein (C_3H_4O). But if the combustion mode is regulated properly and carcinogen is kept for a proper time in high temperature, then it cracks into lower hydrocarbons, which are further oxidized to final combustion products. Therefore, further combustion experiments have been performed to evaluate the remaining concentration of acrolein in the combustion products. Burning the glycerol fraction, the temperature remained ~1000°C all over adiabatic combustion chamber (Fig. 1). The combustion products remain in the combustion chamber up to 2 seconds. According to the results it may be stated that acrolein is not cracked or only very low concentration is produced, which is lower than determinable measuring device margin. According to the methodology used, acrolein concentration may be determined when ≥ 0,092 mg/m^3.

4. CONCLUSIONS

1. According to the results of glycerol combustion experiments it was established that, if combustion process is properly regulated, in all the interval of different load glycerol is fully burnt to CO ~100 mg/m^3, NO_x ~ 90 mg/m^3, SO_2 ~ 0 mg/m^3 remaining concentration. But the measurement of emitted fumes proved that concentration of solid particles is high, because it has achieved the value up to 14,5 g/m^3.
2. After a cyclone (device collecting solid particles) was installed, the results of combustion experiment and ratios of combustion quality did not change, the salt quantity remained the same. It may be concluded, that diameter of solid salt particles is <2µm.
3. In order to clean fumes, a fiberglass filter sleeve was installed, in all intervals of different loading glycerol combustion quality results remained unchanged. It was determined, that concentration of solid particles in the emitted fumes did not exceed 350 mg/m^3 (measured by standard 3% oxygen quantity). The effectiveness of fume cleaning from solid particles amounted to ~98%.
4. A research of remaining acrolein concentration in the products of combustion was performed using the method of gas chromatography. It was established that in high temperature this carcinogen is fully cracked and is not detected according to the used method.

Thus, it may be concluded that if glycerol fraction is burnt at 1000°C, acrolein gas is not formed

5. According to the results of glycerol fraction experiments, it may be stated, that glycerol fraction, comprising in biodiesel manufacture process, may be used as fuel in heat generating systems, if combustion process is properly regulated and effective fume cleaning device is installed.

REFERENCES

1. P. Janulis, V. Makarevičienė, Biodegalų ir bioalyvų naudojimas Lietuvoje. Lietuvos Respublikos ūkio ministerija VĮ Energetikos agentūra, Vilnius 2004 m. ISBN 966-96160-9-3.
2. G. Burneika LŽŪU Žemės ūkio inžinerijos institutas, Šilumos energetika ir technologijos, konferencijų pranešimų medžiaga, "Pjuvenų kuro briketų su glicerolio priedu ruošimo technologijos tyrimų rezultatai". Kauno technologijos universitetas, 2003 m., p. 331–335. ISBN 9955-09-440-0.
3. Directive 2003/30/EC of the European Parliament and the Council of 8 May 2003 on the promotion of the use of biofuels or other renewable fuels for transport. OJEU L123, 2003 m., p. 42–46.
4. LAND 28-98/M-08 "Stacionarūs atmosferos teršalų šaltiniai. Dulkių (kietųjų dalelių) koncentracijos išmetamosiose dujose nustatymas. Svorio metodas". Patvirtinta Lietuvos Respublikos aplinkos apsaugos ministerijos 1998 m. balandžio 30 d. įsakymu Nr. 69. Normatyvinis dokumentas įsigalioja nuo 1998 m. gegužės 30 d.
5. VDI 3862 Part 5. „Gaseous emission measurement. Measurement of lower aldehydes especially acrolein with the 2-HMP-method GC-method. Verein Deutcher Ingenieure e.V., Dusseldorf 2008.
6. И.Е. Кузнецов, К.И. Шмат, С.И. Кузнецов. Оборудование для санитарной очистки газов. Справочник. 1989 Техника, Киев. ISBN 5-335-00299-3.
7. R. Zevenhoven, P. Kilpinen. Control of pollutants in flue gases and fuel gases. 2002 Espoo/Turku, Finland. ISBN 951-22-5527-8.

CYSENI 2009, May 28-29, Kaunas, Lithuania
ISSN 1822-7554, www.cyseni.com

PROPERTIES OF SUPERCAPACITORS FABRICATED BY PLASMA TECHNOLOGIES

Ž. Kavaliauskas, L. Pranevičius,
Vytautas Magnus University
Vileikos str. 8, LT-44404 Kaunas – Lithuania
Phone: +370 37 401 895; +370 37 401 904
+37068269086
E-mail: liudas.pranevicius@ktu.lt

L. Marcinauskas
Kaunas University of Technology
Studentu str. 50, LT-5136 Kaunas – Lithuania
Phone: +370 37 401 895
E-mail: liutauras@mail.lei.lt

A. Baltušnikas
Lithuanian Energy Institute
Breslaujos str. 3, LT-44403, Kaunas – Lithuania
Phone: +370 37 401 895; +370 37 401 905
E-mail: zydrunas@mail.lei.lt; abalt@mail.lei.lt

ABSTRACT

Supercacitors due to their large specific capacitance, high power density and high efficiency of charging are widely used in the electronic devices, uninterrupted power sources, hybrid car and power distribution systems. Plasma technology is used for manufacturing of supercapacitors with electrodes made of carbon derivative coatings. In the present work, the acetylene in the flow of argon is used as plasma working gas. The thick carbon electrodes are deposited on the stainless steel substrates. To improve the electrical parameters of supercapacitors, the thin nickel oxide film is deposited on the top of carbon coating. The experimental results show that the capacity of supercapacitors significantly increases when the nickel oxide is deposited on the surface of carbon electrodes. However, the voltage characterizing the stability of supercapacitor decreases. The studies of surface topography in scanning electron microscope (SEM) show that the structure of electrodes becomes mesh-like when the nickel oxide layer is deposited on the carbon. The electrical characteristics of the supercapacitor device depend on the thickness of the oxide layer. The best results are obtained when nickel oxide film thickness is equal to 50-100 nm.

Keywords: supercapacitors, electrode.

INTRODUCTION

In recent years, a great deal of attention has been devoted to the research of supercapacitors since they exhibit some excellent properties: extremely large capacity (up to 780 F/g), high power density (>1 kW/kg), large number of charge-discharge cycles (>10^4 cycles), and high efficiency of discharge (>90%) [1-3]. Due to these reasons supercapacitors are widely applied in hybrid cars, in systems which need strong electric current pulses, in current supporting systems and various mobile devices (mobile medical equipment and computer equipment and other) [2]. For the manufacturing of supercapacitor electrodes various technologies and materials are used: activated carbon, carbon aerogel, carbon nanotubes, and conductive polymers [2–4]. Metal oxides (ruthenium oxide, nickel oxide, etc.) are used as auxiliary materials to improve charge kinetics properties [5-11]. It is widely accepted that the best material for the manufacturing of electrodes for supercapacitors is the activated carbon [4]. Such carbon has the following distinguished properties: large effective surface area, perfect temperature stability, relatively low price, and simple production technology [7–8]. The ruthenium oxide is the most relevant auxiliary material used to improve the ion kinetics. High specific capacity and high conductivity have been achieved using these materials [5]. However, due to economic reasons and very complicated manufacturing technology other alternatives are considered [6]. One of the alternative materials for the ruthenium oxide is the nickel oxide. The nickel oxide improves kinetics of ions in supercapacitors. The price of this material is relatively small and the manufacturing technology is simple. Nickel oxide has the following physical and chemical properties: good temperature stability, resistance to calcium alkali impact and good dielectric properties [8–10].

EXPERIMENTAL PROCEDURE

The electrodes of supercapacitors were fabricated using a two-stage technology. During the first-stage, the atmospheric plasma torch technology was used for the deposition of thick carbon coating on the stainless steel substrates. During the second-stage, the formation of thin (72 nm) nickel oxide film on the top of carbon layer was performed using the magnetron sputter-deposition vacuum system.

Carbon layer was deposited using atmospheric pressure plasma torch in the mixture of argon and acetylene gases. Argon was used as gas carrier and acetylene as precursor. The ratio of Ar/C_2H_2 was verified in the range 27–55. The arc voltage was 36 V, arc current – 24 A, deposition time – 150 s, and the distance between plasma torch outlet and sample – 0.01 m. The deposition rate was determined from the measurements of the slope of the sample‘s weight changes obtained using a microbalance with a weight uncertainty of 2×10^{-6} g.

During deposition of oxide film, a water cooled substrate holder and a shutter were located in front of magnetron. The target-to-substrate distance was 0.06 m. The chamber was evacuated to a typical background pressure of 10^{-5} to 10^{-4} Pa by a pumping unit including a turbomolecular pump at pumping speed about 150 $\ell\cdot s^{-1}$. The flow of Ar was controlled by a throttle valve. The sample temperature was controlled with the accuracy ±5°C. The sample holder reached steady state temperature 400 K after two minutes of deposition. The main deposition parameters of the nickel oxide films were following: the magnetron voltage – 244 V, the discharge current – 1.5 A, the partial pressure of the oxygen gas - 1.36÷1.85 Pa. The deposition rate was about 1.2 nm/s and sputtering time ~60 s. The previous investigations showed that the highest capacitance value was obtained for the NiO layers thickness of ~72 nm [12].

The analysis of surface topography of fabricated electrodes was carried out using a scanning electronic microscope JSM–5600. Concentrated potassium alkali KOH (10 $mol\cdot dm^{-3}$, 40 ml) was used as an electrolyte.

RESULTS AND DISCUSSIONS

The atmospheric pressure plasma torch carbon coating deposition technology was used for fabrication of supercapacitor electrodes. The electrical characteristics of supercapacitors were investigated in dependence on the parameters of coating deposition. It was registered that surface topography of fabricated electrodes, carbon coating surface effective area significantly depend on the composition of the working gas. The ratio of Ar/C_2H_2 was used as a variable parameter for experimental studies keeping other deposition parameters fixed.

Fig. 1 includes SEM surface views of supercapacitor electrodes after different stages of treatment. It is seen that the surface structure of carbon coatings after the atmospheric plasma torch deposition includes many loosely bonded to the substrate formations (Fig. 1a) which are easily rinsed out in water or electrolytic solution. As Ar concentration in the working gas mixture increases, the surface includes many micrometric formations well adhered to the substrate (Fig. 1c). It is explained considering the peculiarities of plasma interaction with substrate. For the dominantly Ar plasma, the growing C coating is densified by the incident Ar ions. The plasma activated carbon form dense microstructure with the small number of pores.

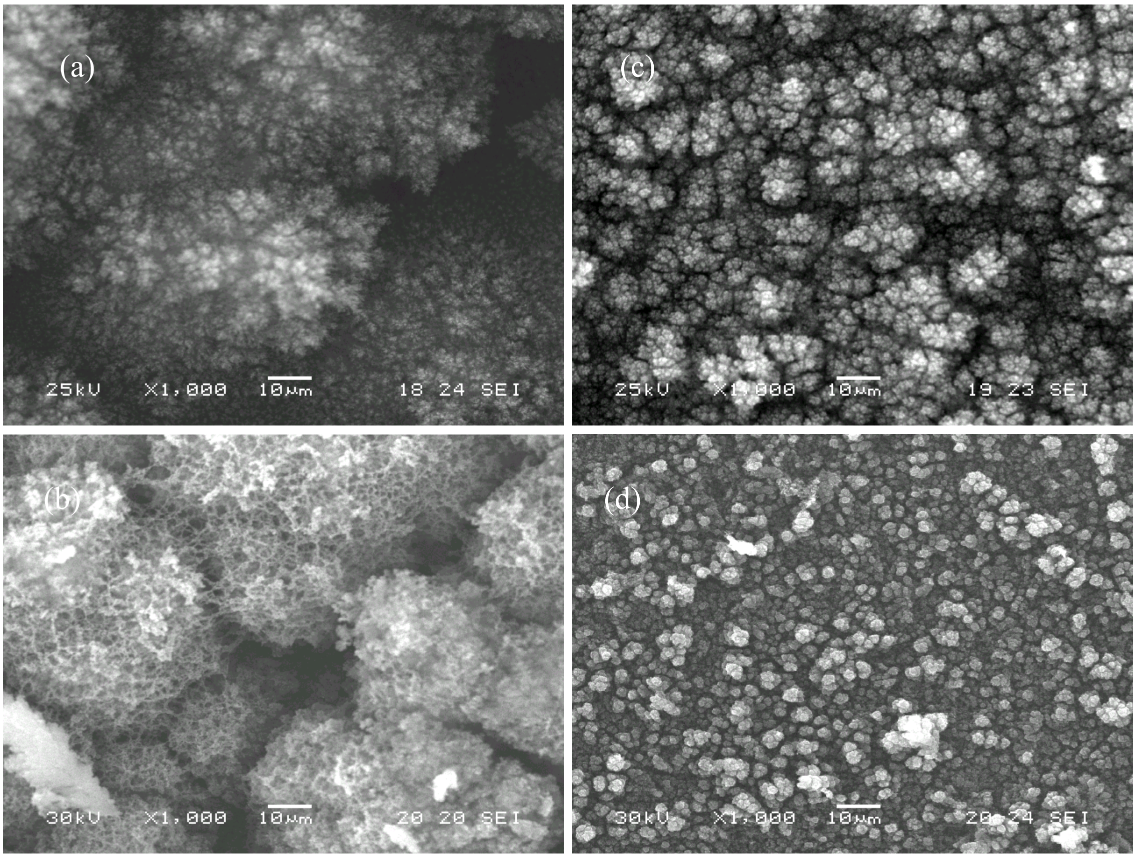

Fig. 1. SEM images of the coatings fabricated for $Ar/C_2H_2 = 27$ (a – without NiO_2, and b – with 72 nm thick NiO_2 film on the top), and for $Ar/C_2H_2 = 55$ (c – without NiO_2, and d – with 72 nm thick NiO_2 film on the top)

For the dominantly C plasma, the coating growth rate is high. However, the film microstructure is porous and the surface topography highly developed with many loosely bonded formations on the surface. After the deposition of the NiO_2 layer, the surfaces include many randomly distributed clusters (Figs.1 b, d). The mesh-like surface formations (Fig. 1b) observed for $Ar/C_2H_2 = 27$ changes to the 1-5 µm size clusters for $Ar/C_2H_2 = 55$ (Fig. 1d). It may be noted that the surface effective area of the carbon produced for $Ar/C_2H_2 = 27$ is very high, and it decreases as the ratio Ar/C_2H_2 increases.

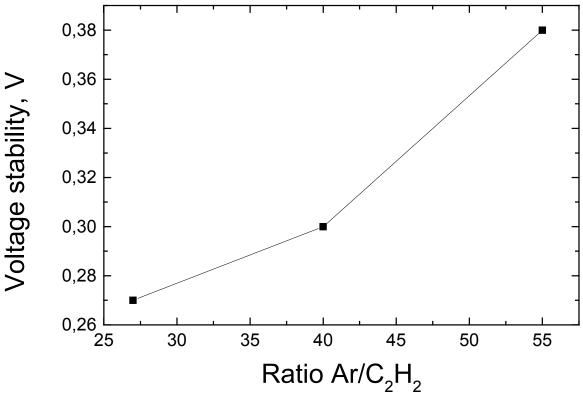

Fig. 2. The dependence of supercapacitor stability voltage on the ratio of Ar/C_2H_2

The dependences of the supercapacitor electrical parameters on the ratio of Ar/C_2H_2 were measured. Fig. 2 and Fig. 3 include the dependences of supercapacitor stability voltage and the supercapacitor capacity, correspondingly, on the ratio of Ar/C_2H_2. The obtained results indicated that with the increase of the ratio Ar/C_2H_2 from 27 to 55 the supercapacitor capacity decreases from 0.085 to 0.02 F (Fig. 3). Meanwhile, the supercapacitor stability voltage increases from 0.275 V up to 0.375 V with the increase of the Ar/C_2H_2 ratio from 27 to 55 (Fig. 2).

Thin NiO_2 film on the surface of carbon changes the charge accommodation and distribution kinetics at the interface carbon–electrolyte. For thin NiO_2 films (less than 100 nm), the charging effects form strong electric field which bind charges on the surface and makes surface stable. Tunneling effects dominate without irreversible damages in the film structure. For thicker films, the discharge currents destroy thin oxide film structure and form conductive breakdown channels.

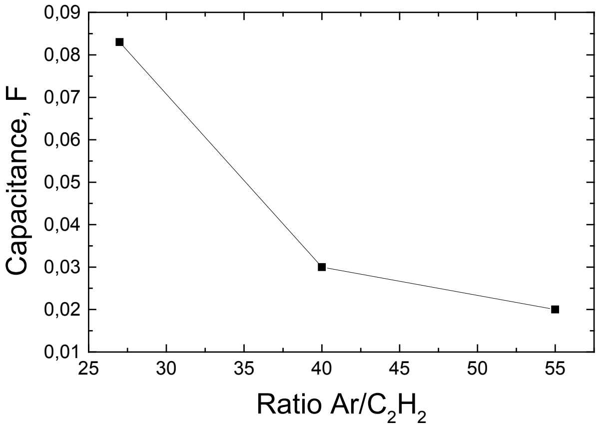

Fig. 3. The dependence of supercapacitor capacitance on the ratio of Ar/C_2H_2

The decrease of the supercapacitor capacity is related due to the fact that the effective surface area of the coating decreases as the ratio Ar/C_2H_2 increases. Li et al. [4] found that the carbon coating, which consists of smaller particles, has higher surface area, hence facilitating ions transport to the pores. Thus the specific capacitance of the supercapacitors also will be higher. This result shows that the surface topography has huge effect on the specific capacitance value.

CONCLUSIONS

1. Supercapacitors including carbon electrodes, fabricated by atmospheric plasma torch deposition, and capped with 72 nm thick NiO_2 film, deposited by the reactive magnetron sputter deposition technique, have been produced and the electrical characteristics investigated.
2. It was obtained that the surface roughness increases with the decrease of the Ar/C_2H_2 ratio.
3. It is shown that the supercapacitor parameters depend on the C_2H_2 flow rate in the argon plasma. The supercapacitor capacity decreases from 0.09 to 0.02 F and the stability voltage increases from 0.275 to 0.375 V as the Ar/C_2H_2 ratio changes from 27 to 55.

REFERENCES

1. A. Burke. R&D considerations for the performance and application of electrochemical capacitors // Electrochimica Acta. 2007, Vol. 53, p. 1083–1091.
2. R. Kotz, M. Carlen. Principles and applications of electrochemical capacitors // Electrochimica Acta. 2000, Vol. 45, p. 2483–2498.
3. A.Pandolfo, A. Hollenkamp. Carbon properties and their role in supercapacitors // Journal of Power Sources. 2006, Vol. 157, p. 11–27.
4. J. Li, X. Wan, Y. Wang, Q. Huang, C. Dai, S. Gamboa. P. Sebastian. Structure and electrochemical properties of carbon aerogels synthesized at ambient temperatures as supercapacitors // Journal of Non-Crystalline solids. 2008, Vol. 354, p. 19–24.
5. X. Liu, P. Pickup. Ru oxide supercapacitors with high loadings and high power and energy densities // Journal of Power Sources. 2008, Vol. 176, p. 410–416.
6. V. Ganesh, S. Pitchumani. V. Lakshminarayanan. New symmetric and asymmetric supercapacitors based on high surface area porous nickel and activated carbon // Journal of Power Sources. 2006, Vol. 158, p. 1523–1532.
7. G.Yuan, Z. Jiang, A. Aramata, Y. Gao. Electrochemical behavior of activated-carbon capacitor material loaded with nickel oxide // Carbon. 2005, Vol. 43, p. 2913–2917.
8. H. Liu, P. He, Z. Li, Y. Liu, J.A. Li. Novel nickel-based mixed rare-earth oxide/activated carbon supercapacitor using room temperature ionic liquid electrolyte // Electrochimica Acta. 2006, Vol. 51, p. 1925–1931.
9. D. Zhao, M. Xu, W. Zhou, J. Zhang, H. Li. Preparation of ordered mesoporous nickel oxide film electrodes via lyotropic liquid crystal templated electrodeposition route // Electrochimica Acta. 2007, Vol. 53, p. 2699–2705.
10. M. Wu, J. Gao, S. Zhang, A. Chen. Effect of carbamate esters on neurite outgrowth in differentiating human SK-N-SH neuroblastoma cells // Journal of Power Sources. 2006, Vol. 159, p. 65–369.
11. M. Wu, L. Zhang, D. Wang, C. Xiao, S. Zhang. Cathodic deposition and characterization of tin oxide coatings on graphite for electrochemical supercapacitors // Journal of Power Sources 2008.
12. Z. Kavaliauskas, L.L. Pranevicius, L. Marcinauskas, P. Valatkevicius. The role of thin NiO film on the top of carbon electrode on the parameters of supercapacitors // Jaunoji energetika 2008.

ASSESSMENT OF PRODUCER GAS CLEANING AND CONDITIONING SYSTEMS

J.L. Marao Jr.
Lithuanian Energy Institute
Breslaujos str. 3, 44403 – Lithuania
Phone: (+370)68731381
E-mail: jose.marao@mail.lei.lt

ABSTRACT

This paper assesses the utilization of producer gas by chemical thermodynamic evaluation of this gas behavior in several treatment alternatives. Nowadays, there is a wide tendency to search for new energy sources other than those related to fossil fuels. Biomass and waste gasification have a potential to be used on electricity generation and also liquid fuels production. However, the producer gases have low calorific value and high levels of unwanted components which should be eliminated, such as tar and particulates, which can harm fuel's transportation and injection systems due to obstruction, corrision and abrasion. Considering the use of these gases in internal combustion engines, the tar levels, for example, should be not higher than 50 mg/Nm^3. Accordingly, there are several alternatives to get rid of these components. Particulates and soot can be eliminated mechanically by filters, scrubbers or cyclones. On the one hand, tars condense on cold surfaces (lower than 300^{o}C) and can obstruct the system. On the other hand, thermal, oxidative and catalytic gas treatment helps to improve quality by cracking tar into smaller species that are not condensable at ambient temperature. Conversely, these methods are not economically reliable as they may require expensive materials, high process temperatures – requiring over 1400^{o}C – and/or long residence times.

Keywords: Gasification, Tars, Cracking, Equilibrium

1 INTRODUCTION

It is not a novelty the search for new energy sources other than fossil fuel utilization. But, nowadays, the utilization of alternative energy sources became reliable and necessary due to: world wide concern with CO_2 and greenhouse gases emissions, reduction of fossil fuel resources, instability of petroleum derived fuel prices and high level of waste generation. In addition, in order to reduce energetic dependence from other countries, nations, which do not provide enough natural sources of energy to supply their internal demand, tend to promote the search of new sources.

In this scenario, gasification of non-food biomass and waste gained a new potential to be one of new energy sources. On one hand, gasification is simple and reliable to produce a calorific fuel to several systems; on the other hand, gasification systems need to meet equipment and environmental requirements. Thus, it is necessary to add equipments and processes in these systems in order to achieve fuels optimized for their utilization and that emissions from them do not be hazardous. Accordingly, the unwanted components of gasification can be tars, particulates, alkali, sulfur and ammonia [1]. The requirements of fuel characteristic – tar and particulates – in accordance with its utilization are presented in the Table 1.

Table 1. End use devices requirements [1, 2]

End use	**Tar – mg/Nm^3**	**Particulate – mg/Nm^3**	**Particulate size – µm**
Internal combustion engine	10–50	50.00	-
Gas turbine	5	15.00	5
Synthetic gas production	–	0.02	–
Compressors	50–500	–	–

There are several equipments - such as cyclone, filters, scrubbers and electrostatic precipitators – which operation is based on mechanical removal of tars and particulates from the gases in order to achieve the requirements presented in Table 1. Alternatively, other methods as thermal and catalytic cracking can condition production gases in order to keep the gas quality (calorific value) at higher levels than the method mentioned previously.

A controlled H_2:CO ratio is required for Fisher-Tropsch synthesis processes for liquid fuel production. This ratio is achieved by utilizing special catalysts and separation mechanisms like CO_2 capture. Usually, catalysts are used in two stages: at first it's used activated carbonated minerals as catalysts – such as dolomite, magnesite and calcite – for larger hydrocarbons (HC) and tars cracking; at second it's used metal catalysts – like commercial Ni based catalysts – which can effectively crack lighter HC such as methane into hydrogen and carbon monoxide.

The by-product – tar from gasification is considered one of the main problems of gasification technology. In addition to environmental hazards causes by tars, they also are the performer of several process-related problems in end use devices (turbines, internal combustion engines, etc.) and processes devices (fans, valves, heat exchangers, etc.). These problems can be fouling, corrosion and abrasion [3].

In literature, there are several definitions for tars. Roughly, it can be defined as condensable organic compounds, with a viscous black or dark brown liqueur aspect. Mainly it is a mixture of aromatics such as benzene, toluene, phenol and 2 and higher rings polycyclic aromatic hydrocarbons (PAH) like naphthalene and anthracene [2, 4].

1.1 Thermal decomposition processes

There are various methods used to improve the quality of syngases. Thermal cracking [5], steam reforming and partial oxidation [3, 5] were analyzed in this work. These processes are analogous as they involve a thermal reactor which can favor reactions that increase the number of permanent gases by cracking tars and hydrocarbons into H_2, CO and CH_4. Accordingly tar cracking reactions can be achieved at high temperatures by:

$$C_nH_m \Leftrightarrow nC + \tfrac{1}{2}mH_2 . \tag{1}$$

Steam reforming is given by:

$$C_nH_m + xH_2O \Leftrightarrow nCO + (x + \tfrac{1}{2}m)H_2 . \tag{2}$$

Under certain temperatures, carbon monoxide can react with radical OH through the following reaction:

$$CO + OH \Leftrightarrow CO_2 + \tfrac{1}{2}H_2 . \tag{3}$$

As discussed by Zevenhoven [4], this reaction is relatively slow. Thus, carbon monoxide conversion is rather promoted by a water shift reaction which has equilibrium on the right side of the equation (4). This situation is favorable for producing H_2 rich synthetic gases to be used in fuel cell from gasification's carbon monoxide together with CO_2 capture mechanisms. The carbon monoxide water shift reaction is represented by:

$$CO + H_2O \Leftrightarrow CO_2 + H_2\,. \tag{4}$$

Soot is also a by-product from gasifier's producer gases. It can be defined as agglomerates of carbonaceous particles forming clusters that are composed of thousands of particles. Soot can be formed during either the gasification or during thermal treatment of producer gas. Both these processes represent a sub-stoichiometric stage of combustion. The soot formation in such situations can be represented as:

$$C_nH_m + xO_2 \rightarrow 2xCO + \tfrac{1}{2}mH_2 + (m-2x)C_{(s)}\text{, with } m > 2x. \tag{5}$$

Jess [5] presented that possible reactions occurred during the conditioning of dust-laden gas through either partial oxidation or thermal treatment. It has five main reactions: HC oxidation, decomposition by hydrogenation, tar cracking, steam reforming and carbon gasification. The last four reactions can also be enhanced by the use of a catalyst in the thermal reactor. There reactions are presented below.

Oxidation:

$$xH_2 + yCH_4 + zO_2 \rightarrow aCO + bCO_2 + cH_2O\,. \tag{6}$$

Hydrogenation (exemplified by naphthalene):

$$C_{10}H_8 + 7H_2 \rightarrow C_6H_6 + 4CH_4\,. \tag{7}$$

Tar cracking and steam reforming reactions are such like (2) and (3) respectively.

Carbon Gasification:

$$C + H_2O \Leftrightarrow CO + H_2 \tag{8}$$

Furthermore, under certain conditions, polymerization may happen by polycyclic aromatic hydrocarbon (PAH) growth through the HACA mechanism (Hydrogen Abstraction and C_2H_2 addition) [6]. This reaction releases H_2 and consumes acetylene.

2 METHODOLOGY

The present work will focus the cleanup and conditioning of tars by thermodynamic evaluation. Kinetic modeling of gaseous phase hydrocarbons can be generalized in three types: empirical, molecular and mechanistic models [7]. On one hand, empirical investigations have the disadvantage due to time and cost factors and level of uncertainty from equipment available. Molecular models can constitute in some cases quick and reliable approaches. On the other hand, only mechanistic models can represent properly real chemical phenomenon with high level of accuracy. To create reliable mechanistic models for large hydrocarbons species is very difficult and require very extensive work (depending on the species to be analyzed). Thus in this work was considered a molecular model for determination the thermodynamic equilibrium of a gas phase mixture of hydrocarbon, nitrogen and tar species and its correlation to temperature.

2.1 Thermodynamic equilibrium

Thermodynamic equilibrium can be defined as the state of a thermodynamic system in which it has a minimum thermodynamic potential. In this state no changes takes place, neither mechanical nor thermal or chemical. So, in this work was chosen the Gibbs free energy (ΔG) method for thermodynamic equilibrium evaluation.

The Gibbs method evaluates the concentration of each species present in the mixture in order to minimize the free energy ΔG of the products. To do so, it uses the relation from the non-expansion work that can be obtained from a closed system to changes in entropy, enthalpy and temperature, constrained with mass balance and elements conservation.

The simulation presented in this work shows the equilibrium state in which minimum chemical potential occurs, considering a constant temperature and pressure system. In this case, the chemical potential of the species can influence the reactions according the criterion of spontaneity. When ΔG of a reaction is greater the zero, the transformation is not suitable to occur; when ΔG is lower than zero, the reaction may be spontaneous; and when ΔG is equal zero, it represents the chemical equilibrium and no changes may occur. Gibbs free energy can be calculated by [8]:

$$G = U + pV - TS\,, \tag{9}$$

where G is the Gibbs free energy, U is the internal energy, p is the pressure, V is the volume, T is the temperature and S is the entropy. Considering the system‘s changes with constant pressure and temperature, we have:

$$\Delta G = \Delta H - T\Delta S\,, \tag{10}$$

where $H = U + pV$, H is the enthalpy. When the system reaches its minimum (ΔG = 0), it defines:

$$\sum \mu_i n_i = 0\,, \tag{11}$$

where, μ_i is the chemical potential of i-th species (J/mol), n_i is number of moles of species i. Expanding equation (11), the equation of equilibrium becomes as follows:

$$\Delta G_i^0 + RT \ln y_i f_i p + \sum_k \lambda_k a_{ik} = 0, \text{ with } i = 1,2,\ldots,N. \tag{12}$$

where ΔGi^o – the standard Gibbs energy of formation of the i-th species, in J/mol; R – the universal gas constant, J/(mol.K); T – temperature, K; y_i – mole fraction of the i-th species in the gaseous mixture, ($y_i = n_i / \sum_i n_i$); f_i - fugacity of the i-th species; p – absolute pressure; a_{ik} – the number of atoms of type k-th element present in each molecule of the i-th chemical species; λ_k – Lagrange multiplier. To determine n_i, the k elements balance is given by:

$$\sum_i n_i a_{ik} = A_k, \text{ with } k = 1,2,\ldots,w\,. \tag{13}$$

The solution of a set of N equilibrium and w elements balance equations yields the mole number n_i of species i involved in the reaction, assuming that all the substances are in the gaseous state. In different conditions, the thermodynamic properties of each species are determined by solving the *Peng – Robinson* equation of gas state:

$$p = \frac{RT}{V-b} - \frac{a}{V(V+b)+b(V-b)}\,, \tag{14}$$

where, a, b – parameters of gas state.

2.2 Problem formulation

The gas inlet for this investigation was assumed a constant source of higher heating value (HHV) fuel 5 MJ/Nm^3, including the heat of combustion of tars. This value was chosen because it represents a typical heating value for a biomass and tire gasification unit. In order to investigate the effect of the main components over the tar components, the gas composition was varied according desired fractions of hydrogen, carbon monoxide, carbon dioxide, steam and oxygen. Accordingly, the tar fraction was assumed to be a value which completes the fixed HHV of the fuel and the nitrogen fraction refers to the amount of gas to complete the volume of the mixture. Besides, the tar species in the inlet gas was considered as of 2 ring aromatic hydrocarbon naphthalene ($C_{10}H_8$).

The molar percentage of H_2 per CO in the producer gas in some investigation was assumed 7.1% and 9% according experimental results on tire gasification under sub-stoichiometric air ratio $\alpha = 0.2$ [9]. These values were chosen to give a more realistic aspect to the simulation and because they represent a case that permanent gases amount corresponds to only 11% of the HHV of the mixture. In such circumstances, conditioning system is substantial for the process when the aim is electricity generation. In other investigations, the CO_2 amount was varied from 0 to 0.15 mol fraction; CO from 0 to 0.15 mol fraction; H_2 from 0 to 0.15 mol fraction; H_2O from 0 to 0.10 mol fraction; and O_2 from 0 to 0.10 mol fraction.

In addition, the following assumptions were considered in this simulation:

- Adiabatic process, i.e., no heat loss from the system;
- Single phase (gaseous) was considered, i.e., the soot formation and condensation were not taken into account in the calculations;
- Sulfur and nitrogen compounds (other than N_2) were not considered.

Besides there is an international standard for tar sampling and analyzing tars [10], it is very difficult to determine the fractions of each tar species in producer gases. So the tar species included in this model were the same as tires pyrolysis experiments identified by S.Chen et al. [11]. The table below shows the chemical species included in the models:

Table 2 – Chemical species considered in the model

Group	Compounds
Hydrogen and oxygen compounds	H H_2 O O_2 OH H_2O HO_2 H_2O_2 HCO
Nitrogen compounds	N_2
Hydrocarbons	CH CH_2 CH_3 CH_4 C_2H C_2H_2 C_2H_3 C_2H_4 C_2H_5 C_2H_6 C_3H_7 C_3H_8 C_4H_6 C_5H_6
Hydrocarbon -Tars	C_6H_6 C_6H_5OH C_7H_8 C_7H_8O C_8H_{10} C_9H_8 $C_{10}H_8$ $C_{12}H_{10}$ $C_{13}H_{10}$ $C_{14}H_{10}$ $C_{16}H_{10}$ $C_{20}H_{12}$ $C_{22}H_{14}$ $C_{24}H_{12}$
Other organic compounds	CH_2O CH_2OH CH_3O CH_3OH HCCO CH_2CO HCCOH CH_2CHO CH_3CHO
Inorganic carbon compounds	CO CO_2

2.3 Solver and database

The thermodynamic equilibrium solver used in this work was the *Cantera* [12] program code – an open source code written in *Python* – which uses the Villars-Cruise-Smith algorithm for the chemical equilibrium calculation according the Gibbs energy presented by Equations 9–14. *Microsoft Excel* was used as post-processor.

The database evaluated in the calculations was the *Third Millennium Ideal Gas and Condensed Phase Thermochemical Database for Combustion* [13], containing thermodynamic properties of 508 chemical species; however, just those presented on Table 2 were considered important for this investigation. Originally this database is not on the format used in *Cantera*, so it had to be converted to this format by the author of this paper.

3 RESULT AND DISCUSSIONS

3.1 The effect of partial oxidation and steam reforming

The results were calculated according several reactor equilibrium temperatures varying from 573 K and 1673 K. In the Figure 1 below, it is possible to identify the possible influence of steam over HC's polymerization. In temperature up to 823 K steam influences tar cracking while at high temperatures it showed a tendency of polymerization of HC into heavier species, which could result in soot formation. In temperatures over 1450 K tars starts to be cracked again; however these temperatures are not reliable for conditioning systems. The legend shows the molar fraction value of the referred species after the decimal point (example: "H2-071" represents 0.071 H_2 mol fraction).

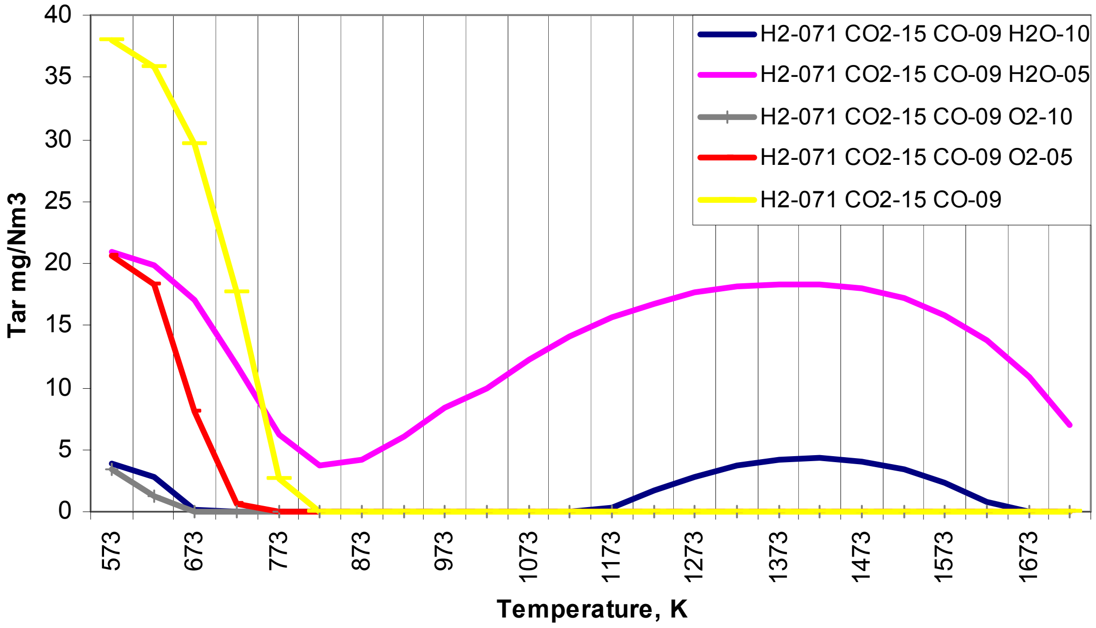

Fig. 1. Sum of tar components in equilibrium state as function of temperature

The Fig. 2 shows the low heating value (LHV) discounted the heat from tar species for the some gas samples. At lower temperatures, the use of steam in cracking seems to enhance the gas calorific value; however, an analysis of a similar gas composition without steam shows higher LHV when the cracking process happens in higher temperatures. This can indicate that steam possibly can be used to promote tars cracking and gas calorific enhancement at lower temperature tars conditioning systems.

The Fig. 3 shows the composition at equilibrium state of gases, comparing the runs with 0.05 steam mol fraction on left side with 0.10 steam mol fraction on the right side (the same showed at Figs. 1 and 2). If compared with the values presented at Table 1 and at Fig. 1, it is possible to assume that steam reforming can be an alternative for lower temperature cracking method with further fuel use in internal combustion engines. But, it is obvious that high level of remainder steam on the gas should be condensed and collected to avoid corrosion.

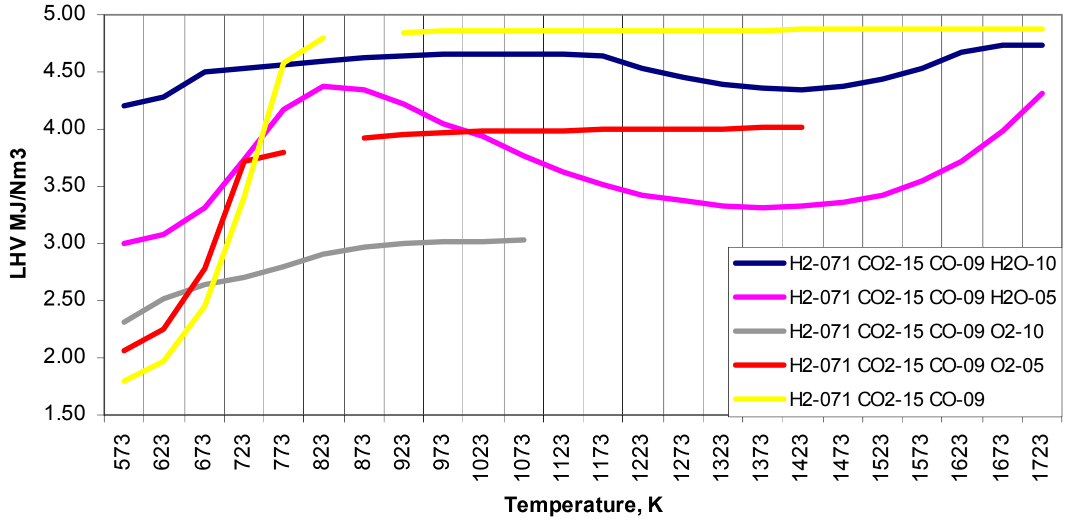

Fig. 2. O_2 and H_2O effect on LHV (discounted LHV from tars as a function of temperature)

One significant aspect of steam reforming is that it presented a temperature zone in which it may produce optimal results for tar cracking. Such perception is important to define the ranges that each process can operate.

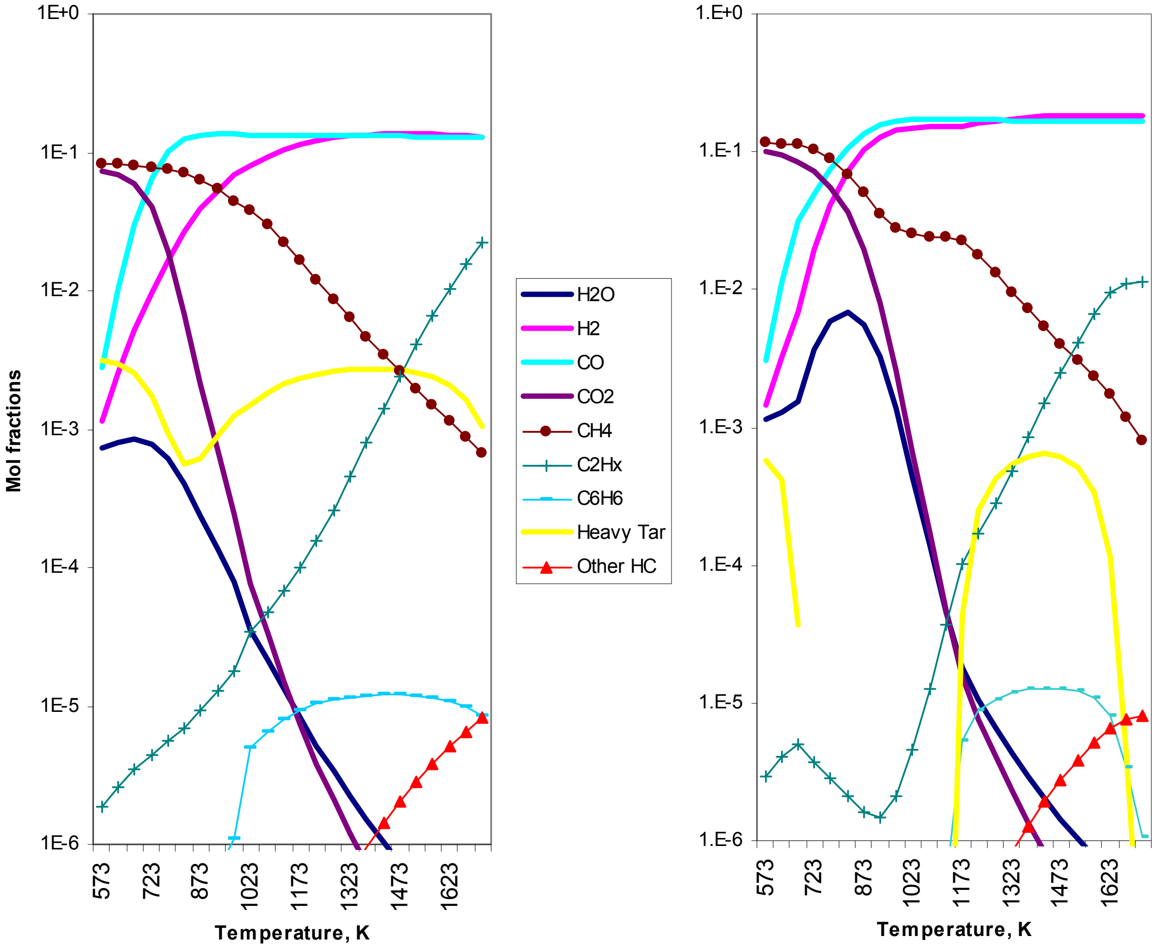

Fig. 3. Equilibrium state product gas composition (left – steam 0.05 mol fraction; right – steam 0.1 mol fraction)

Heavy tars formation (PAH formation, polymerization) – observed at higher temperatures (see benzene and heavy tars at Fig. 3) – and soot formation can be positive to the system, as it consumes HC and releases H bonds, resulting in a cleaner gas after mechanical separation, which can increase equipment life time, especially internal combustion engines and turbines. In addition, such solution can be reliable in the case of producing electricity with H_2 in fuel cells. However, in the case of producing energy in internal combustion engines or turbines, it is clear that polymerization will promote a decrease of calorific value and system output; as these equipments can operate with higher levels of HC and tars.

Partial oxidation can be less expensive alternative for tar reduction than others previously mentioned, as it releases heat and consequently requires lower amount of external heat source to promote tar cracking. However, it has the disadvantage of reducing considerably the heat value of the gas. Thus, according the results on Figs. 1 and 2, this alternative seems to be not reliable enough; but, before making anticipated conclusions, it's necessary to investigate economically and compare the losses from the partial combustion with the heat necessary to run the thermal cracking reactor. Probably a life cycle analysis (LCA) would present very interesting results in this case.

3.2 The effect of hydrogen

In the Figs. 4 and 5 it is observed the influence of H_2 fraction in the mixture. It presented a tendency of decreasing the tar amount at lower temperatures. It is interesting that in the case of no H_2 was given in the input gas; there is a tendency of HC polymerization at higher temperatures similar to that observed with the addition of steam.

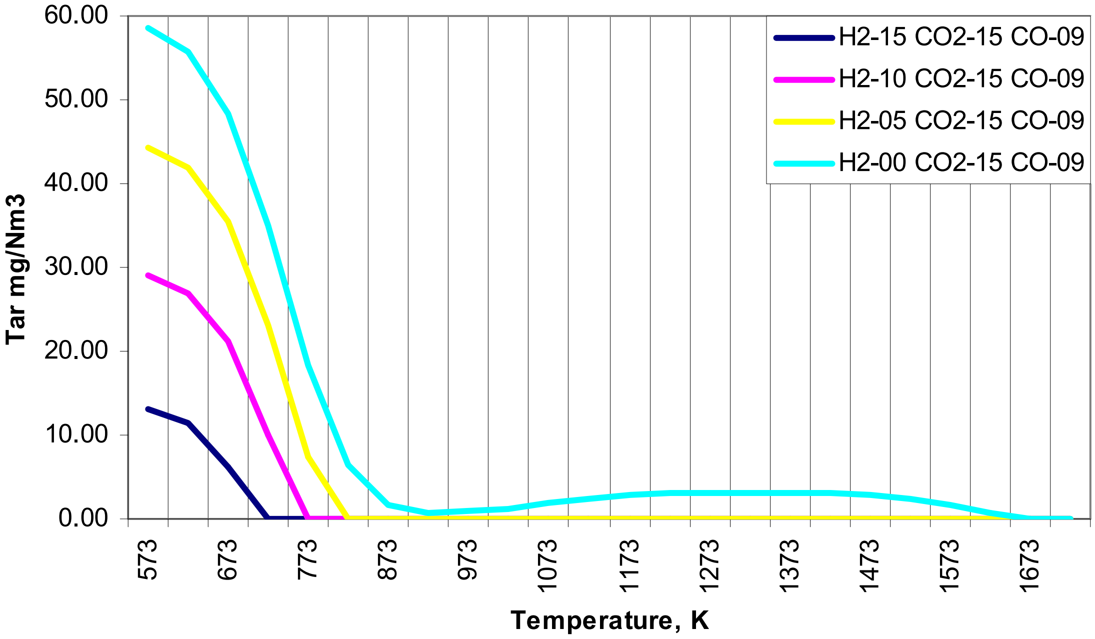

Fig. 4. Sum of tar components in equilibrium state as function of temperature

Another possible relationship is that when the amount of H_2 is higher, for example 0.15 mol fractions, the calorific value tend to be higher after lower temperatures treatment. In addition, it clearly observed that the stagnation temperature for the highest calorific value (Fig. 5) is anticipated progressively with the increase of H_2 in the initial mixture. However, at higher process temperatures, gases with lower initial mol fractions of H_2 results in a higher LHV gas after equilibrium. This suggests that the H_2 mol fraction may positively influence tar cracking and at the same time helps to decrease tar cracking temperature. Such information may be significant in the decision of which gasification system to use – for example, lower temperature gasification may produce lower output but higher H_2 content while higher temperature gasification may produce higher tar content.

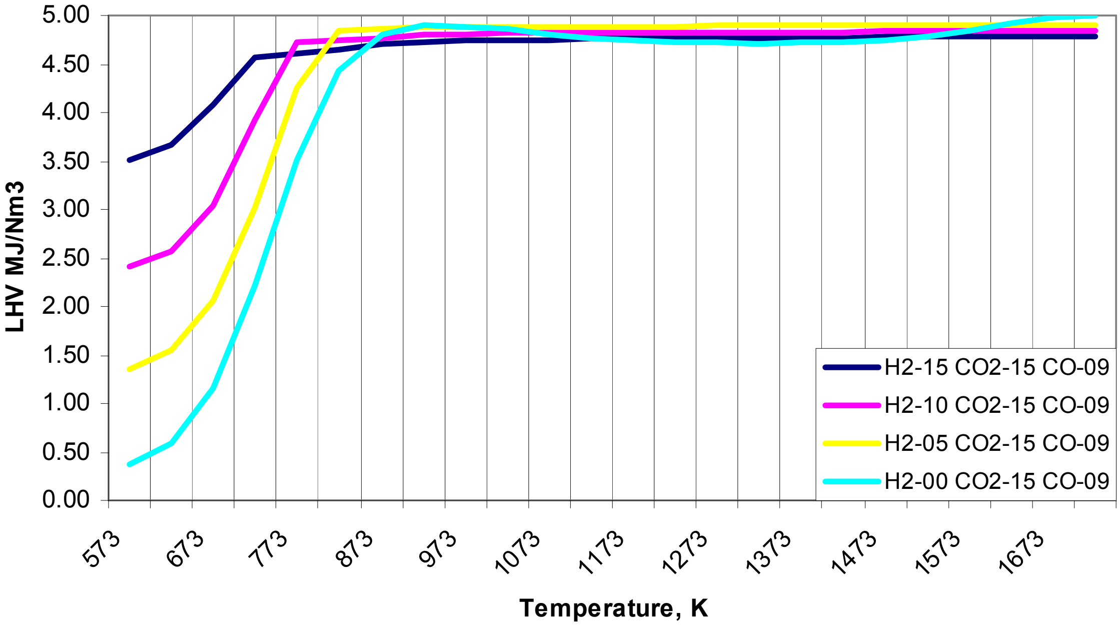

Fig. 5. H_2 effect on LHV (discounted LHV from tars) as a function of temperature

4 CONCLUSIONS

According to the equilibrium model studied, the partial oxidation presented good capability of reducing tar, however when analyzed the calorific value of the gases after equilibrium, the gas calorific value (LHV) is much inferior than of the input gas even in higher temperature equilibrium (over 1000 ^{o}C), which may indicate that this alternative is not reliable enough related to other alternatives for tar cracking.

Conversely, the utilization of steam in thermal cracking reactors presented the best simulated results for the calorific value (LHV discounted the heat from remainder tars) besides the tar levels are one the highest from the analyzed cases. Both cases, with 5 and 10 mol percentages also showed a tendency of increasing the LHV at lower cracking temperatures.

At lower temperatures, the addition of H_2 to the inlet gas presented a notable abatement in tar fraction. However, likewise in the addition of O_2 to the gas – partial oxidation –, the LHV of the equilibrium gas is reduced.

Depending on the fuel utilization, the polymerization observed in the case of steam reforming can be positive, as it increases the H_2 fraction. Also, there are some cases, such as the use of producer gas in cement and lime kilns, that no tar treatment is required if this fuel is used as a secondary fuel, because these processes present long residence times and temperatures that are able to crack heavier HC and tars. However in the case of utilization as fuel to internal combustion engines and turbines, the tar conditioning is essential to enhance gas quality and equipment lifetime.

In order to analyze the economy of each system is also necessary to consider the residence time required for each scenario to reach the equilibrium or close to it. With this information is possible to dimension equipments and estimate material and power consumption.

REFERENCES

1. J. Rezaiyan, N.P. Cheremisinoff, *Gasification Technologies: a primer for Engineers and Scientists*, CRC Press, ISBN 0-8247-2247-7, USA, 2005, p. 165–265.
2. T.A. Milne et al, *Biomass Gasifiers „Tars": Their Nature, Formation and Conversion,* NREL/TP-570-25357, USA, 1998.
3. Houben, M.P. et al. *Tar reduction through partial combustion of fuel gas*, doi:10.1016/j.fuel.2004, Fuel 84, 2005, p. 817–824.
4. R. Zevenhoven, P. Kilpinen, *Control of pollutants in flue gas and fuel gases*, ISBN 951-22-5527-8, 2nd ed., 2002, p. 6.16–6.19
5. A. Jess, H. Depner / *Thermische und katalytische Aufarbeitung von Rohgasen der Vergasung und Verkokung fester Brennstoffe*, Chemie Ingenieur Technik (69), p. 970–973.
6. M. Frenklach and H. Wang, *Soot Formation in Combustion*, Springer-Verlag, Berlin, 1994, p. 165.
7. E. Ranzi et al., Progress in Energy and Combustion Science 27, 2001, p. 99-139
8. N. Striugas, G. Stravinskas, Vandenilio gavyba termiskai skaidant skirtingos koncentracijos glicerolio frakcija su daline oksidacija, ENERGETIKA, Vilnius, 2007, T. 53. Nr. 3, p. 84–89
9. H. Schmidthls, *The pre-combustion chamber for secondary fuels – development status of a new technology*, Cement Industry Technical Conference, IEEE-IAS/PCA, p. 207–218
10. W. van de Kamp et al., Tar measurement *standard for sampling and analysis of tars and particles in biomass gasification product gas*, 14th European Biomass Conference & Exhibition, France, 2005.
11. .Chen et al., *Emissions of polycyclic aromatic hydrocarbons (PAHs) from the pyrolysis of scrap tires*, Atmospheric Environment 41, 2007, p. 1209–1220
12. D. Goodwin, Cantera: chemical kinetics software package, California Institute for Technology - Caltech, <www.cantera.org> (accessed in December 2008).
13. A. Burcat, B. Ruscic, *Third Millennium Ideal Gas and Condensed Phase Thermochemical Database for Combustion with updates from Active Thermochemical Tables*, ANL-05/20 and TAE 960Technion-IIT, Aerospace Engineering, and Argonne National Laboratory, Chemistry Division, September 2005.

CYSENI 2009, May 28-29, Kaunas, Lithuania
ISSN 1822-7554, www.cyseni.com

EROSIVE PLASMA CHARACTERISTICS IN PLASMA-TARGET INTERACTION REGION

V.M. Grishchenko
Heat and Mass Transfer Institute
of the National Academy of Sciences of Belarus
P.Brouki Street 15, Minsk BY-220072 – Belarus
Phone: +375(17)2842246
E-mail: furst2006@tut.by

ABSTRACT

The erosive plasma flow-target interaction parameters are presented. The stable quasistationary bulk plasma formations with lifetimes more than 50 microseconds were obtained in the plasma–target interaction area.

Keywords: erosion, plasma, accelerator, target, spectrum, electron temperature, electron concentration

1. INTRODUCTION

Currently a close attention is paid to the development of physic technical concepts of making new plasma systems to obtain highly concentrated energy flows for photochemistry, high-temperature thermal physics, new material synthesis, and to use them as the base for new technologies and technological processes aimed at the modification of the material properties in extreme regimes of action [1–3]. The investigation of physical processes of interaction between erosive plasma flows can help solving a variety of actual scientific and industrial problems in quantum electronics, photochemistry, and radiation plasma dynamics. When colliding, the accelerated plasma flows [4, 5] may open up certain possibilities in producing new plasma formations.

In [6], the main results of studying the interaction between two oppositely directed rarefied plasma flows in the concentration ratio range of $n_1/n_2=1\div15$ and Mach numbers of $M \approx 1.9–3.5$ are offered. They show that in the case of equal concentrations, the colliding plasma flows do not produce density jumps, which is explained by the leveling of the density spatial disturbance due to the propagation of both symmetrical shock waves and following them substance flows in opposite directions [6].

Studies on plasma flow collisions intended to obtain high-intensity plasma dynamic sources of optical pumping for molecule laser active media are shown in [7–9].

In [7], authors describe in detail the plasma deceleration and the kinetic energy thermalization of two colliding plasma flows. They show that the interaction (or cumulative) area is a dense matter formation confined with two strong shock waves propagating with velocities ten times lower than those of plasma flows. This indicates a high efficiency of dissipation processes resulting in virtually total thermalization of colliding flows kinetic energy and plasma heating in the interaction area. Such a cumulative area is a source of the strong continuous radiation whose radiance temperature is about 32–35 kK in the visible region and 25 kK in the near ultraviolet. In such discharges, the plasma heating up is a result of the kinetic energy thermalization of dense plasma flows on their impact upon gaseous medium which plays the part of an obstacle [7].

The authors of [8–9] present experimental data on high-current plasma dynamic discharges for generators of both the laser and strong thermal radiation. Advantages of their method are associated with the possibility to excite big volumes of active medium and hence to achieve the high-power laser radiation, as well as with the lack of any fundamental restriction on obtaining a high power efficiency of laser generation because of both a wide absorption band in the spectra of active molecules and a relatively small Stokes shift of absorption and radiation spectra.

In this paper I would like to present the results of the experimental investigation into parameters of erosive plasma flow running into the obstacle.

2. GENERATION OF EROSIVE PLASMA FLOWS

The experimental setup for investigations of erosive plasma flows is shown in Fig.1. An erosive plasma accelerator 1 consists of two coaxial copper electrodes separated by an isolator (∅ 30 mm). The outer electrode is of a confuser shape with a ∅ 20 mm exit section. The accelerator is mounted in the vacuum chamber 2 using a copper coaxial current lead. The visual examination and photographic 5 and spectral studies were made through optical windows 3 of the vacuum chamber.

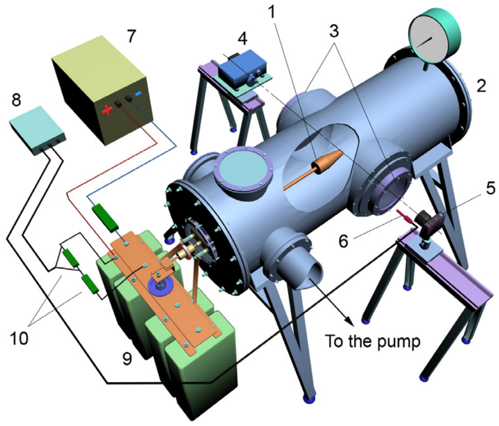

Fig. 1. Experimental setup for investigation of erosion plasma flows

The electrical schematic diagram of the erosion plasma accelerator power supply is shown in Fig. 2. Plasma flows were generated by a high-voltage discharge of the capacitor battery 9 (Fig. 1) (total capacity 600 microfarad) between the accelerator electrodes. The capacitor battery was charged by a high-voltage supply 7 (Fig. 1) (0–6 kV).

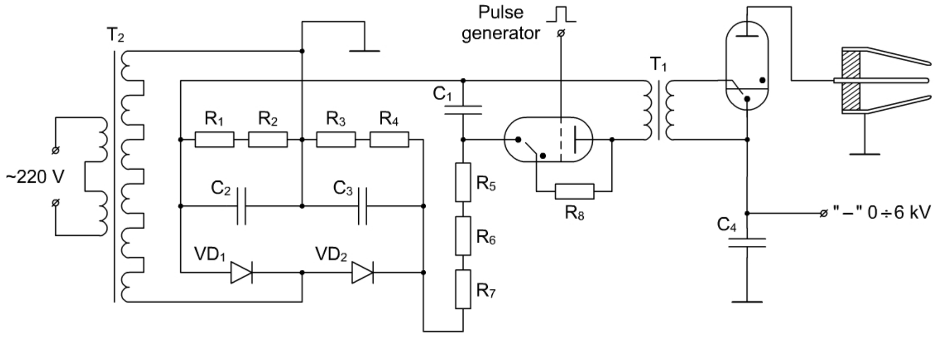

Fig. 2. Electrical diagram of erosion plasma accelerator power supply

3. PARAMETERS OF FREE EROSIVE PLASMA FLOW

The parameters of free erosive plasma flows were measured under a pressure of residual air in the vacuum chamber equal to ~ $3 \cdot 10^{-3}$ Torr. The discharge current peak value varied in the range 90 to 140 kA with an increase in the initial voltage on the capacitor battery from 3 to 4 kV. The discharge duration was about 150 microseconds. Under the conditions described above the compressive plasma flow (∅1 cm and 10 cm long) was formed at the accelerator outlet. The flow diverges with the expansion angle of 20÷30° (Fig. 3).

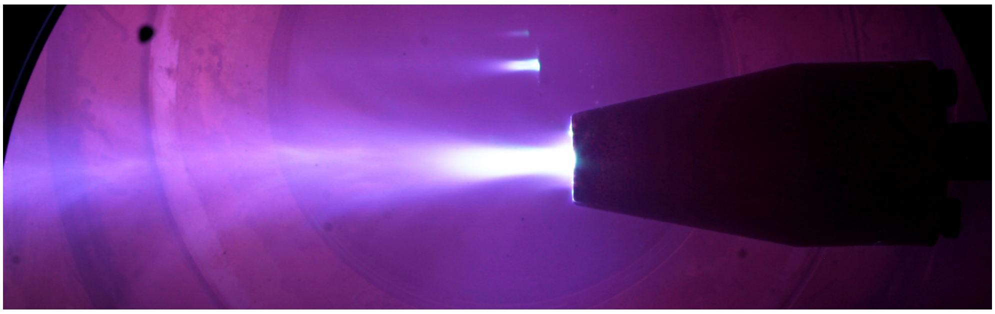

Fig. 3. Photograph of the erosive plasma flow

Typical oscillograms of voltage on the capacitor battery, discharge current, and the temporal dependence of the plasma flow total emission are shown in Fig. 4.

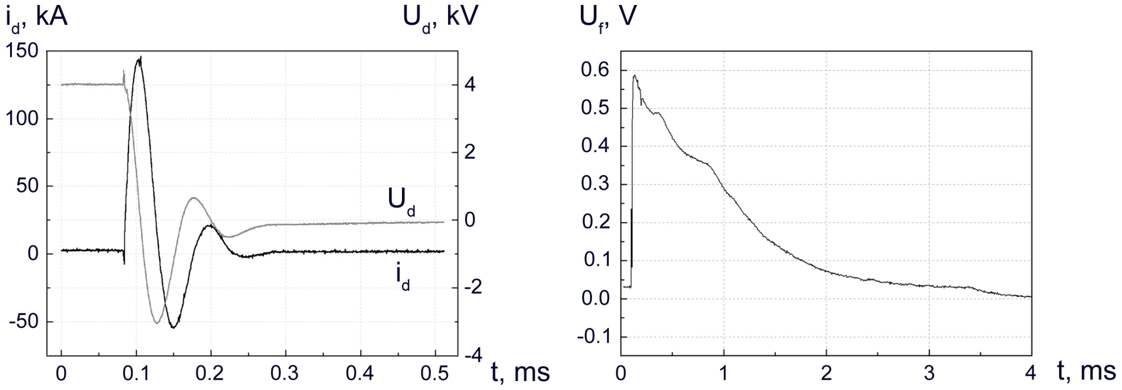

a) b)

Fig. 4. a - Oscillogram of voltage on capacitor battery and discharge current; b - temporal dependence of the plasma flow total emission

The discharge current and voltage on the capacitor battery were traced by a Rogowski loop and a high-ohmic resistive divider 10, respectively (Fig. 1). The total emission was recorded by a photodiode 6 coupled with a digital oscilloscope 8 (Fig. 1).

The spectral studies of plasma formations were carried out using a S150A-IV spectrometer 4 (Fig. 1). A typical spectrum of the erosive plasma emission is shown in Fig. 5. The photo was made using 1 microsecond exposure and 70 microseconds delay from the beginning of the process. The plasma emission spectra obtained in the range of 300÷1200 nm show primarily the continuous radiation, emission lines of the atomic hydrogen, and intense (resonant) lines of the dielectric material atoms. Used as a dielectric material was caprolone, chemical formula $[\text{-NH(CH2)CO-}]_n$. Hence, the resonance lines of hydrogen, nitrogen, oxygen, and carbon were observed in the spectra of erosion plasma emission.

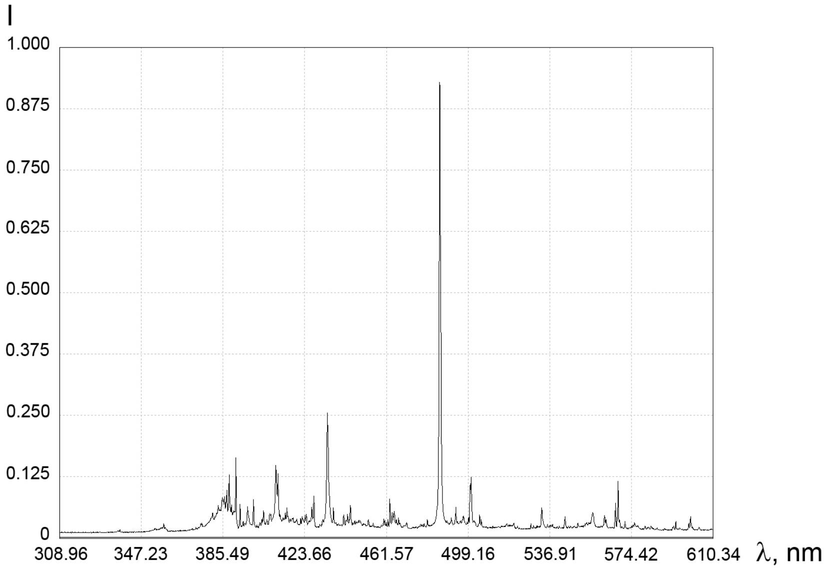

Fig. 5. Spectrum of erosive plasma emission

The electron temperature in plasma was measured from the continuum intensity on either side of the Balmer series limit on the assumption of the local thermodynamic equilibrium. When the discharge current reached the peak value of 140 kA, the electron temperature at a distance of 1 cm from cathode amounted ~ $3 \cdot 10^4$ K.

The electron concentration averaged over the pass of light was determined from the Stark broadening of H_β Balmer line [10]. At the peak discharge current of 140 kA the electron density was $2 \cdot 10^{15}$ cm^{-3} at a distance of 1 cm from cathode.

4. INTERACTION OF EROSIVE PLASMA FLOWS WITH A TARGET

The steel semi cylindrical and the flat cobalt magnet surfaces were used as the targets. The photographs of the erosive plasma–target interaction are shown in Fig. 6.

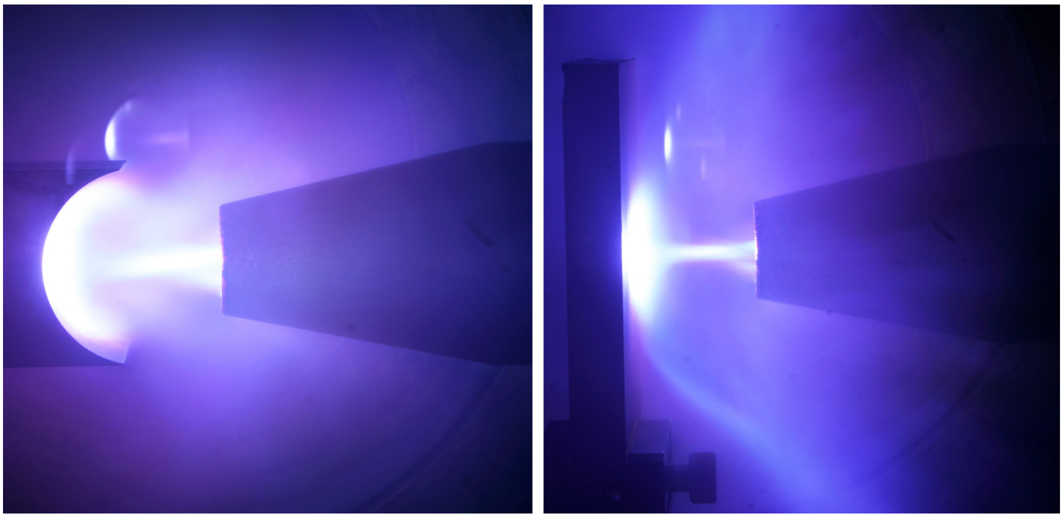

Fig. 6. Photographs of the erosive plasma–target interaction (left – the steel semicylindrical surface; right – the flat cobaltic magnet)

The experiments conducted show that the collision of plasma with the target results in the appearance of quasi-stationary shock compressed plasma layers that exist for over 50 microseconds. The length, location, and other characteristics of the cumulative area can be modified by varying the incident plasma flow parameters and operating regimes of the magnetoplasma compressor.

5. CONCLUSIONS

The main parameters of plasma in free erosive flows such as the electron temperature and concentration have been estimated. The results obtained show that under the experimental conditions the electron temperature and concentration reach $3\cdot10^4$ K and $2\cdot10^{15}$ cm^{-3}, respectively at a distance of 1 cm from cathode and at the peak discharge curent. The stable quasi-stationary bulk plasma formations with lifetimes of over 50 microseconds were observed in the plasma–target interaction area.

REFERENCES

1. Асташинский В.М., Ефремов В.В., Костюкевич Е.А., Кузьмицкий А.М., Минько Л.Я. Интерференционно-теневые исследования процессов в магнито-плазменном компрессоре // Физика плазмы. 1991. Т. 17, № 9. С. 1111–1115.
2. Асташинский В.М., Баканович Г.И., Кузьмицкий А.М. и др. Выбор режимов работы и параметры плазмы магнито-плазменного компрессора // ИФЖ. 1992. Т. 62, № 3. С. 386–390.
3. Асташинский В.М., Маньковский А.А., Минько Л.Я. и др. Исследование физических процессов, обусловливающих режимы работы КСПУ // Физика плазмы. 1992. Т. 18, № 1. С. 90–98.
4. Ананин С.И., Асташинский В.М., Костюкевич Е.А. и др. Интерферометрические исследования процессов в квазистационарном сильноточном плазменном ускорителе // Физика плазмы. 1998. Т. 24, № 11. С. 1003–1010.
5. Асташинский В.М. Формирование компрессионных эрозионных плазменных потоков заданного состава в плотных газах // ЖПС. 2000. Т. 67, № 2. С. 229–233.
6. Еселевич В.Г., Файнштейн В.Г. Турбулентная электростатическая ударная волна при взаимодействии встречных потоков разреженной плазмы // Физика плазмы. 1984. Т.10, № 3. С. 538–547.
7. Плазменные ускорители и ионные инжекторы. / Под ред. А. И. Морозова. М., Наука. 1984. С. 5–49.
8. Генераторы лазерного и мощного теплового излучения на основе сильноточных плазмодинамических разрядов. М., Наука. 1984. С. 50–81.
9. Протасов Ю.С., Протасов Ю.Ю. Импульсный источник коротковолнового ультрафиолетового излучения высокой плотности мощности // Приборы и техника эксперимента. 2003. № 2. С. 72–77.
10. Диагностика плазмы / Под ред. Р. Хаддлстоуна и С. Леонарда. М., Мир. 1967.

CYSENI 2009, May 28-29, Kaunas, Lithuania
ISSN 1822-7554, www.cyseni.com

AVERAGED TEMPERATURE AND CONCENTRATION DISTRIBUTION OF ELECTRONS MEASUREMENTS IN BARRIER DISCHARGE PLASMA

M.Yu. Chernik
Heat and Mass Transfer Institute of the National Academy of Sciences of Belarus
P.Brouki Street 15, Minsk BY-220072 – Belarus
Phone: +375(17)2842246
E-mail: Emerald_@tut.by

ABSTRACT

For numerical modeling of ionized flows about bodies the most important information is electron distribution in modeling flow. That is why the goal of this work is to present the optical method of measurements of electron concentration distribution in ionized flow induced by dielectric barrier discharge in presence of incident flow.

Keyword: electron concentration, electron temperature, high frequency barrier discharge, plasma, drag reduction

1. INTRODUCTION

Nowadays many researchers consider a very perspective and actual investigation of plasma actuators based on dielectric barrier discharge for air flow modifications and aircraft drag reduction. It has to be mentioned that plasma actuators affect lift coefficient like wing flaps, however does not have moving parts. Such fact is a considerable advantage.

Main problems in this field of interest are to increase actuators efficiency and to develop physical mechanism of dielectric barrier discharge influence on aerodynamical flow characteristics. The authors of paper [1] summarized properties of most common dielectrics used for manufacturing of actuators to pick the optimal material with the lowest thermal loses, because sometimes these loses are comparable to the heat input to the dielectric discharge plasma production. It has been shown that for the plasma actuator production caprolone and quartz is the best choice but thickness of the material plays an important role as well.

It has been considered for a long time that drag reduction of bodies with surface dielectric discharge is caused by air temperature rise in the boundary layer but some experiments show insignificant heating in the discharge area [2, 3]. Photograph of plasma luminescence of dielectric barrier discharge with nanosecond exposition enable to reveal the streamers structure [2]. Authors of papers [4, 5] investigated the boundary layer structure formed by ion wind and determined recirculation zone between electrodes.

Investigations of discharge characteristics showed strong dependence on the ion wind speed from shape and frequency impulse on electrodes. Also this research works showed that speed saturation appears while input voltage increases [6, 7].

Plasma actuators enable to solve the flow separation problem on wing [8]. It is possible to prevent flow separation with speeds 2.85 m/s when angle of attack is up to 5° [1]. When the angle of attack reaches 15°–21°, prevention of flow separation becomes possible for flows with speeds up to 75 m/s [1].

Method of numerical modeling of dielectric barrier discharge, described in paper [9], presents plasma actuator as a set of air capacitors and calculates mass forces on the plasma properties and known formulas for flat capacitor. Modeling results are in good agreement with experimental data and light intensity of the discharge depends on voltage on electrodes under the law ~$V^{7/2}$ [9]. Experimental data analysis show that maximal electron density in barrier discharge is 10^{19}–10^{20} m^{-3} [10], which is in good agreement with previously obtained photometric measurements results for shadow patterns under two wavelength probe radiation [11].

2. EXPERIMENTAL SETUP

As an experimental model flat plate made from caprolone (10×180×120 mm) was used. On the sharpen front surface on both sides of plate 2 rows of joint needles were installed (needle spacing was 3 mm, needles rows was placed 3 mm over plate) as the first electrode. The second electrode was an isolated copper wire installed inside the plate. Electrodes were 40 mm apart. When high voltage impulse was applied on electrodes high frequency barrier discharge appeared. Electrical network for this discharge power supply described in details in paper [11]. Peak voltage value on the discharge electrodes varied from 70 to 140 kV.

The discharge induced ionized air flow with speed range 5–10 m/s and the flow formed turbulent boundary layer over flat plate. In presence of the discharge an incident flow from the nozzle with exit section 15×200 mm was applied. Experimental setup and nozzle operation principles are described in paper [12]. The velocity of incident flow was measured by Pitot-Prandtl tube and in the exit section area was about 60 m/s.

To measure distribution of electrons concentration in ionized airflow induced by high frequency barrier discharge, Tepler photograph photometric measurements were performed [13]. Experimental setup for optical measurements is shown in Fig. 1.

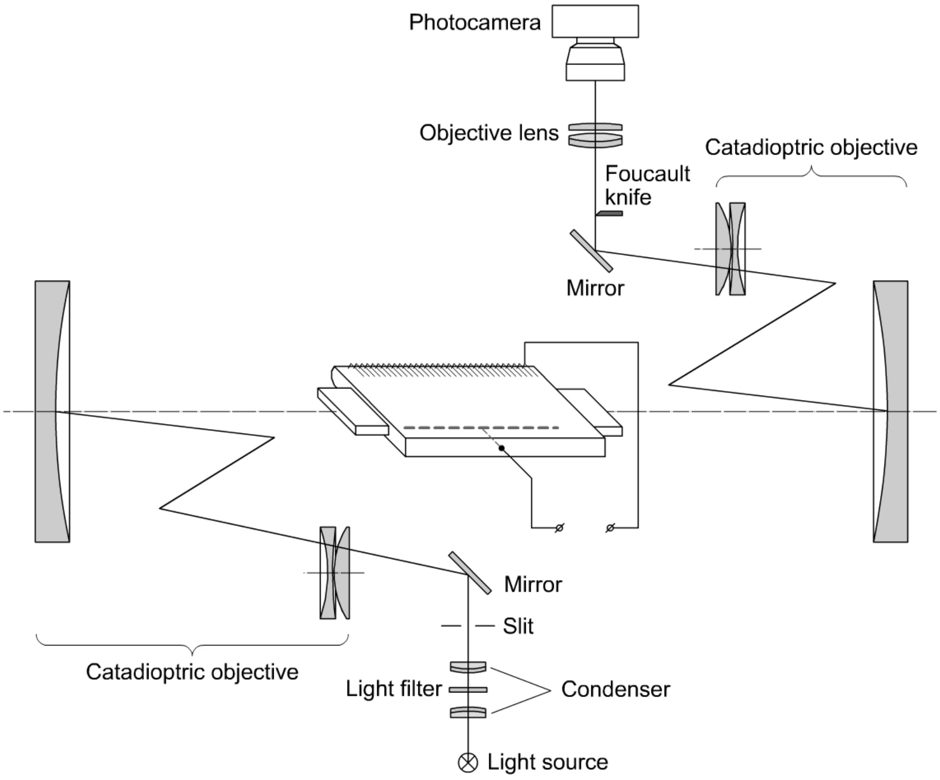

Fig. 1. Experimental setup for optical measurements

Experiments were carried out with the use of holographic interferometer in a shadow device mode. Focus of objective lens was $F = 3213.5$ mm, the diameter of observed field was 800 mm. The diaphragm slit was $\Delta x = 0.1$ mm wide and was oriented parallel to the flat plate. The photograph exposition was held $\Delta t = 2$ s to average turbulent fluctuations in the air flow. In the illuminating part of device blue and red color filters with transparency maximum of $\lambda_b = 420$ nm and $\lambda_r = 640$ nm, respectively, were installed alternately (Fig. 2). Visual observations show constriction of the incident flow to the model surface.

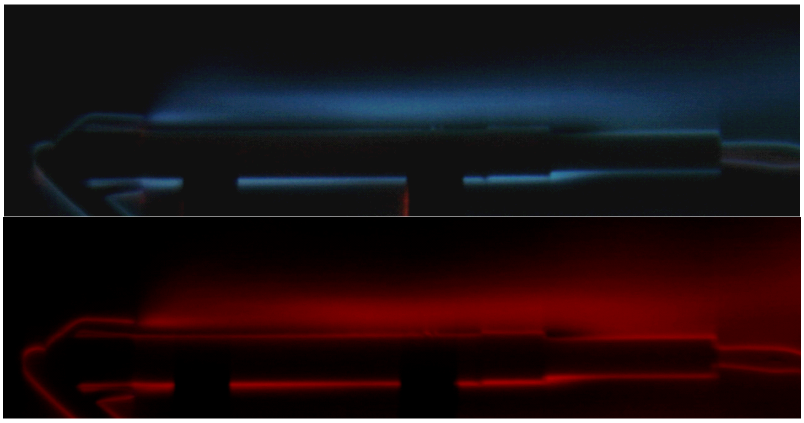

Fig. 2. Tepler snap-shot of boundary layer over flat plate for two wavelengths

3. METHODOLOGY AND EXPERIMENTAL RESULTS

In case of small deviation angles in tested optical inhomogeneity (e.g. propagation of light through turbulent gas flow) propagation of light ray considered almost rectilinear. In rectangular coordinate system when axis z is directed along probe radiation axis x is ortogonal to the model surface, Euler equation can be used in simplified form [13]:

$$tg\varepsilon_x \approx \int_{z_1}^{z_2} \frac{d\{\ln[n(x,y,z)]\}dz}{dx}; \qquad tg\varepsilon_y \approx \int_{z_1}^{z_2} \frac{d\{\ln[n(x,y,z)]\}dz}{dy}. \tag{1}$$

Here ε_y ε_x and ε_y – is a deviation angles projections, z_1 and z_2 – are coordinates of ray entrance and exit from optical inhomogeneity. In the investigated situation, when slit is oriented parallel to the model surface, optical inhomogeneity can be considered as 2D. Therefore $\frac{\partial n}{\partial x}$ is independent function of coordinate z and the quantity of $\frac{\partial n}{\partial y}$ is negligible. So, the set of equations (1) modifies to equation (2):

$$\varepsilon_x = \frac{1}{n_0}\frac{\partial n}{\partial x}(z_2 - z_1). \tag{2}$$

The value of ε_x can be determined experimentally from photometric measurements of Tepler photographs when equation (3) is used [14]:

$$\frac{\Delta I}{I_0} = \frac{\varepsilon_x F}{\Delta x}. \tag{3}$$

Here I_0 is a background light intensity without Foucault knife, ΔI - is an intensity difference between disturbed and undisturbed regions on the Tepler snap-shot in Foucault knife presence.

Absolute value of index of refraction in turbulent boundary layer can be found by using following equation:

$$n(x,y)=n(x_0,y)-\int_{x_0}^{x}\frac{\partial n}{\partial x}(x,y)\,dx=n_0-\frac{n_0}{\Delta z}\int_{x_0}^{x}\varepsilon_x(x,y)\,dx=n_0-\frac{n_0}{\Delta z}\frac{\xi}{F}\int_{x_0}^{x}\frac{\Delta I(x,y)}{I_0}dx. \qquad (4)$$

Here n_0 is index of refraction of undisturbed air.

Index of refraction of plasma can be represented by the equation (5) [13]:

$$n\text{-}1=\kappa\rho(1+\beta T)\text{-}K\lambda^2 N_e. \qquad (5)$$

Where

$K=\dfrac{\pi e^2}{2m_e c^2}$=4,5·10^{-14}, β –is thermal coefficient of volumetric expansion; λ – is probe radiation wavelength; ρ – is medium density; N_e - is electron concentration.

It is assumed that in the self-similar area of the jet the flow is isobaric. So, the equation (5) may be rewritten as:

$$n-1=(n_0-1)\frac{T_0}{T}-K\lambda^2 N_e. \qquad (6)$$

The dispersion formula for air index of refraction [14] is:

$$n-1=\frac{1}{10^6}\left[64,328+\frac{29498,1}{146-10^6/\lambda^2}+\frac{255,4}{41-10^6/\lambda^2}\right], \qquad (7)$$

Equation (5) for two wavelengths λ_r = 650 nm and λ_b = 420 nm forms the set of equations with two unknown variables – electron temperature and concentration:

$$\begin{aligned} n_b-1&=(n_{b0}-1)\frac{T_0}{T}-K\lambda_b^2 N_e,\\ n_r-1&=(n_{r0}-1)\frac{T_0}{T}-K\lambda_r^2 N_e. \end{aligned} \qquad (8)$$

By solving this set (8) for λ_r = 650 nm and λ_b = 420 nm temperature and concentration of electrons can be obtained.

Two-dimensional distribution of averaged values of temperatures and concentrations of electrons in boundary layer are shown in Fig. 3.

Obtained concentration of electrons values is comparable to the relevant values for glow discharge [10]. “Wave-like” behavior of distribution of electron concentration along the flow is due to volume charges generation, leading to potential redistribution. It can be seen from the non uniform temperature distribution. This effect is similar to Faraday dark space and cathode space forming in glow discharge.

Fig. 4 is a cross-section of distributions presented in Fig. 3. The averaged values of temperatures and concentrations of electrons along the flow on distance 10 mm, 6 mm and 3 mm from the plate surface are shown.

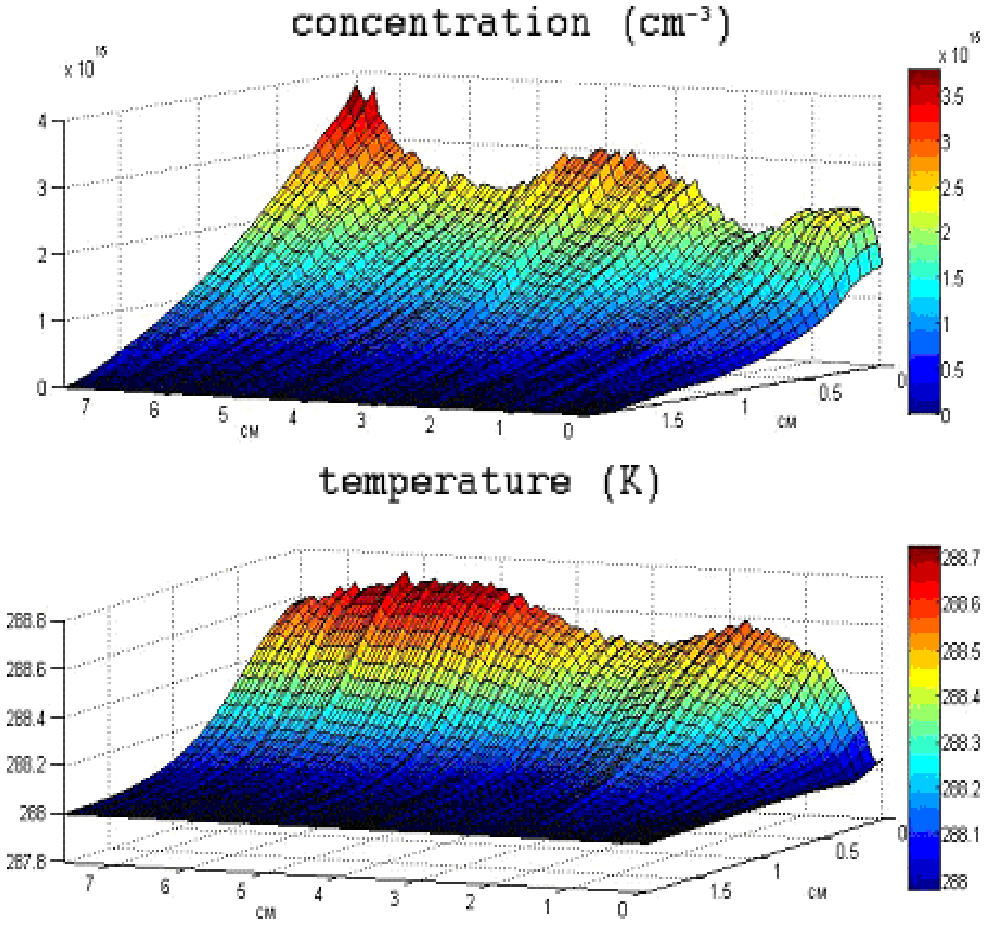

Fig. 3. Two-dimensional distribution of averaged values of temperatures and concentrations of electrons in boundary layer

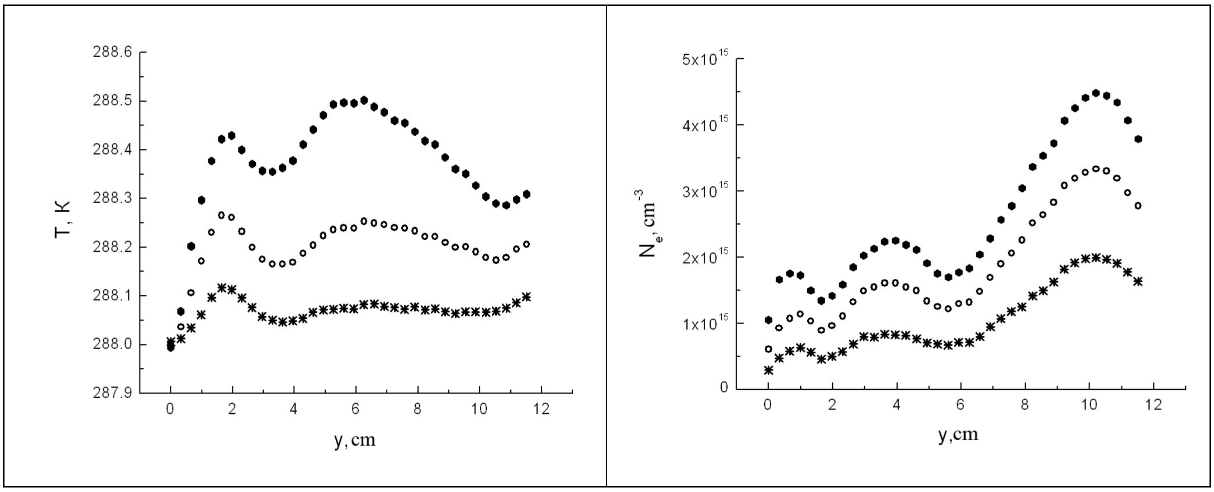

Fig. 4. Distribution of averaged values of temperatures and concentrations of electrons along the flow: • – x = 10 mm; o – x = 6 mm; ∗ – x = 3 mm

4. CONCLUSIONS

Obtained concentration of electrons values is comparable to the relevant values for glow discharge. “Wave-like” behavior of concentration of electrons distribution along the flow is due to volume charges generation, leading to potential redistribution. This effect is similar to Faraday dark space and cathode space forming in glow discharge.

In the induced flow Ion acceleration takes place mostly near minimum of electrons concentration distribution. Extremum of electrons temperature distribution are in antiphase to respective extremum of electrons concentration. So, in investigated discharge few interlaced spaces appear: near minimum of concentration distribution dominance of heating of flow appears and near maximum ion acceleration take place.

5. REFERENCES

1. J.R. Roth and Xin Dai. Optimization of the Aerodynamic Plasma Actuator as an Electrohydrodynamic (EHD) Electrical Device. 44th AIAA Aerospace Sciences Meeting and Exhibit 9–12 January 2006. Reno, Nevada. AIAA 2006-1203.
2. D.V. Roupassov, I. N. Zavyalov, A.Yu. Starikovskii. Boundary Layer Separation Plasma Control Using Low-Temperature Non-Equilibrium Plasma of Gas Discharge 44th AIAA Aerospace Sciences Meeting and Exhibit 9-12 January 2006. Reno, Nevada. AIAA 2006-373.
3. P. Khramtsov, O. Penyazkov, M. Chernik, I. Shatan, I. Shikh. Effect of surface high-frequency barrier discharge on a flat plate drag reduction, The 3rd Int. Workshop «Nonequilibrium processes in combustion and plasma based technologies». Минск, Беларусь. 2008. С. 44–47.
4. G.I. Font, S. Jung, C.L. Enloe, and T.E. McLaughlin. Simulation of the Effects of Force and Heat Produced by a Plasma Actuator on neutral Flow Evolution. 44th AIAA Aerospace Sciences Meeting and Exhibit 9-12 January 2006/ Reno, Nevada. AIAA 2006-0167.
5. О.Г. Пенязьков, П.П. Храмцов, М.Ю. Черник, И.Н. Шатан, И.А. Ших. Влияние плазмы высокочастотного барьерного разряда на структуру динамического пограничного слоя на плоской поверхности // ИФЖ, Т. 81, № 1. 2008. С. 55-62.
6. G.I. Font, C.L. Enloe, T.E. McLaughlin, and D. Orlov. Plasma Discharge Characteristics and Experimentally Determined Boundary Conditions for a Plasma Actuator. 44th AIAA Aerospace Sciences Meeting and Exhibit 9-12 January 2006. Reno, Nevada. AIAA 2006-188.
7. О.Г. Пенязьков, П.П. Храмцов, М.Ю. Черник, И.Н. Шатан, И.А. Ших Влияние иоинного ветра на структуру динамического пограничного слоя на плоской пластине. VI Минский международный форум по тепло- и массообмену. Сборник докладов на CD, Минск, 19–23 мая 2008 г. ISBN 978-985-6456-60-5, Доклад № 1–48].
8. A.A. Sidorenko, B.Yu. Zanin, B.V. Postnikov, A.D. Budovsky, A.Yu. Starikovskii, D.V. Roupassov, I.N. Zavialov, N.D. Malmuth, P. Smereczniak, and J.S. Silkey. Pulsed Discharge Actuators for Rectangular Wing Separation Control. 44th AIAA Aerospace Sciences Meeting and Exhibit 9–12 January 2006. Reno, Nevada. AIAA 2007-941.
9. D.M. Orlov , T.C. Corke, M.P. Patelz. Electric Circuit Model for Aerodynamic Plasma Actuator. 44th AIAA Aerospace Sciences Meeting and Exhibit 9-12 January 2006. Reno, Nevada. AIAA 1206-2006.
10. A.V. Likhanskii, M.N. Shneider, S.O. Macheret, and R.B. Miles. Modeling of Interaction Between Weakly Ionized Near-Surface Plasmas and Gas Flow. 44th AIAA Aerospace Sciences Meeting and Exhibit 9–12 January 2006. Reno, Nevada. AIAA 2006-1204.
11. П.П. Храмцов, О.Г. Пенязьков, М.В. Дорошко, М.Ю. Черник, И.А. Ших. Теневой метод измерения осредненной концентрации электронов в потоке

ионизированного газа, индуцированного высокочастотным барьерным разрядом // ИФЖ, в печати.

12. П.П. Храмцов, О.Г. Пенязьков, В.М. Грищенко, М.Ю. Черник, И.Н. Шатан, И.А. Ших. Аэродинамическое сопротивление пластины в потоке ионизированного газа, индуцированного приповерхностным высокочастотным барьерным разрядом // ИФЖ, в печати.
13. Л.А. Васильев. Теневые методы. М., Наука. 1968.
14. Диагностика плазмы / Под ред. Р. Хаддлстоуна и С. Леонарда. М., Мир. 1967.

CYSENI 2009, May 28-29, Kaunas, Lithuania
ISSN 1822-7554, www.cyseni.com

APPLICATION OF HIGH-FREQUENCY BARRIER DISCHARGE FOR FLAT PLATE DRAG REDUCTION

I.N. Shatan
Heat and Mass Transfer Institute of the National Academy of Sciences of Belarus
15 P. Brouki str., Minsk BY-220072, Republic of Belarus
Phone: +375(17)2842246
E-mail: 2eshnik@gmail.com

ABSTRACT

Application of discharge plasma for drag reduction of aircraft is a wide and active developing research field, which is carried out all over the world. The purpose of this work is an experimental investigation of capabilities of surface high-frequency barrier discharge to influence the total aerodynamic drag of flat plate. Placed on the plate discharge the system produces surface plasma at atmospheric pressure. Discharge system consists of two electrodes. One of them is an exposed multiple-apex electrode. The other electrode is embedded in the plate segment of wire. High-frequency barrier discharge on the flat plate is sustained by high-voltage ac pulses. In experiments the blow on the flat plate is produced by two-dimensional air stream. To determine the influence of plasma actuator on flow structure and boundary layers structure, the shadow patterns of blow on the flat plate by air stream are obtained. In experiments dependence between total aerodynamic drag of flat plate, the velocity of incident flow and electrical parameters of surface discharge is investigated. It is established that the use of high frequency surface barrier discharge allows decreasing profile drag coefficient to 3 – 7 %.

Key words: Plasma drag, discharge plasma, high-frequency barrier discharge, multiple-apex electrode, aerodynamic drag

1. INTRODUCTION

Application of plasma for aircraft drag reduction is of particular interest. Aerodynamic drag is the main source of aircrafts engine power loss. Increase of air vehicle effectiveness and its velocity is an important issue. There have been a wide variety of attempts in the past to achieve drag reduction and flow control in boundary layers and over airfoils by mechanical and fluid dynamic means. These approaches usually make wings more complicated, may add weight to the wing and become sources of airframe noise and vibrations.

Application of discharge plasma for drag reduction of an aircraft is a wide and actively developed research field, which is being carried out all over the world [1–6]. The dielectric barrier discharge is a type of plasma discharge with the unique property that it is self limiting and, therefore, sustainable at atmospheric pressures. Because of its particular properties method of high-frequency barrier discharge is a very perspective way to generate surface plasma at atmospheric pressure and has an effect on aerodynamic drag. The purpose of this work is an experimental investigation of the dependencies between the total aerodynamic drag of a flat plate, the velocity of incident flow and electrical parameters of discharge.

2. EXPERIMENTAL EQUIPMENT AND METHODOLOGY

In these investigations a flat caprolon plate with the peaked front edge was used. Total size of the plate was 10×180×120 mm. Exposed to the air multiple-apex system and insulated copper wire were used as discharged electrodes. The configuration of the electrodes is shown in Fig. 1. The multiple-apex electrode was placed on the front peaked edge of the plate. It consisted of two sets of thin needles arranged on upper and lower surfaces of the plate. The needles were located in the streamwise direction with 3 mm step parallel to the surfaces. The distance between needles and surfaces was 3 mm on both sides of the plate. The other electrode was a segment of copper wire covered by fluoroplastic isolation. It was built-in in the plate parallel to the front edge at 40 mm distance from the needle ends.

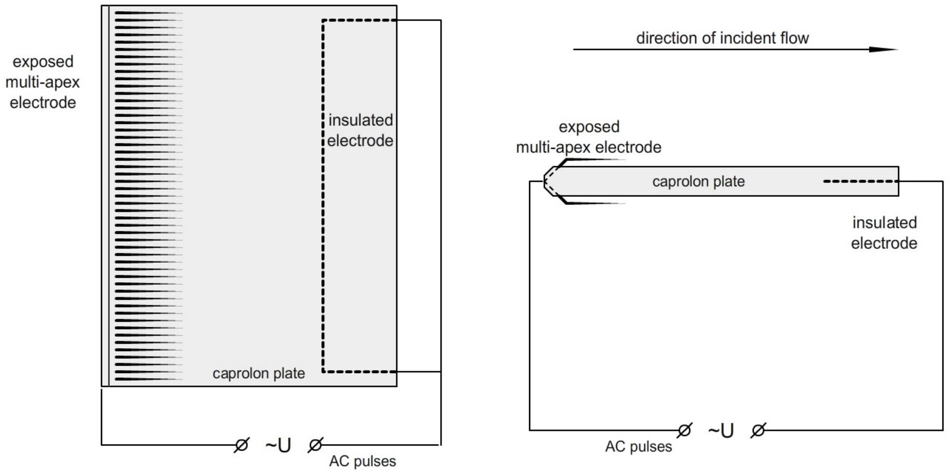

Fig. 1. Configuration of discharge electrodes on the plate. Multiple-apex electrode is exposed to the air while the other is insulated inside the plate

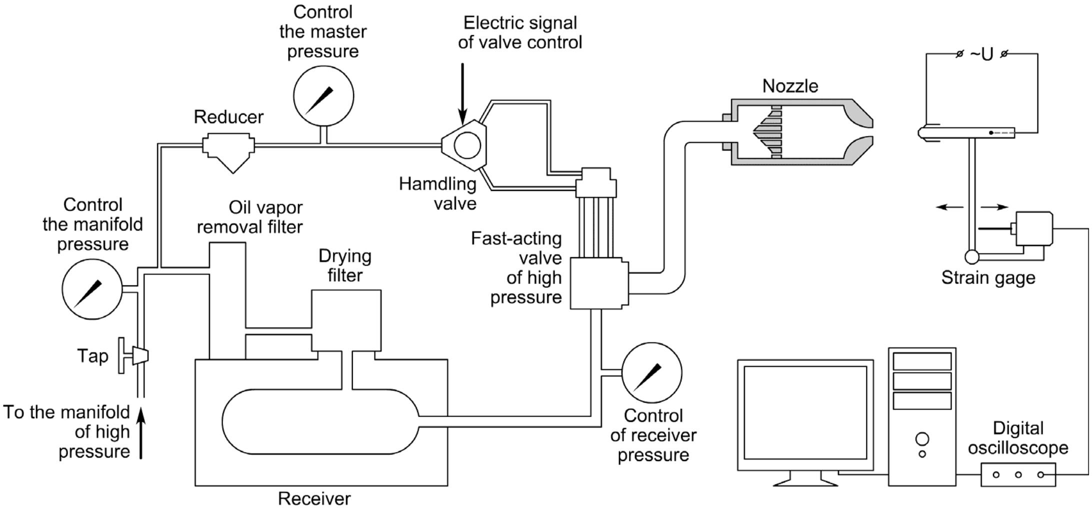

Fig. 2. Experimental equipment for measurement of aerodynamic drag

High-voltage electrical ac pulses with duration 200 microseconds, amplitude 70 kV and frequency 1 kHz were supplied to the electrodes and generated high-frequency barrier discharge on the flat plate. An apparently diffused discharge light was seen by unaided eye. As the result of interaction between charged particles with electrodynamic body forces, the gas flow appeared (its velocity was about 5-10 m/s) and turbulent boundary layers were formed on the surfaces [7]. The blow on the plate was produced by two-dimensional air stream that flowed through a nozzle with exit section 15×200 mm. The scheme of experimental facility for drag measuring is shown in Fig. 2. Compressed air from high pressure manifold was stored in the receiver with enclosed volume 0.2 m^3. The pressure in the receiver was set depending on the required flow velocity.

The plate was placed across the flow axes at 120 mm distance from the nozzle section and was fixed on the hinge. The force acting the plate was transmitted to the strain gauge. Sensor's electric signal was registered by the digital oscilloscope. The flow velocity was measured by Pitot-Prandtl tube. Visualization of the flow structure near the flat plate was carried out with a holographic interferometer. The shadow pattern of blow on the flat plate with barrier discharge is shown in Fig. 3. The flow velocity near the front edge of the plate was equal to $u = 60$ m/s. As follows from the shadow patterns, barrier discharge causes constriction of the boundary layer to the surface.

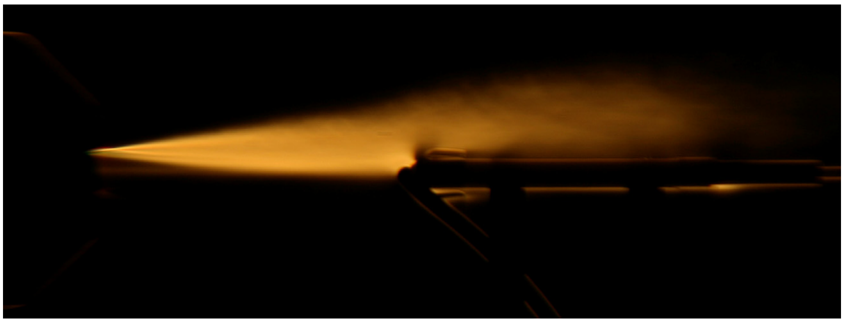

Fig. 3. Shadow pattern of blow on the flat plate by two-dimensional air stream

3. RESULTS AND DISCUSSION

The photography of the plasma light with air flow and without it was used for the evaluation of the flow effect on the barrier discharge structure. For this purpose a digital camera was used. As it is shown in Fig. 4, the flow presence leads to the elongation of the discharge radiating area. The elongation was about 15 % with the flow velocity 60 m/s.

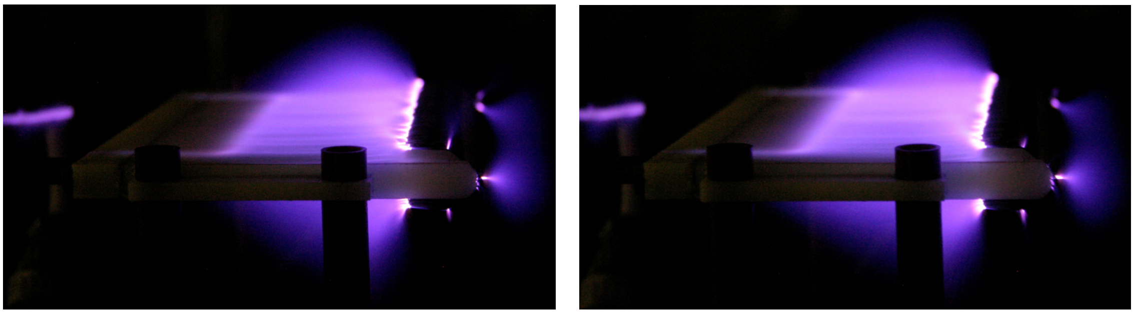

Fig. 4. The photos of the plasma light without air flow (left) and with air flow $u = 60$ m/s (right)

The total aerodynamic drag of the plate was measured by electromechanical strain gauge. The blow on the plate was produced with a discharge and without it, in turn. As the velocity of the incident flow was decreasing, the pressure at the receiver was decreasing. The total plate drag dependence from time with a discharge and without it is shown in Fig. 5.

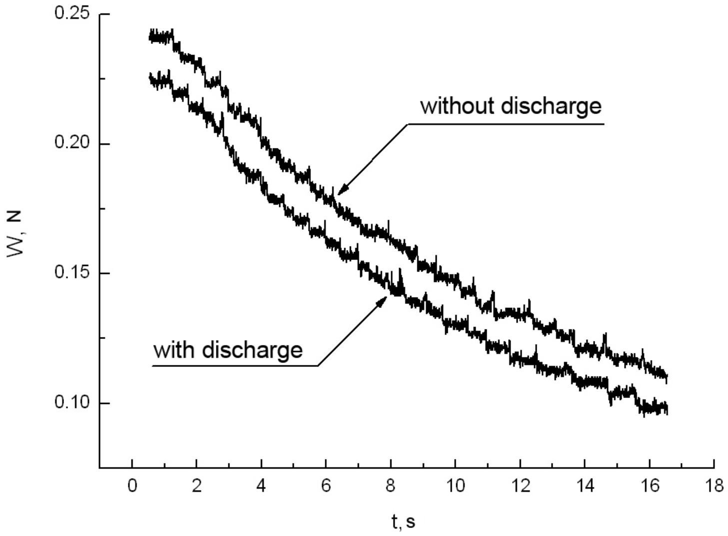

Fig. 5. The time dependences of the total plate drag in the presence of discharge and without it.

The profile drag coefficient of the flat plate was calculated by formula [8, 9]

$$c_W = \frac{F}{\rho u^2 bh}, \tag{1}$$

where b – the plate width; c_W – the profile drag coefficient of the plate; h – the plate thickness; u – the velocity of the incident flow; F – the profile aerodynamic drag; ρ – the air density.

The dependences of profile drag coefficient of the plate on Reynolds number with and without barrier discharge are shown in Fig. 6. The presence of high-frequency barrier discharge on the surface of the plate leads to the profile drag coefficient decrease to 3–7%. It should be mentioned that in the investigated range of Reynolds number profile drag is the sum of two comparable components: friction drag and pressure drag. The plasma boundary of the used electrodes configuration influences only on the friction drag and does not influence on the pressure drag.

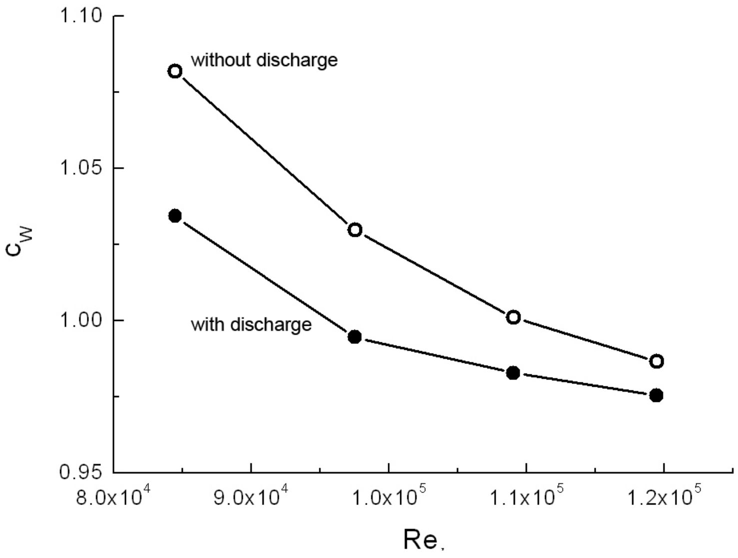

Fig. 6. The dependences of profile drag coefficient of the plate on the Reynolds number with and without barrier discharge

To define optimal discharge conditions for greater influence on aerodynamic drag the investigation of the dependence of profile drag coefficient on the electric power of discharge was carried out. The results are shown in Fig. 7. While increasing electric power, the efficiency of barrier discharge influence on the plate drag increases until some critical point. This value of specific surface density power input is equal to $P_k = 9.5$ kW/m^2. The further growth of electric power leads to the increase of total aerodynamic drag of the plate. It is connected with discharge contraction processes in its own magnetic field and formation of filamentary structure. Filamentary plasma structure shunt discharge gap because of its high electroconductivity. In such conditions electrical power of the discharge is dissipated mainly on heating, and the part of energy which is used for ion wind generation decreases.

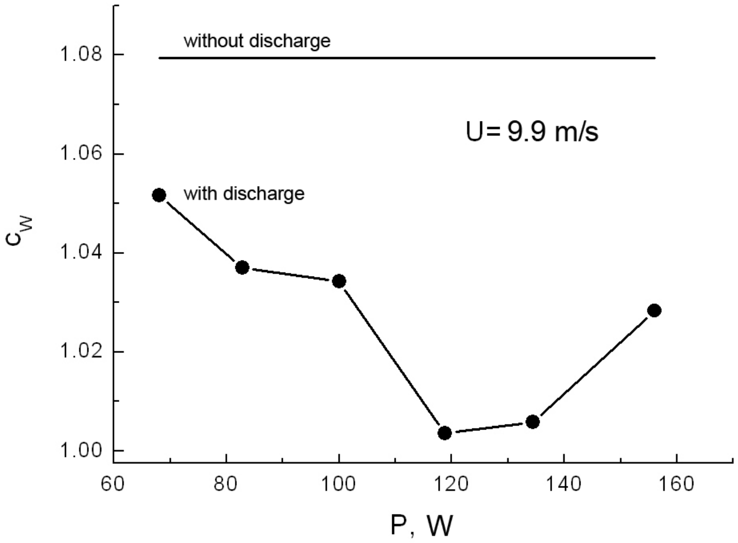

Fig. 7. Dependence of profile drag coefficient on electric power of discharge

4. CONCLUSIONS

In this work it is shown experimentally that the use of high frequency surface barrier discharge allows to decrease the profile drag coefficient by 3–7 %. The discharge is bound inflexibly to the electrodes and almost isn't blown out by incident flow. The critical value of specific surface density power input P_k, which has maximal efficiency of barrier discharge influence on the plate drag, is high enough to use it in engineering design of aircrafts in wide range of electrical parameters.

REFERENCES

1. Roth J.R. Plasma Processing Applications of a One Atmosphere Uniform Glow Discharge Plasma // Int. Symp. Plasma 2001. Warsaw, Poland, September 19–21, 2001.
2. Fadeev V. M., Jusupaliev U., Shyteev S. A. Barrier discharge in the modern technologies [Internet resource] // Access mode: http://www.optics.phis.spbu.ru/
3. Boubnov E., Udovenko D., Sharshembiev K., Borombaev M.K. Voltage-charge characteristic of barrier discharge on duplex wire // The materials of the first republican science workshop of students physicist and young scientists. Kharakol, 2001. Pp. 92-101.
4. Samoilovich V.T., Gibalov V.I., Kozlov K.V. Physical chemistry of barrier discharge. // Moscow, MSU, 1989. p. 176.

5. Philipov U.V., Emelyanov U.M. About active power of ozonizers // Journal of Chemical Physics. 1959. Vol. 33, N. 5, p. 1042–1046.
6. Uniform barrier discharge [Internet resource] // Access mode: **Http://www.Optics.Phis.Spbu.Ru/**
7. P. Khramtsov, O. Penyazkov, M.Chernik, I. Shikh, Shadow method of measuring of average electron concentration in ionized gas flow induced by high-frequency barrier discharge. // Journal of Engineering Physics and Thermophysics, in print.
8. Hantly G. Dimensional analysis.// Moscow, Mir, 1970.
9. Schlichting G. The theory of boundary layer.// Moscow, Nauka, 1969.

CYSENI 2009, May 28-29, Kaunas, Lithuania
ISSN 1822-7554, www.cyseni.com

COMBUSTION OF METAL PARTICLES IN OXYGEN ATMOSPHERE IN RAPID COMPRESSION MACHINE

V. V. Leshchevich
A.V. Luikov Heat and Mass Transfer Institute
P. Brovka str. 15, 2000072 Minsk – Belarus
Phone (+37517) 284 15 20
E-mail: V.Leschevich@dnp.itmo.by

ABSTRACT

This work has been conducted to determine conditions that can provoke spontaneous autoignition of the iron particles in oxygen atmosphere. The rapid compression machine (RCM) was used in this study to generate thermodynamic conditions (oxygen pressures 1.5-3.7 MPa and temperatures 750-1000 K) at which autoignition can occur. The iron powder consisted of different size particles (0-200 μm) and iron powders, consisting of one particle fraction, were studied. The critical conditions for iron particle layer autoignition were established. The influence of different factors (a rate of heat removal from the combustion region and particle size) on the ignition and combustion properties of iron powders was determined. The obtained data are useful for understanding the basics of multiphase media combustion.

Keywords: combustion, autoignition, rapid compression machine, multiphase media, iron particles, oxygen atmosphere, critical conditions

1. INTRODUCTION

In the recent years much attention has been given to combustion in multiphase media where a liquid or solid fuel burns in a gaseous oxidant. Particular interest was paid to the ignition and combustion of metal particles. Today metal powders are widely used as fuel additives in various energetic materials such as explosives and pyrotechnics due to its high combustion enthalpy.

Metal particle combustion has been reviewed by I. Glassman [1], F.A. Williams [2] and recently by R.A. Yetter and F.L. Dryer [3, 4]. For oxygen-containing environments, in which the final product is a refractory metal oxide, early studies recognized the importance of two factors. The first is the volatility of the metal relative to the volatility of the metal oxide and the second is the relationship between the energy required to gasify the metal or metal oxide and the overall energy available from the oxidation reaction. For a given metal-oxygen system, the magnitudes of these energies and the metal and metal oxide volatilization temperatures have been used to classify the metal combustion process. The combustion mechanisms for different metals can be divided into two categories: the metal is relatively nonvolatile and the combustion consists of heterogeneous surface reactions; the metal easily vaporizes and the combustion process takes place in the vapor phase. Most metals have high boiling point temperatures, and thus, for a metal to burn in the vapor phase, the oxide vaporization–dissociation or volatilization temperature must be greater than the boiling point temperature of the metal. If the oxide's vaporization–dissociation temperature is less than the boiling point of the fuel, combustion must proceed heterogeneously on the particle surface. This concept has become known as “Glassman's criterion” for the vapor phase combustion of metals. Metals that will burn in the vapor phase in oxygen can be determined by comparing the metal's boiling point temperature to the temperature at which the metal oxide is decomposed or dissociated to vapour phase. According ‘‘Glassman’s criterion” Al, Be, Cr, Fe, Hf, Li, Mg and Ti fall into this category and have the ability to burn as vapour phase diffusion flames at 1 atm in pure oxygen [1]. If the form of the oxygen reactant is varied, then the available enthalpy will change as a result of a change in the heat of reaction, and thus, the mode of combustion may change as well. The condition for vapour phase combustion versus heterogeneous combustion may be influenced by pressure by its affect on the vaporization temperature of the metal reactant [4].

The ignition characteristics of metal particles can strongly depend on the experimental technique which governs the pressure and temperature fields of the media surrounding the particles. A common technique for metal particles combustion investigations is the so-called “method of tracks” developed by Russian researcher V.A. Fedoseev in the late 1950’s [5, 6]. This technique involves maintaining a flow of hot oxidizer gas inside a tube. Single metal particles are injected into the tube and the subsequent ignition and combustion of the particles is recorded photographically. G. Young et al. [7] used a commercially available McKenna flat flame burner using a mixture of methane/air/oxygen to provide a test bed for determining critical parameters of the ignition and combustion of boron nanoparticles. The products of combustion in the burner post flame region were used in order to provide an environment for particle combustion. Lower ignition temperatures have been found with other techniques. For example, N.M. Laurendeau and I. Glassman [8] used an induction furnace to heat magnesium particles and observed ignition temperatures of about 635 °C. The dust flammability experiments were conducted in the PRL 20-L laboratory chamber, using strong pyrotechnic igniters [9, 10].

All experimental studies were concentrated on the combustion characteristics of metal particles. The used experimental equipment makes it possible to obtain complete information about metal particle ignition and combustion phenomena. But this information doesn’t include experimental data (the pressures and temperatures of the gaseous oxidant) concerning autoignition of metal powders at elevated pressures. With the view of determining these conditions this research was carried out.

2. EXPERIMENTAL SETUP

Rapid compression machine models a single compression event of an engine. Gases contained in the test chamber are compressed to high pressures and temperatures for few milliseconds and the reaction is allowed to proceed at a constant volume. Typically, post compression pressure greater than 5 MPa and temperature greater than 1000 K can be obtained. In order to avoid significant heat losses and reaction happening before the end of the compression stroke, the piston should be travelled very fast. To achieve these high velocities, the piston is usually driven pneumatically and stopped hydraulically. The compression ratio, initial pressure, temperature of the mixture can be varied to control the pressure and temperature after compression.

The design of the developed for this study RCM is based on several other compression machines described elsewhere in the literature [11–13]. The general view of the machine is shown in Fig. 1. The RCM system consists of a driving cylinder, a compression cylinder, a hydraulic system of motion control and a driving air tank. The driving cylinder and the compression cylinder of the RCM have a bore of 100 mm and 50 mm, respectively. This allows the driving air pressure to be 4 times smaller than the final desired pressure achieved by the compression piston.

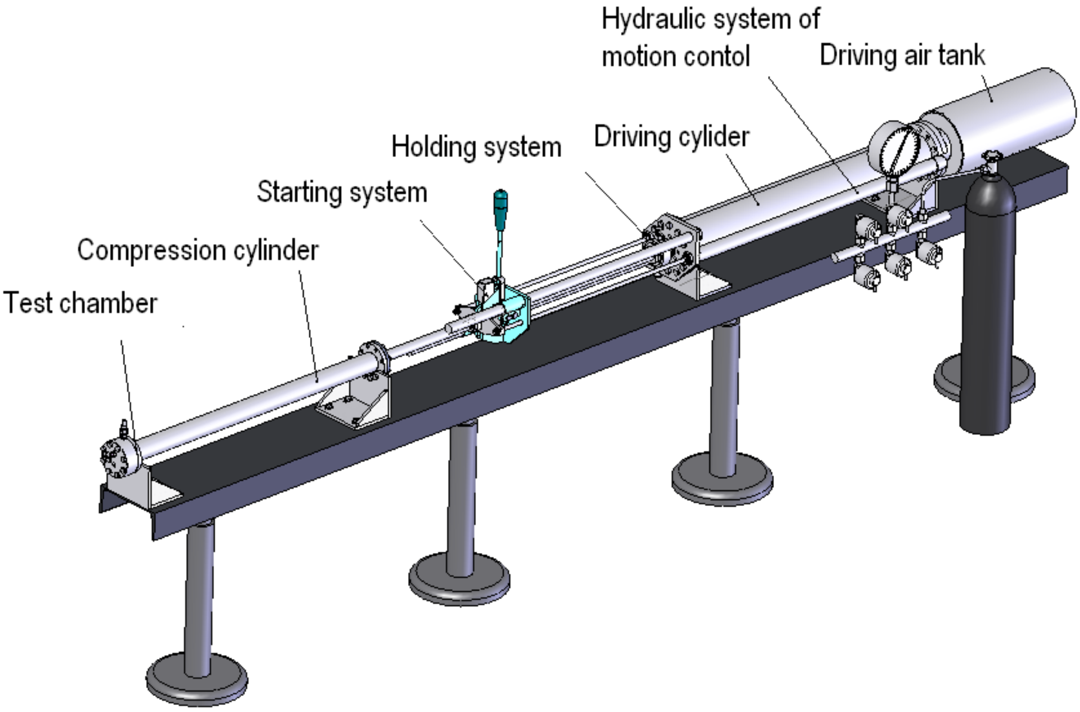

Fig. 1. General view of the developed RCM

The test chamber (the end part of compression cylinder) is designed to withstand high pressures generated under compression and is equipped with a pressure transducer, a gas inlet/outlet port for pumping and filling it with oxygen. For optical excess, a quartz cylinder was mounted into the wall of the test. The doubled optical fibbers transferred the recording luminescence at metal particles ignition and combustion to the photomultiplier tubes. In these experiments the volume luminescence was only as the indicator of the presence of the reaction in the test chamber.

The compression ratio is regulated by varying the initial volume of the compression cylinder. Volume variations are achieved by changing the initial position of the system of the pistons and, hence, of the piston stroke (the maximal piston stroke is 865 mm). When the test chamber height is 15 mm the compression ratio of 55 can be achieved and further increased by reducing the test chamber height. Pressure and temperature of a compressed gas media is varied by changing the initial gaseous oxidant pressure in the test camber and compression ratio.

Experimental data on a rapid compression machine include the temporal measurements of pressure and volume of gas media. Temperature then was calculated from the Clapeyron constitutive equation considering that mass of mixture didn't change during compression event.

In this study the iron powder consisted of different size particles was used as fuel and pure oxygen as oxidant. Iron powder was placed into the test chamber. Experiments were performed at constant initial pressure of oxygen in the compression cylinder channel equal to 25.0 kPa and at the initial temperature of 293 K. The piston stroke and the tank pressure of RCM were varied to obtain different conditions in test chamber at the end of compression. Particle samples of iron from Brovar's State Plant of Powder Metallurgy (Ukraine) were used in these experiments. The particle size distribution of this iron powder and the range of size of the separated particle fractions are presented in Table 1.

Table 1. Characteristics of iron particle fractions used in combustion experiments

Fraction number	0	1	2	3	4	5	6
Range of size , µm	> 200	160–200	100–160	80–100	63–80	50–63	≤ 50
Particle size distribution of total mixture, mass %	0.2	6.6	29.7	20	11.8	15.8	15.9

3. EXPERIMENTAL RESULTS

In the first experimental series a total mixture of iron particles was placed to the bottom of the test chamber. The particle ignition in this series was not observed for the pressures less than 1.8 MPa and temperatures less than 750 K. At these conditions the incomplete combustion of particles was occurred.

The ignition of a combustible metal particle depends on a variety of parameters, including the particle material, size, shape, surface characteristics, as well as the rate of heating and the oxidizing atmosphere. Heat released on metal oxidation may causes fast self-heating of the metal particles at high temperature. Thus, metal ignition, and therefore the explosion, occurs as a result of thermal self-acceleration of the chemical reaction [14]. In some cases, the heat released at oxidation of particles has time to be removed into the surroundings, and the ignition does not take place. Then the particle temperature reaches a maximum and decays to reach the initial gas temperature (subcritical regime). In other cases heat released in the particle causes self-acceleration of the oxidation reaction, which leads to a rapid increase in particle temperature and cause complete combustion of the whole particle layer (supercritical regime). The existence of the critical regime for metal particle oxidation has been mathematically shown [15]. The critical conditions for iron particle layer ignition were experimentally detected in this study. From photos in Fig. 2 it is seen that the local ignition does not result in combustion of whole particle layer (pressure above 2.16 MPa, temperature above 835 K). This is subcritical regime of auto-ignition. The heat released at oxidation of particles is removed into the chamber's wall due to thin particles layer. As known, the thicker particle layer has lower conductivity due to the particle packing factor and resistances of particles contacts in the layer. If the local oxidation have been started at the thick layer the heat released in the particle causes self-acceleration of the oxidation reaction, which leads to a rapid increase in particle temperature and causes complete combustion of particle layer. Photos on Fig. 3 demonstrate this case of autoignition at the pressure above 2.17 MPa and temperature above 840 K. Thus, the critical conditions delimited subcritical and supercritical regimes of autoignition for investigated iron powder and experimental parameters (test chamber geometry, heat flux from particles layer, the rate of oxygen compression, thickness of particles layer and etc.) are occurred at the oxygen pressure 2.16–2.17 MPa and temperature 835–840 K.

Besides a rate of heat removal from the particle layer there are a number of factors that also affect the behaviour of metal particles in high pressure oxygen medium. These are a rate of oxygen compression and a particle size distribution. Combination of these factors also determines the combustion regime. To evaluate the influence of particle size distribution on the ignition properties the individual particle fractions have been studied separately. To facilitate the comparison different fractions (the characteristic sizes cited in Table 1) were tested at the same time and therefore at the same thermodynamic parameters of the oxygen. To do that, particle fractions were located within separate cells of special racks made of stainless steel and inserted into the test volume. This experiments demonstrated that at the pressure about 2.17 MPa and temperature about 780 K all fractions of metal particles are not ignited. The higher compression ratio experiments (pressure about 3.07 MPa and temperature about 970 K) demonstrated the ignition and combustion of fractions 3, 5, 6 and not separated total mixture of particles. In addition, the localize autoignition and combustion of individual particles were revealed in fractions 2 and 4. Only the biggest fraction 1 with particle size ranged from 160 to 200 μm was not ignited. The combustion completeness was largest in fractions 6, 3 and total mixture of particles.

Fig. 2. Photographs of particle samples after compression for subcritical regime

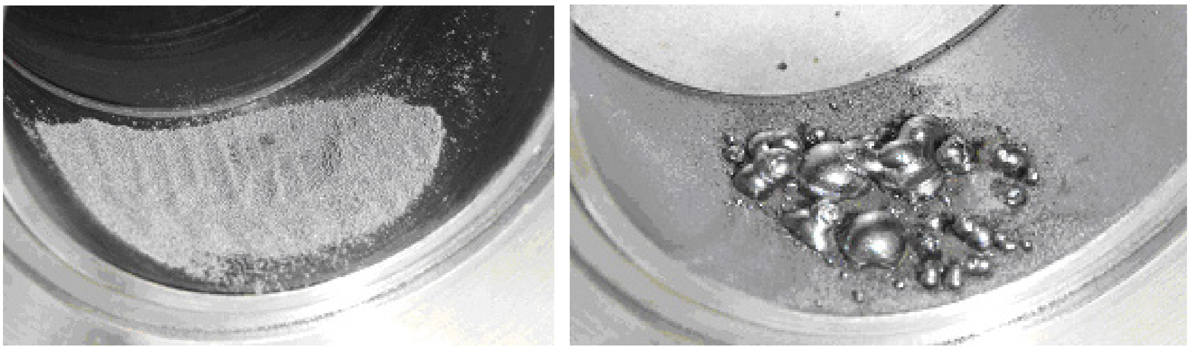

Fig. 3. Photographs of test chamber with particle sample before (left) and after compression (right) for supercritical regime

4. CONCLUSIONS

The autoignition and combustion studies of iron particles in oxygen atmosphere were performed in the rapid compression machine. In spite of, the used technique is rather new for such type investigations; preliminary experiments demonstrated the suitability of the developed RCM for metal powders autoignition studies. This is associated with high accuracy and repeatability of thermodynamic conditions of gaseous oxidant generated in the test chamber of RCM.

Experiments with iron powder consisted of different size particles shows the existence of the critical conditions for metal particle autoignition phenomenon. The transition between subcritical and supercritical regimes for investigated iron powder and for experimental conditions was observed at the pressure above 2.16–2.17 MPa and temperature over 835–840 K. For the quantitative description of this phenomenon and for the establishment of pressure and temperature correlations these results must be verified by statistical analysis of the extensive amount of experimental data.

To evaluate the influence of particle size on the ignition properties the individual particle fractions have been studied. As it was expected, the ignition ability of the iron powder decreases with increasing particle sizes.

The unique correlation between the occurrence of autoignition and the oxygen pressure and temperature, stoichiometry of the iron–oxygen system can't be obtained due to shortage of experimental data at this stage of investigation.

REFERENCES

1. I. Glassman. Combustion, 3rd Edition // Academic Press, Orlando. 1996, Ch. 9.
2. F.A Williams. Combustion Theory // Addison-Wesley, Redwood City, CA. 1985.
3. R.A. Yetter and F.L. Dryer. Metal particle combustion and classification // Microgravity Combustion: Fire in Free Fall, Academic Press. 2001, p. 419–478.
4. R.A. Yetter, G.A. Risha, S.F. Son. Metal particle combustion and nanotechnology // Proceedings of the Combustion Institute. Vol. 32. 2009, p. 1819–1838.
5. V.A. Fedoseev. Evaporation and Combustion kinetics of fine drops and particles // Physics of the aero dispersed systems.. Vol. 1. 1969, p. 98–114.
6. V.A. Fedoseev, V.E. Glushkov and L.A. Sokolov. Ignition of magnesium particles in different media // Physics of the aero dispersed systems. Vol. 6. 1975, p. 83–88.
7. G. Young, K. Sullivan, M.R. Zachariah and K.Yu. Combustion characteristics of boron nanoparticles // Combustion and Flame. Vol. 156. 2009, p. 322–333.
8. N. M Laurendeau, and I. Glassman. Combustion Science and Technology, Vol. 3, 1971, p. 77–82.
9. K.L. Cashdollar, I.A. Zlochower. Explosion temperatures and pressures of metals and other elemental dust clouds // Loss Prevention in the Process Industries. Vol. 20. 2007, p. 337–348.
10. K.L. Cashdollar. Overview of dust explosibility characteristics // Loss Prevention in the Process Industries. Vol. 13. 2000, p. 183–199.
11. D. Lee, S. Hochgreb. Rapid compression machines: heat transfer and suppression of corner vortex // Combustion and flame. Vol. 114. 1998, p. 531–545.
12. M.T. Donovan, X.He, T.R. Palmer, B.T. Zigler, M.S. Wooldridge and A. Atreya. Demonstration of a free-piston rapid compression facility for the study of High Temperature Combustion Phenomenon // Combust. Flame. Vol. 137. 2004, p. 351–365.
13. W.S. Affleck and A. Thomas. An opposed piston rapid compression machine for preflame reaction studies // Proc. Inst. Mech. Eng. Vol. 183. 1968, p. 365–387.
14. D.A. Frank-Kamenetskii. Diffusion and heat transfer in chemical kinetics // New York: Plenum Press. 1969.
15. E. Shchepakina and V. Sobolev. Modelling of critical phenomena for ignition of metal particles // Journal of Physics: Conference Series. Vol. 138. 2008, 012025, doi:10.1088/1742-6596/138/1/012025.

CYSENI 2009, May 28-29, Kaunas, Lithuania
ISSN 1822-7554, www.cyseni.com

ENVIRONMENTAL EFFECTS OF PAKRI AND VIRTSU WIND FARMS

I. Pertmann
Tallinn University of Technology
Department of Thermal Engineering
Kopli 116, 11712 Tallinn – Estonia
Phone: +372 620 3915
E-mail: pertmann@sti.ttu.ee

ABSTRACT

Pakri and Virtsu are two first Wind Farms in Estonia, established respectively in 2005 and 2002. Pakri Wind Farm consists of 8 Nordex N-90 wind turbines. Their nominal power is 2.3 MW, hub height 80 meters and rotor diameter 90 meters [9]. Total power of the Pakri wind farm is 18.4 MW. Virtsu wind farm consists of three Enercon E-40/6.44 wind turbines, hub height 65 meters and rotor diameter 44 meters, and one Enercon E-48 wind turbine, hub height 65 meters and rotor diameter 48 meters. Enercon E-40 nominal power is 600 kW and Enercon E-48 800 kW [10]. Wind farm total power is 2.6 MW. To show the real wind farm effects to the environment and people, different measurements and observations were carried out in both wind farms. Main investigated effects of the wind farms were wind turbine noise levels at different distances from wind turbines, effects on birds and animals. In order to investigate working wind farm's effects on birds and bird behavior, bird observation and count was carried out. In every visit to the wind farm bird corpse searches were made. To investigate the noise distribution in the wind farm area and near the wind farm site, different noise measurements were carried out. Noise was measured in four different cases – at low wind speeds (1–2 m/s, wind turbines did not work), at middle wind speeds (3–5 m/s and 6–8 m/s) and at strong wind speeds (13–15 m/s). In first case noise of not working wind farm was compared with other noises in wind farm area (bird voices, noise form the cars, etc.).

Keywords – wind farm, environmental effects, noise.

1. INTRODUCTION

There is a big discussion about what power sources to use in the future in Estonia. While wind energy is one of the renewable energy sources, all the positive and negative aspects of wind energy and wind turbines are under attention. Unfortunately, most of the wind turbine negative effects are magnified or shown through the examples of other countries. Every wind farm is different from the others (different types of turbines, number of turbines in wind farm, wind farm location) and therefore generalizations are not reasonable. The aim of the current investigation and measurements is to show the real measured noise levels and independent research results in two different Estonian wind farm areas.

Pakri and Virtsu wind farms were selected because they differ by many characteristics. Virtsu wind farm is the first wind farm in Estonia, so it is quite little (2.6 MW). Because it was the first wind farm in Estonia, that is also the reason, why it is little bit poorly sited (too near to the local houses) and there are problems with noise and light flashing caused by rotor blades. Virtsu wind farm nearest neighbours are complaining about noise and also light flashing problems in winter, when sun is low.

Pakri wind farm was the first bigger wind farm in Estonia. There are no local houses near the Pakri wind farm area and the noise and light flashing are not such big problems there. Hence two wind farms with different types of generators, different numbers of turbines in wind farm and different wind farm locations are compared.

2. METHODOLOGY

Virtsu wind farm consists of three Enercon E-40/6.44 600 kW turbines and one Enercon E-48 800 kW turbine making total power of 2.6 MW. Pakri wind farm consists of eight Nordex N-90 2.3 MW wind turbines. Total power of Pakri wind farm is 18.4 MW.

Location of the Pakri and Virtsu wind farms' turbines is shown in Fig. 1.

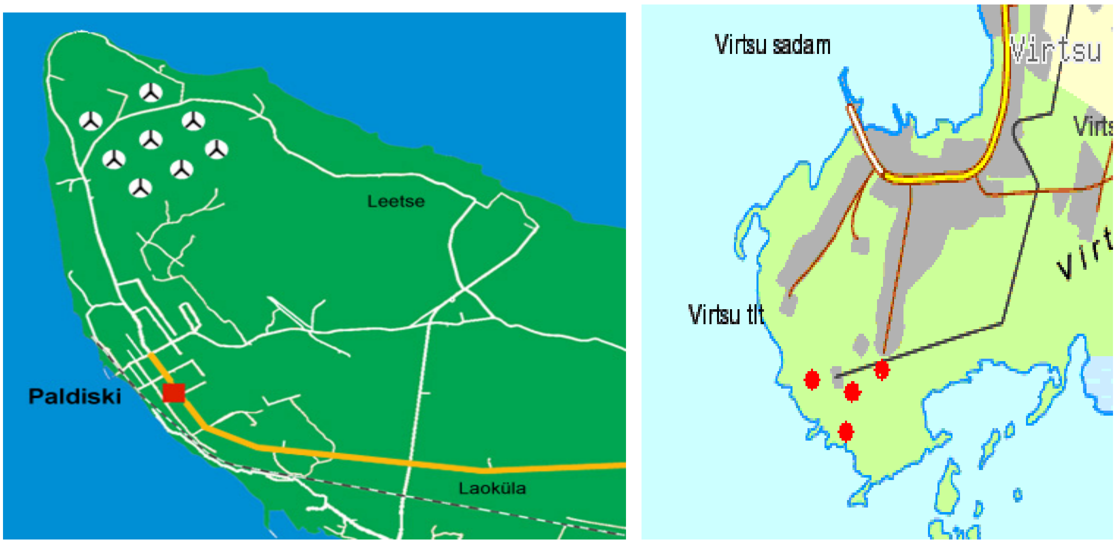

a b

Fig. 1. Location of the Pakri (a) and Virtsu (b) wind farms' turbines

During every visit to the wind farms bird and animal observations were made. All the bird and animal activities were registered. All the anthills and animal footprints were mapped. Elaborated bird observation in Pakri wind farm was carried out in October 2006 (when the migratory birds were leaving). In October 2008 Tallinn Bird club carried out a bird count in different places including Paldiski and top of Pakri peninsula. Also search for bird corpses was made during each visit to the wind farms.

Virtsu wind speed data were registered in Virtsu Meteorological Station and Pakri wind speed data were available from one of the wind farm turbine nacelle anemometers. Wind direction did not change during the measurements. Wind turbine noise measurements were carried out with Digital Sound Level Meter, Model 407764. Range of the sound level meter is 30 dB to 130 dB. Accuracy of the device is ± 1.5 dB. The noise levels in dB with frequency weighting A were measured at different distances from turbines and compared with overall background noise levels away from the wind farm site. At lower wind speeds (up to 3 m/s) noises caused by wind turbines were compared with other noise sources in wind farm area (bird sounds, passing cars etc). Noise was measured in four different cases:

- at wind speeds of 1–2 m/s, when wind turbines did not work,
- at wind speeds of 3–5 m/s, when wind turbines were working very slowly
- at wind speeds of 6–8 m/s, when wind turbines were working below nominal power,
- at wind speeds of 13–15 m/s, when wind turbines were working at their nominal power.

Measurements were made at every 30 meters starting right next to the turbine and up to distance where the noise levels are in the same level with overall background level or up to distance, which can be achieved due to landscape (too dense forest, sea, etc.). One measurement series was made upwind and the other – downwind from the wind farm.

3. RESULTS AND DISCUSSIONS

3.1. Wind farm effects to birds and animals

The main three potential hazards to birds from wind turbines are: disturbance leading to bird displacement (barriers to movement), collision mortality and damage to habitat resulting from wind turbines and associated infrastructure. Wind farm effects are variable and also species-, season- and site-specific. Wind farm disturbance can lead to bird displacement and exclusion from areas of suitable habitat, which can lead to loss of birds' habitats. Disturbance may also arise from increased human activity in the wind farm area.

Many different studies have been made in different countries [3–6] and the main results are:

- Overall bird densities at wind farm sites were not significantly lower than those at reference sites;
- There was no evidence of clumped distributions of breeding birds and no significant difference in the extent of clustering between wind farm sites and reference sites;
- Bigger wind turbines, longer rotor blades, and larger wind farms were not associated with lower bird densities;
- Avoidance of wind turbines was observed at only one of the ten study sites [1].

Collision risk and mortality studies [3, 7–8] have quoted low collision mortality rates per turbine. In large and poorly sited wind farms (Altmont Pass in California, USA and Navarra in Spain), wind farm total collision mortality rates are a little bit bigger, but in Estonia the biggest operating wind farm today is Pakri wind farm with only 8 turbines, so the relative collision mortality should be low in this area.

Relatively high collision mortality rates have been recorded at large, poorly sited wind farms in areas where large concentration of birds are present, also migrating birds. One quite important factor, which influences the collision risk, is the height of individual wind farms. Different weather conditions have different influence on the risk of collision. Also species, age, behavior and stage of the bird's annual cycle influences the collision risk [2].

Habitat loss or damage, resulting from wind farm infrastructure, is not a major concern for birds, if the sites are not of national and international importance for biodiversity. If large developments are sited in such locations as on sandbanks in shallow waters or on peat lands, then there can be loss of or damage to sensitive habitats [1].

In Pakri and Virstu wind farms over 40 site visits were made during the last four years. Most of them were made in Pakri wind farm. No bird corpses have been seen in wind farm areas so far. During one visit to Pakri wind farm in autumn 2007 some brown bird feathers were found near the turbine number 7. The bird itself was eaten by some wild animal, so there is no certain proof that the bird was killed by the turbine rotor blades. Estonian wind farm opponents say that there are no bird's corpses near the wind farm areas because the foxes eat the birds, which are killed or injured by turbine rotor blades, but even if this bird was killed by a turbine, this is nevertheless only one bird during over 40 visits. Much more birds perish in high-voltage lines and near the high-rise buildings with mirror-glass windows.

During one October observation day the total of 716 birds were registered. There were 674 ciconias (migrating), 27 passerines and 15 other birds. During that time and also during other visits no wind turbine disturbance to the birds was registered. The migrating storks flew a lot higher than wind turbine rotor areas and also further from wind farm site. Little birds flew through or below rotor area and were also not disturbed at all [2]. One Pakri wind farm turbine and migrating storks are shown in Fig. 2:

Fig. 2. Pakri wind farm turbine and migrating storks

During Bird watch on 5 October 2008, Tallinn Bird Club counted 2259 birds in Paldiski and 1353 in Pakri foreland. The birds that figured the most were gulls (Larus, 840 birds), fieldfares (Turdus pilaris, 410 birds), siskins (Carduelis spinus, 629 birds) and goldeneyes (Bucephala clangula, 280 birds) [11]. In the period from 2005 to 2008 Estonian Ornithological Society counted over 90 bird species in Paldiski region and about 80 bird species in Virtsu region [12].

In wind farm like Pakri, which is already in work and is not poorly sited, i.e. located not in the sites of bird habitats, there are no major effects on the birds. Most likely birds are used to wind turbines and know how to avoid colliding with them.

In the building phase the wind farm is of course a very disturbing factor to the animals and insects, because in that phase there is a lot of human activity in wind farm area, for example, transportation, cranes, etc. However, every power plant incorporates building phase and that influences animals and local inhabitants. When the wind farm is ready and working, there are no more disturbances to the animals. Estonian wind farm opponents say that wind turbines frighten away the ants, but in Pakri wind farm there are a lot of anthills in wind farm site area. The nearest anthill to the turbines is only 100–150 meters away from the turbine number 3. Next anthill is about 300 meters away from the turbine. So in Pakri wind farm ants are not disturbed.

In addition to ants, animal have also been seen in Estonian wind farms: rabbits, adders, foxes and footprints of the wild boars. So it can be assumed that animals, like people, accustom to the changes in their place of habitation. Pakri wind farm turbine number 3 and anthill are shown in Fig. 3.

Fig. 3. Pakri wind farm turbine and anthill

3.2. Noise in Pakri and Virtsu wind farms

Two types of noise can be heard in a wind farm: continuous noise and intermittent noise. Continuous noise comes mainly from wind turbine generators and substations and intermittent noise is caused by rotor blades (when rotor blade passes the wind turbine mast). The noise, caused by mast passing rotor blades is not very annoying. It is like swash and reminds common wind. In wind farms like Pakri and Virtsu, which are located near the sea, the overall background noise level is quite high due to stronger winds and heavy sea. In such kind of wind farms rotor blade noise is not so disturbing. Much more annoying is generator noise, because it is clearly distinguishable from other background noises.

The height of the noise measurements was 1.8 meters above the ground level (the height of human ears). The noise measurements were performed east-west direction upwind and downwind from the wind farm.

Noise levels in wind farms were measured in the first case at very low wind speeds (1–2 m/s), when none of the turbines were working. Enercon E-40 cut-in wind speed is 2.5 m/s and Nodex N-90 cut-in wind speed is 3 m/s [4, 5]. In that case the only noise caused by wind farm was the noise from transformers and substations. Some short-term bigger noises were made when the turbine turned to the wind, began to operate or braked. Registered wind turbine noise levels are shown in Table 1:

Table 1. Wind turbine noise levels in Pakri wind farm when turbines were not working

Location	Noise level, dBA
2 km away from wind farm	33.3
At the center of the wind farm	34.2
Near the substation	53.9
On turbine steers (8 turbine average)	43.8
15 m away from turbines (8 turbine average)	37.1

When wind speeds are quite low and the wind turbines are not working, there is almost no noise at the wind farm area. Some bigger intermittent noise appears when turbine turns to the wind (46.5 dB) or begins to operate (60.8 dB – 300 meters away from turbine), but these are very short-term noises. Much bigger intermittent noise occurs when any car drives by (75.2dB) or a mobile phone rings (68 dB).

In the second case the noise levels were measured when the average wind speed was 3–5 m/s and the wind turbines were working at minimal power. In both wind farms 6 different experiments were made and the results are shown in Fig. 4 and 5. The noise levels in Pakri wind farm depending on the distance from the wind farm are shown in Fig. 4.

Average noise level near the turbines was 65.4 dBA. Average noise level 1 km away from wind farm was 41.0 dBA. 780 meters away from the wind farm the wind turbine noise was not any more distinguishable from overall background noise level.

The noise levels in Virtsu wind farm depending on the distance from turbines are shown in Fig. 5.

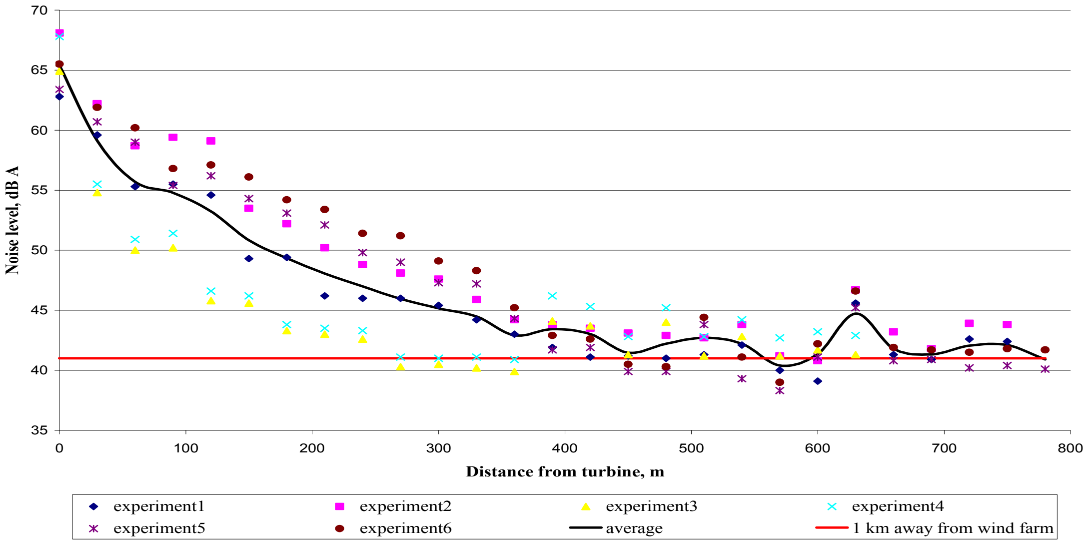

Fig. 4. Noise levels in Pakri wind farm at wind speeds of 3-4 m/s at different distances from the wind farm

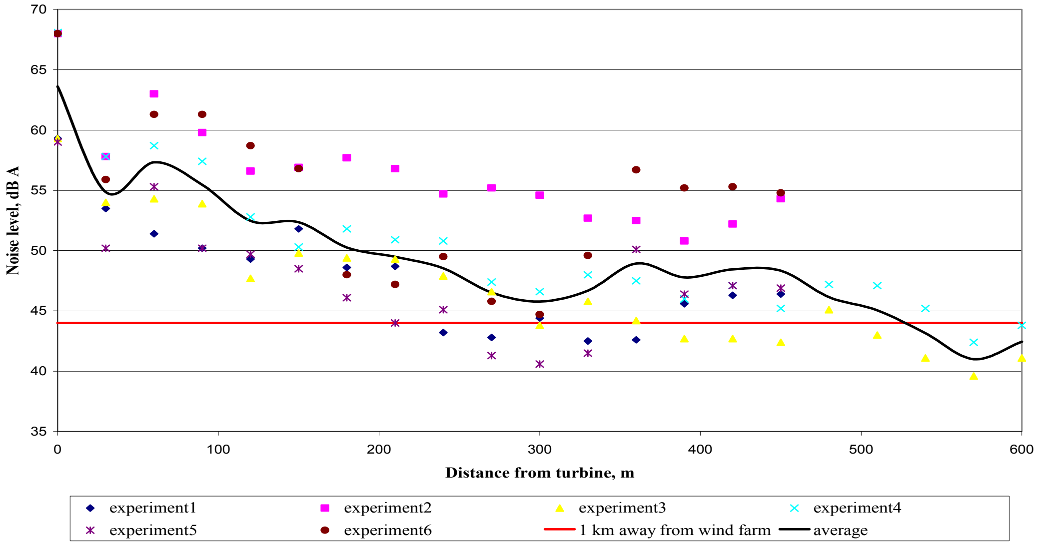

Fig. 5. Noise levels in Virtsu wind farm at wind speeds of 3–5 m/s at different distances from the wind farm

Average noise level near the turbines was 63.6 dBA. Average noise level 1 km away from the wind farm was 44.1 dBA. 540 meters away from the wind farm the wind turbine noise was not any more distinguishable from overall background noise level.

In third case the noise levels were measured when the average wind speed was 6–8 m/s and the wind turbines were working below the nominal power. Virtsu wind farm turbines Enercon E-40 are working at full power, when the wind speed is higher than 12.5 m/s. Pakri wind farm wind turbines Nordex N-90 obtain their nominal power when wind speed reaches 13 m/s. The noise levels in Pakri wind farm depending on the distance from turbines are shown in Fig. 6.

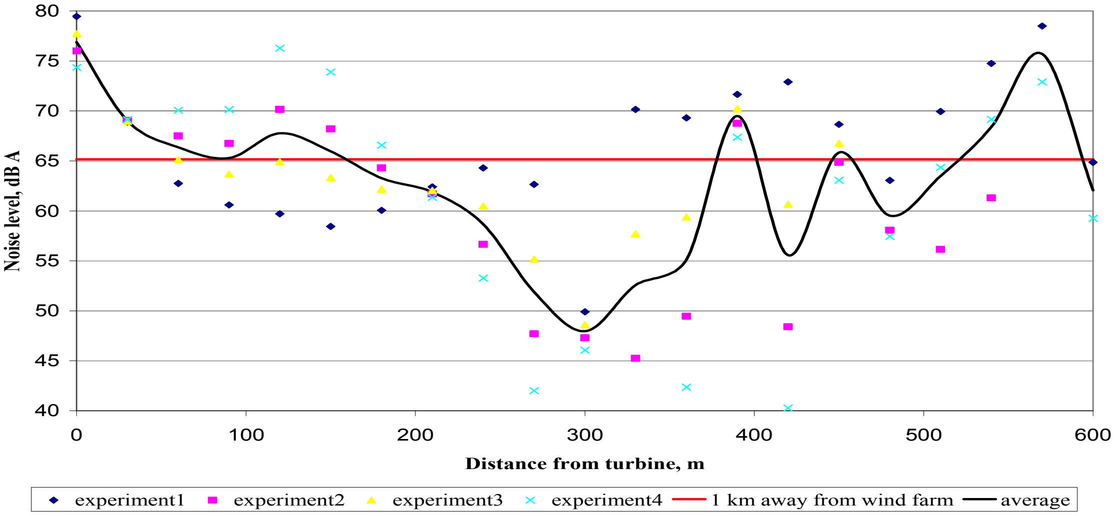

Fig. 6. Noise levels in Pakri wind farm at wind speeds of 6-8 m/s at different distances from the wind farm

Average noise level near the turbines was 76.9 dBA. Average noise level 1 km away from wind farm was 65.2 dBA. 600 meters away from the wind farm the wind turbine noise was not any more distinguishable from overall background noise level. Some noise level downtrends might be caused by the fact that some of the measurements points are between the trees or junipers and also in lower places. Measurement points between 200 and 400 meters are in the boscage and because of that the noise levels are below the value 1 km away from wind farm.

The noise levels in Virtsu wind farm depending on the distance from turbines are shown in Fig. 7.

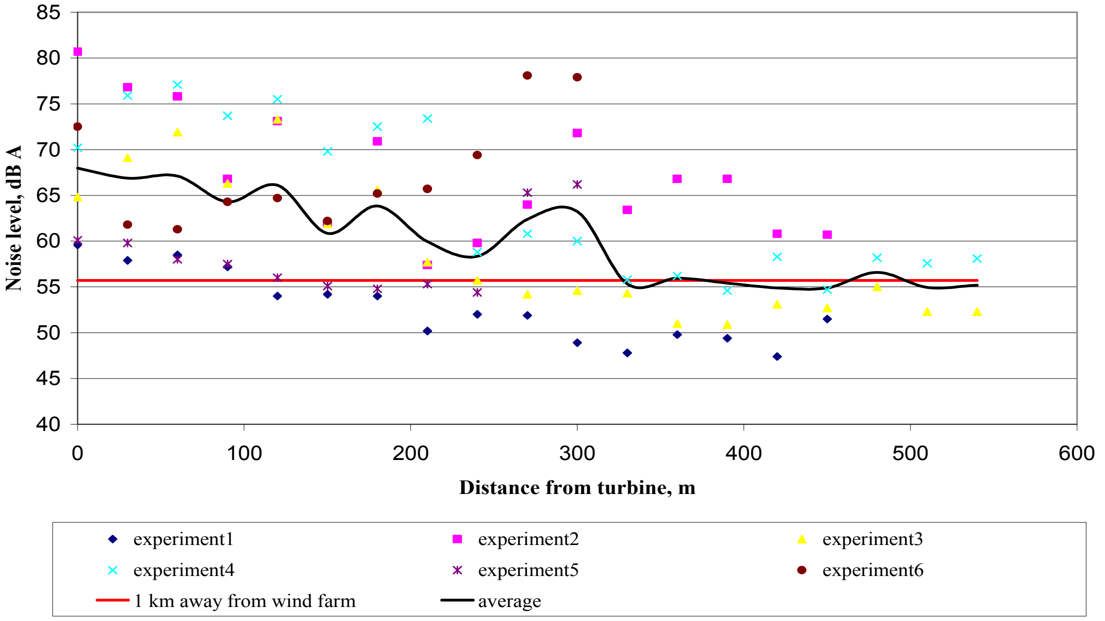

Fig. 7. Noise levels in Virtsu wind farm at wind speeds of 6-8 m/s at different distances from the wind farm

Average noise level near the turbines was 67.9 dBA. Average noise level 1 km away from wind farm was 55.7 dBA. 510 meters away from the wind farm the wind turbine noise was not any more distinguishable from overall background noise level. Some noise level downtrends might be caused by the fact that some of the measurements points are between the trees or junipers and also in lower places.

In fourth case the noise levels were measured when the average wind speed was 13–15 m/s and the wind turbines were operating at nominal power. The noise levels in Pakri wind farm depending on the distance from turbines are shown in Fig. 8.

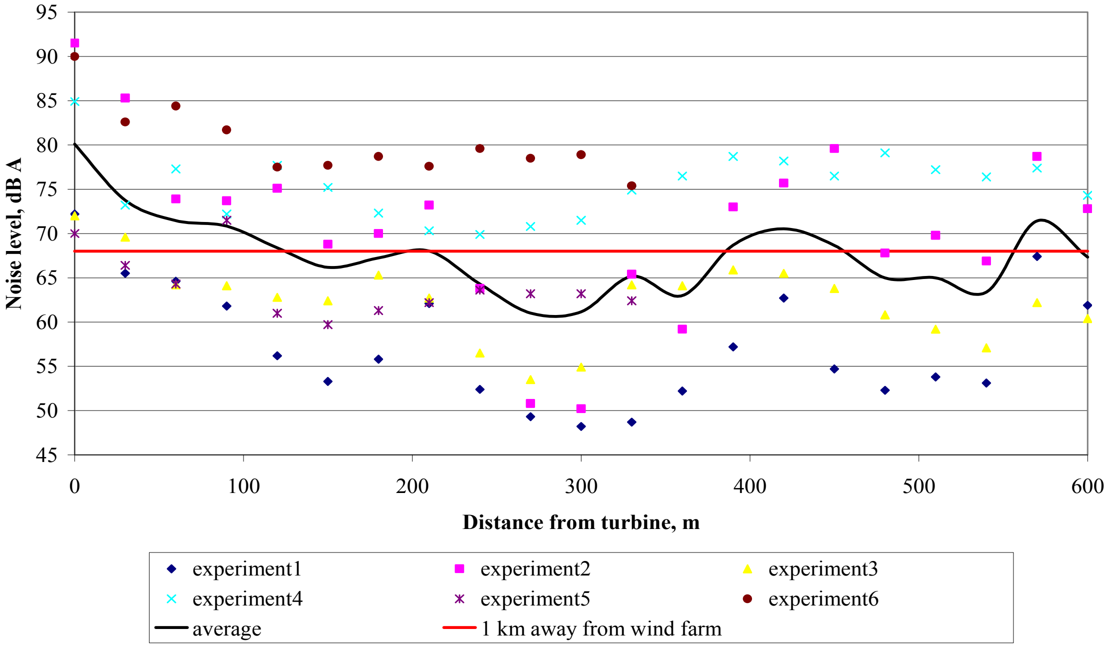

Fig. 8. Noise levels in Pakri wind farm at wind speeds of 13–15 m/s

Average noise level near the turbines were 80.1 dB A. Average noise level 1 km away from wind farm was 68.2 dB A. 600 meters away from the wind farm the wind turbine noise was not any more distinguishable from overall background noise level. Some noise level downtrends might be caused by the fact that some of the measurements points are between the trees or junipers and also in lower places.

While Virtsu wind farm consists of smaller turbines (600 kW and 800 kW), the noise levels near the turbines are little lower than in Pakri wind farm. In Virtsu wind farm wind turbine noise falls below the overall background noise level at the distance of about 540 meters away from the wind farm, in Pakri wind farm about 780 meters away from wind farm. Unlike Pakri wind farm, where there are no houses nearby, in Virtsu houses are just 240 meters away from the closest turbine. Because of this some noise problems arise near the Virtsu wind farm.

When wind is stronger, also overall background noise level is higher than at middle wind speeds. In Pakri wind farm about 600 meters away from wind farm the noise level does not exceed overall background noise level 1 km away from wind farm, in Virtsu this distance is 510 meters.

Also landscape around the wind farm area has much influence to noise levels. If there are some trees or other obstacles between the wind farm and measurement point, the noise level drops, depending on the size of the trees and obstacles.

3.3. Light flashing caused by rotor blades

In January, when the sun is the lowest, the wind turbine shadow measurements were carried out in Pakri and Virtsu wind farms. In Pakri wind farm wind turbine rotor blade flashing shadow reached 1100 meters away from wind farm. Pakri wind turbine rotor blade top is up to 125 meters above the ground level.

In Virtsu wind farm the rotor blade flashing shadow reached 600 meters away from wind farm and the wind turbine rotor blade top is in its upper position 85 meters above the ground level.

4. CONCLUSIONS

To minimize wind farm effects to the animals and birds, exhaustive investigations of the wind farm must be carried out. If the wind farm is well sited, there are no nesting places exactly on the site and therefore wind farms like Virtsu and Pakri have very little effect on birds. During every visit to the wind farms different animals, ants, snakes and many kinds of footprints have been seen. Because of this fact one can say that operating wind farms do not disturb animals and insects as well.

If wind speeds are lower than 3 m/s, there is no loud and continuous noise in the wind farm areas. Little higher noise levels are only exactly near the wind turbine substations. Some bigger intermittent noise is generated when some turbine turns to the wind or begins to operate.

At wind speeds 3-5 m/s, when the wind and sea wave noise is minor and the wind turbines are working at minimal power, wind turbine noise is audible at longer distance. In Pakri wind farm with 2.3 MW turbines wind farm noise is distinguishable up to 780 meters away and in Virtsu wind farm with three 600 kW and one 800 kW turbine – up to 540 meters away from the wind farm.

If wind speeds are about 6–8 m/s, there is already more noise in the wind farms, but also the overall background noise level is then higher. Noise made by rotor blades is not very distracting and reminds of wind blow. More distracting is wind turbine generator noise, because it is clearly distinguishable from other noises. Overall background noise level in wind farms is from 56 to 65 dB A, depending on landscape around the wind farm.

With quite high wind speeds (13–15 m/s) the overall background noise level is even higher (up to 70 Db A). Distance, where the wind turbine noise is not anymore distinguishable, is about 600 meters away from the wind farm.

From noise point of view the local houses in Pakri wind farm area could be more than 800 meters away from wind farm and in Virtsu wind farm about 600 meters away. Taking into consideration the light flashing, caused by rotor blades, the distances should be more than 1 km in Pakri wind farm area and over 600 meters in Virtsu wind farm area.

Landscape around the wind farm area has much influence on noise levels. If there are some trees or other obstacles between the wind farm and measurement point, the noise level drops, depending on the size of the trees and obstacles. If wind farm builders follow the distance rules from the houses, there is no wind farm noise problem. In Virtsu one turbine is too close to the local houses and there are also some noise problems.

REFERENCES

1. R. Langston, D. Pullan. Wind farms and Birds: An analysis of the effects of wind farms on birds and guidance on environmental assessment criteria and site selection issues // Convention on the Conservation of European Wildlife and Natural Habitats, Strasbourg, 2003.
2. I. Pertmann. Wind Turbine Effects to the Environment and People // 5th International Symposium „Topical Problems in the Field of Electrical and Power Engineering“, Kuressaare, 2008, p. 133–139.

3. J.E. Winkelman. The impact of the Sep wind park near Oosterbierum, the Netherlands, on birds // RIN-raport 92, Arnhem, 1992.
4. C. Ketzenberg, K.-M. Exo, M. Reichenbach, M. Castor. Einfluss von Windkraftanlagen auf brütende Wiesenvögel // Natur und Landschaft 77, 2003, p. 144–153.
5. J.P. Gill. Baseline breeding bird survey of the Dun Law wind farm // Report to Renewable Energy Systems Ltd., Edinburgh, 2000.
6. R. Thomas. Renewable energy and and environmental impacts in the UK: Birds and wind turbines //Master of Research Degree Thesis, University Collece London, 1999.
7. S. Dirksen, J. Van der Winden, A.L. Spaans. Nocturnal collision risks of birds with wind turbines in tidal and semi-offshore areas // Wind Energy and Landscape Balkema, Rotterdam, 1998, p. 99–108.
8. D. Still, B. Little, S. Lawrence. The effect of wind turbines on the bird population at Blyth Harbour, Northumberland // ETSU W/13/00394/REP, 1996.
9. http://www.nordex-online.com/en/products-services/wind-turbines/
10. http://www.enercon.de/en/_home.htm
11. http://www.tallinna-linnuklubi.ee/
12. http://www.eoy.ee/

CYSENI 2009, May 28-29, Kaunas, Lithuania
ISSN 1822-7554, www.cyseni.com

PRELIMINARY STUDY ON IMPLICATION OF CLIMATE VARIABILITY ON WATER RESOURCES AND HYDRO-POWER GENERATION IN NIGERIA

I.A. Balogun, S.O. Gbuyiro, A. Oluleye, A. Akinbobola
Department of Meteorology
School of Earth and Mineral Sciences
Federal University of Technology
P.M.B 704, Akure 340001 – Nigeria
Phone: +234-8039194212
E-mail: iabalogun@futa.edu.ng, kleverchaps@yahoo.com

ABSTRACT

This paper seeks to investigate and address the relative impact of changing climate and variability extremes on dams and lakes that are major sources of hydroelectric power generation in Nigeria. The Kainji hydroelectric power generating station is being used as a pilot study in this paper. In this regard, the hydropower generation from Kainji hydroelectric station in Niger State, Nigeria has been investigated. Power generation records from the station up to 28 years (1970–1998) with data of some climatic and hydrologic parameters covering minimum of 50 years and above were used in this study. The trend and variability of these parameters were investigated. Rainfall anomaly index was used to determine the wet and dry extremes of the trend and the best and worst rainfall decades were noted. Before applying the analytical method, the normality of the data were tested and found to be normally distributed. The rainfall change point exhibited downward shift that coincided with the prolonged sahelian drought episode of 1970's. More importantly, the shift is recognized as result of recent climate change that began in the 70's. The best and worst rainfall decades were also noted. The rapid and often drastic changes in rainfall especially in the last two decades are today issues of immense concern to the scientific world. Consequences of this to agriculture and health are common, but little emphasis has been placed on its effects on the energy sector, with respect to its exploration, distribution and availability. Consequence of this changing climate and its variability extremes have been noted to impact negatively on the Kainji hydro-electric power generation

Keywords: climate change, rainfall variability and energy

INTRODUCTION

There is an overwhelming evidence of climatic changes over the past decades in many parts of the world. Precipitation patterns have been found to be deviating from their normal values. Changes in the precipitation regime directly affect water resources management and hydrology. This situation is investigated for Kainji hydroelectric dam in Nigeria and the strength of the change determined. Impacts of future climate change on hydrological systems and water resources management in West Africa are expected to be adverse and extensive, and the environmental and socio- economic problems that would be associated with the potential impacts may prove to be among the major problems facing the entire region [1]. The current situation in the Nigeria is that energy supply is not covering the energy demand [2]. In recent years, the sensitivity and vulnerability of hydroelectric energy generation to climate variations and change have been a source of concern to the people and governments of the country. Kanji Dam reservoir is one of the biggest dams in Nigeria designed in 1970 to supply about 40% of the energy needs in the country [3]. Dams are constructed for several purposes among which include domestic, agricultural, industrial water supply, irrigation, hydroelectric power supply, etc. However, Kainji dam was also constructed for these purposes but with higher priority to augment electricity generation for the country**.** There has been paucity of inflow of water and hence the difficulty for it to maintain its maximum operating head (465 ft) and to attain optimum power generation. Hydropower generation is the energy source most likely to be affected by climate change, owing to its sensitivity to the amount, timing, and geographical pattern of precipitation, as well as temperature. As noted by [4], there will be changes in magnitude and timing of water resources and these would necessitate changes in water resources management strategies and greater water conservation efforts would be required to balance water supplies and demands. In a generalized global view, there is a potential for more intense rainfall events (which would require more conservative water storage strategies to prevent flood damage), greater probability of drought (less hydroelectric production), and less precipitation (less water available during warm months); all of which point to less hydroelectric capacity of the power generating station.

It has been noted that in West Africa in the 1950s changes in the sahelian rainfall were particularly dramatic [5]. Wet conditions prevailed during that decade with averages from 15% above normal in the southern area to 35 to 40% above normal along the sahelian fringe. Favorable rainfall conditions ended in the 1960 and average rainfall deficits from 1968 to 1973 matched the excess of the 1959s with extremes reached in 1972 and 1973. Rainfall deficits also occurred in the subsequent years and continued till 1983. The drought which began in the 1968 never really ended though some areas wee characterized by favourable distribution of rainfall throughout the season.

Reduced and changing rainfall pattern especially in the 1970's and particularly the 1980's over the northern part of Nigeria have tasked the ingenuity of water resources managers in the region. Previous research works in the country covering most and all climatic region has established that rainfall over the region has been very erratic both in time and space. River runoff is affected by the amount of water available from rain [6]. Experts say that there has been consistent reduction in water inflow into the Kanji River over the years because of climate change [7].

In no doubt, climate change will have impact on both electricity demand and supply. The potential for hydroelectric generation approximately follows runoff, so here it can be seen that hydroelectric potential would also be affected. Reduced flows in rivers and higher temperatures reduce the capabilities of hydroelectric generation. Higher temperatures also reduce transmission capabilities. Hydropower generation will be affected by decreasing run-off. Excessive drought will lead to higher evapo-transpiration, which adversely affects water volume, and will thus reduce hydroelectric capacity. It was pointed out that increase in evaporation, as a result of higher temperatures, together with changes in precipitation patterns, might alter the timing and magnitude of river flows. This would affect the ability of hydropower stations to harness the resource and may result in reduced energy production implying lower revenue and poorer financial returns [8].

In the past, feasibility studies have relied on historical rainfall and river flow data for the assessment of hydroelectric potential at a proposed site [9]. The case of Climate change and hydro electric power generation is double edged as it directly and indirectly affects each other in its feed-back processes.

DATA AND METHODOLOGY

Kainji dam is an area drained by the river Niger to the northwestern part of Nigeria. Fig. 1 shows the map of Nigeria with the study area (Hydrological Area I being understudied). The study reservoir (Kainji) is man made. Its geographical location is 09°48'N, 04°38'E and its tailrace is at 09°08'N, 04°48'E just around Jebba. It is within Hydrological Area 1(HA 1) to the Northwest of Nigeria and it is constructed on River Niger. It occupies a land area of about 1270 km^2. The man made reservoir has a total capacity of 15×109 m^3 of water, with a maximum operating head of 141.73 m and 136 km in length upstream. The reservoir lies within the semi-arid zone of the country.

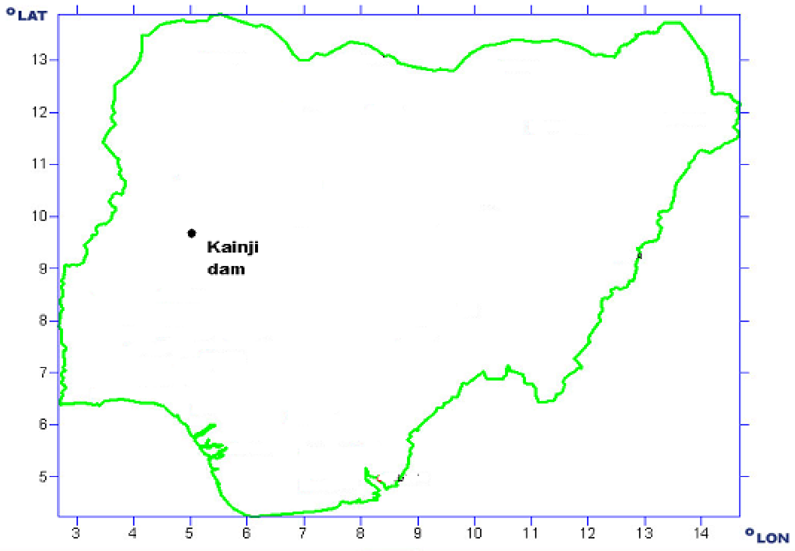

Fig. 1: Map showing location of Kainji hydroelectric dam

Data used for this work were collected from three major sources; monthly climatological parameters (rainfall, minimum and maximum temperature, evaporation) covering minimum of 50 years and above (1943–2000) were obtained from the Nigerian Meteorological agency (NIMET), Lagos, other data such as run-off from Department of water resources and hydroelectric power generation and consumption data were obtained from the Kainji hydroelectric power generating station, Kainji.

The data were subjected to normality test by plotting both Weibull probability curve (WPC) and Normal probability curve (NPC). The data appeared to fit well into NPC, which suggest that the data come from normally distributed samples. In the determination of wet and dry periods, method of Nicholson [10] was used.

Method used for this work is purely statistical approach, which involves the calculation of standardized anomaly in which a period having values greater than zero and less than zero are regarded as wet and dry period respectively. Mann – Whitney method of change detection in a trend was applied to determine the nature and extent of abrupt change in rainfall trend.

RESULTS AND DISCUSSION

Climate change affects the magnitude and timing of river runoff. In general, consideration of climate change impact on hydropower has been concerned with the potential annual production of electricity only and not the impact of changes on the monthly availability. Month-to-month changes in electricity demand are generally greater than year-to-year, so a consideration of the monthly availability is likely to have more relevance. Consideration of spillage and the likely actual production under climate change will allow a more realistic representation. Fig. 2 shows the normalized long-term rainfall variation over Kainji dam. The trend shows that rainfall was generally above normal between 1951 and 1965, a period of 16 years. There was a gradual marked change in the rainfall pattern over the station from 1966 through the year 2000, a period of 35 years except year 1979, 1981, 1994, but a slight increase was noticed from 1998 to 2000.

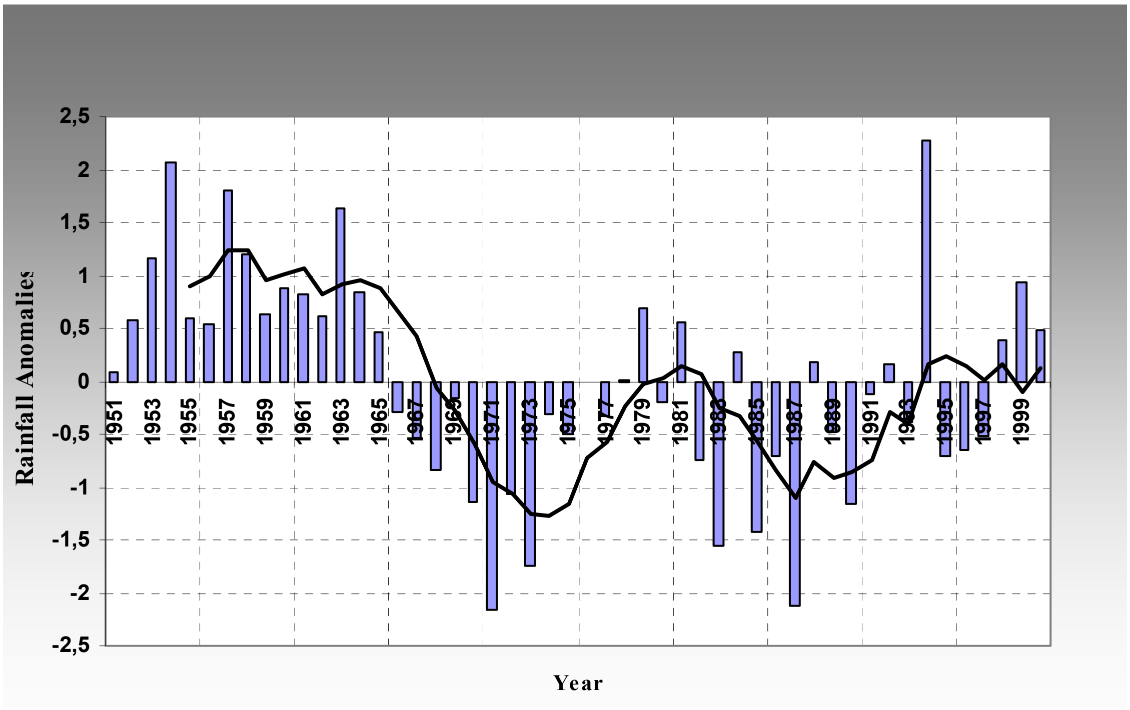

Fig. 2: Annual Rainfall Variation and the 5-year running mean over Kainji Station (1951–2000)

Unlike the rainfall pattern, the minimum temperature trend shows (Fig. 3) the station recorded generally below normal nighttime temperature between 1951 and 1971, a period of 21 years, giving an indication that the area was generally cool perhaps due to minimal anthropogenic influence on the vegetation around the station. Previous research findings have shown that the nighttime temperature is increasing faster than the daytime temperature; this has also been noted in Kainji station. The predominance of this increase accounts for why minimum temperature was considered in this study rather than the maximum temperature. There was a notable but gradual change in the pattern from 1972. This station began experiencing warmer nighttime temperature, which became intense between1986 and 1988. Although the minimum temperature is still above normal, there is a gradual decrease in the minimum temperature from 1995.

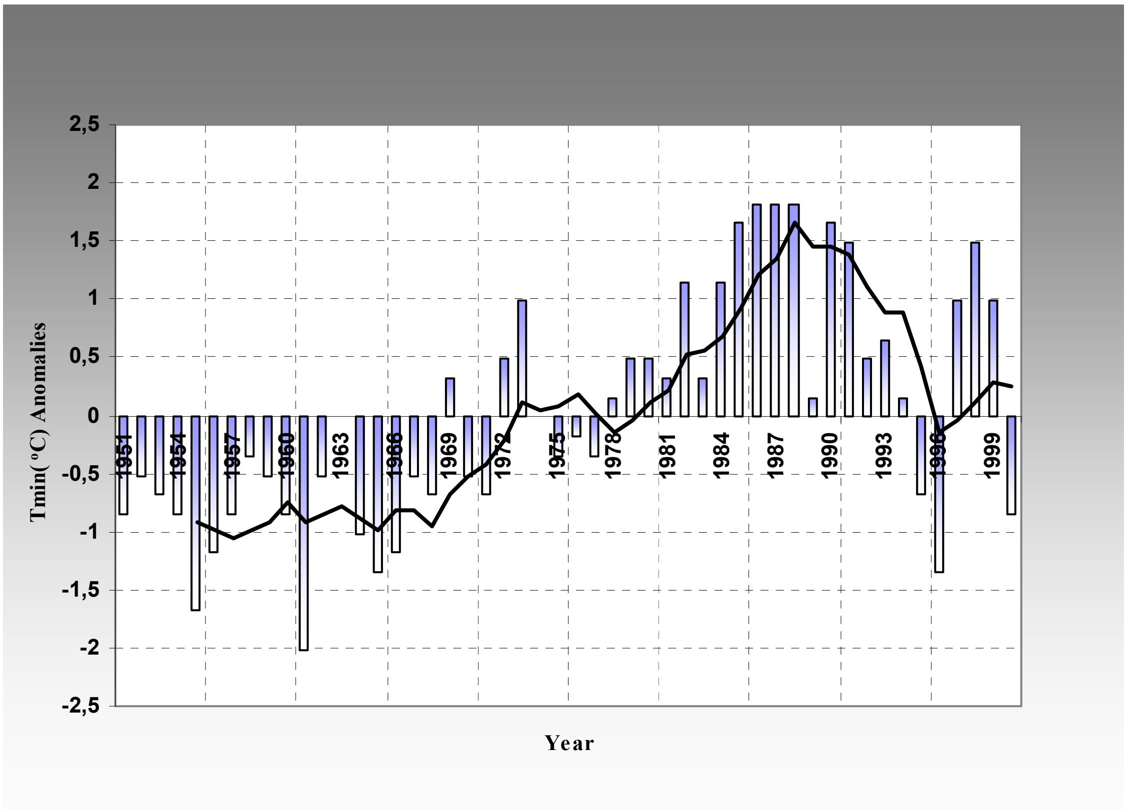

Fig. 3. Annual Minimum Temperature and the 5-year running mean in Kainji Station (1951–2000)

The evaporation trend as shown in Fig. 4, have the same pattern as rainfall but in opposite direction. A period of surplus rainfall, evaporation was below normal and vice versa. This is perhaps due to the fact that during the period of much rainfall, substantial amount of cloud cover could be a factor to reduce evaporation rate, hence the low evaporation recorded during the high rainfall period. Although cloud amount is not the only factor responsible for evaporation, other factors such as wind gradient, availability of moisture and solar energy are equally important. But it appears high amount of cloud cover during the rainy season and the reduced solar energy appeared to be the major factor.

The water discharge by the dam as indicated by the runoff trend in Fig. 5 shows that the runoff from the dam was between normal and above normal from 1951 to 1971. Subsequently, from 1972 to 2000, the runoff was below normal which means that lesser amount of water are allowed to discharge because of deficit in rainfall and high rate of evaporation over the station.

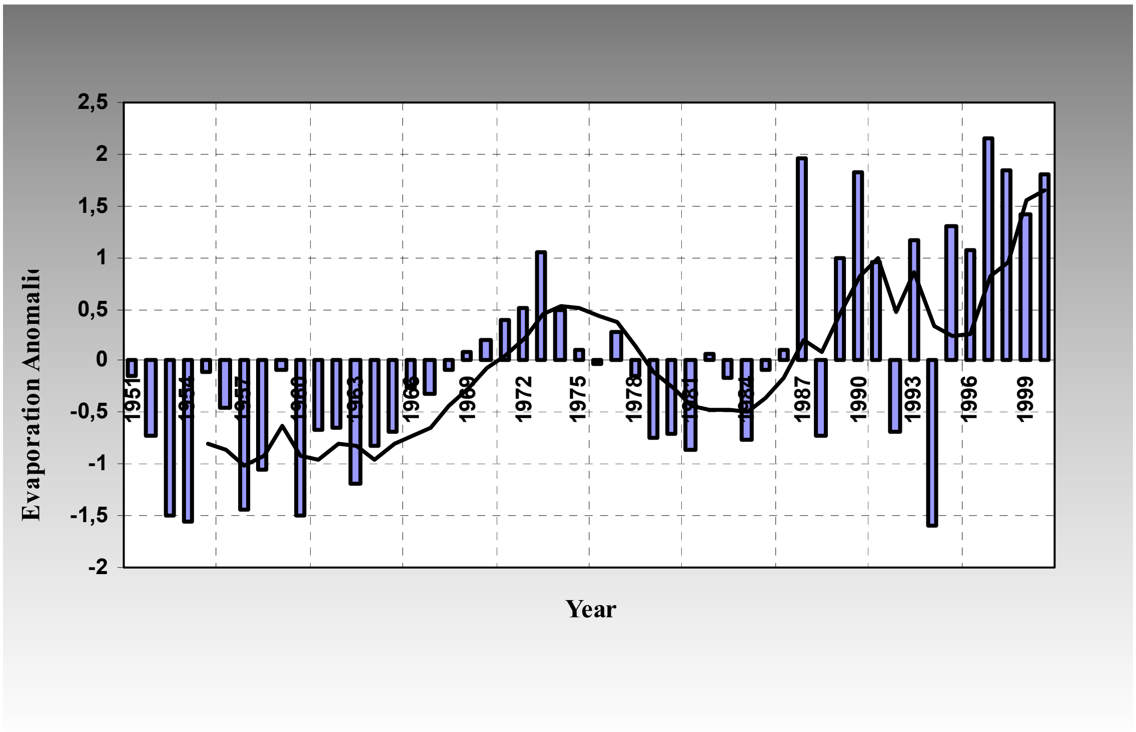

Fig. 4. Annual Evaporation variation and the 5- year running mean in Kainji Station (1951–2000)

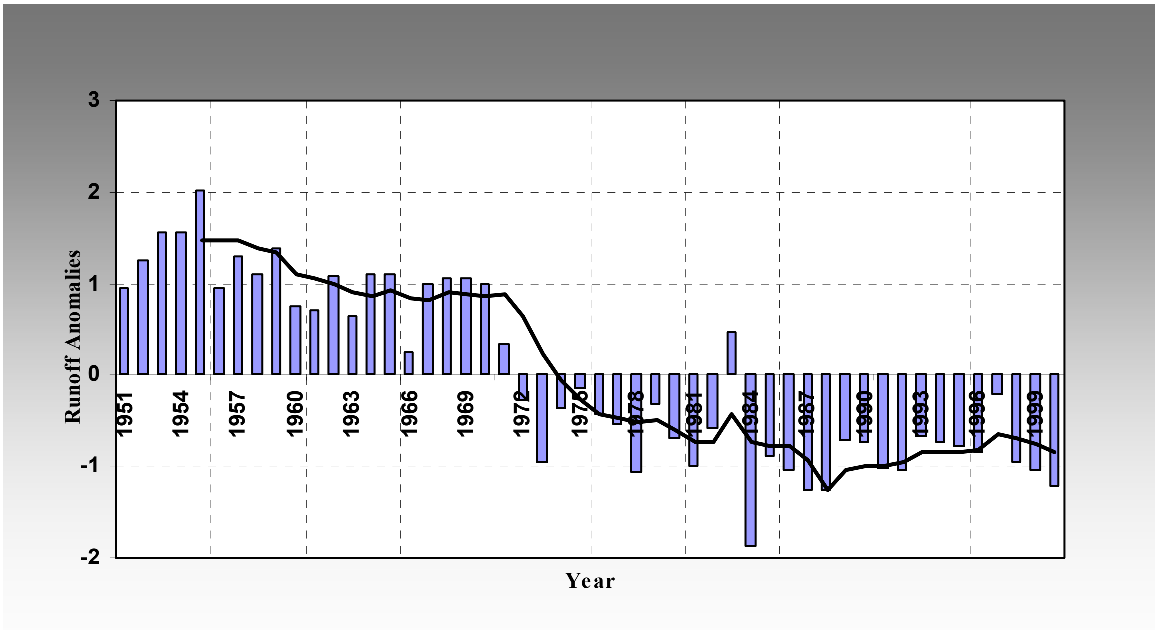

Fig. 5. Annual runoff variation and 5-year running mean over Kainji Station (1951–2000)

The hydro-power generated from the dam has been noted to follow the same trend as the rainfall (Fig. 6). During the period of less predominantly dry rainfall (1975–1982), power generation from the station was substantial but subsequently became low during the period of prolonged rainfall deficit observed to start from 1983 which fall within the worst rainfall decades in the country. This suggests that rainfall availability is a crucial factor for optimum power generation in the station.

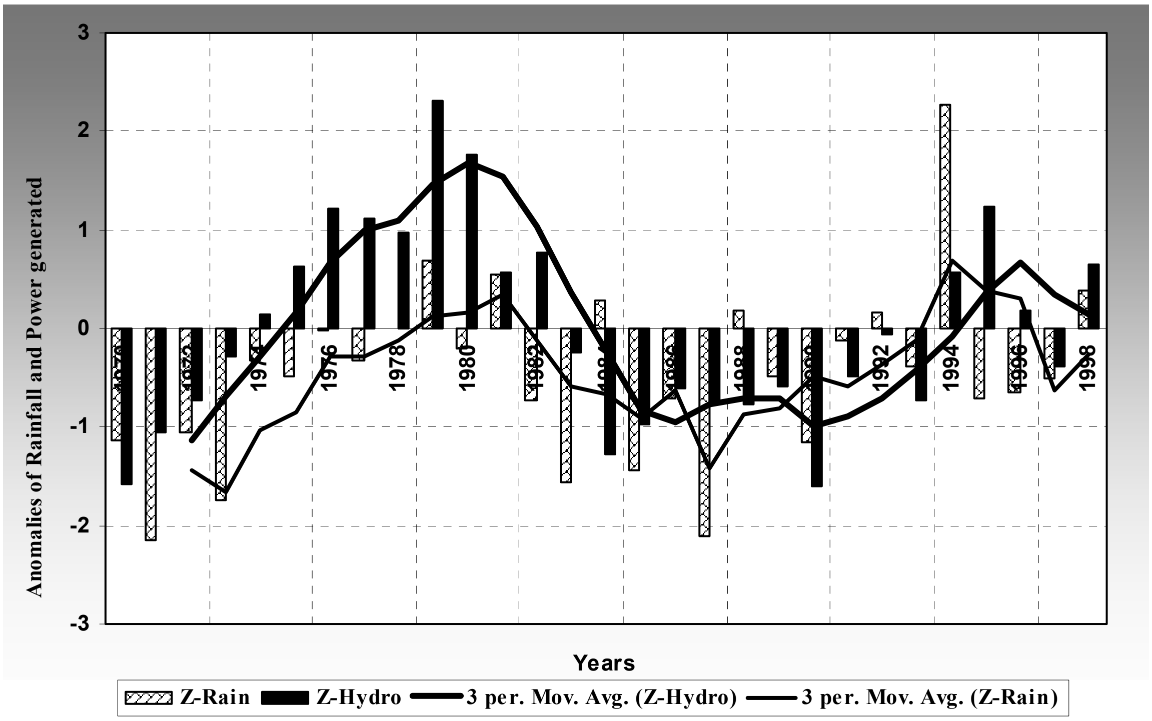

Fig. 6. Annual variation of Rainfall and Hydropower generated from the Kainji hydro station from 1970 to 1998 with their respective 3-year running mean.

Fig. 7 reflects the decreasing efficiency of the power generating station consequently upon the impact of long period of rainfall deficit, which spanned into the 90's with its attendant increase in air temperature and evaporation led to reduction of water storage in the dam. The average energy generated from Kainji reservoir for the period 1970–1998 was 2009.9 MWh. Trend analysis reveals that hydroelectric energy generated from Kainji decreases at the rate of 2.4 MWh/hr for the period of study.

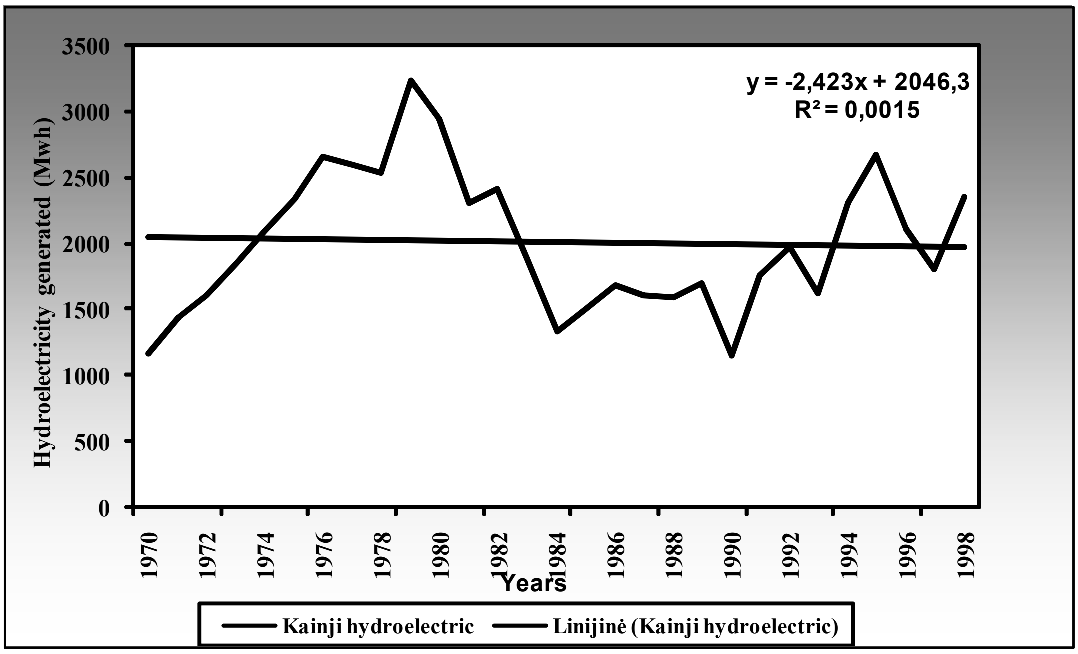

Fig. 7. Annual Variation of Hydroelectricity generated from Kainji Dam (1970–1998) with the linear trend

The decadal climatic characteristic of the station since the 1950's through the period of study with the percentage contribution of the dam to the total from other sources is shown in Table 1 below. It is evidently clear that the level at which it is degenerating is alarming. The decadal changes in the climatic parameters are also glaring.

Table 1. Long term climatic characteristics of Kainji and its percentage hydroelectric contribution to the national total. *Note: n/a means not available since the station was designed in 1970

	Rainfall (mm)	ET (mm)	Tmax (°C)	Tmin (°C)	Kainji hydroenergy generated (MWh/hr)	Installed capacity (MW)	% hydroenergy generated at Kainji dam to National Total
50's	914.2	3544.5	33.9	19.9	n/a	n/a	n/a
60's	840.1	3644.5	34.0	19.9	n/a	n/a	n/a
70's	664.2	4112.7	34.0	20.5	2155.4	320	61.9 %
80's	721.0	3980.0	34.4	21.1	1898.1	760	19.4 %
90's	725.2	4499.7	34.4	20.7	1972.7	960	13.1 %
1998	790.0	5037.5	34.5	21.3	2358.9	960	14.4 %

CONCLUSIONS

Human activities are expected to lead to substantial changes in climate. One outcome may be reductions in river runoff with potentially serious ramifications for the provision of hydroelectric power. The runoff is also strongly affected by the amount of water available from rainfall. In the foregoing analysis, effects of climate change are noticeable on the basic meteorological and hydrological parameters considered in this study starting from the 70's. As already noted, rainfall is reducing, evaporation is increasing, and temperature is increasing while runoff is decreasing in the area studied. They will generally affect generation of hydroelectric energy, which is sensitive to river flow. As observed, a change or variation of rainfall results in a change in hydroelectric energy generated from Kainji. It is also noted that the consequence of the changing climate and its variability extremes have impacted negatively on the hydropower generation in Nigeria. This study has shown that epileptic power supply currently being experienced in the country is in consonance with the plummeted power supply occasioned by the climate change effect on the hydro resources of the dam, given that the percentage hydro power contribution of the dam to the total power generated in country has substantially dropped from 62% to less than 20%.

References

1. O. Ojo, S.O.Gbuyiro, and C. U Okoloye: Implications of Climate variability and climate change for water resources availability and management in West Africa, *GeoJournal* 61, p. 111–119, 2004.
2. K. Kevelaitis, R. Museckaite, G. R.Obialo and V. Raudonis: Solar energy implementation in Nigeria Bachelor level in Business Studies, House rudar.ruc.dk/bitstream/1800/3750/1/, 2008.
3. S.O. Gbuyiro, O.Ojo, O. Iso, C. Okoloye and O. Idowu: Climate and water resources management, 27th WEDC Conference on People and systems for water, sanitation and health, Lusaka, Zambia, 2001.
4. A.O. Ojo: Implications of Climate change for water supply demand systems in Lagos Metropolitan Area, Proceedings of the International Conference on Implications of Climate Change, Global warming and environmental degradation in Africa, 1998.
5. World Climate Programme, (WCP): Data and Monitoring: Detecting Trend and Other changes in Hydrological Data. Edited by Zbigniew, W. Kundezewicz and Alice Robson. Compiled from the International Workshop on Detecting Changes in Hydrological Data held in the institute of Hydrology, Wallingford UK, 2nd –4th December 1998, contribution to WCP-water project A. p. 5–45, Published in June 2000.
6. D.D. Orkuma: Rainfall variation and water resources management in the semi-arid zone of Nigeria. *J. Met & Clim. Sci* , 3 (3), p. 6–11, 2002.
7. M. Ayankola: Niger's new dam threatens Nigeria's power supply www.businessdayonline.com/index.php?option=com_content&view=article&id= 1118: nigers.nigerias-power.Friday, 07 November, 2008.
8. G.P. Harrison, H.W. Whittington and S.W. Gundry: Climate change impacts on hydroelectric power. Proceedings of the 33rd University Power Engineering Conference (UPEC' 98), Edinburgh, September, p. 391–394, 1998.
9. H.W. Whittington, and S.W.Gundry: Global Climate Change and Hydroelectric Resources, *IEE Engineering Science & Technology Journal*, March, 1998.
10. S.E. Nicholson: Sub – Saharan rainfall 1981 – 1984. *J. Climate Appl. Meteor.* 24, 1388–1391, 1985.

ANALYSIS OF THE W7-X FACILITY VACUUM VESSEL WITH THE COCOSYS LUMPED-PARAMETER CODE IN CASE OF 40 MM DIAMETER PIPE RUPTURE

M. Povilaitis, E. Urbonavičius
Lithuanian Energy Institute
Breslaujos str. 3, LT-44403 – Lithuania
Tel. +370 37401920
E-mail: mantasp@mail.lei.lt

ABSTRACT

This paper deals with an analysis of the W7-X facility vacuum vessel with the COCOSYS lumped-parameter code in a case of 40 mm diameter pipe rupture. W7-X is a stellarator type experimental fusion device, developed by Max Planck Institute of plasma physics. It was evaluated during the presented analysis if the area of the burst disk installed in the vacuum vessel of the facility is sufficient to prevent the overpressure of the vacuum vessel in the case of a 40 mm diameter pipe rupture. Rupture of one of the 40 mm inner diameter coolant pipes providing water for the divertor targets during the baking regime of the facility operation is considered to be the most severe accident in terms of the vacuum vessel pressurization. Baking regime is the regime of the facility operation during which vacuum vessel structures are heated to the temperature acceptable for the plasma ignition in the vessel. In the paper nodalisation scheme of the facility vacuum vessel developed for the lumped-parameter code COCOSYS and performed numerical analysis are presented. Results of the presented analysis show that area of the burst disk is sufficient to prevent overpressure of the vacuum vessel of the W7-X facility in the case of simulated accident.

Fusion, COCOSYS, W7-X

1. INTRODUCTION

Practical use of the atomic nuclei fusion energy is a promising direction of the nuclear power development. Possibilities associated with the probable future use of fusion energy are so large, that nuclear fusion is sometimes referred as “the energy source of the future” [1].

Nuclear fusion would allow us to have environmentally-friendly high power energy sources. However, before reaching efficient electricity generation from the fusion energy sources and use of fusion power in the practical activities, a number of technical and engineering problems has yet to be solved.

One of the organizations performing research and development of the nuclear fusion technologies in Europe is European Fusion Development Agreement (EFDA). Starting 2007, Lithuanian energy institute (LEI) is a member of this organization. LEI is cooperating with Max Planck plasma physics institute (IPP, Germany) in the frame of EFDA project by performing safety analysis of fusion device WENDELSTEIN 7-X (W7-X), which is currently being developed and built by IPP in Greifswald [2].

There are two main types of devices initiating fusion in the plasma confined by magnetic field – tokamaks and stellarators. Both types of magnetic confinement fusion devices have toroidal geometrical form. However, while the cross-section of the tokamak device stays constant along the circumference of the torus, devices of the stellarator type have varying cross-sections. Wendelstein 7-X is stellarator type experimental nuclear fusion device (Fig. 1).

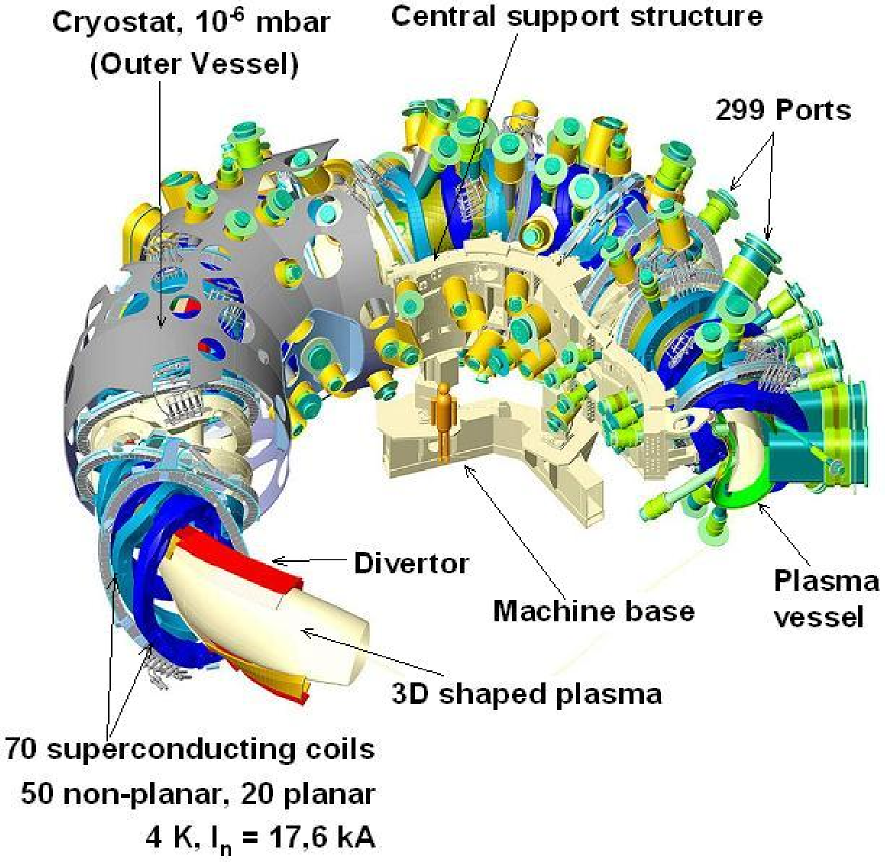

Fig. 1. Fragment of the 3D schematic view of the W7-X device [3]

The purpose of the development of the W7-X device is to demonstrate the feasibility of the stellarator devices for the creation of stable plasma conditions for as long as half an hour.

While performing safety analysis of the W7-X device, simulations and analysis of the possible accident were done. Simulated accident was the rupture of the device cooling water pipe. This accident was chosen for the analysis, because rupture of such 40 mm diameter pipe, largest of the ones entering plasma vessel, providing water for the divertor, during “baking” mode (mode of the device operation before plasma initiation, during which structures of the device plasma vessel (also called vacuum vessel) are heated) is considered to be the most severe accident in terms of vacuum vessel pressure increase [4].

Performed safety analysis consisted of two parts:

1. Simulation of the cooling circuit of the device and pipe rupture, and the calculation of the parameters of the water flow into the vacuum vessel.
2. Simulation of the thermodynamic processes following water ingress in the vacuum vessel and calculation of the thermodynamic parameters.

The main purpose of the analysis was to calculate whether the planned diameter of the burst disk, which will be installed in the wall of the vacuum vessel, would be sufficient to prevent overpressure of the vacuum vessel.

In this paper the second part of the performed analysis (simulation of thermodynamic processes following water ingress in the vacuum vessel of the W7-X stellarator device) is presented.

2. PERFORMED SIMULATIONS

2.1. Nodalisation

The simulation of the evolution of the thermodynamic parameters in the vacuum vessel of the W7-X stellarator was performed with the lumped-parameter code COCOSYS [5]. COCOSYS is a German containment code system developed by GRS. COCOSYS code is based on mostly mechanistic models and intended for comprehensive simulation of all relevant processes and plant states during severe accidents in the containment of light water reactors. In order to perform accident simulations, nodalisation scheme of the vacuum vessel was developed.

Complicated three-dimensional geometry of the stellarator in the developed model is simplified to the geometry of horizontal cylinder. Ends of the cylinder are open and joined together, simulating closed circle of torus geometry. Whole volume of the vacuum vessel, and surface area and mass of vessels structures in the model correspond to the available design data, presented in the accident specification [4].

Device is composed out of five parts with similar configurations, called modules. Each module of the vacuum vessel is subdivided into nine virtual control nodes (zones) in the scheme (figure 2): four in the central part of the scheme cross-section (nodes C**), four in the outer part (nodes O**) and one in the bottom part (node BOT), in which released water is collected. Fig. 2 shows cross-section of one module nodalisation scheme. All five modules are simulated in the analysis.

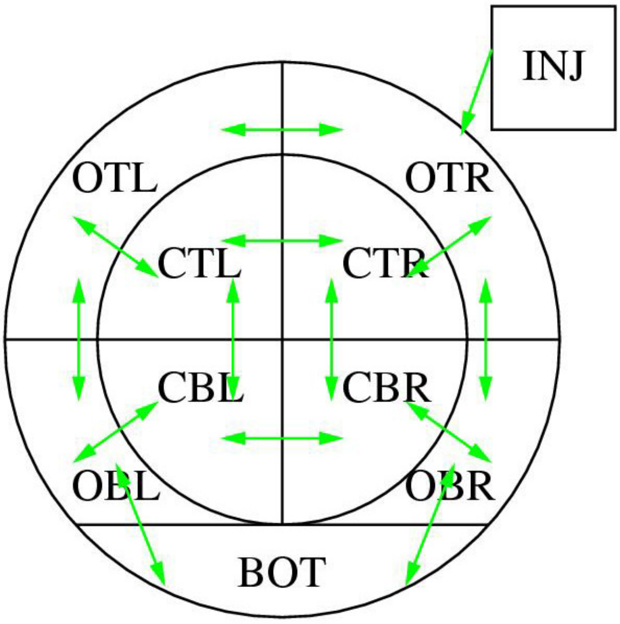

Fig. 2. Cross-section of the developed nodalisation scheme of the vacuum vessel for one module (black – nodalisation nodes, green – atmospheric junctions)

Volumes of the zones are calculated from the geometry of the cylinder assuming volume and length of the cylinder equal to the free volume and circumference of the torus, presented in the specification [4]. All adjacent zones of one module are connected by atmospheric junctions. Areas of these junctions and their lengths are calculated from the cylinder geometry. Corresponding zones of the adjacent modules (e.g., CBL zones of the first and second modules) except BOT zones also are connected by atmospheric junctions, properties of which are calculated from the geometry of cylinder.

INJ zone is the zone into which the water release from the ruptured pipe is simulated. It is defined for the aims of simulation – it helps to more realistically model the water flowing from the ruptured pipe to the wall of the vacuum vessel. INJ zone is present only in one module. Geometric parameters of this zone were selected according to port data and the initial thermodynamic parameters are the same is in the whole vacuum vessel.

Two zones not presented in the Fig. 2 were also simulated – torus hall and environment. The former is a 16800 m^3 volume hall in which stellarator torus is situated. Conditions in the hall were selected according to planned normal operation of W7-X device. OTL node of the vacuum vessel third module and torus hall node are separated by the simulated burst disk. It is possible in COCOSYS to simulate burst disk by defining an atmospheric junction, which is closed at the beginning and opens if pressure difference between the zones it connects reaches indicated value (direction considered). In the case of W7-X this value is equal to 0.1 bar. Area of this junction was set equal to the area of the burst disk. The environment node was used to simulate hot environment of the outer side of the simulated vacuum vessel walls. This node has no connections with other nodes and is needed only for modeling purposes.

Simulated heat transfer structures are presented in Fig. 3. Surface areas of the structures were calculated from the known mass and thickness of the structures [4], assuming steel density equal to 7900 kg/m^3. Structures are assumed to be composed only of steel. WBOT wall is divided into two parts – vertical and horizontal.

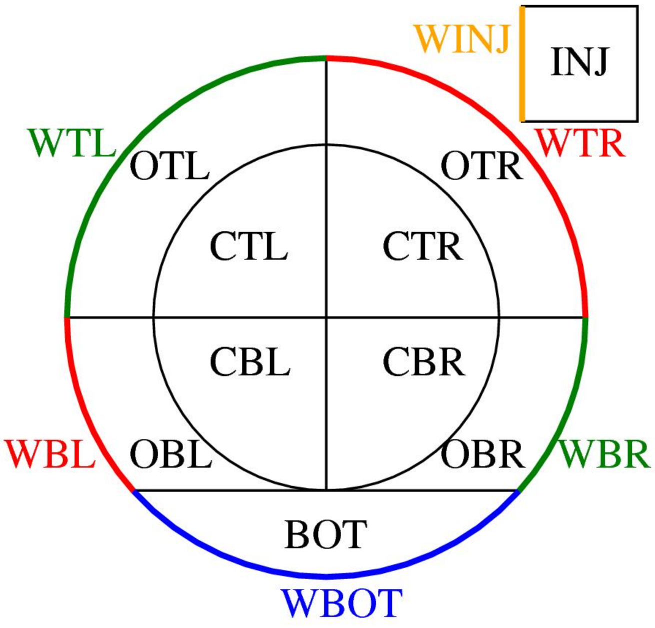

Fig. 3. Cross-section of the developed nodalisation scheme of the vacuum vessel for one module with the simulated structures displayed

To simulate water flow along the vessel walls, three water flow junctions are defined in the first module (there is no water in other modules during the accident), connecting:

1. INJ node with the WTR wall,
2. OTR node with the WBR wall and
3. OBR node with the WBOT vertical wall.

2.2. Initial parameters and calculations

When the W7-X device is working in the “baking” mode, pressure in the cooling circuit is 10 bar, while inside the vacuum vessel it is only 0.0001–0.01 bar. Therefore, due to pressure drop, the coolant flowing out of the rupture into the vacuum vessel partially evaporates. The unelaborated part of the coolant flows on the hot steel structures and also partly evaporates. Steam formed due to evaporation causes pressure inside the vacuum vessel to rise. Increase of pressure in excess of 1.1 bar in the vacuum vessel must be avoided. Simulated burst disk is a passive safety device which should prevent pressure from rising above 1.1 bar. Presented simulation was performed in order to verify suitability of given diameter burst disk for this objective in the case of postulated one of the most critical failure event.

Initial and boundary conditions for the simulations were defined in [4] by the IPP. It was assumed that initial pressure inside the vacuum vessel is 1 kPa. Temperature of the vacuum vessel structures (steel walls) was set to be constant during whole length of calculations and equal to 150°C.

The diameter of the simulated burst disk was equal to 250 mm [4].

For the presented simulations results of the first part of the analysis (calculation of the parameters of the water flow into the vacuum vessel) were needed – mass flow of the coolant through the rupture and its specific enthalpy. First part of the analysis was performed by specialists from LEI using the RELAP5 code. The RELAP5 computer code has been developed by Idaho National Engineering Laboratory. It is a one-dimensional non-equilibrium two-phase thermal-hydraulic system code. The RELAP5 code has been successfully applied to PWR and BWR reactors. Results of their analysis, presented in Fig. 4, were used as initial parameters in the COCOSYS simulations presented in this paper. At the start of the accident coolant starts to flow out of the ruptured pipe into the containment. However, the flow is decreasing. Specific enthalpy of the flowing coolant is increasing until fluctuations of its value start at ~70 s due to numerical instabilities. However, the mass flow rate at this time is small (<1 kg/s) and continuing to decrease, therefore these fluctuations don’t have significant influence on the results.

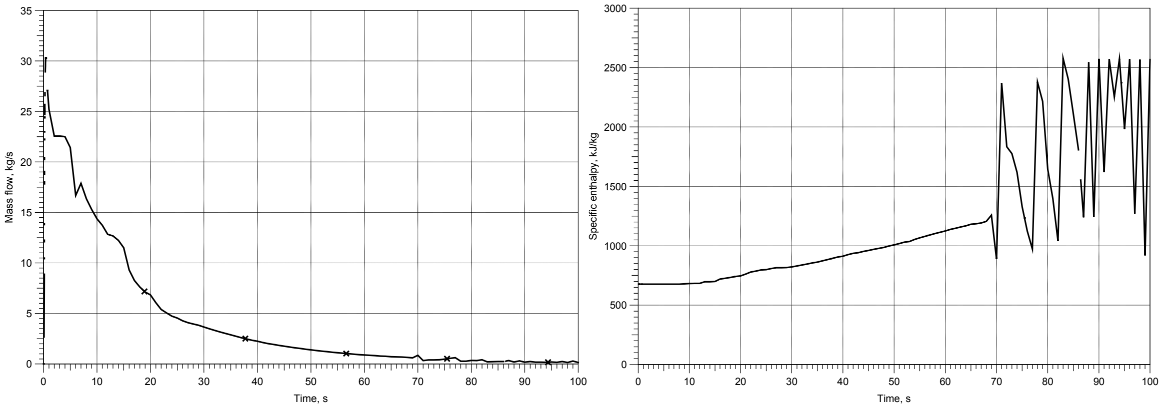

Fig. 4. Evolutions of coolant mass flow rate through the rupture and its specific enthalpy used in the calculations

3. RESULTS OF THE SIMULATIONS

Calculations were performed using COCOSYS version V2.3v20 and the presented nodalisation scheme of the vacuum vessel (Fig. 2).

Results obtained from the calculations show that after pipe rupture takes place, pressure inside the vacuum vessel starts to rise and during 30 seconds reaches value of 1.1 bar (Fig. 5). When this value is reached, burst disk opens. Opening of the burst disk is followed by the pressure decrease in the vacuum vessel.

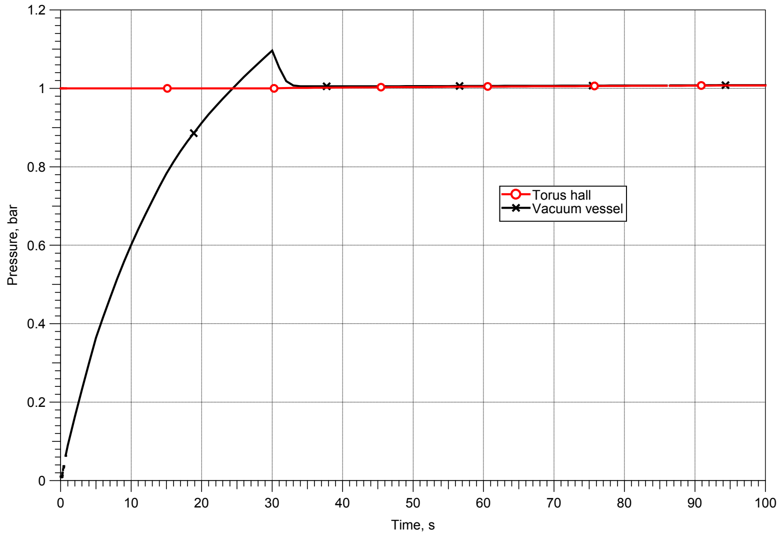

Fig. 5. Obtained pressure evolutions inside the vacuum vessel and torus hall during the accident

Pressure is decreasing due to the steam flowing out of the vacuum vessel to the torus hall. Pressure inside the torus hall stays almost constant, because the volume of this room is large, and flow rate of the steam is low and decreasing (Fig. 6). Burst disk opens while the release of coolant from the ruptured pipe is still taking place.

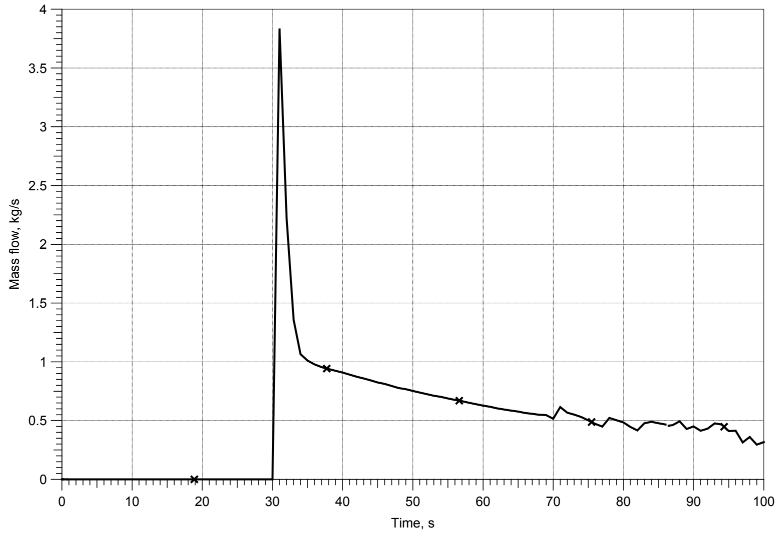

Fig. 6. Obtained mass flow rate through the burst disk

Mass flow rate through the burst disk reaches its biggest value (almost 4 kg/s) just after it has opened. However this initial big flow rapidly decreases to the values below 1 kg/s, due to decreasing flow of the coolant into the vessel and small pressure difference between torus hall and torus.

Pressure differences inside the vacuum vessel are small (Fig. 7), because whole volume of the vacuum vessel is open for mass transfer and coolant release from the ruptured pipe is small enough.

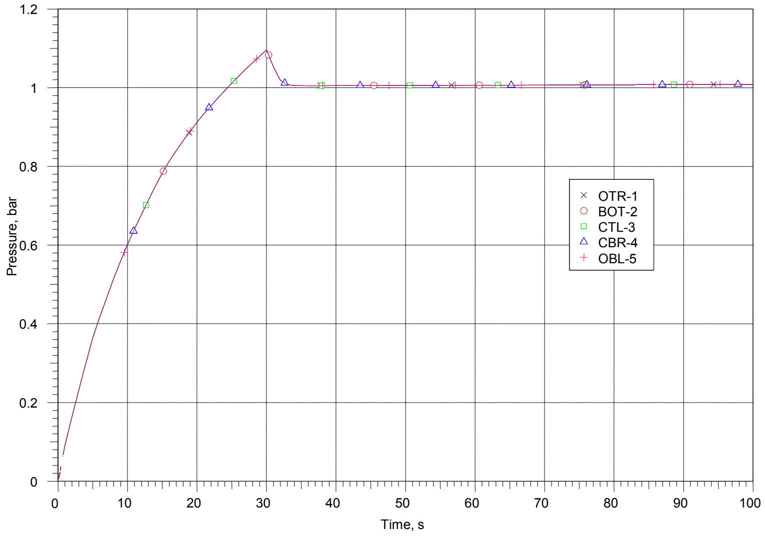

Fig. 7. Pressure evolutions inside the selected parts (control nodes of the nodalisation scheme, where a number after the control node name denotes the module number) of the vacuum vessel during the accident

Obtained results show that the area of the burst disk is sufficient to prevent pressure inside the vacuum vessel exceeding 1.1 bar in the case of simulated accident.

4. CONCLUSIONS

Calculations of the W7-X fusion facility vacuum vessel response to the rupture of the 40 mm diameter pipe using COCOSYS lumped-parameter code were performed. During the analysis, nodalisation scheme of the vessel for the calculations was developed according to simplified vessel geometry. Data available from the accident specification and analysis of the accident with the RELAP5 code were used in the simulations. Obtained results showed that the planned area of the burst disk should be sufficient to prevent pressure inside the vacuum vessel exceeding 1.1 bar in the case of simulated accident.

5. ACKNOWLEDGEMENT

Authors acknowledge the support of Agency for International Science and Technology Development Programmes in Lithuania and European Commission for the preparation of this paper.

REFERENCES

1. W.D. D’haeseleer, Plasma Phys. Control. Fusion 12, 41 (1999).
2. V. Erckmann et al., The W7-X Project: Scientific Basis and Technical Realization, 17th IEEE/NPSS Symposium on Fusion Engineering, October 6-10, 1997, San Diego, CA.
3. The WENDELSTEIN 7-X Project: http://www.ipp.mpg.de/ippcms/eng/for/projekte/w7x/
4. Naujoks D., Initial and Boundary Conditions, 1-NBF-T0008.0, Max-Plank-Institut für Plasma Physik, 2006.
5. H.-J. Allelein, S. Arndt, W. Klein-Heßling, S. Schwarz, C. Spengler, and G.Weber, “COCOSYS: status of development and validation of the German containment code system,” Nuclear Engineering and Design, vol. 238, no. 4, p. 872–889, 2008.

CYSENI 2009, May 28-29, Kaunas, Lithuania
ISSN 1822-7554, www.cyseni.com

THE ANALYSIS OF LOSS-OF-COOLANT ACCIDENT IN FUSION FACILITY W7-X WITH ASTEC CODE

T. Kačegavičius
Lithuanian Energy Institute
Breslaujos st. 3, LT-44403 – Lithuania
Phone: +370 37 401928
E-mail: tomas@mail.lei.lt

ABSTRACT

Fusion is the newest of energy production technology, which could potentially solve problems with growing energy demand of population in the future. Wendelstein 7-X (W7-X) is a stellarator under construction at Greiswald, (Germany). Which shall demonstrate that in the future energy could be produced in such type of fusion reactors. This paper presents the collected information, which is required for development the analysis of water ingress during the W7-X operation mode "Baking. This paper presents the model of W7-X targets cooling circuits developed with ASTEC code. The analysis of loss-of-coolant accident during operation mode "Baking" (rupture of the 40 mm target cooling pipe) has been performed using developed model. The performed analysis showed the response of W7-X "baking" and cooling circuits in case of 40 mm pipe rupture. The amount of coolant released through the ruptured pipe into the vacuum vessel is estimated.

1 INTRODUCTION

At present there are two experimental fusion reactors under construction: ITER, which is constructed in Cadarache (France) and Wendelstein 7-X (W7-X) (in Germany). ITER will be designed to produce ~500 MW of fusion power sustained for up to 400 seconds. Wendelstein 7-X (W7-X) is a stellarator, which shall demonstrate that in the future energy could be produced in such type of fusion reactors. It is presently under construction at the Max-Planck-Institute for Plasmaphysics, Greifswald, Germany. The superconducting magnet system enables continuous operation, limited only by the plasma exhaust cooling water system whose capacity is designed for 30 minutes full power operation.

Prior to start of the operation of the facility its safety has to be demonstrated by performance of the safety analyses. The ingress of water during the W7-X no-plasma operation modes "Baking" and "Hot Liner" into the plasma vessel represents one of the most critical failure events, since primary and secondary steam production leads to a rapid increase of the inner pressure in the vessel. It should be noted that during "Baking" no plasma in the plasma vessel exists, i.e. no special models for plasma simulation are required. Such event could lead to loss of vacuum condition up to overpressure in the plasma vessel, damage of in-vessel components and diagnostics as well as bellows of the ports. Therefore increase of pressure in excess of 1.1 bar must be avoided by means of active (safety valves) and passive safety devices (burst disk, mass loaded disk).

This paper presents the analysis of LOCA in W7-X facility. This paper also includes short description of ASTEC code, which was selected for the analysis of the event, the description of W7-X cooling system. This is the first time when the ASTEC code, which is developed for the analysis of Light Water Reactors, is applied for the analysis of fusion type facility.

2. W7-X TARGET COOLING SYSTEM

The zero point for the W7-X elevation is in the centre of the torus. The highest point (pipes to the upper ports of the outer vessel) is about +3.5 m. The connections to the lower ports are at -3.5 m. The components Heater, Pump, Nitrogen Pressure Vessel are located at -8.1 m. The automatic valves at the module manifolds are at ~0 m.

The height of the pressuriser is 2850 mm (2100 mm for the cylindrical part), the diameter is 1250 mm, leading to total volume of 2500 l. Volume ratio nitrogen/water is about 0.5. The nitrogen pressure in the pressuriser is controlled between 9-11 bar leading to 10 bar static pressure [1].

The power of the heater is 180 kW. The heater is a simple cylinder of diameter 270 mm and length 1950 mm in horizontal position. The electrical heater wires are just inside the vessel. There is no inner pipe system inside the heater.

There is only one pump for all target loops in the operation mode “Baking”. For the operation mode “cooling” there is another pump available, but here for the defined analysis not of concern.

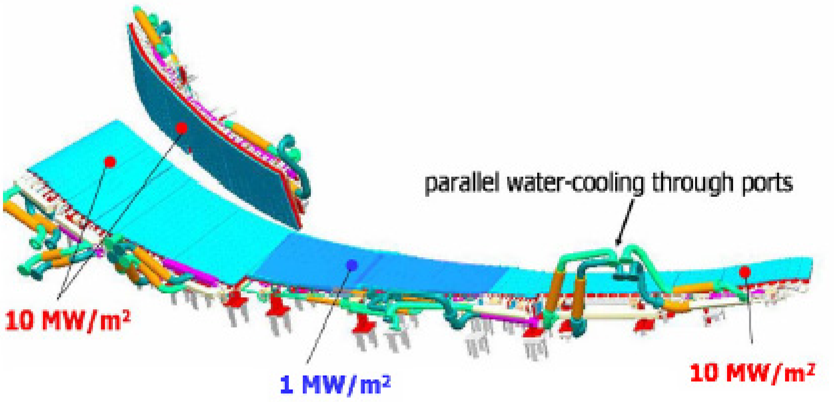

Fig. 1. W7-X divertor target module with horizontal and vertical targets

Fig. 1 shows model of one divertor target module with a total plasma facing surface of about 2 m^2. Most part of the target can withstand heat loads of up to 10 MW/m^2, the middle part of the horizontal target plate has to withstand only power loads up to 1 MW/m^2. These sections of the ten divertor modules with a total area of about 5.6 m^2 composed of 20 target modules with a total of 240 target elements [2].

1800 litres is the volume of all targets in one module. This is roughly the amount of water closed between the valve at the manifold to the 5 modules and the non-return valve. So that 5 times the 1800 litres plus the amount in the outer circuit is ~10 m3. Since there is ~1800 l x 5 modules = 9000 l in the pipe system from the automatic valves (through the torus) to the automatic valves at the manifolds, there are 9000–2640 = 6360 l left for the pipe system near the torus (from the outer vessel to the automatic valves in both directions). There are 120 target circuits (loops) for the torus. That means 24 loops for each module. These 24 loops provide the upper and lower divertor in one module through lower and upper ports.

The maximum water temperature is 160 °C. The water pressure is about 10 bar under the W7-X baking conditions. The corresponding mass flow of water in the cooling circuit target is 177 m^3/h, the flow velocity through the cooling tubes of the target elements during baking operation is about 1 m/s. Simplified scheme of the cooling loop is shown in Fig. 2.

According to [3] the plasma vessel should be modeled using a simplified geometry of the torus with a major radius of 5.5 m and a minor radius of 1 m with a free volume of

108.5 m^3. A rupture of the 40 mm diameter target module pipe near the flange of the outer vessel, right at a place at the inner surface of the torus, during vessel “baking” is assumed [3].

The wall surface of the plasma vessel made of steel is 150°C. The thickness of the wall is 17 mm. The weight of the plasma vessel is 32.6 t, the weight of the ports, which are also hot , is 62.5 t. The plasma vessel consists of the five modules having the same configuration and volume. The burst or rupture disk with a diameter of 250 mm is located at a T-flange, which is mounted on a pipe of diameter of 300 mm and length of 4 m. It was assumed that this pipe is attached to the part of the PV that only steam can be released into the torus hall with free volume of ~16800 m^3. In another scenario, it was assumed that the water steam from the torus volume is directed outside the torus hall to atmosphere via the exhaust pipe of diameter 500 mm and length 25 m. The maximum volume flow in the operation mode “baking” is 177 m^3/h. The whole water volume in the baking circuit of the targets is 10.3 m^3 and of the baffles/wall 12.4 m^3.

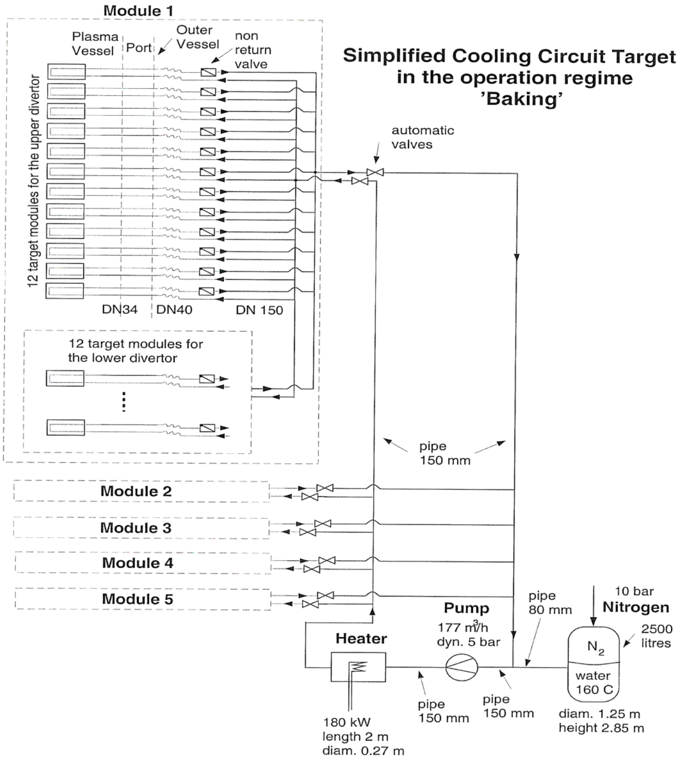

Fig. 2. Flow diagram in “baking” mode

3. ASTEC CODE

The analysis of LOCA in W7-X facility was performed using the integral code ASTEC. ASTEC (Accident Source Term Evaluation Code) – is an integral code for Light Water Reactors source term severe accident calculation, from the initiating event until radioactive release out of the containment [4]. ASTEC code consists of several modules, which are developed for the analysis of separate tasks. Each module will be shortly presented further.

CESAR module simulates the whole front-end phase in the vessel (with a simplified core modelling) and in the loops, and then, after the beginning of core degradation phase, two-phase thermal-hydraulics in the loops and in the vessel upper plenum only. The models are based on a thermal-hydraulics simulator code, the physical models of which were derived from the reference French CATHARE thermal-hydraulics code. Two phases are considered: water and gas (steam + 1 non-condensable gas). The system is made of 5 scalars mass and energy conservation equations associated with 5 state variables.

The reactor cooling system is discretised in volumes (one mesh), either homogeneous or with a swollen level, in axial meshed volumes and in junctions. Thermal non-equilibrium is simulated by separated mass and energy balance equations supported by interfacial mass and heat transfer models. The wall heat transfer models close the energy balance equations. Mechanical non-equilibrium is simulated by a set of algebraic drift correlations for vertical and horizontal flow paths. The wall shear model closes the momentum balance equation. Special components could be defined to simulate pumps and ruptures of the piping.

This paper presents the analysis of W7-X target 40mm pipe rupture. The results of LOCA analysis will be further used in the plasma vessel model developed for CPA module. CPA [4] module is used for simulation of thermal-hydraulics and aerosol behaviour in containment. Lumped-parameter approach (volumes represented by nodes connected by junctions) in simple or multi-compartment containments (tunnels, pit, dome…) with possible leakages to the environment or to normal buildings, with more or less large openings to the environment.

The other modules DIVA, ELSA, SOPHAEROS, RUPUICUV, MEDICIS and IODE are not relevant for the selected accident scenario simulation in the fusion type facility.

4. DEVELOPMENT OF MAIN COOLING CIRCUIT AND “BAKING” CIRCUIT MODEL USING ASTEC CODE

ASTEC/CESAR module was used for the analysis of divertor target cooling circuit response and calculation of water release to W7-X vessel. The simplified scheme of main cooling and “Baking” circuits was developed (see Fig. 3). The simplified scheme was used for development of ASTEC code model nodalisation. The measurements (pipe lengths, elevations, pump parameters, heater power and valves parameters) and configuration of pipes (it is necessary for evaluation of form loss coefficients) were taken from W7-X designs.

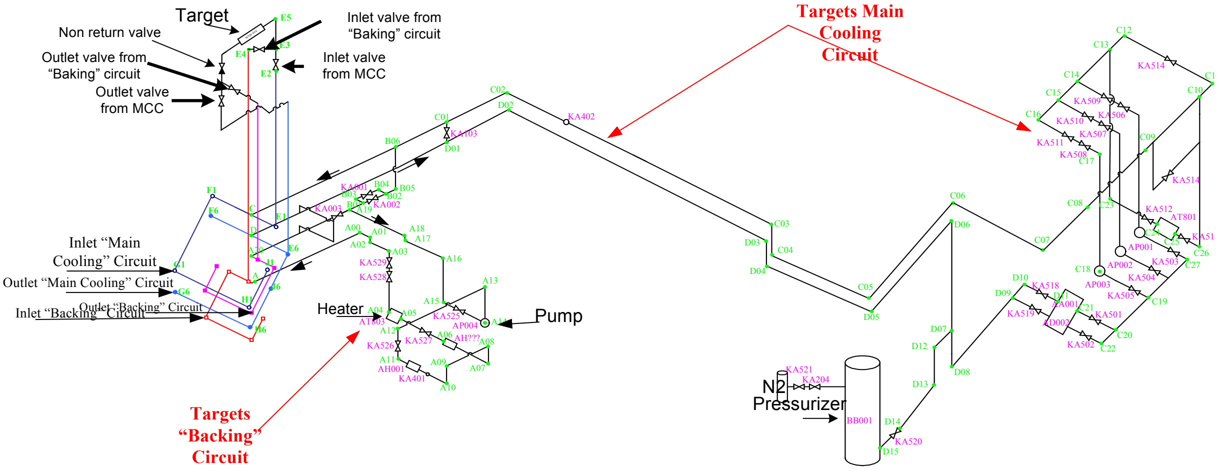

Fig. 3. Simplified scheme of main cooling and “Baking” circuits.

The simplified scheme for modeling of targets (nodalisation scheme) was developed (see Fig. 4). As it is seen from presented scheme, 4 Target Modules are modeled as simplified one equivalent element: “F5-F5’”, “G5-G5’”, “H5-H5’”, “J5-J5’”.

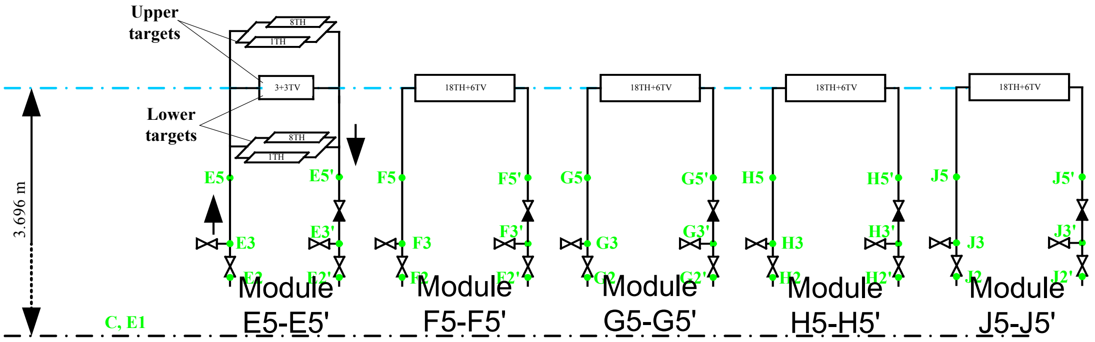

Fig. 4 Modelling of targets (nodalisation scheme)

One Target Module is modeled in more extended format: the two single targets were selected (one in upper and one in lower position). These upper single elements allows to model rupture of single target feeder pipe. One Target Module “E5-E5” is modeled in more detailed manner (see Fig. 5). The pipe elements “136”, “137”, “139” and “140” are used for modeling of upper and bottom horizontal Targets. 6 vertical Targets are modeled by employing “138” pipe element. Element “146” is identical to “130”, element “139” – to “136” and element “140” – to “137”. The modeling of double ended guillotine break is used the ASETC/CESAR connection module BREAK. Element “199” models the volume inside plasma vessel with pressure equal 0.01 bar.

The pump in the model was described by a pressure difference as a function of the flow rate. Pump model STRU PUMP available in the ASTEC code is used.

For the modelling of the pressurizer a special type of node “swollen water level” was used. Volume ratio nitrogen/water is about 0.5.

The valves from MCC and “Baking” circuit on inlet and outlet were modelled by used ASTEC/CESAR module STRU SYSTEMS/VALVE. The non-return valves were modelled by a difference of the proportionality coefficients used in the calculation of the local pressure loss for reverse flows.

The heater was modelled by the heat structure with defined initial temperature and the heat source of 180 kW. In this modelling is used ASTEC module STRU WALL.

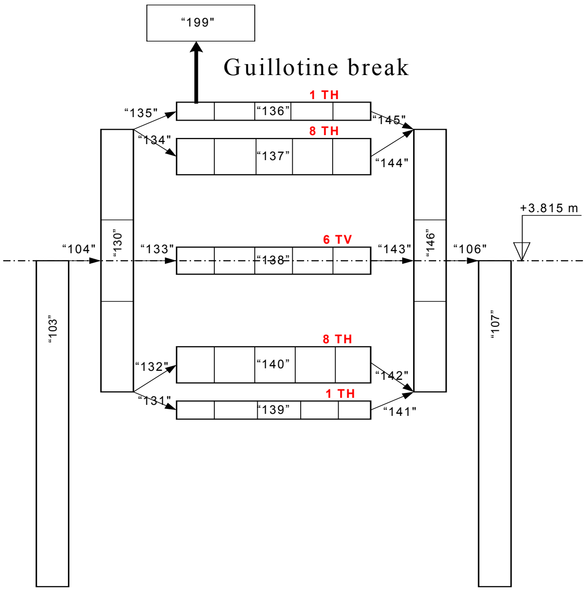

Fig. 5. Nodalisation scheme of affected module

5. ANALYSIS OF 40 MM DIAMETER PIPE RUPTURE

It was assumed that in the “Baking” circuit the water temperature is 433.16 K (160 ^{0}C) and density – 907 kg/m^3. The water flow rate through “Baking” circuit is 177 m^3/h=44.6 kg/s. Pressure in plasma vessel is equal 0.01 bar. Valves from MCC to the targets are closed on inlet and opened on outlet. Valves from “Baking” circuit on inlet and outlet are opened.

Table 1. The following events were assumed to occur:

1.	T = 0.0 s	Double ended guillotine break of DN40 (inner diameter 0.0443 m) occurs.
2.	T = 2.0 s	Closure of valves on Target inlets begins (due to pressure increase in plasma vessel).
3.	T = 5.0 s	Valves on Target inlets are fully closed.
4.	T = 10.0 s	Trip of pump on “Baking” circuit

In the model it was assumed that the break occurs in the Module in piping “E5-E5’” (see Fig. 4). The break occurs in DN40 mm feeder pipe, connecting single upper horizontal Target (element “136” in Fig. 5).

As it is seen from Table 2, the flow rates through different Target Modules (they are identical) are different. The differences are due to differences in flow resistances of inlet and outlet rings. The biggest water flow rate is through the first Target Module, the smallest flow is through the last Target Module. This result indicates that the inlet and outlet rings should be modelled very carefully.

Table 2 Water flow rates through different Target Modules

	Mark	**Flow rate, kg/s**
1	E5-E5’	**12,99**
2	F5-F5’	9,005
3	G5-G5’	8,2602
4	H5-H5’	7,6024
5	J5-J5’	6,7250

Fig. 6 shows that the water flow in the “Baking” circuit stops after the closure of automatic valves.

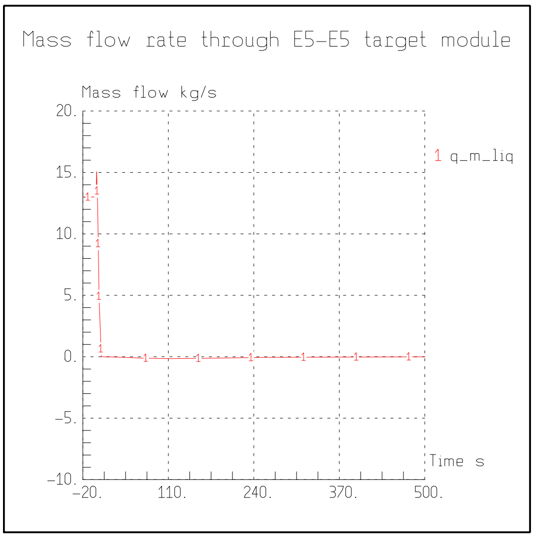

Fig. 6. Flow rate through E5-E5’ (“Baking” circuit)

The discharge of coolant through the break is presented in Fig. 7. 1s after guillotine break of 40 mm pipe mass flow through the break is maximum (14.6 kg/s). After close of automatic valve the discharge of coolant through the break slightly decreases, but the water from other Targets in this Module is discharged till pressure in the intact Targets decreases down to the pressure in plasma vessel (Fig. 8).

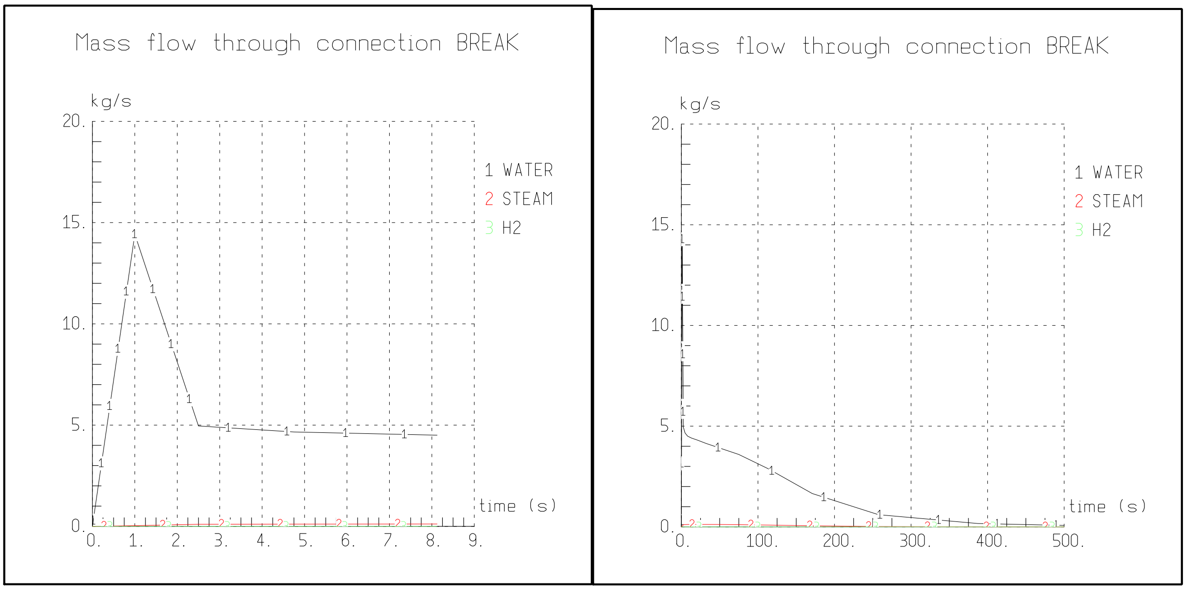

Fig. 7. Discharge of coolant through the break

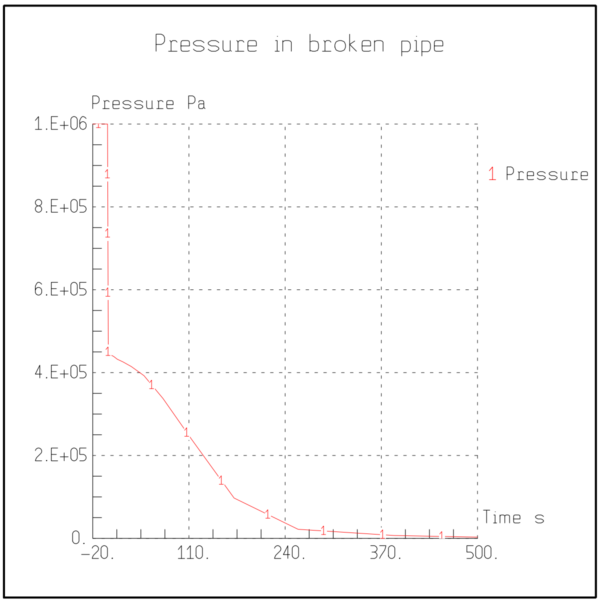

Fig. 8. Pressure in broken pipe

The information about emptying of targets in affected Target Module is presented in Fig. 7 and Figure 8. In these figures the behaviour of water and steam mass in the broken pipe is presented. As it is shown in Fig. 9, the upper Target will be empty after approximately 400 s. From this Figure we can see that the water mass decreases very sharply due to pressure difference between circuit (10 bar) and plasma vessel (0.01 bar).

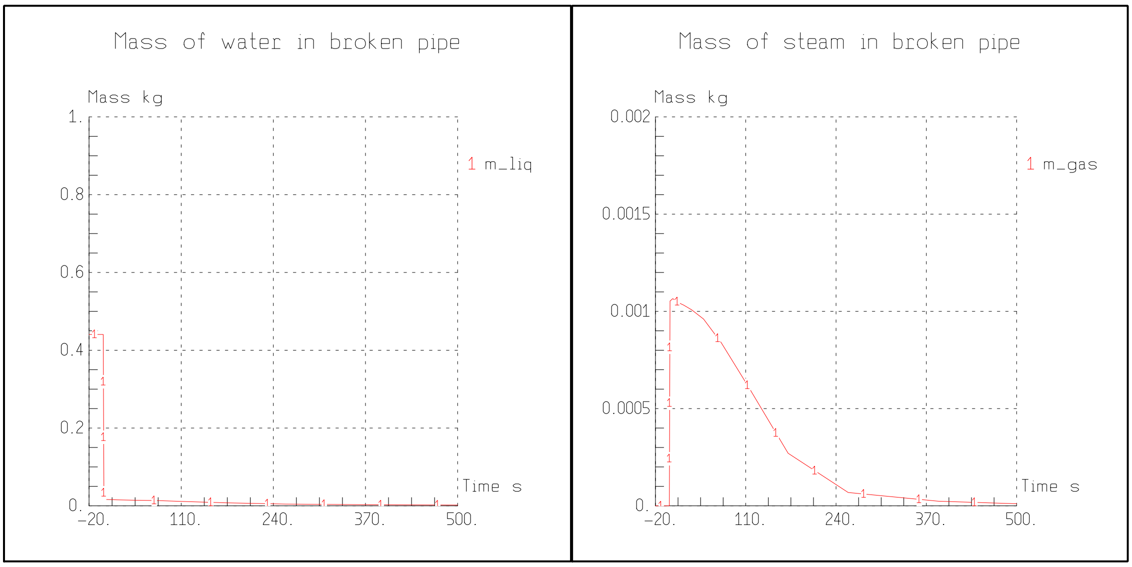

Fig. 9. Behaviour of water and steam mass in the broken pipe

The information, which will be used in latest phases of analysis for the calculation of pressure behaviour in plasma vessel (discharge of coolant and enthalpy behaviour) is presented in Fig. **10** and Fig. 11.

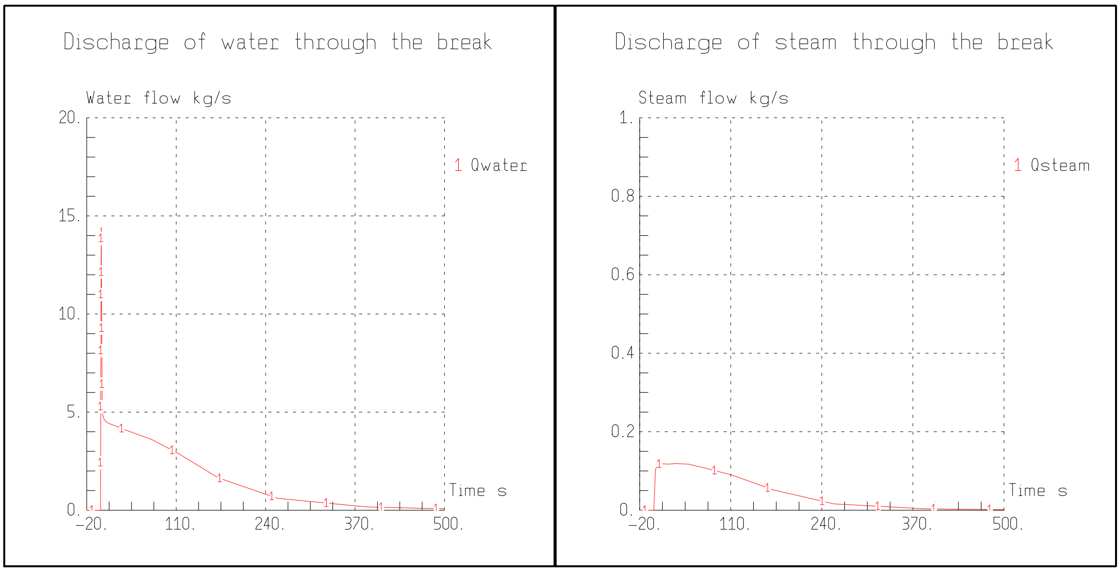

Fig. 10. Discharge of coolant through the break

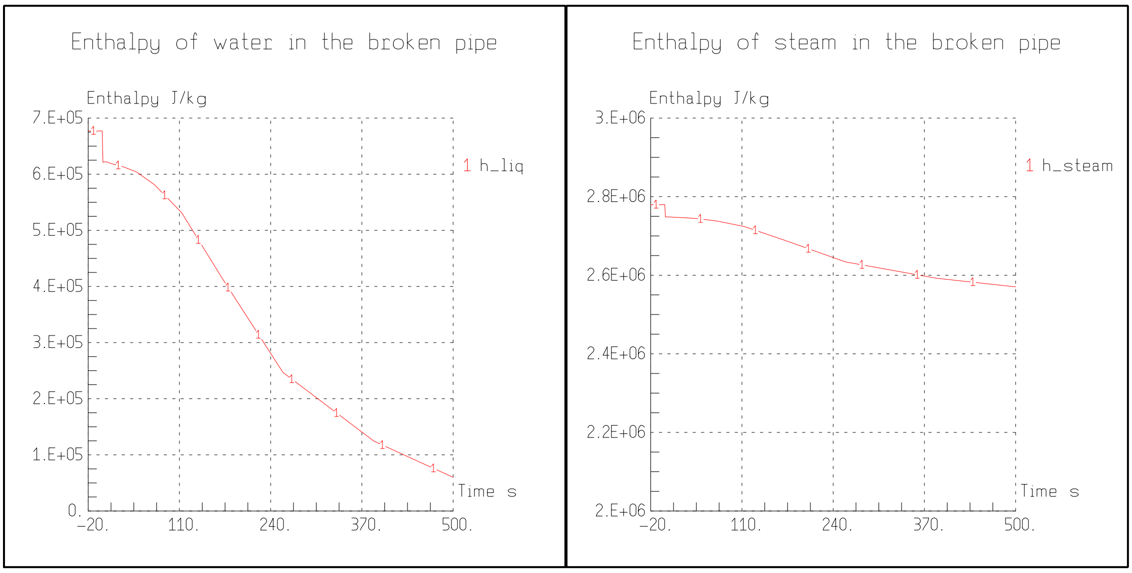

Fig. 11. Enthalpy behaviour of coolant in broken pipe

6. SUMMARY

Based on presented information the ASTEC model was developed. The steady - state condition was reached using the model and rupture of DN40 mm feeder pipe, connecting single upper horizontal Target in “Baking” mode was performed. The selected boundary conditions guarantee the conservative results. The received results of calculations (discharge of coolant and enthalpy behaviour) will be used in latest phases of analysis for the calculation of pressure behaviour in plasma vessel.

The calculation result is very sensitive to assumptions and boundary conditions. Thus in the nearest future it is necessary to clarify:

The construction of inlet and outlet headers in connection of “Baking” circuit and Targets. The contraction influences the form loses and initial flow rates of water through different Modules. In present model the flow rates through different Modules differs very significant.

Delay between signal generation and start of valve actuation

Full valve closure time

Set-point of signal for automatic pump trip and delay between parameter reaches the set-point and pump trip.

In the next steps it is planned to add the model of the W7-X plasma vessel for CPA module. After connection of both modules (CESAR and CPA) the integral analysis of W7-X facility response to loss-of-coolant accident will be performed. And in further steps it is planned to perform uncertainty and sensitivity analysis of computation results.

7. ACKNOWLEDGEMENT

Authors acknowledge the support of Agency for International Science and Technology Development Programmes in Lithuania and European Commission for preparation of this paper.

REFERENCES

1. D. Naujoks, Initial and Boundary Conditions, 1-NBF-T0008.0, Max-Plank-Institut für Plasma Physik, 2006.

2. B. Streibl et al., “Manufacturing of the W7-X divertor and wall protection”, Proc. 23rd Symp. Fusion Technology, Venice, Italy (2004).
3. “Wendelstein 7-X, Overview and Status of Construction”, Hans-Stephan Bosch a and the Wendelstein 7-X Team, a Max-Planck Institut für Plasmaphysik, Branch Institute Greifswald, Euratom-IPP Association, D-17491 Greifswald, Germany
4. J.P Van Dorsselaere, B. Schings, ASTEC V1.3 rev0 Users Manuals (modules CESAR, DIVA, ELSA, SOPHAEROS and SYSINT) CD, December 2006.

CYSENI 2009, May 28-29, Kaunas, Lithuania
ISSN 1822-7554, www.cyseni.com

CONSERVATIVE CONDITIONS IN MODERNIZED RBMK-1500 REACTOR CORE DURING REACTIVITY INITIATING ACCIDENT

A. Slavickas, R. Pabarčius
Lithuanian Energy Institute
Breslaujos str., LT-44403 Kaunas, Lihuania
Phone: +370 (37) 401920
E-mail: andriussl@mail.lei.lt

ABSTRACT

This paper deals with the transient modelling of reactivity accident which was caused by erroneous spontaneous withdrawal of a bank of control rods in Ignalina NPP reactor core. The withdrawal of control rods in the power peak zone causes a drastic increase of reactivity and fuel temperatures. Modelling was performed in different initial conditions to find the most conservative case. For this purpose a made-up peak of radial power distribution in reactor core was formed and six variants with different power and fuel burn-up axial profiles in fuel channels were investigated. The simulations of this accident were performed using QUABOX/CUBBOX-HYCA software.

Keywords: RBMK, reactor, conservative conditions, withdrawal of control rods

1. INTRODUCTION

The Ignalina NPP operates with a RBMK-type boiling water channelized reactor with graphite moderator. The reactors thermal power and energy release distribution in the reactor core is controlled by movement of control rods. There are 211 control rods, which move in Control and Protection System (CPS) channels. Reactor protection system consists of several subsystems, which are designed to reduce the reactor power or to shut down the reactor in response to a variety of trip signals [1].

The Diverse Shutdown System (DSS) was implemented at the Ignalina NPP Unit 2 in 2004 in accordance with SAR-2 recommendations [2]. The implementation of DSS makes two independent shutdown systems in CPS: fast power reduction (BSM) and emergency reduction (AZ). BSM system provides normal shutdown and is able to ensure long-term maintenance of the reactor in the sub-critical state as well. AZ system provides emergency protection in a case of accident. The control rods are divided into two systems. AZ system includes 24 fast acting rods and in addition 49 rods out of the remaining 187 control rods. The BSM system includes all remaining 138 rods and in addition the same 49 rods, which are included in the AZ system. These 49 rods are called AZ/BSM rods.

AZ system is actuated from two sets of the detectors. Each of them has its own sensors and operation logics based on the algorithm 2 out 3. This system performs the emergency protection function. The operation of logics of the initiating equipment of the BSM shutdown system is based on the same algorithm 2 out 3 and it is intended for fast power reduction until reactor shutdown and its continuous hold-down in a sub-critical state. A subsystem of AZ/BSM rods, which is part of both systems, fulfils the control functions during normal operation or the emergency protection function during the reactor accident modes.

Emergency protection signal AZ and normal shutdown signal BSM are controlled by signals coming from Outside Core Detector (ODC), Inside Core Axial (ISA) and Inside Core Radial (ICR) detectors. It is variety of CPS modes, which can be initiated by variety signals of detectors.

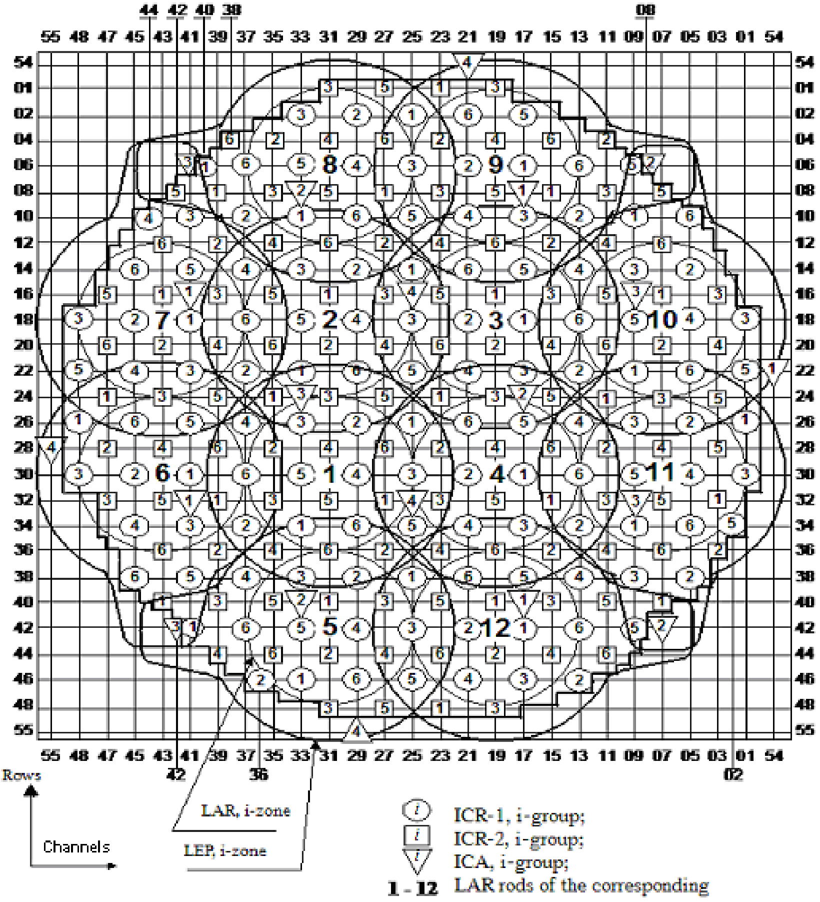

Fig. 1. The scheme of the in-core radial and axial detectors locations

The reactor core is divided into 12 zones of local automatic regulation (LAR) and local emergency protection (LEP) (Fig. 1). Each LAR-LEP zone has 1 LAR and 2 LEP rods. Each LAR zone receives signals from 6 detectors that belong to 6 different detectors groups. Signals from 2 detectors are summed up and form one signal. In this way, 3 signals from one LAR zone are available. According of this signals (2 out 3) LAR rods are compensating power changes in each LAR zone. LAR rods are moving with velocity of 0.2 m/s.

Either LAR and LEP modes warning or emergency signal from a single detector is initiated if locally neutron flux increases set value above mark. If 2 emergencies overpower signals are coming from LEP ICA detectors, which belong to different detectors groups, in one LEP zone at the same time, AZ-6 signal in that zone is initiated. The same general logic is applied for signals of ICR detectors. LEP rods are moving with velocity of 0.4 s.

AZ-6 signal initiates AZ-3 signal if reactor power is above half nominal reactor power. According to AZ-3 signal reactor power is reducing to half nominal reactor power with the rate of 2% of nominal power per second. If AZ-6 signal is still available when reactor power are below a half of nominal power, reactor power is reducing further with the rate of 1% of nominal power per second until the signal disappears. If actuation of AZ-6 regime in three or more LAR-LEP zones occur emergency AZ signal is generating. The full description of Ignalina NPP Unit 2 CPS logic can be found in [3].

RBMK-1500 reactor core is very heterogenic in comparison with other type reactors. Several types of CPS rods and four type of fuel assembles (uranium-erbium compositions) are used at Ignalina NPP. After DSS implementation and during continuous modification of fuel type RBMK-1500 reactor core was changed significantly [4]. Then the most conservative conditions for accident analysis are needed to review once again.

The specific physical models and correlations ensuring a necessary level of conservatism should be used for the conservative approach analysis in general. Initial condition of reactor core should be chosen in such way that the received calculations results were conservative for parameters, for which the acceptance criteria are selected.

This paper deals with determination of the most conservative conditions during investigation of reactivity initiated accident at Ignalina NPP. It was assumed the spontaneous withdrawal of a control rod bank at full power (4200 MW) in this study. Such reactivity accident influences reactor core and perturbs its parameters the most. The probability of this design basis accident is greater than 0.01 over the lifetime of the plant.

The axial power peak in RBMK reactor core usually is in the upper part of reactor core in reference core state. The axial fuel burn-up distribution influences the excursion of axial power distribution in fuel channels during the withdrawal of the control rod bank. A performance of analysis with changed axial power and burn-up distributions in reactor core was made in this study. 6 different initial core states with different axial power and fuel burn-up distribution profiles were investigated. Thereby the main purpose of this study was to find the most conservative conditions of initial state for accident analysis performance in modernized RBMK-1500 reactor core.

2. MODELLING OF REACTIVITY ACCIDENTS

2.1. QUABOX/CUBBOX-HYCA code

QUABOX/CUBBOX-HYCA (Q/C-H) [5-8] code was used during investigation. State-of-the-art code Q/C-H was originally developed by the German company GRS mbH for the Light Water reactors and was used for the licensing purposes of the Western LWRs. Since 1990 the code was also applied for the analysis of RBMK-1500 reactor safety and since 1995 it was additionally adapted to account for the special features of RBMK-1500 reactors.

Q/C-H code consists of neutron-kinetic (QUABOX/CUBBOX) and thermal-hydraulic (HYCA) parts. The 3D neutron kinetics code is solving the two-group neutron diffusion equation, using a polynomial approximation method, and is applied to the analysis of static and dynamic reactor core. The thermodynamics part of code is solving conservation equations for single phase flow and two-phase flow using drift-flux correlations. Coolant flow and fuel rod model are part of parallel coolant channel model in the thermodynamic part of the code.

During the review process of the SAR-1 [9] Q/C-H code was used in the independent review calculations. The code was used for the preparation of SAR-2 [2] during performance of the accident analysis. After DSS implementation in 2004 modified CPS layout and its full DSS operation logic was implemented in Q/C-H code. The code is continuously used for RBMK-1500 core calculations and for the surveillance of the reactivity behaviour of the changing core loading using higher enriched erbium fuel and control rods of the new design. So, Q/C-H code is widely applied for static and dynamic safety analysis of RBMK-1500 reactor.

The neutron kinetics calculations are based on two neutron energy group's cross sections library. This two-group macroscopic cross sections library is developed using the lattice code WIMS-D4 [10] and it is constituent part of the STEPAN code, which is being used as an operational tool for performing the every-day neutronic-dynamic calculations of RBMK-1500 reactors at the Ignalina NPP. The library contains macroscopic cross sections for all type of fuel used in RBMK reactor core, as well as macroscopic cross sections for non-fuel lattice (including cross sections for cluster control rod). The cross sections contains the dependencies on the fuel temperature, cool density, fuel burn-up level and other parameters determining the neutron balance.

2.2. Initial reactor core states

As the basic state for the formation of initial conditions for investigation Ignalina NPP Unit 2 reference reactor core state registered by the TITAN information computer system on 28 July 2006 was used. Reactor at that time was operated at the thermal power level of 4052 MW, the average fuel burn-up was 12.67 MW days/kg and the operative reactivity margin was 54.9 manual control rods [11]. Calculated reactivity parameters and coefficients of this reactor state falls into the allowable range defined in reactor passport.

Reactivity accidents are caused by rapid reactivity increases. Reactivity increases can be caused by withdrawal of control rods, CPS cooling circuit voiding or erroneous fuel refueling. The spontaneous withdrawal of a control rod bank at full power (4200 MW) was assumed in this study as inclusive case. It was chosen 4 accident control rods in reactor core center for the investigation. The withdrawal of control rods bank in reactor core center can cause immediately reactivity changes because the efficiency of control rod in reactor core center is higher than in reactor core periphery. The parameters of chosen reactor condition at full power are closest to operational limits.

The selected central rod bank was fully inserted into the core at the beginning of modeling. The radial neutron flux distribution had been shifted toward the accident rods to create the radial power peak. Such perturbed power distribution was constructed by changing surrounding burn-up of fuel channels and insertion depth of surrounding CPS rods. These means enabled to generate perturbed power peak about accident rod bank several percent higher than those of reference core state.

The process of reactivity accident depends on axial power and fuel burn-up distributions. So it was investigated 6 cases with different initial core states by changing axial power and burn-up profiles to determinate the most conservative condition for performance of reactivity accident analysis. Note that the axial power peak is in the upper part of reactor core in reference core state. All of analyzed cases are represented in Fig. 2, Fig. 3 and Fig. 4.

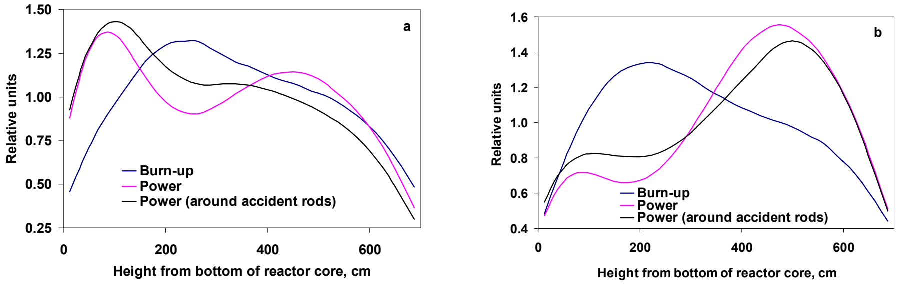

Fig. 2. Cases of reactor core states when axial burn-up peak is in bottom part of reactor core. Power peaks are in bottom (a) and in upper (b) part of reactor core

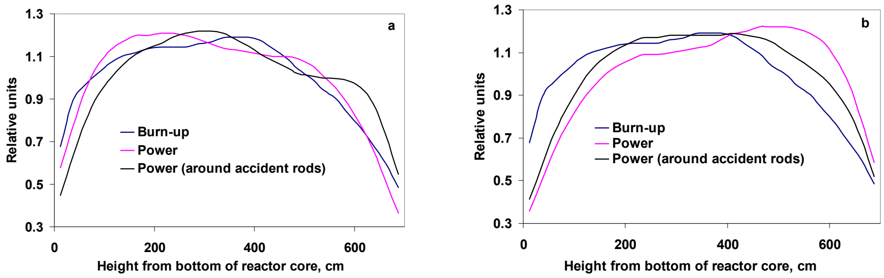

Fig. 3. Cases of reactor core states with average burn-up profile in reactor core. Power peaks are in bottom (a) and in upper (b) of reactor core

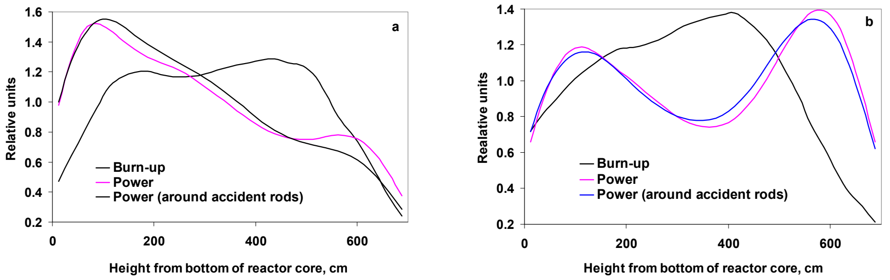

Fig. 4. Cases of reactor core states when axial burn-up peak is in upper part of reactor core. Power peaks are in bottom (a) and in upper (b) part of reactor core

2.3. Methodology of investigation

In general the following principles shall be applied for definition of initial conditions and for fulfillment of the conservative approach analysis during control rod withdrawal accident:

- Radial neutron flux distribution is shifted towards the accident rods;
- One fresh fuel assembly is located in the vicinity of the accident rods;
- Accident rods are chosen so as to minimize the effect of the LAC system;
- The most effectiveness control rod is assumed not operable;
- First initiated emergency or protection signal is neglected;

Control rods with coordinates 22–27, 24–25, 26–23, 26–27 (see Fig. 1) were chosen for reactivity accident analysis presented in this paper. The erroneous spontaneous withdrawal of control rods bank took place at time t=0.0 s. The speed of control rods bank withdrawal was 0.4 m/s. Control rods were withdrawn fully from reactor core within 17 s. A detector signal, which initiates first emergency or shutdown signal, was neglected because of need to meet the condition of conservatism. So two sets of reactivity accident modeling were performed for each case. First calculation was needed to find the detector signal which initiates first emergency or shutdown signal. The second calculation neglecting this signal was performed. The most effectiveness control rod around accident control rods bank was assumed not operable because of need to meet the condition of conservatism too. The most effectiveness control rod was found by making variation calculations of steady states with fully inserted and fully withdrawn control rod in reactor core. The effectiveness of control rod was determined as difference between these two states. Skipped first detector signal and the most effectiveness control rod were found separately for initial reactor core states with different axial fuel burn-up and power profiles.

The acceptance criteria for reactivity initiated accidents presented in Table 1 were applied in this study. One of main criteria is maximum fuel temperature. Maximum fuel temperature can't to exceed fuel melting point, approximately 2800 ^{0}C for dioxide uranium. The criterion of fuel cladding temperature assumes that in case of fuel cladding temperature above 700 ^{0}C a possibility to lose integrity of the cladding appears and a release of fission products may take place. The criterion of fuel channel temperature is related to fuel channel integrity.

Table 1. Acceptance criteria applied for analysis [2]

Parameter, component or system	Acceptance criteria (safety limit)
Reactor power	below 4800 MW
Fuel pellet temperature	below 2800 ^{0}C
Fuel cladding temperature	below 700 ^{0}C
Fuel channel temperature	below 650 ^{0}C

2.4. Calculations results

Reactivity accident analysis was performed for all described cases of initial reactor core states (Fig. 2-4). The main important calculations results are summarized in Table 2. The difference in maximal fuel cladding and fuel channel temperatures vary in the range 18 ^{0}C and 10 ^{0}C accordingly. Difference of maximal fuel pellet temperature all over the cases does not exceed 540 ^{0}C. As can see from Table 2 maximum value of reactor power during investigated accident differs not more than 118 MW. Acceptance limits were not exceeded during all investigated cases. Calculation results show that CPS was enable to prevent reactivity accident excursion before reactor operating state becomes critical.

The highest fuel temperature and reactor power were determined in reactor core state when axial fuel burn-up peak was in upper part of reactor core and axial power peak was in bottom part of reactor core. AZ signal was generated at the earliest in this case too (in 2.35 s). So according obtained calculations results this case (burn-up peak in upper and power peak in bottom part of reactor core) is the most conservative. This most conservative reactivity accident in comparison to other investigated cases is described below.

Table 2. Summary of reactivity accident analysis results

Maximal values	Acceptance limit	Case of reactor core state related to profiles (related to Fig.2-4)					
		Fig. 2a	Fig. 2b	Fig. 3a	Fig. 3b	Fig. 4a	Fig. 4b
Reactor power, MW	< 4800	4374	4289	4359	4345	4407	4343
Fuel pellet temperature, ^{0}C	< 2800	1970	2055	1697	1664	2237	1892
Fuel cladding temperature, ^{0}C	< 700	355	357	348	343	361	352
Fuel channel temperature, ^{0}C	< 650	323	325	320	317	327	322
AZ signal generation, s	–	2.43	2.77	2.43	2.52	2.35	2.49

The accident started at the time 0.0 s. Spontaneous withdrawal of control rod bank in reactor core centre caused the increase of reactor power and fuel temperatures. At the time 0.3 s LAR rod movement started to compensate power changes. But reactivity continued to increase. The first accident signals appeared at the time 1.35 s. Accident signal at the time 1.81 s, which had to actuate AZ-6 regime, was ignored (conservative approach). At the time 1.83 s follow-up AZ-6 regime was generated, which initiated AZ-3 regime. Reactivity and reactor power continued to increase despite actuated AZ-3 regime, which should had to reduce reactor power to half of nominal power. It is because the center rod bank still was moving out of core and reactivity was increasing. AZ regimes were actuated in 3 LAR/LEP zones at the time 2.06 s. At this time point AZ signal was generated. CPS control rods started to move for reactor shutdown according to AZ signal with the delay of 0.29 s. Starting from this point of time reactivity and reactor power began to decrease. The full sequence of events during reactivity accident of this case is presented in Table 3. During control rod bank withdrawal reactor power increased from 4200 MW to 4407 MW (at time 2.36 s) and maximal fuel temperature increased from 2195 ^{0}C to 2237 ^{0}C (at time 2.7 s). These values remained in allowable operating margins (Fig. 5).

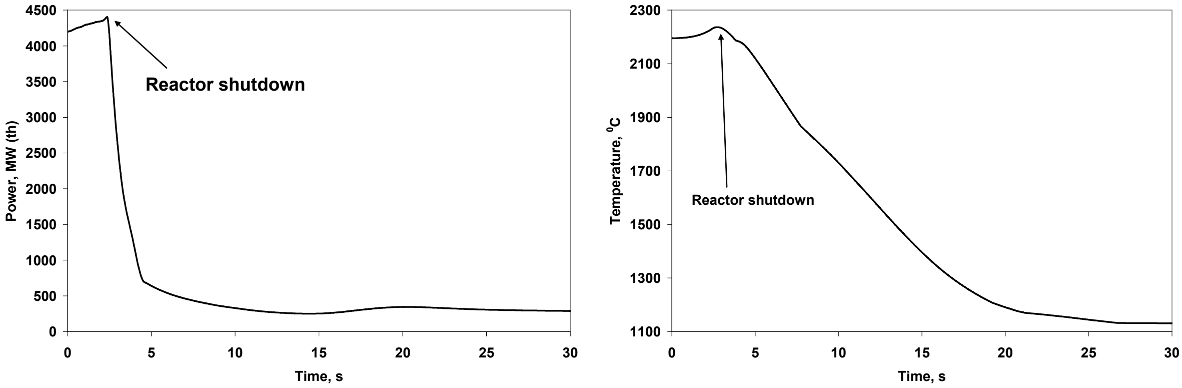

Fig. 5. Reactor power and fuel temperature variations during accident

Table 3. Sequence of events during spontaneous withdrawal of rod bank

Time, s	Event
0.0	Start of control rod banks withdrawal accident
0.3	LAR rods movement starts
1.35	Generation of accident signal by ICA detectors in zones No.1 and No.4.
1.47	Generation of accident signal by ICA detectors in zones No.2 and No.3.
1.81	Generation of accident signal by ICA detectors in zone No.1. Signal ignored.
1.83	Generation of accident signal by ICA detectors in zone No.4. Actuation of the AZ-6 regime in zone No.4.
1.86	Generation of accident signal by ICA detectors in zone No.2. Actuation of the AZ-6 regime in zone No.2.
1.94	Generation of accident signal by ICR detectors in zones No.1 and No.4.
2.06	Generation of accident signal by ICR detectors in zones No.1 and No.2. Actuation of the AZ-6 regime in zone No.2.
2.35	With a delay of 0.29 s CPS control rods are moved for reactor shutdown according to AZ signal.

3. CONCLUSIONS

The modeling of reactivity accident caused by erroneous spontaneous withdrawal of the bank of control rods is presented in this paper. Cases with different power and fuel burn-up profiles in fuel channels were investigated to determine the most conservative case for the reactivity accident analysis.

During the analysis of calculations results was shown that the most conservative reactivity accident appears in the case of reactor core state when axial power peak is in bottom part and axial burn-up peak in upper part of RBMK-1500 reactor core. Because of significant perturbations in the core AZ signal is generating fastest in this case in comparison to other investigated cases. Later on the emergency protection is initiating more quickly because of high positive reactivity insertion around accident control rods. Reactor power and maximal fuel temperature increase very quickly and reach the highest values comparing to other investigated cases.

Based on obtained calculation results can be stated that during analysis of reactivity initiated accident, which is related to control rod withdrawal, for preparation of initial reactor core for investigation axial fuel burn-up profile shifted to upper part and axial power profile shifted to bottom part of the RBMK-1500 reactor core shall be used. Such conditions allow to determine the most possible consequences of accident.

REFERENCES

1. K. Almenas, A. Kaliatka, and E. Ušpuras, Ignalina RBMK-1500. A Source Book, Extended and Updated Version, Lithuanian Energy Institute, Kaunas, Lithuania, 1998.
2. Safety Analysis Report for INPP Unit 2, INPP, 2002.
3. Ignalina NPP. Technical Specification for INPP. Tender Documentation of the Second Shutdown System for Ignalina NPP Unit 2, 2001.
4. Bubelis E., Pabarcius R., Langenbuch S., Clemente M. Analysis of nuclear characteristics of Ignalina NPP RBMK-1500 reactors using new uranium-erbium fuel of 2.6% enrichment // Proc. of Annual Meeting on Nuclear Technology, 20-22 May 2003, Berlin, Germany, 2003, p. 21–24.
5. S. Langenbuch Die modellgleichungen des 3D-kern-modells QUABOX-HYCA fur leichtwasser-reaktoren. GRS mbH report No. GRS-A-256 (Januar 1979), Auftrags-Nr. 82150 (SR 122/1.2.1).
6. Langenbuch S., Maurer W., Werner W. “Coarse mesh flux expansion method for the analysis of space-time effects in large LWR cores”, Nucl. Sci. Eng. 63, 1977, p. 437–356.
7. Langenbuch S., Maurer W., Werner W., “High-Order schemes for neutron kinetics calculation based on a local polynomial approximation”, Nucl. Sci. Eng. 64, 1977, p. 508–516.
8. QUABOX/CUBBOX-HYCA manual, GRS, 1993.
9. Ignalina NPP Safety Analysis Report, VATTENFALL, 1996.
10. Askew J.R., Fauers F. J., Kemshell P. B. “A general description of the lattice code WIMS”. J. Of the Brit. Nucl. Energy Soc. 1996.
11. Measurement Act of reactor physical and dynamical characteristics of Unit 2, INPP, 28-07-2006.
12. Бубялис Э., Пабарчюс Р., Тонкунас А. Моделирование аварийной ситуации с самоходами и падением стержней СуЗ, используя программный комплекс QUABOX/CUBBOX-HYCA // Energetika, 2003, Nr. 3, p. 11–20.

CYSENI 2009, May 28-29, Kaunas, Lithuania
ISSN 1822-7554, www.cyseni.com

HUMAN RELIABILITY ANALYSIS FOR PROBABILISTIC SAFETY ASSESSMENT OF IGNALINA NPP

R. Voronov
Lithuanian Energy Institute
Laboratory of Nuclear Installation Safety
Breslaujos str. 3, LT-44403 Kaunas – Lithuania
E-mail: roman@mail.lei.lt

ABSTRACT

Despite the high reliability of safety systems of nuclear power plants (NPP), human actions still play an important role in NPP safety. Evaluation of human reliability is therefore important for full scope Probabilistic Safety Assessment (PSA) and risk analysis.

In PSA, which include modeling of interaction of safety systems during an accident sequence, human errors are modelled together with hardware failures. Methods for modelling of human errors and evaluation of probabilities of such errors are different comparing methods used for modelling and probabilities estimation of equipment failures.

This paper describes modelling of dynamic actions, which are to be performed by Ignalina NPP operators during accident sequence. Such modelling was applied for Ignalina NPP PSA. A combination of ASEP (Accident Sequence Evaluating Procedure) and THERP (Technique for Human Error Rate Predicion) was applied. Such methodology allows to evaluate operators' error probability at different phases of action: identification, decision-making and implementation, also allowing to properly account different factors that impact human performance: interface, alarm, indications, procedures, training, stress, time, etc..

Human Reliability Analysis (HRA) presented in the paper allows to refine Ignalina NPP PSA model. Application of such method is possible in the areas, where operators play an important role in ensuring safety: nuclear power, oil, chemistry, and transport industry.

Keywords: Human Reliability Analysis, Ignalina NPP, ASEP, THERP, operators' dynamic actions.

1. INTRODUCTION

An integral part of Probabilistic Safety Analysis (PSA) of Nuclear Power Plants is Human Reliability Analysis (HRA), which identifies possible human actions that could impact safety of the facility being analysed. Human actions influence safety in different ways, like making safety equipment unavailable due to errors during repair or maintenance, or initiating an abnormal event, or making errors during accident mitigation. Like equipment failures, human errors are characterized by probability. However, statistics of human errors is rarer than equipment failures and humans cannot be "tested" to get such statistics. Also reasons for human errors and factors that impact them are wider and differs from ones for equipment failures. Analyst's task is to identify human actions that are vital for the plant safety, adequately evaluate factors that have the highest impact performance of plant operators, evaluate human error probability (HEP) for each action and include the actions in the PSA model. There is a number of HRA methods used for different stages of analysis. HRA specialist can apply different methods taking into account their advantages and disadvantages, thus creating his own method for a specific study. Despite of the methods used HRA should satisfy at least these criteria:

- Sufficient detail to understand and document all important performance-shaping factors (PSF) that affect human actions.
- Identify and account for dependencies.

- Human error rates are internally consistent and consistent with plant experience and other evidence.
- Uncertainties shall be identified, quantified and displayed.
- Well-documented.
- Probabilistic Safety Analysis model of Ignalina Nuclear Power Plant (INPP) was being developed and progressing more that ten years. Initially post-initiator human actions in INPP PSA were modelled using simplified time dependency model where HEP was dependent only on time window available to perform corresponding human action. Such approach was acceptable for rough estimate at the initial stage of PSA, when less information was available. Later, when the PSA model and data became more accurate, more precise analysis of human performance was required. The main drawback of simplified approach is that HEPs are the same for different accident scenarios having the same time windows. In real life, operators' actions are affected by many different factors, most important of them are:
  - Time
  - Stress
  - Experience and training
  - Availability of written procedures
  - Recognition of the event and plant status.

These factors are scenario-specific, i.e. their impact may be different for the same operators' actions performed in different circumstances depending on the initiating event and accident scenario. Valid HRA should account for such differences and provide consistent HEPs. No such analysis was performed neither for INPP nor for other industrial objects in Lithuania before.

A need for new HRA was recognized by INPP PSA team and recommended by expert missions. HRA was performed in scope of INPP PSA update [1] (so-called "Living PSA"). Various HRA methods used worldwide were analysed, methodology for INPP PSA was developed and analysis was carried out both for pre-initiator human actions and dynamic post-initiator human actions.

This paper presents a short overview of the analysis that was performed for post-initiator dynamic actions.

2. HUMAN RELIABILITY ANALYSIS

2.1. Post initiator dynamic actions

After abnormal event (accident initiating event) plant operators must accomplish well defined tasks for manual initiation, control and alignment of plant systems that are required to ensure the plant safety and avoid an accident. Normally plant safety systems are designed to be initiated automatically in case of emergency and operators' role is to align and control the systems. These tasks are an integral part of plant response to initiating events. Operator actions are well-defined and described in plant emergency procedures. However, there is always a probability that emergency sequence of events does not correspond to the expected scenario, e.g. safety systemd do not start automatically or fail to run, also additional failures may occur. . In such cases importance of operators' actions becomes much higher, Operators must backup startup signals, initiate redundant systems or equipment instead of failed ones and take additional measures to keep the plant parameters within the safety limits.

2.2. Main stages of analysis

Main stages of human reliability analysis are:

1. Identify operators' actions. Key actions important for INPP safety are identified in PSA model. These actions were verified using INPP operating and emergency procedures, interviews with operators.
2. For each action identify:
    a. Success criteria: what action shall be performed; how many operators are required to perform an action; what level of operator skill or training is required; where must the action be performed.
    b. Boundary conditions: what is the initiating event; what equipment failures or human errors preceded the action.
    c. Time: when the action shall be performed, what indications are signal to start the action, how much time is available to operator to perform the action; how much time is required to perform the action.
    d. Dependencies: actions that affect the same function; possible options and which option has a priority.

    Different sources of information are analysed at this stage: Plant operating and emergency procedures, safety reports, PSA model and documentation, thermal-hydraulic analyses, interviews with operators.
3. Perform quantitative analysis of personnel errors.

Approximately 75% of human reliability analysis work takes to identify actions and include them into the model and 25% takes to estimate human error probabilities.

2.3. Modelling of human actions in PSA

PSA uses event tree method for modelling of possible accident scenarios and fault tree method for modelling of plant safety systems required for accident mitigation. Human actions and corresponding errors are included in both event trees and fault trees.

Fig. 1 illustrates incorporation of human action into an event tree.

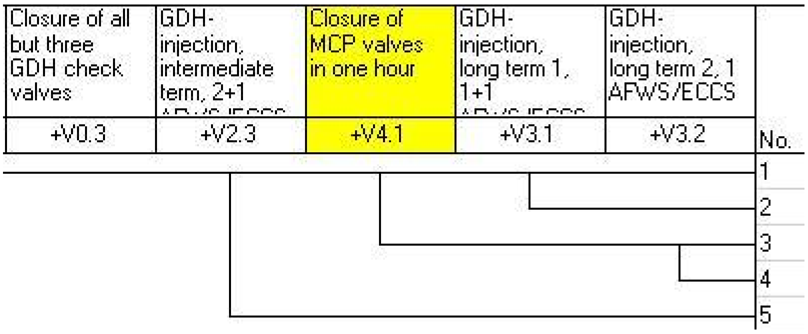

Fig. 1. Operator action in accident event tree

Presented example is a fragment of the event tree for accident sequence "Medium Loss-of–Coolant Accident (LOCA) in Zone 1". Highlighted event represents human action "Operator closes Main Circulating Pump valves in one hour".

Fig. 2 illustrates incorporation of human action into a fault tree.

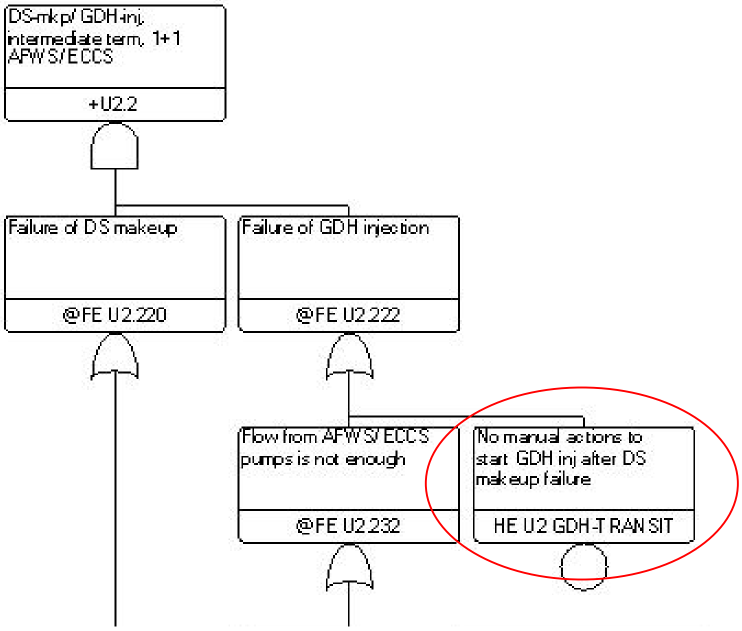

Fig. 2. Operator action in system fault tree

Presented example is a fragment of the fault tree for failure of water supply to the primary circuit at intermediate stage of an accident. Highlighted event represents operator's failure to initiate water supply to group distribution header (GDH) when water supply to drum separator fails.

2.4. Overview of HEP Quantification Methods

In this analysis a combination of THERP (Technique for Human Error Rate Prediction) and ASEP (Accident Sequence Evaluation Procedure) methods was used.for quantification of human error probabilities.

2.4.1. Technique for Human Error Rate Prediction (THERP)

As described in [2], THERP is a method for identifying, modeling, and quantifying human failure events (HFEs) in a PSA. It is a reasonably complete approach to HRA, and has probably been used more than any other HRA technique. Besides its application to NPPs, THERP has recently been used in the maritime, chemical process, and other industries. It has also been applied worldwide since its publication, and a sizeable knowledge base now exists for using THERP.

With respect to modeling, THERP does not provide explicit guidance on how to model an HFE in a PSA. Nonetheless, its qualitative guidance can be useful in doing so. THERP decomposes non-diagnosis HFEs into lower-level errors and identifies important performance shaping factors (PSFs) via task analysis (one of the principal features of a THERP analysis). This decomposition is graphically represented with HRA event trees. THERP also contains a database of nominal HEPs, a few of which have some basis in empirical evidence, but probably involved adaptation/extrapolation by the authors' to fit the NPP domain. The rest of the data represents the expert judgment of the authors, which is based on an understanding, gathered over decades of research and practice, of human-machine interactions in industrial and military facilities, including NPPs.

The resource-intensive nature of THERP limits its application in full-scale PRAs to the extent intended by the method (e.g., perform task analyses, use HRA event trees), but it can be supplemented with a screening procedure (e.g., ASEP, see below) to quantify the majority of HFEs in the analysis. The full THERP task analysis can then be reserved for a subset of the HFEs, which represent the dominant contributors to risk [4].

2.4.2. Accident Sequence Evaluation Program HRA Procedure (ASEP)

As described in [3], ASEP is a less-resource-intensive version of THERP. In contrast to THERP, ASEP is intended to be able to be implemented by systems analysts who are not HRA specialists. Given the "short-cuts" in the method (compared to THERP), the ASEP quantification approach is purposely intended to provide somewhat conservative estimates. ASEP addresses the quantification of both pre-accident and post-accident HFEs, and provides specific guidance for deriving both screening and nominal values for both types of HFEs. It is based upon THERP, but purposely simplifies parts of THERP, such as the model for dependency. In addition, ASEP is almost entirely self-contained; the user need not be familiar with THERP and is not required to use any of the THERP models or data.

ASEP does not address most activities related to the HRA process, such as identification of HFEs, and does not provide detailed guidance on how to model the HFEs. Thus, in using ASEP, it is assumed that the HFEs have already been identified and modeled and only quantification of the associated HEPs is required [4].

2.5. Quantification using ASEP and THERP methods

Each post-initiator dynamic action includes two stages: cognitive stage, i.e. to notice and recognize situation that require operator's intervention, to think and to take a decision; and implementation stage, when the action itself is performed. Each stage is affected by a different set of factors. Thus cognitive and decision-making stage is affected mostly by availability of information about the plant status (alarms, indications), availability and quality of written procedures and operator's skills and training and his ability to recognize the situation and make a decision. Implementation stage is mostly affected by physical possibility to perform the action, i.e. number of personnel, number of operations, access to the equipment, procedures, equipment labelling. Both stages are affected by stress level of operators and time available. Human error probabilities at each stage, therefore, are estimated separately.

Probability of error P_{err} is a sum of probability of failure to correctly diagnose the required response and make correct decision P_d and probability to perform the required action P_a:

$$P_{err} = P_d + P_a. \qquad (1),$$

Main steps of evaluation are:

For each action identify maximal time window T_M, that is available to perform the action, or, in other words, after which it is too late to take any actions. Examples of time window are time that a reactor can survive without cooling before it's overheating or pump can run without cooling of bearings until it's failure. Time T_m can be evaluated using results of deterministic analysis. This time window includes time to diagnose and make a decision T_d and time to perform an action T_a .(Fig. 3).

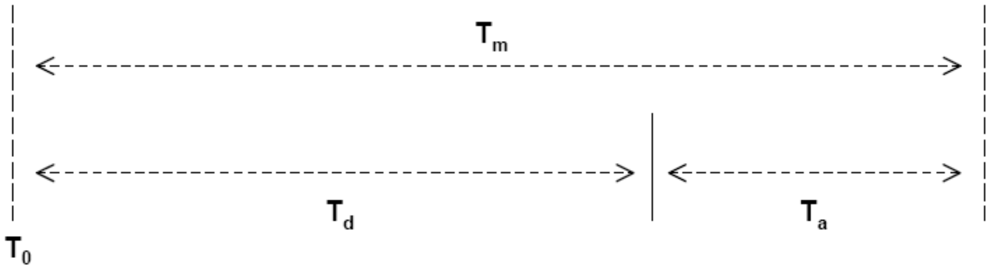

T_0 = annunciation (or other compelling signal) of abnormal event
T_m = estimated maximum allowable time to complete diagnosis and required post-diagnosis actions to satisfy PSA success criteria ("available time window")
T_d = estimated allowable time for correct diagnosis that permits sufficient time to complete post-diagnosis actions before Tm
T_a = estimated time to perform required actions after correct diagnosis

Fig. 3. Time to diagnose and perform an action

Time T_a sufficient to perform the action after decision is made is estimated next. This time could be very short, like pressing a button on a control panel, or longer, like manually open a valve located in another unit.

Probability P_a of failure to perform the action is estimated by using THERP tabulated data [2] depending on action complexity, procedures, skills and training. This is very simplified application of THERP method.

Use of ASEP method is based on assumption that the time is a key factor to cognitive and decision-making stage ant that error to recognize and make a decision means failure of the entire action. Time T_d available to recognize the situation (diagnose) and make a decision on what actions shall be performed is calculated as

$$T_d = T_m - T_a. \qquad (2),$$

Nominal diagnosis human error probability (HEP) P_d depends on time T_d and is evaluated using ASEP time-dependency curve and tables [3] (Fig. 4). Uncertainty bounds of HEP are assigned based on the same tables or curve.

ASEP method contains guidances and tables that allow to adjust nominal help in order to account for another factors like alarms, stress, procedures, training etc., and estimate several actions that shall be performed closely in time.

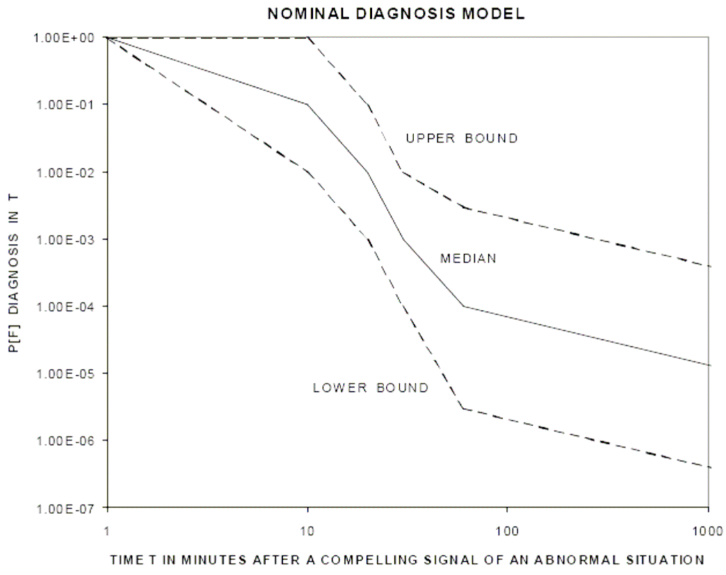

Fig. 4. Error probability on diagnostics and decision-making stage

2.6. Human Reliability Analysis for INPP PSA

Seven post-initiator dynamic actions, important for reactor cooling, were analysed.

- Water supply from Emergency Core Cooling System (ECCS) to Group Distribution Header (GDH) in case of Loss-of-Coolant Accident (LOCA);
- Primary circuit (PC) makeup in case of loss of feedwater;
- Transition to PC water supply from long-term ECCS instead of Main Feedwater Pumps;
- Closure of valves of Main Circulation Pumps (MCP) in case of LOCA;
- Service Water from Unit 1 supply to Intermediate Cooling Circuit #2 (ICC-2) and Diesel Generators (DG) of Unit 2;
- Alternative cooling of ECCS pumps in case of ICC-2 failure;
- Alternative cooling of Auxiliary Feedwater Pumps (AFWP) in case of ICC-2 failure.

Each action was analysed in context of different initiating events and accident scenarios. Number of such scenarios in different groups of initiating events was from 5 to 18. Analysis process for one such action is presented below as an example.

2.6.1. Example of operators' action analysis

Action name: Water supply from ECCS to GDH in case of LOCA

Description: In case of loss-of-coolant accident (LOCA) automatic startup of Emergency Core Cooling System (ECCS) with water supply to Group distribution Header (GDH) is provided in accordance to ECCS algorithms 1-4. If ECCS automatic startup fails, operator shall manually initiate necessary equipment and provide water supply to the primary circuit (PC).

Functional success criteria:

- Plant conditions to start the action: presence of ECCS startup conditions and absence of ECCS operation indications (pumps work, valves open, water flow from water pressurized tanks and pumps)
- Time window end conditions: reactor core overheat.
- Action goal: to prevent reactor core overheat.
- Actions to be taken: recognize LOCA; recognize ECCS startup failure; start water supply from short-term ECCS (pressurized tanks and MFWP); start water supply from long-term ECCS (ECCS and AFW pumps).

Physical success criteria:

- Equipment to be initiated: for short-term ECCS – open valves; for long-term ECCS – start the pumps and opens valves.
- Who performs the action: Leading Engineer for Unit Control under supervision of Deputy Shift Supervisor.
- Where the action is performed: Main Control Room, workplace of LEUC
- Procedures to be used: Symptom-Oriented Emergency Procedure, Accident Mitigation Procedure.

Time success criteria.

Time is scenario-context factor that depends on initiating events. Therefore, the action has to be analysed for two groups of initiating events – Large LOCA and Medium LOCA. Time window is defined in accordance with the results of thermal-hydraulic analysis. According to [2] in case of large LOCA reactor core temperature will exceed acceptability criteria after 600 seconds. For medium LOCA this time is 1500 seconds. Therefore time windows T_m to start short-term ECCS for these groups of initiating events are 10 minutes and 25 minutes correspondingly.

Operation of at least one of three trains of short-term ECCS adds two minutes to reactor overheat time. Thus, time window T_m to initiate long-term ECCS in case of short-term ECCS success is 12 minutes for large LOCA and 27 minutes for medium LOCA.

This is a good example showing that PSF could be different for the same action under different scenarious. Here the time window for medium LOCA is almost twice longer allowing more time to diagnose, make decision and implement the required action.

Analysis of boundary conditions is the most difficult and important part of the analysis. All factors that have an impact on operator during the action has to be identified, analysed and documented. Brief description of boundary conditions analysis findings is presented below.

Time required to perform the action is assumed one minute. As soon as during large and medium LOCA plant parameters change rapidly, a high stress level is anticipated. Operators are monitoring main plant parameters and start take actions in accordance with their experience and emergency procedures. Operators in main Control Room has a good indication of main parameters and processes. Operation of ECCS is one of the important parameters to follow and failure of ECCS is recognized very soon. Recognition and decision making is affected by competing actions and priority of actions. At the same time the operator shall monitor PC parameters, feedwater flow, pressure in DS, operation of protections. Also he is monitoring startup of Accident Localization system (ALS) and Emergency Deaerators Makeuo (EDM) pumps. However, monitoring of ECCS startup has the highest priority and it is assumed that competing actions will not disturb the action to start ECCS manually.

Quantification

In the previous version of PSA model HEP for this action was 1. i.e. it was assumed that the action is impossible due to very short time window.

In the current analysis Pd is estimated using medium ASEP curve [3] dependent on time window Td, Pa is estimated using THERP [2]

Results are presented in the **Error! Reference source not found.**.

Table 1. Human error probabilities for action “Water supply from ECCS to GDH”

IE Group	**Action**	**T_m, min**	**T_a, min**	**T_d, min**	**P_a**	**P_d**	**P_{err}**
Large LOCA	Start of short-term ECCS	10	1	9	1.58E-02	3.75E-03	1.61E-01
	Start of long-term ECCS	12	1	11	7.94E-03	3.75E-03	1.03E-01
Medium LOCA	Start of short-term ECCS	25	1	24	3.98E-04	3.75E-03	1.02E-02
	Start of long-term ECCS	27	1	26	2.51E-04	3.75E-03	7.80E-03

In previous version of INPP PSA operator action “Manual Start of ECCS” was conservatively assumed to be impossible. During the systematic analysis process this action was analysed against different initiating events. As a results four scenario-specific actions were identified and four HEP values were calculated that are more optimistic than HEP=1 used in previous version of INPP PSA.

3. RESULTS AND DISCUSSION

The example provided in 2.6.1 shows how during the analysis different conditions were identified for the actions under different scenarios. Output of single action analysis is four different actions with their own probabilities. After the analysis of seven actions 23 scenario-specific actions were identified, as shown in Table 2

Table 2. Human error probabilities for analyzed operator's action

Action title	**Mean**	**Error Factor**	**5%**	**50%**	**95%**
Start of short-term ECCS, Large LOCA	1,61E-01	4,73	4,88E-01	1,03E-01	2,18E-02
Start of long-term ECCS, Large LOCA	1,03E-01	4,73	3,12E-01	6,60E-02	1,39E-02
Start of short-term ECCS, Medium LOCA	1,02E-02	7,02	3,54E-02	5,04E-03	7,19E-04
Start of long-term ECCS, Medium LOCA	7,80E-03	7,02	2,72E-02	3,87E-03	5,51E-04
Drum-separator makeup	3,96E-03	9,92	1,49E-02	1,50E-03	1,51E-04
Drum-separator makeup after MFWP trip	3,96E-03	12,82	1,53E-02	1,19E-03	9,28E-05
Closure of MCP valves	5,78E-03	7,02	2,01E-02	2,87E-03	4,08E-04
SW supply to ICC-2	4,01E-03	12,82	1,54E-02	1,20E-03	9,39E-05
SW supply to DG	1,46E-03	9,92	5,48E-03	5,52E-04	5,57E-05
SW supply to ICC-2, Large LOCA	4,33E-02	4,73	1,31E-01	2,77E-02	5,86E-03
SW supply to DG, Large LOCA	1,00E+00	-	-	-	-
SW supply to ICC-2, Medium LOCA	1,26E-02	7,02	4,38E-02	6,24E-03	8,89E-04
SW supply to DG, Medium LOCA	1,26E-01	4,73	3,82E-01	8,08E-02	1,71E-02
SW supply to ICC-2, Transients	8,44E-03	7,02	2,94E-02	4,18E-03	5,96E-04
SW supply to DG, Transients	6,09E-03	7,02	2,12E-02	3,02E-03	4,30E-04
ECCS pumps alternative cooling	1,50E-03	12,82	5,79E-03	4,52E-04	3,52E-05
ECCS pumps alternative cooling, Large LOCA	1,45E-02	7,02	5,03E-02	7,17E-03	1,02E-03
ECCS pumps alternative cooling, Medium LOCA	7,17E-03	7,02	2,49E-02	3,55E-03	5,06E-04
ECCS pumps alternative cooling, Transients	5,87E-03	7,02	2,04E-02	2,91E-03	4,14E-04
AFW pumps alternative cooling	1,50E-03	12,82	5,79E-03	4,52E-04	3,52E-05
AFW pumps alternative cooling, Large LOCA	1,37E-02	4,73	4,16E-02	8,80E-03	1,86E-03
AFW pumps alternative cooling, Medium LOCA	8,48E-03	7,02	2,95E-02	4,21E-03	5,99E-04
AFW pumps alternative cooling, Transients	5,87E-03	7,02	2,04E-02	2,91E-03	4,14E-04

The presented analysis was performed for reactor cooling actions and does not cover all post-initiator dynamic actions. The following areas was not analysed: reactor shutdown; recovery of systems, manual startup of redundant equipment, manual opening of failed valves. For the analysed events more reasonable values were obtained. Use of such values makes PSA model more realistic and consistent and allows use of PSA for practical applications.

Another important output of HRA is thoroughly documented analysis process, similar to one described in 2.6.1. Use of such records allows to identify main factors that affect operators' performance during abnormal events and accident mitigation. Such findings can be used by NPP to improve reliability of operators actions.

The performed analysis is the first experience of systematic and comprehensive HRA. The approach and methodology used for INPP HRA could be applied in other areas, where operators play an important role in ensuring safety: nuclear power, oil, chemistry, and transport.

REFERENCES

1. Ignalina NPP Probabilistic Safety Analysis, Final Report, Lithuanian Energy Institute, 2007.
2. Handbook of Human Reliability Analysis with Emphasis on Nuclear Power Plant Applications. Final Report, NUREG/CR-1278, A.D. Swain, H.E. Guttmann, Prepared for U.S. Nuclear Regulation Comission, 1983.
3. Swain, A. D., "Accident Sequence Evaluation Program Human Reliability Analysis Procedure", NUREG/CR-4772, Nuclear Regulatory Commission, February 1987.
4. Evaluation of Human Reliability Analysis Methods Against Good Practices. Final Report, NUREG-1842, U.S. Nuclear Regulatory Commission, September 2006.
5. Additional Deterministic Calculations for Support of PSA Model Assumptions and Limitations, Lithuanian Energy Institute, 2004.

CYSENI 2009, May 28-29, Kaunas, Lithuania
ISSN 1822-7554, www.cyseni.com

MODELLING PECULIARITIES OF RADIONUCLIDE MIGRATION FROM BITUMINIZED WASTE

R. Kilda
Laboratory of Nuclear Engineering
Lithuanian Energy Institute
Breslaujos g. 3, LT-44403 Kaunas
Phone: +370 37 401992
E-mail: raimond@mail.lei.lt

ABSTRACT

The proper management of radioactive waste (RAW) is very important in Lithuania today in relation with decommissioning of Ignalina NPP. The radioactive waste should be managed in accordance to its type as well as activity level. Bituminized radioactive waste is produced at Ignalina NPP among other types of waste and should be managed in proper way.

As usual the radioactive waste management process is concerned by safety analysis. Therefore potential radionuclide migration from the storage or repository of bituminized radioactive waste should be analyzed. In order to perform safety analysis it is necessary to identify key properties of the waste under consideration as well as to understand the processes governing radionuclide migration from the repository of bituminized RAW.

The key properties of bituminized RAW which are important considering analysis of radionuclide migration are identified in the paper. The key processes governing radionuclide releases from bituminized waste by water pathway, i.e. water uptake and leaching are discussed in the paper considering long-term behaviour of bituminized waste. Development of conceptual models of radionuclide migration from the waste taking into account the specific behaviour of bituminized RAW like water uptake, swelling, formation of pores and leaching of radionuclides is provided. The mathematical models applied to radionuclide migration from bituminized waste as well as the preliminary results of the modelling are presented and discussed also.

Keywords: bituminized radioactive waste, bitumen matrix, water uptake, leaching, safety assessment.

1. INTRODUCTION

Since the late 60s bitumen has been widely used by nuclear industry as a matrix for the immobilization of low- and intermediate level radioactive waste.

The main advantages of RAW bituminization are as follows [1, 2]: *i)* matrix material (bitumen) is relatively inexpensive; *ii)* the process temperature is low (up to ~200°C; *iii)* bitumen is compatible with wastes having various compositions; *iv)* the stability to RAW leaching is extremely high; *v)* the volume of wastes disposed off is ~20% less in comparison to cemented waste.

At present bitumen is used for solidification of RAW (radioactive waste) such as sludge, liquid concentrates and ion exchange resins in several countries, e.g. Sweden, Finland, Denmark, France, Belgium, Germany, Switzerland, Lithuania, Russia and Japan.

The concentrate residuals (evaporator concentrates) are obtained after evaporation of the liquid radioactive waste. Afterwards the residuals are mixed with bitumen. Usually the concentration limit of 35-45 % by mass of the residuals should not be exceeded in order to avoid sedimentation of the salts as well as exothermic reactions inside the waste matrix.

Therefore considering safety analysis the long-term performance assessment of bituminized RAW storage or disposal relies on the behaviour of the bitumen matrix. Bitumen is considered to have favourable chemical and physical properties to act as a waste immobilization material. Diffusion of radionuclides as well as diffusion of water vapour in bitumen is insignificant. However, during interim storage and subsequent disposal the properties of bitumen may change. This may influence the behaviour of bitumen matrix. Therefore it is important to identify key properties of the bituminized waste as well as to understand the processes governing radionuclide migration from the bitumen matrix.

The leaching of radioactive components embedded in the bitumen matrix is modelled and preliminary results are discussed in the paper.

2. LONG TERM BEHAVIOUR OF BITUMINIZED WASTE

The phenomena taking place in bitumenized waste are still a matter of discussion in scientific community. In general the behaviour of the bituminized waste depends on three main factors:

i) the physical properties of bitumen,
ii) the chemical composition of embeded waste, and
iii) the chemical environment at the repository.

A comprehensive review of literature concerning characteristics of bitumenized waste is provided in document [3]. According to [3] the key processes relevant to bituminized waste that should be considered in a safety assessment are as follows: radiolytic effects, biodegradation; ageing; water uptake and leaching. First of all radionuclide migration through the water pathway usually is of great concern in the safety analysis therefore the realease of radionuclides as the component process including water uptake and leaching is considered in the paper.

2.1. Water uptake

In consequence of chemical process used to solidify liquid concentrates bituminized RAW contain some soluble salts ($NaNO_3$, Na_2SO_4 in most cases) and insoluble elements (sludge particles, radionuclides, etc). Although bitumen is generally considered as an impermeable material it has been shown experimentally [4] that water can diffuse in pure bitumen due to undissolved salts in bitumen matrix cause the water uptake. The waste is dispersed in the form of particles in a continuous phase of bitumen. Water vapour can diffuse through the surrounding layer of bitumen to the waste particles. When the waste particles absorb water they begin to swell. The swelling of the particles can have several consequences [3]:

- internal stresses will be generated within the matrix;
- the bitumen matrix may increase in size;
- the distance between the particles and thus the thickness of the bitumen layer between them can decrease.

When enough water is taken up the waste particles increase in size until the touch each other an open communicating porosity is formed.

2.2. Leaching

The term “leaching” is mostly used to refer to the release of radioactive components embedded in the bitumen matrix. However, other substances (e.g. salts) are simultaneously leached from the matrix. The diffusivity of radionuclides in undisturbed bitumen is negligible. Thus, a network of pores or fractures in the matrix is a necessity for release of nuclides. As discussed in the previous sections there are several mechanisms by which such an open porosity can be formed. Once a communicating porosity is established, the radionuclides dissolve and are released from the bitumen matrix by diffusion [3].

The release rate is dependent upon type of bitumen, type of waste, waste loading, concentration of nuclides in solution and also all factors influencing the diffusivity of radionuclides (e.g. temperature). The conditions determining the leaching rate may not be constant in time. For example, open pores may close, external conditions (e.g. temperature, pressure, water flow rate, water chemistry) may change and physical ageing of the bitumen matrix will result in a progressive hardening of the matrix. One therefore has to be cautious in applying the results of experiments of a relatively short duration (up to few years) in a safety assessment that extends over a much longer period of time [3].

3. MATHEMATICAL MODELS OF RADIONUCLIDE LEACHING FROM BITUMINIZED WASTE

As pointed out in previous section water uptake by bituminized RAW can be important and lead to the development of a solution-filed pore structure in which radionuclides and dissolved salts can migrate. In other words the leachability of bituminized RAW is the development of a solution-filled pore structure. Leaching experiments performed in many laboratories on synthetic bitumen have shown that the water uptake is diffusion controled [4]. The water diffusing into bitumen matrix is absorbed by the salt particles which are swelling. The particles grow with a constant supply of water. The excessive local swelling leads to interconnection of particles therefore a connected porosity is formed, see Fig. 1. The porous structure allows then the release of salts (as well as radionuclides) from the waste. The nuclides initially in the salt particles are now in the pore water and the nuclides are free to diffuse out of the bitumen matrix.

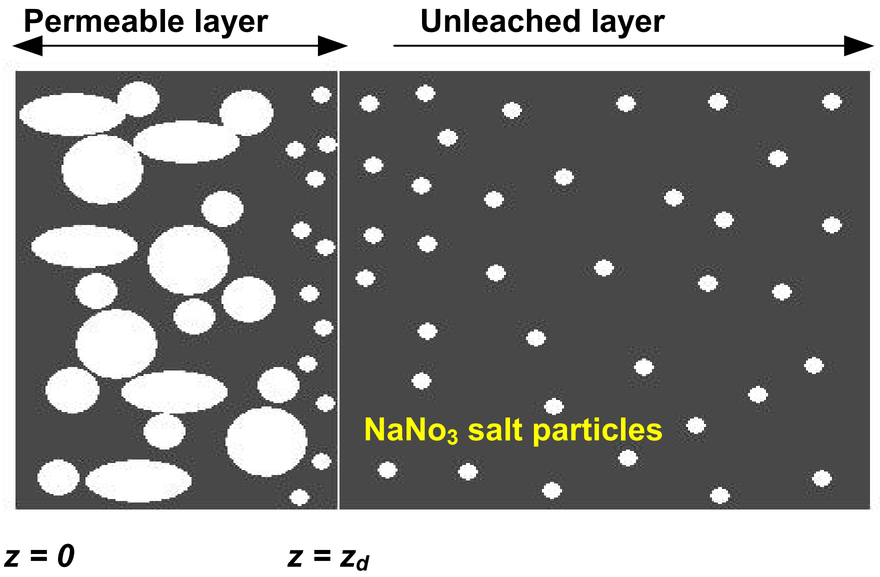

Fig. 1. Schematic representation of the development of solution-filled pore structure in bituminized waste. z_d gives the position of the dissolution front (disturbed zone thickness) within the depth of bitumen matrix (z direction) (adapted from [4])

Model of activity release from bitumen is presented in [5]. The model indicates that the release of radionuclides from the bitumen is determined by the water uptake. Assuming that all radionuclides in the bitumen volume into which water has penetrated are released from the bitumen matrix, i.e. the amount of released activity is given by the following expression:

$$I_{release}(t) = I_{total} \cdot \frac{V(t)}{V_{total}}, \tag{1}$$

where

$I_{release}$ – activity of released radionuclide, Bq/year;

I_{total} – activity of radionuclide present in the bitumen matrix, Bq;

$V(t)$ – volume of bitumen affected by the penetrating water (disturbed volume), m^3;

V_{total} – volume of the bitumen matrix, m^3;

t – time, years.

Taking into account that the water uptake is diffusion controlled and thus it is proportional to the square root of time the expression to calculate the thickness of disturbed zone is indicated in [6]:

$$z_d(t) = \gamma \cdot \sqrt{t}, \tag{2}$$

where γ stands for factor describing water uptake rate, m/yr$^{1/2}$. As the disturbed volume is given by:

$$V(t) = A \cdot z_d(t), \tag{3}$$

where A is a cross-section area available for water uptake, m^2, then the equations (1), (2) and (3) lead to the following expression:

$$I_{release}(t) = I_{total} \cdot \frac{A \cdot \gamma \cdot \sqrt{t}}{V_{total}}, \tag{4}$$

Hence, the process of radionuclide release from the bitumen matrix is proportional to the square root of time (in other words, it is diffusion controlled by water uptake) and is expressed by a dependence proportional to the rate of water uptake (γ) and the cross-section area (A) available for water uptake.

In order to investigate the importance of the radionuclide release mechanism further transportation through the engineering barrier is considered. A bitumen matrix is assumed to be directly in contact with the concrete engineering barrier (wall) of certain width (L), see Fig. 2.

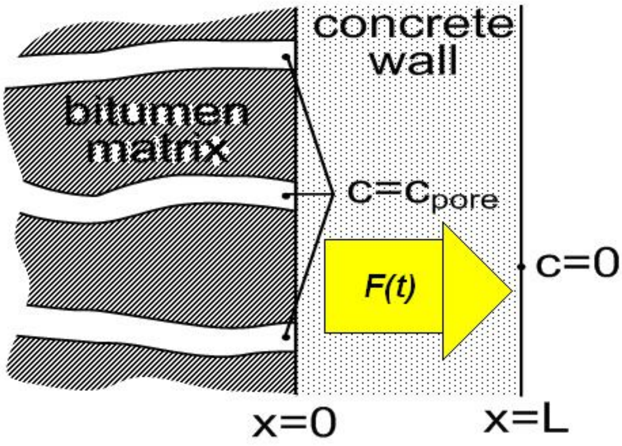

Fig. 2. Conceptual model of the radionuclide transport out of the bitumen matrix through the concrete wall of thickness L. c_{pore} – activity concentration in bitumen matrix , $F(t)$ – flux of radionuclides across the wall

The transport through the wall is described by one-dimensional diffusion equation:

$$\frac{\partial C}{\partial t} = D_e \frac{\partial^2 C}{\partial x^2}, \tag{5}$$

where

C –activity concentration of radionuclides in the pores of the wall, Bq/m^3;
D_e – effective diffusion coefficient in the considered media (material), m^2/s;
t – time, s.

Boundary and initial conditions are described by the set of equations:
$C(x,0) = 0$;
$C(0,t) = C_{pore}$;
$C(L,t) = 0$.

where

C_{pore} –activity concentration in the pores of the bitumen matrix, Bq/m^3;
x – distance in the diffusion direction, m;
L – wall thickness, m.

An analytical solution of equation (5) under boundary and initial condition indicated above is given by [7]. Finally taking into account the exponentially decaying pore concentration the radionuclide flux across the concrete wall is expressed as follows:

$$F(t) = 2C_{pores} \sum_{m=0}^{\infty} \sqrt{\frac{D_e K}{\pi t}} \cdot \exp\left[-\frac{(2m+1)^2 L^2}{4D_a t}\right] \cdot e^{-\lambda t}, \tag{6}$$

where

$F(t)$ – activity flux of the radionuclides transported across the wall, Bq/(m^2·s);
C_{pores} – activity concentration in pores of the bitumen matrix, Bq/m^3;
D_e – effective diffusion coefficient in the considered media (material), m^2/s;
D_a – apparent diffusion coefficient in the considered media (material), m^2/s;
K – retention (delay) factor;
λ – decay constant, s^{-1}, for certain radionuclide;
t – time, s.

4. MODELLING OF THE RADIONUCLIDE TRANSPORT

4.1. Input data

The list of some representative radionuclides and values of their physical and chemical parameters used for the modelling are presented in Table 1. It should be pointed out that the sorption of radionuclides in the bitumen matrix was not taken into account assuming conservative value 0.

Table 1. Physical and chemical parameters of the radionuclides

Radionuclides	**Half-life, years**	**Sorption coefficient (K_d) in medium (material), m^3/kg**	
		Bitumen matrix $^{1)}$	**Concrete** $^{2)}$
^{14}C	5.73 E+03	0	0.2
^{94}Nb	2.03 E+04	0	0.5

Radionuclides	**Half-life, years**	**Sorption coefficient (K_d) in medium (material), m^3/kg**	
		Bitumen matrix [1)]	**Concrete** [2)]
^{14}C	5.73 E+03	0	0.2
^{94}Nb	2.03 E+04	0	0.5
^{129}I	1.57 E+07	0	0.003
^{134}Cs	2.06E+00	0	0.001
^{137}Cs	3.00 E+01	0	0.001

1) Conservative values.

2) Values selected according to the data presented in the document [8].

Initial activity (I_{total}) equals to 1 TBq for each radionuclide under consideration that is embedded in the bulk of bitumen. Volume of bitumen matrix of 1 m^3 is assumed. The thickness of concrete wall equals to 0.2 m. The bitumen type used for RAW bituminization as well as solubility limits of radionuclides in water are not taken into account. Values of the parameters used in the expressions (4) and (6) are presented in Table 2.

Table 2. Parameter values used for modelling

Parameter (notation), units	**Value**
RAW volume (V_{total}), m^3	1
Water uptake rate (γ), m/yr$^{1/2}$	1.0E-03 [1)]
Thickness of the wall (L), m	0.2
Area available to water uptake and radionuclide migration through the side walls of the building (A), m^2	1
RAW porosity (ε), -	0.4 [2)]
Concrete porosity (ε), -	0.15 [3)]
Concrete density (ρ_b), kg/m^3	2 300 [3)]
Effective diffusion coefficient in concrete (D_e), m^2/s	1.0E-11 [3)]

1) Average value.

2) Assuming 40% of evaporated concentrate in bitumen matrix.

3) Values selected according to the data presented in the document [8].

4.2. Modelling results

The equations (4) and (6) were implemented and solved using MS Excel environment.

The modelling of activity flux *F(t)*, Bq/(m^2·yr), through the concrete wall was assessed for two cases:

- *Case 1:* assuming instant release of the radionuclides from the bitumen matrix;
- *Case 2:* considering the water uptake and radionuclide leaching from bitumen matrix.

The time period for each radionuclide is selected until the maximum flux value is reached. The results obtained in *Case 1* are presented in Fig. 3 and Table 3.

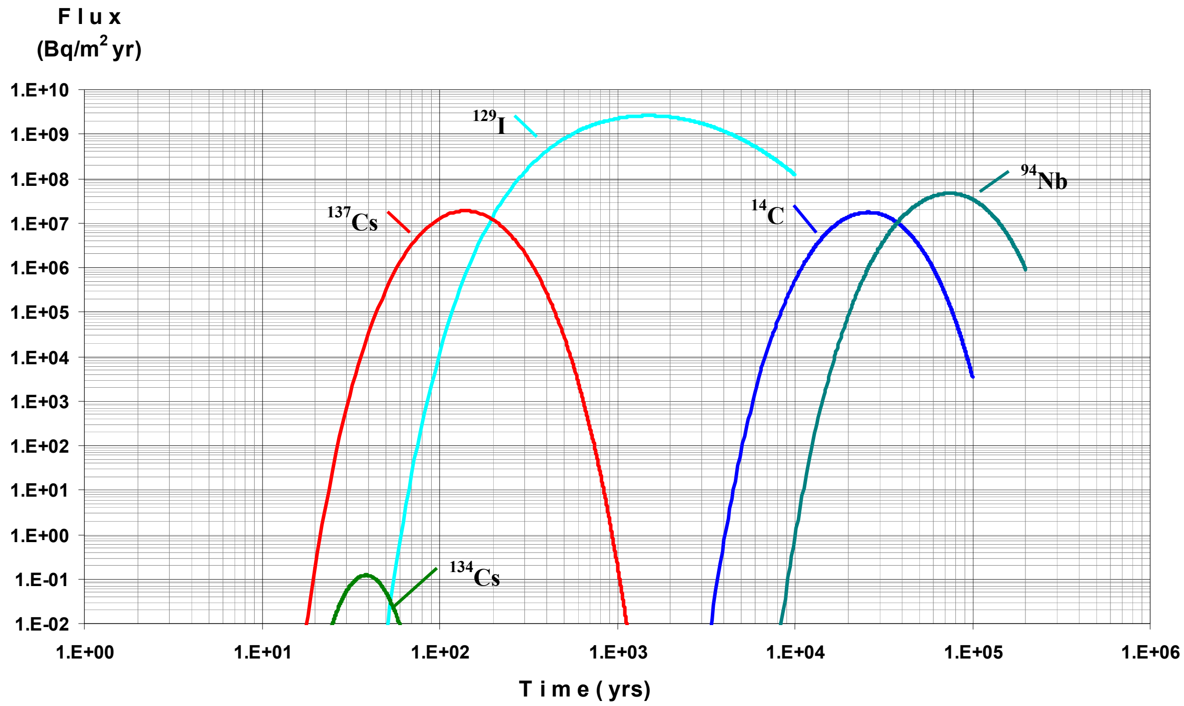

Fig. 3. Activity flux versus time, *F(t),* in case of instant radionuclide release from the bitumen matrix

Table 3. Estimated values of maximum flux in *Case 1*

Radionuclides	**Flux maximum**	
	Time, yrs	**Value, Bq/(m2·yrs)**
^{14}C	25 700	1.75E+07
^{94}Nb	73 000	4.65E+07
^{129}I	1 470	2.60E+09
^{134}Cs	38	1.22E-01
^{137}Cs	135	1.87E+07

Radionuclide release from the bitumen matrix according to model expressed by formula (4) is presented in Fig. 4. The assessed release values were used as input data for modelling of radionuclide transport through the concrete wall in *Case 2*.

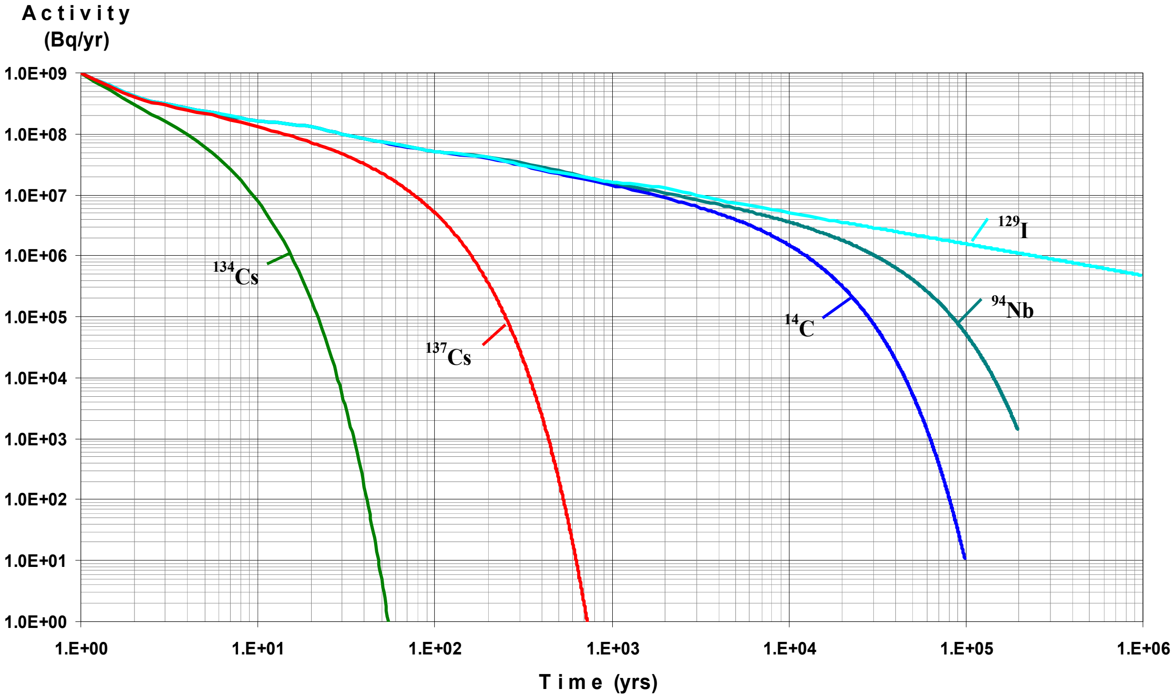

Fig. 4. Radionuclide release, $I_{release}(t)$, from the bitumen matrix

The results obtained in *Case 2* are presented in Fig. 5 and Table 4.

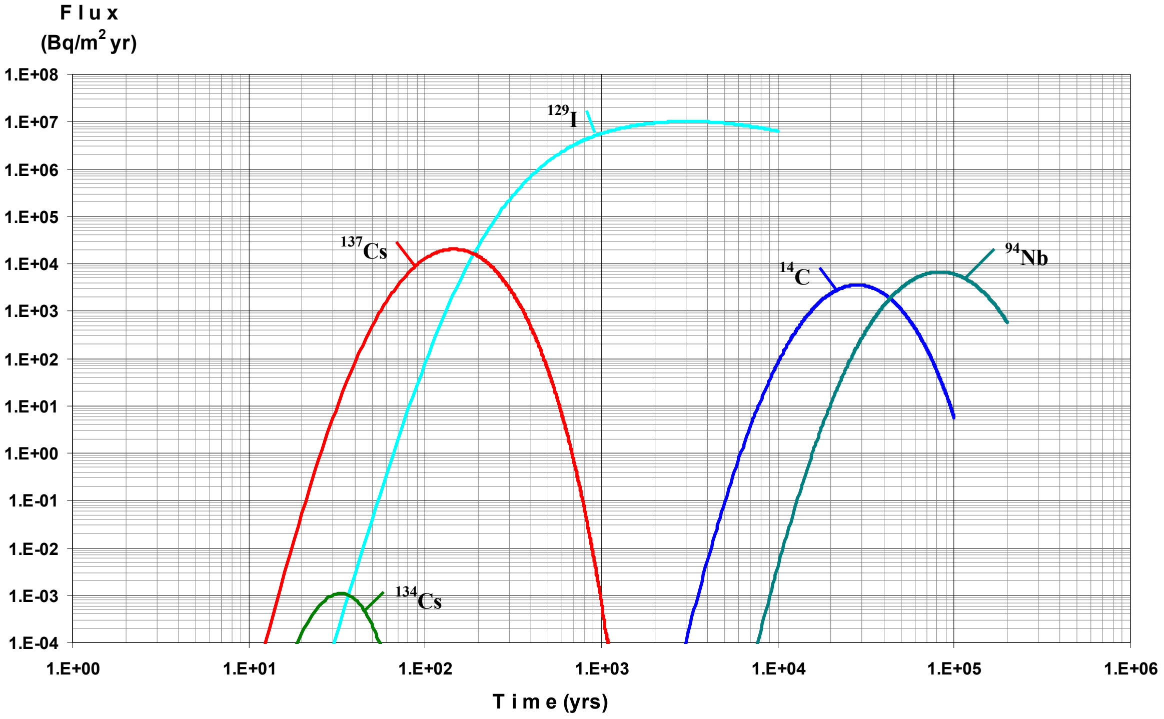

Fig. 5. Activity flux versus time, $F(t)$, in case when the radionuclide leaching from the bitumen matrix is taken into account

Table 4. Estimated values of maximum flux in *Case 2*

Radionuclides	**Flux maximum**	
	Time, yrs	**Value, Bq/(m2·yrs)**
^{14}C	27 900	3.57E+03
^{94}Nb	82 800	6.73E+03
^{129}I	2 680	1.01E+07
^{134}Cs	33	1.11E-03
^{137}Cs	140	2.02E+04

Two main factors should be considered when analysing the radionuclide transport through the material (or engineered barriers), radioactive decay and sorbtion particularly. A fast decay and low sorbtion of ^{134}Cs with respect to concrete has determined the early appearance of flux maximum, the least one among the radionuclides under consideration. An opposite is observed for ^{14}C and ^{94}Nb that are characterized by slow decay and rather high sorption. As the decay of ^{129}I is the slowest one and it is with the relatively low sorbtion among radionuclides under consideration the highest value of the activity is obtained.

In general after comparison of two cases under consideration a significant decrease (from two to four orders of magnitude) of the maximum flux through the concrete wall is obtained in *Case 2*, i.e when the radionuclide leaching from the bitumen matrix is taken into account.

The shift of maximum flux value in time scale is also considerable for long-lived radionuclides. A maximum is observed more than 1000 yrs. later in comparison with the case of instant release. However radioactive decay is prevailing in case of short-lived *Cs* isotopes therefore maximum flux times are very close in both cases under consideration.

It should be pointed out that the bitumen is a waste form effectively containing the radionuclides because of the processes prevailing in the bitumen matrix: slow water uptake, swelling of evaporator concentrate particles and formation of pores.

5. CONCLUSIONS

After quantitative comparison of radionuclide releases in case of regarding the water uptake as well as radionuclide leaching from bitumen matrix with the case of instant release of radionuclides a significant decrease of activity flux values (approximately in 2-4 orders of magnitude) is observed.

Realistic models for safety analysis in case of bitumenized waste as a highly effective waste containment should be used instead of too conservative assumption neglecting the processes of water uptake and formation of pores in bitumen matrix.

REFERENCES

1. B.S. Kolychev et al. Inclusion of radioactive waste in bitumen. Atomnaya Energiya, Vol. 26, No. 6, p. 530–536, 1969.
2. K.P Zakharova and O.L. Masanov. Bituminization of liquid radioactive wastes. Safety assessment and operating experience. Atomnaya Energiya, Vol. 89, No. 2, p. 135–139, 2000.

3. M. Pettersson, M. Elert (Kemakta Konsult AB). Characterization of bitumenised waste on SFR1. SKB Report R-01-26. Swedish Nuclear Fuel and Waste Management Co, Stockholm, Sweden, 2001.
4. J. Sercombe, B. Gwinner et al. Modelling of bituminized radioactive waste leaching. Journal of Nuclear Materials 349, p. 96–118, 2006.
5. S. Brandber, M. Elert and A.Rasmuson. Development of a calculation Model for Radionuclide Release from Bituminized Waste, Intakta France SARL, France, 1985.
6. K. Brodersen, B. Mose Pedersen. Characterization of low and medium-level radioactive waste forms. Report EUR 9423, Ed. O.Vejmelka and R. A. J. Sambell. Commission of the European Communities, Luxemburg, 1984.
7. J. Crank. The Mathematics of Diffusion. 2nd edition, Oxford University Press, London UK, 1975.
8. Project SAFE. Compilation of Data for Radionuclide Transport Analysis. SKB report R-01-14, November 2001.

ESTIMATION OF RADIATION DOSES DURING DISMANTLING A PRESSURED TANK OF RBMK-1500 REACTOR EMERGENCY CORE COOLING SYSTEM

A. Šimonis
Lithuanian Energy Institute
Laboratory of Nuclear Engineering
Breslaujos str. 3, LT-44403 Kaunas – Lithuania
Phone: 370 37 401885
E-mail : audrius@mail.lei.lt

ABSTRACT

Preparation for the decommissioning of Ignalina Nuclear Power Plant involve multiple problems. One of them is the personnel radiation safety during performance of dismantling works. In order to assess the optimal personnel radiation safety, modelling is performed by means of computer program "VISIPLAN 3D ALARA Planning tool" developed by SCK CEN (Belgium). This program allows assessing gamma radiation exposure from various sources, considering shielding geometry (structure), and shielding materials. The program is used for designing of gamma radiation shielding, assessing of existing and planned accumulative effective doses to personnel when carrying out operation, maintenance, and dismantling activities. Estimation of radiation dose during dismantling of a pressured tank of the RBMK-1500 reactor emergency core cooling system has been carried out in this work. Also, by means of radiation safety optimization (ALARA) principle, accumulated effective doses to the operators performing dismantling works have been optimized.

Keywords: Emergency Core Cooling System, Pressured Tank, modelling, optimisation, doses to the workers

1. INTRODUCTION

The only one nuclear power plant in Lithuania, i.e. Ignalina Nuclear Power Plant (INPP) is situated in the Northeastern part of Lithuania close to the borders with Latvia and Belarus and on the shore of Lake Druksiai. It is approximately one hundred and twenty kilometers away from the capital city Vilnius. The power plant possesses two RBMK-type water cooled graphite-moderated pressure-tube reactors each of a design capacity of 1500 MW(e). They were commissioned (first grid connection) in 1983 and 1987, respectively.

In accordance with the National Energy Strategy [1] adopted by the Lithuanian Parliament the first unit of INPP was shut down on December 31, 2004. The shutdown of the second unit is scheduled for the end of 2009. The Lithuanian Government by resolution "On State Enterprise Ignalina NPP First Unit Decommissioning Concept" [2] has approved an immediate dismantling concept for the decommissioning of the first power unit of INPP.

After shutdown of the first unit of INPP, the high pressure part of the Emergency Core Cooling System (ECCS) – presured tanks (PT), big diameter pipes, fast acting valves and the Helium Make-up Station, located in Building 117/1, became redundant and were no longer needed for safety or operational purposes and now can be progressively dismantled.

In Building 117/1 contamination of internal surfaces of some equipment (big diameter pipes, small pipes, ECCS pressure vessels) that had been in contact with the reactor core cooling water was detected [3].

Building 117/1 is the first one where dismantling is planned at Ignalina NPP. Therefore the presented modelling information in this paper is quite unique and essential as it addresses future challenges.

In this paper only a part of Building 117/1 equipment of ECCS PT installed in Room 101-401 has been analyzed and investigation results have been presented. The estimation of radiation dose during dismantling of a part of big diameter pipes of ECCS was carried out in paper [4]. There was performed optimization (principle ALARA) of accumulated effective doses to the operators performing dismantling works. The selection of dismantling strategy when starting dismantling from more contaminated pipe shown that it is possible to reduce the accumulated effective dose by 10 % (from 1.68E-01 to 1.52E-01 mSv).

2. DESCRIPTION OF THE INSTALLED EQUIPMENT

There are total 16 ECCS PT with outside diameter – 1.76 m, height – 14 m and wall thickness – 0.08 m in Room 101-401 (see Fig.1). The material of ECCS PT is carbon steel. So the mass of one ECCS PT is about 47.6 tons.

Fig. 1. Photo of the ECCS PT in Building 117/1

According to radiological measurements performed by INPP staff in 2007 the ECCS PT internal surface is contaminated with radioactive corrosion products. There was measured internal contamination only for two ECCS PT during radiological measurements. So conservatively high contamination level for ECCS PT was used for modelling (see Table 1). Only two measurement points at different levels were measured for ECCS PT. One measurement point is at the very bottom (level 0.0) and next one at 7.2 m (middle height of PT).

Table 1. Contamination level of internal surfaces of ECCS PT [3]

Nuclide	Measurement point at level 0.0		Measurement point at level +7.2	
	Surface contamination, Bq/cm^2	Percentage	Surface contamination, Bq/cm^2	Percentage
Co-60	37.52	47	0	0
Cs-137	42.91	53	25.58	100
Total	80.43	100	25.58	100

ECCS PT consists of a welded vertical cylinder with two ellipsoidal bottoms, support structure, nozzles and a man-hole.

All ECCS PT will be cut with oxy-flame track mounted cutting equipment. The dismantling strategy of ECCS PT is presented in Fig. 2 (marks a dash line cut seam), the process of dismantling will be as follows:

1. Upper ellipsoidal bottom will be cut into two pieces. Cutting operation will be performed with oxy-flame cutting equipment manually. The cut two pieces will be lifted at once.

2. ECCS PT cylinder body will be cut into 20 rings by track mounted cutting equipment.

2.1 First of all four vertical cuts of the ECCS PT will be performed at length up to 0.65 m.

2.2 Then, a radial cut of a ring will be performed. Thus each ring will be divided into four segments; the sections will be fixed and lifted as one piece.

3. The ellipsoidal bottom and support structure of ECCS PT will be cut into two pieces. Cutting operation will be performed with oxy-flame cutting equipment manually.

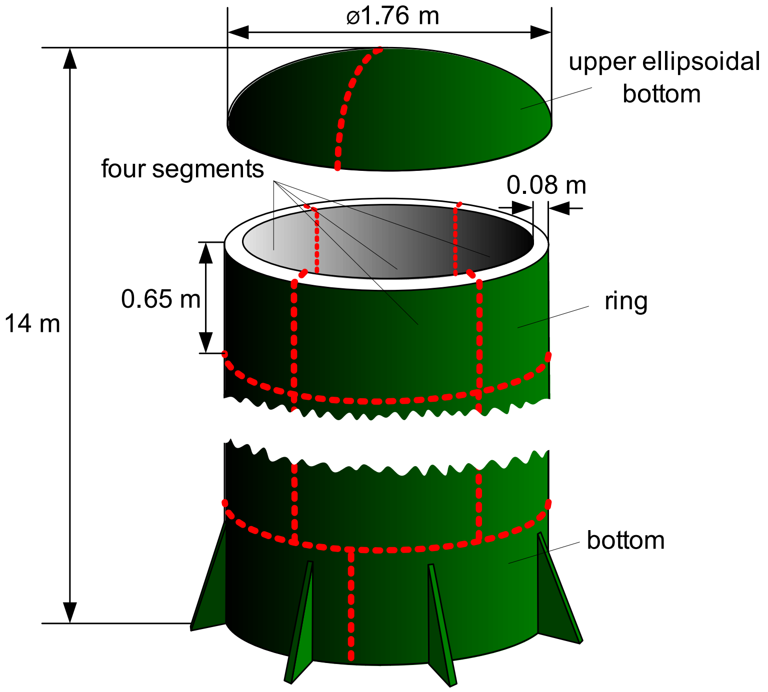

Fig. 2. Dismantling strategy of ECCS PT in Building 117/1

As was mentioned above, the height of ECCS PT is 14 m, so the scaffolding is needed for operator to mount a track for cutting equipment.

3. METHODOLOGY OF MODELLING

As all 16 ECCS PT are contaminated [3] it is necessary to find out and to compare personnel doses if used cutting equipment is with remote controlled torch or without it. One phase of implementation of ALARA principles is dose planning and forecasting, therefore the selection of different methods of employment of the dismantling equipment allows to reduce personnel collective doses.

The comparison of operations durations during dismantling of the ECCS PT is presented in Table 2. It is assumed that two workers perform all dismantling operations at a distance of 0.3 m from the ECCS PT surface in case when the track mounted cutting equipment has no remotely controlled torch.

Another option for the analysis is the track mounted cutting equipment with remotely controlled torch. It is assumed that two workers perform preparations for cutting operation, and cut upper elipsoidal bottom and lower bottom at a distance of 0.3 m from the ECCS PT surface. Its is assumed that workers leave working area during the ECCS PT cutting.

Table 2. Workers operations and corresponding duration for dose calculation

No.	Operation	Operation duration corresponding to the time when a worker is affected by radiation exposure	
		cutting equipment **without** remotely controlled torch, hours	cutting equipment **with** remotely controlled torch, hours
1.	Preparation for cutting upper elipsoidal bottom	0.5	0.5
2.	Cutting upper elipsoidal bottom into two pieces	1	1
3.	Preparation for radial cutting	0.5	0.5
4.	Radial cutting	0.5	0
5.	Preparation for vertical cutting four times	0.5	0.5
6.	Vertical cutting four times	0.5	0
7.	Removal of cutting slag from the bottom	1	1
8.	Preparation for cutting lower bottom into two pieces	0.5	0.5
9.	Cutting lower bottom into two pieces	1	1

It is assumed in the model, that the ECCS PT body is a cylinder with normal shape ends. The body length is 14 m, outer diameter is 1.76 m, and wall thickness is 0.08 m with carbon steel density 7.9 t/m^3. The used scaffolding has seven levels and height of one level is 2 m.

A radioactive source is modelled as cylindrical (thickness is 2 mm) and homogeneous. During the radiological measurements there were measured only two points of the ECCS PT. So conservatively it is assumed that the contamination at the level 0.0 is the same as that up to 7.2 m, and contamination at the level 7.2 is the same as that up to 14 m. Values of contamination level used during the modelling are presented in Table 1. In the modelling it is assumed that only one ECCS PT causes dose effect to the workers.

It is also assumed in the model, that all molten slag after cutting the ECCS PT falls down on the ECCS PT bottom. It is also a radioactive source. The amount (height in this case) of the source proportionally increases during the cutting. The maximum height of the source (when part No. 21 is removed, see Fig. 3) is 0.28 m and the source activity is 5 MBq (Co-60 – 33% and Cs-137 – 66.5%).

The model of dismantling of the ECCS PT is presented in Fig. 3. There are 22 cut lifted parts (20 rings and 2 ends) of the ECCS PT in total.

It is assumed in the model that durations for preparation and cutting of vertical cut seams in the parts No. 4, 7, 10, 13, 16 and 19 are divided into two equal parts for operation in the upper level of the scaffolding and in the lower level of the scaffolding, because the scaffolding level is in the middle of the cutting seam.

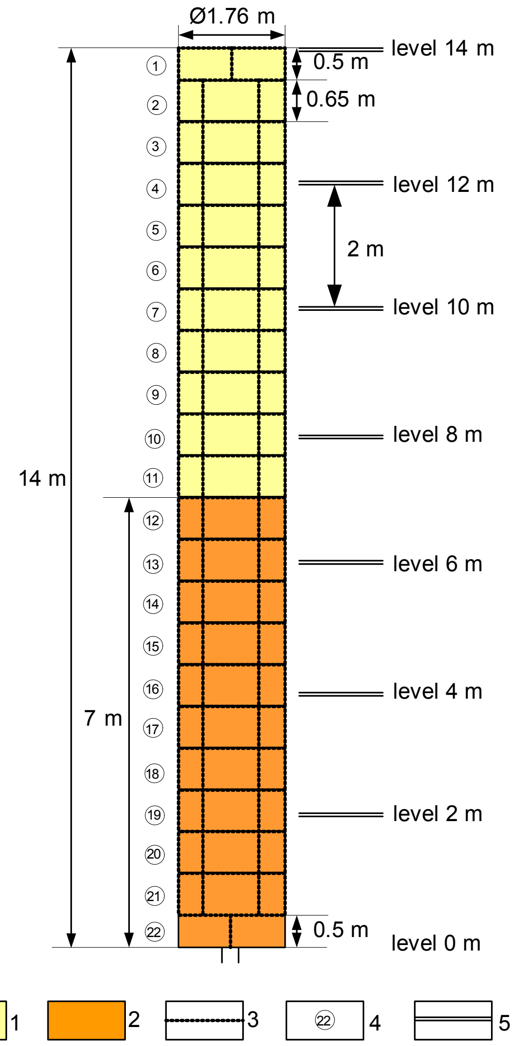

Fig. 3. Model of dismantling ECCS PT

1 – Surface activity according measurement point at level 7.2 (see Table 1);
2 – Surface activity according measurement point at level 0.0 (see Table 1);
3 – Cut seam;
4 – Number of ECCS PT part;
5 – Scaffolding and its level.

In this paper a computer program “VISIPLAN 3D ALARA Planning Tool” [5] was used for gamma dose rate modelling. This program is intended for estimation of gamma radiation dose rates in simple and complex 3D geometries. In this program the calculation of dose rate for radiation sources is based on “point kernel” method. Each small source is called a kernel and the process of integration, where the contribution to the dose of each point is added up, is called “point kernel” integration.

Before calculation with the VISIPLAN, the validation was made based on comparison of the VISIPLAN results with the results from reference calculation from ANSI/ANS 6.6.1 [6]. A comparison was also made for the ESIS problem 1 from ESIS [7].

The photon fluence rate ϕ (cm^{-2}×s^{-1}) at a dose point near a volume source, the program can be determined by considering the volume source as consisting of a number of point sources. By adding the contribution of every point source to the dose at the dose point we find the photon fluence rate at the dose point from the entire source.

$$\phi = \int_V \frac{S \cdot B \cdot e^{-b}}{4 \cdot \pi \cdot \rho^2} dV \,. \tag{1}$$

Where S – source strength representing the number of photons emitted by the source per unit time and volume [n×s^{-1}×cm^{-3}], B - built-up factor (values tabulated according [8]), b – represents the mean free paths (the attenuation effectiveness of a shield), ρ – density of material.

Based on the photon fluence rate at a point, the program can calculate the effective dose equivalent D (name of term according [9] or the effective dose depending on the dose conversion factors h_i). The dose rate D is calculated as:

$$D = \sum_i h_i \cdot \phi_i \tag{2}$$

Where,

h_i – the dose conversion coefficient [9] for photons of energy E_i, ϕ_i – the fluence rate of the photons at energy E_i. The dose conversion coefficient represents different exposure geometries of the man (anterior, dorsal, isotropic, rotation, lateral) and the dose conversion coefficients are adapted to calculate dose rate for the standing human at 1.2 m above floor, because at this height there are more sensitive organs of the human.

The main input data for “VISIPLAN 3D ALARA Planning tool” are: the geometry of an analyzed system, composition and density of materials, parameters of the radiation sources and coordinates of the points where the dose rate is going to be determined.

4. RESULTS OF MODELLING

The modelling results were generated with the software “VISIPLAN 3D ALARA Planning tool”.

The initial operations (removal of two third parts) of 3D view model are presented in Fig. 4. Dismantling operations for other parts of ECCS PT are done in the same way.

After performing the modelling, the dose rates are obtained for each cutting operation of the ECCS PT part in every scaffolding level (there are total 8 levels). So, total 29 dose rate calculation points are obtained and results are presented in Fig. 5. As it can be seen from this figure, it is expected that the higher dose rate levels are in the lower level of the ECCS PT. The variation of dose rates from the top level to lower level are uneven, because the height of the ECCS PT (shielding) is changing during dismantling, so the dose rates are in the rage from 6.6E-07 to 1.4E-02 mSv/h.

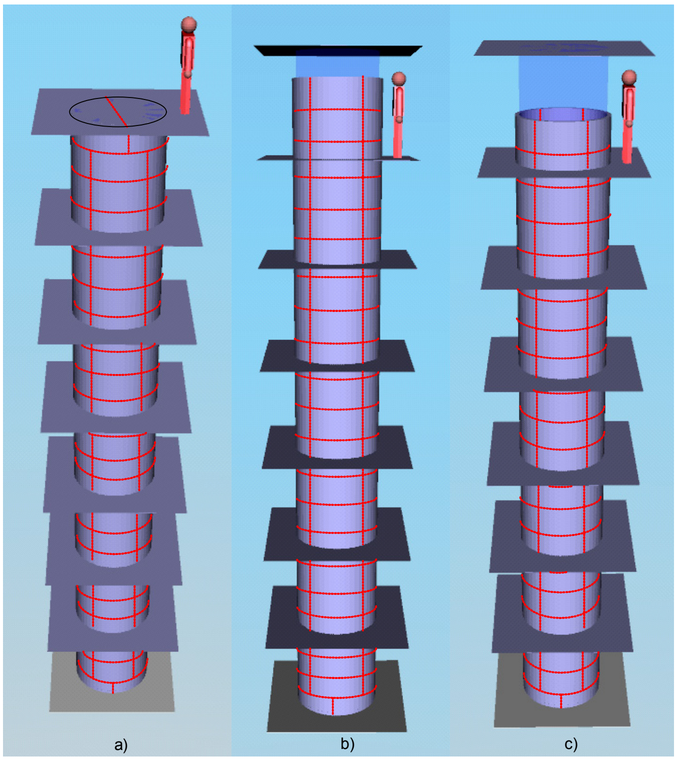

Fig. 4. The 3D view of the ECCS PT dismantling model

a) preparation/cutting of upper elipsoidal bottom; b) segment No.1 is removed and operations of preparation/cutting of segment No.2 are performed; c) segment No.2 is removed and operations of preparation/cutting of segment No.2 are performed)

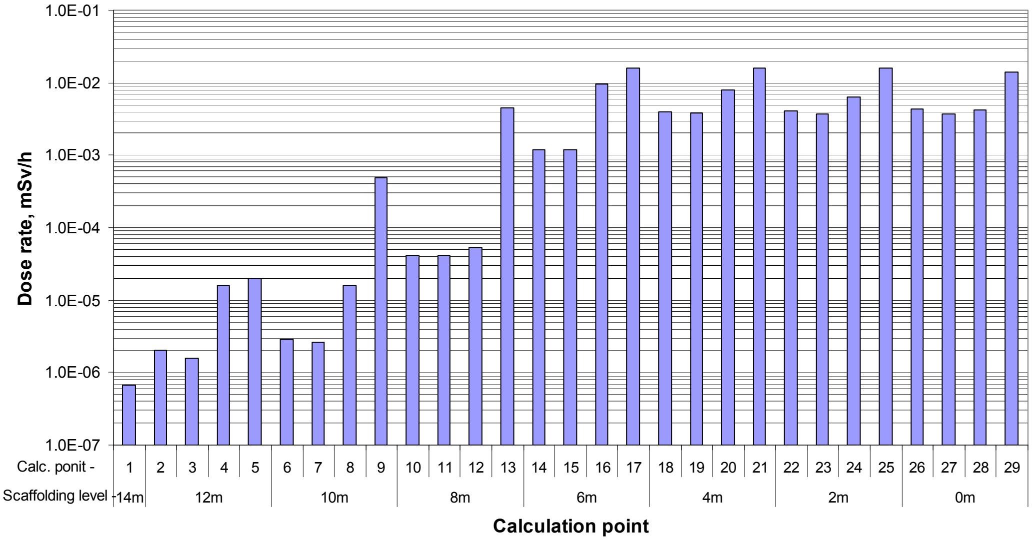

Fig. 5. Dose rates for workers standing on the scaffolding

5. ANALYSIS OF THE RESULTS

After performing the modelling and grouping the dose rates values and durations according to the operations the effective doses are assessed.

The comparison of effective dose for one worker during dismantling ECCS PT is presented in Fig. 6.

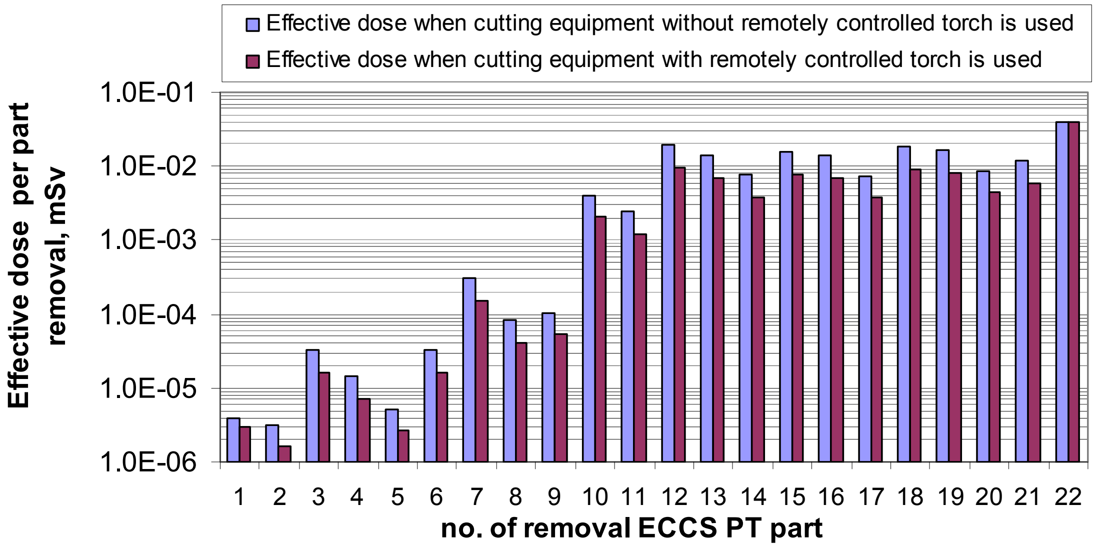

Fig. 6. Comparison of effective doses for one worker per removal of ECCS PT segment

The comparison of collective doses for two workers during dismantling of the ECCS PT when the cutting equipment is without the remotely controlled torch and with the controlled torch is presented in Fig. 7. As it can be seen from Fig. 7 the collective dose after 45 working hours when using the cutting equipment without the remotely controlled torch is 0.36 man-mSv and when using the cutting equipment with the remotely controlled torch is 0.22 man-mSv. The difference between the collective doses during the dismantling of the ECCS PT is 0.14 man-mSv and if the dismantling strategy with the remotely controlled torch is selected, it is possible to reduce the collective dose about 40 %.

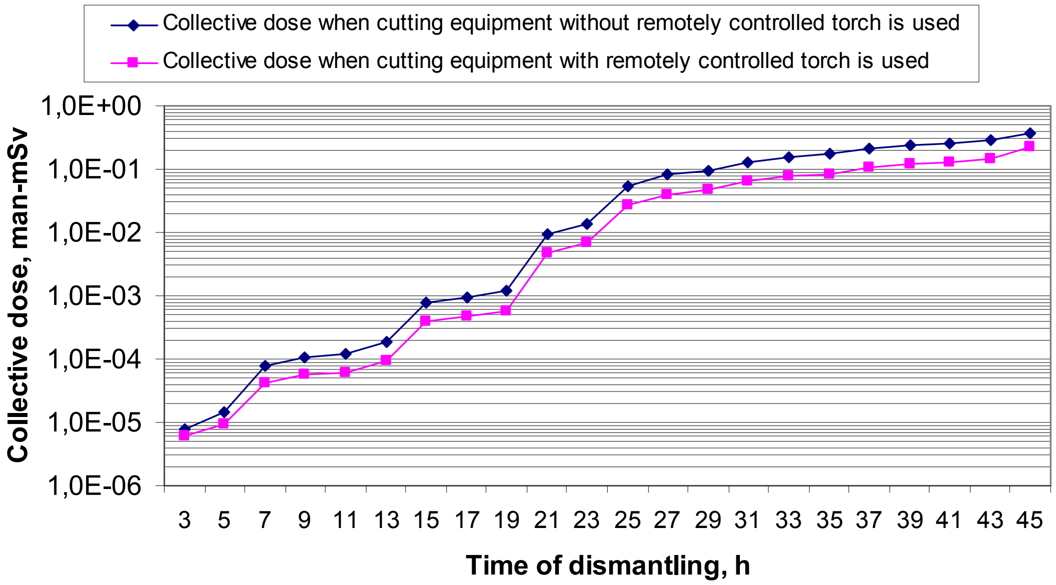

Fig. 7. Comparison of the collective dose during the dismantling of one ECCS PT

6. CONCLUSIONS

After performing the modelling with program “VISIPLAN 3D ALARA Planning tool” and analysis of the results for two dismantling techniques (cutting equipment without and with remotely controlled torch), it can be concluded that:

1. The dose rates during dismantling of the ECCS PT are in the range from 6.6E-07 to 1.4E-02 mSv/h.
2. After dismantling of one ECCS PT over 45 working hours the collective dose for two workers is 0.36 man-mSv when using the cutting equipment without the remotely controlled torch and 0.22 man-mSv when using the cutting equipment with the remotely controlled torch.
3. If the dismantling strategy with the remotely controlled torch is selected, it is possible to reduce the collective dose about 40%.

REFERENCES

1. The Republic of Lithuania Parliament Decision No. IX-1130 dated October 10, 2002, On Approval of National Energy Strategy. State news 2002 No. 99-4397.
2. The Republic of Lithuania Government Resolution No. 1848 dated November 26, 2002, On State Enterprise Ignalina NPP First Unit Decommissioning Concept. State News 2002, No. 114-5095.
3. Environmental Impact Assessment Report. Ignalina NPP Building 117/1 Equipment Decontamination and Dismantling. VT Nuclear Services Ltd and Lithuanian Energy Institute (Laboratory of Nuclear Engineering), 2008.
4. Simonis A. Estimation of radiation dose in dismantling pipelines of RBMK reactor emergency core cooling system; Lithuanian energy institute, Laboratory of Nuclear Engineering, CYSENI 2008, ISSN 1822-7554.
5. F. Vermeersch. VISIPLAN 3D ALARA PLANNING TOOL. Training Guide. Exercises. Calculation Method & Validation Tests. SCK CEN, 2005, 64 p.
6. ANSI/ANS 6.6.1 “The calculation and measurement of direct and scattered radiation from LWR Nuclear Power Plants”, 1979.
7. ESIS “Specification for gamma ray shielding benchmark applicable to a nuclear radwaste facility”. Newsletter #37, European Shielding Information Service, 1981
8. ANSI/ANS-6.4.3.-1991 „American National Standards for Gamma-Ray Attenuation Coefficients and Build-up Factors for Engineering Materials“.
9. International Commission on Radiological Protection (ICRP 51). Data for Use in Protection Against External Radiation. A Report of a Task Group of Committee 3 of the ICRP (adopted 1987); Annals of the ICRP, Vol. 17, No. 2/3 (1987).

CYSENI 2009, May 28-29, Kaunas, Lithuania
ISSN 1822-7554, www.cyseni.com

MOBILE PHONE RADIATION AT DIFFERENT OPERATION MODES

D. Dvarvietis, V. Stanevičius, A. Kanapickas
Department of Physics, Vytautas Magnus University
Vileikos str. 8, LT-44404 Kaunas – Lithuania
Phone: +37037327922
E-mail: a.kanapickas@gmf.vdu.lt

ABSTRACT

Radiofrequency radiation is widely used to empower modern everyday devices such as mobile phones or microwave ovens. In this work the results of radiation power densities of over 20 mobile phones are presented. Measurements were carried out using Smart Fieldmeter RFP-04CE/PI-01 connected to the computer. Analysis of recorded data has shown that there are several modes of mobile phone operation: “quiet” mode (usually when phone is locked), “active” mode (usually when just unlocked), “call” mode (phone is ringing), “conversation” mode and “pause” mode (i.e., complete silence during conversation). It is found that there are typical radiation power densities for each operation mode different for every specific phone model investigated. According to the Lithuanian occupational exposure standart (HN 81:2005) period of time one can use phone safely depends on radiation power density. It follows that at the “quiet” operation mode this time exceeds 24 hours for all phones analyzed whereas at the conversation mode the time for active conversation is limited to 50 minutes per day for the phone with the strongest radiation.

Keywords: mobile phone; high-frequency electromagnetic fields; radiation measurement; measurement system

1. INTRODUCTION

GSM system (Global Standart for Mobile Communications) uses microwave frequency range and as such is non-ionizing radiation. Dominant effect of this is thermal invoked by rotation and vibration of water molecules in our body. As a reference level, 10 W/m^2 is used as a power density where the thermal effect on humans is negligible [1]. However, RF radiation penetrates into the tissue and can influence the internal organs.

The total number of mobile phone subscribers in the world is continuously increasing. Concerns have been raised by a lot of researchers and non-governmental organizations about the possible exposure of consumers to the radiofrequency (RF) fields from mobile phones or the impact of radiation from their base stations on the health of those within its vicinity. The World Health Organization (WHO) has noted for its part in its assessment conclusions that the present scientific knowledge calls for no specific precautions concerning mobile phone use. If people are concerned, they can restrict their children’s or their own exposure to RF radiation by controlling the mobile phone call durations and using hands-free devices [1].

However, scientific reasoning for the research of possible health impact of mobile communication equipment can be based on several facts. Since the risk of long-term use of mobile phones cannot be assessed with certainty until mobiles phones have been in use for several decades, there is no plausible knowledge about the possible health outcomes. Another reason for the concern is children who will have much more time to use mobile phones than adults today who started their regular mobile phone use only about ten years ago [2].

In the communication link, two sources of radiation are present: base and mobile station. Measurements show that the radiofrequency and microwave radiation in public accessible areas around the base stations is indeed very low and comparable to the radiation levels found in places away from the facilities [3]. Measurements of mobile phone emitted radiation [4–6] show that radiation levels around phone antena are comparable with the exposure limits [1], i.e. mobile phone radiation should be investigated in more details. Since it is very difficult to determine the intensity of these fields inside the body, they are being measured through Specific Absorption Rate (SAR). However, SAR depends on conductivity and dencity of biological tissue under the investigation. Therefore, more fundamental value to account RF exposure levels is power density, usualy measured in μW/cm^2. In presented work radiation characteristics of several models mobile phones during call are investigated and the resulted exposure analyzed according to occupational exposure standarts.

2. EXPERIMENTAL SET-UP

2.1.1. Referenced quantities

Exposure on human body to the EM field is determined by electric and magnetic field level inside the body. These values differ from the ones measured outside the body. Since it is very difficult to determine the intensity of these fields inside the body, they are being measured through Specific Absorption Rate (SAR). This parameter represents the dissipation of energy on unit of time and mass, and also takes into account the type of source as well as its frequency and time of exposure. SAR can be calculated as follows:

$$\mathrm{SAR} = \frac{\sigma E^2}{\rho} \quad [\mathrm{W/kg}], \tag{1}$$

where σ is conductivity of the material given in [S/m], E is the electric field given in [V/m] and ρ is density of the material given in [kg/m^3].

Since SAR, time rate of RF energy absorbed per unit mass, is very difficult and complex to be measured in biological tissues, standards permit the use of reference levels of power flux density S [W/m^2] in free space [7]. To evaluate flux density the following expression can be used:

$$S = \frac{E^2}{Z}. \tag{2}$$

Where Z – air impedance equal to $Z = 120\,\pi$ and E – electrical field strength measured in [V/m]. For practical purpose expression (2) is used straightforwardly to get values of power dencity expressed in [μW/cm^2]: $S = E^2/\,377$.

2.1.2. Measurement description

Fig. 1 presents registration system: Smart Fieldmeter RFP-04CE with detachable isotropic probe PI-01 and computer with data acquisition software – WinDaq DI-194 installed. During measurements field gauge was used for the calibration of the meter. Calibration was used every time when uncertainty about the measurement results arose.

Measurement of Smart Fieldmeter is based on isotropic E probe sensor. E probe sensor is located in plastic enclosure at the end of nonmetal handle. This sensor uses 3 dipole antennas positioned normal to each other. Signals from each antenna are combined to allow meter to measure the absolute value of the field regardless of the field direction. The equipment has wide frequency range from 200 kHz to 3 GHz covering all common mobile communications services.

Probe can be mounted on the meter through SMA male connector mating the SMA female connector at the top of the meter, or it can be attached to the meter with flexible cable.

During experiments this cable was used since it allows keeping phone and probing at the distance avoiding influence of operator on measurement results.

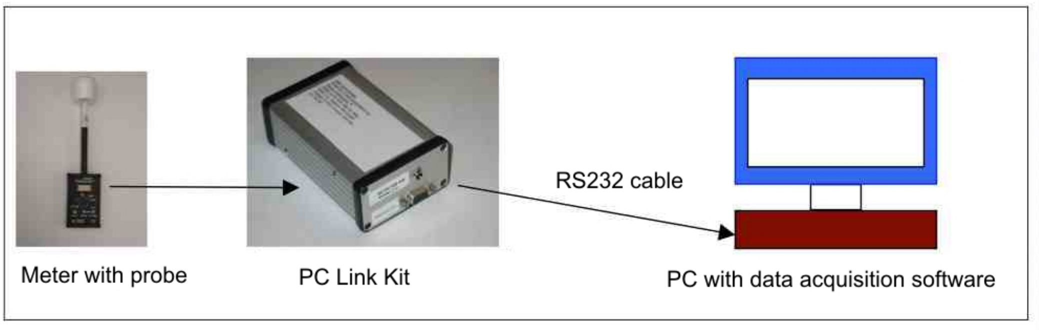

Fig. 1. Measurement set-up: Smart Fieldmeter RFP-04CE with detachable isotropic probe PI-01, data acquisition software – WinDaq DI-194

Smart Fieldmeter has three modes of operation: average, pulse and peak. For near field measurements of RF radiation more correct values could be obtained using "average" mode [8]. Response time of the instrument in average mode is $T_{av} = 2$ s, i.e. the result of measurement is RMS (Root mean square) averaged over T_{av}. At the measurement range 20 V/m resolution of the meter is 0.1 V/m. PC data streaming allows data transfer 120 samples/s through AC/RF decoupled DAQ box to serial RS232 port.

3. RESULTS

Different model of mobile phone handsets were collected for the measurement. The mobile phones are: Nokia 1200, 2630, 3500 Classic, 5200, 6021, 6080, 6230, 6300i, 5160, 3260, 3020, 7060, N95, Samsung SGH D500, x400, E900, Siemens CF75, S40, Sony Ericsson K500i, T100, T630, W300, K810i, W200, W302i (25 models).

Characteristics of radiation during complete call was measured for all phones. Typical radiation chart is presented in Fig. 2.

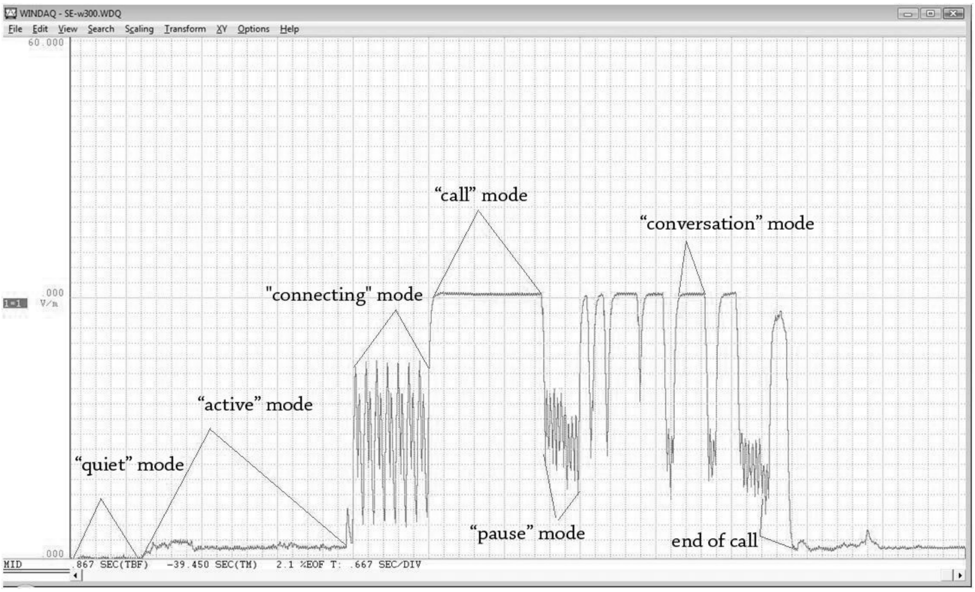

Fig. 2. Typical variation of the strength of electrical field [V/m] radiated by mobile phone during a call

The whole scale on the left side of the graph corresponds to 60 V/m (~2 V/div). The division of the time scale is equal to 0.666 s/div. Each experiment lasted about 30 s starting from the activation of phone, ringing to some dummy recipient, conversation and finishing the call. Analysis of recorded data has shown that there are several modes of mobile phone operation: “quiet” mode (usually when phone is locked), “active” mode (usually when just unlocked), “call” mode (phone is ringing), “conversation” mode and “pause” mode (i.e. complete silence during conversation). For several cases additional modes were possible to distinguish: we name them “connection” mode (some different type of radiation when searching-waiting for recipient connection) and after disconnection “end of call” finishes with short period of increased radiation for some phone models.

It was found that there are typical radiation power densities for each operation mode different for every specific phone model investigated. However, the variation of radiation in time has irregular nature. To describe quantitatively radiation properties during each mode the average field strength and its variation (standard deviation) were calculated. Standard deviation appears to be appropriate parameter to describe the time variation of phone radiation during corresponding operation type.

The results of the investigation are summarized in Table 1, where mobile phone radiation characteristics at the different operation mode are presented. Average field strength is noted by <*E*> and its variation Δ*E* (standard deviation). “Quiet” and “active” operation modes are not included because of very small values.

Table 1. Mobile phone radiation characteristics at different operation mode. Average field strength is noted by <*E*> and its variation Δ*E* (standard deviation)

Mobile phone model	“Connection”		“Call”		“Conversation”		“Pause”		“End of call”	
	<*E*>, V/m	Δ*E*, V/m	<*E*>, V/m	Δ*E*, V/m	<*E*>, V/m	Δ*E*, V/m	<*E*>, V/m	Δ*E*, V/m	<*E*>, V/m	Δ*E*, V/m
Nokia 1200	10.90	5.55	17.10	5.62	19.67	0.35	8.65	1.45	0.91	1.95
Nokia 2630	14.56	4.36	17.49	5.35	25.97	2.90	10.45	1.45	8.61	3.76
Samsung SGH D500	9.78	4.77	29.61	3.30	23.49	0.21	6.52	2.64	11.58	11.57
Samsung SGH x460	12.74	4..4	27.58	5.47	29.42	0.33	10.83	1.58	10.65	11.28
Sony-Ericcson K500i	12.56	4.07	10.55	1.17	12.94	0.22	7.42	0.51	9.15	10.42
Sony-Ericcson T100	3,54	1,70	7,79	1,72	5,54	0,14	1,03	0,67	2,20	1,33
Sony-Ericcson T630	12.42	4.99	29.48	4.73	28.30	0.21	8.31	3.49	9.30	11.11
Sony-Ericcson W300	13.08	5.95	29.82	3.34	30.43	0.16	11.94	1.76	13.35	7.50
Siemens CF75	11.02	5.63	30.46	2.06	30.67	0.16	7.92	1.66	1.92	4.42
Siemens S40	8.52	3.65	22.62	3.74	17.02	0.72	6.33	1.84	10.00	5.72
LG KE800	8.86	1.16	11.69	4.04	14.23	0.27	6.03	0.26	1.18	0.30
Motorola P7389	15.73	5.13	30.51	0.64	12.00	0.25	7.05	0.66	17.88	9.27
Nokia 3500 Classic	12.27	1.18	31.19	0.15	31.20	0.16	13.35	2.18	2.22	0.70
Nokia 5200	8.58	1.07	21.05	5.53	17.94	1.26	7.07	0.35	12.64	4.76
Nokia 6021	14.34	1.23	30.91	0.11	28.94	1.86	11.51	0.39	4.53	4.40
Nokia 6070	14.26	7.24	10.76	3.73	28.99	0.11	6.70	1.24	4.81	4.22
Nokia 6080	11.56	2.74	17.44	6.05	30.15	1.48	7.66	1.47	11.90	8.16
Nokia	10.39	0.90	25.03	5.74	9.68	0.13	5.31	0.29	2.95	0.93
Nokia 6230	7.45	0.58	20.31	1.81	20.02	0.23	6.89	1.07	14.84	7.90

Nokia 6300i	14,32	1,66	28,79	3,10	18,46	1,18	9,26	0,82	4,43	1,00
Nokia 5160	13,82	1,25	14,52	1,35	13,74	3,39	3,85	0,19	5,59	2,36
Sony-Ericcson K810i	5,49	0,24	5,62	0,46	5,09	0,24	4,77	0,14	4,85	0,13
Sony-Ericcson W200	6,31	0,51	21,93	0,34	12,63	1,25	8,13	0,54	9,53	5,21
Sony-Ericcson W302i	15,61	3,81	16,00	0,49	30,09	1,69	12,71	1,84	3,27	2,54

Scientists have devoted a great deal of effort to deciding upon safe RF-exposure limits. This is a very complex problem, involving difficult public health and economic considerations. The recommended safe levels have been revised downward several times in recent years – and not all scientific authorities agree on this question even today. The most recent assessment was published in 2007 by the European Commission Scientific Committee on Emerging and Newly Identified Health Risks [9]. It states that studies on neurological effects and reproductive effects have not indicated any health risks at exposure levels below the ICNIRP-limits established in 1998 [10].

For the interpretation of results two exposure standards currently valid in Lithuania can be used: HN 80:2000 and HN 81:2005. First one states exposure limits to less than 10 $\mu W/cm^2$ for residential places. At workplaces there are different exposure limits depending on irradiation time. The standard HN 81:2005 is devoted for the safety control of mobile communication networks. For the evaluation of the exposure limit the following equation is used:

$$\mathrm{EST} = K\frac{200}{T} \quad \left[\mu\mathrm{W/cm}^2\right], \tag{3}$$

where EST is the limit of the radiation power density, expressed in $\mu W/cm^2$; K denotes the coefficient of biological efficiency decrement, which is equal to 1 for high frequency radiation; and T is the maximal allowed irradiation time per 24 h, expressed in hours.

The two approaches used in Lithuanian exposure standards are applied in Table 2, where allowed maximal irradiation time T_1 and T_2 during the conversation mode is shown. For the discussion it is more convenient to use T_2, which is calculated using equation (3). It follows that depending on model T_2 varies in wide range. Minimal T_2 value reaches ~ 50 min for several phone models. This means that according to the Lithuanian occupational exposure standard HN 81-2005 one may use mobile phone for direct conversation no more that 50 minutes per 24 hours with minimal risk to the health.

Table 2. Maximal irradiation time (T) during the conversation mode according to the standards valid in Lithuania: HN 80:2000 (T_1) and HN 81-2005 (T_2). S denotes power flux density, calculated using (2). Time, calculated by (3), is rounded to minutes

Mobile phone model	<E>, V/m	S, $\mu W \cdot cm^{-2}$	T_1, min HN 80:2000	T_2, min HN 81-2005
Nokia 1200	19,67	102,61	120-149	117
Nokia 2630	25,97	178,91	90-119	67
Samsung SGH D500	23,49	146,36	90-119	82
Samsung SGH x460	29,42	229,62	30-59	52
Sony-Ericcson K500i	12,94	44,41	270-299	270
Sony-Ericcson T100	5,54	8,13	> 480	1475
Sony-Ericcson T630	28,30	212,44	30-59	56

Sony-Ericcson W300	30,43	245,62	30-59	49
Siemens CF75	30,67	249,44	30-59	48
Siemens S40	17,02	76,86	180-209	156
LG KE800	14,23	53,72	240-269	223
Motorola P7389	12,00	38,20	330-359	314
Nokia 3500 Classic	31,20	258,17	60-89	46
Nokia 5200	17,94	85,40	150-179	140
Nokia 6021	28,94	222,15	60-89	54
Nokia 6070	28,99	222,91	60-89	54
Nokia 6080	30,15	241,06	60-89	50
Nokia	9,68	24,87	>480	483
Nokia 6230	20,02	106,30	120-149	113
Nokia 6300i	18,46	90,39	150-179	133
Nokia 5160	13,74	50,07	240-269	240
Sony-Ericcson K810i	5,09	6,87	> 480	1747
Sony-Ericcson W200	12,63	42,33	300-329	284
Sony-Ericcson W302i	30,09	240,18	60-89	50

Table 3 presents average values of power flux density during all operation modes. It can be concluded that on average it is safe to use mobile phone for conversation no more that 90 minutes per 24 hours.

Table 3. Average values of power flux density S_{aver} during all operation modes. S_{min} and S_{max} denotes measured minimal and maximal power flux density, respectively, for each operation mode. T_2 is given only for conversation mode pointing out that the cause of exposure usually is direct conversation

Operation modes	S_{min}, μW· cm^{-2}	S_{max}, μW· cm^{-2}	S_{aver}, μW· cm^{-2}	T_2, min HN 81-2005
“Quiet”	0.01	0.04	0.30	
“Active”	0.04	2.78	0.80	
“Connecting”	3,3	65,7	35.9	
“Call”	8.9	246.5	136.1	
“Conversation”	6.9	249.4	132.4	90
“Pause”	3.9	42.8	18.7	
“End of call”	0.2	84.5	20.5	

4. CONCLUSIONS

In this work the radiation characteristics of over 20 mobile phones are studied. Analysis of recorded data has shown that there are several modes of mobile phone operation: “quiet” mode (usually when phone is locked), “active” mode (usually when just unlocked), “call” mode (phone is ringing), “conversation” mode and “pause” mode (i.e., complete silence during conversation). It is found that there are typical radiation power densities for each operation mode different for every specific phone model investigated. During “quiet” mode average radiation levels are, depending on phone model, in the range (0.01–0.04) μW/cm^2; during "active" mode – (0.04–2.78) μW/cm^2; "call" mode – (10.2–246.5) μW/cm^2; "conversation" mode – (6.9–249.4) μW/cm^2; "pause" mode – (3.9–42.8) μW/cm^2. According to the Lithuanian occupational exposure standart (HN 81:2005) period of time one can use phone safely depends on radiation power density. The average power flux density during conversation mode is equal to 132.4 μW/cm^2, which means that the maximal allowed time for the conversation by a mobile phone is equal to about 90 minutes per 24 h. It follows that at the "quiet" operation mode this time exceeds 24 hours for all phones analyzed whereas at the conversation mode the time for active conversation is limited to 50 minutes per day for the phone with the strongest radiation.

REFERENCES

1. WHO (World Health Organization). Electromagnetic fields and public health: mobile telephones and their base stations. WHO Fact sheet No. 193. Geneva: World Health Organization; 2000.
2. Statement of Finnish Radiation and Nuclear Safety authority (STUK) concerning mobile phones and health // STUK press releases, 2009 01 07. <http://www.stuk.fi/sateilytietoa/sateilyn_terveysvaikutukset/matkapuhelin_terveysvaikutus/en_GB/stukin_matkapuhelinkannanotto/#>.
3. Y. Ali, R. Rahim, A. Majid, A. Thani. Microwave Radiation from Mobile Telephone Base Stations // RF and Microwave Conference: 386 – 389, 2006.
4. M.R. Usikalu and M.L. Akinyemi. Monitoring of Radiofrequency Radiation from Selected Mobile Phones // Journal of Applied Sciences Research, 3(12): 1701-1704, 2007.
5. L. McLean. The impacts of radiofrequency radiation from mobile phone antennas // EMR Australia, 2008.
6. W. Joseph, G. Vermeeren, L. Verloock, M. Heredia, L. Martens. Characterization of personal RF electromagnetic field exposure and actual absorption for the general public // Health Physics 95(3): 317–330, 2008.
7. M. Ibrani – Pllana, L. Ahma, E. Hamiti. Human exposure assessment in the vicinity of 900 MHz GSM base station antenna // International journal of communications 2 (1): 57–61, 2007.
8. J. Karpowicz, K. Gryz. Practical aspects of occupational EMF exposure assessment // Environmentalist (27): 525–531, 2007
9. SCENIHR (Scientific Committee on emerging and newly identified health risks). Possible effects of Electromagnetic Fields (EMF) on Human Health // European Commission, 21 March 2007.
10. IEEE Standard for Safety Levels with Respect to Human Exposure to Radio Frequency Electromagnetic Fields, 3 kHz to 300 GHz, ref. IEEE Standard C95.3, 2002.
11. Lietuvos higienos norma HN 80:2000 „Elektromagnetinis laukas darbo vietose ir gyvenamojoje aplinkoje" // Valstybės žinios: Nr. 5-195, 2002.
12. Lietuvos higienos norma HN 81:2005 „Judriojo radijo ryšio sistemų bazinės stotys" // Valstybės žinios: Nr. 153, 2005.

CYSENI 2009, May 28-29, Kaunas, Lithuania
ISSN 1822-7554, www.cyseni.com

PRELIMINARY ANALYSIS OF AEROSOL DEPOSITION AND DISTRIBUTION IN PHEBUS CONTAINMENT UNDER FPT-3 EXPERIMENT CONDITIONS

A. Kontautas, E. Urbonavičius
Lithuanian Energy Institute
Breslaujos str. 3, LT-44403 Lithuania
Phone: 8 37 401983
E-mail: aurkon@mail.lei.lt

ABSTRACT

Since the Three Mile Island accident in 1979, a worldwide effort has been undertaken to understand and model severe accident phenomena in nuclear reactors in case of a hypothetical loss of core cooling. The international Phébus Fission Product (FP) program, which deals with light water reactor source term research, was initiated in 1988 by the French "Institut de Radioprotection et de Sûreté Nucléaire" (IRSN), and the Joint Research Center of the Commission of European Communities (CEC) [1].

The Phebus Fission Product (FP) test series concern integral in-pile experiments to study the mechanical and physico-chemical phenomena in the course of a severe accident in a nuclear reactor. The aim of the PHEBUS fission product (FP) experimental program is to study the degradation phenomena and the behaviour of the fission products released in the reactor coolant system and the containment building. The FPT-3 test is the last in the series of 5 in-pile integral experiments of the FP programme, performed in November 2004.

This paper presents preliminary analysis of processes in PHEBUS containment during FPT-3. For the preliminary analysis a lumped parameter code COCOSYS (Containment Code System) was used. COCOSYS model of 19 nodes for analysis of FPT-3 experiment, already, with good agreement, was used for FPT-1 calculation. Thermo hydraulic parameters are in good agreement with measured experimental results. Analysis of aerosol aerodynamic mass median diameter and dynamic shape factor on aerosol deposition rate and deposition distribution performed in paper.

Keywords: PHEBUS FPT-3, aerosol, aerodynamic mass median diameter, dynamic shape factor

1. INTRODUCTION

According to the general safety objective the Nuclear Power Plants (NPP) shall be designed to be safe and operated without significant effect on individuals, society and environment. However, severe accidents involving significant core degradation leading to fuel melting and fission product release beyond limits of NPP could not be completely excluded even though they are of low probability. After major severe accidents in nuclear reactors at Three Mile Island (TMI), USA, in 1979 and at Chernobyl, Ukraine, in 1986, a worldwide effort has been undertaken to understand and to model severe accident phenomena in nuclear reactors in case of a hypothetical loss of core cooling. The most extensive international program, which covers the whole accident progression and full spectrum of severe accident phenomena in the reactor core, cooling circuit and containment, is international PHEBUS Fission Product program.

The aim of this experimental program is to study the degradation phenomena and the behaviour of the fission products released in the reactor coolant system and the containment building. The program matrix consists of five in-pile tests, performed under different conditions concerning the thermal hydraulics and the environment of fuel rods, in particular the amount of steam (strongly or weakly oxidizing atmosphere). Five experiments have been successfully performed so far in 1993 (FPT0), 1996 (FPT1), 1999 (FPT4) and 2000 (FPT2). The last test of this program (FPT3) has been performed in November 2004 [1].

This paper presents the analysis of processes that occur in PHEBUS containment under FPT-3 experiment conditions. The first part of this paper deals with PHEBUS containment geometric, initial and boundary conditions, hydrogen and carbon compounds, and aerosols injection to containment. For simulation of the aerosols deposition distribution in PHEBUS containment the model for COCOSYS code was developed and described in the second part of this paper. The third part presents the analysis of aerodynamic mass median diameter (AMMD) and dynamic shape factor (CHI) influence on the aerosol deposition and deposition distribution in PHEBUS containment.

2. DESCRIPTION OF EXPERIMENT FPT-3

2.1. Geometric conditions

The PHEBUS containment vessel is a 10 m^3 tank (see Fig. 1), made of stainless steel (AISI 316L), in which aerosols and gases conveyed through the experimental circuit during the test are collected. Height of containment is 5 m with an inner diameter of 1.8 m. The containment wall represents a surface of about 25 m^2. The containment has cylindrical form with rounded bottom and top. The outer vessel walls were heated to avoid steam condensation and subsequent aerosol deposition on the containment top vault and vertical walls during the test. The top vault is equipped with a group of three condensers, which are designed to control heat transfer, steam condensation and thus simulate the cold structures of a reactor building. Total surface area of condensers is 3.33 m^2. The condenser surface is divided into two parts: the cooled condensing or “wet” condenser surface (area: 0.775 m^2 per condenser) and the non-condensing or “dry” condenser surface (area: 0.336 m^2 per condenser). A diameter of one condenser is 0.15 m. The lower part of each condenser is kept dry by heaters and contains equipment to collect condensate from the upper cooled part. When the collection device is full, the condensate is sequentially drained into the sump. The temperature of the non-condensing or “dry” part is regulated by electrical heaters and can be increased up to 150 °C. The cooled surfaces of condensers (about 0.81m^2 per condenser) are covered with epoxy paint as a source for organic iodine formation. The sump is a lower vessel part closed by a curved bottom structure with volume of 0.1 m^3. The sump has a diameter of only 0.584 m and height is 0.6 m. The sump was initially filled with 120 l water. The injection pipe tag to the containment of steam, hydrogen and aerosols is defined – 2.86 m in height. Pipe tag has cone form is in the centre of containment and is pointed to condensers [2].

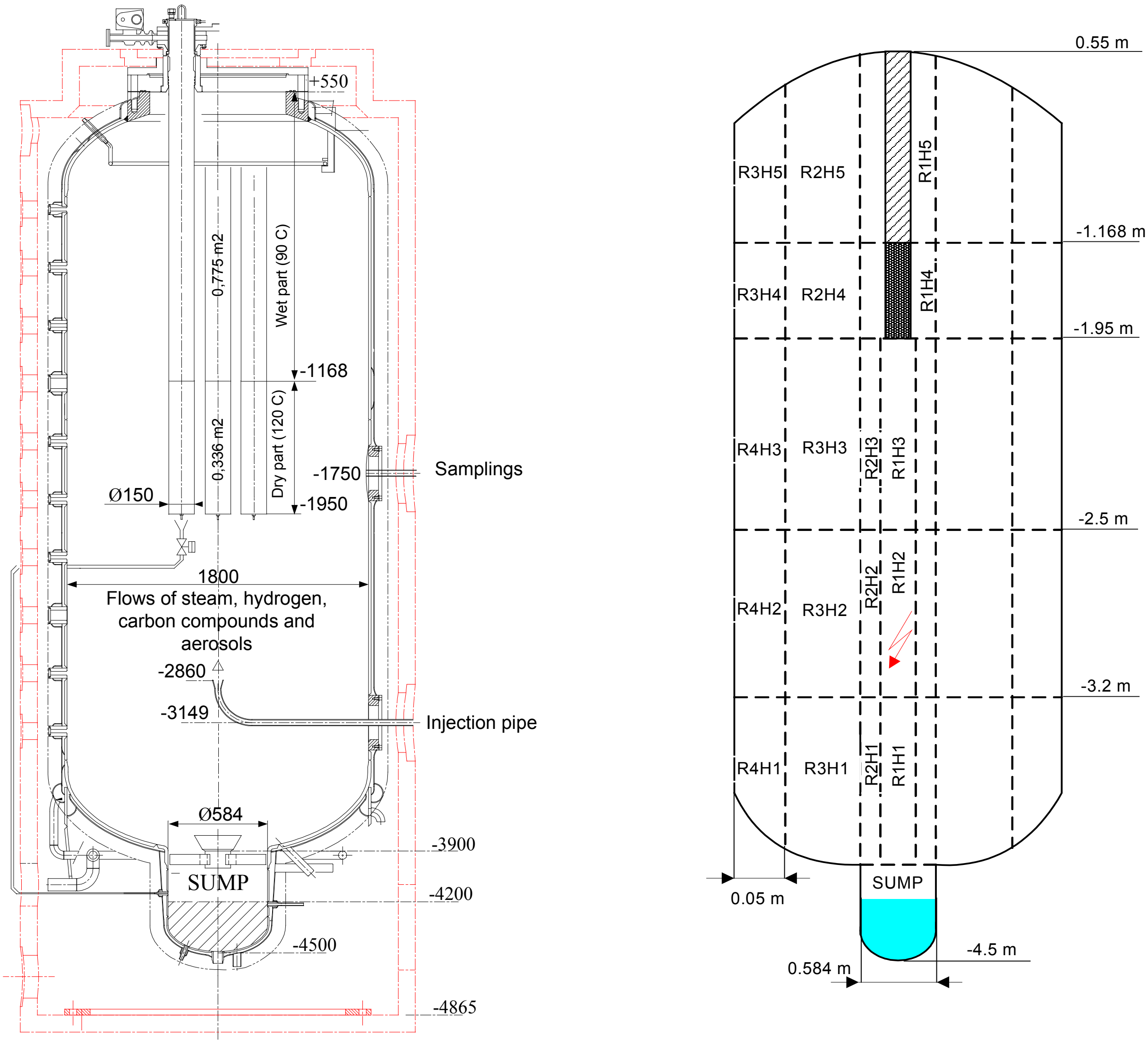

(a) (b)

Fig. 1. Schematic view of PHEBUS containment presented in figure (a). Nodalization scheme of PHEBUS containment presented in figure (b)

2.2. Initial and boundary conditions

Initially the containment is filled with air. During test preparation phases the nitrogen is injected into the containment to reach 2.0 bar pressure in containment. The objective of this operation is to obtain, after depressurisation to 1 bar, the desired reduced containment oxygen concentration 4 % O_2 in volume. Before the test transient, the obtained oxygen concentration in the containment is also 4 vol. %, the remaining volume is occupied by nitrogen. Average atmosphere temperature is 108 ^{o}C, average relative humidity – 52%.

The composition of the containment atmosphere consists of condensable gases (i.e., steam) and non-condensable gases (i.e., H_2, O_2, N_2, CO and CO_2). Measured steam and hydrogen flows rates released to containment are shown in Fig. 2. As one could see the steam mass flow rate is kept constant at the low value of 0.5 g/s through all injection interval. Maximum hydrogen flow rate released to containment is ~0,06 g/s after 10000 s. In Fig. 3 are shown CO and CO_2 flows rates released to containment after absorber material oxidation in the reactor core. Injected aerosol mass is shown in Fig. 4. According to the test procedure the containment was isolated after 22500 s.

The regulation temperatures of various containment walls is set to the values required by the test protocol for the test transient, i.e. 110 °C for the containment walls in contact with the gas phase, 90 °C for the condensing surface of the painted condensers (dry condenser surfaces are maintained at 120 °C) and 90 °C for walls in contact with the sump. The containment vessel boundary conditions are chosen to limit the relative humidity ratio to about 50 to 70% during the transient. Conditions inside containment are regulated to prevent steam condensation on the walls in contact with the gas. Steam condensation in the containment was controlled by the cooled condensing surfaces of the painted condensers [2, 3].

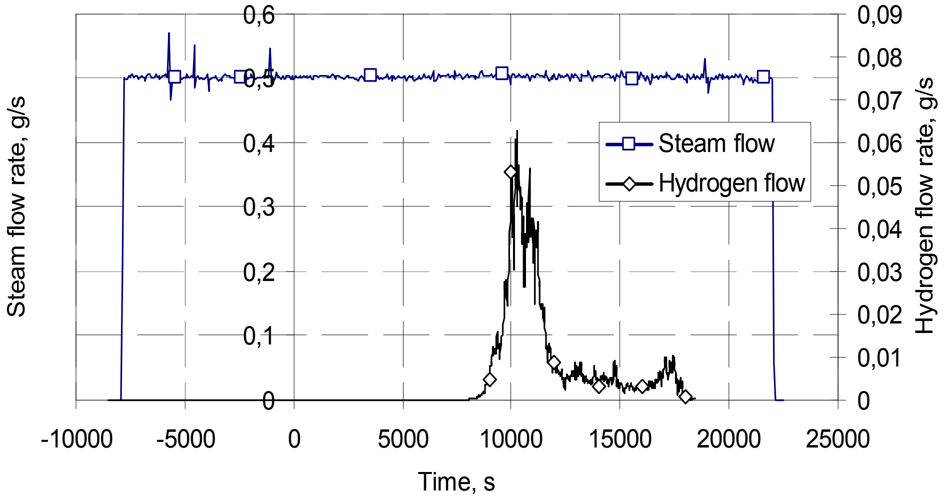

Fig. 2. Steam and hydrogen flow rates to containment during FPT-3

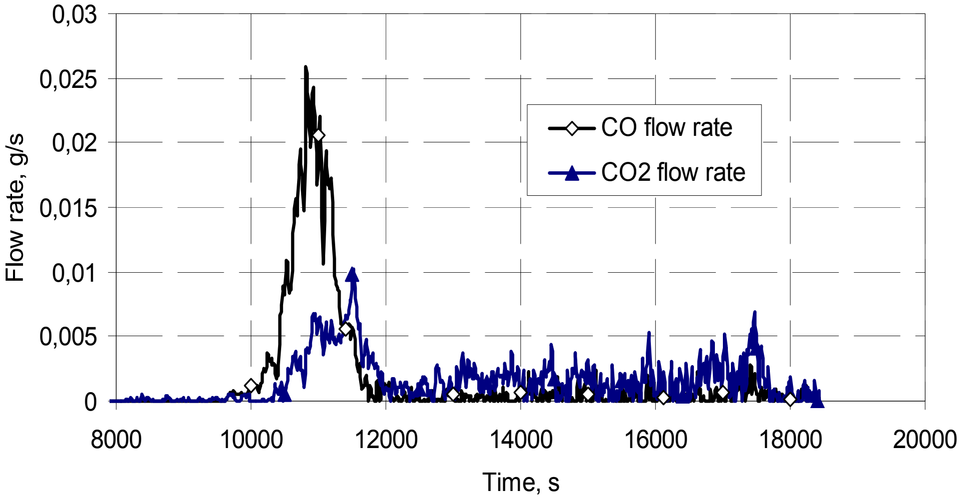

Fig. 3. CO and CO_2 flow rates to containment during FPT-3

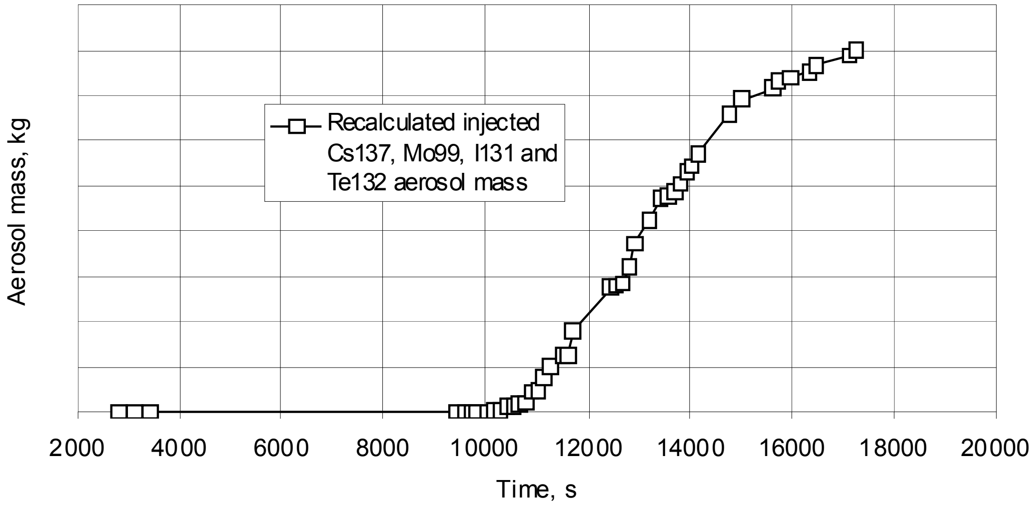

Fig. 4. Injected aerosol mass to containment during FPT-3

3. MODEL OF PHEBUS CONTAINMENT

For simulation of the aerosol distribution and deposition in the PHEBUS containment the model for COCOSYS code was developed. The nodalisation scheme of model is shown in Fig. 1. Radial subdivision consists of 4 rings above the sump and below condensers, and there are 3 rings at level of condensers. The diameter of one ring in radial subdivision corresponds to the diameter of the sump. The diameter of the central part of the subdivision was defined in such way that the injected plume of gases could be better defined in the model. There are defined 6 levels for vertical subdivision. Containment part between "wet" condensers bottom and sump is divided into three almost equal parts ~0.7 m height. The pipe through which the gases and aerosols from the reactor core are injected to the containment is located in the node R1H2. The sump is simulated by a single node.

Junctions are defined for simulation of the gas and water flows between the nodes in the model. The real geometric areas are defined for the atmospheric junctions. Detailed description of the nodalisation and assessment of the developed nodalisation for PHEBUS containment simulation are presented in [4].

In the developed model the initial and boundary conditions (e.g. initial pressure, temperature, humidity, etc) are defined according to FPT-3 test specification, presented above.

The aerosols are divided to 20 size classes assuming diameter range 10^{-8}–10^{-4} m. The models of gravitational, diffusiophoretic deposition mechanisms are considered in the model. The thickness of diffusion boundary layers in PHEBUS containment is 10^{-4} m. For the analysis it was estimated that the solubility factor of generic aerosol component is 1.9, which means that aerosols are very hygroscopic. Average aerosol mass density is not defined in PHEBUS FPT-3 preliminary report. According to presentation of Ammirabil et al. [5], it was recommended, that average aerosol density have to be lower than 6350 kg/m^3. Therefore, in this analysis average density is defined 6000 kg/m^3.

4. RESULTS OF ANALYSIS

4.1. Influence of aerodynamic mass median diameter

Fig. 5 presents comparison between different calculations of aerosol mass suspended in containment atmosphere. The airborne aerosol mass continuously increases until the injection of aerosols to the containment is terminated after 17340 s (see Fig. 3). After aerosol injection to the containment is terminated, then due to deposition processes, the airborne aerosol mass decreases. Before termination of injection the maximal aerosol mass in suspension is approximately 95 g. Fig. 5 presents the results of the parametric analysis determinative the influence of aerosol aerodynamic mass median diameter (AMMD). The AMMD is not given in the FPT-3 preliminary report. Also, it is noticed, in preliminary report of FPT-3 test, that aerosol deposition by sedimentation is slower than in previous tests and this may be attributed to lower AMMD [2]. In FPT-1 final report aerodynamic mass median diameter of aerosols is $2.79\cdot10^{-6}$m [4]. For the performed analysis AMMD was varied between $2.79\cdot10^{-6}$m and $2.42\cdot10^{-6}$m. As one could see there is only minor influence of the AMMD on the deposition rate of the aerosols.

Distribution of aerosol deposition is shown in Table 1. The results received with COCOSYS show that the largest deposition of aerosols (~71%) is on the containment floor around the sump. On the condensers and in the sump there are deposited ~ 28%, on the vertical containment walls and removed by the sampling only ~0.8% of aerosol mass. In containment atmosphere sedimentation deposition of aerosol particles is significant process on the containment floor and is directly proportional to AMMD. Therefore, decrease of AMMD leads to stay particles longer in suspension. More aerosol particles stay longer in suspension, so aerosol deposition on condensers surfaces increases. Diffusion deposition is the main process for aerosol deposition on the containment walls. Deposition on the containment walls is inversely proportional to AMMD. After aerosol AMMD decreases till $2.42\cdot10^{-6}$m, aerosol deposition on containment walls increases only 0.05%.

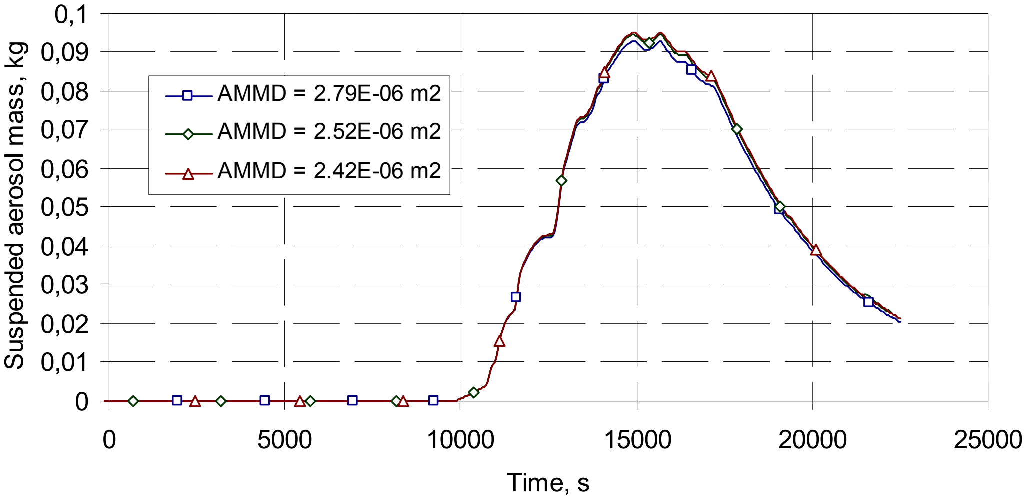

Fig. 5. Aerosol mass suspended in containment atmosphere

Table 1. Influence of AMMD. Distribution of aerosol deposition

	Floor of containment	Condenser surfaces and sump	Containment walls + samplings
COCOSYS (AMMD = $2.79\cdot10^{-6}$m)	71.49%	27.73%	0.35+0.43=0.78%
COCOSYS (AMMD = $2.52\cdot10^{-6}$m)	70.94%	28.24%	0.39+0.43=0.82%
COCOSYS (AMMD = $2.42\cdot10^{-6}$m)	70.74%	28.44%	0.4+0.43=0.83%

4.2. Influence of aerosol dynamic shape factor

Aerosol dynamic shape factor represents aerosol particles sphericity. In COCOSYS code spherical aerosol particles are defined with coefficient CHI = 1.0. If CHI > 1.0, particles form deflects from spherical. In containment atmosphere aerosol sphericity is significant for aerosol agglomeration and deposition processes. Aerosol dynamic shape factor is inversely proportional to aerosol agglomeration processes, because changing particles form leads to worse sticking probability. Furthermore, this coefficient is also inversely proportional to deposition by sedimentation. In PHEBUS FPT-3 preliminary report is noticed that aerosol deposition by gravitational settling is slower than in previous tests and this may be attributed to reduced agglomeration [2]. As we can see from Fig. 6, deflect from spherical particles has significant influence on aerosol deposition, and could be a reason for a slower aerosol deposition by sedimentation.

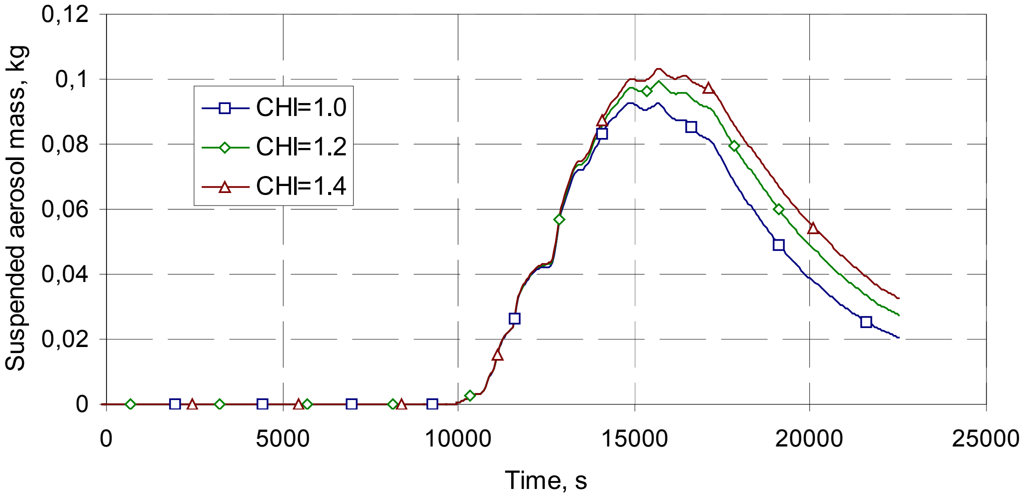

Fig. 6. Suspended aerosol mass in PHEBUS containment

Distribution of aerosol deposition is shown in Table 2. When aerosol dynamic shape factor is 1.0, aerosol deposition on the containment floor is 71.49%. On the condensers and in the sump there are deposited 27.73%, on the vertical containment walls and removed by the sampling 0.78% of aerosol mass. After aerosol dynamic shape factor increases till 1.4, aerosol deposition on containment floor and on the condensers decreases approximately 5%. However, aerosol deposition on the vertical containment walls increases monotonically (not exceeding 1%). Aerosol dynamic shape factor is significant for aerosol deposition by sedimentation. Nevertheless, the difference of diffusion deposition on the containment walls is small. The reason for such small difference should be further investigated.

Table 2. Influence of aerosol dynamic shape factor. Distribution of aerosol deposition

	Floor of containment	Condenser surfaces and sump	Containment walls + samplings
COCOSYS (CHI = 1.0)	71.49%	27.73%	0.35+0.43=0.78%
COCOSYS (CHI = 1.2)	68.49%	30.69%	0.4+0.42=0.82%
COCOSYS (CHI = 1.4)	66.46%	32.67%	0.46+0.41=0.87%

5. CONCLUSIONS

Analysis of aerosol deposition and distribution processes in the containment according to FPT-3 preliminary report was performed using lumped parameter code COCOSYS. The influence of aerosol aerodynamic mass median diameter and dynamic shape factor were investigated.

According to preliminary report, evolution of aerodynamic mass median diameter strongly influences the deposition mechanisms in containment and specially the gravitational settling. In the performed analysis AMMD was varied between $2.79 \cdot 10^{-6}$m and $2.42 \cdot 10^{-6}$m. According to calculated results, aerodynamic mass median diameter has only minor influence on the aerosol deposition and distribution.

Aerosol particles deflection from spherical form plays important role on the aerosol agglomeration and deposition processes, and could be a reason for slower aerosol deposition by gravitational settling.

REFERENCES

1. G. Repetto, O.De Luze, J. Birchley, T. Drath, T. Hollands, M.K. Koch, C. Bals, K. Trambauer, H. Austregesilo. Preliminary analyses of the PHEBUS FPT3 experiment using Severe Accident Codes (ATHLET-CD,ICARE/CATHARE, MELCOR) // The 2nd European Review Meeting on Severe Accident Research (ERMSAR-2007), Germany. 12-14 June 2007, 1 p. .
2. B. Biard, Y. Garnier, J. Guillot, C. Manenc, P.March, F. Payot. PHEBUS FPT3 preliminary report // IRSN and Commission of the European Union Institute for Energy, 2007.
3. A.M.Chretien, Data book FPT-3, IRSN and Commission of the European Union Institute for Energy, 2007.
4. A. Kontautas, E. Urbonavičius, S. Rimkevičius. Calculation model and simulation parameters influence to aerosol deposition in PHEBUS experimental facility // Energetika, 2008.
5. Ammirabil, L., Bielauskas, A., Bujan, A., Toth, B., Gyenes, G., Dienstbier, J., Herranz, L., Fontanet, J., Reinke, N., Rizoiu, A., Jancovic, J. Progress of ASTEC validation on fission product release and transport in circuits and containment // The 3rd European Review Meeting on Severe Accident Research (ERMSAR 2008), September 23–25, 2008.

INVESTIGATION OF PHOTONUCLEAR REACTION PRODUCTS ON SILVER AND INDIUM ISOTOPES FOR ENDPOINT BREMSSTRAHLUNG ENERGIES FROM 34 TO 90 MEV

O.A. Bezshyyko, L.O. Golinka–Bezshyyko, I.M. Kadenko, O.A. Kovalenko
Taras Shevchenko National University of Kiev
Glushkova str. 6, b.11, 03022 – Ukraine
Phone: 38–044–2597533
E-mail: obezsh@univ.kiev.ua

A.N. Vodin, A.N. Dovbnya, S.N. Olejnik, G.E. Tuller
National Science Center "Kharkov Institute of Physics & Technology" (NSC KIPT)
Kharkiv, Academicheskaya str. 1, 61108 – Ukraine
Phone: 38–057–3356873
E-mail: vodin@kipt.kharkov.ua

V.A. Kushnir, V.V. Mitrochenko
Research and Development Complex "Accelerator" of NSC KIPT
Kharkiv, Academicheskaya str. 1, 61108 – Ukraine

A.I. Levon
Institute for Nuclear Research,
Kyiv, Prospect Nauk, 47, 03680 – Ukraine

ABSTRACT

Values of the isomer ratios for nuclei ^{104}Ag, ^{110}In, ^{108}In as products of the photonuclear reactions ^{107}Ag(γ,3n)^{104m,g}Ag, ^{113}In(γ,3n)^{110m,g}In, ^{109}Ag(γ,5n)^{104m,g}Ag, ^{115}In(γ,5n)^{110m,g}In, ^{115}In(γ,7n)^{108m,g}In were obtained using bremsstrahlung of the electron linear accelerator LU-40 with endpoint energies ranged within (34–90) MeV for irradiation of targets. Energy resolution of electron beam was about 1% and mean electron current was near 5 μA. Method of the induced activity was used to obtain experimental isomer ratios.

INTRODUCTION

Using high energy gamma-quanta as projectiles in nuclear reactions has some essential advantages for study of nuclear structure and nuclear reaction mechanisms. Indeed, gamma-quanta do not introduce large angular momentum into compound nucleus and additional contribution to excitation energy of compound nucleus due to binding energy of projectile is absent. In addition, the precise nondiscrete control of the gamma-quanta energy is possible.

Characteristics of photonuclear reactions are well studied in the energy region of Giant Dipole Resonance (GDR) and above the pion-producing threshold (PPT). The energy region between GDR and PPT (from about 30 to about 100 MeV) was studied to a smaller extent both theoretically and experimentally. The reason is due to small values of photonuclear reaction cross sections in this energy region and limited availability of high intensity quasi mono-energetic gamma ray sources with well controlled gamma-quanta energy.

During the last several years essential progress has been achieved in development of the new theoretical models for the photonuclear reactions and in improvement of the existing ones in the considered energy region. The quasi-deuteron model was further improved [1], some new pre-equilibrium models have been developed for description of the multi-particle emission [2, 3]. Permanently growing interest to Accelerator Driven Systems and progress in the design of high intensity quasi mono-energetic gamma-quanta sources [4, 5] also stimulate study of the photonuclear reactions above the GDR energy region. Very limited experimental data for the photonuclear reactions in the energy range (30-100) MeV for testing newly developed and available theoretical models was the major motivation for the present work.

The main purpose of this study is to obtain the experimental isomer ratios for nuclei ^{104m,g}Ag, ^{110m,g}In, ^{108m,g}In as the products of the ^{107}Ag(γ,3n)^{104m,g}Ag, ^{113}In(γ,3n)^{110m,g}In, ^{109}Ag(γ,5n)^{104m,g}Ag, ^{115}In(γ,5n)^{110m,g}In and ^{115}In(γ,7n)^{108m,g}In reactions and compare them with predictions of the modern theoretical models.

METHODOLOGY

The de-excitation time of nuclei by the γ-cascade irradiation usually does not exceed 10^{-12} s [6]. In some cases transitions between levels of nucleus are suppressed due to the large difference of angular momentum of these levels involved and the nucleus can live long enough in a specific state called the isomer state. Usually these isomeric states have not large excitation energies and its angular momentum differs from a spin of the ground state by a few units of $\hbar$.

The isomer or ground levels with large values of spin are populated mainly from highly excited states with large spin values. Population of isomer or ground levels with smaller values of spin can occur mainly from highly excited states with small values of spins. Therefore investigations of relative populations of the isomer and ground states [7, 8] can be very useful to derive spins of highly excited levels and to study the de-excitation mechanisms via gamma emission.

For mono-energetic gamma beam with energy E the isomer ratio is determined as the cross sections ratio $\frac{\sigma_m(E)}{\sigma_g(E)}$, where $\sigma_g(E)$ is the cross section of the photonuclear reaction leading to the ground state, $\sigma_m(E)$ is the cross section for the same nucleus leading to the isomeric state. Also the isomer ratio is often determined as a ratio of the cross section σ_H for state with higher spin to the cross section σ_L for state with lower spin:

$$\xi = \frac{\sigma_H(E)}{\sigma_L(E)}. \tag{1}$$

If a gamma beam is non-monoenergetic (what is the case for experiments with bremsstrahlung sources), the isomeric yield ratio is determined as:

$$d(E_{\max}) = \frac{Y_m}{Y_g}, \tag{2}$$

where the reaction yield is given by

$$Y_{m,g} = N_t \int_{E_{thr}^{m,g}}^{E_{\max}} \sigma_{m,g}(E) \cdot W(E, E_{\max}) dE, \tag{3}$$

N_t – number of the target nuclei , $Y_{m,g}$ – reaction yield for nucleus in the isomer (m) or ground (g) state, $E_{\max}$ – maximal gamma energy, $W(E,E_{\max})$ – bremsstrahlung spectrum, $\sigma_i(E)$ with i=m,g – the reaction cross section for nucleus to be formed in meta-stable (ground) state for gamma energy E, E_{thr}^{i}, i=m,g – the energy threshold of the reaction leading to the meta-stable (ground) state.

Production of isomeric pair and its decay can be described by the following differential equation system:

$$\begin{cases} \dfrac{dN_m}{dt} = Y_m - \lambda_m \cdot N_m \\ \dfrac{dN_g}{dt} = Y_g - \lambda_g \cdot N_g + p \cdot \lambda_m \cdot N_m \end{cases}, \tag{4}$$

where N_i –- population of i-state (i=m - isomer state, i=g – ground state), Y_i – reaction yield according to (3), λ_m, λ_g – decay constants for isomer and ground state, p – branching factor (transition probability from isomer to ground state) [9, 10]. The equation system is valid under such conditions: gamma-quanta flux is time invariable; contribution from interfering reaction may be considered as negligible; simple decay scheme, when the isomer level decays by gamma transition to the ground state in competition with β-decay and the ground state decays by β-decay branch.

Solution of system (4) is:

$$\begin{cases} \dfrac{S_m}{C \cdot \varepsilon \cdot f_m} = Y_m \Lambda_3 \Lambda_6 \Lambda_9 \\ \dfrac{S_g}{C \cdot \varepsilon \cdot f_g} = Y_g \Lambda_2 \Lambda_5 \Lambda_8 + \\ + Y_m (\Lambda_1 \Lambda_5 \Lambda_8 + \Lambda_3 \Lambda_4 \Lambda_8 + \Lambda_3 \Lambda_6 \Lambda_7) \end{cases}, \tag{5}$$

where S_i, i=g,m – photo-peak area (in the gamma spectrum of the activation products), coefficient C includes self-absorption factor, summation effects of cascade gammas and other effects, ε –- full efficiency of gamma detection for the analysed gamma-line; f_i, i=g,m – quantum yield of gamma-line for i-state decay (transition probability for this line); coefficients Λ_j, j=1,9 are defined by t_1, t_2, t_3, – irradiation time, cooling time and measurement time, respectively:

$$\Lambda_1 = \frac{p}{\lambda_g} \left[1 - \frac{\lambda_m \lambda_g}{\lambda_m - \lambda_g} \left(\frac{e^{-\lambda_g t_1}}{\lambda_g} - \frac{e^{-\lambda_m t_1^g}}{\lambda_m} \right) \right]$$

$$\Lambda_2 = \frac{1}{\lambda_g}\left(1 - e^{-\lambda_g t_1}\right), \; \Lambda_3 = \frac{1}{\lambda_m}\left(1 - e^{-\lambda_m t_1}\right)$$

$$\Lambda_4 = p\frac{\lambda_m}{\lambda_m - \lambda_g}\left(e^{-\lambda_g t_2} - e^{-\lambda_m t_2}\right)$$

$$\Lambda_5 = e^{-\lambda_g t_2}, \; \Lambda_6 = e^{-\lambda_m t_2}$$

$$\Lambda_7 = p\left[1 - \frac{\lambda_m \lambda_g}{\lambda_m - \lambda_g}\left(\frac{e^{-\lambda_g t_3}}{\lambda_g} - \frac{e^{-\lambda_m t_3}}{\lambda_m}\right)\right]$$

$$\Lambda_8 = 1 - e^{-\lambda_g t_3}, \; \Lambda_9 = 1 - e^{-\lambda_m t_3}.$$

As a result, the following expression is obtained

$$F = Y'_m X + Y'_g, \tag{6}$$

where F and X are defined as

$$F = \frac{S}{\varepsilon \cdot f_g \Lambda_2 \Lambda_5 \Lambda_8}, \; X = \frac{(\Lambda_1\Lambda_5\Lambda_8 + \Lambda_3\Lambda_4\Lambda_8 + \Lambda_3\Lambda_6\Lambda_7) + \frac{f_m}{f_g}\Lambda_3\Lambda_6\Lambda_9}{\Lambda_2\Lambda_5\Lambda_8}, \tag{7}$$

with $S = S_g + S_m$ peak area sum, $Y'_{m,g} = CY_{m,g}$ - values, proportional to reaction yields.

In this particular case isomer yield ratio was calculated by fitting the experimental data (X, F) using expression (6).

Experimentally, the method of induced activity was applied to obtain the isomer ratios. Irradiations of Ag and In targets have been carried out with bremsstrahlung endpoint energies within the region (34 ÷ 90) MeV. Linear accelerator LU-40 (Research and Development Complex “Accelerator” NSC KIPT) was used as a source of fast electrons [11]. Instability of electron beam intensity was within 2%. Inner monitor of electron beam was calibrated by values from Faraday cup of the magnetic analyzer, placed at the accelerator outlet. The tantalum converter with 1.05 mm thickness was placed on the exit window of the accelerator facility, close to which the cylindrical aluminium gamma absorbers (thickness 5.5 and 10 cm) were installed. Diameter of beam spot on the conversion target was less than 9 mm. Energy of electron beam was determined using magnetic analyzer and was double checked in the low energy region by reaction thresholds. A distance between tantalum converter and absorber was 2 and 4 cm, between tantalum converter and target – 20 and 30 cm (depending on electron energy). We used metallic silver and indium targets with natural isotopic abundance to study the reactions ^{107}Ag(γ,3n)^{104m,g}Ag, ^{113}In(γ,3n)^{110m,g}In, and highly enriched targets (with enrichment more than 98% for silver and more than 99% for indium) of ^{109}Ag and ^{115}In for the reactions ^{109}Ag(γ,5n)^{104m,g}Ag, ^{115}In(γ,5n)^{110m,g}In, ^{115}In(γ,7n)^{108m,g}In. Irradiation time for every sample was 20 min. Then within (3 – 8) seconds the irradiated sample was moved with pneumatic transfer system to the measurement area. HPGe detector with the energy resolution <2.0 keV for ^{60}Co γ-line 1332 keV was used to acquire the instrumental gamma-ray spectra of the activation products as a set of serial measurements with various time periods. Cooling times varied for silver from 5 seconds to few hours and for indium – up to dozens of hours. Distances between sample and detector (dozens centimetres just after irradiation and few centimetres at the end of measurement period) were chosen to optimize both statistics and time restrictions when large contribution of interfering reactions took place, minimum distance was restricted by condition of negligible contribution of cascade gammas summing. Efficiency calibration of spectrometer was carried out for each detector-to-sample distance. The efficiency-energy dependence in double logarithmic scale showed a good quality and linearity in the energy range of interest, with deviations between experimental data and linear fitted values not exceeding 2%. Examples of spectra from the induced activities for the silver and indium targets are shown in Fig. 1.

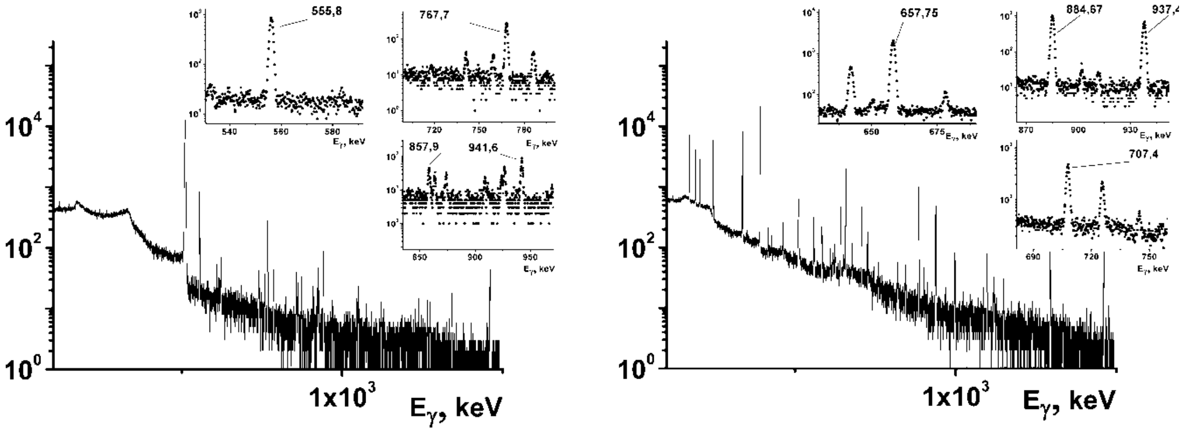

Fig. 1. Gamma-ray spectra from the induced activities in the silver target enriched in ^{109}Ag (left) and in the indium target enriched in ^{115}In (right). The analytical gamma lines used for determination of the isomer ratios are indicated separately

RESULTS AND DISCUSSION

Isomer ratios were obtained as $IR(E_\gamma)=\frac{Y_H(E_\gamma)}{Y_L(E_\gamma)}$, where $Y_H(E_\gamma)$ is the reaction yield for the state of final nucleus with larger angular momentum (ground state), $Y_L(E_\gamma)$ is the reaction yield for the state of final nucleus with smaller angular momentum (meta-stable state). Simplified decay schemes for ^{104m,g}Ag and ^{110m,g}In nuclei are shown below (see Fig. 2 and Fig. 3) [6].

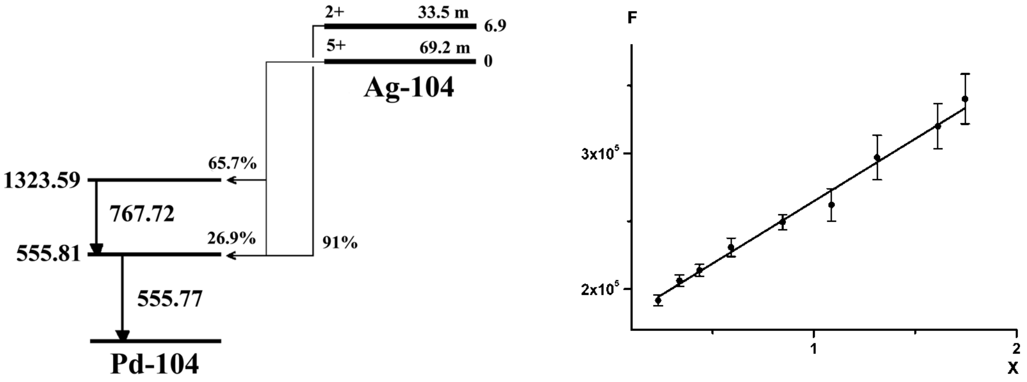

Fig. 2. Simplified decay scheme for ^{104m,g}Ag (left) and decay line of the nucleus ^{104m,g}Ag (reaction ^{109}Ag(γ,5n)^{104m,g}Ag) in presentation of Eqs. (6, 7)

One can see in these figures also the fitting result of the decay line in presentation (X, F) according to Eqs. (6, 7). Gamma transitions and corresponding lines with the energies 767.7 keV (EC+β^+ decay of the ground state) and 555.8 keV (common line for decay of the ground and isomer states) were used to calculate the isomer ratio for ^{104m,g}Ag. Additional transitions with energies 857.9 keV and 941.6 keV occurring in a cascade with above specified ones were used to controll correctness of these calculations.

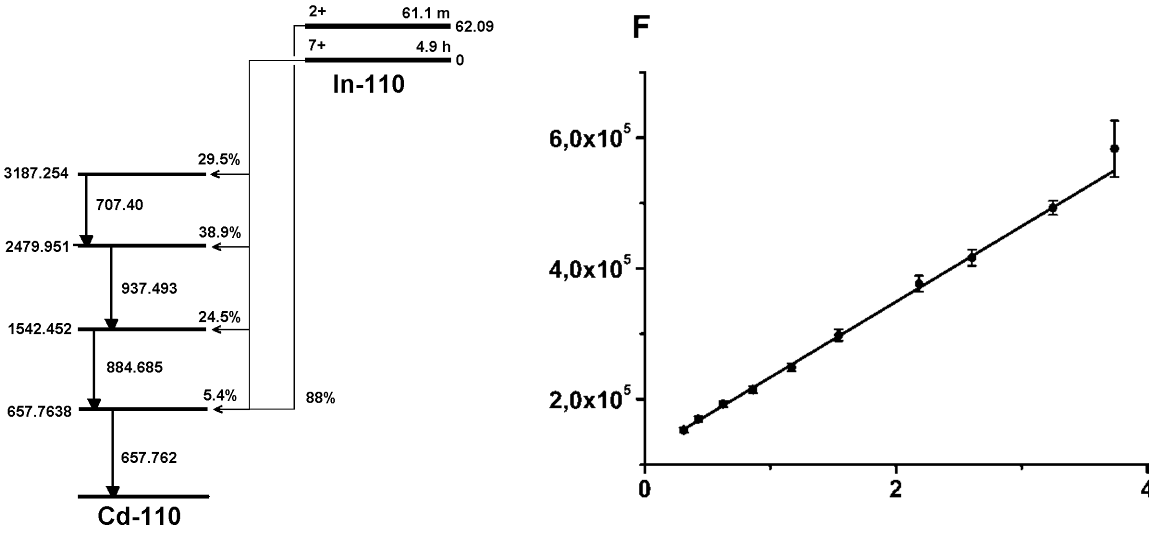

Fig. 3. Simplified decay scheme for ^{110m,g}In (left) and decay line of the nucleus ^{115m,g}In (reaction ^{115}In(γ,5n)^{115m,g}In, E_γ=90 MeV) in presentation of Eqs. (6, 7)

The gamma lines 884.7 keV, 937.5 keV, 707.4 keV (EC+β^+ decay of the ground state) and 657.8 keV (common line for decay of the ground and isomer states) were used to obtain the isomer ratio for ^{110m,g}In.

The gamma lines 875.5 keV (EC+β^+ decay of the ground state) and 633.0 keV (common line for decay of the ground and isomer states) were used to obtain the isomer ratio for ^{108m,g}In.

All obtained experimental values of the isomer ratios, corresponding reactions and characteristics of investigated nuclei are presented in Table 1.

Table 1. Reactions, the bremsstrahlung energy end-points $E\gamma_{max}$, spins of the target nuclei, spins of the meta-stable and ground states and obtained experimental isomer ratios $IR=Y_H/Y_L$

Reaction	$E\gamma_{max}$	I^{π}_{tar}	I^{π}_{m}	I^{π}_{g}	IR
^{107}Ag(γ,3n)^{104m,g}Ag	35	$1/2^-$	2^+	5^+	0.88 ± 0.14
	36,5	$1/2^-$	2^+	5^+	1.04 ± 0.10
	38,5	$1/2^-$	2^+	5^+	1.26 ± 0.05
	40	$1/2^-$	2^+	5^+	1.39 ± 0.08
^{109}Ag(γ,5n)^{104m,g}Ag	90	$1/2^-$	2^+	5^+	1.88 ± 0.08
^{113}In(γ,3n)^{110m,g}In	34	$9/2^+$	2^+	7^+	0.31 ± 0.07
	36	$9/2^+$	2^+	7^+	0.44 ± 0.07
	38	$9/2^+$	2^+	7^+	0.62 ± 0.06
	40	$9/2^+$	2^+	7^+	0.54 ± 0.04
	43	$9/2^+$	2^+	7^+	0.52 ± 0.05
^{115}In(γ,5n)^{110m,g}In	60	$9/2^+$	2^+	7^+	0.4 ± 0.04
	80	$9/2^+$	2^+	7^+	0.67 ± 0.13
	85	$9/2^+$	2^+	7^+	0.83 ± 0.08
	90	$9/2^+$	2^+	7^+	1.02 ± 0.02
^{115}In(γ,7n)^{108m,g}In	90	$9/2^+$	2^+	7^+	0. 9± 0.25

The uncertainties given in Table 1 include contributions from photopeak efficiency calibration, abundance, geometry configuration and intensities of gamma-rays (photopeak areas). Statistical uncertainties of photopeak areas made the main contribution to total uncertainty of result. Also number of experimental points of F,X dependency and range of X determination influenced total experimental error. These values were limited by experimental conditions.

We used code TALYS [12] for theoretical calculations of isomer ratios for investigated nuclei (see Fig. 4). Optimal default parameters were applied for calculation.

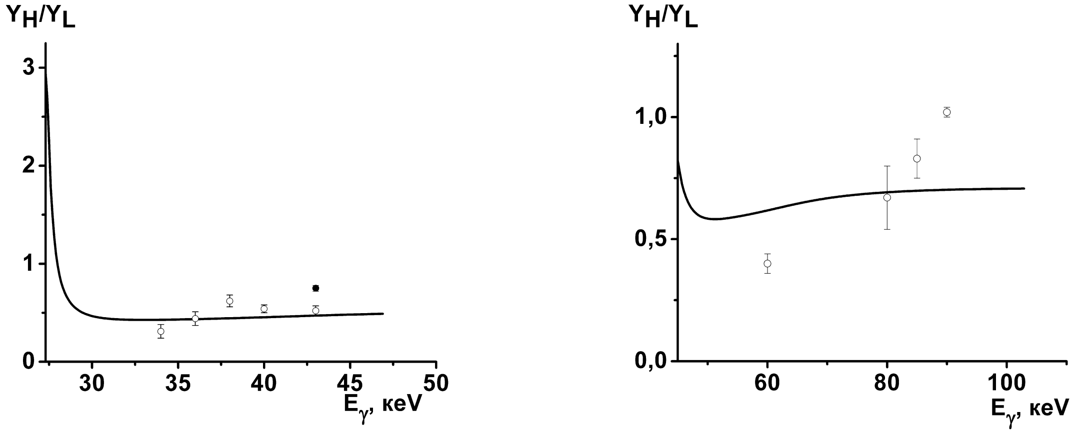

Fig. 4. Isomer ratios of yields for ^{110m,g}In from reaction ^{113}In(γ,3n)^{110m,g}In (left) and reaction ^{115}In(γ,5n)^{110m,g}In (right). Solid line – calculation with using code TALYS, circles – experimental data obtained in this work, filled circle – experimental value from ref. [10]

CONCLUSIONS

Experimental values of the isomer ratios are obtained for ^{104m,g}Ag, ^{110m,g}In and ^{108m,g}In nuclei as products of the photonuclear reactions ^{107}Ag(γ,3n)^{104m,g}Ag, ^{113}In(γ,3n)^{110m,g}In, ^{109}Ag(γ,5n)^{104m,g}Ag, ^{115}In(γ,5n)^{110m,g}In and ^{115}In(γ,7n)^{108m,g} In using bremsstrahlung endpoint energies in the region from 34 to 90 MeV.

Theoretical calculations of isomer ratios have been performed using code TALYS. Experimental values of isomer ratios for ^{110m,g}In from reaction ^{113}In(γ,3n)^{110m,g}In and reaction ^{115}In(γ,5n)^{110m,g}In are in a sufficiently good agreement with theoretical calculation results. In the same time the trends of these value dependencies are different. For reaction ^{115}In(γ,5n)^{110m,g}In calculated line has a weak energy dependence in comparison with experimental data. For other reactions differences between experimental data and theoretical calculations are well observable (1.5–2.3 times). For ^{104}Ag calculated values are underestimated more than 2 times.

This work was supported partly by grant of NAS Ukraine “NMRT X-9-535”.

REFERENCES

1. M.B. Chadwick, P. Oblozinský, P.E. Hodgson, G Reffo. Pauli-blocking in the quasideuteron model of photoabsorption // Phys. Rev. – 1991. – Vol. C44. – P. 814–823.
2. M. Herman, P. Oblozinsky, R. Capote et al. Recent Development of the Nuclear Reaction Model Code Empire // Proc. of International Conf. on Nuclear Data for Sci. and Technology "ND2004". Sept. 26 – Oct. 1, 2004. – Santa Fe (USA). – N.-Y., 2005. – AIP Conf. Proc. Vol. 769. – P. 1184 – 1187.
3. P. Talou, T. Kawano, P.G. Young and M.B. Chadwick. The McGNASH nuclear reaction code and its use for gas production cross-section calculations // Nucl. Instrum. Meth. – 2006. Vol. A562 – P. 823 – 826.
4. P. A. Gokhale, S. Deokattey and V. Kumar. Accelerator driven systems (ADS) for energy production and waste transmutation: International trends in R&D // Progr. in Nucl. Energy. – 2006. Vol. 48 – P. 91 – 102.
5. http://higs.tunl.duke.edu.
6. http://www.nndc.bnl.gov/ensdf.
7. B.C. Ishkhanov, I.M. Kapitonov. Interaction of electromagnetic radiation with nuclei. – M.: MSU, 1979. – 215 p.
8. Yu.P. Gangrsky, A.P. Tonchev, N.P. Balabanov. Excitation of isomer states in photonuclear reactions. // PEPAN. – 1996. – V. 27, No. 4. – P. 1043–1098.
9. R. Vänskä., R. Rieppo. The experimental isomeric cross-section ratio in the nuclear activation technique // Nucl. Instr. and Meth. – 1981. – Vol. 179. – P. 525–532.
10. D. Kolev, E. Dobreva, N. Nenov, V. Todorov. A convenient method for experimental determination of yields and isomeric ratios in photonuclear reactions measured by the activation technique // Nucl. Instr. and Meth. in Phys. Res. – 1995. – Vol. A356. – P. 390–396.
11. A.N. Dovbnya, M.I. Aizatsky, V.N. Boriskin, I.V. Khodak, V.A. Kusnir, V.V. Mytrochenko, A.N. Opanasenko, S.A. Perezhogin et all. Beam parameters of an S-band electron linac with beam energy of 30...100 MeV // Problems of Atomic Science and Technology. -2006. - №2(46). – P. 11–13.
12. A.J. Koning, S. Hilaire, M.C. Duijvestijn. TALYS: Comprehensive nuclear reaction modeling // Proc. of International Conf. on Nuclear Data for Sci. and Technology "ND2004". Sept. 26-Oct. 1, 2004. - Santa Fe (USA). – N.-Y., 2005. – AIP Conf. Proc. Vol. 769. – P. 1154–1159. http://www.talys.eu.

CYSENI 2009, May 28-29, Kaunas, Lithuania
ISSN 1822-7554, www.cyseni.com

ANALYTICAL SOLUTIONS OF THE SCHRODINGER EQUATION FOR FINITE HARMONIC-OSCILLATOR POTENTIAL WELLS

G.P. Kamuntavičius, A. Mašalaitė, S. Mickevičius
Department of Physics, Vytautas Magnus University
Vileikos 8, LT-44404, Kaunas, Lithuania
Phone: +37060526384
E-mail: s.mickevicius@gmf.vdu.lt

ABSTRACT

An analytical approach for finding Schrodinger equation solutions in finite harmonic oscillator (HO) potential wells is developed in this report. The structure of spectra and corresponding wave-functions is investigated in one and two finite potential wells. The dependence of the ground state eigenvalues on the wells depth and the distance between wells is presented there in.

Key words (Mathematical methods in physics, Schrodinger equation, potential wells)

1. INTRODUCTION

The importance of the double- and many-wells potentials in quantum mechanics can hardly be overestimated. The potentials of this kind appear in condensed matter physics, in an atom theory, as well as in statistical physics and in solving different other problems of theoretical physics.

The best known application of a potential consisting of the periodic repetition of N neighboring wells is the theory of conductivity in a condensed matter. Each single-well eigenvalue splits into a set of N bound states of the periodic system of the many-wells potential. The spacing of the energy values of these states may be very narrow and depends on the parameters of the well, as well as on a distance between wells [1]. These levels form an energy band necessary to understand the motion of approximately free electrons in a lattice of a metal.

This problem is also very interesting from the point of view of the fundamental quantum mechanics. The tunneling of wave-functions of identical fermions, trapped in different wells, causes correlations of these particles. How far these wells have to be situated in order to be sure that antisymmetrization of these wave functions is not necessary? Thus, it is only one of the problems arising in this situation.

Recently, many studies have been devoted for understanding the nucleon-nucleon interaction starting from quark models [2, 3]. The success of the point-like constituent quark model in a barion spectroscopy demonstrates that the application of this approach for two nucleons could be a good choice for the understanding the nucleon-nucleon interaction and it constitutes the modification in nuclei due to presence of “spectator” nucleons. The way for the solution of this problem selected by the authors is based on a nontraditional consideration of the confinement of quarks in the cases when two nucleons approach each other and the corresponding confinement potentials come into contact. The overlap of wave-functions of valence quarks, trapped in different nucleons, causes correlations thus giving the possibility to understand the peculiarities of the nucleon-nucleon interaction. In work [4] an infinitely deep confining HO well was applied as often as it is applied in the Standard Model of elementary particles [5]. The main result of this investigation is that the introduced modification of the confinement potential in a six quark system is consistent with the characteristic features of the realistic potential. Let us now investigate the more realistic situation when the deepness of the confining potential is finite.

2. SINGLE FINITE HO POTENTIAL WELL

Let us refer to the simplest model, starting from a single HO potential well. In case of the infinite HO potential well the time – independent Schrodinger equation is expressed as follows [6]:

$$\left(-\frac{\hbar^2}{2m}\frac{d^2}{dx^2}+\frac{m\omega^2}{2}x^2\right)\phi(x)=E\phi(x), \tag{1}$$

where m is the mass of particle in the potential well, ω is frequency and E is energy. With the help of the dimensionless variable

$$\xi=\frac{x}{b}, \quad b=\sqrt{\frac{\hbar}{m\omega}} \tag{2}$$

the Eq.(1) is simplified to the following reduced form

$$\left(-\frac{1}{2}\frac{d^2}{d\xi^2}+\xi^2\right)\varphi_n(\xi)=e_n\varphi_n(\xi). \tag{3}$$

The dimensionless eigenvalue $e_n=\frac{E}{\hbar\omega}$ measures the energy of the oscillator. The solutions of the Schrodinger Equation for the infinite HO well can be normalized for the eigen values

$$e_n=n+\frac{1}{2}, \quad n=0,1,2,.... \tag{4}$$

The eigenfunctions, normalized in ξ can be represented in the form [6]

$$\varphi_n(\xi)=\frac{1}{\sqrt{2^n n!\sqrt{\pi}}}H_n(\xi)e^{-\frac{\xi^2}{2}}; \quad n=0,1,2,... \tag{5}$$

where $H_n(\xi)$ are the Hermite polynomials.

Let us examine how the picture of energy levels changes when the HO potential becomes finite. An example of the finite HO potential well is presented in Fig.1. The potential in the well area $|x|<x_0$ is negative and for $x=0$ equals to $-V_0$, where V_0 is the positive number. The potential equals to zero outside the area $|x|\geq x_0$. The analytical expression for the potential is as follows (see Fig. 1):

$$V(x)=\begin{cases}\frac{m\omega^2x^2}{2}-V_0, & |x|<x_0;\\ 0, & |x|\geq x_0.\end{cases} \tag{6}$$

For $x=x_0$ the potential equals to zero and the parameter x_0 can be expressed through the parameter V_0:

$$x_0^2 = \frac{2V_0}{m\omega^2}. \tag{7}$$

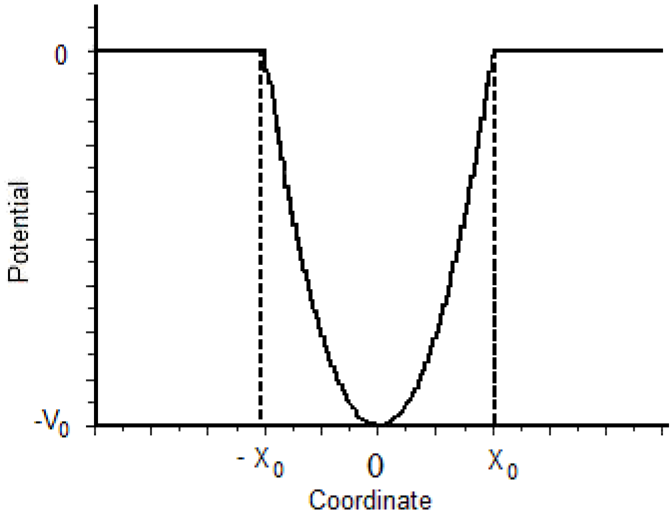

Fig. 1. Single HO potential well with finite ends

The Shrodinger equation for a particle moving in a such potential well is expressed in:

$$\left[-\frac{\hbar^2}{2m}\frac{d^2}{dx^2} + \left\{\frac{m\omega^2 x^2}{2} - V_0\right\} - \mathrm{E}\right]\varphi_{\mathrm{E}}(x) = 0, \quad |x| < x_0; \tag{8}$$

$$\left[-\frac{\hbar^2}{2m}\frac{d^2}{dx^2} - \mathrm{E}\right]\varphi_{\mathrm{E}}(x) = 0, \quad |x| \geq x_0. \tag{9}$$

Using dimensionless variables from Eq. (2) the Eq. (8) and Eq. (9) are simplified to the reduced form:

$$\left[\frac{d^2}{d\xi^2} - \xi^2 + \frac{2(V_0 + \mathrm{E})}{\hbar\omega}\right]\varphi_{\mathrm{E}}(\xi) = 0, \quad |\xi| < \xi_0; \tag{10}$$

$$\left[\frac{d^2}{d\xi^2} + \frac{2\mathrm{E}}{\hbar\omega}\right]\varphi_{\mathrm{E}}(\xi) = 0, \quad |\xi| \geq \xi_0. \tag{11}$$

As $\xi_0^2 = \frac{x_0^2}{b^2} = \frac{2V_0}{\hbar\omega}$, the depth of the potential well in the dimensionless coordinates equals to $\frac{\xi_0^2}{2} = \frac{V_0}{\hbar\omega}$. Let us introduce new parameter $q = \frac{2(V_0 + \mathrm{E})}{\hbar\omega}$, where E is the bound state energy in the finite HO potential well. As E is negative, the parameter $\varepsilon^2 = -\frac{2\mathrm{E}}{\hbar\omega}$ takes positive values, hence q can be present in the form of $q = \xi_0^2 - \varepsilon^2$.

One can rewrite Eq.(10) and (11) using the newly introduced parameters:

$$\left[\frac{d^2}{d\xi^2} - \xi^2 + q\right]\varphi_q(\xi) = 0, \quad |\xi| < \xi_0; \tag{12}$$

$$\left[\frac{d^2}{d\xi^2}-\varepsilon^2\right]\varphi_q(\xi)=0, \quad |\xi|\geq\xi_0. \tag{13}$$

Eq.(13) is the Schrodinger equation for the free particle and its solutions are:

$$\Psi_1(\varepsilon,\xi)=A_1e^{-\varepsilon\xi}, \quad \xi>\xi_0; \tag{14}$$

$$\Psi_2(\varepsilon,\xi)=A_2e^{\varepsilon\xi}, \quad \xi<-\xi_0. \tag{15}$$

Eq.(12) has two independent kinds of solutions: the first one is symmetrical

$$\varphi_1(q,\xi)=B_1\exp\left(-\frac{\xi^2}{2}\right)\cdot M\left(\frac{1-q}{4},\frac{1}{2},\xi^2\right) \tag{16}$$

and the other is antisymmetrical ones

$$\varphi_2(q,\xi)=B_2\cdot\xi\cdot\exp\left(-\frac{\xi^2}{2}\right)\cdot M\left(\frac{3-q}{4},\frac{3}{2},\xi^2\right). \tag{17}$$

Here A_1, A_2, B_1 and B_2 are the normalization constants. Function $M(x,y,z)$ is degenerated hypergeometric function [7].

In order to find the energy values of bound states in the finite HO potential well, functions (14), (15), (16), (17) and their derivatives have to satisfy the continuity conditions at points $\xi=-\xi_0$ and $\xi=\xi_0$. As the potential, presented in Fig.1, is symmetric with respect to point $\xi=0$ only one condition at the point $\xi=\xi_0$ is necessary instead of two continuity conditions. As the normalization constants A_1, B_1 and B_2 are unknown, the continuity conditions for logarithmical derivatives are used, thus allowing us to avoid the calculations of A_1, B_1 and B_2. The continuity condition for functions (14) and (16)

$$\left.\frac{\varphi_1'(q,\xi)}{\varphi_1(q,\xi)}\right|_{\xi=\xi_0}=\left.\frac{\Psi_1'(\varepsilon,\xi)}{\Psi_1(\varepsilon,\xi)}\right|_{\xi=\xi_0} \tag{18}$$

gives the equation for the symmetrical solution

$$\frac{-\xi_0\cdot M\left(\frac{1-q}{4},\frac{1}{2},\xi_0^2\right)+\xi_0(1-q)M\left(\frac{5-q}{4},\frac{3}{2},\xi_0^2\right)}{M\left(\frac{1-q}{4},\frac{1}{2},\xi_0^2\right)}=-\sqrt{\xi_0^2-q}. \tag{19}$$

The similar condition for functions (14) and (17)

$$\left.\frac{\varphi_2'(q,\xi)}{\varphi_2(q,\xi)}\right|_{\xi=\xi_0}=\left.\frac{\Psi_1'(\varepsilon,\xi)}{\Psi_1(\varepsilon,\xi)}\right|_{\xi=\xi_0} \tag{20}$$

gives the equation for the antisymmetrical solution

$$\frac{\left(1-\xi_0^2\right)\cdot M\left(\frac{3-q}{4},\frac{3}{2},\xi_0^2\right)+\xi_0^2\cdot\frac{3-q}{3}\cdot M\left(\frac{7-q}{4},\frac{5}{2},\xi_0^2\right)}{\xi_0\cdot M\left(\frac{3-q}{4},\frac{3}{2},\xi_0^2\right)}=-\sqrt{\xi_0^2-q}. \qquad (21)$$

From the Eq.(19) and Eq.(21) the values of the parameter q are found. The calculation results for the ground state energy in the finite HO potential well are presented in Table 1.

As can be seen from Table 1, when the potential well is shallow, the ground level eigenvalue is situated near the bottom of the well. When the well becoming deeper, the eigenvalue approaches the eigenvalue of the ground level in infinite HO potential well.

Table 1. The energy eigenvalues in the finite HO potential well as the function of the well depth $\xi_0^2/2$. The ground state eigenvalue in the infinite HO potential well equals to 0,5.

$\xi_0^2/2$	q, finite HO well
0.6	0.399
0.78	0.438
1.13	0.475
1.53	0.491
2	0.498
2.2	0.498
2.42	0.499
2.65	0.5
2.88	0.5

3. ENERGY LEVELS IN DOUBLE FINITE HO POTENTIAL WELLS

Now let us investigate the band energy spectra in double finite HO potential wells, presented in Fig. 2. The analytical expression for that potential in the dimensionless coordinates is:

$$V(\xi)=\begin{cases}\dfrac{\left(|\xi|-a\right)^2}{2}-\xi_0^2, & |a|<|\xi|<|a+2\xi_0|;\\ 0, & |\xi|\le a,\ |\xi|\ge a+2\xi_0.\end{cases} \qquad (22)$$

A new parameter a is introduced, where $2a$ equals to dimensionless distance between the ends of the potential wells.

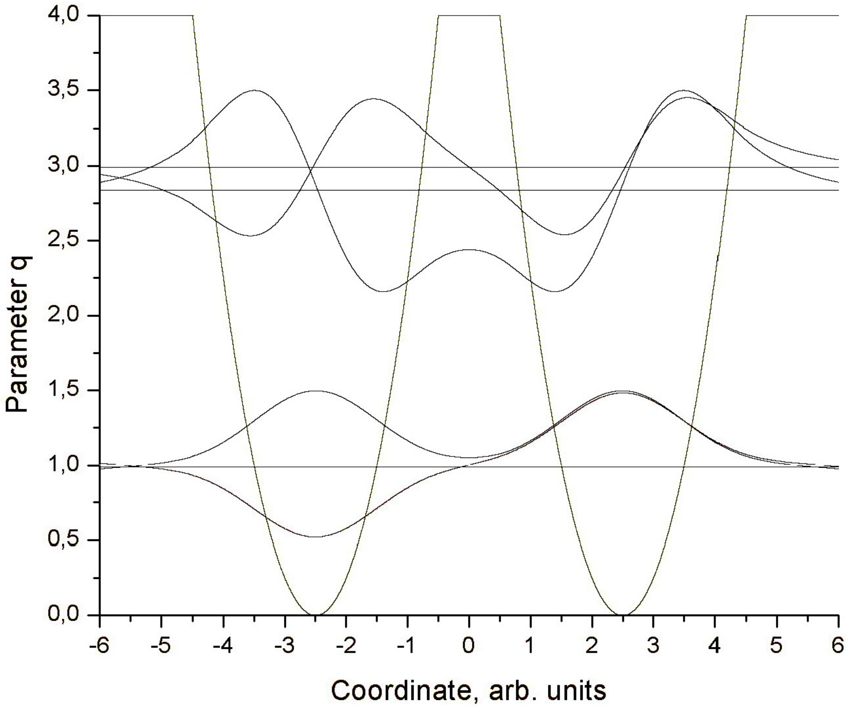

Fig. 2. Bound-state wave functions and energy spectra for double finite HO potential wells. The horizontal lines also serve as zero lines for the functions shown

In regions outside the wells the wave function must show the exponential fall for large values of $|\xi|$. The behaviour of the wave function is determined in particular by its structure in the region between the potential wells which encompass the original. In this domain the wave function is a linear combination of real exponentials which, due to the problem of the symmetry, are either symmetric

$$\varphi_s(\varepsilon_s,\xi) = N_1 \cosh(\varepsilon_s \cdot \xi) \tag{23}$$

or antisymmetric

$$\varphi_a(\varepsilon_a,\xi) = N_2 \sinh(\varepsilon_a \cdot \xi). \tag{24}$$

N_1 and N_2 are the normalization constants, ε_s and ε_a are the dimensionless bound state energies of the symmetric and antisymmteric solutions respectively. The wave function in the region between wells connects the wave functions in the first and second square wells. It therefore determines the overall symmetry. Since the antisymmetric solution has the large average curvature, it possesses the greater kinetic energy compared to the symmetric solution. This explains why the splitting of the two energy eigenvalues of the bound states increases when two wells approach each other.

The wave functions in the regions $|a| < |\xi| < |a + 2\xi_0|$ are equal to the linear combination of the functions (16) and (17). In the region $-a > -\xi > -a - 2\xi_0$ the wave functions are

$$\eta_1(q,\xi+\xi_0+a) = \varphi_1(q,\xi+\xi_0+a) + C_1\varphi_2(q,\xi+\xi_0+a) \tag{25}$$

and the corresponding wave functions in the region $a < \xi < a + 2\xi_0$ are

$$\eta_2(q,\xi-\xi_0-a) = \varphi_1(q,\xi-\xi_0-a) + C_2\varphi_2(q,\xi-\xi_0-a), \tag{26}$$

where C_1 and C_2 are coefficients of the linear combination.

As the potential presented in Fig. 2 is completely symmetric with respect to point $\xi = 0$ the continuity conditions for logarithmical derivatives only at points $\xi = a$ are used

$$\left.\frac{\eta_1'(q,\xi-\xi_0-a)}{\eta_1(q,\xi-\xi_0-a)}\right|_{\xi=a} = \left.\frac{\varphi_s'(\varepsilon_s,\xi)}{\varphi_s(\varepsilon_s,\xi)}\right|_{\xi=a}; \quad \left.\frac{\eta_1'(q,\xi-\xi_0-a)}{\eta_1(q,\xi-\xi_0-a)}\right|_{\xi=a} = \left.\frac{\varphi_a'(\varepsilon_a,\xi)}{\varphi_a(\varepsilon_a,\xi)}\right|_{\xi=a} \tag{27}$$

and $\xi = \xi_0 + 2a$

$$\left.\frac{\eta_1'(q,\xi-\xi_0-a)}{\eta_1(q,\xi-\xi_0-a)}\right|_{\xi=\xi_0+2a} = \left.\frac{\Psi_1'(\varepsilon,\xi)}{\Psi_1(\varepsilon,\xi)}\right|_{\xi=\xi_0+2a}. \tag{28}$$

As C_2 can be eliminated from these equations and the final equation for q in the symmetrical case becomes:

$$\frac{M\left(\frac{1-q}{4},\frac{1}{2},\xi_0^2\right)\left(\xi_0-\sqrt{\xi_0^2-q}\right)-\xi_0(1-q)M\left(\frac{5-q}{4},\frac{3}{2},\xi_0^2\right)}{M\left(\frac{3-q}{4},\frac{3}{2},\xi_0^2\right)\left(\xi_0\cdot\sqrt{\xi_0^2-q}-\xi_0^2\right)+\xi_0^2 M\left(\frac{7-q}{4},\frac{5}{2},\xi_0^2\right)} = \frac{M\left(\frac{1-q}{4},\frac{1}{2},\xi_0^2\right)\left(\tanh\left(\sqrt{\xi_0^2-q}\cdot a\right)\cdot\sqrt{\xi_0^2-q}-\xi_0\right)-\xi_0(1-q)M\left(\frac{5-q}{4},\frac{3}{2},\xi_0^2\right)}{M\left(\frac{3-q}{4},\frac{3}{2},\xi_0^2\right)\left(1-\xi_0^2+\xi_0\cdot\sqrt{\xi_0^2-q}\cdot\tanh\left(\sqrt{\xi_0^2-q}\cdot a\right)\right)+\xi_0^2\frac{3-q}{3}M\left(\frac{7-q}{4},\frac{5}{2},\xi_0^2\right)}. \tag{29}$$

The equation for q in the antisymmetrical case is:

$$\frac{M\left(\frac{1-q}{4},\frac{1}{2},\xi_0^2\right)\left(\xi_0-\sqrt{\xi_0^2-q}\right)-\xi_0(1-q)M\left(\frac{5-q}{4},\frac{3}{2},\xi_0^2\right)}{M\left(\frac{3-q}{4},\frac{3}{2},\xi_0^2\right)\left(\xi_0\cdot\sqrt{\xi_0^2-q}-\xi_0^2\right)+\xi_0^2 M\left(\frac{7-q}{4},\frac{5}{2},\xi_0^2\right)} = \frac{M\left(\frac{1-q}{4},\frac{1}{2},\xi_0^2\right)\left(\coth\left(\sqrt{\xi_0^2-q}\cdot a\right)\cdot\sqrt{\xi_0^2-q}-\xi_0\right)-\xi_0(1-q)M\left(\frac{5-q}{4},\frac{3}{2},\xi_0^2\right)}{M\left(\frac{3-q}{4},\frac{3}{2},\xi_0^2\right)\left(1-\xi_0^2+\xi_0\cdot\sqrt{\xi_0^2-q}\cdot\coth\left(\sqrt{\xi_0^2-q}\cdot a\right)\right)+\xi_0^2\frac{3-q}{3}M\left(\frac{7-q}{4},\frac{5}{2},\xi_0^2\right)}. \tag{30}$$

The dependence between the energy eigenvalues of this double well and the distance between wells has been investigated by the authors. The energy levels corresponding to the symmetrical and the antisymmetrical wave-functions show the dependence on the distance between wells $2a$, presented in Fig.3. If comparing eigenvalues in single and double HO potential wells it is clearly seen that the symmetrical ground state in the system of double wells is situated at lower energy than in the single separate HO well.

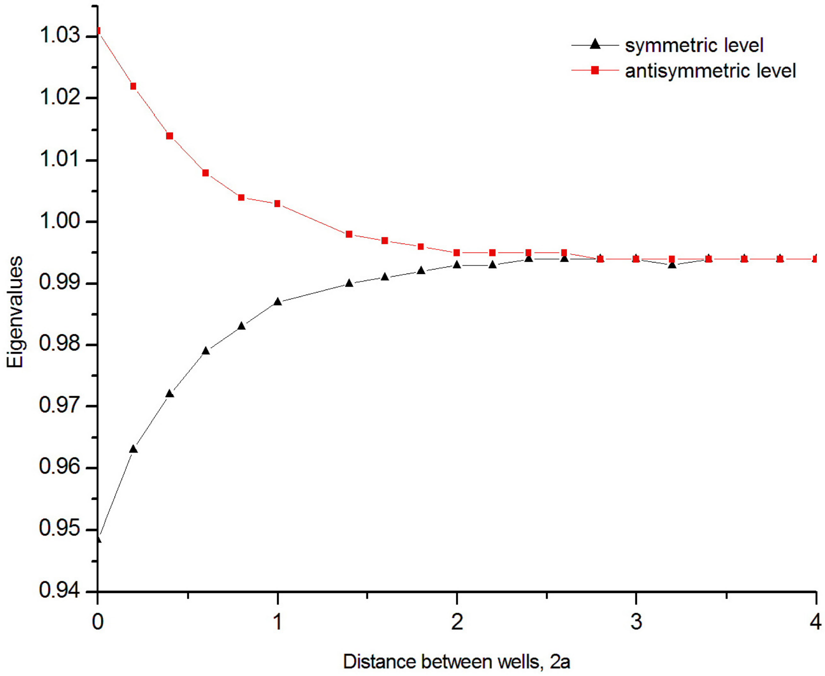

Fig.3. The dependence of the two lowest wave functions eigenvalues on the distance between double finite HO potential wells. The wells depth equals to 2

4. CONCLUSIONS

The investigated system of double finite HO wells opens new possibilities for describing modifications of the recent realistic nucleon-nucleon potentials taking into account the substructure of interacting nucleons. The finite depth of confining wells for constituent quarks causes significant correlations of quarks from interacting nucleons necessary to understand and describe in a simple manner the effects, well-known as the three – and may be four- nucleon potentials, necessary for more or less acceptable microscopic description of the atomic nuclei. The appearance of the system of two levels in double well potential instead of one level in the single well case, the lowest of whom is situated at a lower energy than in the single well, gives us the possibility to understand the under-binding of the lightest atomic nuclei, observable for all recent realistic potentials. Nucleons entering the interaction area change due to the intrinsic structure and the presence of other nucleons. This phenomenon is particularly what we need for the observable under-binding explanation.

REFERENCES

1. H. Kamada et al., Phys. Rev. C 64, 044001, (2001).
2. M.J. Savage, Nucl. Phys. A **7**21, 94, (2003).
3. P.A.M. Guichon and A.W. Thomas, Phys. Rev. Lett. 93, 13, (2004).
4. G.P. Kamuntavičius, A. Mašalaitė, S. Mickevičius, Toy model of the nucleon-nucleon potential, Lithuanian Journal of Physics, 46 (4), 407–411, (2006).
5. W.N. Cottingham and D. A. Greenwood, *An Introduction to the Standard Model of Particle Physics*, (Cambridge University Press, 2003).
6. S. Brandt, H.D. Dahmen, *The Picture Book of Quantum Mechanics,* (Springer, 2000).
7. M. Abramowitz and I.A. Stegun, Handbook of Mathematical Functions with Formulas, Graphs, and Mathematical Tables, (Dover, New York ,1964).

General sponsor :

Lithuanian Energy Institute

Sponsors :

Lithuanian State Science and Studies Foundation

Lithuanian District Heating Association

CALL FOR PAPERS FORS CYSENI 2010:
www.cyseni.com

Lithuanian Energy Institute
Young Scientists Association
3 Breslaujos str. LT-44403 Kaunas, Lithuania
www.lei.lt , jms.lei.lt